Catalytic Performance, Thermo-elastic, Surfaces and Coating Properties of Transition Metal Nitrides

A Thesis Submitted for the Degree of Doctor of Philosophy in Physics

By

Zainab N. Jaf

School of Engineering & Information Technology at Murdoch University

2018

Declaration

I declare that this thesis is my own work of my project and has not previously been submitted for a degree at any other university or institution.

……..

Zainab N. Jaf

December 2018

Supervisory Statement

It is to certify that the work embodied in the thesis entitled “Catalytic Performance, Thermo-elastic, Surfaces and Coating Properties of Transition Metal Nitrides” by Zainab N. Jaf, has been carried out under our supervision and that this work has not been submitted elsewhere for a degree at any tertiary education institution.

DR.Mohammednoor Altarawneh

DR.Zhong-Tao-Jiang

Dedication

For my first teacher who had given me tremendous support throughout my life "My Late Father-Mr.Naji Abdullah Jaf ".

To my beloved husband "Hussein" and my gorgeous daughters "Zahraa, Noor, and Fatima" for their overwhelming support and encouragement.

Zainab

Acknowledgments

First of all, I thank Allah for enabling me finishing my study and writing this thesis. This thesis is the result of a series of fruitful discussions over the past three and a half years with my supervisors DR. Mohammednoor Altarawneh and DR. Zhong-Tao Jiang without which I would have never achieved my goal. Valuable advice, feedback and encouragement given by them significantly contribute to the pursuit of this dream.

I am grateful to the Iraqi government represented by Ministry of Higher Education and Scientific Research for the award of a postgraduate research scholarship and financial support provided along the period of study.

I'm also thankful to the National Computational Infrastructure (NCI) and the Pawsey Supercomputing Centre in Perth, Australia for the grant of computational time.

I owe great deal of appreciation and gratitude to my beloved husband Hussein for his incredible support, love, patience, and encouragement during the PhD journey.

I am pleased to express my supreme thanks to my gorgeous girls Zahraa, Noor, and the little one, Fatima.

Many thanks Zahraa and Noor for your patience, encouragement and understanding during these years….

Fatima, the smile and joy that never leave your little cute face always inspired me to achieve more.... you are the greatest gift that I gained in my life.

No words will be adequate to express how much I'm indebted to my parents for all the things that they've done for me since born…. Thanks for all the moral support and love.

I would like to offer my special thanks to DR. Hantarto Widjaja for his cooperation, providing valued discussions and suggestions. Much appreciated, DR.Widjaja.

The quick response, professional and technical assistance provided by Mr. Kris Parker is highly appreciated. Thank you, Kris …

Finally, my esteems and dedications to all of those who supported me in any respect during the completion of this task…

Abstract

Among transition metal nitrides (TMNs), refractory molybdenum nitrides have been deployed in a wide array of strategic industrial applications due to their remarkable mechanical electrical and catalytic properties. This dissertation has a two-fold aims; first to comprehensively report electronic, thermo-mechanical and electronic characteristics of the bulk and surfaces of molybdenum nitride, and secondly to construct robust mechanistic pathways for prominent catalysed reactions. Most parts of this thesis utilise the density functional theory (DFT) framework to acquire these two objectives. I have carefully benchmarked the accuracy of theoretically-obtained results against experimental quantities pertinent to investigated systems, most notably, lattice parameters of bulk phases, bulk modulus, surface relaxations, and chemical conversion values.

Atomic charge distributions and density of states enabled to illustrate the bonding nature of investigated phases of molybdenum nitrides. For instance, we found that the MoN phase largely exhibits a metallic character with strong Mo-N ionic bonds. Based on estimated Gibbs free energies, the cubic phase of molybdenum nitrides incurs higher thermodynamic stability than the hexagonal phase, with no detected phase transition in the selected *T*–*P* ranges, as experimentally observed. The elastic stiffness coefficients of MoN in the hexagonal structure indicated higher mechanical stability in reference to the cubic structure. The optical conductivity of both phases near zero-photon energy coincides well with their metallic character inferred by their corresponding density of states curves.

Motivated by the fact that, the hexagonal structure δ-MoN is a potential replacement for cubic boron nitride (*c*-BN) and diamond (ultra-incompressible materials), we elect to computationally study the electronic properties, thermodynamic stability phase diagram, and vacancy formation energies of all plausible atomic terminations of NiAs and WC-type configurations of δ_3-MoN and δ-WN hexagonal phases, correspondingly. Various low Miller indices of surface terminations of δ_3-MoN and δ-WN have been considered. *Ab* initio atomistic thermodynamic analysis predicts that N-terminated (111) and (100) slabs to be the most energetically favourable surface terminations amongst the explored surfaces of δ_3-MoN and δ-WN, respectively. Evidenced by plotted density of states, bulk and surfaces of δ_3-MoN and δ-WN display a metallic character. In terms of surface relaxation and reconstructions, most investigated surfaces experience mainly downward displacements of their topmost layers. Most notably, the relaxed Mo-termination in (111) and (100) surfaces of δ_3-MoN, demonstrate significant reconstructions resulted in the first layer to be solely truncated with nitrogen atoms

instead of molybdenum in the un-relaxed initial geometry. Nevertheless, no significant surface reconstruction has been noticed in most of considered δ-WN configurations. Calculated Bader's electronic charges reveal charge transfer from Mo/W atoms to N atoms, largely retaining the ionic bond nature in their bulk phases. Moreover, computed vacancy formation energy calculations indicated that creation of surface nitrogen vacancies are a highly endothermic process.

After considering bulk and surface properties, mechanistic and kinetics aspects for several hydrogen-transfer involved reactions have been investigated. The selective hydrogenation of acetylene (ethyne), present in hydrocarbon feed into ethylene (ethene) plays a critical importance in petroleum unit operations. The dissociative adsorption of hydrogen over the γ-Mo_2N surface preferentially occurs over the vacant nitrogen sites. Our calculated overall uptake rate of hydrogen molecules by the γ-Mo_2N surface correlates very well with analogous experimental findings. Likewise, accessible energy barriers for hydrogen migration from a low energy site (N-vacant) to a higher energy site (atop N) accounts for the experimentally observed facile mobility of hydrogen atoms over surfaces of Mo_2N. The constructed detailed mechanisms for the partial and full hydrogenation of C_2H_2 into C_2H_4 and C_2H_6; respectively, highlight several thermodynamic and kinetic factors that underline the selective occurrence of partial rather than full hydrogenation of alkynes over transitional metal nitrides in general. For instance, we demonstrate that a higher barrier for the initial hydrogenation step in the full hydrogenation route in comparison to the analogous step in partial hydrogenation pathway (17.4 kcal mol^{-1} versus 10.8 kcal mol^{-1}) to contribute significantly in the selective occurrence of partial hydrogenation of alkynes cuts.

It is well-known that catalytic removal of the S-content from thiophenic compounds is an essential step in efforts aiming to diminish the environmental burdens of transportation fuels. We therefore investigate the hydrodesulfurization HDS mechanisms of thiophene C_4H_4S over γ-Mo_2N catalyst via DFT calculations. We found that the thiophene molecule preferentially adsorbs in a flat mode over 3-fold *fcc* nitrogen hollow sites. The HDS mechanism may potentially proceed either unimolecularly (direct desulfurization) or via H-assisted reactions (hydrogenation). Due to a sizable activation barrier required for the first C−S bond scission, we predict that the direct desulfurization to contribute insignificantly in the HDS mechanism. Migration of adsorbed hydrogen atoms from the γ-Mo_2N surface to the thiophene ring significantly reduces activation barrier required in the C−S bond scission. Estimated conversion values predict a 50-70% consumption of thiophene at temperature as low as 700 K

and at low values of gas hourly space velocities. Our computed conversion values were in a qualitative agreement with analogous limited experimental estimates.

I also probed the reduction mechanism of *p*-chloronitrobenzene (*p*-CNB) to *p*-chloroaniline (*p*-CAN) over the γ-Mo_2N (111) surface. Our findings display that, *p*-CNB prefers to be adsorbed over two distinct adsorption sites namely, hollow *fcc* and N-hollow *hcp* sites with relatively sizable adsorption energies. We establish that, the activation of nitro group proceeds through direct pathway along with forming several reaction intermediates. Most of these intermediaries reside in a significant well-depth in reference to the entrance channel. Central to the constructed mechanism is H-transfer steps from *fcc* and *hcp* hollow sites to the NO/-NH groups through modest reaction barriers. Our computed rate constant for the conversion of *p*-CNB correlates very well with the experimental finding at the temperature window of the catalytic tests. Plotted species profiles via a simplified kinetics model confirm the experimentally reported high selectivity toward the formation of *p*-CAN at relatively low temperatures.

In this dissertation, not only binary TMNs, but also ternary TMNs have been investigated in the form of Cr−Mo−N thin films. Closed field unbalanced magnetron sputtering ion plating (CFUMSIP) was deployed to fabricate the aforementioned films with different Mo contents. XRD results confirmed the face centered cubic (*fcc*) structure of pure CrN film. The incorporation of molybdenum (Mo) in the CrN matrix, however, was confirmed by both XRD and XPS analyses. The CrMoN coatings demonstrate various polycrystalline phases including CrN, γ-Mo_2N, Cr with oxides layers of MoO_3, CrO_3, and Cr_2O_3. Microstructure results show that the grain size of Cr-Mo-N coatings increases with the increase of Mo content due to the formation of MoN phase, when Mo atoms interact with N atoms around the grain boundaries of CrN phase. The optical results revealed that, the synthesised coatings exhibit low reflection magnitudes in the visible region of the solar spectrum, introducing them as good antireflection surfaces. Mo-containing samples improved solar absorptance of about 76% was recorded in the wavelength range of 200 – 800 nm. However, low thermal emittance of about 20% was obtained at 2500 – 15000 nm. Measured experimental and DFT computed values exhibited absorption coefficients (α) with a matching trend, across the wavelength range of 200 to 800 nm.

Table of Contents

Contribution Toward Publication

The research work embodied in this thesis includes published and submitted joint-authored papers as listed below;

[1] **Jaf, Z.N.,** Jiang, Z-T, Miran, H.A. and Altarawneh, M. (2016) Thermo-elastic and optical properties of molybdenum nitride. Canadian Journal of Physics, 94 (9). pp. 902-912.

[2] **Jaf, Z.N.**, Altarawneh,M., Miran, H.A., Jiang, Z.T and Dlugogorski, B.Z. (2017) Mechanisms governing selective hydrogenation of acetylene over γ-Mo_2N surfaces. Catalysis Science & Technology, 7 (4). pp. 943-960.

[3] **Jaf, Z.N.** , Altarawneh, M., Miran, H.A., Jiang, Z-T, Dlugogorski, B.Z.(2018) Hydrodesulfurization of Thiophene over γ-Mo_2N catalyst. Molecular Catalysis, 459. pp.21-30

[4] **Jaf, Z.N**., Altarawneh, M., Miran, H.A., Jiang, Z-T. (2018) Geometries, electronic properties and stability of molybdenum and tungsten nitrides low-index surfaces. Materials Research Express. 5(12).

[5] **Jaf, Z.N.** , Altarawneh, M., Miran, H.A., Jiang, Z-T, Almatarneh, M., Dlugogorski, B.Z. (2018)

Catalytic Hydrogenation of p-chloronitrobenzene to p-chloroaniline Mediated by γ-Mo_2N

ACS Omega. 3 (10), pp 14380–14391.

[6] **Jaf, Z.N.,** Jiang, Z-T., Altarawneh, M., Veder, J-P, Manickam Minakshi, Miran, H.A., Zhou, Z-F, H. N. Lim, N. M. Huang, Dlugogorski, B.Z. "Synthesis, Physico-chemical Properties, Combined Experimental, and Computational Studies of $Cr_xMo_{1-x}N$ Coatings" Submitted to Surface coating and technology. Under review-Thin Solid Film.

[7]Miran, H.A., Altarawneh, M., Widjaja, H., **Jaf, Z.N**., Rahman, M.M., Veder, J.P.,Dlugogorski, B.Z. and Jiang, Z-T (2018) Thermo-mechanical properties of cubic lanthanide oxides. Thin Solid Films, 653. pp. 37-48.

[8]Miran, H.A., Altarawneh, M., **Jaf, Z.N**., Dlugogorski, B.Z. and Jiang, Z-T (2018) Structural, electronic and thermodynamic properties of bulk and surfaces of terbium dioxide (TbO_2). Materials Research Express, 5 (8).

[9] Miran, H.A., Jiang, Z-T, Altarawneh, M., Veder, J-P, Zhou, Z-F, Rahman, M.M., **Jaf, Z.N.** and Dlugogorski, B.Z. (2018) Influence of DC magnetron sputtering reaction gas on structural and optical characteristics of Ce-oxide thin films. Ceramics International, 44(2018). pp. 16450-16458.

Conference Papers

[1] **Jaf, Z.N.**, Altarawneh, M., Miran, H.A. and Jiang, Z-T (2016) Selective hydrogenation of Acetylene over γ-Mo_2N (100) catalytic surface. In: 2016 Australian Institute of Physics (AIP) WA 2016 Postgraduate Conference, 13 October 2016, University of Western Australia. Perth.

[2] **Jaf, Z.N**., Altarawneh, M., Miran, H.A. and Jiang, Z-T (2017). An atomistic approach of thiophene hydrodesulfurization over γ-Mo_2N catalyst. In: 13th International Conference and Exhibition on Advanced Materials and Nanotechnology, 26 - 28 October 2017, Osaka, Japan.

[3] **Jaf, Z.N.,** Altarawneh, M., Miran, H.A. and Jiang, Z-T (2017) Mechanisms and kinetics of thiophene hydrodesulfurization over γ-Mo_2N catalyst. In: 2017 Australian Institute of Physics WA Postgraduate Student Conference, 16 November 2017, University of Western Australia, Perth.

[4]Miran, H.A., Altarawneh, M., **Jaf, Z.N**., Widjaja, H., Veder, J.P. and Jiang, ZT (2017) Electronic properties, mechanical stability and reduction reaction energies for cubic lanthanide oxide composites: A computational modelling approach. In: 9th International Conference on Materials for Advanced Technologies (ICMAT) 2017, 18 - 23 June 2017, Suntec Singapore.

[5]Miran, H.A., Jiang, Z-T, Veder, J.P., Rahman, M.M., **Jaf, Z.N**. and Altarawneh, M. (2017) Influence of reaction gases on the structural and optical characteristics of Ce-oxide thin film coatings. In: 2017 Australian Institute of Physics WA Postgraduate Student Conference, 16 November 2017, University of Western Australia, Perth.

[6]Miran, H.A., Jiang, Z-T, Veder, J.P., **Jaf, Z.N.** and Altarawneh, M. (2017) Influence of reaction gases on the structural and optical characteristics of Ce-oxide thin film coatings. In:

13th International Conference and Exhibition on Advanced Materials and Nanotechnology, 26 - 28 October 2017, Osaka, Japan.

[7]Miran, H.A., Altarawneh, M., Widjaja, H., **Jaf, Z.N.** and Jiang, Z-T (2016) Dissociation of chlorobenzene (C_6H_5CI), Chlorothane (C_2H_5CI) and isopropyl chloride (C_3H_7CI) on ceria (CeO_2) 111 surfaces. In: Australian Institute of Physics (AIP) WA 2016, Postgraduate Conference, 13 October 2016, University of Western Australia, Perth.

Statement of Contribution

Journal publications

[1] Jaf, Z.N., Jiang, Z-T, Miran, H.A. and Altarawneh, M. (2016) ***Thermo-elastic and optical properties of molybdenum nitride.*** Canadian Journal of Physics, 94 (9). pp. 902-912.

Author's name	Contribution	Overall Percentage (%)	Signature
Jaf, Z. N.	Computational modeling, data collection and analysis, writing the manuscript and revision	70	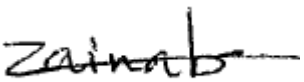
Jiang, Z-T	Discussions and manuscript preparation	30	
Miran, H. A.	Discussions and manuscript preparation		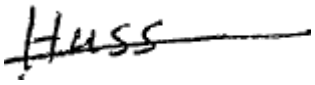
Altarawneh, M.	Project leader, discussions, manuscript preparation and revision		

[2] Jaf,Z.N., Altarawneh, M., Miran, H.A., Jiang, Z-T. **(2018)** ***Geometries, electronic properties and stability of molybdenum and tungsten nitrides low-index surfaces***. Material Research Express. 5 (12).

Author's name	Contribution	Overall Percentage (%)	Signature
Jaf, Z. N.	Computational modelling, data collection and analysis, writing the manuscript and revision	70	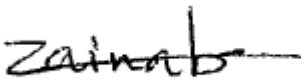
Altarawneh, M.	Project leader, discussions, manuscript preparation and revision	30	
Miran, H. A.	Discussions and manuscript preparation		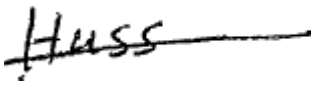
Jiang, Z-T	Discussions and manuscript preparation		

[3]Jaf,Z.N., Altarawneh,M., Miran,H.A., Jiang,Z-T and Dlugogorski, B.Z. (2017) ***Mechanisms governing selective hydrogenation of acetylene over γ-Mo_2N surfaces.*** Catalysis Science and Technology, 7 (4). pp. 943-960.

Author's name	Contribution	Overall Percentage (%)	Signature
Jaf, Z. J.	Computational modelling, data collection and analysis, writing the manuscript and revision	70	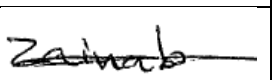
Altarawneh, M.	Project leader, discussions, manuscript preparation and revision	30	
Miran, H.A.	Discussions and manuscript preparation		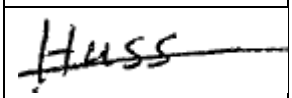
Jiang, Z-T	Discussions and manuscript preparation		
Dlugogorski, B.Z.	manuscript preparation		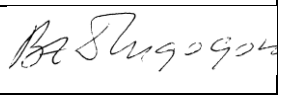

[4] Jaf,Z.N., Altarawneh, M., Miran, H.A., Jiang, Z-T and Dlugogorski, B.Z. (2018) ***Hydrodesulfurization of Thiophene over γ-Mo_2N catalyst***. Molecular Catalysis, 459. pp. 21-30.

Author's name	Contribution	Overall Percentage (%)	Signature
Jaf, Z. J.	Computational modeling, data collection and analysis, writing the manuscript and revision	70	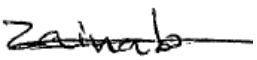
Altarawneh, M.	Project leader, discussions, manuscript preparation and revision	30	
Miran, H.A.	Discussions and manuscript preparation		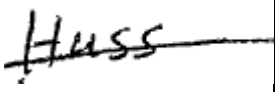
Jiang, Z-T	Discussions and manuscript preparation		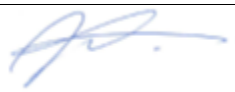
Dlugogorski, B.Z.	manuscript preparation		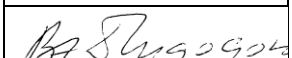

[5] Jaf,Z.N., Altarawneh, M., Miran, H.A.,Almatarneh, M., Jiang, Z-T and Dlugogorski, B.Z. ***Catalytic Hydrogenation of p-chloronitrobenzene to p-chloroaniline Mediated by γ-Mo_2N.*** ACS Omega, 3 (10), pp 14380–14391

Author's name	Contribution	Overall Percentage (%)	Signature
Jaf, Z. J.	Computational modeling, data collection and analysis, writing the manuscript and revision	70	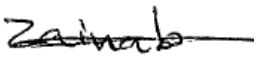
Altarawneh, M.	Project leader, discussions, manuscript preparation and revision	30	
Miran, H.A.	Discussions and manuscript preparation		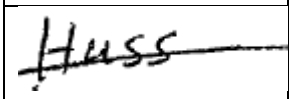
Almatarneh, M.	manuscript preparation		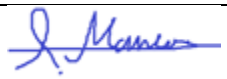
Jiang, Z-T	Discussions and manuscript preparation		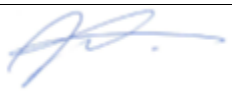
Dlugogorski, B.Z.	manuscript preparation		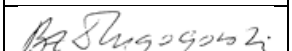

Abbreviations

Transition metal nitrides	TMNs
Density functional theory	DFT
Molybdenum nitride	MoN
Quais harmonic approximation	QHA
Face centred cubic	fcc
Hexagonal closed packed	hcp
Body centred cubic	bcc
Density of states	DOSs
Partial density of states	PDOSs
Valence electron concentration	VEC
Vickers hardness	H_V
Direct current	DC
High power impulse magnetron sputtering	HPIMS
Radio frequency	RF
Generalized gradient approximation	GGA
Vienna Ab initio Simulation Package	VASP
Local density approximation	LDA
CAmbridge Serial Total Energy Package	CASTEP
X-ray diffraction	XRD
Plasma-enhanced chemical vapour deposition	PECVD
Universal Structure Predictor: Evolutionary Xtallography	USPEX

Chemical vapour deposition	CVD
Physical vapour deposition	PVD
Atomic layer deposited	ALD
arc ion plating	AIP
Transition state theory	TST
Two dimensions	2 D
Arc ion plating	AIP
Bias voltage	V_b
Temperature-programmed reaction	TPR
Scanning electron microscope	SEM
Sacrificial support method	SSM
Temperature programmed desorption	TPD
Temperature programmed adsorption	TPA
Hydrogenation	HYD
Hydrodenitrogenation	HDN
Hydrodeoxygenation	HDO
Hydrodesulfurization	HDS
Hydrodechlorination	HDC
Direct desulfurization	DDS
Hydrogen evolution reaction	HER
p-chloronitrobenzene	*p*-CNB
p-chloroaniline	*p*-CAN
Hydrodemetallization	HDM

Dry reforming of methane	DRM
Oxygen reduction reaction	ORR
Direct methanol fuel cells	DMFCs
Methanol Oxidation Reaction	MOR
Specific surface area	SSA
Benzothiophene	BT
Dibenzothiophene	DBT
Gas hourly space velocity	GHSV
van der Waals	vdW
Crystallite size	D_g
Refractive index	n
Extinction coefficient	k
Real part of the complex dielectric function	$\varepsilon_1(\omega)$
Imaginary part of the complex dielectric function	$\varepsilon_2(\omega)$
Loss tangent	$tan\delta$
Volume energy loss function	V_{el}
Surface energy loss function	S_{el}
Full width at half maximum	FWHM
Wavelength	λ
Optical emission monitor	OEM
Standard cubic centimeter per minute	sccm

List of Figures

List of Tables

Chapter 1 : Introduction and Thesis Outline

1.1 Introduction

Owing to unique chemical, electronic and mechanical properties, transition metal nitrides (TMNs) are now widely deployed in a wide array of industrial applications. Their remarkable attributes encompass high hardness, elevated melting points, high wear resistance, profound chemical stability, low electrical resistivity, and a superior catalytic selectivity. They find direct utilizations in diverse fields spanning cutting machineries, absorbance of solar energies, and catalysis. Of particular importance are molybdenum nitrides-based materials (MoN_x, x = 0.5-2.0). Facile synthesis routes for MoN_x surfaces and films coupled with their remarkable aforementioned properties; render their increasing replacements of precious metals in various applications. Doping Mo with nitrogen drastically alters its electronic structure and renders it suitable for a niche category of applications. Great deal of recent theoretical and experimental research on MoN_x has focused on the γ-Mo_2N phase that crystalizes in randomly distributed nitrogen atoms in the unit cell structure. The electronic structure of γ-Mo_2N is mainly dominated by the contribution of mixed and strongly hybridized states of Mo-4*d* and N-2*p* states. This in turn modified the electronic properties of γ-Mo_2N to mimic analogous behaviour of precious metals. In addition to their deployment as protective layers for machineries that work under harsh conditions of elevated temperatures and pressure in excessively corrosive media, Mo-nitrides have long been utilized as catalysts in prominent chemical applications. Among various chemical applications, great deal of research has focused on hydrotreating catalysts by molybdenum nitride with a focus on hydrogenation HYD, hydrodesulfurization HDS, and hydrodenitrogenation HDN reactions.

Variant characterization techniques have revealed that introducing alloying elements largely enhance mechanical, electronic and optical properties of parent materials. Comprehensive experimental studies of ternary transition metal nitrides in the form $Cr_xMo_{1-x}N$ coatings grown by different deposition methods have been carried out. Although it is very well known that CrN to be a super-hard material on its own right, mechanical properties of Cr–Mo–N coatings represented by micro-hardness values and residual stress have shown that adding various ratios of molybdenum systematically improves its hardness. Moreover, friction of coefficients has been reduced by integrating certain contents of molybdenum, pointing to plausible tribological applications. However, there is still much room to investigate the role of molybdenum in

enhancing the optical behaviour of CrN coatings as potential solar selective surfaces. This could be achieved by investigating the Ultraviolet–visible (UV-vis) and Fourier-transform infrared (FTIR) spectra of Cr-Mo-N coatings. Atomic-scale understanding significantly contributes in the advancement in materials science nowadays. Therefore, it is insightful to couple surface measurements with analogous results sourced from accurate materials simulations.

Computational modelling by implementing accurate density functional theory (DFT) calculations has emerged as a powerful and an accurate tool to describe the physics and chemistry of materials, and their course of interactions with gas phase molecules. Several important aspects that underline the catalytic capacity of a material could only be accessible via DFT calculations. For instance, reaction intermediates in catalytic reactions are too-short lived for successful experimental identification. In this thesis, we have utilized DFT calculations and surface measurements to report thermo-mechanical, optical, electronic, structural and catalytic-based properties of transition metal nitride materials. Overall, I have provided a theoretical elucidation into catalysis by γ-Mo_2N phase, properties of Mo-N and tungsten nitride (W-N) surfaces, and optical characteristics of Cr–Mo–N films. It is hoped that acquired theoretical and experimental results will aid in the fine-tuning of TMN properties into desired practical applications spanning chemical reactions and optical devices.

1.2 Hypothesis

"The unique structural and electronic attributes of transition metal nitrides is expected to afford these materials catalytic, optical and mechanical applications. The underlying aim of the thesis is to link the aforementioned properties with the experimentally observed characteristics of these materials. For instance, it was shown experimentally that γ-Mo_2N displays a profound catalytic capacity toward a wide array of selective hydrogenation reactions. We envisage that hosting hydrogen atoms in structural voids of Mo2N to be a key mechanistic factor in these industrially important hydrogenation reactions. Likewise, a plausible absorbance of light by transition metal oxides in the near visible light spectra is expected to derive significant optical applications"

1.3 Scope of This Thesis

Via combined theoretical and experimental approach, this dissertation has;

1-Reported thermo-mechanical properties for the two stoichiometric configurations of MoN phases; namely, *c*-MoN (cubic) and δ_3-MoN (hexagonal) phases via DFT calculations coupled with the quasi-harmonic approximation (QHA) calculations.

2-Constructed a stability phase diagram that encompasses all Mo and W nitrides plausible surface terminations via applying the *ab* initio atomistic thermodynamics approach.

3-Estimated the formation energies required to create a surface nitrogen vacant sites in hexagonal MoN and WN surfaces, and their corresponding equilibrium concentrations at a temperature range of 300-1000 K. The underlying aim is to determine the surface density of these potent active catalytic sites.

4-Exlored chemical reactions governing the hydrogen uptake by γ-Mo_2N surfaces, constructed reaction routes for the hydrogenation mechanisms of triple and double bonds in C_2H_2 and C_2H_4, correspondingly, and provided global-like kinetics models that satisfactorily accounts for experimentally observed profiles of products.

5-Theoretically investigated the hydrodesulfurization HDS mechanisms of thiophene C_4H_4S over γ-Mo_2N catalyst by means of DFT calculations. This process is central in ongoing efforts to remove the S-content from sulfur rich fuels such as transportation fuel for example.

6-Reported reaction pathways and kinetic parameters for the reduction mechanism of *p*-chloronitrobenzene (*p*-CNB) to *p*-chloroaniline (*p*-CAN) over γ-Mo_2N (111). The latter compound is an important intermediate in various chemical products, most notably pesticides, perfumes, and pigments.

7-Provided experimental measurements and matching DFT calculations to inspect structural, chemical bonding state, and optical properties of Cr-Mo-N coatings. The significance of such ternary coatings is manifested by enhancing optical and mechanical properties of parent CrN coatings.

1.4 Thesis Outline

This thesis embodies comprehensive studies investigating the catalytic activities, bulk and thin film properties of MoN-based materials. Practical applications of materials stem from their microscale properties. For this reason, a significant part of this thesis reports pertinent thermo-mechanical, optical and electronic properties of bulk and surfaces of molybdenum nitrides. Throughout chapters of the thesis, I execute DFT calculations, carry out phonon frequencies

computations, construct reactions mechanisms, and estimate kinetic parameters. While catalysis by molybdenum nitride has been the main focus in the thesis, sophisticated thin films characterizations of Cr-Mo-N system had been carried out with the objective to assess its potential usage in solar selective devices. Figure 1.1 displays thesis structure. Herein, I present an overview of thesis outlines.

Chapter 2 demonstrates an inclusive literature review focused on the recent development of transition metal nitrides with a particular focus on their synthesis routes and profound catalytic activities. This Chapter presents detailed accounts of metal nitrides chemistry, their structural, electronic, and mechanical properties. The Chapter also critically surveys related theoretical and experimental studies that report catalysis by molybdenum nitrides. Moreover, the Chapter comprehensively review relevant experimental studies encompassing magnetron sputtering, temperature programmed reaction (TPR), x-ray diffraction (XRD) measurements, surface morphologies, and catalytic tests. On the theoretical side, I mainly summarised DFT-related studies that illustrate reaction networks for catalytic-assisted reactions and how their reported thermo-kinetic parameters correlate with related experimental findings.

Chapter 3 briefly accounts for implemented theoretical methodologies throughout chapters of the thesis (DFT methodology, functionals and procedures of DFT implementation, *AB* initio atomistic thermodynamics, phonon frequencies calculations, and the transition state theory (TST)). This Chapter also presents deployed DFT codes. Experimental techniques utilized in Chapter 9 are also illustrated.

Chapter 4 reports thermo-elastic and optical properties of cubic and hexagonal phases of molybdenum nitride. First, I present the geometric and electronic properties of these two phases and found that cubic phase exhibits higher thermodynamic stability and thermal expansion coefficients than the hexagonal δ_3-MoN phase. However, the hexagonal phase was predicted to be harder and more mechanically stable. Predicted reflectivity in the wavelength range of 250–800 nm indicates a promising potential utilisation of MoN films in antireflection coating applications. The plotted energy-dependent spectrum of the real and imaginary parts shows that the considered two phases share matching optical properties. Density of states DOSs curves suggest that, the chemical reactivity of the MoN materials is primarily controlled by their unfilled Mo-*d* orbital.

Chapter 5 demonstrates a comprehensive DFT study to investigate geometries, electronic properties and stabilities of molybdenum and tungsten nitrides low-Miller indices surfaces. *Ab*

initio atomistic thermodynamics computations point out to the thermodynamic stability of N-terminated (111) and (100) configurations in δ_3-MoN and δ-WN, respectively. DOSs plots, predicted a metallic character for bulk and surfaces of δ_3-MoN and δ-WN. Geometrically, most of the investigated surfaces experience mainly downward displacements of their topmost layers.

Significant part of this thesis has focused on hydrotreating processes over γ-Mo_2N. Theses catalysed chemical reactions incur strategic industrial applications. Investigated reactions encompass partial and full hydrogenation of C_2 and C_4 adducts HDS of thiophene, and hydrogenation of *p*-(CNB) into *p*-(CAN).

Chapter 6 investigates the selective hydrogenation of ethyne into ethene rather than ethane over γ-Mo_2N surfaces. The reported results on the interaction of hydrogen with the γ-Mo_2N surfaces concur very well with the analogous experimental findings pertinent to preferable adsorption on nitrogen vacant sites, number of active sites, reaction rate constants and overall uptake of hydrogen molecules by Mo_2N surfaces. The constructed reaction mechanism and computed reaction rate constants serve to compute the chemical conversion values with analogues experimental values and to deduce for the first-time thermo-kinetics factors that underpin the occurrence of selective partial hydrogenation rather than full hydrogenation of alkynes over transition metal nitrides.

Chapter 7 inspects the HDS mechanisms of thiophene over γ-Mo_2N surface catalyst. Herein, I investigate all physisorbed and chemisorbed modes of the thiophene before calculating reaction and activation energies for all involved reactions steps. Findings from this Chapter highlight predominant reaction routes for the HDS of thiophene (a major S-carrier in coal). For example, due to a sizable activation barrier required for the first C−S bond scission, the direct desulfurization (DDS) contributes marginally in the HDS mechanism. This Chapter constructs mechanisms for the experimentally observed conversion of thiophene into an adsorbed C_4 species and H_2S assisted by migration of pre-adsorbed H atoms into the thiophene molecule. The last section in the chapter illustrates thermodynamic and kinetic factors that dictate the occurrence of the partial hydrogenation of adsorbed C_4H_4 adduct.

Chapter 8 provides an insight into the reduction mechanisms of *p*-(CNB) to *p*-(CAN) over the γ-Mo_2N (111) surface. The findings display that, *p*-(CNB) prefers to be adsorbed over two distinct adsorption sites. Hydrogen transfer from N-vacant site activates the nitro group. Synthesis of *p*-(CAN) from *p*-(CNB) proceeds through a complex reaction mechanism in which

several reaction intermediates subsequently form via H-transfer reactions into O, N and NH sites in the adsorbed chemical moieties. The computed rate constant for the overall conversion of *p*-(CNB) correlates very well with the experimental finding.

Chapter 9 illustrates a combined experimental and computational study that sheds light on structural, chemical composition, and optical behaviour of ternary Cr-Mo-N coatings synthesised by magnetron sputtering plasma. The Obtained UV-vis spectra coincide very well analogous DFT-plotted profiles.

Chapter 10 conveys concluding remarks that would be useful in the rational design of molybdenum nitride catalysts/ and or films for commercial applications. Potential future research directions are also presented.

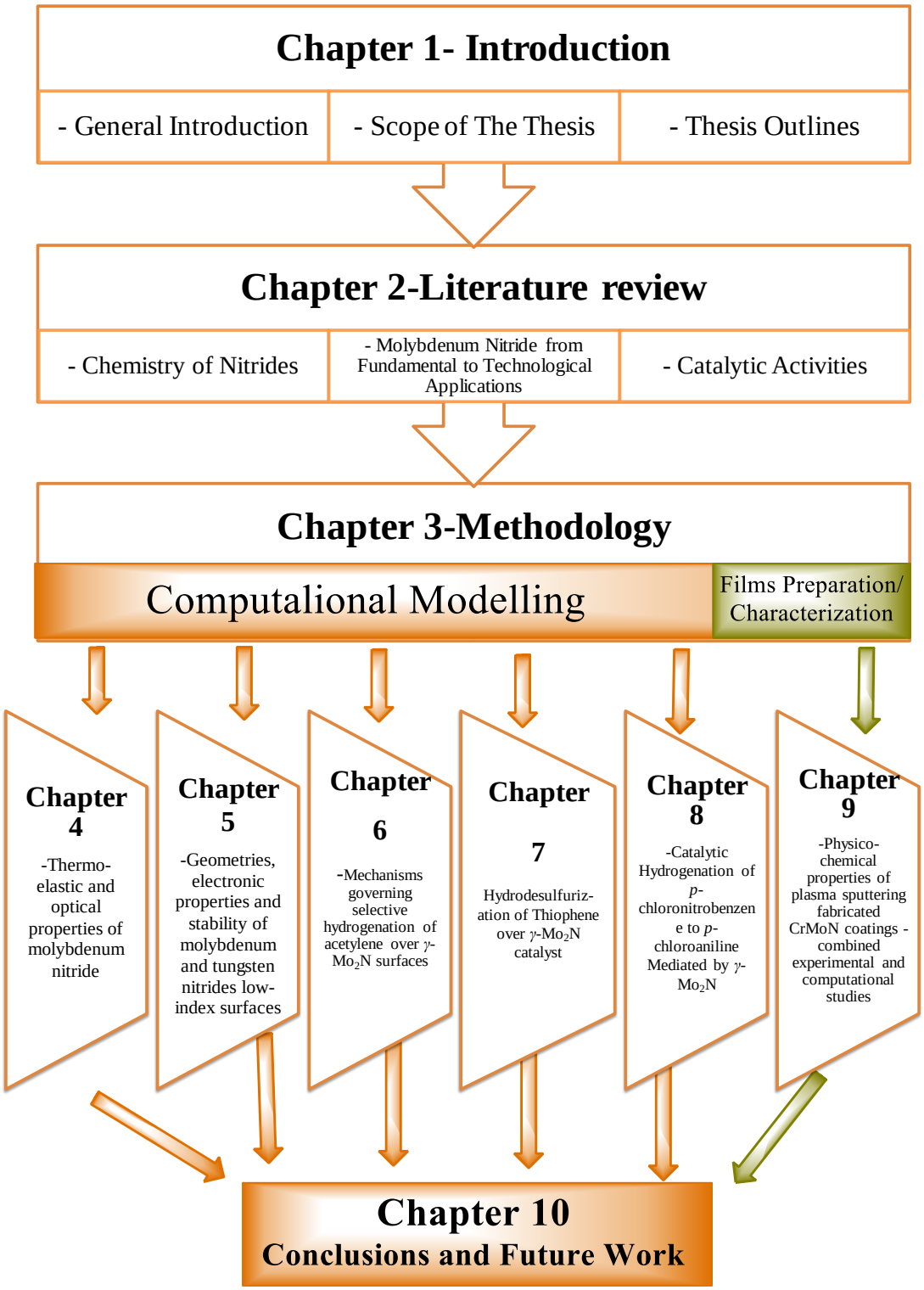

Figure 1.1 : Thesis outline.

Chapter 2 : Literature Review

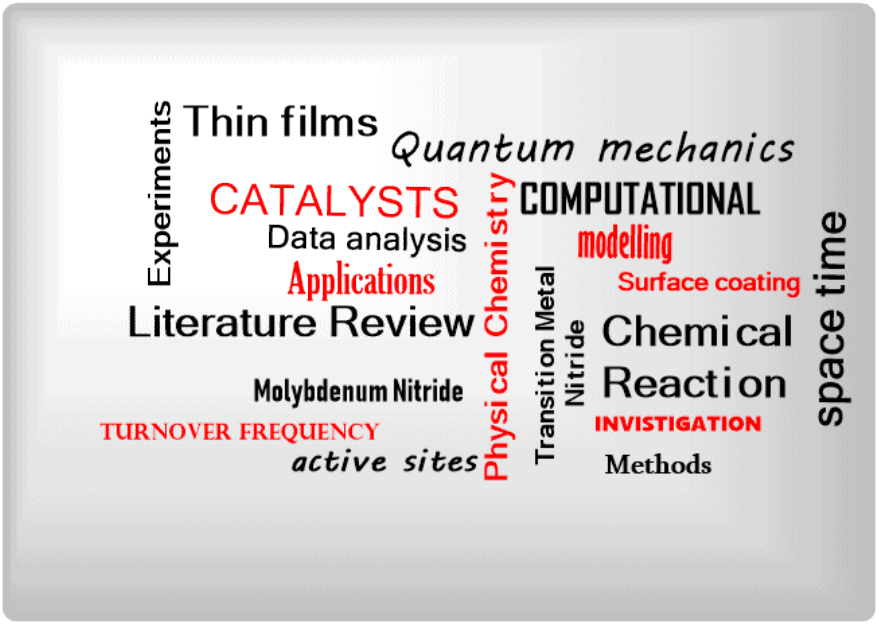

2.1 An Overview

Nitride-based materials capture considerable interest owing to their unique physical and chemical properties such as, high melting point, superior hardness, and excellent corrosion resistance [1-4]. Synthetic methods of nitride-base materials generally require high temperatures and long reaction time [5]. Indicating that synthesis routes of nitride-containing compounds is hampered primarily by the high bond dissociation energy required in the fission of the triplet bond in nitrogen molecules (945 $KJmol^{-1}$) in contrast to only (498 $kJmol^{-1}$) , the bond dissociation energy in the oxygen molecules; i.e., a primary reaction in the synthesis of metal oxides [6]. This high energy prevents nitrogen atoms from developing ionic bonds with electropositive elements. Overall, thermodynamic considerations may have contributed to the scarcity of nitrides and their propensity to form unique geometries compared to those of the oxides or carbides. To this end, number of comprehensive reviews has addressed various aspects of nitride-based compounds including structural, thermodynamics, bonding nature, synthetics methods, catalysis, and characterizations [4, 7, 8]. This chapter briefly introduce two main aspects pertinent to nitride-based materials;

- The chemistry of transition metal nitrides, particularly molybdenum nitrides, most notably, applications synthesis methods, phase stability diagrams, and properties.

- Recent studies that report catalysis by molybdenum nitride with a particular focus on governing reaction mechanisms, operating conditions, products, and chemical conversions.

TMNs are refractory ceramic compounds that enjoy wide array of fascinating properties and applications. This class of compounds have been pursued vigorously due to demonstrating high melting points, good resistance against wear and corrosion, chemical inertness, excellent electrical conductivity [1, 3]. These remarkable properties primarily stem from their unique their electronic and geometrical structures. For instance, geometries of these compounds comprise a mixture of covalent, metallic and ionic contributions rendering them suitable for a niche categories of application that requires facile switching of the bonding nature; for example uptake and release of their nitrogen surface content [4]. Studies on properties and applications for TMNs have focused on the various plausible configurations of TMNs, including thin films [9, 10], nanoparticles [11], and powders [12].

The most commonly deployed TMNs comprise TiN, CrN, MoN, ZrN, WN, AlN, and BN [13-15]. The interests in TMNs have been mainly derived by their potential replacements of noble metals [16-19]. Figure 2.1 displays the main applications of TMNs as high temperature coatings that work under hostile conditions of elevated temperatures and pressures; catalysts, and solar selective surfaces.

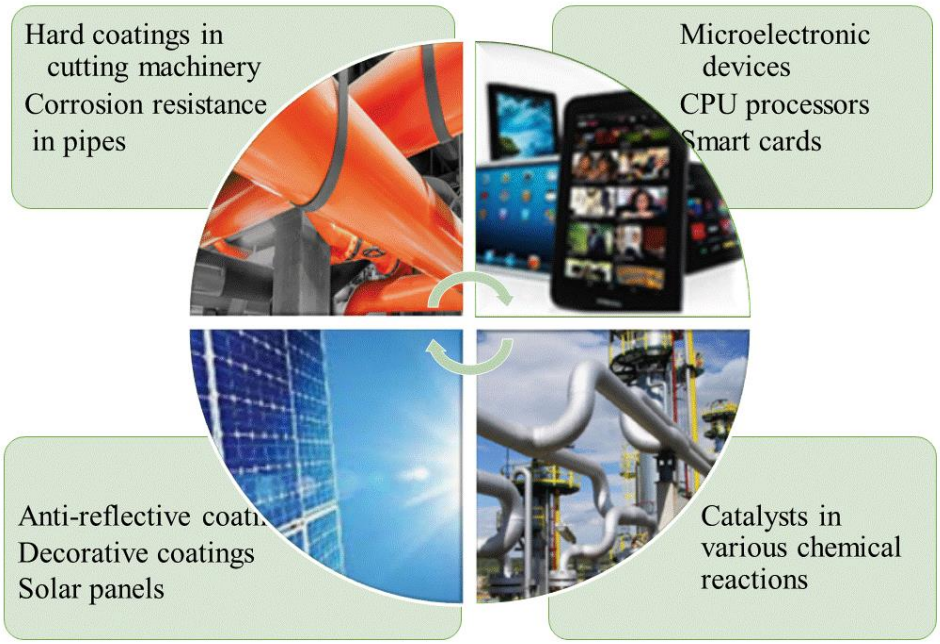

Figure 2.1: Main applications of TMNs.

The elements of groups III-XII on the periodic table are termed as transition metals as highlighted in Figure 2.2. In the subsequent sections, our discussion will be centred on the crystalline structures and electronic properties of binary TMNs.

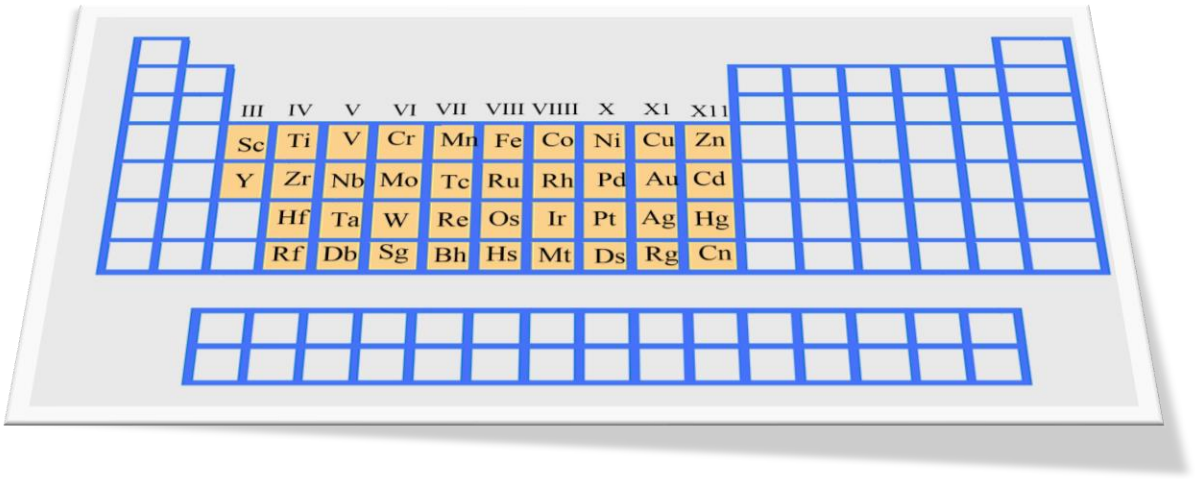

Figure 2.2: Transition metal elements (*d*-block).

2.2 Structural Properties

In this section, the crystal structures of the TMNs are reviewed. An extensive efforts were devoted to provide an insight into geometric and electronic aspects of TMNs [1, 4, 20]. It is well known that Group III-XII (*d*-block elements) assume an intermediate transition state between the metallic and interstitial nitrides (*i.e.* diffusing non-metal atoms into the metal lattices)[3]. Row 1 metals (Ti, V, Cr, Mn, Fe, Ni and Co) named as the intermediate compounds, while Row 2 and 3 metals including (Zr, Nb, and Mo) and (Hf, Ta, W and Re), respectively, termed as interstitial compounds. In TMNs, nitrogen atoms nest in the interstitial sites in which, they randomly distributed in half of the octahedral interstices. while, metal atoms occupy lattices of face centered cubic (*fcc*), or hexagonal closed packed (*hcp*), or simple hexagonal structures [4]. These sites may also be occupied by other atoms such as carbon or oxygen forming carbonitride and oxynitride, respectively. Furthermore, the empirical formula proposed by Hägg [21], suggested that when the radius ratio of the non-metal atom to the metal atom is less than 0.59, interstitial compounds groups typically adapt the so-called B1-NaCl structure [22].

Although, nitrides assume simple crystal structures, they typically differ from those of their corresponding parent metals. The stable version of metallic molybdenum Mo for instance crystallises in body centred cubic (*bcc)* phase, nonetheless its analogous stable nitride (Mo_2N)

exhibits *fcc*- like structure as shown in Figure 2.3. These structural modifications between the parent metal and nitrogen-containing transition metal is ascribed to electronic factors [1].

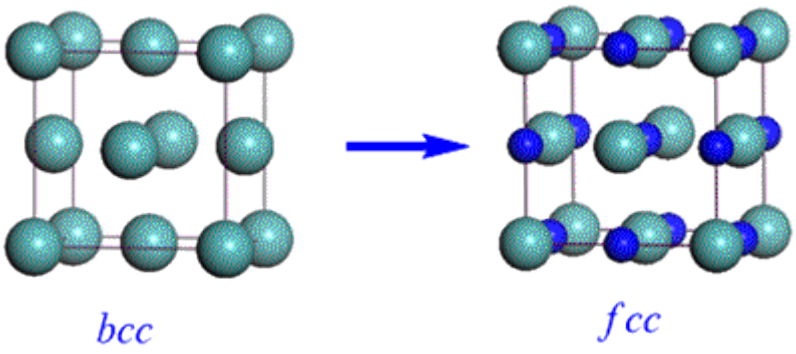

Figure 2.3: The typical crystalline structures of metallic molybdenum (bcc) and molybdenum nitride (fcc) unit cell's. Light blue and dark blue spheres refer to Mo and N atoms, respectively.

Table 2.1 shows transition metals of group IV–X and their possible nitrides. The predominant stoichiometry in the early transition metal nitrides follow the formulas TMN and TM_2N (where TM refers to transition metal). However, later transition metals mainly adapt the stoichiometry of TM_3N [23]. This is due to the fact that size of atoms decreases with the t group number. Subsequently, the lattice of high group metals is not able to host interstitial nitrogen atoms while maintaining close-packed (*cp*) or hexagonal close-packed (*hcp*) metal atoms [24, 25].

Table 2.1: Transition metals of group (IV-X) and their analogues possible nitride positions in the periodic table [17, 26].

Group IV	Group V	Group VI	Group VII	Group VIII	Group VIIII	Group X
Ti_2N, $TiN_{0.9}$, TiN	V_2N, VN	Cr_2N, CrN	Mn_4N, Mn_2N, Mn_3N_2	Fe_4N, Fe_2N	Co_3N, Co_2N, CoN_3	Ni_3N, NiN_2
ZrN, Zr_3N_4	Nb_4N_3, Nb_2N, NbN, Nb_4N_5, $NbN_{0.95}$	MoN, Mo_2N, MoN_2, Mo_5N_6	$TeN_{0.75}$	RuN, Ru_2N, Ru_3N, Ru_4N, RuN_2	RhN_3	PdN_2
HfN, Hf_3N_2, Hf_3N_4	TaN, Ta_3N_5, Ta_2N, $TaN_{0.8}$, $TaN_{0.1}$	WN, W_2N, W_3N_4, W_2N_3	Re_2N	OsN_2	IrN_2, Ir_3N_4	PtN_2

2.3 Electronic Properties

It has been established that, the number of valence electrons plays significant role of having unique properties [24]. In particular, the DOSs of TMNs afford parallel trend to their corresponding transition metals in terms of the shape and ordering of the bands [27]. For the transition metals, the *d*-band starts to fill from Ru and Os to Pd and Pt. Furthermore, group IV–VI TMNs share similar catalytic properties with group VIII–X transition metals due to possessing similar *d*-band. The electronic structure strongly correlates with properties of TMNs studied by various spectroscopic techniques [4, 28].

Brewer *et.al.* [29] reported thermodynamic properties of the various crystalline transition metals based on the Engel correlation which combines electronic and crystal structures of *bcc* and *hcp* configurations with spectroscopic data for the gaseous transition metal atoms to calculate thermodynamic properties of various crystalline configurations of the transition metals. In addition to experimental measurements, semi-empirical formulas have been widely used to acquire properties and predict geometries of TMNs in general. For instance, the Engel correlation relates electronic arrangements and crystal structures of metals with spectroscopic data. Likewise, based on the Engel-Brewer theory of metals and alloys [30], the structure of a metal or substitutional alloy strongly depends on the *s-p* electron. According to this theory, the number of *s-p* valence electrons per atom *(e/a)* determines the shape of the unit cell. For instance, (1-1.5), (1.7-2.1), and (2.5-3) ratios correspond to *bcc, hcp and fcc* configurations, respectively.

It has been reported that valence electron concentration (VEC) provides a detailed picture of the mechanical properties of groups IV to XII in rock salt structure nitrides, carbides and carbonitrides [31]. Earliest first-principles investigations into the electronic properties of bulk TMNs group V and VI have been conducted by Papaconstantopoulos *et al.*[32]. Energy separations in DOSs of TMNs increases from 3*d* to 5*d* nitrides (i.e. CrN→MoN→WN). Furthermore, investigations of the electronic DOSs in valence and core states of TMNs were interpreted in relation with the degree of covalency in the chemical bonding. Various properties strongly depend on the magnetite of the band gap. Along the same line of enquiry, it has been shown that a low stability of the cubic MoN phase is related to an increase in the charge transfer of Mo-*d* electrons to N-*p* with increasing stoichiometric ratio N/Mo[33]. Figure 2.4 depicts theoretically predicted total density of states DOSs for some selected metal mononitride[34]. The absence of a band gap in the DOSs curves highlights the metallic character for all the considered configurations.

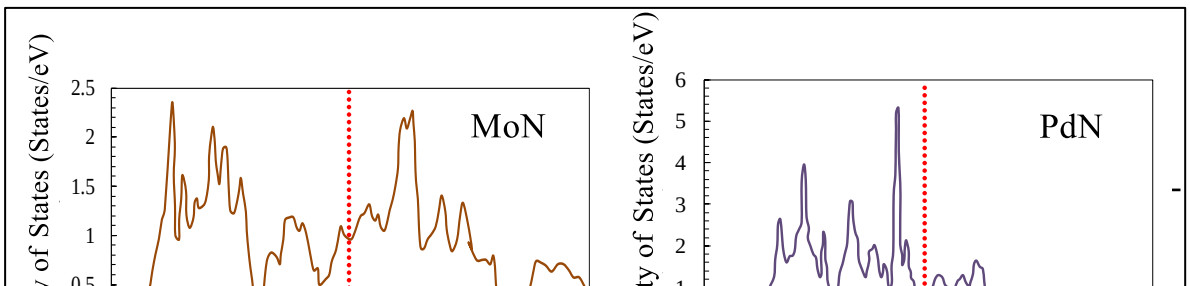

Figure 2.4: Theoretically predicted total density of states for several transition metal mononitrides. The arbitrary Fermi energy level is set at zero; denoted by an upright dotted line [34].

By transferring further towards right-hand of the periodic table, the size of the metal atom gradually increases hindering nitrogen atoms from being situated at the metal lattice. Therefore, the thermal stability of the nitride decreased [3]. Non-metallic group elements however tend to develop mono-nitride-compounds such as (BN, Si_3N_4, AlN, InN, GaN, and InN), which are well characterised by their covalent bonding and insulating or semi-conductive nature [35]. Those compounds have been utilized in wide variety of applications such as, diffusion barriers[36] in semiconductors and optoelectronic devices [2]. The catalytic performance of non-metallic nitrides is restricted and they could be deployed as catalyst supports only [37]. In fact, BN is typically utilized as a non-catalytic surface.

2.4 Mechanical Properties

Hardness is a measure of a material to resist plastic deformation. The hardness of TMNs' compounds strongly alters with their M/nitrogen ratios in which hardness decreases with the nitrogen contents. Hones *et al.* [38] observed that hardness of *fcc* γ-Mo_2N is lower than that of over-stoichiometric phases. The strength of metal-nitrogen bonds in TMNs in another contributing factor in their relative hardness. The decrease of the hardness (*i.e.* elastic modulus) values is mainly derived by a diminishing of the covalent character of bonding-N. At low nitrogen loads, electrons in the low-lying bonding bands are only partially occupied, resulting in a higher hardness. However, by increasing nitrogen contents, the low-lying bonding bands become all occupied. This breaks covalent bonds and weaken the ionic bonds; and hence the hardness decreases [32]. The subsequent sections aim at presenting recent relevant literature focusing on the methods of thin film synthesis and catalytic performance of the Mo-N system. Table 2.2 enlists selected mechanical, thermal and geometrical properties for TMNs compounds.

Table 2.2: Central properties of some selected transition metal nitrides at high temperature [14].

Phase	Lattice constants (Å)	Density (g/cm^3)	Microhard -ness (GPa)	Melting Point (^oC)	Young's modulus (GPa)	Heat conductivity ($Wm^{-1}K^{-1}$)	Linear thermal expansion coefficient (10^{-6} K^{-1})	Electrical resistivity ($\mu\ \Omega$ cm)	T_c (*K*)
TiN	4.242	5.39	17	3050	420	29	9.9	27	5.8
ZrN	4.570	7.32	15	3000	460	11	7.8	24	10.4
HfN	4.516	13.8	18	3330	380	11	8.5	27	6.9
VN	4.138	6.04	5.7	2350	380	11	10.8	65	8.9
NbN	4.392	8.16	11	d	360	3.8	10.2	60	17.2
TaN	4.238	15.9	32	d	-	-	8.0	-	8.9
CrN	4.148	6.14	13	d	450	11.7	-	640	-

Nitrides of the molybdenum possess number of unique properties including high hardness and superconducting temperature [39, 40] that enable this compound to find direct application in many niche fields such as hard coatings for high temperature machinery [41, 42], diffusion barrier in microelectronic devises [43, 44], and enriching of the tribological properties of hard coatings via the formation of the so-called Magnéli phase [45]. Technological applications of molybdenum nitrides strongly depend on their phase structures. Depending on the nitrogen concentration, nitrides of the molybdenum adapt several phases. Table 2.3 reports structural properties of all plausible phases of molybdenum nitrides.

Table 2.3: Lattice parameters of various phases of MoN collected from numerous studies.

Mo-N system	Structure and Space group	Lattice Parameters (Å)	Reference
γ-MoN_x (x~0.5)	*fcc* rock salt structure with randomly distributed nitrogen in octahedral sites with a space group of $Fm\bar{3}m$	a =4.16	high-pressure–high-temperature synthesis [46].
Mo_2N	*fcc*	a= 4.16-4.19	Reactive dc sputtering [47].
γ-Mo_2N	*fcc*	a =4.124	pulsed laser irradiation [48].
c-Mo₂N	*fcc*	a=4.2	plasma immersion ion implantation [49].
β- Mo_2N	Body centred tetragonal phase with ordered nitrogen sites and a space group of I41/amd	a = 4.16 c = 8.0	plasma immersion ion implantation [49].
β-$Mo_2N_{0.85}$	Tetragonal	a = 4.199 c = 7.996	Reactive DC magnetron sputtering [50]

β-Mo_2N	Tetragonal	a = 4.18 c = 7.99	expanding plasma microwave discharge [51].
β-$Mo_{16}N_7$	Tetragonal	a = 8.4 c = 8.0	Heat treatment of calcium nitride and molybdenum [52].
$MoN_{(0.5-1)}$	Cubic	a=4.16-4.28	Density functional theory (DFT) as implemented in VASP code within the local density approximation (LDA) [53].
δ_1-MoN	Hexagonal WC type $p\bar{6}m2$	a = 2.868 c = 2.810	Plasma-enhanced chemical vapour deposition and ammonolysis of $MoCl_5$ [54].
δ_3-MoN	Hexagonal NiAs-type $P6_3mc$	a = 5.73 c = 5.62	DFT as implemented in CASTEP code within full-potential linearized augmented plane waves and local orbitals method [55].
Mo_5N_6	Combination of Hexagonal WC and NiAs structures	a = 4.89 c = 11.06	Plasma-enhanced chemical vapour deposition and ammonolysis of MoS_2 [54].
δ_1-MoN	Hexagonal WC-like structure with space group $p\bar{6}$ m2	a = 2.86 c = 2.80	DFT as implemented in CASTEP code within full-potential linearized augmented plane waves and local orbitals method [55].
δ_3-MoN	Hexagonal NiAs-type $P6_3mc$	a = 5.71 c = 5.62	DFT as implemented in CASTEP code within full-potential linearized augmented plane waves and local orbitals method [55].
δ_1-MoN	Hexagonal WC-like structure with space group $p\bar{6}$ m2	a = 2.86 c = 2.84	DFT as implemented in CASTEP code within

			Vanderbilt ulterasoft pseudopotential [56].
B1-MoN	Cubic NaCl -type structure with space group of $Fm\bar{3}m$	a = 4.25	Self-consistent augmented-plane-wave calculations [32].
B1-MoN	Cubic NaCl -type structure with space group of $Fm\bar{3}m$	a = 4.21–4.25	Experimental work [57].
Mo_5N_6	Filled 2H-MoS_2 structure	a = 4.893 c =11.06	Ammonolysis of MoS_2 [58].
B1- $MoN_{(0.9\text{-}1.8)}$	Cubic NaCl -type structure with space group of $Fm\bar{3}m$	a = 4.20 - 4.26	Reactive dc sputtering [47].

2.5.1 γ-$Mo_2N_{1 \pm x}$ Phase

The gamma phase (γ-Mo_2N) reveals *fcc* structure with space group of ($Fm\bar{3}m$) and a repeated layer of ABCABC stacking sequence. Moreover, this phase is stable at high temperature with N atoms randomly (*i.e.* disordered) distributed and half-occupied the octahedral sites of N atoms [59]. The measured superconducting transition temperatures T_c was found to be 5.5 K [60]. Another phase of the γ-$Mo_2N_{1 \pm x}$ involves an ordered array of vacancies with the Pm3m space group that differs from the $Fm\bar{3}m$ space group in the presence of superstructure reflections [61]. Since Mo-N system crystallizes over a wide range of stoichiometries, thus, in a fully stoichiometric geometry (*i.e.* the Mo: N stoichiometric ratio is 1:1), the coordination environment of Mo cations would contain MoN_6 octahedra, while if nitrogen site was half-occupied, (*i.e.* the Mo: N stoichiometric ratio is 2: 1), Mo would comprise a reduced coordination number [62, 63]. It has been predicted that the fully stoichiometric configuration affords the highest superconducting transition temperature at T_c ~30 K [60]. Suggesting that the impact of a disorder (N vacancies) on high-temperature superconductivity of the nonstoichiometric cubic structure $MoN_{0.5}$, resulted in reducing its transition temperature [64]. Figure 2.5 (a) portrays unit cell structure of the gamma phase.

2.5.2 β-Mo_2N Phase

β-Mo_2N phase is an ordered tetragonal structure that is mechanically stable at low temperatures. This structure is often considered as a tetragonal adjustment of the cubic *γ*-Mo_2N phase with the lattice constant *c* doubled (I41/amd, space group)[52]. At high temperatures, the *γ*-Mo_2N transforms to *β*-Mo_2N. Literature presents a rather very limited account on synthesis routes and characterization of *β*-Mo_2N [65]. Inumaru *et al.* [66] synthesized a crystalline phase of *β*-Mo_2N by pulsed laser deposition of molybdenum metal. XRD analysis revealed that the prepared material is composed of $Mo_2N_{0.85}$. Figure 2.5 (b) depicts unit cell structure of this tetragonal phase.

2.5.3 Metastable Cubic B1-*MoN*

While the stoichiometric cubic B1-MoN phase is thermodynamically unstable, it could be stabilised via careful control of the nitrogen concentration during synthesis[67]. It was reported that the nitrogen amounts in MoN_x films can be regulated from $Mo_1N_{0.5}$ to Mo_1N_1 via varying the growth rates (*i.e.* N/Mo flux ratio) during the film deposition process[68]. In a separate work accomplished by the same group, the deposition of epitaxial B1-MoN_x ($0.98 < x < 1.03$) on *α*-Al_2O_3, has observed mechanical stability in samples which have been exposed to thermal treatments lower than 650 ºC [69]. A number of XRD studies reported very similar lattice structure of the *NaCl*-$MoN_{0.5}$ phase at $a = 4.16$ Å [70]; $a = 4.151$ Å [71]. The *B_1*-MoN phase entails a stoichiometry between $MoN_{0.5}$ to $MoN_{1.0}$. The increase in lattice parameter is expected to accompany any increase in nitrogen content. The concentrations of nitrogen vacancy primarily rely on synthesis parameters, most notably availability of nitrogen cations during sputtering [72, 73], and temperature treatments [70]. Figure 2.5 (c) represents unit cell of *B1*-MoN type structure.

2.5.4 δ-MoN Phase

The hexagonal δ-MoN configuration exhibits arrangements of metal layers with ABAB staking sequence and T_c of ~13.8 K [60]. Nonetheless, due to the poor quality of the detected crystals, it was very challenging to unequivocally pinpoint the positions of the N atoms [74]. Fabrication of this phase was carried out via the reduction of MoO_2 with NH_4Cl at high temperature and high NH_3 pressure of (1773 K) and (2 MPa), respectively [75]. Bull *et al.* [63] synthesised hexagonal (δ_1-MoN) via high temperature ammonolysis of $MoCl_5$. The produced crystal occurs along the space group of $P6_3mc$ with lattice constants of a=2.87 Å and c=2.81 Å. Ammonolysis at high pressure affords hexagonal highly N-ordered phase δ_3-MoN with nearly doubled lattice parameters, (*i.e.* a=5.73 Å and c=5.61 Å. Ganin *et al.* [54] carried out by plasma-enhanced chemical vapour deposition (PECVD) method and ammonolysis of $MoCl_5$ and MoS_{2-} to produce several stoichiometric phases of hexagonal molybdenum nitrides. The synthesised nitrides are termed as δ_1-MoN (*WC* type, $P\bar{6}m2$), δ_3-MoN (*NiAs*-type, $P6_3/mmc$), and nitrogen rich phase (Mo_5N_6). The hexagonal δ_3-MoN phase demonstrates the highest bulk modulus among Mo-N phases. Soignard *et al.* [39] measured bulk modulus of δ-MoN and γ-Mo_2N to be 345 GPa and 301 GPa, accordingly. The higher bulk modulus in the case of δ-MoN is attributed to the high compressive stress. Figure 2.5 (d) shows unit cell of hexagonal-δ_3-MoN type structure.

2.5.5 Mo_5N_6 Phase

The Mo_5N_6 phase feature displays unequal layers of nitrogen prisms and octahedral-type arrangements along the c axis, as Figure 2.5 (e) shows [58]. Nitrogen atoms form an AABB-type arrangement, in an analogy to sites of sulfur atoms in MoS_2. The molybdenum atoms saturated all the trigonal prismatic sites along with partial filling of octahedral sites. The Mo_5N_6 structure mimic the configurations of the *WC*- and *NiAs*-type building blocks, with partially filled Mo sites[54].

2.5.6 Nitrogen-Rich Molybdenu

Figure 2.5 (f) presents the 3R-MoN_2 geometrical unit cell that features a MoS_2-type structure along with a rhombohedral R3m arrangement. Wang *et al.* [76] utilized a solid-state ion-exchange reaction to produce the nitrogen-rich molybdenum nitride at a relatively moderate pressure of 3.5 GPa.

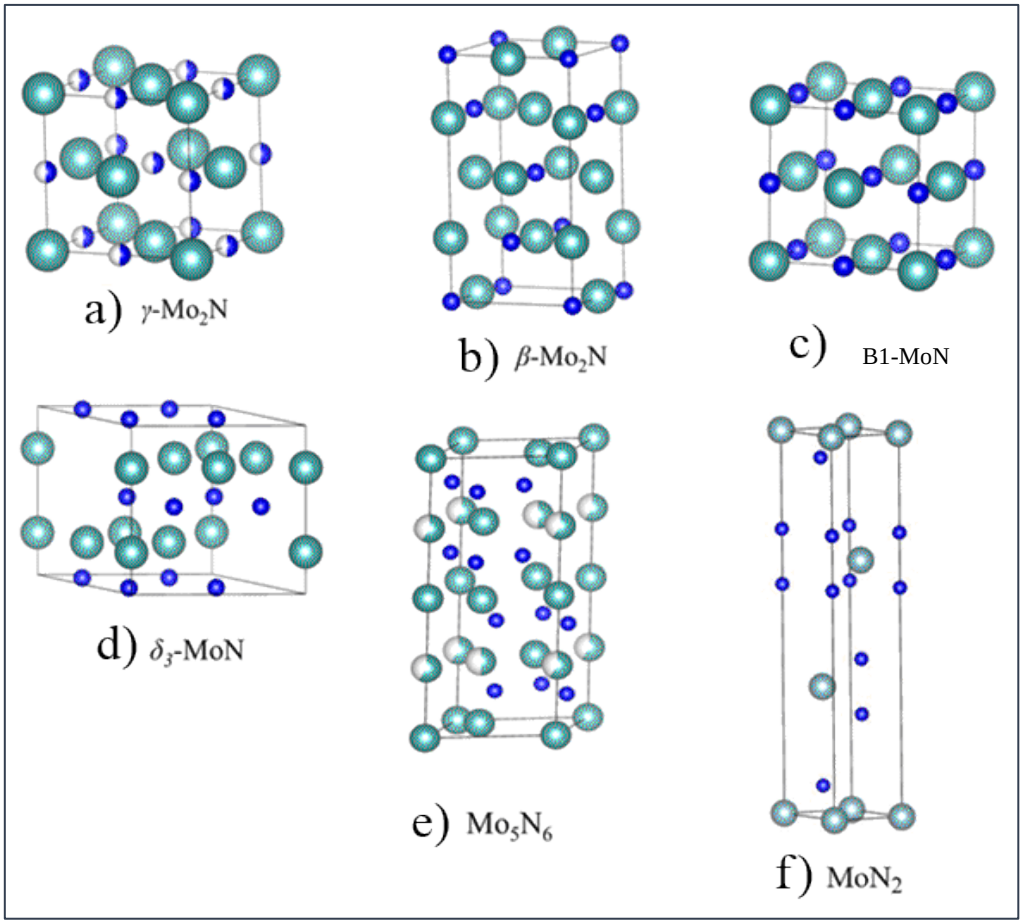

Figure 2.5: Phases of molybdenum nitrides.

The variation of XRD data for γ-Mo_2N, δ-MoN and Mo_5N_6, display that γ-Mo_2N adapts different crystal structure system compared to hexagonal δ-MoN and Mo_5N_6 systems as revealed in Figure 2.6.

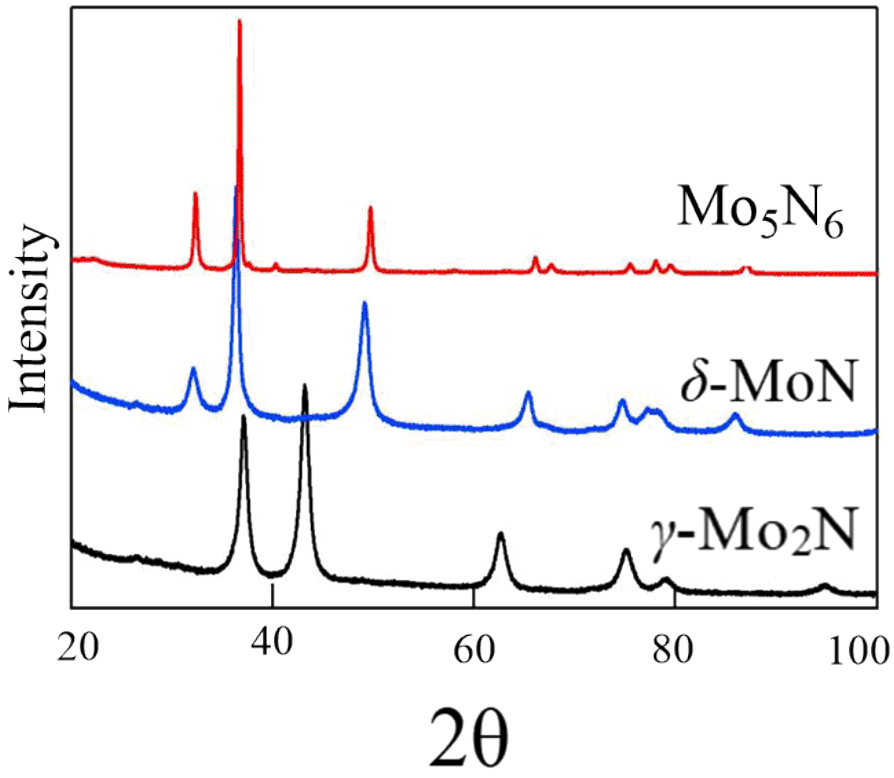

Figure 2.6: XRD patterns of Mo-M phases [62].

Yu *et al.* [77] explored ground-state properties of bulk MoN_2 via DFT calculations. They proposed that Mo atoms are sandwiched between N atoms. Surprisingly, they concluded that the experimentally proposed MoS_2-type MoN_2 structure by Wang *et al.* [76] was unstable from thermodynamic and mechanical prospects. This claim was supported by computing negative elastic stiffness coefficients (C_{44}) value, multiple imaginary phonon frequencies, and a positive enthalpy of formation. Likewise, Wang *et al.*[78] carried out first-principles calculations to inspect the structural stabilities and electronic properties for the 2D layered MoS_2-like molybdenum and tungsten dinitride nanosheets. They pointed out that in the contrary to their corresponding disulphide, the presence of durable soft modes in the dinitride nanosheets in the MoN_2 phase render them as dynamically, thermally, and mechanically unstable. They also postulated that surface hydrogenation can effectively eliminate these soft modes. The hydrogenated MoN_2H_2 and WN_2H_2 sheets described in Figures 2.7 and 2.8, respectively reveal structural stability and excellent electronic properties. In another related study, it has been reported that the ground state geometry of the two-dimensional transition metal dinitrides sheet named tetra-MoN_2 that is significantly more stable than the H-MoN_2 phase with a flexible strain tenability based on the applied stress. With an indirect band gap of only 1.41 eV, the tetra-MoN_2 is a semiconductor

[79]. More recently, the structural, mechanical, and thermal stabilities of MoN_2 nanosheets were confirmed via DFT calculations [80].

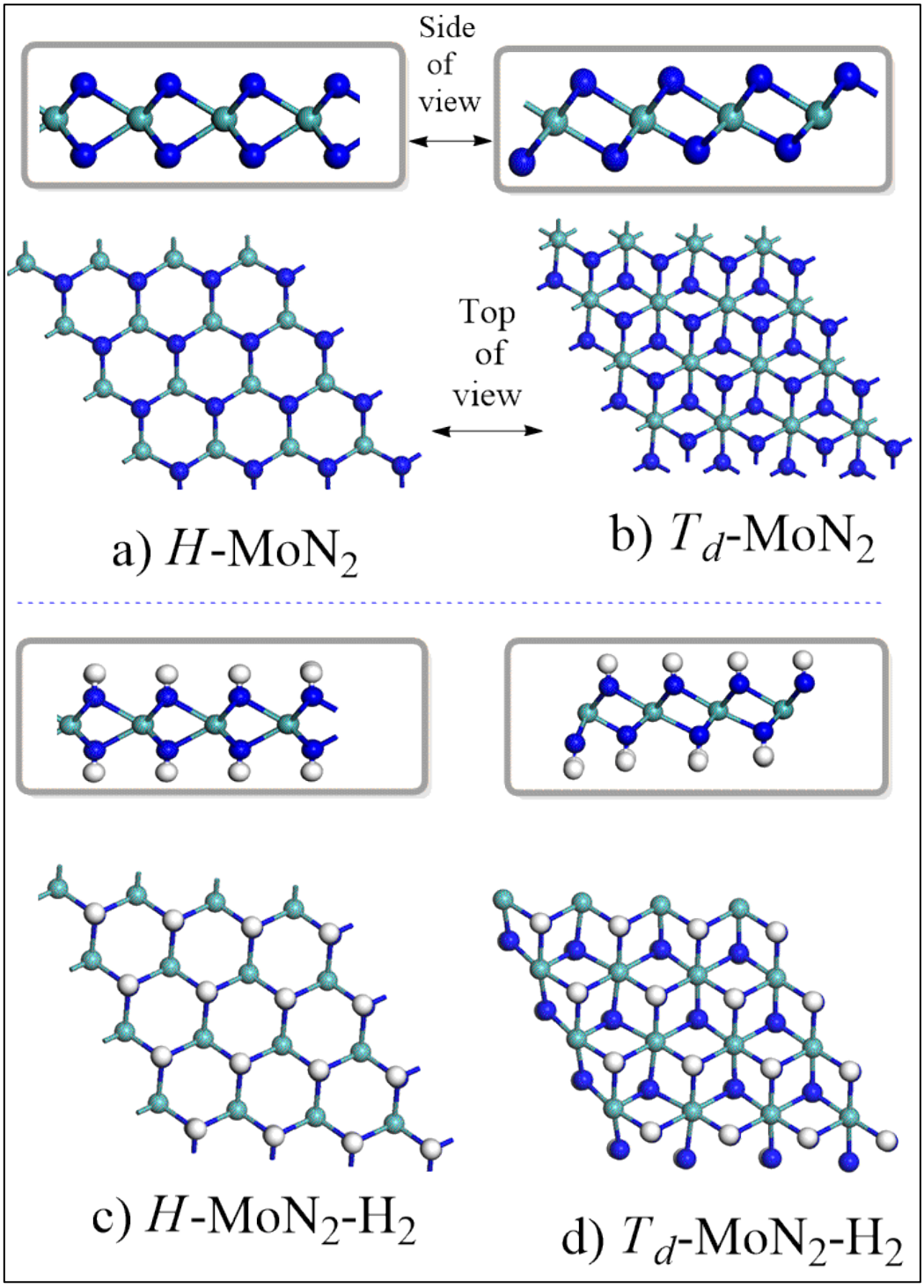

Figure 2.7: Structural configurations of *H*-MoN_2, T_d-MoN_2, *H*-MoN_2-H_2, and T_d-MoN_2-H_2 sheets. Light blue, dark blue, and white spheres correspond to Mo, N, and H atoms, respectively [78].

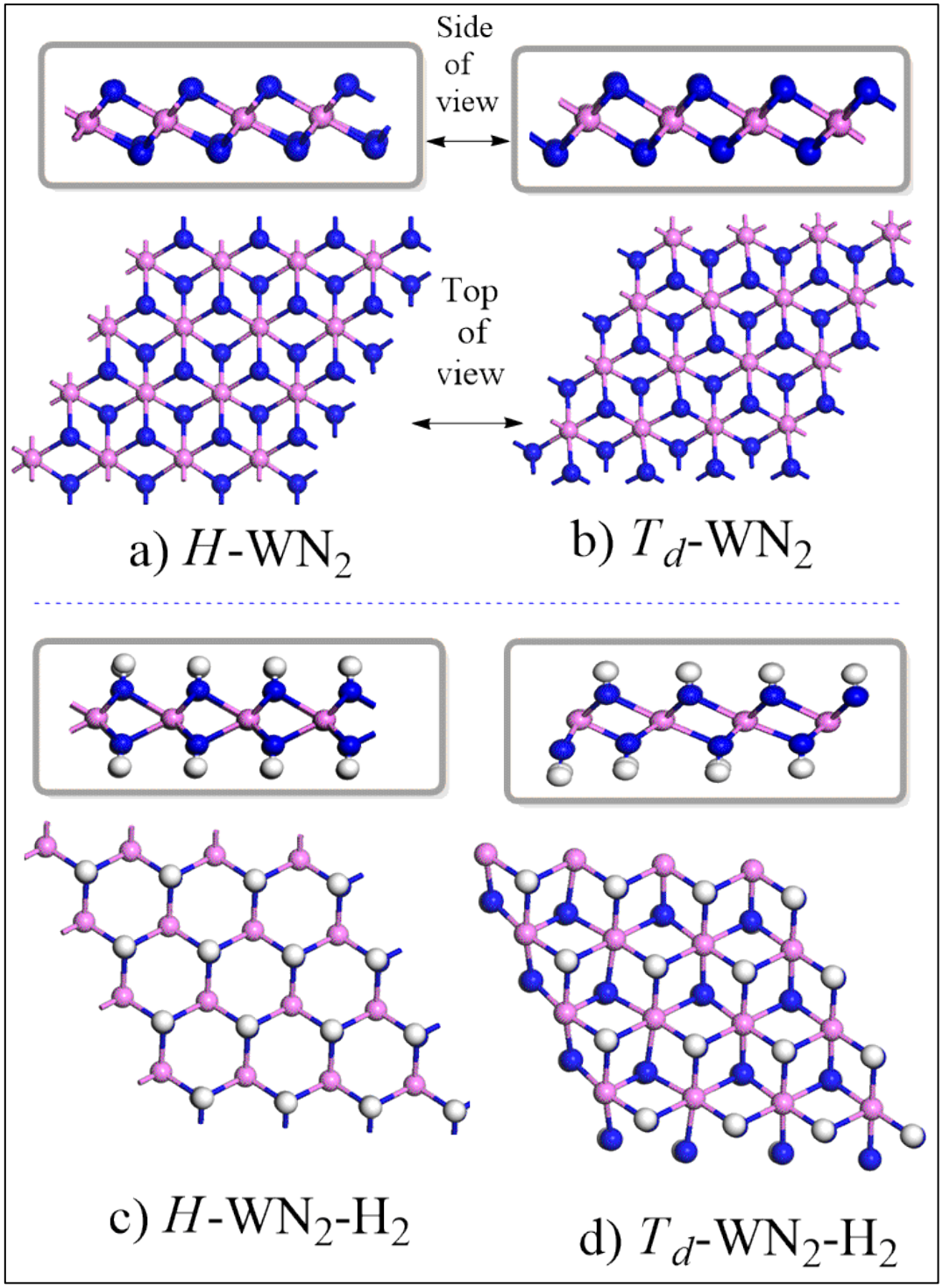

Figure 2.8: Structural configurations of H-WN_2, T_d-WN_2, H-WN_2-H_2, and T_d-WN_2-H_2 sheets. Pink, dark blue and white spheres denote W, N, and H atoms, respectively [78].

Li *et al.* [81] performed a DFT-based study to investigate the possibility of deploying MoN_2 nanosheet as catalysts for electrochemical synthesis of ammonia. Results indicated that in

order for dinitrogen to be adsorbed and activated over MoN_2, high energy is required. However, they recommended that Fe-doping can significantly enhance the catalytic performance.

2.6 Phase Stability Diagram of Mo-N System

The phase diagram of the Mo–N system is depicted in Figure 2.9. Starting with the α-phase, molybdenum hosts an atomic nitrogen load in the range of 0 to 1.08 atomic weight (at. %). At temperatures lower than 1000°C, the concentration of atomic nitrogen remains very negligible in α-Mo and attains a maximum value of 1.08 at. %. A temperature of 1860°C and an equilibrium pressure of 670 atm. signify the *T-P* condition for Mo to dissolve 1.08 at.% N [59]. Mändl *et al.* [49] suggested a transformation from the cubic γ-Mo_2N phase to tetragonal β-Mo_2N phase to took place at around 580°C.

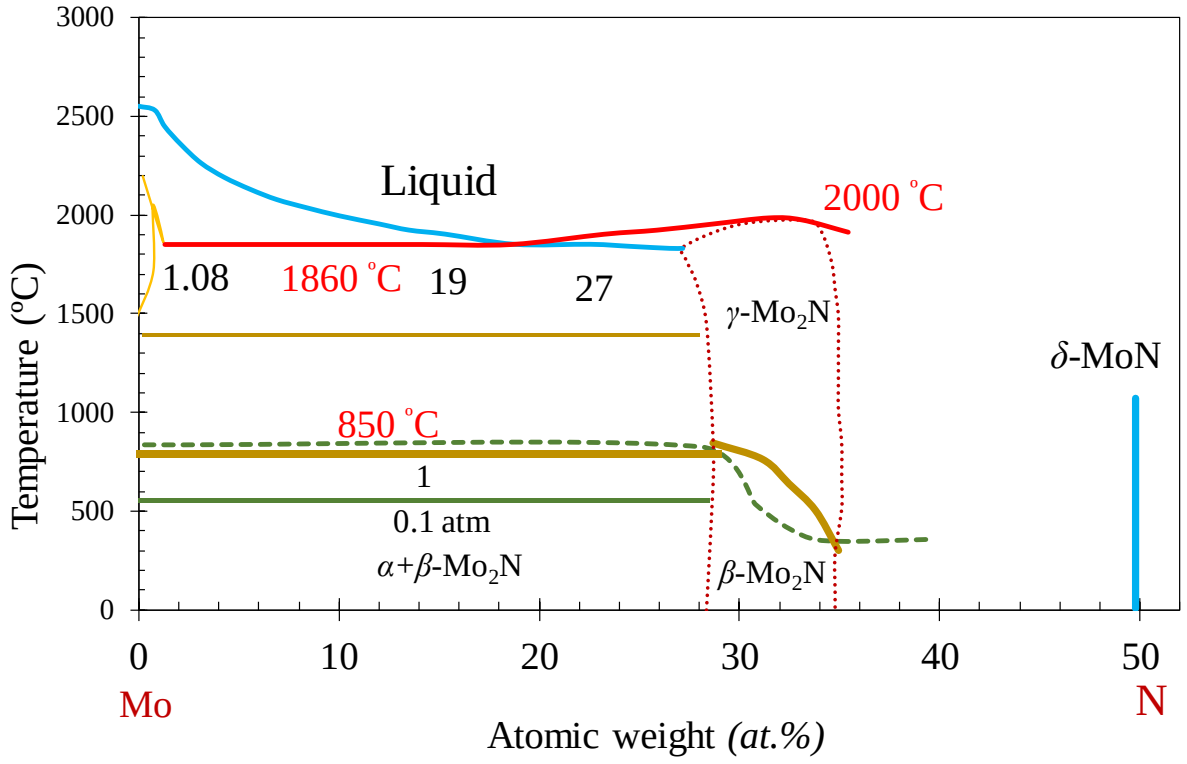

Figure 2.9 : *T-P* phase stability diagram of Mo-N system [59].

the formation of gamma phase is governed by nitrogen ratios. Furthermore, the transformation to another phase proceeds at the temperature window of 400 -850ºC [14]. Moreover, according to the proposed phase diagram by Jehn and Ettmayer, the γ-Mo_2N phase appears at high temperatures as a defective B1- structure in which half of the nitrogen lattice positions are vacant sites at a nitrogen composition of around 27-35 at.%. As discussed earlier, the B1-MoN phase could be produced via gradual filling of the vacant nitrogen sites in the defective γ-Mo_2N phase and because of being non-equilibrium phase, it is preferred to transform to the thermodynamically more stable hexagonal phase. The absence of the *B1*-MoN phase from the stability diagram shown in Figure 2.9 is ascribed to its thermodynamic instability. In another word, the B1-MoN is readily transformed into the hexagonal δ-MoN phase [82]. Via careful analysing of XRD spectra, Saito *et al.* [83], suggested the transformation sequence γ-$Mo_2N \rightarrow$ B1-type MoN $\rightarrow$ δ-MoN phase. Moreover, they conveyed that in addition to *bcc*-Mo (110) and (200) directions and after nitrogen ion dose of 1×10^{17} ions/cm^2 implanted into Mo thin films, new diffraction lines belong to γ-Mo_2N phase appear. At a maximum dose of 16×10^{17} ions/cm^2, the reflection lines of the *bcc*- Mo crystal tend to vanish. In addition to the *T-P* conditions, the amount of nitrogen is a controlling factor in the dominant phase. A combined experimental and theoretical study by Klimashin *et al.* [84] assessed the influence of nitrogen contents and their vacancies on geometries and mechanical properties of Mo–N thin films. The relative concentration of N-vacant sites alters the Mo-N bonding types, and hence the relative thermodynamic hardness. Balasubramanian *et al.* [85], conducted a DFT calculations coupled with the universal structure predictor evolutionary xtallography (USPEX) evolutionary phase-search algorithm to estimate the thermodynamic plausibility of Mo-N phases and their stoichiometries. Theoretically, eight thermodynamically stable molybdenum nitride phases were predicted. These phases encompass N-rich and N-deficient configurations, including, hexagonal δ-Mo_3N_2, cubic γ-$Mo_{11}N_8$, cubic γ-$Mo_{14}N_{11}$, orthorhombic ε-Mo4N3, monoclinic σ-MoN, σ-Mo_2N_3, tetragonal β-Mo_3N, and hexagonal δ-MoN_2. Finally, the thermodynamic stability diagram in displayed in Figure 2.9 conveys a very important concluding remark stoichiometric and near- stoichiometric adapt hexagonal type structures, whereas values of N-atoms ratio and occupation in un-stoichiometric phases may determine their phases; namely, B1-MoN, gamma γ-Mo_2N, tetragonal β-Mo_2N.

Chemical vapour deposition (CVD) [86, 87], and physical vapour deposition (PVD) techniques [88] are the major techniques in the synthesis of molybdenum nitride films. In this regard, polycrystalline and amorphous molybdenum nitride were fabricated via a wide range of physical vapour deposition processes [89, 90]. Most notably, the reactive magnetron sputtering methods either by radio frequency (RF) or direct current (DC) procedures [89, 91, 92]. The state-of-art magnetron sputtering was shown to yield high purity and homogeneity films. A comprehensive recent review by Jauberteau *et al.* [67] surveyed the crystal structures, preparation methods, mechanical, and electrical properties of molybdenum nitride films. We therefore focus on presenting recent advances in the deposition of MoN thin films. Nandi *et al.* [93] prepared molybdenum nitride thin films using the atomic layer deposition (ALD) method. The molybdenum hexacarbonyl ($Mo(CO)_6$) was used as the source of Mo while ammonia signifies the nitrogen precursor. Furthermore, an ion-exchange reaction at high pressures was utilized to produce stoichiometric hexagonal and cubic phases of molybdenum nitrides. Ozsdolay *et al.* [94] deposited epitaxial layers of MoN_x over MgO(001) substrates via DC magnetron sputtering system. Adjusting the substrate temperature (*Ts* 600-1000 ºC) enabled to vary the nitrogen stoichiometry in MoN_x (001) layers between $x = 0.69-1.25$. The change in the N/Mo ratios also altered lattice parameters (a = 4.16–4.26 Å and the layer density (ρ = 8.7–6.8 g/cm^3)). As expected, a softening (*i.e.* transformation from ductile-to-brittle) took place with increasing nitrogen concentration. Bouaouina *et al.* [95] deposited multilayer of Mo_2N/CrN thin films via RF magnetron sputtering. They considered the influence of the bi-layer thickness of Mo_2N/CrN films on the mechanical and micro structural properties. They had illustrated that increasing the thickness of multilayer systematically enhances the hardness, the elastic modulus, and the tensile stress. In another related work by the same group, Bouaouina *et al.* [96] synthesized molybdenum nitride thin films over (100) silicon substrates by means of RF magnetron sputtering of a Mo target in a (Ar-N_2) gas flow rates. They investigated the microstructure, residual stress and mechanical properties of the produced films. They pointed out that within the range from 20% to 40% nitrogen in the plasma, the predominant phase is the *fcc* γ-Mo_2N. However, at higher nitrogen content (50%), hexagonal δ-MoN and cubic B1-MoN phases form. Kommer *et al.* [97] fabricated molybdenum nitride films with various stoichiometries and structure morphologies by high power impulse magnetron sputtering (HPIMS). The mechanical properties such as hardness, elastic modulus and tribological

behaviour were reported. Tribology measurements have been performed at various temperatures under heavy load. Measured properties prompted the authors to propose that synthesized thin films could enhance wear resistance of steel parts at elevated temperatures. Higher hardness and elastic modulus were obtained by reducing the working gas pressure. Wicher *et al.* [98] prepared molybdenum nitride thin films by DC pulsed magnetron sputtering method operating at 100 kHz as main frequency and modulated by an additional adaptable frequency ranging from 10–1000 Hz. Results indicate that by deploying various modulated frequencies, the morphology, phase composition, electrical and mechanical properties of the deposited films are enhanced. Very recently, Durai *et al.* [99] studied the effect of Cu doping on the microstructural and supercapacitive properties of Mo_3N_2 deposited by reactive magnetron co-sputtering technique. They pointed out that the (XRD) examination evidenced the cubic phase of Mo_3N_2 and the incorporation of Cu has no impact on the crystal structure. Furthermore, the electrochemical supercapacitive behaviour was enhanced and the measurements showed increasing the capacitance of 173.4 mF cm^{-2} for the un-doped to 619.5 mF cm^{-2} for the Cu doped Mo_3N_2. Suggesting that the fabricated Mo_3N_2 exhibits high-performance supercapacitors.

2.8 The influence of Deposition Parameters on the Growth of Molybdenum Nitride

Fine-tuning of molybdenum nitride films toward the desired properties is often acquired via adjusting the sputtering parameters. Targeted properties of microstructures including grain size, preferred orientation, lattice defects, phase composition, and surface morphologies. Several studies have addressed the influence of deposition conditions on the growth and properties of the deposited films. A study conducted by Kazmanli *et al.*[100] assessed the effect of various preparation factors such as nitrogen pressure, bias voltage and substrate temperature on the structure of Mo–N coatings produced by arc PVD. Stöber *et al.* [101] deposited thin films of metallic molybdenum and molybdenum nitride on silicon wafers by reactive DC magnetron sputtering. The deposition conditions include a plasma power in the window of 300 to 700 W and a total pressure ranging from 2 to 8 Pa. They investigated the impact of deposition parameters including the nitrogen contents, plasma powers, and sputtering gas pressures during film growth on mechanical and electrical properties. The remarkable role of sputtering gas and nitrogen content was clearly detected through structural and

morphological analyses [102]. Xiang and Wu [103] developed crystalline molybdenum nitride films via RF magnetron sputtering. They illustrated that the mechanical properties, corrosion resistance and tribological performance could be fine-tuned via regulating RF input power and Ar/N_2 gas flow ratios. At modulating an Ar/N_2 gas flow ratio for instance from 10/10 to 18/2 and RF input powers from 150 to 300 W, the crystal structure of molybdenum nitride films altered from crystalline to amorphous. However, the deposited films at an Ar/N_2 ratios of 16/4 and an input power of 300 W, showed an exaggerated Mo_2N microstructure with preferred (111) reflections. Conversely, when applying an input power of 150 W and at an Ar/N_2 ratio of 10/10, the crystalline phase of the films was curbed. Recently, it has been proposed that MoN multilayer films revealed microstructure evolution and cracking resistance with adjusting gas inlet and input power [104].

2.9 Recent Literature on the Synthesis and morphology of Various forms of Molybdenum-Nitride System

As illustrated in preceding sections, molybdenum nitride-based compounds have been in a main stream research topic that aims to report their crystalline phases via several synthesis, methodologies and characterisations techniques. Herein, we briefly present recent literature pertinent to molybdenum nitride morphologies. Choi *et al.* [105] fabricated nanocrystalline powders of MoN_x (x = 0.77 – 1.32) at low temperature ($\geq 600^oC$) via NH_3 ammonolysis and nitridation of the $MoCl_5$ with the aim to test their effectiveness as super capacitors. Results indicate that the highest specific capacitance attains a value of 111 F/g d for γ-Mo_2N crystallites at a scan rate of 2mV/s. Xie and co-workers [106] systematically investigated the hydrogen evolution reaction (HER) activity of atomically-thin hexagonal phase of molybdenum nitride (MoN) nano-sheets synthesised by liquid exfoliation of MoN nanosheets with a thickness of only 1.3 nm leading to 100% exposure of Mo atoms on the surface of the nanosheets. Via DFT calculations, the active surface sites of the atomically-thin MoN nano-sheets were determined. These sites are assumed to be surface Mo atoms through catalysing protons into hydrogen. The analysis of DOSs revealed that the atomically-thin MoN nanosheets display metallic characteristics. Joshi *et al*.[107] proposed a synthesis technique for obtaining micrometer-size 2D nanosheets of hexagonal δ-MoN via a two-step process. The synthesis process commences by the formation of 2D nanosheets from MoO_3 precursor followed by the transformation of the oxide phase to the respective nitride through a reductive annealing process. Phase

transformation of metal oxide to respective nitride, sulfide or carbide occurs via reduction of the oxide phase in NH_3, H_2S or CH_4 environment, respectively. Very recently, formation mechanism of molybdenum nitrides nanosheets has been reported by Sun *et al.* [108]. In their study, several phases of molybdenum nitride nanosheets including Mo_5N_6, δ-MoN, and γ-Mo_2N were synthesized via incorporating MoS_2 with nitrogen in a nanosheet configuration. Figure 2.10 pictured a graphical illustration of the temperature-dependent reduction reaction of MoS_2 and NH_3, (*i.e* a process that is very sensitive to the working temperature). At 750°C, Mo_5N_6 is generated directly without the presence of an immediate product. At 820°C, Mo_5N_6 is synthesized in one step in a process. The latter commences decomposition to δ-MoN when MoS_2 was spent. At 920°C, the only detected product is the δ-MoN phase. By the gradual conversion of MoS_2, MoN decomposition to γ-Mo_2N and β-Mo_2N starts to merge. At 1020°C, the phase evolution process (after complete consumption of the MoS_2) follows the sequence δ-MoN→ γ-Mo_2N→ β-Mo_2N→ Mo. At a higher temperature of 1120°C, the β-Mo_2N structure is the only intermediate that eventually transforms into Mo.

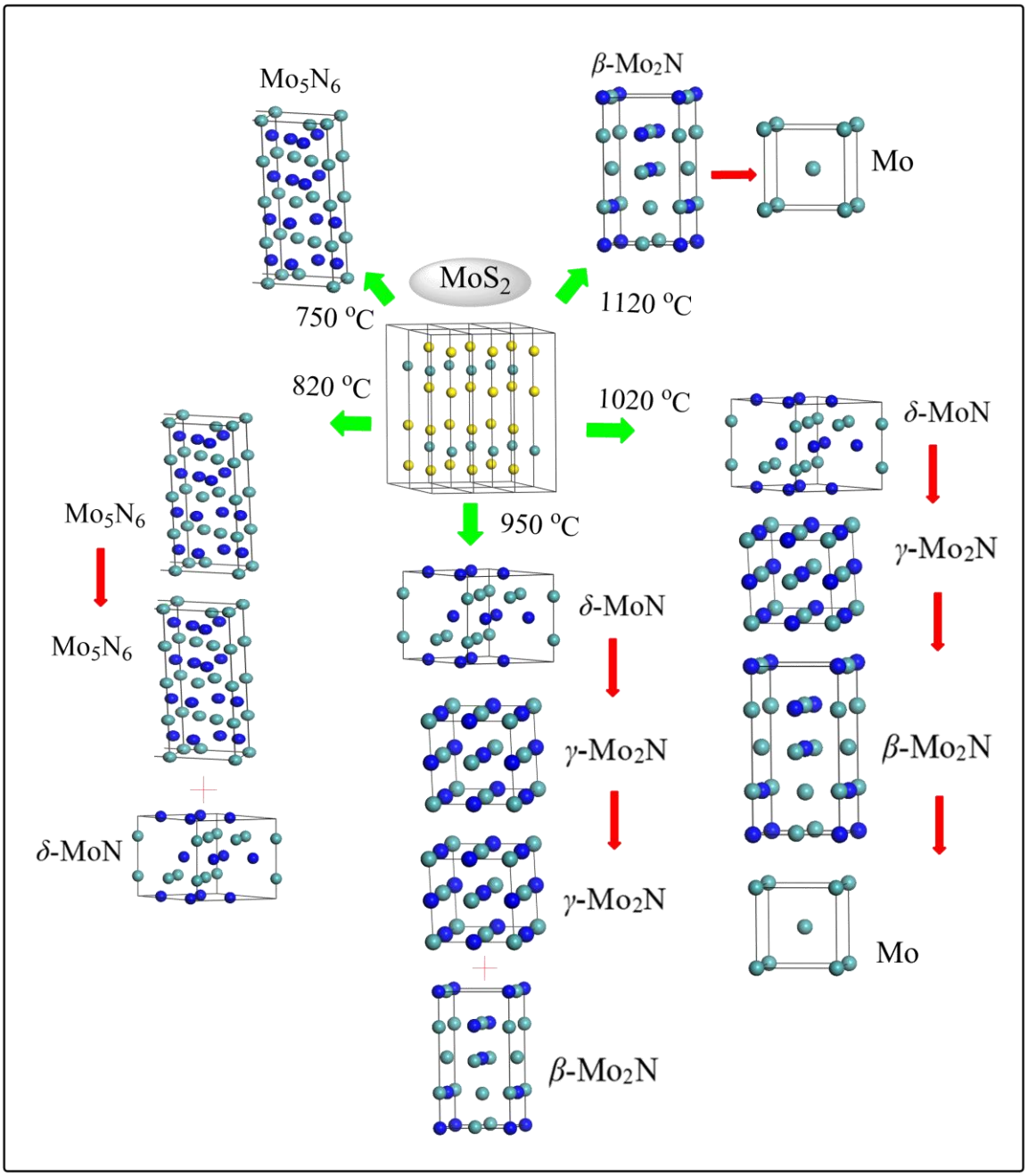

Figure 2.10: Schematic demonstrating the phase MoN_x evolution process of reducing MoS_2 with NH_3 at various temperatures [108].

2.10 Computational Modelling Studies in Predicting Ground-State Properties of Mo-N system

Motivated by the growing need for reliable and representative data that can be utilized for shortlisting of materials and tailoring their attributes toward a category of desired applications, a great deal of efforts using the state-of-the-art computational methods have been deployed to gain an atomic-base insight into potential applications and properties of Mo-N based materials. The development of robust theoretical methodologies and the availability of powerful high-performance computational facilities have enabled to carry out very accurate materials modelling. Obtained results basically include any experimentally measurable quantity. The list includes thermo-mechanical properties, lattice parameters, adsorption energies, XRD patterns, reaction rate constants and turnover frequencies. First principles calculations in the framework of DFT are presently the most widely used approach to acquire the aforementioned properties. In this context, I will introduce the recent advances of DFT in predicting the bulk and surface properties of molybdenum nitrides.

Stevens *et al.* [109] investigated the accuracy of DFT methods in calculating some properties including equilibrium bond length, dipole moment, and harmonic vibrational frequency in a series of group VI (Cr, Mo, W) transition metal containing diatomic molecules. By using flexible basis sets, they examined a wide range of exchange-correlation functional. Later on, results are compared with analogous experimental measurements. Generalized gradient approximation (GGA) seems to be the most appropriate functional that accurately reproduce the experimental parameters. Isaev *et al.* [110] investigated ground state properties and phonon spectrum of B1-type mononitrides of group III-VI transition metals. Likewise, structural, elastic, and electronic properties for several MoN phases have been studied by Kanoun *et al.* [55] and summarize in Table 2.4.

Table 2.4: Computed and measured equilibrium lattice parameters (*a*) Å, (c) Å, bulk modulus (*B*) GPa, Young's modulus (*E*) GPa, and Poisson's ratio (*v*).

	NaCl-MoN	ZB-MoN	δ_1-MoN	δ_3-MoN	CsCl-MoN
a	4.304[a]	4.616[a]	2.868[a] , 2.868[b]	5.710[a] , 5.735[b]	2.67[a]
c	-	-	2.80[a] , 2.81[b]	5.625 [a], 5.628[b]	-
B	351.5[a]	274.8 [a]	376.7 [a]	379.4, 380[b]	354.8 [a]
E	461.6 [a]	139.6 [a]	640.0 [a]	611.3 [a]	695.9 [a]
v	0.23 [a]	0.41 [a]	0.24 [a]	0.28 [a]	0.13 [a]

[a] DFT calculations using CASTEP code [55].

[b] Experimental findings[54].

Zhao *et al.* [34] reported DFT results on structural, mechanical and electronic properties of 4-*d* transition metal mononitrides considering NaCl, NiAl and WC-type structures. They indicated that among the investigated geometries, MoN with NiAs-type structure displays the highest hardness (bulk modulus of 351 GPa and shear modulus of 239 GPa). Investigations on the elastic response of the cubic (*B1*-NaCl structure) of early binary transition metal nitrides have been performed by Holec *et al.*[111]. A satisfactory agreement with the available experimental data has been attained. Cohesive energy, lattice constant and elastic constants C_{11}, C_{12} and C_{44}, have been determined. In another DFT study conducted by Liu *et al.* [112], group V-IIX transition metal nitrides have been inspected. They concluded that CrN, MoN and WN in NbO structure display the highest values of Vickers hardness (H_V) (*i.e.* higher than 20 GPa).

2.11 γ-Mo_2N Clean Surfaces

In addition to bulk phases, several DFT studies have provided electronic and structural properties for surfaces of Mo-N; most notably the γ-Mo_2N configuration. Commonly reported results include surface relaxation, reconstructions in reference to bulk positions, and reaction rate *etc.*

Cleaving the optimized bulk of γ-Mo_2N along the three Miller indices afford several configurations[113]. Some of these surfaces contain Mo/N mixed terminations while other display only N atoms in their topmost layers. Figures 2.11 and 2.12 portray optimized (*i.e.* minimum energy structures) for γ-Mo_2N surfaces and potent active sites are highlighted.

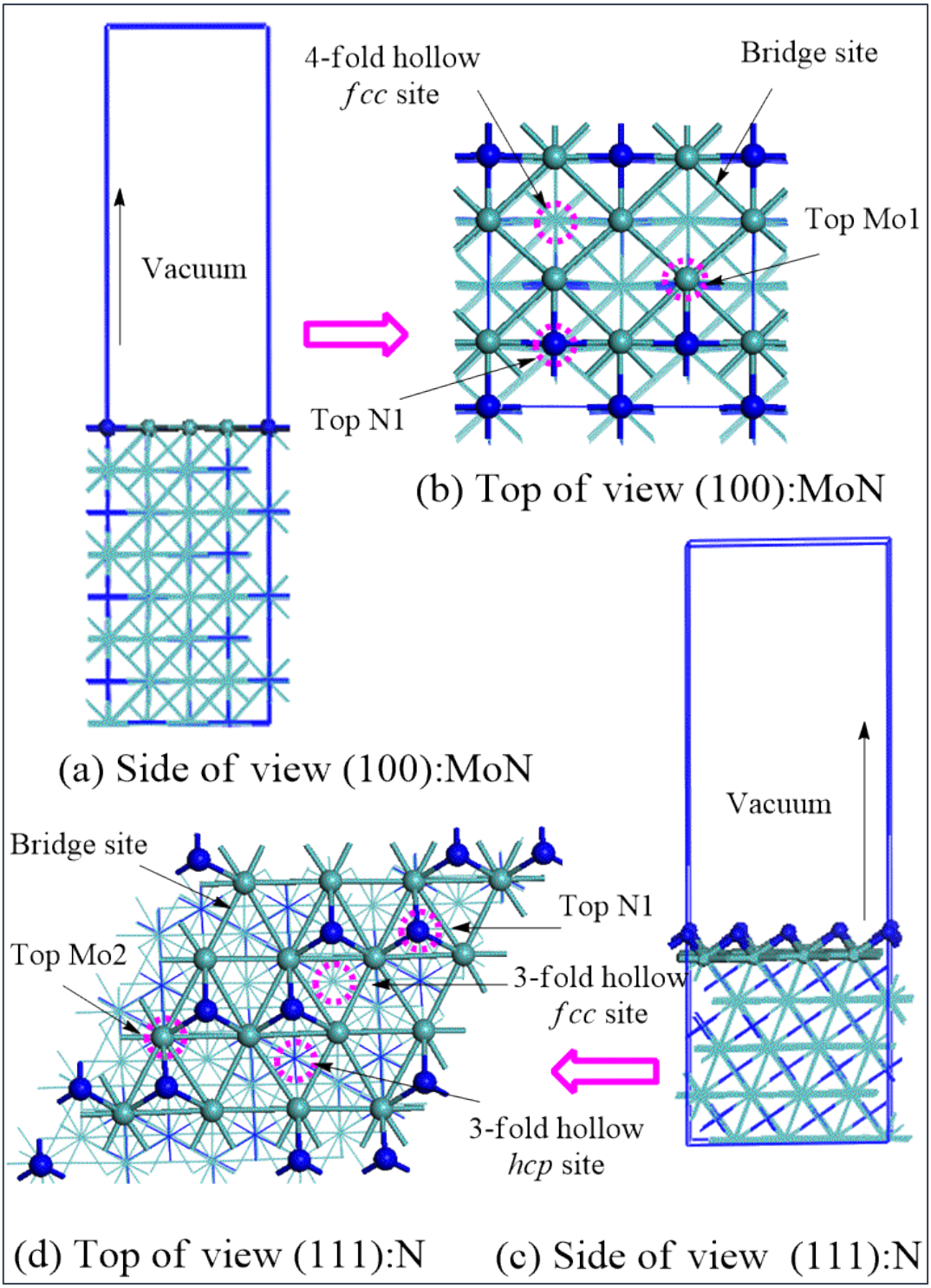

Figure 2.11: The optimised configurations of the γ-Mo_2N (100): MoN and γ-Mo_2N (111): N terminated surfaces and their possible adsorption sites. Molybdenum atoms are described in light green while nitrogen atoms are depicted in blue.

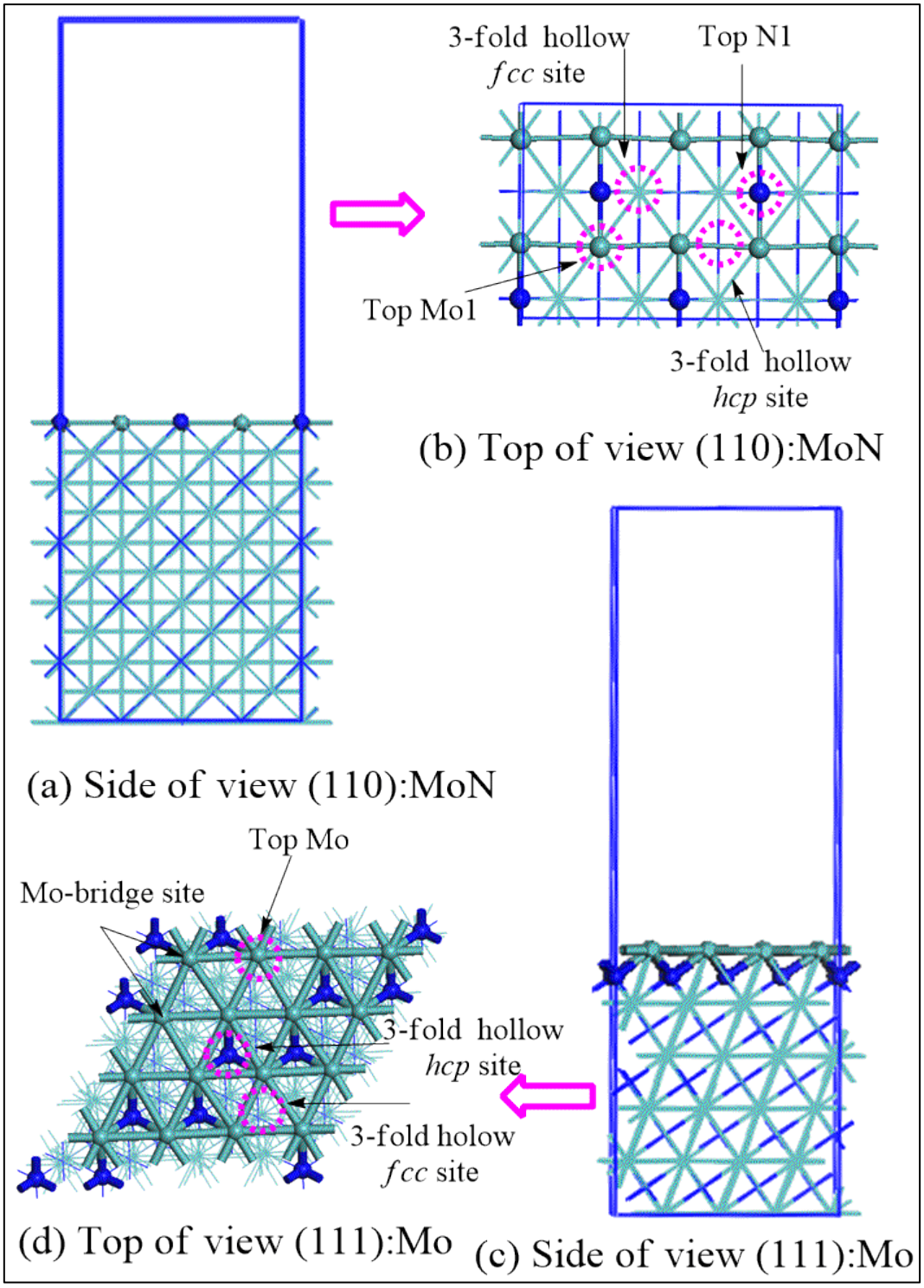

Figure 2.12: The optimised configurations of the γ-Mo_2N (110): MoN and γ-Mo_2N (111): Mo terminated surfaces with emphasized possible adsorption sites.

According to the constructed phase stability diagram via *AB* initio atomistic thermodynamics calculations shown in Figure 2.13, the γ-Mo_2N (111) is the most thermodynamically stable γ-Mo_2N [113]. This surface has been the subsequently utilized in several DFT-based studies that target catalysis by γ-Mo_2N [113, 114].

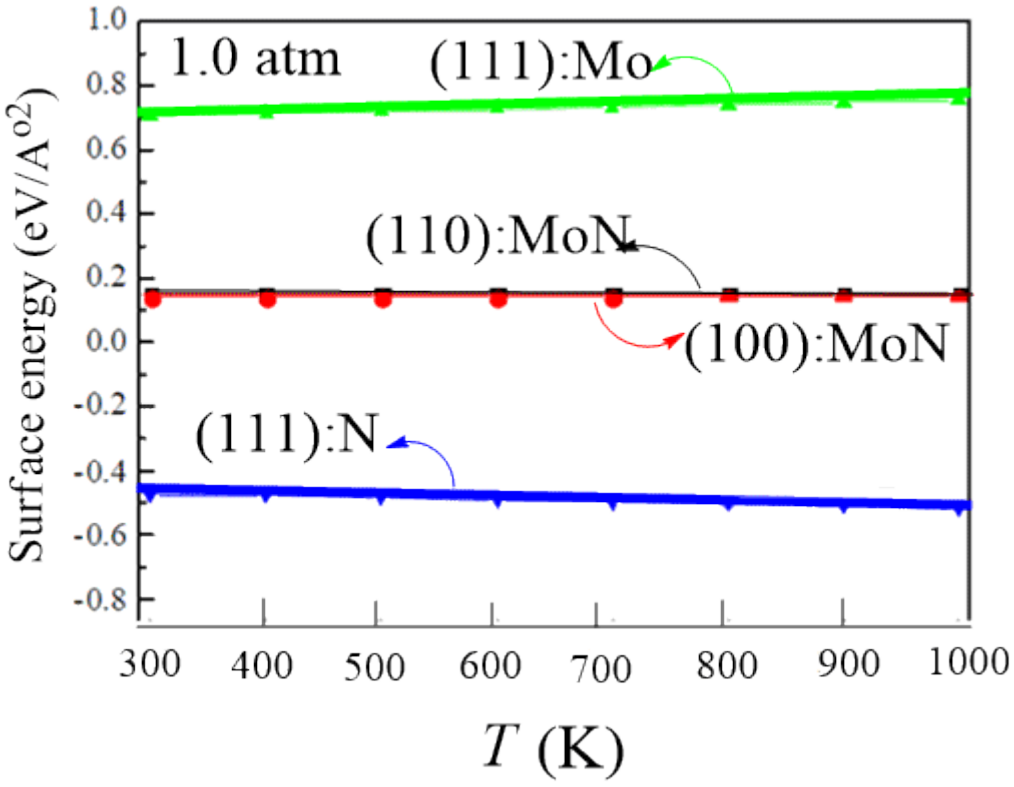

Figure 2.13: Phase stability diagram for molybdenum nitride surfaces [113].

2.12 An Overview into Ternary Transition Metal Nitride Coatings: Cr-Mo-N System the Case of Study

It is well-known that mechanical and optical properties of Cr-N thin films and coatings are systematically improved when doped with other transition metals. Figure 2.14 illustrates different types of generic coatings; namely, multicomponent coatings such as binary, ternary) gradient layers, gradient coating, solid solutions or multiphase/composite (solid solutions and/ or intermetallic compounds) [115, 116].

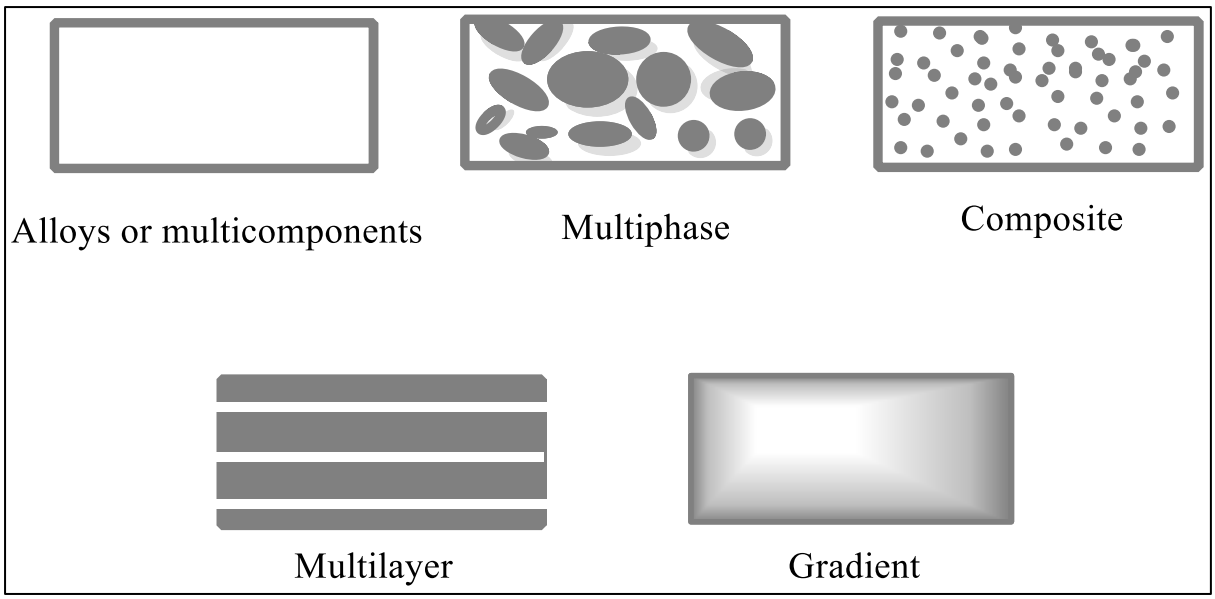

Figure 2.14: Graphical illustration of different type of coatings [115].

As mentioned above, an effective way to enhance and tune properties of material involves introducing alloying elements. Particularly, inserting molybdenum (Mo) or tungsten (W) into CrN coatings was shown to improve their structural, mechanical, and tribological properties [117-119]. Ceramic TMN coatings are typically utilised as protective coatings to increase lifetime of machineries that operate in elevated *T-P* operational conditions and or corrosive media. As discussed in section 2.7, PVD techniques have widely been deployed to deposit variety of hard coatings. The first generation of protective hard coatings in cutting and forming tools deposited by PVD was TiN [120]. However, the main shortcoming of TiN coating is that it suffers from low oxidation resistance and hardness. Presently, CrN represents the state-of-the-art of commercial PVD. Applications of CrN coatings originate from their profound properties as effective corrosion, oxidation and wear resistance [121]. To further improve these unique characteristics, Multicomponent coatings of Cr-*X*-N where *X* corresponds to one of the alloying elements including Al, Ti, Zr, W, and Mo etc. have been taken into consideration in literature [118, 122-125].

By implementing a hybrid coating method of arc ion plating (AIP) on a Cr target, a DC magnetron sputtering technique for Mo target, and N_2/Ar as the nitrogen precursor, Kim *et al.* [118] inspected the effects of Mo content up to 30.4 at.% on the microstructure and mechanical properties of the ternary CrMoN coatings. The fabricated coatings experience the formation of a substitutional solid solution of (Cr,Mo)N owing to the displacement of Cr atoms by the

larger Mo atoms in CrN crystals. At moderate mass ratio of Mo, the CrMoN coatings incur a higher hardness value of around 34 GPa, in reference to only 18 GPa for pure CrN.

CrWN and CrMoN films were deposited on high speed steel substrate by unbalanced DC reactive magnetron sputtering by Gu *et al.* [117]. XRD patterns illustrated that the CrWN films were composed of mixed CrN and W_2N crystalline phases, whereas the CrMoN films mainly encompasses crystalline CrN and amorphous/nanocrystalline Mo_2N phases. Authors confirmed the superior mechanical properties of CrWN and CrMoN coatings in reference to pure CrN coatings. Qi *et al.* [126] reported the influence of DC reactive magnetron sputtering parameters on the mechanical and tribological properties of the CrMoN films. Investigated parameters include substrate negative bias voltage (V_b), substrate temperature (T_s), and gas flow ratio ($R = N_2/ (N_2 + Ar)$).

2.13 General Synthetic Routes of Mo-N Catalysts via Temperature-Programmed Reaction (TPR)

Typically, the synthesis of TMNs carried out at high temperature by metallurgical processes producing low specific surface area powders [24], unsuitable for catalytic applications that requires high surface area materials. Temperature-programmed reaction (TPR) is currently the most commonly implemented approach in the synthesis of high surface area TMNs for catalytic applications [127]. In this section, I will review the synthesis of transition metal nitrides; with a specific focus on the molybdenum nitride surfaces. Figure 2.15 illustrates the basic synthesis apparatus for metal nitride. In general, the NH_3 is the preferred nitridation agent since it provides nitrogen atoms more easily than other sources such nitrogen molecules. The main synthetic methods of TMNs catalysts were reported in several studies [127, 128]. The commonly deployed fabrication procedure of TMNs occurs through the gas-solid reaction between of MO_3 (M refers to a metal atom *i.e.* Mo or W) and NH_3 or a mixture of NH_3 and Ar.

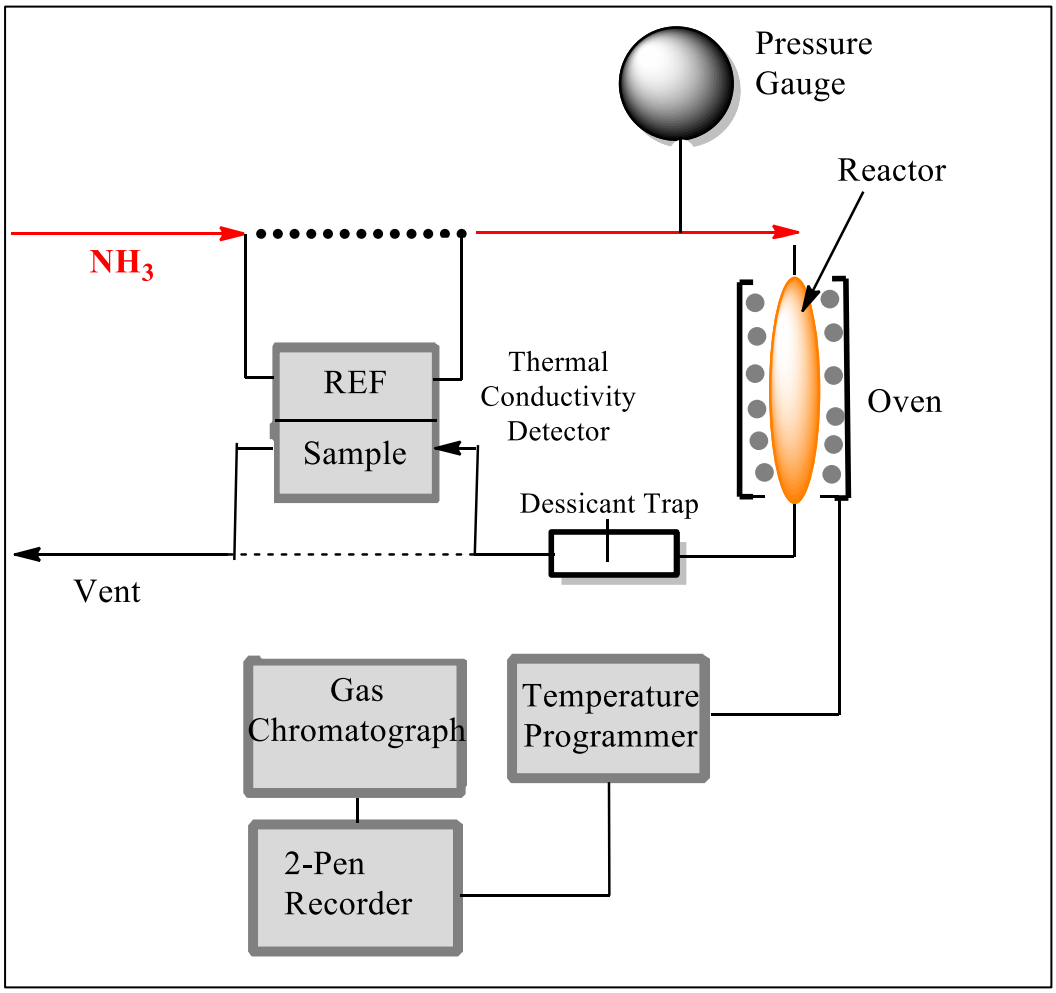

Figure 2.15: Graphical illustration of the synthesis apparatus for metal nitrides [129].

Jaggers *et al.* [130] proposed a reaction pathway to produce molybdenum nitride with high surface area *via* nitriding MoO_3 precursor with ammonia producing a mixture of MoO_xN_{1-x} or MoO_2. The oxynitride MoO_xN_{1-x} is then transformed to nitride's phases. *fcc*-Mo_2N and hexagonal MoN, albeit the former is produced at a higher temperature. However, products of this direct nitridation methods are associated with low surface areas. Inspired by promising catalytic application of MoN-based materials, efforts were devoted to modify synthesis procedure toward higher surfaces areas of these materials [131]. Volpe and Boudart [127] were the first to report synthesis of high-surface area of metal nitride catalysts by the reaction of ammonia with MoO_3 precursor. The reported surface area of produced nitride attains a high value of 220 m^2g^{-1}. Electron diffraction measurements illustrated that the N-induced conversion of MoO_3 platelets is topotactic. A study conducted by Marchand *et al.* [132] documented that the morphology and surface area of the prepared nitride materials is controllable via adjusting ammonia space velocity, and operating temperature to ensure

enhancing the surface area. The impact of the preparation parameters on the structural properties of synthesised catalyst has been reported by Choi *et al.* [128]. They proposed that, molybdenum trioxide MoO_3 exposed to heat treatment in NH_3 atmosphere over two heating steps, first from 623 to 723 K then from 723 to 973 K. These two temperature processes occur at various space velocities. Results suggest that the fabrication of high surface area molybdenum nitride takes place through several reactions depending on the deployed space velocity and heating rates. They concluded that high surface area of γ-Mo_2N ensued via the conversion of MoO_3 precursor into H_xMoO_3 and γ-$Mo_2O_yN_{l-y}$ intermediates. However, the reaction pathway via intermediates such as, MoO_2 resulted in the production of medium and low surface area molybdenum nitrides. These categories of ammonolysis operations were shown to also promote the production of pseudo-morphic configurations [133].

Haddix *et al.* [134] used proton NMR to characterize the adsorption of H_2 over high surface area of γ-Mo_2N (~120 m^2g^{-1}). They proposed that H_2 strongly bounded to the surface of the catalyst. Ranhotra *et al.* [135] fabricated porous powders of Mo_2N (fcc) by H_2 reduction of MoO_3 to metallic Mo in the presence of H_2. Results indicate that this phase contains pores of about 17 Å in diameter and a high BET surface area of 180 m^2/g. Recently, Roy *et al.*[136] have also prepared high surface area (116 $m^2\,g^{-1}$) of bulk γ-Mo_2N.

In the programmed ammonolysis procedure, nitrided materials are typically cooled in inert gas (helium, argon or nitrogen) or in a diluted ammonia atmosphere [137]. This is followed by passivating nitrides through passing a low diluted oxygen mixture (usually < 1%) in an inert gas [138, 139]. Any formed oxide layer is then removed by reduction with H_2 or N_2/H_2.

It is well documented that ammonolysis of $MoCl_5$ and MoS_2 precursors can yield various nitrides, most notably, δ-MoN and Mo_5N_6[54]. In a study conducted by Wise *el al.* [140], they synthesized a high surface are topotactic (150 m^2g^{-1}) γ-Mo_2N via N_2/H_2 treatment of MoO_3. One of the main advantage of such nitridation procedure is the facile elimination of heat transfer emitted from the endothermic decomposition of ammonia, (*i.e.* the N-H bond dissociation in ammonia is 93.21 Kcal/mol [6]). The surface area of the molybdenum nitride phases strongly depends on the synthesis conditions; namely, flow rate of nitrogen source, temperature and the heating rate. In their TPR synthesis of γ-Mo_2N, Li *et al.* [141] proposed that the surface area of the final nitride phase increases due to the pseudo morphological nature of the NH_3 + MoO_3 overall pyrolysis reaction.

Claridge *et al.* [129] developed a complex procedure to produce nitrides from carbide precursors. This procedure fabricated high surface area of carbide and nitride materials from binary and ternary oxide precursors of vanadium, niobium, tantalum, molybdenum, and tungsten. Figure 2.16 shows TPR reactions that operate in the formation of various Mo-N and M0-C phases starting from the MoO3 precursor. TPR analysis showed that by applying various gas mixtures, such as CH_4/H_2, C_2H_6/H_2, or NH_3, materials with surface areas >40 $m^2\ g^{-1}$ can be obtained.

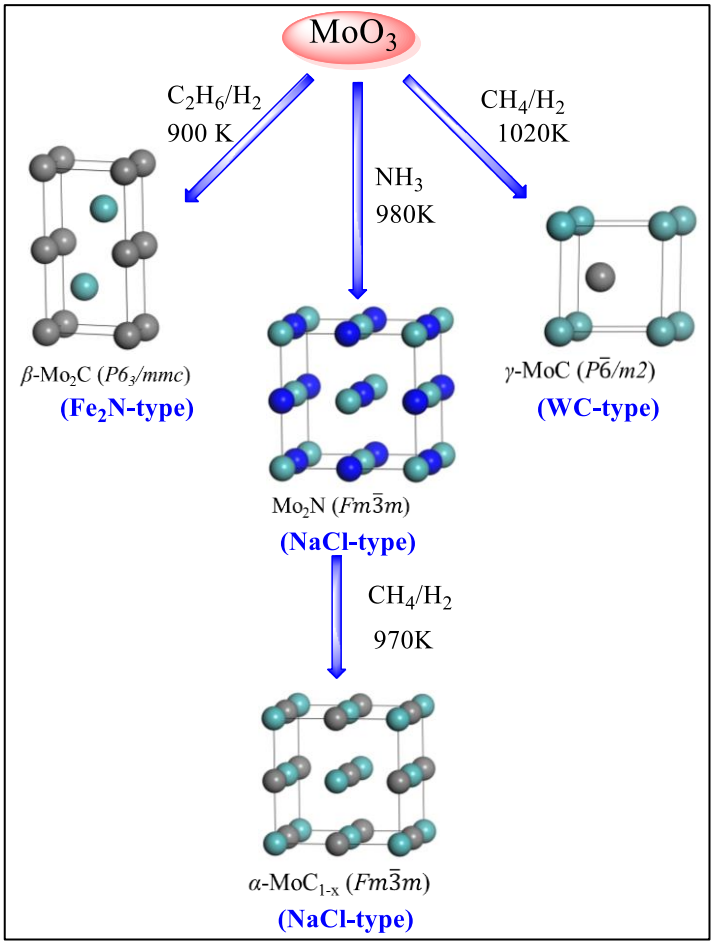

Figure 2.16: Pathways to Mo-N and Mo-C phases via temperature programmed reaction (TPR) of MoO_3 [129].

Investigating the influence of impurities level on the β-Mo_2N phase prepared by N_2/H_2 treatment of MoO_3 precursors has been explored by Cairns *el al.*[142]. Results demonstrated that adding minor loads of 1 wt % Pd, Au, Ni and Cu prompt significant alternation of the surface area of produced β-Mo_2N phase at 750 °C. The impact of using different sources of precursors was illustrated in another work by Cairns *et al.* [143]. Different MoO_3 precursors provided by AnalaR and Sigma–Aldrich, namely source A and source S, respectively, affords different morphologies of β-Mo_2N phase; (*i.e.* plate-like structures and deformed rectangular blocks as evidenced by SEM images). As an alternative procedure of using the TPR of MoO_3 (in where ammonia serves as the source of nitrogen), novel synthesis techniques were developed, for example the sacrificial support method (SSM) [136]. The advantage of this method was to convert the MoO_2 intermediate using $MgMoO_4$. Xu *et al.* [144] have suggested a synthetic approach termed as self-assembly method to fabricate hexagonal -like MoN hierarchical nanochex, composed of single-crystal nanowires.

2.14 Catalysis by Molybdenum Nitrides

Catalysis by metal nitrides rests on two important aspects; the presence of N-vacant sites, and the electronic structures that mimic that of Pt-based catalysts. In hydrogenation reactions by γ-Mo_2N, N-vacant sites act as hosts for dissociated hydrogen atoms. The weakly bounded surface H atoms migrate to adsorbed hydrocarbon species via relatively facile reactions. Previous DFT studies have mainly mapped out governing catalytic reactions for rather limited groups of reactions. Experimental catalysis work on Mo-N based catalysts provided chemical conversion values and surface characterisation of adsorbed species. Implementing high resolution transmission electron microscopy combined with Fourier analysis, NMR measurements, and X-ray photoelectron spectroscopy (XPS) characterizations were deployed to detect the near-surface structures and compositions of a series of molybdenum nitride catalysts [139]. In the next sections, prominent surface-mediated reactions by γ-Mo_2N is surveyed.

2.15 Adsorption and Activation of Simple Molecules

Molybdenum nitride compounds display profound high catalytic performance in a wide array of chemical reactions including CO hydrogenation, ethane hydrogenolysis, NO reduction, and hydro-treatment processes. The availability of potent active sites on the surface of the catalyst signifies a crucial aspect in the catalytic activity of a material. For a material to be catalytically potent, it must be capable to adsorb and activate the commonly deployed probe molecules such as CO, H_2, NO, NH_3, C_5H_5N, and O_2. Kinetically, the activation route will be shut down if the molecular adsorption and activation are not faster than surface mediated reactions. To avoid deactivation or positing of active sites, rapid desorption of produced radicals is an important factor. Desorption of products from the surfaces makes the active site to be available for another adsorption–activation–transfer–desorption cycle. Figure 2.17 depicts typical catalytic cycle steps [139].

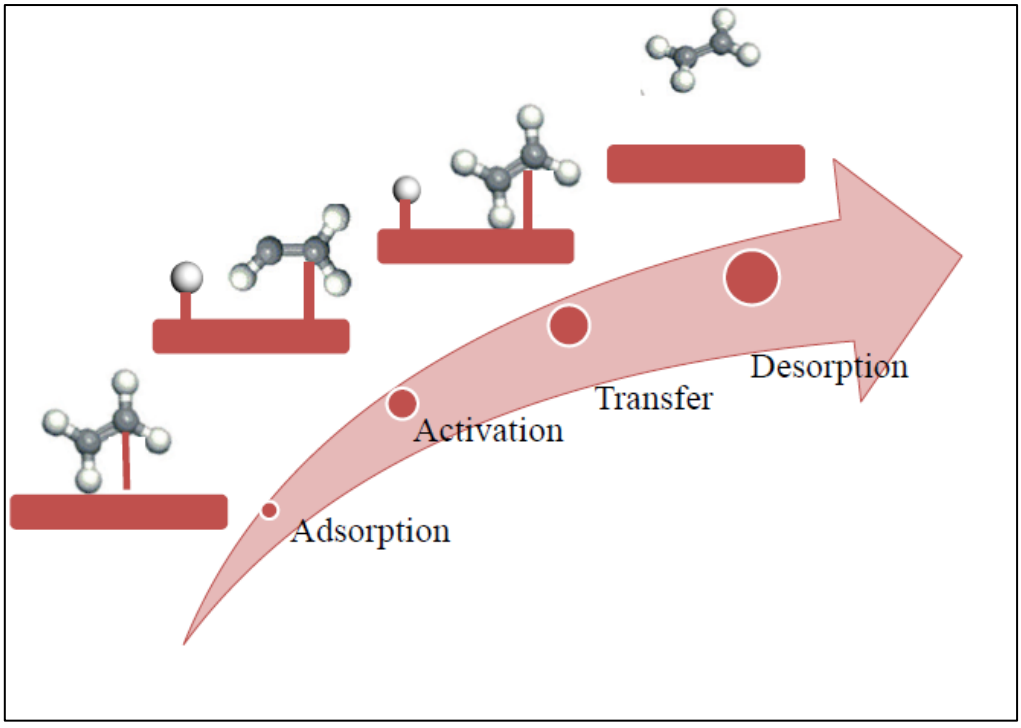

Figure 2.17: The main cycle that involves the reactions of any molecule over a surface catalyst. Ethene (C_4H_4) adsorption, deactivation, transfer to saturate radicals, and finally desorption.

2.15.1 Hydrogen (H_2)

Hydrogen is the most commonly used probe molecule to examine catalysis by metal nitride surfaces. Typically, a catalyst is active when it can adsorb and activate molecular hydrogen (H_2) at a sufficient reaction rate for a proposed period of time and at a specific temperature window. It is well established that Hydrogen interaction is desired on coordinatively unsaturated Mo (*i.e.* nitrogen deficient sites). At room temperature and over a polycrystalline γ-Mo_2N, the adsorption of hydrogen commences sluggishly, meaning that it is an activated process [145].

Figure 2.18 displays hydrogen uptake at 673K for Mo_2N [145]. H_2-uptake measurements over Mo_2N with a surface area of 79 m^2g^{-1} and reduced (*i.e.*, purging the surface with hydrogen) at 673 K were carried out by *Li et al.* [145]. The uptake isotherms in the temperature range of 308–623 K inferred that the total and reversible hydrogen uptake increased with the temperature. However, the irreversible hydrogen uptake augmented suddenly when the uptake temperature was raised up to 423 K. The maximum of irreversible hydrogen uptake was found to proceeds at 473 K. One of the proposed mechanisms for hydrogen adsorption took place via heterolytic dissociation on surface Mo-N pairs.

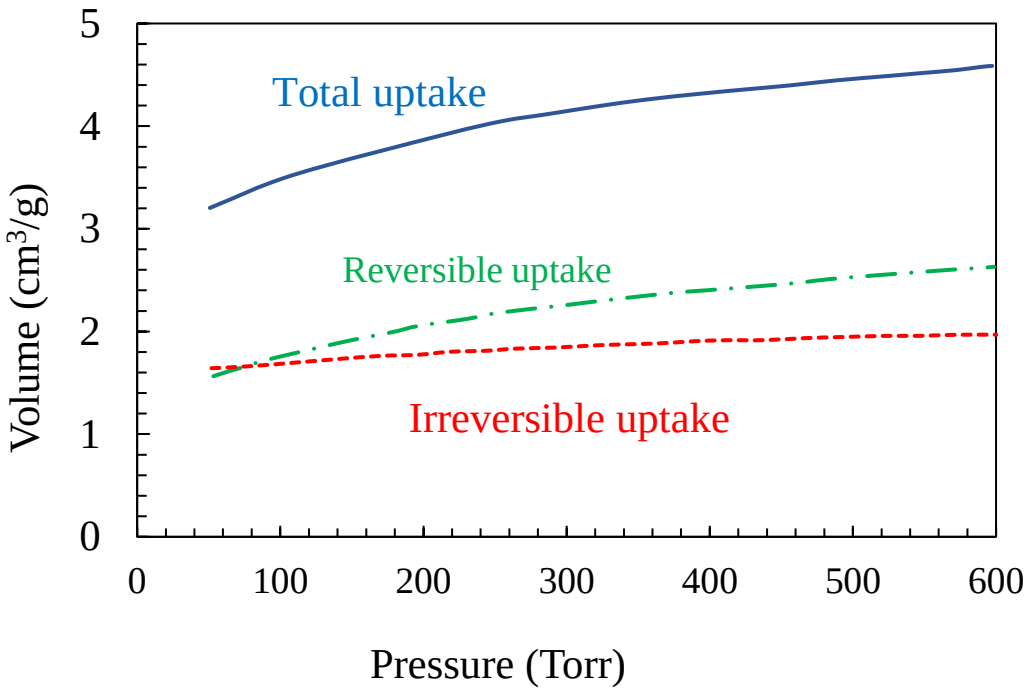

Figure 2.18: Hydrogen uptake at 673K for Mo_2N [145].

Based on nuclear magnetic resonance NMR measurements, Haddix *et al.* [146] stated that hydrogen dissociatively adsorbed over γ-Mo_2N with high surface area ~120 m^2/g. The maximum total uptake of hydrogen is limited to about 10% of the total available BET surface area of γ-Mo_2N, suggesting that the activation of hydrogen molecules is hindered by a relatively high temperature. The preferred adsorption site was also predicted to be nitrogen deficient sites. The interactions of H_2 and NH_3 with clean Mo(100) and nitrided Mo(100)-c(2×2)N surfaces were investigated via temperature programmed desorption (TPD) and Auger electron spectroscopy [147]. They suggested that at a given hydrogen coverage, the nitrided surface seems to adsorb ~ 4–10 times less than the expected concentrations of H_2 molecule than the clean Mo (100) surface.

The H_2-TPD profiles reported by Li *et al.* [148] are shown in Figure 2.19. High surface area γ-Mo_2N (134m^2/g) was treated in a hydrogen environment at specific temperatures. This has been followed by cooling to room temperature in the flow of H_2 before the TPD experiments were carried out.

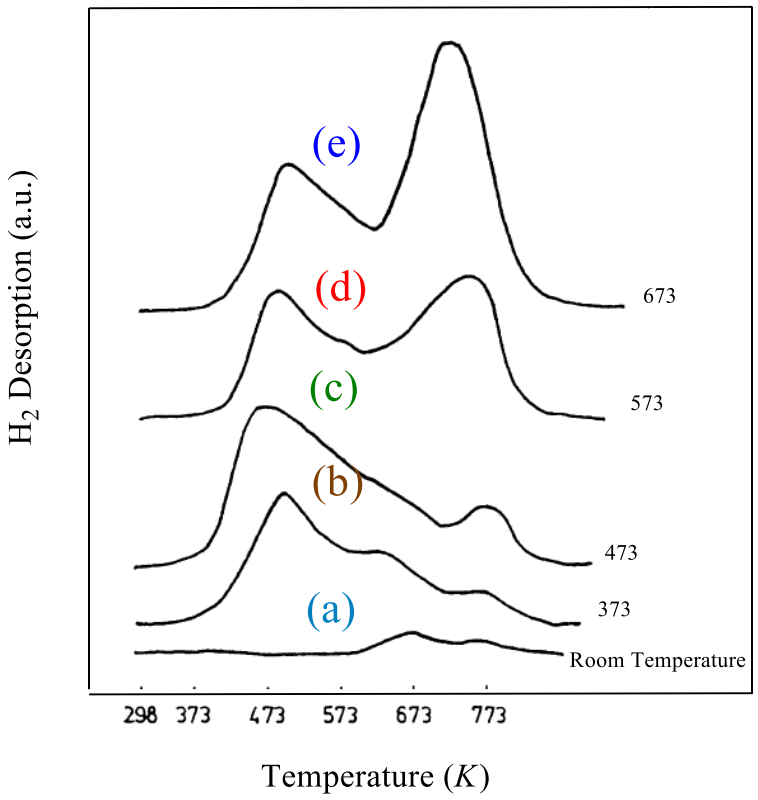

Figure 2.19: The H_2-TPD profiles reported by by Li *et al.* [148].

Zhang *et al.* [149] found that by TPD and temperature programmed adsorption (TPA) techniques, the adsorbed hydrogen species were able to mobile and migrate from low adsorption energy sites (N vacant sites) to high adsorption energy sites (atom N sites). This facile surface diffusion sustains the dynamic equilibrium. Two hydrogen adsorption peaks at 517 K and 736 K were detected. These peaks were assigned to belong to low and high adsorption sites, respectively. TPD and TPA measurements overall indicate a rapid equilibrium between adsorption and desorption reactions.

2.15.2 Oxygen (O_2)

It has been reported that oxygen can diffuse into the subsurface layers of molybdenum nitrides. During exposure to dilute O_2 mixture, a thin oxide passivating layer may form. The rates of oxygen diffusion into the subsurface and react with Mo are accelerated at higher temperatures. The potential occurrence of oxygen subsurface diffusion indicates that higher operating temperatures systematically enhances the overall uptake of oxygen as additional oxygen atoms are to be sub-surface adsorbed [150]. Figure 2.20 reveals that the oxygen uptake at 298 K is greater than the corresponding uptake at 195 K, due to either oxidation of subsurface layers or incomplete surface coverage. Markel *et al.* [137] indicated that the developed passivation layer does not produce a distinct oxide phase but rather an oxynitride phase.

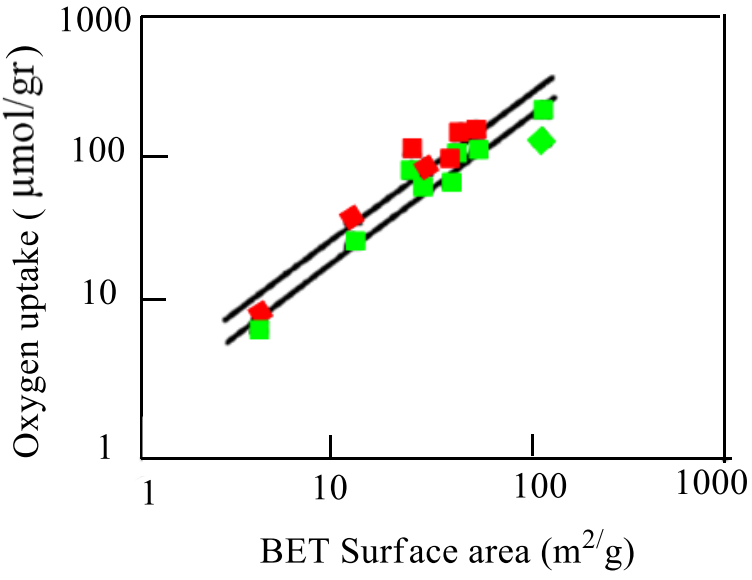

Figure 2.20: A comparison of the BET surface areas and O_2 uptakes following pre-treatment in flowing H_2 at 673 K for three hours uptake at 298 K (red) and the uptake at 195 K (green) [150].

2.15.3 Carbon monoxide (CO)

Yang *et al.* [151] have investigated surface active sites and adsorption properties of CO on the fresh and reduced passivated samples of Mo_2N/Al_2O_3. The Infrared (IR) spectrum of the CO adsorption displayed distinct patterns over fresh and reduced passivated samples. For the fresh sample, the IR spectrum of adsorbed CO showed that CO molecule adsorbed on the top of molybdenum and nitrogen sites forming a surface CO and NCO species. However, in the case of reduced passivated sample, an oxynitride layer was formed.

Generally, the adsorbed CO molecule undergoes a dissociative adsorption to C and O atoms. Furthermore, the IR results clearly demonstrated that the pre-adsorption of H_2 on fresh Mo_2N/Al_2O_3 hinders the CO adsorption, presumably due to the pre-occupation of active sites by dissociated hydrogen molecules.

Through DFT calculations, Frapper *et al.* [152] determined the most favorable energetic sites for CO molecular adsorption over γ-Mo_2N (100) plane. CO was positioned at several adsorption sites. Results indicate that four lowest adsorption positions can be distinguished as illustrated by Figure 2.21, namely, on-top Mo_1, on-top Mo_2, on-top nitrogen surface N atom, and on 4-fold vacant site. However, the 4-fold vacant site is predicted to have the lowest coordination mode with adsorption energy of -1.49 eV (~ -34.3 kcal/mol). Comparable adsorption energies were obtained for the three sites. However, the chemisorbed CO molecules have not been observed experimentally on the Mo_2N catalyst. Nonetheless, 4-fold hollow in (100) fcc surface were a promising active site for diatomic molecules on the basis of IR interpretation. The computed binding energies were -1.43 eV (~ -32.9 kcal/mol) and -1.32 eV (~ -30.4 kcal/mol) for the Mo_1 and Mo_2 sites (refer to Figure 2.21), correspondingly. This adsorption energy matches very well the corresponding adsorption energy of CO over the Pd(100), i.e., 1.44 eV (~33.2 kcal/mol) proving the well-known Pt-like catalytic properties for nitride molybdenum catalysts [153]. CO adsorption over atom N sites leads to the formation of a chemisorbed NCO species. The calculated adsorption energy corresponds to a slightly endothermic reaction by 0.23 eV (~ 5.3 kcal/mol), however, no activation barrier was reported. Despite of this low endothermicity, removal of a surface N atom is expected to incur a sizable energy barrier.

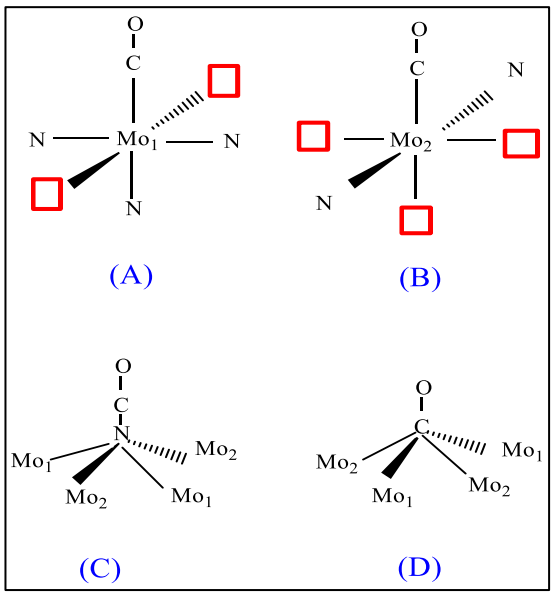

Figure 2.21: Schematic showing the possible active sites of CO adsorption on clean (100) 1×1 surface: (A) on-top Mo_1, (B) on-top Mo_2, (C) on-top nitrogen surface atom N_{surf}, and (D) on 4-fold site μ_4-CO. The red square symbols correspond to the vacant 4-fold hollow sites [154].

2.15.4 Adsorption of N_2

It has been reported that N_2 dissociativly adsorb over Mo_2N and at high temperature forming nitrogen-saturated surface. DFT calculations predicted the dissociation energy to be around -2.04 eV/N_2 molecule [154]. Along the same line of enquiry, Hillis *et al.* [155] predicted very weak adsorption of molecular nitrogen over the molybdenum dioxide (MoO_2) surfaces during the process of ammonia synthesis.

Moreover, Aika and Ozaki reported that about 146 ml(STP)/(3.39g molybdenum) of N_2 was absorbed on a molybdenum metal after 69 h of nitriding in a pure N_2 atmosphere [156]. Molybdenum containing ternary nitrides such as Co_3Mo_3N assumes high possibility to act as nitrogen transfer agents via Mars−van Krevelen-like mechanism in cyclic involving activating nitrogen that can be released and replenished. In these reactions, Co_3Mo_3N serve as a nitrogen storage medium [157, 158].

2.16 Catalytic Activity of Molybdenum Nitride Compounds

The catalytic performance of group V and VI metal nitrides and carbides in catalysing various reactions including, butane dehydrogenation, isomerization and hydrogenolysis etc. have been surveyed in several reviews [147, 159-161]. Neylon *et al.* [159] observed that turnover frequencies estimated for the nitride and carbide catalysts were of the same order of magnitude as that for the Pt–Sn/Al_2O_3 catalyst. Figure 2.22 demonstrates Arrhenius-type plots for the hydrogen evolution reaction over selected metal nitrides of group V and VI along with corresponding values of Pt–Sn/Al_2O_3. Nitrides of molybdenum, tungsten and vanadium were found to be considerably active during number of reactions. However, herein we focused on Mo_2N-mediated reactions. Table 2.5 shows various chemical reactions catalysed by MoN.

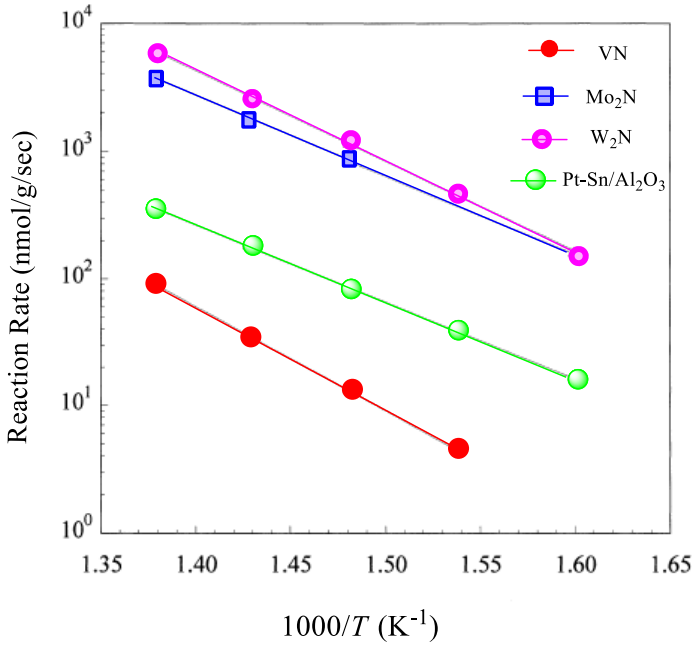

Figure 2.22: Reaction rate constants for hydrogen evolution over transition metal carbides and nitrides during electrocatalysts [159].

Table 2.5: Summarizes catalytic activities of various geometries of molybdenum nitride.

Catalyst	Preparation method	Shape and Morphology	Surface area	Reaction Products	Applications	Catalytic activity	Ref.
γ-Mo_2N	TPR of MoO_3 with NH_3	Spherical and cubic particles	100 m^2g^{-1}	-	Pyridine hydrodenitrogenation catalysts.	-	[150]
Mo_2N	TPR of MoO_3 in N_2/H_2 treatment at 573K, pressure of 5 MPa	-	9-115 m^2 g^{-1}	Phenol	hydrodeoxygenation HDO of guaiacol	10% conversion of guaiacol	[162]
γ-Mo_2N	TPR NH_3	-	$150m^2g^{-1}$	Ammonia	ammonia synthesis	Reaction rate at 673K under 0.1MPa was 43 μ mol h^{-1} g^{-1}	[163]
Mo_2N/graphite	TPR of carbon-supported Mo precursors with NH_3	-	91 m^2g^{-1}	unsaturated alcohol	Crotonaldehyde hydrogenation	High selectivity to the unsaturated Alcohol and crotylalcohol selectivities exceed the 60%	[164]
γ-Mo_2N	TPR reduction of MoO_3 in flowing NH_3	porous particle	108 m^2g^{-1}	butane	Thiophene hydrodesulfurization HDS	38.1% Conversion efficiency at 673 K	[165]

$NiMoN_x/C$	treating the NiMo/C in NH3 flow at 700^OC	Nanosheets	-	-	hydrogen evolution reaction HER	78 mV at 0.24 mA cm^{-2} in acid	[166]
Mo_2N	TPR of MoO_3 with the mixture of N_2/H_2 gases	-	165 $m^2 g^{-1}$	methane	hydrogenation of CO	high activity and selectivity of methane formation	[167]
β-Mo_2N	A temperature programmed treatment of MoO_3 in flowing N_2 + H_2	platelet	17 $m^2 g^{-1}$	*p*-chloroaniline	hydrogenation of *p*-chloronitrobenzene	100% selective towards NO_2 group reduction with reaction rate constant (k = 2.0 min^{-1})	[168]

2.16.1 Hydrotreating Reactions

It is well recognized that hydrotreating reactions are considered as one of the most essential catalytic processes in petrochemical industries. They refer to a chemical process in which heteroatoms such as, S, N, and O or metals are removed from crude oil feedstock. Depending on the target molecule/atomic constituents, several catalyzed hydrogenation operations were developed, this includes HDS, HDN, HDO and hydrodemetallization (HDM) [139, 147, 155]. Owing to environmental concerns from the increasingly emissions of SO_x and NO_x gases from thermal processes, strict rules and regulations to diminish the releases of such pollutants have been imposed. As such, this has promoted catalysts scientists to fabricate and test the capacity of Mo-N as cost-effective materials in hydrogenation applications [169-171]. Figure 2.23 summarizes fundamental catalytic activities of molybdenum nitride.

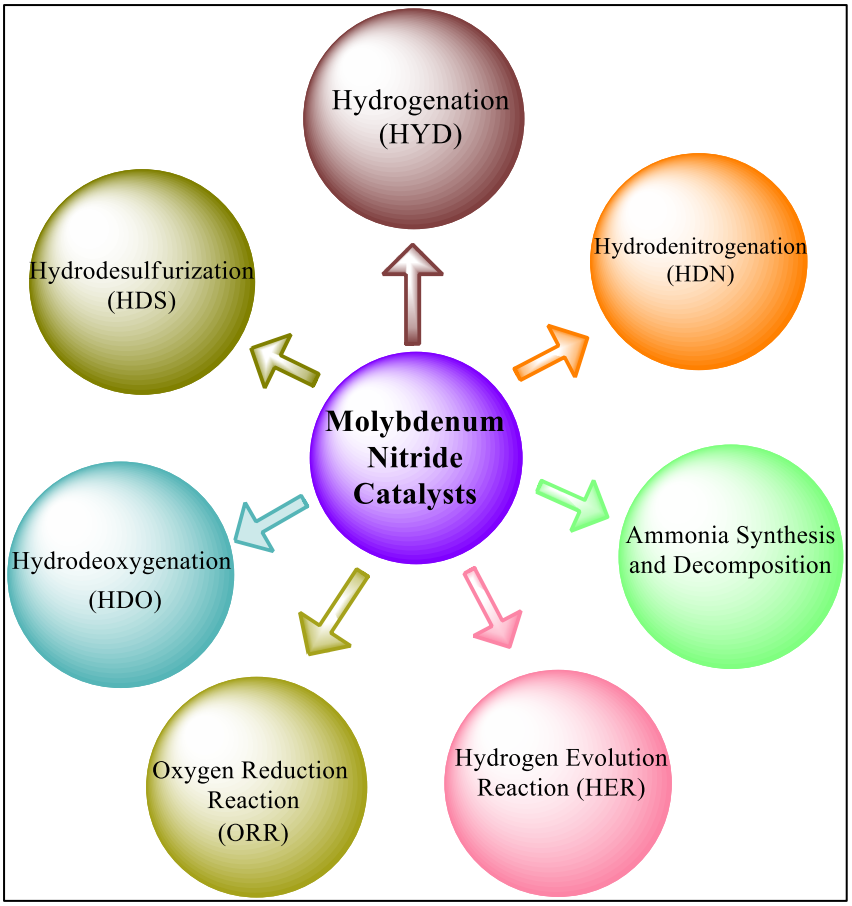

Figure 2.23: The main applications of molybdenum nitride catalysts.

2.16.1.1 Hydrogenation (HYD)

It is well established that the availability of surface hydrogen plays crucial role in hydrogenation-based reactions. The inclusion of nitrogen induces significant alternation of the catalytic activities of the host metals (*i.e.* Mo) via adjusted bonding strengths and improved electronic structure [172]. TMNs show high catalytic activity and selectivity as compared to their metal hosts. This is stemmed from electronic effect of metal nitrides which is in turn governed by density of states of the *d*-orbital.

In a nutshell, when a metal-nitrogen bond forms, the resulting smaller deficiency in the *d*-band occupancy of the metal motivates an electron donating character [173] from the metal toward N atoms. These significant electronic changes render Mo-N based materials to mimic the capacity of noble metals- as catalysts in hydrotreating processes [4, 139, 174].

The catalytic performance of transitional metal nitrides was shown to be highly sensitive to the transitional metal: nitrogen ratios as well as the structural phase (*i.e.* cubic δ versus hexagonal β). In this regard, β-Mo_2N affords generally higher specific turn over frequencies in reference to the δ phase. Recent DFT studies have provided a molecular-level understanding of catalytic reaction mechanisms operating over surfaces of transitional metal nitrides. As mentioned earlier, measurements by NMR and TPD techniques provided insightful information pertinent to hydrogen dissociative adsorption on Mo_2N [145, 148, 175]. While literature has answered many intriguing questions pertinent to electronic dictating factors contributing to catalysis by transitional metal nitrides, governing mechanisms and surface modifications during the course of gaseous molecules – surface interactions. Nonetheless, several aspects necessitate further investigations; most importantly, phenomena leading to poisoning of catalytic active sites at higher temperatures; potential influence of dopants and atomic-type terminations on surface diffusion, and the effect of oxygen-rich streams versus pyrolytic conditions on the catalytic activity.

Reviews on transitional metal nitrides have mainly focused on their structures and experimental findings related to hydro processing. Discussing results from TPD technique pertinent to hydrogen interaction with Mo_2N without accounting for mechanisms and structural/electronic factors contributing to the catalytic behaviour of TMNs. Selective hydrogenation occupies the core of many chemical industries. Additionally, several factors influence the hydrogenation activity and / or selectivity. These factors include the specific surface area (SSA), the nature of the surface-active sites and crystalline phase of particular catalysts [170, 176]. Detailed descriptions of chemical phenomena pertinent to γ-Mo_2N-assited catalysis are extensively discussed in Chapters six, seven, and eight of this dissertation.

2.16.1.1a Selective hydrogenation of ethyne over γ-Mo_2N

The selective hydrogenation of ethyne over γ-Mo_2N surface catalyst has been investigated by Hao *et al.* [177] at 50–210 ºC. The selectivity of producing ethene as a reaction outcome steadily increased at 150ºC. They proposed that a conversion of ca. 85% ethyne and selectivity of ca. 85% for ethene were obtained at 130°C. The influence of reaction time and temperature on the conversion and selectivity of ethyne hydrogenation is clearly seen from Figure 2.24a and b, respectively. At the start of the reaction (*i.e.,* the first 30 min), the selectivity for ethane and butane improved and the conversion of ethyne reached about 100%. The key reaction products referred to ethane and butane. Pointing out that the reduced passivated catalyst

ensured high hydrogenation activity, so that ethyne is hydrogenated directly to alkanes (ethane and butane). Besides, via the analysis of Figure 2.24b the data demonstrate that the conversion of ethyne improved from 3 to 99%, at temperature ranged from 50 to 210◦C. In addition to increasing the selectivity of ethene from 75 to 90%. However, the selectivity of butene rapidly diminished at higher temperatures as compared with ethane which was trivial at all reaction temperatures [177]. They attributed that the high activity and selectivity towards ethene formation was governed by thermodynamic selectivity [178]. Implying that, high coverage of ethyne over γ-Mo_2N active sites suppresses ethene from re-adsorption resulted in high selectivity of ethene. However, selectivity of ethane and butene were low due to lower coverage of ethyne on the surface of γ-Mo_2N. In another expression, high selectivity for alkenes in the hydrogenation reaction suggests that alkenes have a weaker adsorption than alkynes over the γ-Mo_2N catalyst covered by ethyne.

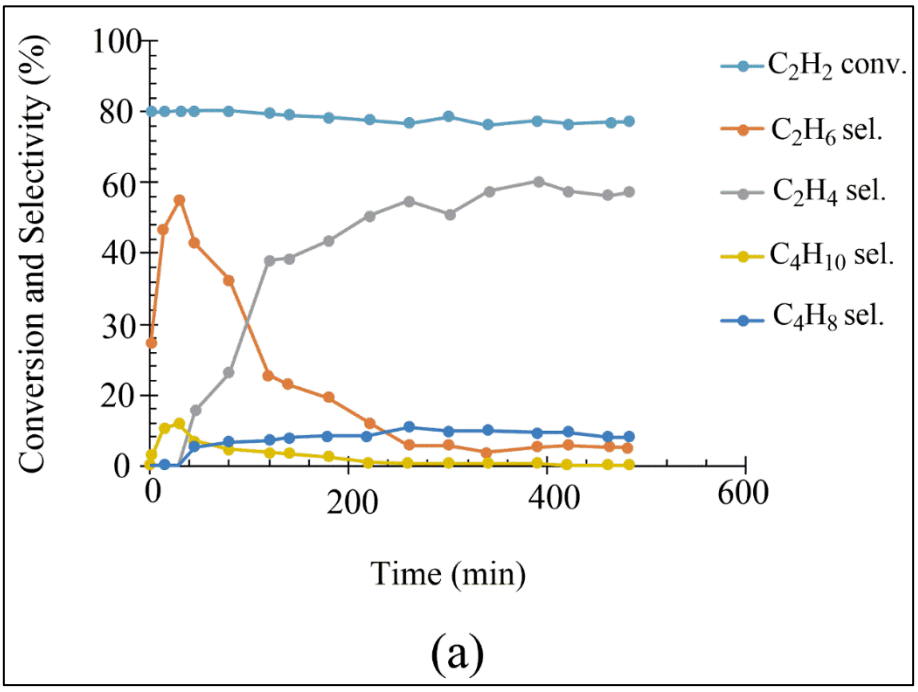

(a)

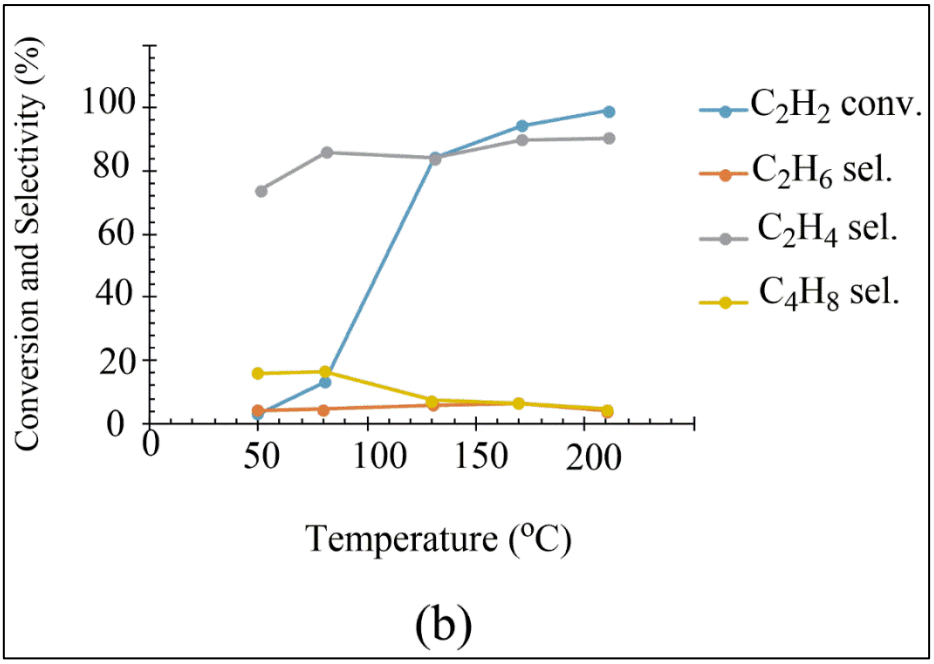

Figure 2.24: Activity and selectivity of ethyne hydrogenation on γ-Mo_2N as a function of (a) reaction time at 150ºC, SVD 7000 h^{-1}. (b) at different reaction temperatures, SVD5000 h^{-1} [177].

A Recent study performed by Cárdenas-Lizana *et al.* [179] reported the synthesis of two crystalline phases of molybdenum nitride namely, tetragonal β-Mo_2N with specific surface area (SSA = 6–15 $m^2\ g^{-1}$) and cubic γ-Mo_2N (45–135 $m^2\ g^{-1}$) for selective hydrogenation of alkyne. Results showed that those materials exhibit high selectivity (77–90%) in acetylene hydrogenation to ethylene. They proposed that, β- and γ- phases exhibited steady-state conversion and similar selectivity with time on-stream, as demonstrated for 13 h of nonstop operation over γ-Mo_2N as displayed in Figure 2.25. They attributed the stability of the both prepared catalysts to the trivial amount of undesired formation of green oil, which could deactivate the catalyst by blocking the active sites. Governed by H_2 and acetylene uptake, β-Mo_2N crystallography delivered higher formation of Green oil with selectivity of ($S \leq 15\%$) due to higher C_2H_2/H_2. However, Green oil production was lower ($S = 3\%$) over γ-Mo_2N due to lower C_2H_2/H_2 as XPS results predict.

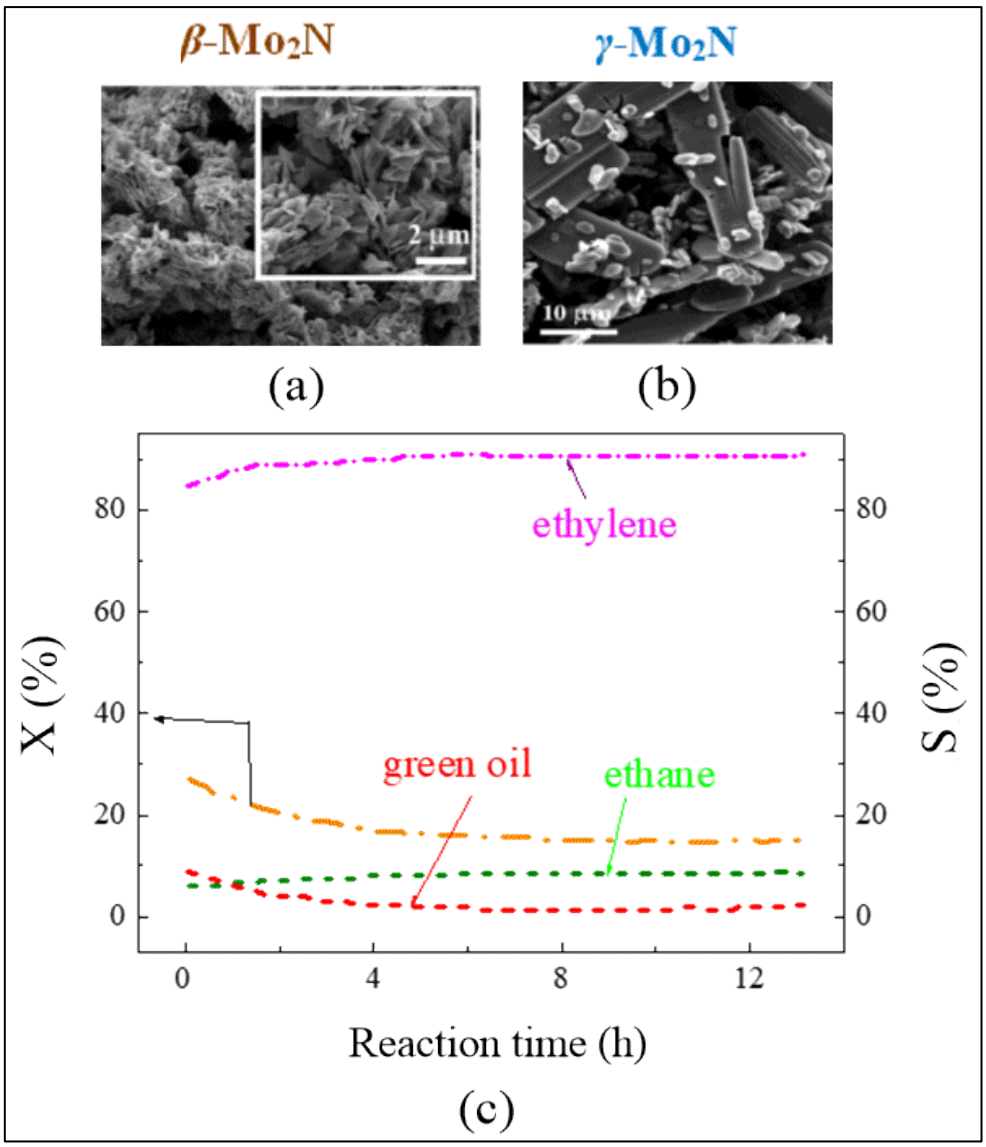

Figure 2.25: SEM images of (a) Small crystalline aggregates of β-Mo_2N phase via a non-topotactic conversion of MoO_3. (b) Large platelets with secondary smaller rod-like structure of γ-Mo_2N phase. (c) Variation of acetylene conversion (X-orange dash dots) and selectivity (S) to ethylene (pink dash dots), ethane (green dash dots) and green oil (red dash dots) with time on-stream over γ-Mo_2N [179].

2.16.1.1b Selective Hydrogenation of 1,3-Butadiene

As an industrially important reaction to prevent catalyst poisoning, the selective hydrogenation of butadiene to butane is of great significance.

In an experimental study carried out by Wu *et al.* [180] to investigate the selective hydrogenation of 1,3-butadiene and 1-butene over Mo_2N/γ-Al_2O_3 catalyst. In situ FT-IR spectroscopy detected the formation of several chemisorbed surface species. Furthermore, the occurrence of the πd-adsorbed butadiene considerably inhibits 1-butene from being adsorbed. The high selectivity in the hydrogenation of 1,3-butadiene to 1-butene can also be ascribed to the surface nitrogen atoms that weaken the interaction between 1,3-butadiene and the catalyst surface. In another study, the selective hydrogenation of 1,3-butadiene has been assessed on γ-Mo_2N catalyst. The γ-Mo_2N catalyst was found to be selective to hydrogenate 1,3-butadiene to 1-butene. Surface hydrocarbonaceous species were probed by both IR and H2-TPSR, in charge of deactivating and poisoning the active sites of the nitride catalyst[181]. The selectivity behaviour could also be interpreted according to the C=C bond nature by which 1,3-butadiene exhibits strong adsorption energy owing to possessing two C=C double bond, and 1-butene displays weak adsorption energy owing to holding one C=C double bond[182].

2.16.1.2 Hydrodesulfurization (HDS)

Mo-based catalysts have comprehensively been deployed in the HDS of petroleum feed stocks to eliminate the heteroatoms from thiophenic compounds such as thiophene (T), benzothiophene (BT), and, dibenzothiophene (DBT) [137, 183-186]. The latter group of compounds signify major *S*-carriers in coals and transportation fuels. Ozkan *et al.* [187] prepared an unsupported γ-Mo_2N catalyst for the HDS of BT in the presence/absence of NH_3. The catalyst was highly active towards formation of ethylbenzene at temperature range of 473–653 K.

In order to investigate the catalytic activity of DBT towards HDS reaction , Park *et al.* [188] prepared Co and Ni promoted nitrided Mo/γ-$A1_2O_3$, and unsupported molybdenum nitride catalysts by the TPR approach under NH_3 environment. It was demonstrated that carefully-

monitored variation in temperature, pressure, and contact time increases the reactivity and selectivity toward producing biphenyl (BPN) and cyclohexylbenzene (CHB).

Liu *et al.* [189] prepared γ-Mo_2N and Co-promoted molybdenum nitrides Co−Mo−N catalysts with high surface area have been prepared and characterized by XRD and BET. The findings of measurement of HDS of DBT indicate that γ-Mo_2N and Co−Mo−N have higher HDS activity and selectivity for C−S bond rupture. Furthermore, adding Co as a promoter considerably enhanced the HDS activity of the γ-Mo_2N. The network displayed in Figure 2.26 points out to two main reaction corridors designated as the HYD of one aromatic ring to give a mixture of 4H-DBT and 6H-DBT and HDS of these intermediates proceeds rapidly to produce CHB. While, the second possible corridor corresponds to the direct hydrodesulfurization (DDS) forming (BPN), occurs by hydrogenolysis.

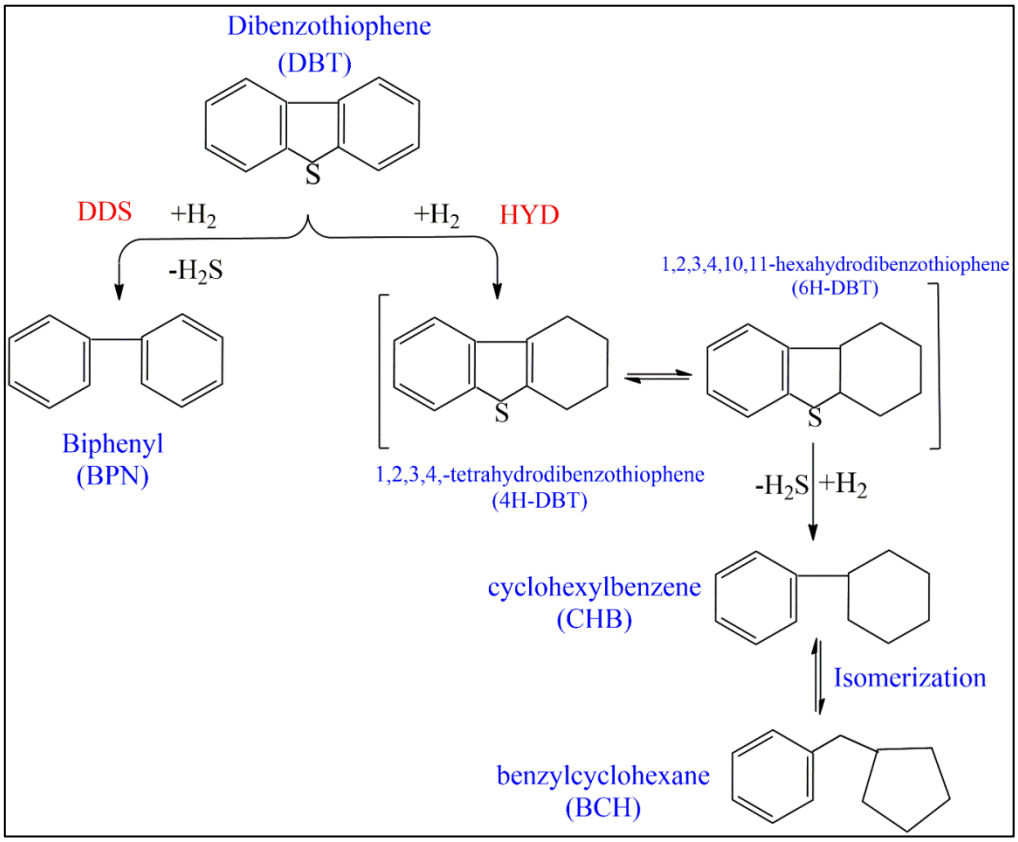

Figure 2.26: HDS reaction routes of dibenzothiophene over Co-promoted molybdenum nitrides Co-Mo-N catalysts [189].

An experimental study performed by Ramanathan and Oyama [190] focused on exploring catalytic activities of a series of transition metal carbides and nitrides of Mo, W, V, Nb, and Ti. Nitrides of these metals were prepared via TPR of their oxide precursors with a reactant gas (20% CH_4/H_2 for the carbide samples and 100% NH_3 for the nitride samples). BET chemisorption measurements were carried out using N_2 and CO as probe molecules. The catalysts were tested in a three-phase trickle-bed reactor for their activity in HDN, HDS, and HDO. Figure 2.27 displays the HDS activity of the studied catalysts. The commercial Ni-Mo/Al_2O_3 catalyst showed highest activity than the transition metal carbides and nitrides for the desulfurization of DBT. The observed catalytic activities follow a sequence of $NiMo/Al_2O_3$ > Mo_2C > WC > Mo_2N > NbC > VC > VN > TiN (*i.e.* group 6 > group 5 > group 4, with very minor ratios of NbC, VC, and VN therefore they haven't been shown in Figure 2.27. In all considered catalysts, the only distinguished product from the HDS of DBT was BPN. Moreover, the inferior HDS activity of the carbides and nitrides may attribute to the uptake of quinolone on the available active sites.

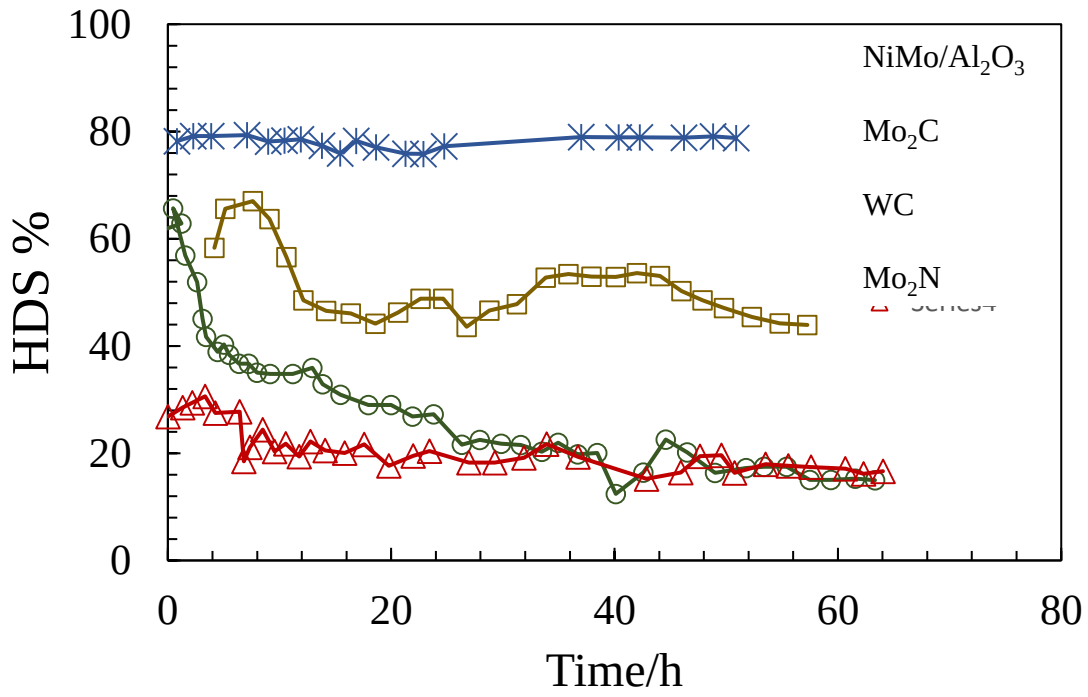

Figure 2.27: HDS activities of carbides and nitrides as compared with $NiMo/Al_2O_3$ at 643K, 3.1MPa, and liquid hourly space velocity (LHSV) of 5 h^{-1} [190].

2.16.1.3 Hydrochlorination (HDC)

The emerging interest in transition metal nitride to promote the production of industrially important aromatic chloroamines, demonstrates a significant importance in the field of catalysts. Of particular interest is the selective hydrogenation of *p*-chloronitrobenzene (*p*-CNB) to *p*-chloroaniline (*p*-CAN).

The Hydrogenation of (*p*-CNB) to (*p*-CAN) comprises two main reaction routs motivating the formation of several intermediates as Figure 2.28 discloses. According to the direct pathway, the hydrogenation of (*p*-CNB) commences via generating chloronitrosobenzene (CNSB) and chlorophenylhydroxylamine (CPHA) as a reaction by-product. Further hydrogen transfer reaction giving rise to the production of (*p*-CAN). Nevertheless, the condensation pathway involves the formation of nitroso, and hydroxylamine intermediates resulting in producing several side products such as chloroazobenzene (CAB) and chlorohydrazobenzene (CHAB), which also subsequently undergo hydrogenation to give (*p*-CAN).

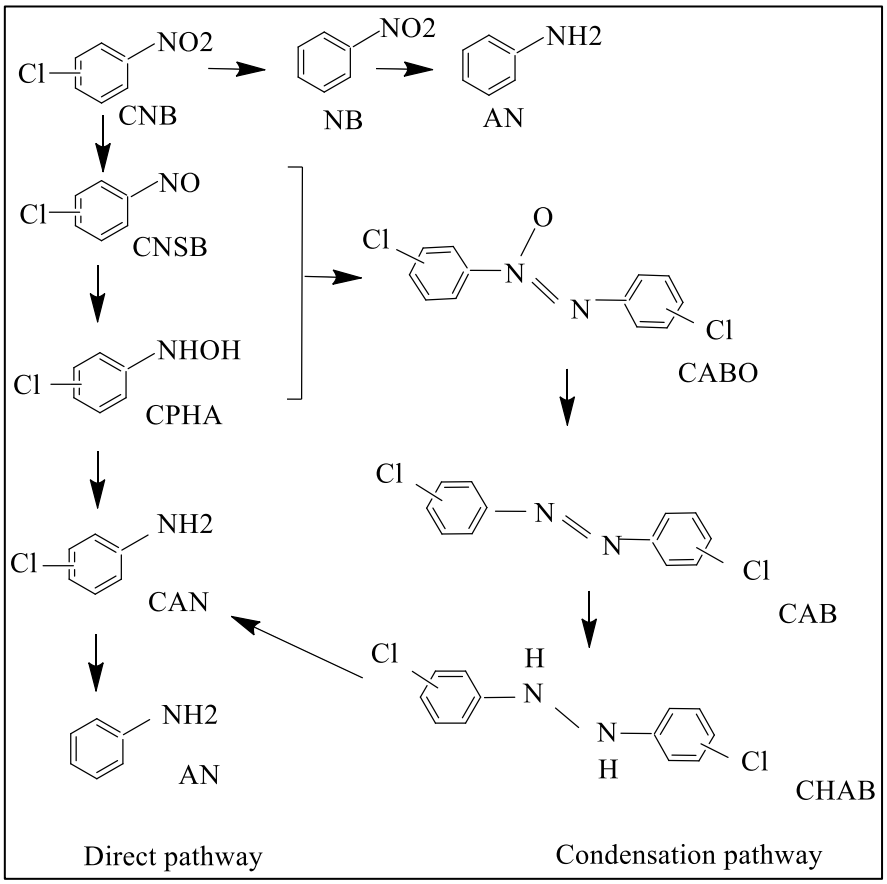

Figure 2.28: Reaction pathways for the hydrogenation of *p*-CNB to *p*-CAN.

Literature reported that selectivity towards the desired haloamines was attained using several catalyst systems, examples including, MgF2/ Ru-Cu catalysts[191], Pd catalysts [192], activated carbon supported Pt(Pt/AC) and Fe promoted Pt (Pt–Fe/AC) catalysts[193], and on Au_{13} and Au_{55} nanoclusters [194], Ni/TiO_2[195]. Additionally, molybdenum and tungsten carbide (Mo_2C, W_2C) and nitride (Mo2N) were prepared from MoO3 and WO3 by temperature-programmed treatment with C_2H_6/H_2 and N_2/H_2 atmosphere. The catalytic action in the gas phase HDC of *1,3*-dichlorobenzene (*1,3*-DCB) to [196]. Results suggest that Ni/SiO_2 favoured concerted removal of both Cl substituents to chlorobenzene had been observed. Wang *et al*.[197] fabricated an onion-like morphology of nanostructured *δ*-MoN catalyst for selective hydrogenation application of functionalized nitroarenes compounds.

2.16.1.3 Hydrodenitrogenation (HDN)

Hydrogenolysis of aromatic and non-aromatic hydrocarbons is currently utilized as a main stream strategy in the production of environmentally friendly fuel that contains no heteroatomic contents, most notably S and N. Central in this strategy is the development of cost-effective catalysts that resists rapid activations and provide high hydrogenation catalytic efficiency [198, 199]. Early studies reported the catalytic performance of high surface area transition metal carbides, nitrides, and borides for quinoline HDN in a batch autoclave reactor[200]. They pointed out that high surface area molybdenum carbide and nitride catalysts were able to effectively remove the N content in quinolone with less hydrogen consumption in reference to commercial Ni-Mo/$A1_2O_3$ catalyst. It has been reported that the structure-sensitivity (*i.e.* site density examined by chemisorption of CO) holds a minor effect on catalytic activity during HDN and HDS reactions. Figure 2:29 shows the quinoline HDN activities of carbides and nitrides as compared with NiMo/Al_2O_3 at 643K and 3.1MPa. It is clearly seen that the HDN activity of Mo_2C was found to be analogous to that of a commercial NiMo/Al_2O_3 catalyst. The identified products from quinoline HDN were hydrogenated quinoline compounds and denitrogenated hydrocarbons [190].

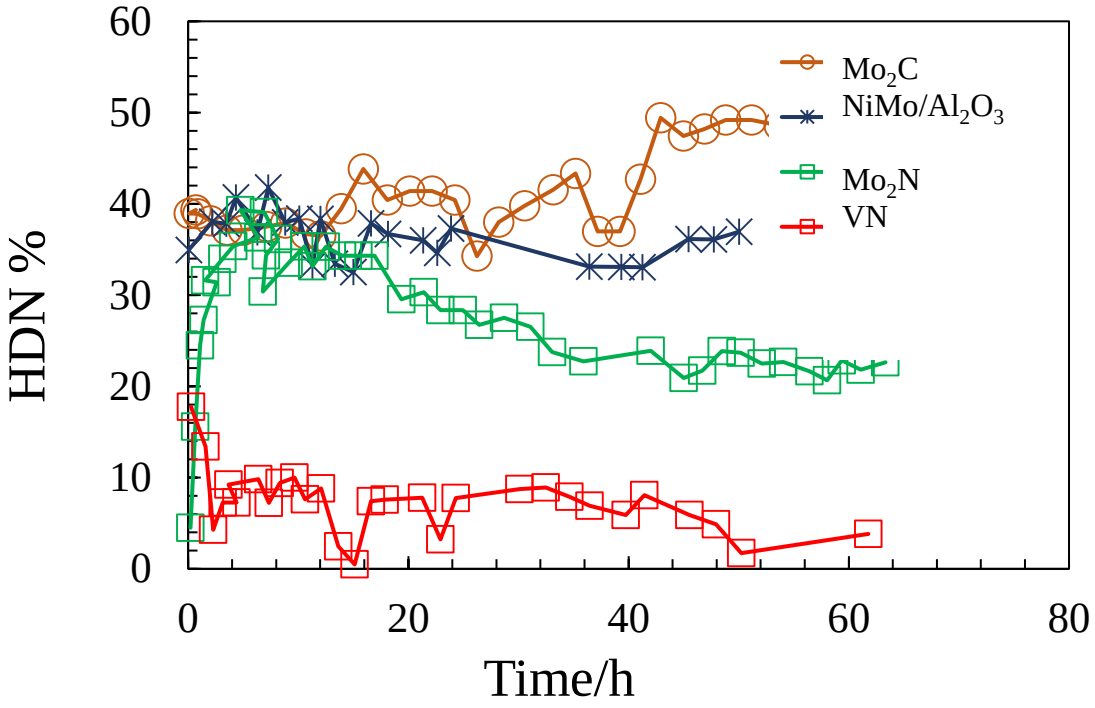

Figure 2.29: HDN activities of carbides and nitrides as compared with $NiMo/Al_2O_3$ at 643K, 3.1MPa, and liquid hourly space velocity (LHSV) of 5 h^{-1} [190].

Lee *et al.* [201] proposed reaction routes for nitrogen removal from quinolone over Mo_2N surface. They explained that quinoline HDN exhibited a high selectivity for the formation of propylbenzene from 1,2,3,4-tetrahydroquinoline instead of propylcyclohexane from decahydroquinoline. Senzi *et al.* [202] reported the HDN behaviour of indole over Mo_2N catalyst. They indicate that Mo_2N exhibits high activity towards the HDN of indole as compared to that of $MoNi/\gamma\text{-}Al_2O_3$ with less hydrogen consumption. Concerning the HDN of pyridine over $\gamma\text{-}Mo_2N$, the major reaction products includes alkanes and pentane [150]. Less H_2 consumption and high catalytic performance in indole HDN has been observed by Li *et al.* [203]. In their study, they tested the HDN's activity and selectivity of indole over *fcc*-Mo_2N prepared by TPR method and sonochemically synthesized *hcp*-Mo_2C. It was concluded that structure, composition and crystallinity of the catalysts play a significant role on the activity and selectivity of indole's HDN.

Nagai *et al.* [170] stated that the activity of Mo_2N strongly depends on surface structure and the availability of active phases which are distinguished to be metallic Mo (modest activity sites) and N deficient (high activity sites). In addition to that, the catalytic performance of 12.5% Mo nitride supported on Al_2O_3 for the HDN of carbazole have been determined [204]. Via the inspection of temperature-programmed reduction, nitrided Mo/Al_2O_3 catalysts showed

a wide peak which deconvoluted to six nitrogen peaks. Four peaks were resulted from the desorption of nitrogen gas on the surface molybdenum species including MoO_2, γ-Mo_2N, Mo metal, and alumina. The extra two peaks were due to nitrogen release from the bulk molybdenum nitride. The activity of nitrided catalysts for the HDN of carbazole was not ascribed to a surface acidity, however, it was concluded that the reduced molybdenum ions Mo^{+2} plays a vital role in the HDN mechanism.

Nagai and Miyao [205] demonstrated that alumina-supported molybdenum nitride catalyst reveals superior activity in the HDN of carbazole at 553-633 K and 10.1 MPa total pressure in reference to the sulfided and reduced treated phases. Figure 2.30 contrasts the HDN's performance of carbazole between several treated conditions including nitrided, sulfided and reduced (*i.e.*, the surface was purged with hydrogen flow then the surface was cooled down prior to the experiment).

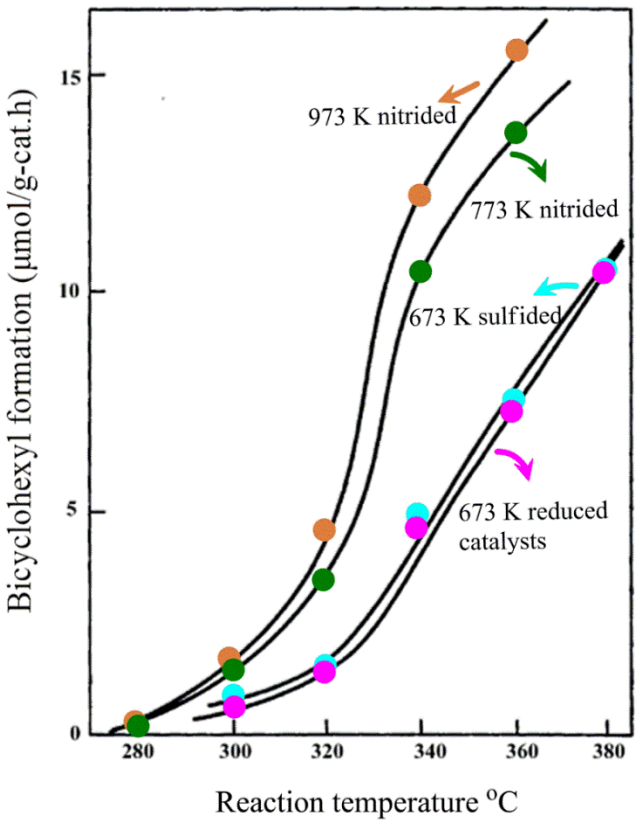

Figure 2.30: The HDN of carbazole [205].

Catalytic decomposition of hydrazine (N_2H_4) over fresh and reduced passivated Mo_2N catalyst were studied [206]. It was suggested that N_2H_4 is adsorbed mainly on the Mo site. Depending on the nitriding temperature, fragmentation of hydrazine affords NH_3 and N_2 at temperatures

below ~ 700 K. Above this temperature, decomposition of ammonia forms hydrogen and nitrogen molecules. Similar products were observed over the Ir/γ-Al_2O_3 catalysts.

2.16.1.4 Hydrodeoxygenation (HDO)

The HDO reaction of oxygen-containing structural entities has been successfully implemented in petrochemical industries on commercial scales [207, 208].

A study conducted by Ghampson *et al.* [209] investigated the influence of nitriding procedure and support on properties in HDO of guaiacol molecule over molybdenum nitride catalysts. The Mo-N catalyst that was synthesised by the N_2/H_2 mixture and ammonolysis routes was reported to be a more active HDO catalyst. This was ascribed to higher dispersion of the molybdenum oxynitride phase. Another study conducted by the same group reported that the un-promoted Mo_2N catalysts with the highest N/Mo concentration affords the maximum activity in the HDO of guaiacol [162]. Furthermore, the HDO activity of guaiacol over alumina- and silica-supported molybdenum nitride catalysts has been reported. The alumina supported nitrides was found to afford significant conversion of guaiacol to catechol whilst, slight catechol production, and maximum phenol production have been detected over silica supported catalysts [210]. Proposed reaction mechanism of guaiacol HDO over Mo_2N supported on commercial activated carbons is depicted in Figure 2.31. It is obviously realized from the figure that the predominant products were phenol and catechol [211].

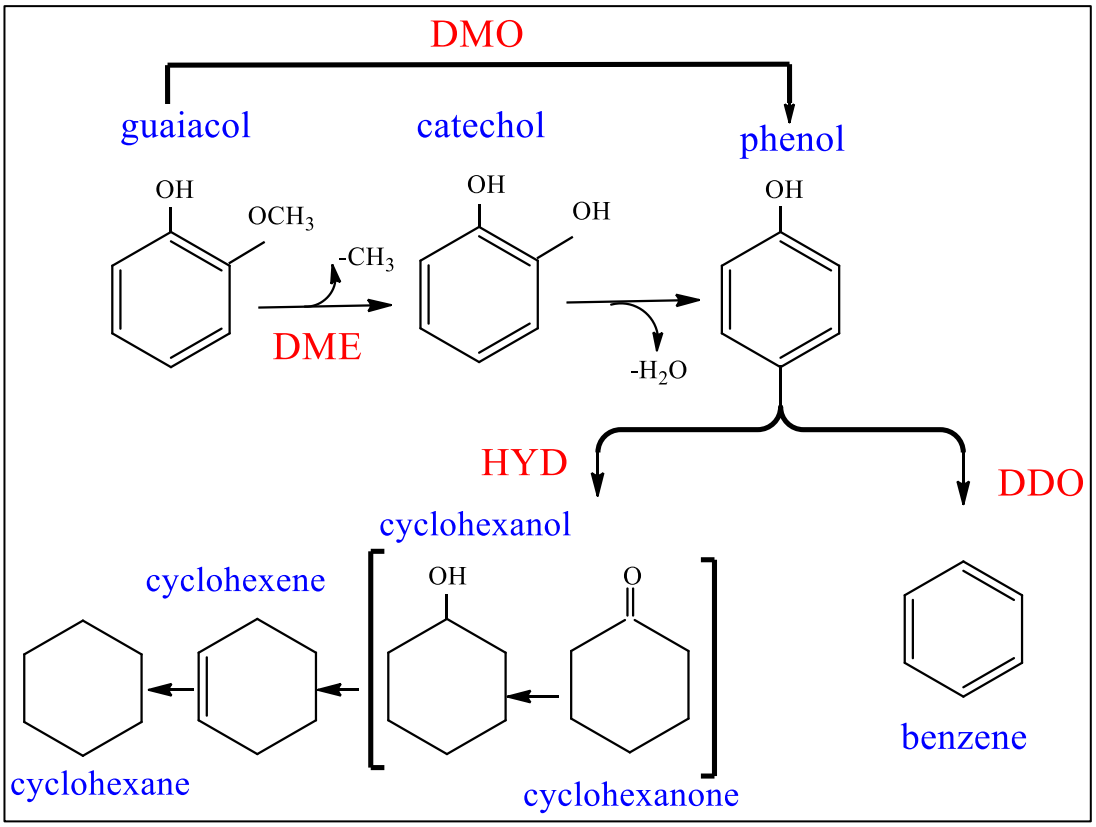

Figure 2.31: The reaction network for HDO of guaiacol [211].

2.16.2 Hydrogen Evolution Reaction (HER)

The proficient production of hydrogen from the electrolysis of water has been a main theme in catalysis research [212-214]. A commercially sustainable production of H_2 from sunlight and H_2O require light absorbers and electrocatalysts made out from inexpensive materials [215, 216]. The typical electrocatalytic systems for H_2 generation integrate noble metals mainly Pt as a catalysts due to superior activity, low over potential and fast kinetics for driving the HER [217] [218]. Not only the high costs but also limited availability of these noble metals hinder their commercial applications [219]. In addition to Pt-based catalysts, non-noble metal compounds have been broadly synthesised and characterized to be applied in the form of supported or promoted catalysts for HER application. Examples including, MoS_2 nanoparticles [220], WC [221], and Pyrene-functionalized Nickel complexes [222], in addition to as metal alloys including Ni and Ni–Mo alloy [223].

The performance of molybdenum or tungsten nitride containing compounds as a catalyst in the hydrocarbons hydrogenolysis was shown to overshoot that of precious metal [150]. A study conducted by Chen *et al.* [224] reported the synthesis of $NiMoN_x/C$ nanosheets by reduction of a carbon-supported ammonium molybdate and nickel nitrate mixture in a tubular oven in H_2 environment at 400ºC, followed by the reaction with ammonia at 700ºC. The prepared heterogeneous catalyst exhibited high HER activity. Moreover, biomass-derived electrocatalytic composites for hydrogen production is an interesting area of research since it combines catalyst made from earth-abundant metals (*i.e.*, molybdenum) and soybeans (a common source of high protein biomass). One of the recently developed catalyst in this regard is the MoSoy [225]. Basically, this catalyst consists of β-Mo_2C phase and an acid-proof γ-Mo_2N phase. The so-called MoSoy catalyst mediates the occurrence of the HER. The merits of this catalyst are high durability in a corrosive acidic solution over exceeding period spanning more than 500 hours. The MoSoy catalyst supported on graphene sheets attains very fast charge transfer kinetics with an overall performance that is in accord with those of Pt for hydrogen production. The development of MoSoy establishes that catalysts with hybrid mixing of transition metals with high-protein biomass is a novel synthesis procedure for materials with potential applications the emerging hydrogen economy. Chen *et al.* [226] stated that the growth of the W_2C–WN nanoparticles onto graphene nanoplates would be more efficient in the HER. The graphene -supported W_2C and WN had an over potential of nearly 120 mV at current density of 10 mA/cm, while the bulk W_2C catalyst required 336 mV at the same current density.

2.16.3 Ammonia Synthesis and Decomposition Reactions

Ammonia currently constitutes a viable hydrogen carrier in potential applications of hydrogen fuel cells. For this reason, synthesis and decomposition of ammonia have been extensively investigated from both fundamental and commercial aspects [227]. Ammonia synthesis reaction represents an industrially important feedstock in the production of strategic chemicals; most notably, fertilizers and nitric acid derivatives [228]. In the opposite-direction process, decomposition of ammonia affords hydrogen molecules in a process that is environmentally friendly as it does not produce the toxic species (*i.e.*, CO). The commercial method to produce ammonia is termed as the Haber process based on the ruthenium (Ru) as catalyst [229]. The Haber process generally involves mild conditions of temperatures, concentrations, and

pressures [230, 231]. Metal nitride catalysts were regarded as better replacement for the Ru-based catalysts [232] based on the involved costs and required synthesis conditions. Their activities are very comparable to those commonly attained on noble-metal [233]. Liang *et al.* [234] fabricated $MoN_x/\alpha\text{-}Al_2O_3$ and $NiMoN_y/\alpha\text{-}Al_2O_3$ catalysts for ammonia decomposition reaction. The demonstrated that the synthesised catalysts were active for ammonia decomposition with 98.7% and 99.8% conversions over nitrided $MoN_x/\alpha\text{-}Al_2O_3$ and $NiMoN_y/\alpha\text{-}Al_2O_3$, correspondingly. Ammonia decomposition activity as a function of Mo loading is depicted in Figure 2.32.

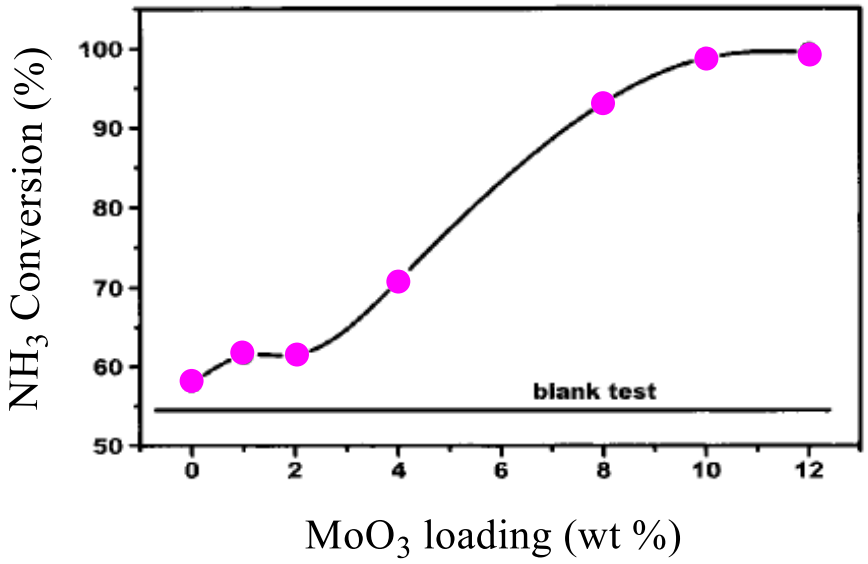

Figure 2.32: Ammonia decomposition over $MoN_x/\gamma\text{-}Al_2O_3$ catalyst with different MoO_3 loading (wt%) at 650 ºC and 1800 h^{-1}GHSV[234].

Tagliazucca *et al.* [61] fabricated molybdenum-based catalysts from MoO_3 and NH_2 to be used in the decomposition of ammonia into hydrogen and nitrogen molecules. Likewise, literature presents several accounts of the catalytic-assisted decomposition of ammonia [235]. It has been postulated that the morphology of fabricated molybdenum nitrides displays slight effect on the catalytic performance for ammonia synthesis [133]. This implies that the nanorod forms of $\beta\text{-}Mo_2N_{0.78}$ and $\gamma\text{-}Mo_2N$ reveal parallel activities. As previously illustrated in various sections of this chapter, prominent steps in the dissociative decomposition of a molecule were assumed to occur over N-vacant sites. Similarly, Podila *et al.* [236] showed the catalyst stability of hydrogen production from ammonia utilising high surface area Mo_2N and Co_3Mo_3N catalysts. Suggesting that at a constant hydrogen production rate, no catalytic deactivation had been noticed for all the prepared catalysts as demonstrated in Figure 2.33.

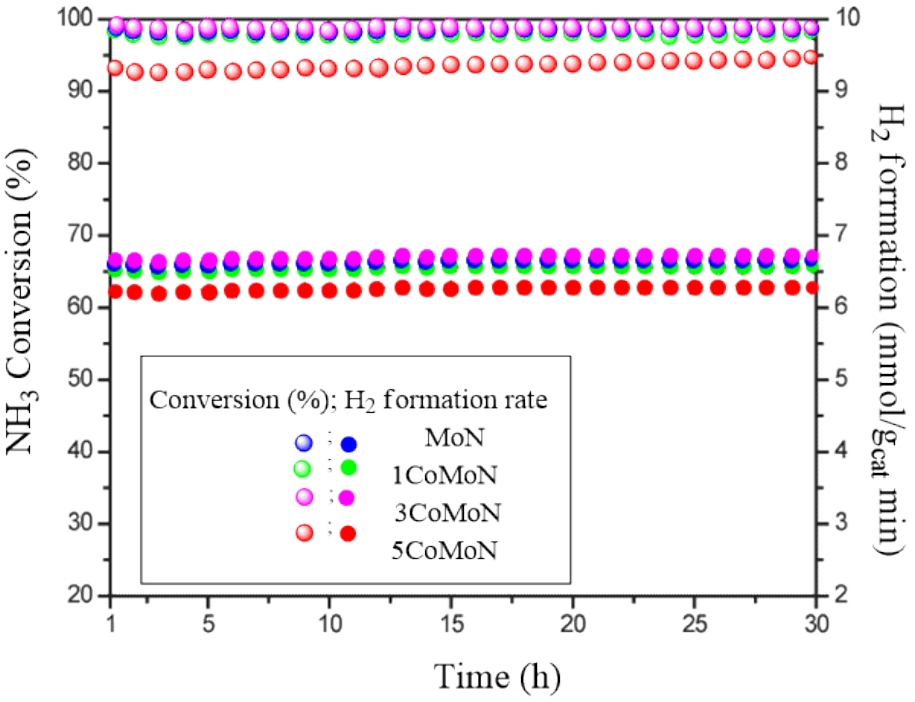

Figure 2.33: Ammonia conversion and the catalyst stability over MoN, 1CoMoN, 3CoMoN, and 5CoMoN catalysts at 600ºC and GHSV of 6000 h^{-1} [236].

2.16.4 Reforming Reactions

Dry (CO_2) reforming of methane (DRM) reaction carries a substantial importance in both scientific and industrial sectors. This reaction converts CH_4 and CO_2 into syngas (*i.e.*, CO and H_2) with low ratio of H_2 /CO:

$$CH_4+CO_2 \rightarrow 2CO+2H_2$$

A wide range of catalysts were utilized to perform this reaction, most notably Ni, Co, Rh, Ru, Pt, and Pd metals. However, these catalysts are highly deactivated owing to carbon deposition and inefficient in terms of high prices and limited availability. Commercial application of the DRM process requires the development of non-noble metal catalysts that resist carbon deposition. While the effect of several operating parameters on the yield of syngas are adequately comprehended, elementary steps involved in the activation and conversion of CH_4 and CO_2 remain highly speculative [237, 238]. Recently, Fu *et al.* [239] synthesised non-precious monometallic and

bimetallic molybdenum nitrides-based catalysts for DRM reaction. Findings indicated that the Mo_2N, Ni_3Mo_3N and Co_3Mo_3N materials were catalytically active toward the DRM reaction at temperature higher than 550°C. Moreover, they observed that the bimetallic nitrides Co_3Mo_3N and Ni_3Mo_3N showed enhanced catalytic activity, stability and resistant to oxidation as compared with molybdenum mononitride. Figure 2.34 shows SEM images of fresh catalysts and temperature versus CH_4 and CO_2 conversion DRM over Mo_2N, Ni_3Mo_3N and Co_3Mo_3N catalysts.

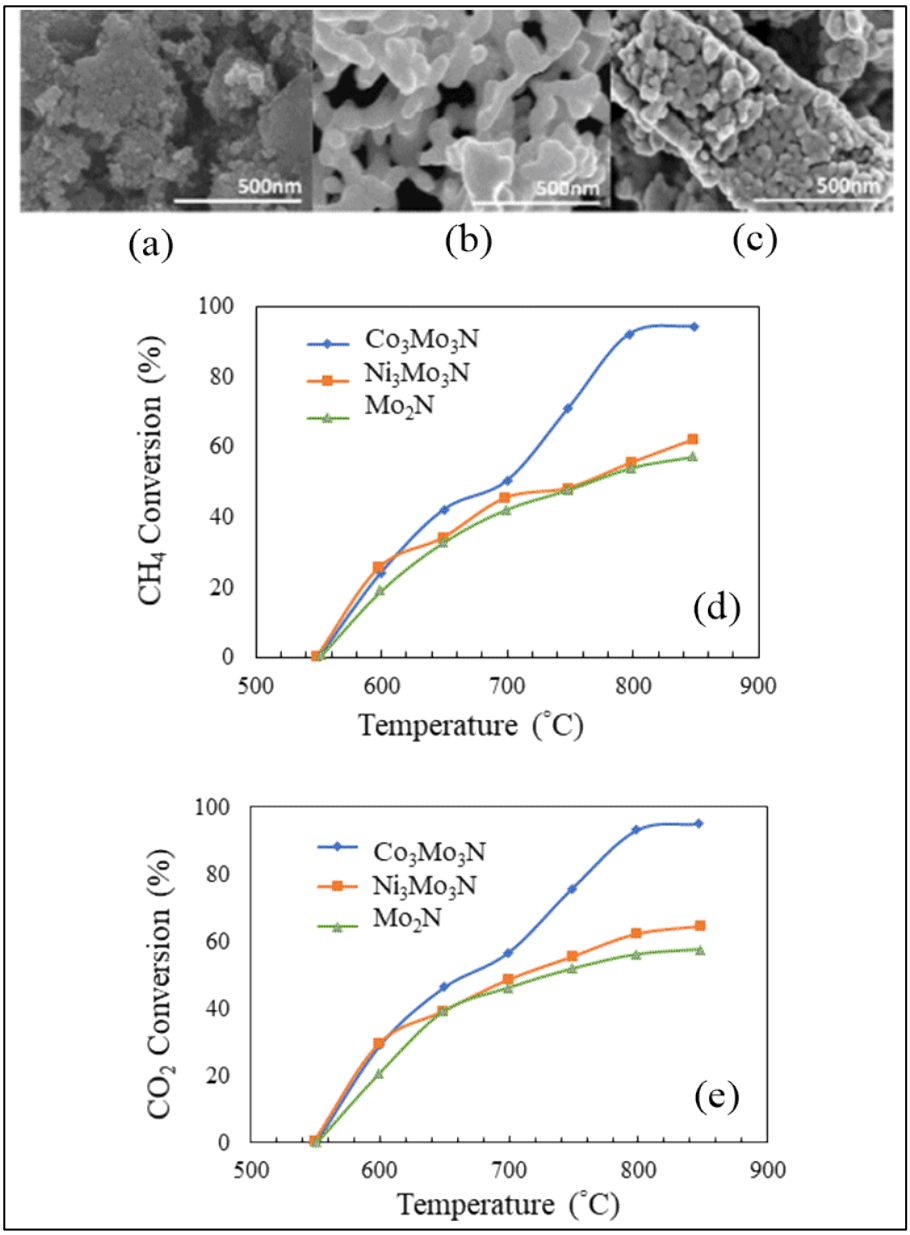

Figure 2.34: SEM morphologies of fresh catalysts (a) Mo_2N, (b) Ni_3Mo_3N, (c) Co_3Mo_3N, (d) temperature versus CH_4 conversion for DRM over Mo_2N, Ni_3Mo_3N and Co_3Mo_3N catalysts (e) Temperature versus CO_2 conversion for DRM over Mo_2N, Ni_3Mo_3N and Co_3Mo_3N catalysts [239].

2.16.5 Oxygen Reduction Reaction (ORR) and Methanol Oxidation Reaction (MOR)

Direct methanol fuel cells (DMFCs) now stand out as a sustainable energy source. In the process of DMFC, adsorbed CO species are produced in the course of electro oxidation of methanol. Polar methanol molecules can diffuse through membrane materials. This in turn gradually blocks the air electrode. A great deal of efforts has targeted synthesis of catalysts that can adsorb produced CO molecules. The high cost incurred from the use Pt-based catalysts has hindered commercialization of DMFCs. The development of innovative non-noble catalysts has the potential to substantially decrease the cost of DMFCs [240].

Xia *et al.* [241] produced cost- effective MoN electrocatalyst with an approximate particle size of 4 nm to be deployed as oxygen reduction catalysts for DMFCs applications via heat treatment of molybdenum tetraphenylporphyrin in the presence of an NH_3 atmosphere at different temperatures (from 600 to 1000 ºC). The electrochemical measurements disclosed that the synthesised MoN catalyst has a durable ORR activity and methanol-tolerant property.

Literature reported the relationship between the structures of molybdenum nitrides and their catalytic activities toward the ORR and MOR. Qi *et al.* [242] synthesized two carbon-supported molybdenum nitrides namely, MoN/C and Mo_2N/C in NH_3 environment. The catalytic activities of the MoN/C and Mo_2N/C in the ORR and MOR operations were examined in O_2-saturated 0.5M$HClO_4$ solution and N_2-saturated 0.5M$HClO_4$ + 1MCH_3OH solution, correspondingly. The stability of the MoN/C and Mo_2N/C in oxygen atmosphere was confirmed via measurements in a fast scanning in O_2-saturated solution. Monometallic hexagonal molybdenum nitrides MoN/C displayed enhanced activities as compared with rock salt type molybdenum nitride Mo_2N/C. This phenomenon was ascribed to either the higher molybdenum valence or a more favourable coordination environment in the hexagonal phase. DFT calculations enabled to gain a molecular level understanding into the relationship between the structures of molybdenum nitrides and their catalytic activities [242]. Findings suggest that both molybdenum nitride phases mediate the dissociation of O_2. The appropriately selected configuration of the MoN and the preferred oxygen adsorption site are contributing factors in the observed high catalytic activity of the MoN/C toward the ORR. Figure 2.35 pictured the highest catalytic activity of MoN/C toward the ORR operation.

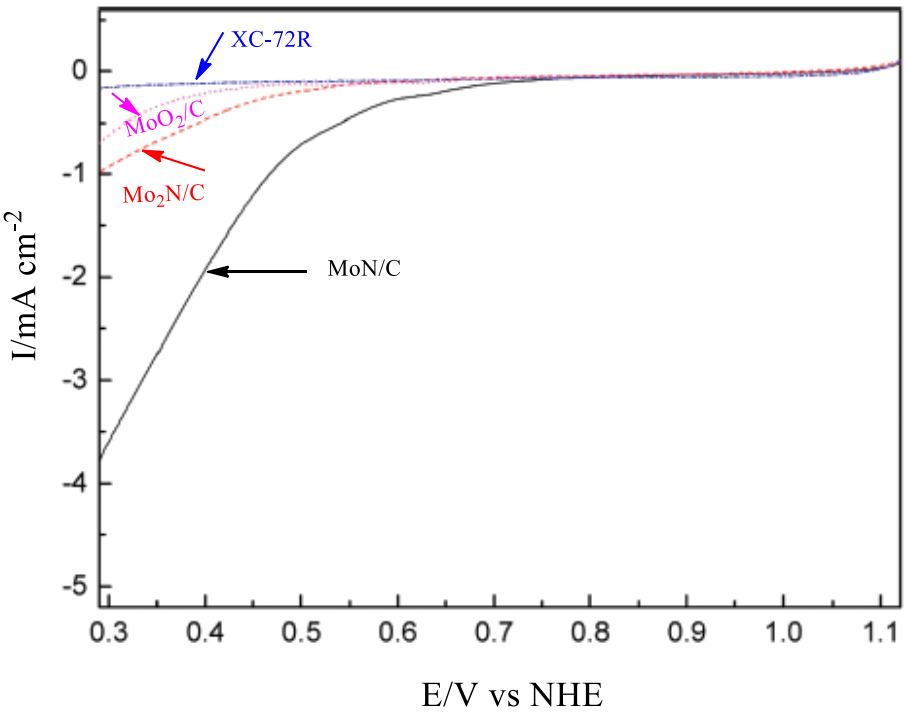

Figure 2.35: ORR curves for MoN/C, Mo_2N/C, XC-72R and MoO_2/C [242].

Cao *et al.* [62] synthesised several monometallic and bimetallic molybdenum nitrides by ammonolysis of several precursors at temperatures ranged from 600-750ºC. Prepared phases included, *δ*-MoN, Mo_5N_6, Mo_2N, and $Co_{0.6}Mo_{1.4}N_2$ to be deployed as electrocatalysts particularly as polymer electrolyte membrane fuel cells (PEMFCs) for the oxygen reduction reaction (ORR). Findings indicate that *fcc*−Mo_2N prepared via MoO_3 displayed poor ORR activity (E_{onset} = 0.420 V) in acid electrolyte while hexagonal *δ*-MoN synthesised by $MoCl_5$ and Mo_5N_6 accordingly exhibited higher ORR activities as can be observed from Figure 2.36.

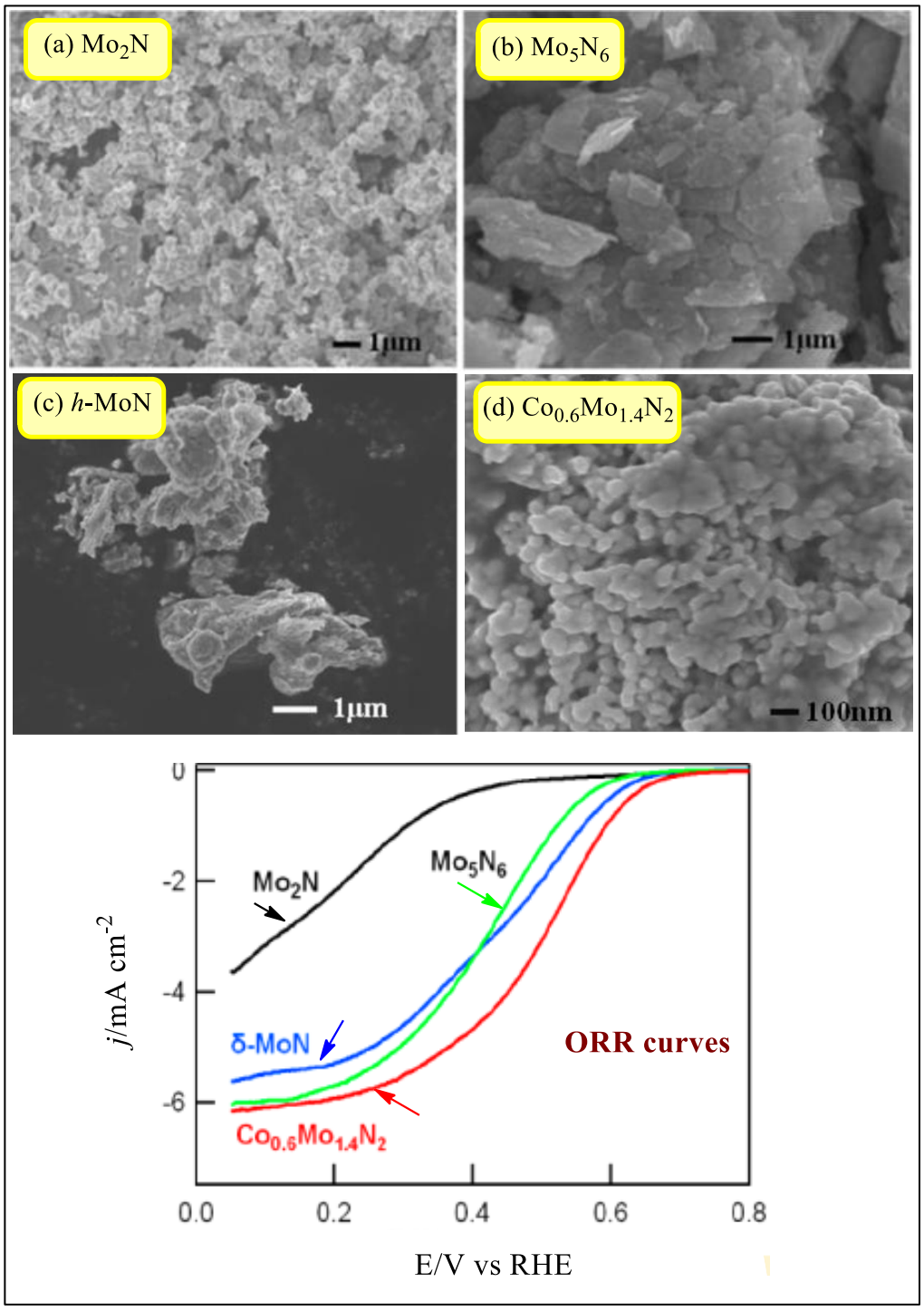

Figure 2.36: SEM images of nitrides Mo_2N, Mo_5N_6 and δ-MoN, and $Co_{0.6}Mo_{1.4}N_2$. The bottom figure refers to Linear sweep voltammetry curves [62].

2.17 Gap in Current Knowledge

1- Great deal of literature has been devoted to investigating structural and electronic properties of bulk molybdenum nitride, however, thermo-elastic and optical properties of this material haven't been investigated. To underpin this, theoretical predictions of volume dependent is necessary to acquire thermo-mechanical properties at high temperatures (up to melting point) and high pressures (up to 12 GPa).

2- Literature presents no account on surface, bulk properties and thermodynamic stability trends of molybdenum-nitride MoN and tungsten nitride WN. For this reason, electronic and structural, phase stability diagram, vacancy formation energies of hexagonal phases of MoN and WN surfaces have been comprehensively studied in this thesis.

3- The catalytic role of molybdenum nitride γ-Mo_2N catalysts in facilitate cleaving various chemical bonds is very critical and has been evaluated experimentally. However, the underlying mechanisms governing these reactions are yet to be established. In the following chapters of the thesis, I provided detailed mechanisms for various surface-mediated hydrogenation reactions. This includes selective HYD of acetylene over γ-Mo_2N (100) and (111) catalytic surface, HDS of thiophene over (111) γ-Mo_2N surface, and the reduction mechanism of *p*-chloronitrobenzene (*p*-CNB) to *p*-chloroaniline (*p*-CAN). The overall aim is to attain an insight into the experimentally acquired chemical conversion values and the reaction routes that are catalysed by a stand-alone Mo-N system.

4- Motivated by the fact that, the influence of dopant elements is expected to improve material's properties, it is required investigating optical properties of Cr-Mo-N thin films with various molybdenum concentrations using sputtering techniques coupled with theoretical-based elucidation.

Chapter 3 Research Methodology

The supercomputer

3.1 General Introduction

Computational chemistry combined with experimental techniques is becoming the major and backup power that contributes to design new materials at a macroscopic level. Simulation modelling motivates widespread interests and plays a distinct role in material science, since it facilitates conducting calculations that are hard to be achieved experimentally via selecting the proper methodology. Density functional theory (DFT) is an effective and efficient approach emerged to solve many body problems and to calculate the electronic structure. *Ab* initio atomistic thermodynamics find direct applications of materials at realistic operational conditions. In this chapter, I briefly summarize the theories behind the development of these tools, followed by a terse picture of the implemented computer codes within the framework of this thesis (*i.e.*, DMol^3, VASP, and CASTEP codes). From another prospect, characterization facilities including XRD, XPS, FESEM, UV_vis, and FTIR hold great advantages in providing insightful information about crystalline phases, surface chemistry, and morphologies, etc. Therefore, I'll concisely look at the principal concepts of those tools. Figure 3.1 displays the flow chart of the methods that utilized in this thesis.

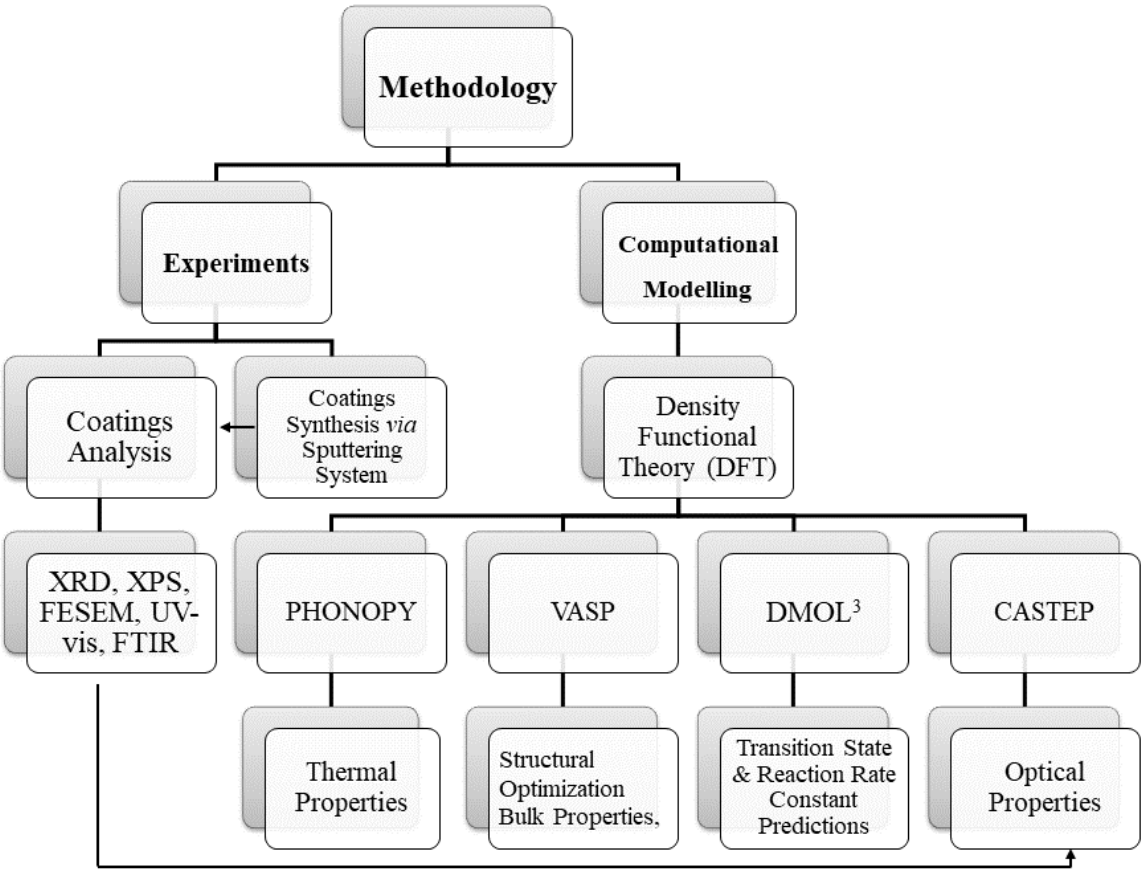

Figure 3.1: The research methodology chart.

3.2 Theoretical Section

3.2.1 Schrödinger Equation

In 1926, Erwin Schrödinger attempts to describe the "matter waves" behaviour, when employed de Broglie's relations to describe plane waves. Afterward, the most general form of the famous equation named as Schrödinger equation has been emerged [243]. According to quantum mechanics, the well-known time-dependent (non-relativistic) Schrödinger equation can be written as:

$$\frac{-\hbar^2}{2m}\left(\nabla^2 + V(r,t)\right)\psi(r,t) = -i\hbar\frac{\partial}{\partial t}\psi(r,t) \qquad 3.1$$

Where, $\hbar$ represents reduced Planck's constant (1.05457×10^{-34} J/s^{-1}), m refers to the mass of the particle, ∇^2 signifies Laplacian operator (kinetic energy of the system), $V(\boldsymbol{r},t)$ indicates to the potential energy of the system in which the particle is moving, $\psi(\boldsymbol{r},t)$ corresponds to the wave function of the system, i denotes imaginary number, $-i\hbar\frac{\partial}{\partial t}$ symbolizes the energy operator; $\boldsymbol{r}$ stands for position vector; t designates time. The equation above resembles an eigenvalue problem, with two unknown quantities ($\boldsymbol{r}$) and its time derivative $-i\hbar\frac{\partial}{\partial t}\varphi(\boldsymbol{r},t)$. These two unknown quantities must be figured out to simultaneously satisfy equation 3.1 Planck's constant is a quantised angular momentum. Its existence in any equation suggests that this equation is subjected to quantum mechanics effect.

The operator on the left hand of the Eq. (3.1) can be given according to the partial differential with respect to x, y, and z coordinates as shown below;

$$\nabla^2 = \left(\frac{\partial^2}{\partial x^2} + \frac{\partial^2}{\partial y^2} + \frac{\partial^2}{\partial z^2}\right) \qquad 3.2$$

By solving the Schrödinger equation, the energy of the system and many other properties can easily be obtained. Equation 3.1 can be re-formulated to not include the time (*i.e.* the time-independent version of Schrödinger equation) can be written as;

$$H\varphi(\vec{r}) = E\varphi(\vec{r}) \qquad 3.3$$

Where $\varphi(\vec{r})$ refers to wave function (*i.e.* wave function of many-body system), *E* denotes the total energy of the system and $\hat{H}$ is the Hamiltonian operator for a molecular system which consists of the summation of the kinetic energy ($\hat{T}$) and ($\hat{V}$) potential energy.

The Hamiltonian operator can be formulated as;

$$\hat{H} = \hat{T} + \hat{V} \quad 3.4$$

$$\hat{H} = \frac{-\hbar^2}{2m}(\nabla^2 + V) \quad 3.5$$

For many body problem, the kinetic energy operator $\hat{T}$, is the summation of ∇^2 for all particles (electrons and nuclei) involved in a system.

$$\hat{T} = \frac{-\hbar^2}{2m}\sum_k \nabla_k^2 \quad 3.6$$

$$\hat{T} = \frac{-\hbar^2}{2m}\sum_k(\frac{\partial^2}{\partial x_k^2} + \frac{\partial^2}{\partial y_k^2} + \frac{\partial^2}{\partial z_k^2}) \quad 3.7$$

$\hat{V}$ signifies the potential energy and it refers to the coulomb repulsion between each pair of charged particles;

$$\mathrm{V} = \frac{1}{4\pi\epsilon_0}\left[\sum_i \sum_{j<i}\left(\frac{e^2}{\Delta r_{ij}}\right) + \sum_I \sum_{J<I}\left(\frac{Z_I Z_J e^2}{\Delta R_{IJ}}\right) - \sum_i \sum_I \left(\frac{Z_I e^2}{\Delta r_{iI}}\right)\right] \quad 3.8$$

Herein, *e* and *Z* correspond to electron charge and nucleus charge of *Ze* (*Z* is the atomic number), respectively. *Δrij* denotes the distance between two pair of electrons and Δ*R*IJ states to the distance between two nuclei. The first term in Eq. 3.8 describes electron-electron repulsion; the second term stands for nuclear-nuclear repulsion while the last term represents electron-nuclear attraction.

$$H = -\frac{\hbar^2}{2m}\sum_i \nabla_i^2 - \sum_{i,I}\frac{Z_I e^2}{|r_i - R_i|} + \frac{1}{2}\sum_{i\neq j}\frac{e^2}{|r_i - r_j|} - \sum_I \frac{\hbar^2}{2M_I}\nabla_I^2 + \frac{1}{2}\sum_{I\neq J}\frac{Z_I Z_J e^2}{|R_I - R_J|} \quad 3.9$$

With m and M_I represent the electron mass and nuclei mass, respectively. r_i and R_I designate the positions of electron and nuclei. The charges of electron and nuclei are indicated to be *e* and Z_I correspondingly. The equation above refers to the Hamiltonian operator for the molecular system. Due to the electron-electron repulsion term in the equation above, the limitation of Schrödinger equation is that it can be solved and applied exactly only for the simplest cases, *i.e.* hydrogen (H) atom, however, an accurate wave function needs to be applied for atoms such as (helium and lithium). However, for the many-body problem, approximations or numerical calculations must be implemented in atoms of higher atomic number[244].

3.2.2 Density Functional Theory (DFT)

It is mainly used by physicists working on condensed systems, solid state physics, quantum chemistry and nanotechnology. In fact, the publications conducted using DFT has gained an increasing interest since last three decades. Various material properties and purposes can be addressed spanning from electronic structure to catalytic activity. DFT deals with the electron density $\rho(r)$ that can be measured experimentally. Implying that, ground-state properties (*i.e.* $T = 0K\ , P = 0$) and in particular the ground-state energy as a functional of the electron density in order to evaluate different electron properties of the molecule. By using this method, it becomes easy to calculate the ground state properties of many body systems, such calculations can be performed for atomic, molecular and crystal structures. Moreover, for an N electron system, the wave function depends on $3N$ coordinates whereas electron density $\rho(r)$ depends only on 3 coordinates. The attractive feature is that it converts the many-body system into a system of non-interacting fermions in an effective field. In addition to consuming much less time in calculating various properties of complex systems compared to other Quantum Mechanics methods which are predominant in the case of small clusters of atoms. Within the framework of DFT, there are two ways of calculating ground-state properties by employing either time-independent DFT or the time-dependent TDDFT. A major component in successful DFT calculations is the selection of the optimal approximation for the exchange-correlation functional which arises from the Kohn-Sham approach. Therefore, Schrodinger equation should be solved to get the wave functions of the system [245]. The first formulated Model in which the total energy of a system is described by its electron density are described mathematically by Thomas and Fermi [246].

3.2.3 Density Functional Theory with Dispersion Correction (DFT-D)

Non-bonded interactions such as dispersion van der Waals (vdW), is of vital importance in assessing the structure and stability of various systems including adsorption of molecules on surfaces, however, computational modelling of those interactions is not an easy task. Presently, high-level quantum-chemical wave functions and approximations are required for proper prediction of vdW interactions. While, the correct long-range interaction tail (for example for separated molecules) is absent from all popular corrected exchange-correlation (XC) functional of DFT such as, local-density approximation (LDA), generalized gradient approximation (GGA) and the Hartree-Fock (HF) approximation which underestimate to correctly describe the long–range dispersion interaction between molecules[247]. However, due to the failure of

the aforementioned approximations to consider the long-range correlation interactions, density functional methods are anticipated to significantly miscalculate the interaction energies for molecules on graphitic surfaces. In recent years, several hybrid semi-empirical approaches that provide the best combination between the cost of first principles evaluation of the dispersion terms and the need to improve non-bonding interactions in the standard DFT description have been introduced. The state of the art in the semi-empirical correction methods is represented by the dispersion correction have been proposed by Grimme (G06) [248], Jurecka *et al.*[249]. Ortmann, Bechstedt, and Schmidt (OBS)[250], and Tkatchenko and Scheffler (TS) [251].

3.2.4 Ground State Properties Predictions of Materials at 0K via DFT

DFT plays a powerful role in determining the ground state properties of a material via solving the fundamental equations of quantum mechanics in an effective mode. It allows for dealing with unit cells comprising up to 1000 atoms, which opens the opportunity to deal with bulk, surfaces, alloys, and lattice defects by computer [252, 253]. In regard to the bulk properties of a material, the initial task when performing DFT calculations is to achieve the lowest energy configuration by approaching a proper methodology. In the present section, special attention is paid on mechanical properties of periodic systems. The study of elasticity of transition metal nitrides has attracted spatial interest in materials science, solid state physics and chemistry [254]. It describes the macroscopic response of crystals to external forces and directly relates to hardness and strength of materials. Symmetry plays an important role in determining the number of elastic constants needed to describe the elastic response of crystalline materials. Usually, cubic crystals require three elastic constants: C_{11}, C_{12} andC_{44}. Hexagonal crystals require five and trigonal and tetragonal crystals require six or seven depending on the point group. Orthorhombic crystals require nine constants and monoclinic crystals require thirteen [255]. Elastic modulus is the ratio of the stress and strain in the elastic region where the strain increases linearly with stress. If the material is subjected to elastic deformation, the material will return to the original dimension once the applied load is removed. The mechanical properties of most solids and alloys under hydrostatic pressure provide valuable information about the binding characteristic between adjacent atomic. Based on *Ab* initio molecular dynamics, elastic constants are calculated for single crystals using the Reuss and Voigt approaches we can obtain expressions below to calculate the elastic modulus [256]. Chapter

four of this thesis will comprehensively describe the governing equations, however, some important relations to calculate mechanical properties are shown in the equations below;

$$B = B_V = B_R = \frac{1}{3}(C_{11} + 2C_{12}) \quad 3.10$$

Shear modulus $G = \frac{G_V + G_R}{2}$ 3.11

Where $G_V = \frac{(C_{11}+C_{12}+3C_{44})}{5}$ and $G_R = \frac{5(C_{11}-C_{12})C_{44}}{4C_{44}+3(C_{11}-C_{12})}$ represent Voigt and Reuss approaches, respectively.

Young modulus $E = \frac{9BG}{3B+G}$ 3.12

Poisson's ratio $v = \frac{3B-2G}{2(3B+G)}$ 3.13

Anisotropy ratio $A = \frac{2C_{44}}{C_{11}-C_{12}}$ 3.14

3.2.5 Ab initio Atomistic Thermodynamics and Phase Stability Diagram

In material science and engineering, multiscale simulation of material properties has emerged as one of the outstanding challenges. It is well-known that DFT calculations are performed at T = 0 K and P = 0 kPa, however, in reality, materials experience harsh environment (*i.e.* high pressure and temperature). Under these operational conditions, a material might exhibit various characteristics. To this end, knowledge of macroscopic scale of material based on microscopic analysis necessitates covering a very broad range of time and length scales (*i.e.* at each length and time-scale, well-established and efficient computational approaches are required) [257].

In this thesis, the *Ab* initio atomistic thermodynamics approach is implemented. Detailed accounts relevant to this approach is found on literature [258, 259]. A brief discussion will be presented focusing mostly on the main equations. In one-component gas phase and at a certain temperature and pressure, $\gamma(T, P)$ surface free energies linearly relay on the chemical potential of nitrogen, $\mu_N(T, P)$;

$$\gamma(T,P) = \frac{1}{2A}\left[G^{slab}(T,P,N_M,N_N) - N_M E_{MN}^{bulk} - (N_N - N_M)\mu_N(T,P)\right] \quad 3.15$$

According to the above formula, the surface Gibbs free energy at a given temperature and pressure, γ (T, P) alters with the chemical potential of nitrogen. In the above formula, $G^{slab}(T,P,N_M,N_N)$ denotes the energy of the studied surface, N_M, N_N stand for the number of metallic and non-metallic atoms in the slab, respectively. E_{MN}^{bulk} refers to the energy of bulk compound per formula unit and $\mu_N(T,P)$ denotes to the chemical potential of nitrogen. The chemical potential of nitrogen is calculated based on;

$$\mu_N(T,P) = \Delta\mu_N(T,P) + \frac{1}{2}E_{N2} \quad 3.16$$

The change in chemical potential of nitrogen $\Delta\mu_N(T,P)$ is extracted from thermodynamic NIST tables[260].

3.2.6 Quasi-Harmonic Approximation (QHA)

Recently, application of DFT calculations in materials science has greatly expanded owing to the development of high-performance computers and the emerging of an accurate and DFT codes, a large set of first principles calculations are now practical with the precision comparable to experiments using ordinary computers. Results from DFT calculations, describe electronic structure, energy, and the force on each atom in a system. In crystals, it is assumed that atoms travel around their equilibrium positions with displacements [261]. In solid state physics, the quasi-harmonic approximation (QHA) is a phonon-based model that illustrates the volume-dependent thermal effects, such as the thermal expansion. It assumes that the harmonic approximation holds for every value of the lattice constant (*i.e.* the harmonic approximation is applied at each volume) [262, 263]. For the solid phase, the Helmholtz free energy at equilibrium lattice volume *V* and temperature *T* is usually describes as [264, 265];

$$F(V,T) = E_C(V) + F_{vib}(v,t) + F_{Ele}(V,T) \quad 3.17$$

Where V refers to the volume, T denotes the temperature, $E_C(V)$ corresponds to the static energy at $0K$, $F_{vib}(v,t)$ implies the vibrational contribution to Helmholtz

energy, $F_{Ele}(\mathrm{V},\mathrm{T})$ describes the thermal electronic contribution to free energy. The Helmholtz energy is commonly used for systems held at constant volume. Different thermodynamic properties as the relationship between volume and temperature, heat capacity at constant pressure, and thermal extension coefficients can be obtained. Using phonopy results of thermal properties, thermal expansion and heat capacity at constant pressure can be calculated under the (QHA) collects the values at volumes and transforms into the thermal properties at constant pressures and/or temperatures. The procedure is based on the small displacement method, and can be used in combination with any program capable to calculate forces on the atoms of the crystal[266].

3.2.7 Transition State Predictions

The capability of solid surfaces to form and split bonds in molecules, from the atmospheres, is the basis for the phenomenon of heterogeneous catalysis. Transition state determinations provide an insight into the nature of chemical reactions. However, the conversion of the reactants into products, leave behind some changes on the product geometry, including, the length or an angle or a combination of angles and/or bond lengths. Starting from the reactants, the energy increases relevant to the catalytic performance of various compounds. It has been observed that only trivial portion of collisions produce a reaction. The amount of energy required for a chemical reaction to commence is known as the activation energy. Furthermore, the geometry equivalent to this energy is called the transition state geometry. If the added energy was not enough to the reactants to approach the energy barrier, it is impossible for the reaction to proceed. Along the reaction pathway, transition state structures play a crucial role in understanding and designing chemical reactions. It is of significant to locate the transition state configuration and energy at other stationary points (reactants and products) since it allows attaining thermochemical and kinetic factors. A schematic diagram for the potential energy surface is shown in Figure 3.2.

Transition state theory (TST) was first established in 1935 by Eyring [267]. Via TST approaches, the challenges of calculating a reaction rate for a hardly happening elementary reaction by dividing space into two lowest energy states termed as, the initial state (IS) and the final state (FS). The reactant region (IS) describes the general region in which the system can be found before reacting, and the product region (FS) denotes to what is thought of as a product

of the elementary reaction in question. The border between the two regions shows the transition state (TS).

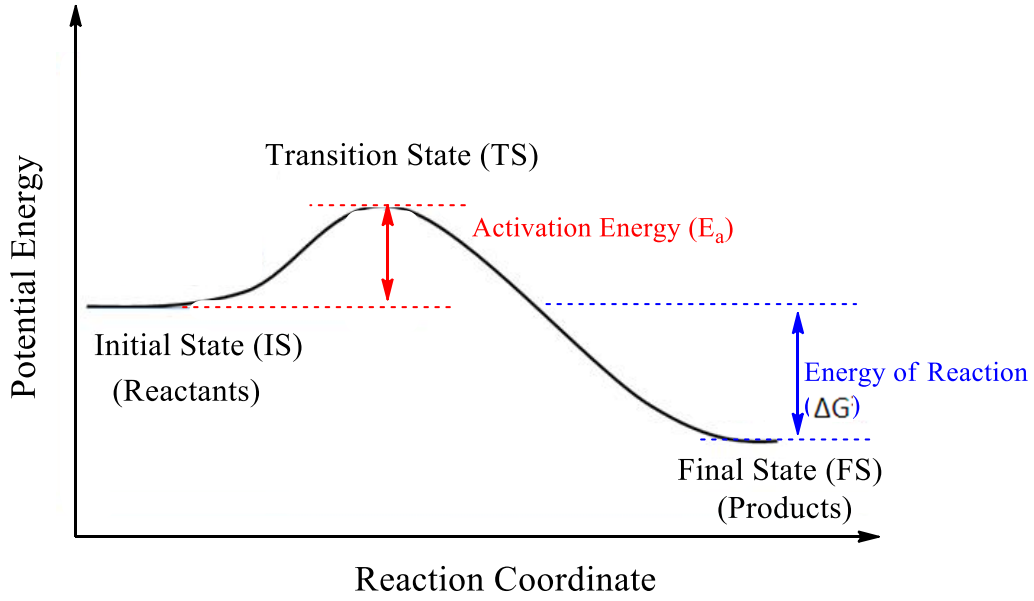

Figure 3.2: Potential energy as a function of reaction coordination.

Moreover, the reaction rate constant in the present study is calculated within the framework of transition state theory (TST) [268]. This theory is first developed in 1935, it reports that there are three kinds of treatments; (1) thermodynamic treatments, (2) kinetic-theory treatments, and (3) statistical-mechanical treatments. The TST proposes that there is a thermodynamic equilibrium between the reactants and the transition structure and the rate of the reaction is proportional to the concentration of particles in the activated complex state or the transition state. The transition state geometries (TSs) were obtained by a combination of the linear synchronous and quadratic synchronous transit LST/QST methods[269]. Nowadays, the influence of temperature on the rates of chemical reactions is almost always interpreted in terms of what is now known as the Arrhenius equation. According to this, a rate constant k is the product of a pre- exponential "frequency" factor A and an exponential term [270]. In another expression, the reaction rate constant in the TST can be calculated via vibrational frequencies yielding activation enthalpies and entropies as a function of selected temperatures between reactants and products based on the formula: $k\ (T)\ =\ A\ exp\ (-Ea\ /\ RT)$. Where, Arrhenius parameters (A-factors and activation energy, Ea) can be estimated by fitting reaction rate

constants, $k(T)$ with the inverse of temperature *(1/T)*. Figure 3.3 presents computational simulation flowchart using DFT.

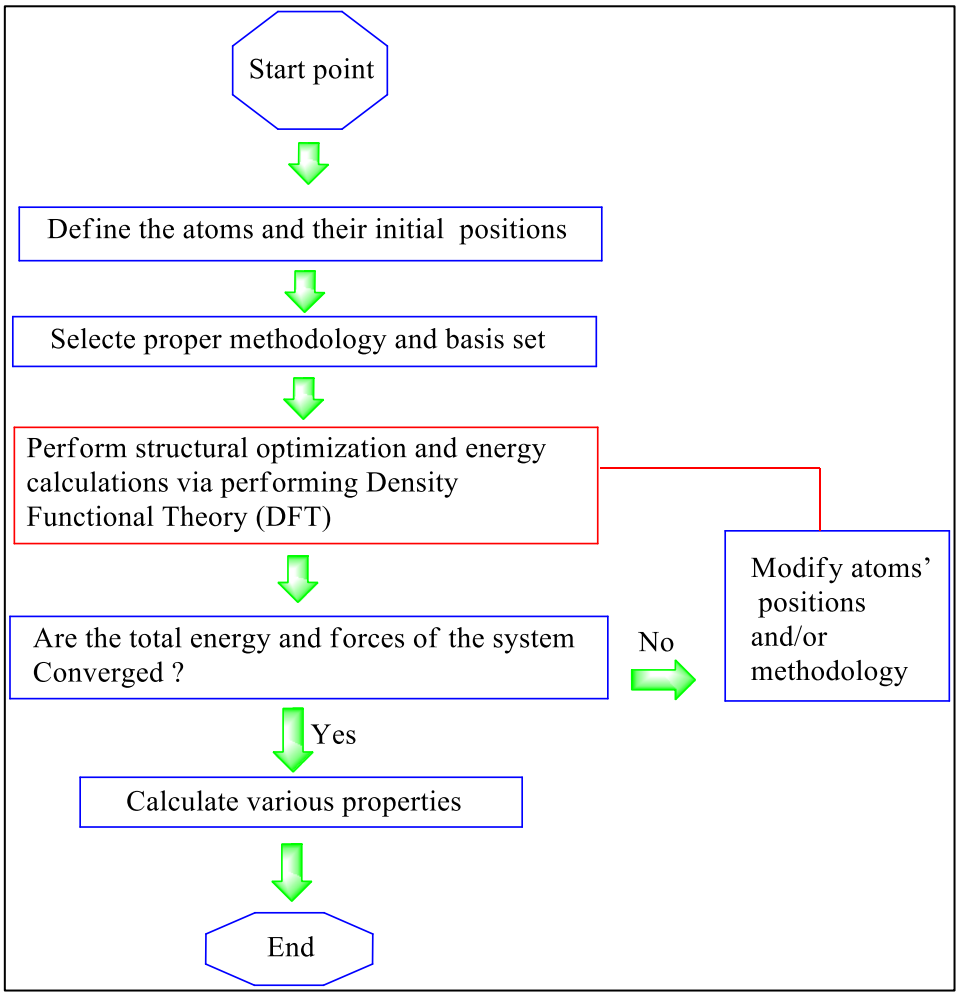

Figure 3.3: Computational simulation flowchart using DFT.

3.2.8 Codes Supporting DFT

Owing to the high performance computers and developing precise and efficient computational modelling approximations, computer codes have witnessed rapid developments resulted in releasing an array of various packages such as ABINIT[271], Quantum Espresso [272], Amsterdam Density Functional (ADF)[273], Gaussian, DMol^3[274], Crystal^{14} [275], CASTEP[276], and VASP[277] were released with different operating systems as Windows,

Linux, and Mac. In this thesis, we are focusing on the software probably used to perform the modeling in this work which is DMol^{3,} VASP, CASTEP, and PHONOPY.

3.2.8.1 DMol^3

DMol^3[278] is a DFT-based modeling program, to simulate chemical processes and model the electronic structure and energetics of a broad range of systems such as, organic and inorganic molecules, crystals (*i.e.* 3D periodic structures), solids, and surfaces. DMol3 can achieve number of calculations and tasks hastily and precisely including, single-point energy calculation, geometry optimization, elastic constants calculations, spin-restricted and unrestricted calculations, molecular dynamics, transition-state optimization/search, a reaction path, reaction kinetics. Furthermore, DMol^3 also able to predict various properties of chemical reaction for instance, heats of reaction, energy barriers, bond orders, charges, and adsorption energies.

Several functionals have been implemented in DMol^3, that are;

1-Local functionals; the specific local functionals provided in DMol^3 are the VWN [279] and PWC [280].

2-Gradient-corrected functionals (GGA); those non-local functionals offer a considerable increase in the accuracy of predicted energies and structures, but with further computation time.

Examples of the most popular non-local functionals involved in DMol^3 package are;

Perdew-Wang generalized-gradient approximation (PW91) [280]. BP Becke exchange plus Perdew correlation (BP)[280, 281]. Perdew-Burke-Ernzerhof correlation Perdew (PBE) [282]. Revised PBE functional (RPBE) [283]. PBE functional optimized for solids (PBEsol) [284]. Hamprecht, Cohen, Tozer and Handy functional Boese and Handy (HCTH) [285]. Becke exchange plus Lee-Yang-Parr correlation (BLYP) [281, 286].

3-Hybrid functionals are supported by DMol^3; for example, the B3LYP functional attempts to improve the exchange-correlation energy functional by combining a portion of exact exchange from Hartree-Fock theory along with exchange and correlation contributions from other, mainly local functionals [287, 288].

DMol^3 allow four options to treat core electrons, which are;

- **All electrons:** is a term used to reflect considering all electrons in the calculations; *i.e.*, valence and core electrons are treated equally. (no special treatment of cores electrons).
- **Effective core potentials (ECP):** substitutes core electrons by a single effective potential, reducing the computational cost. ECPs introduce some degree of relativistic correction into the core [289, 290].
- **All electrons relativistic:** comprise all electrons explicitly and introduce some relativistic effects into the core. (*i.e.* the most accurate and the most computationally expensive option).
- **DFT Semi-core Pseudopots (DSPP):** replaces core electrons by a single effective potential, reducing the computational cost. DSPPs introduce some degree of relativistic correction into the core [291].

$DMol^3$ uses a localized numeric basis sets to describe the atomic orbital basis set that will be used in the calculation. In terms of accuracy and rapidly, they span from low accuracy and fast computation time to high accuracy but expensive computation, minimal basis set (MIN), double numerical (DN), double numerical plus d-functions (DND), double numerical plus polarization (DNP) and triple numerical plus polarization (TNP) where additional polarization functions are applied over the DNP basis set. Furthermore, three sets of dispersion correction methods (DFT-D) are considered in $DMol^3$, namely, TS, Grimme, and OBS.

3.2.8.2 VASP

VASP (Vienna Ab-initio Simulation Package)[292] is one of the popular simulation codes a package for performing *Ab*-initio quantum mechanical calculations using pseudopotentials (all-electron strategies are permitted) and a plane wave basis set. This code deals with a variety of systems including, zero-dimensional (molecules), one-dimensional (polymers), two-dimensional (slabs), and three-dimensional (3D; crystals). Electronic structure and energy calculations from the first principle can be achieved. In addition, a diversity of density functionals is available, such as, Hartree–Fock. Furthermore, a very efficient implementation of global hybrids, such as popular B3LYP and PBE0 treatments, allows for such calculations to be performed at relatively low computational cost.

3.2.8.3 CASTEP

CASTEP stands for Cambridge Serial Total Energy Package, this code is designed and written to meet both academic and commercial requirements [276, 293]. Electronic minimisation of crystalline solids, surfaces, molecules, liquids and amorphous materials can be performed via implementing density functional theory (DFT) calculations together with choosing a proper plane wave basis set. This code allows for utilizing exchange and correlation effects in electron-electron interactions via either the local density or generalized gradient approximations, (LDA) and (GGA), accordingly. Furthermore, CASTEP can efficiently envisage various properties including lattice parameters, elastic constants, band-structures, density-of-states, charge distributions and optical properties.

3.2.8.4 PHONOPY

Phonopy is an open source code implementing number of thermodynamic relations combined with (QHA) to evaluate thermal spectra of materials, including, the linear thermal expansion coefficient, constant volume heat capacity C_V, constant pressure heat capacity C_P, entropy S, etc. This code can handle force constants obtained by density functional perturbation theory (DFPT) from VASP outputs to compute the vibrational frequencies. Phonon properties with essential governed equations are described in Ref.[294]. Figure 3.4 shows the capability of Phonopy code in obtaining various thermal properties.

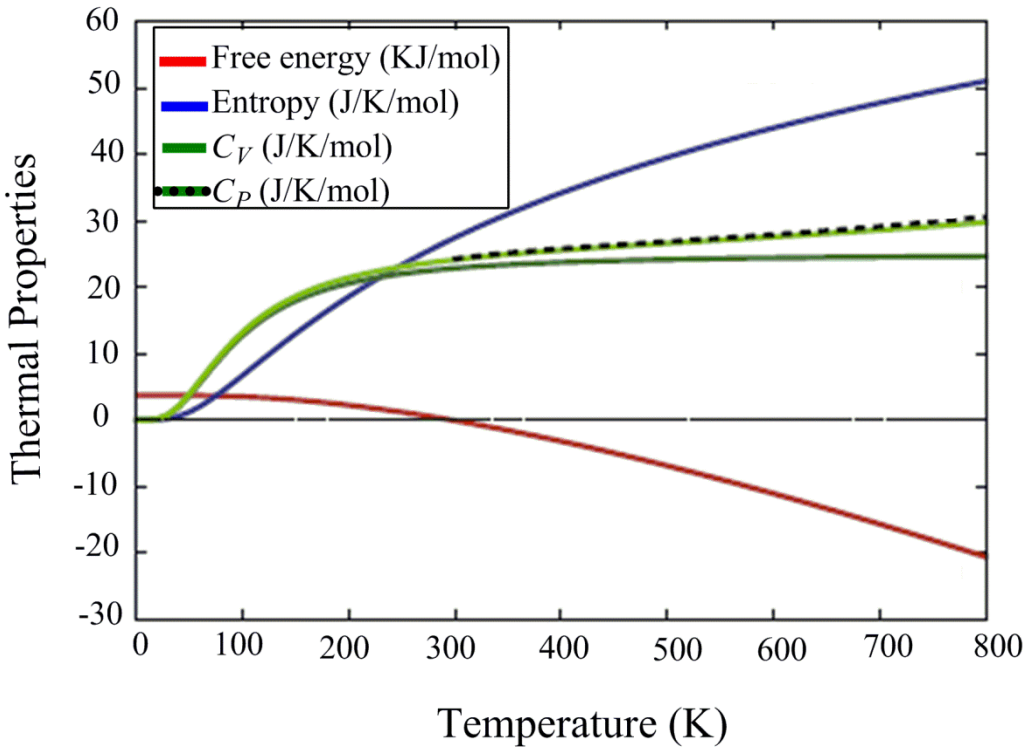

Figure 3.4: A typical thermal properties computed via Phonopy code[294].

3.3 Experimental Section

3.3.1 Sample Preparation by Magon Sputtering System

Physical vapour deposition (PVD) represents one of the key vacuum deposition technologies utilised nowadays to fabricate high quality and uniform films. PVD-based techniques tolerate depositing wide range of materials including metals, alloys, ceramic, and polymers onto various substrates such as glass, silicon, stainless steel, *etc.* Typically, to enable the deposition process to take place successfully, a high vacuum of about 10^{-2}-10^{-4} millibar and temperature of 150 to 500 ºC are required. Sputtering is the most widely employed method to fabricate high quality and adherent coatings. Sputtering process initiates by glowing discharge plasma that generates energetic ions and momentum transfer between the ions and atoms in the material. Mainly, when atoms are knocked from a target (cathode), after being bombard with energetic particles (*i.e.* ions) [88, 227, 295]. However, it proceeds when the desired surface (substrate) to be coated is placed in a vacuum chamber containing an inert gas (*i.e.* Ar^+ as working gas). Then, negative charge is applied to a target source material that will be deposited onto the substrate causing the plasma that is located in front of the target to glow. The

bombardment process causes the removal of target's atoms, which will condense on a substrate as a thin film [228, 229, 296]. Secondary electrons are also emitted from the target surface as a result of the ion bombardment. These electrons are involved in this process by maintaining the plasma. In brief, the incorporation of plasma technique with sputtering method, greatly enhances the formation of the films at early stages of condensation and nucleation [297]. To enrich the sputtering process, a magnetic field configuration positioned in a way that the plasma can be confined in front of the target. This technique is called magnetron sputtering. The word magnetron implies that the targets are placed in a magnetic field to avoid the loss of electrons in the plasma. As a result, the produced magnetic field traps the electrons in the plasma (*i.e.* plasma whose electrons are confined by magnetic fields), in a region between the target and the substrate, and hence the Ar^+ ions could be more efficiently ionised. This permits working at low gas pressures and low target voltages [298]. Window and Savvides [299, 300] investigated the effect of varying the magnetic arrangement in a conventional magnetron by reinforcing the outer ring of magnets relative to the central pole. In this case, some electrons in the plasma were no longer trapped to the target zone but were able to track the magnetic field lines and flow out towards the substrate. Consequently, ion bombardment at the substrate was increased followed by improving the coating structure. By applying the unbalanced magnetron arrangements, high quality coatings can be successfully deposited because of transporting high ion currents to the substrate [301].

In this thesis, the UDP650 closed field unbalanced magnetron sputtering (Teer Coatings Ltd, UK) facility installed at the City University of Hong Kong was utilised to deposit Cr-Mo-N coatings studied in this thesis. Cr-Mo-N coatings were deposited onto Si (100). Two elemental Cr and one elemental Mo have been deployed as target materials. The recorded background pressure prior to coating before the deposition process and working gas pressure during sputtering were set at 4×10^{-4} Pa and 0.15 Pa, respectively. Ar (99.999 %) is used as working gas for sputtering and the flow rate is fixed at 50 sccm and N_2 (99.999 %) is used as reactive gas to form nitrides fixed at 60 sccm. Optical emission monitor (OEM) is used to control dynamically the reactive gas (N_2). Detailed preparation procedure was given in Chapter 9 of this thesis.

3.3.2 Characterization Techniques

The main characterization techniques that interest us in this dissertation are shown below;

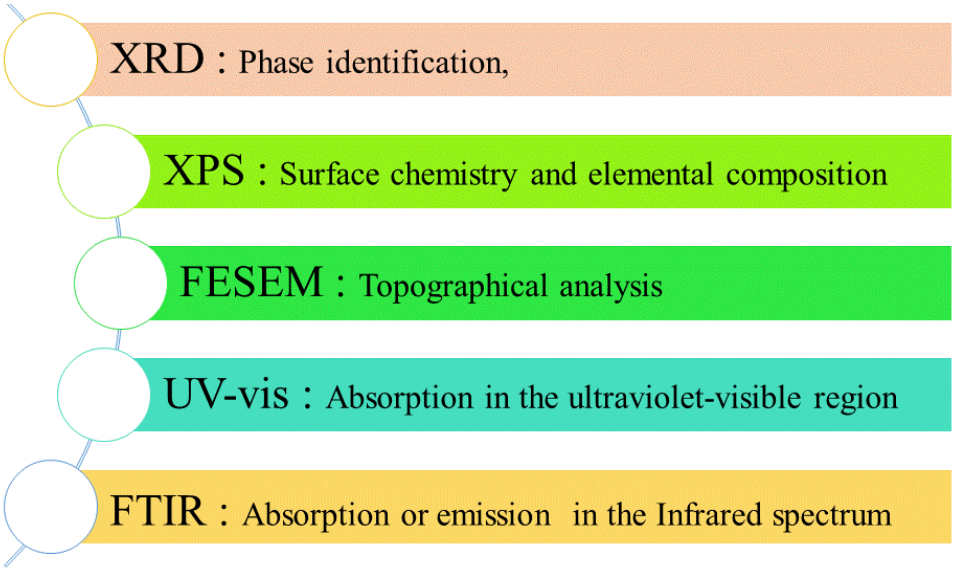

Figure 3.5: The characterisation techniques that used in this thesis.

3.3.2.1 X-ray Diffraction (XRD)

XRD is one of the fundamental and most popular characterization techniques widely deployed for the phase identification and determination of lattice parameters of a crystalline material [302]. Generally, the principle that governs this non-destructive instrument is constructive interference of monochromatic scattered X-ray beam with an incident angle (θ) and wavelength (λ) and a crystalline material. This interference proceeds when the X-ray beam hitting the crystalline material resulted in generating XRD pattern[303, 304].

It is well known that Bragg's law links the wavelength of electromagnetic radiation with the diffraction angle and the lattice spacing in a crystalline material. The angle between the incident and diffracted ray, however, plays distinctive role in diffraction-based methods. When conditions satisfy the criteria of Bragg's Law ($n\lambda=2d\ sin\ \theta$), where n symbolizes an integer number, λ denotes the wavelength of the incident X-ray radiation, d represents the inter-planar distance (d-spacing) and θ signifies the angle between the incident radiation and the surface of the specimen which is also called (Bragg's angle). The interaction of the incident X-ray beam with the sample yields constructive interference. Consequently, the diffracted X-ray can be

detected. Moreover, when scanning the crystalline material within a range of *2θ*, all possible diffraction orientations of the lattice can be detected. Converting the diffraction peaks to *d*-spacings permits the identification of the crystal because each crystal has a set of unique *d*-spacings [305].

In this dissertation, powder diffraction XRD, Bruker AXS D8 Advance, Germany, installed at Curtin University of Technology as shown in Figure 3.6, has been utilised to perform XRD measurements. The wavelength was determined by LynxEye detector with a Cu-*Kα* radiation source for rapid detection. The operating voltage and current were fixed at of 40 kV and 40mA, accordingly. The scan parameters used for phase identification such as, scan range 2*θ* (degree) extending 7.5 – 90, step size (degree) of 0.015, and 0.2 s was the interval time per each step. Collected crystalline phases were identified by using the Search/Match algorithm, DIFFRAC.EVA 3.2 (Bruker-AXS, Germany) to search the Powder Diffraction File. The software is linked to the ICDD crystallographic database Powder Diffraction File (PDF4+ 2016 edition) identified by matching the diffraction peaks with data reported in ICDD.

From the collected XRD data and based on the Debye-Scherrer equation[303], the crystallite size of the film at the reflection plane that exhibits the highest intensity can be determined from XRD data as shown below;

$$D_g = \frac{k\,\lambda}{\beta\,\cos\theta} \qquad 3.18$$

where, *k* refers to Scherrer constant that depends on the crystal's shape *(in our films, k* = 0.90), β corresponds to full width at half maximum (FWHM) of Bragg peak and λ signifies wavelength of X-ray beam.

Figure 3.6: Powder diffraction X-ray diffraction (XRD), Bruker AXS D8 Advance.

3.3.2.2 X-ray photoelectron spectroscopy (XPS)

XPS is a key surface analysis technique, mainly implemented to determine chemical bonding state, elemental composition of the scanned sample such as oxidation state and provide information about elements that involved in the sample's surfaces. In XPS measurements, the sample is located in a high vacuum environment and the beam of low-energy X-ray irradiates the sample and produces photo-ionization. The energy of the ejected photoelectrons is a function of its binding energy and is characteristic of the element from which it was emitted[306]. Basically, when a high energy photon (such as in the X-ray range) inelastically collides with an atom, the atom is converted into an excited state. Such a state is not stable and an atom spontaneously de-excites losing the excess energy. This de-excitation can take place in several ways, one of which is the emission of an electron (in this effect known as a photoelectron).

Herein, Kratos Axis Ultra DLD XPS spectrometer (Manchester, UK) operated with an Al-Kα monochromatic radiation Al (photon energy = 1486.6 eV) source has been utilised. The XPS machine was operated at a power of ~10 mA and ~15 kV and equipped with a cold stage, and an Ar ion gun for etching the coatings is shown in the following Figure 3.7. The X-rays irradiate the sample at an incidence angle of about 45°. The analysis chamber was set at a uniform pressure of 2.9 $\times 10^{-9}$ Torr. The collected XPS spectra were analysed using CASA XPS software.

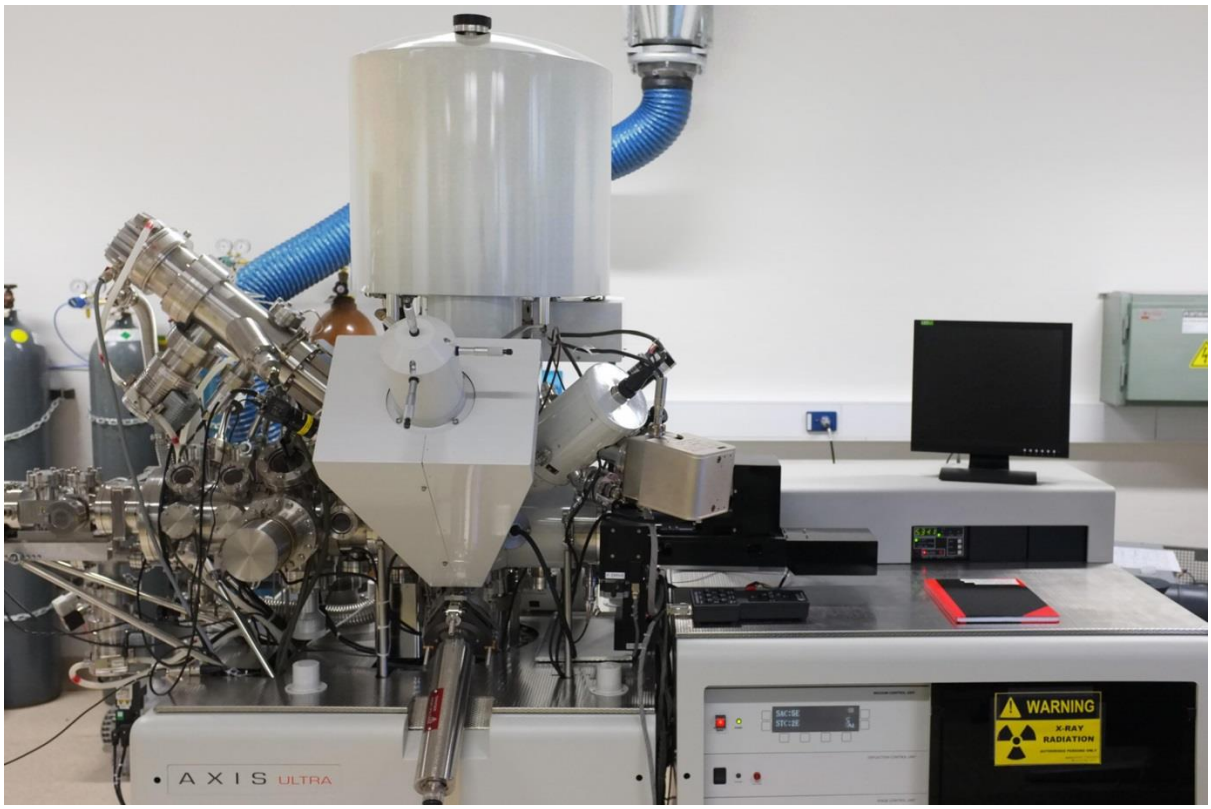

Figure 3.7: Kratos Axis Ultra DLD XPS spectrometer.

3.3.2.3 Field Emission Scanning electron microscope (FESEM)

Field emission scanning electron microscopy (FESEM) is a technique employed to image and investigates the morphological and topographical features of coating materials which provides crucial information regarding the growth mechanism, shape and particle size of the coating

materials. This instrument functions with relatively low applied voltages and small working spaces. A field emission source in FESEM instrument ejects the so- called primary electrons, in elevated vacuum column, and targets the selected material. In addition, the electrons are undergone to acceleration process via applying an intensive electrical field component. In order for the primary electrons to be in a narrow beam concentrating and hitting the studied object, electronic lenses are installed to achieve this aim. The electron bombardment of the material will result in emitting secondary electrons that would be captured or detected by a detector equipped for this purpose. This detector in turn will produce a signal that is going to be subsequently amplified and converted to a video scan-image providing good characteristic information about the morphologies and topographies [307, 308].

3.3.2.4 Ultraviolet–visible spectroscopy (UV-vis)

Ultra violet visible spectroscopy (UV-vis) is a tool utilized to shed light on the optical properties of a solid in the ultra violet visible range of the electromagnets spectrum such as, reflectance, absorptance, and transmittance. Data obtained from UV-vis spectroscopy is useful to estimate the solar selectivity of a material used in solar panel applications for instance. Furthermore, the transmittance data derived by UV-vis are utilized in electrochemical industries such as batteries [309].

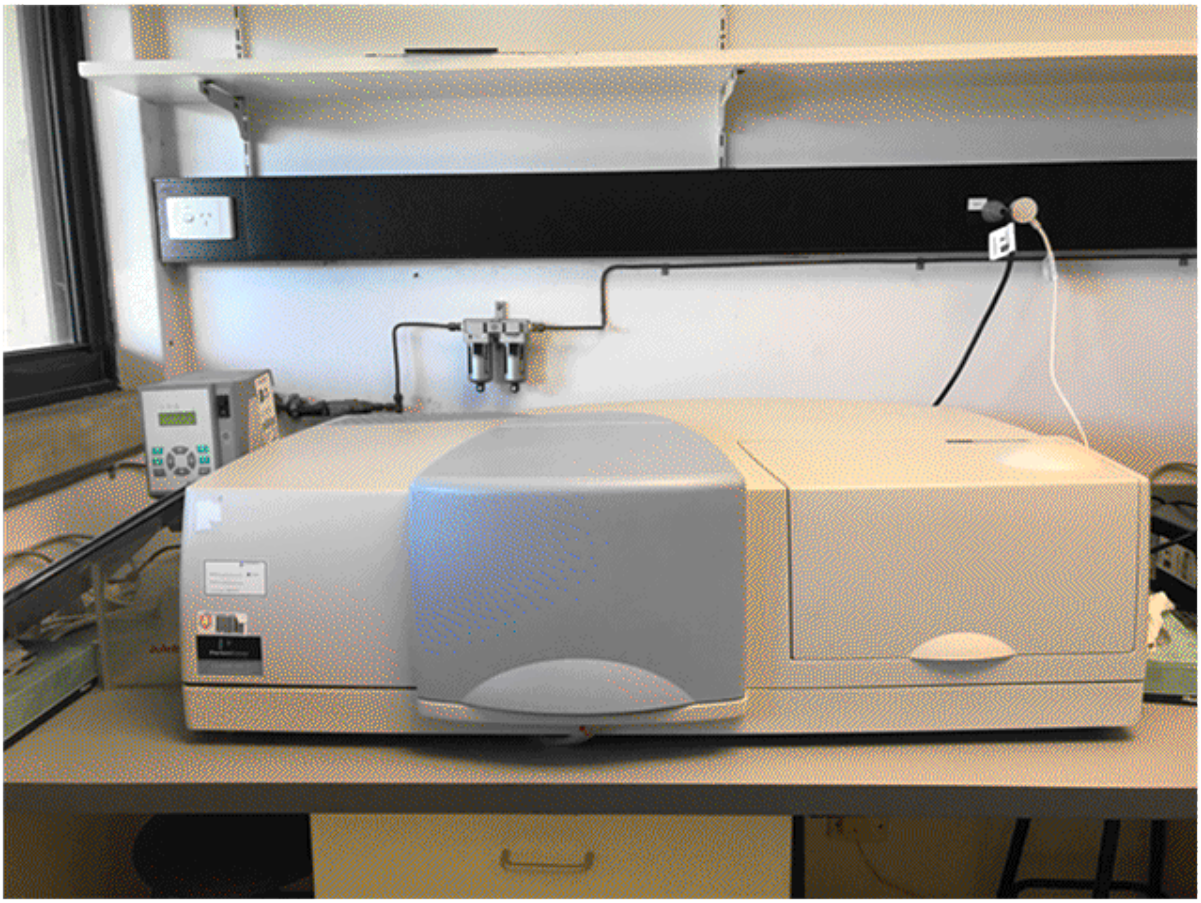

Figure 3.8: UV-vis machine.

3.3.2.5 Fourier-transform infrared spectroscopy (FTIR)

Fourier-transform infrared spectroscopy (FTIR) is an important technique deployed to survey the optical properties such as the emittance for a material in deferent phases, solid, liquid and gas. It must be mentioned that FTIR provides information about the chemical groups present in the material as these functional groups are bonded by energy values reside in the range of infrared wave length. In this technique, a source emits a broad infrared range of electron frequency of infrared on the material. Then, FTIR measures the amount of energy being absorbed by the material or determines those specific wave lengths resulting in exploring the chemical functional groups in the material [310].

Figure 3.9: FTIR machine.

Chapter 4 : Thermo-Elastic and Optical Properties of Molybdenum Nitride

Paper I

Zainab N. Jaf, Zhong-Tao Jiang, Hussein A. Miran, and Mohammednoor Altarawneh ***Thermo-elastic and optical properties of molybdenum nitride.*** Canadian Journal of Physics, 2016, 94 (9). pp. 902-912.

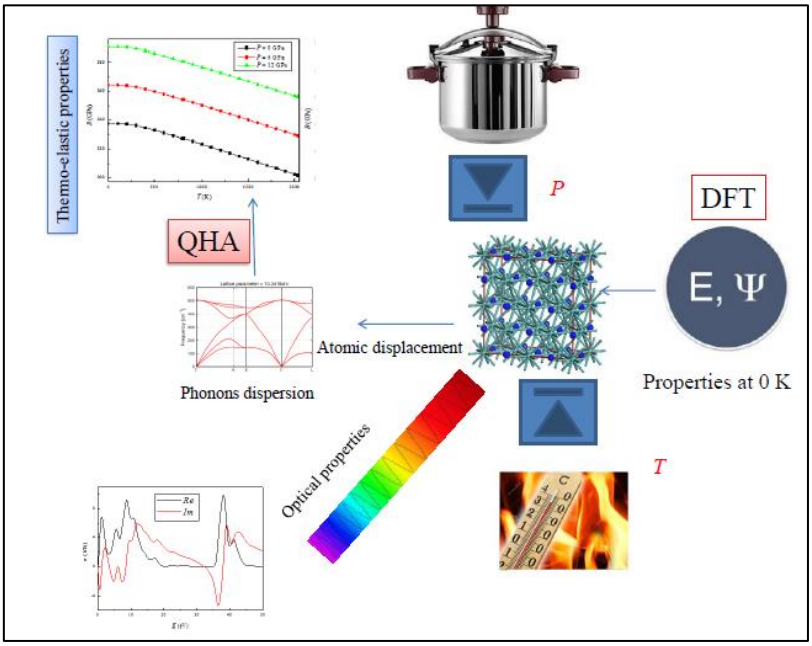

4.1 Abstract

This chapter aims to investigate volume-dependent thermal and mechanical properties of the two most studied phases of molybdenum nitride (c-MoN and h-MoN) by means of the quasi-harmonic approximation approach (QHA) via first principles calculations up to their melting point and a pressure of 12 GPa. Lattice constants, band gaps, and bulk modulus at 0 K match corresponding experimental measurements well. Calculated Bader's charges indicate that Mo–N bonds exhibit a more ionic nature in the cubic MoN phase. Based on estimated Gibbs free energies, the cubic phase presents thermodynamic stability higher than that detected for hexagonal, with no phase transition observed in the selected *T–P* conditions as detected experimentally. The elastic stiffness coefficients of MoN in hexagonal structure revealed that it is stable elastically; in contrast to the cubic structure. The temperature dependence on the bulk modulus is more profound on the dense cubic phase than on the hexagonal phase. Overall, the two considered structures of molybdenum nitride display very minimal harmonic effects, evidenced by the slight variation of thermal and mechanical properties with the increase of pressure and temperature. The optical conductivity of both phases near a zero -photon energy coincides well with their metallic character inferred by their corresponding DOSs curves. It is expected that the thermo-elastic properties of saturated molybdenum nitrides reported in this study will aid in the continuous pursuit to enhance their catalytic and mechanical utilizations.

4.2 Introduction

Owing to an array of remarkable properties, molybdenum has been in the centre of a great deal of research as it constitutes the parent metal of various carbides, sulphides, and nitrides [311]. Of particular importance is molybdenum nitride which assumes direct and prominent applications in harsh operating media such as those encountered in turbine engines, cutting tools, and potent heterogeneous catalysts in many reactions such as, hydrodenitrogenation (HDN) [312]. Furthermore, molybdenum nitride displays high hardness (28 - 34 GPa) [313], high melting point (2023 K), superior chemical stability, and high superconducting transition temperature[314, 315]. The unit cell of bulk MoN belongs to five various stoichiometric and non-stoichiometric crystal structures. This includes a non-stoichiometric cubic NaCl structure (a space group of Fm3m, in which Mo atoms are arranged in fcc lattice while N atoms occupy

octahedral sites, having one formula unit in a unit cell). Furthermore, a CsCl configuration and zinc blende ZB–oriented structure with space group of Pm3m and F43m, respectively. On the other hand, it also exhibits hexagonal structures, as disordered WC-like structure with the composition of δ_1-MoN and space group P6m2[316]. The stoichiometric δ_3-MoN adoptes NiAs structure along the space group P63mc. This phase contains eight formula units of MoN in which Mo atoms are arranged in a hexagonal-like structure while, N atoms occupy trigonal prismatic sites between Mo metallic planes [317].

MoN composites have been fabricated via various deposition procedures such as direct current (DC) and radio frequency (RF) magnetron sputtering [318, 319] and through high temperature-high pressure experiments.[317, 320] The growth of MoN by solid state techniques under ambient conditions resulted in a disordered tungsten carbide (WC) type structure δ_1-MoN [317]. Annealing at a temperature as high as 2500 °C at a pressure of 5.6 GPa alter the WC structure from disordered to ordered nickel arsenide (NiAs) crystal structure, δ_3-MoN, in which lattice parameters *a* and *c* are doubled in reference to the original WC structure. Although molybdenum displays low reactivity towards nitrogen, alloying with nitrogen leads to a harder and less compressible structure in reference to pure molybdenum [321]. Several experimental investigations have addressed the compressibility of such high hardness materials [317, 321-325]. Bezinge *et al.* [74] reported no phase transition between hexagonal and cubic structures under high-pressure (*i.e.*, 6 GPa) and high temperature (*i.e.*, 1800 K). Measured and theoretically calculated bulk modulus of stoichiometric hexagonal δ_3-MoN phase are reported to be 345[317] and 379 GPa[316], respectively. Analogous estimates for nonstoichiometric cubic MoN were found to be 304 GPa (experimental) [325] and 348 GPa (computational modelling)[326]. Apart from experiments, number of theoretical studies has aimed to elucidate both electronic and mechanical properties of various molybdenum nitride phases. For instance, a first-principles study showed that a high pressure of 84.5 GPa is required for a phase transition from WC to NaCl [327]. More recently, Liu and co-workers derived thermodynamic properties of WC type δ_1-MoN and NiAs type δ_3-MoN theortically under high pressure using a Debye model in which the dependency of heat capacity C_V on temperatures was reported [328]. Recent investigation by Zhou *et al.*[329] addressed mechanical and electronic properties of Mo_3N cubic nitrides. They estimated Vicker hardness to be 6.62 GPa. Along the same line of

enquiry, the corresponding value obtained for the NbO-like structure of MoN amounts to 24.86 GPa [330].

The applications always give a guideline for searching particular properties of materials which then pave the way toward tuning to the required specifications. However, most density functional theory (DFT) investigations are performed at 0 K, whereas applications of MoN-based thin films proceed at elevated temperatures and pressures. This calls for a through consideration of mechanical and thermal properties of such materials in a broad combination of temperatures and pressures. Over the last decade, quasi-harmonic approximation (QHA) [331] has emerged as a powerful tool in extending the commonly obtained 0 K DFT-derived properties to any set of operational temperatures and pressures. The QHA formalism[332, 333] has been widely deployed to assess the thermal stability of naturally occurring materials at elevated temperatures and pressures encountered in geological reservoirs. Molybdenum nitrides adopt various phases among which are the cubic and hexagonal forms of fully saturated MoN; with no vacant nitrogen lattice. Optical, structural and most importantly catalytic properties of MoN phases strongly rely on their atomic structures. In this regard, *c*-MoN and δ_3-MoN incur more hardness rendering them suitable candidates for applications related to harsh conditions as in cutting machinery. In this study, we elect to consider the two stoichiometric configurations of MoN; namely *c*-MoN (cubic) and δ_3-MoN (hexagonal) phases.

4.3 Computational details

4.3.1 Structural optimisation

All structural optimisation and energy calculations were done via the Vienna *ab initio* simulation package (VASP) [277] along with the Generalized gradient approximation (GGA) of Perdew and Wang PW91[334]. The interaction between the ion and electron is considered through implementing the projector augmented-wave method PAW [335] which combines the accuracy of all electrons method with the efficiency of pseudo-potentials. The latter are numerically engineered entities mimicking the atomic nuclei and the core electrons. The wave function of the valence electron is expanded by a plane wave basis with an energy cut off of 600 eV. Birllouin-zone integrations were performed using a Monk horst–Pack scheme [336] with a k-points grid size of 12×12×12. Forces on each ion and total energies on atoms were

converged to less than 0.02 eV/Å and 10^{-5} eV, respectively. It is well-known that plain DFT methods (such as LDA and GGA) suffers from fundamental shortcoming in predicting the correct band gap necessitating either hybrid DFT or DFT + U treatment. However, pure DFT methods suffice to reproduce the metallic behaviour of the two considered MoN phases[337].

4.3.2 Mechanical properties at 0 K

The stress–strain method acquires reasonably accurate elastic constants that entail important information pertinent to the mechanical stability of the inorganic compounds [338]. Hook's law states that the elastic stiffness constants correlate with stress and strain tensors. Via applying a small strain to a relaxed structure, the linear elastic stiffness tensor can be easily determined by calculating the produced stress. Shang provides insightful description covering the second-order elastic constants [339].

Within this formalism, the elastic stability of rock salt structure is attained when the three independent elastic constants C_{ij} agree with the Born criteria [340]; $C_{44} > 0, C_{11} > |C_{12}|$, and $C_{11} + 2C_{12} > 0$. Whereas for hexagonal structure, there exists six symmetry elements to consider (C_{11}, C_{12}, C_{13}, C_{33}, C_{44}, and C_{66}); however, only five are independent because $C_{66} = (C_{11}-C_{12})/2$. For NaCl and NiAs-oriented crystals, the polycrystalline bulk and shear modulus were calculated by strain-stress method as mentioned above and derived from the Voigt-Reuss-Hill averaging model as [341, 342] [343]:

$$B_c = \frac{C_{11}+2C_{12}}{3} \quad 4.1$$

$$G_c = \frac{(C_{11}-C_{12}+3C_{44})}{5} \quad 4.2$$

$$B_h = \frac{2}{9}\left[C_{11} + C_{12} + 2C_{13} + \left(\frac{1}{2}\right)C_{33}\right] \quad 4.3$$

$$G_h = \frac{2(C_{11}+C_{33})}{15} - \frac{(C_{12}+2C_{13})}{15} + \frac{3[2C_{44}+(1/2)(C_{11}-C_{12})]}{15} \quad 4.4$$

Here, B_c, G_c, B_h, and G_h stand for bulk, Shear moduli for cubic and hexagonal, in that order. Descriptions of formulas dictating other quantities as Young's modulus Y, Poisson's ratio v anisotropy A (*i.e,* a measure of the material's resistance to microcrack) [344] and Vickers hardness ($H_v = 0.92\, k^{1.137}\, G^{0.708}$) can be found elsewhere [345, 346].

4.3.3 QHA for thermo-elastic properties

Constant-volume heat capacity (C_V) and standard entropies (S) have been obtained via applying statistical thermodynamic relations on phonon dispersions for the equilibrium zero T and zero P lattice volume. The QHA yields T-dependent values of isobaric heat capacity (C_P), thermal expansion coefficients (β) and bulk modulus (B). The QHA formalism treats phonons in solids as independent harmonic oscillators; i.e., a gas-phase representation. Acquiring phonon frequencies enables to compute thermodynamic functions, from which all thermal properties could be obtained [114]. Description and derivations of the QHA is covered in great detail elsewhere [347]. Herein, only the basic governing equations are discussed. For a solid lattice with vibrational frequencies (ν_i), the total free energy of the system (F) at a given temperature is expressed as:

$$F(T,V) = U^{\mathrm{DFT}}(\mathrm{V}) + \sum_i \frac{1}{2} h\nu_i + k_B T\left(\sum 1 - e^{\frac{h\nu_i}{k_B T}}\right) \qquad 4.5$$

In which U^{DFT} signifies the static 0 K DFT energy. Deriving eq. (5) with respect to volume and modifying the thermal pressure affords a natural combination for the effect of volume and pressure on thermal and elastic properties. The Phonopy code [348] executes QHA calculations. In the implementation of these computations, eleven volumes with displacements have been explicitly considered in the range of -5.0 % contractions to 5.0 % expansion on 2×2×2 supercells comprising 64 atoms and 128 atoms in cubic and hexagonal MoN; respectively. The convergence of computed thermodynamic properties with respect to the adapted supercell is covered in section 4.3.3. The QHA has been widely recently deployed to derive thermo-mechanical properties of materials. Our approach in this study is similar with the recent work by Erba *et al.* [349] in which they estimated a wide array of thermal and mechanical properties of alumina (Al_2O_3) up to its melting point.

4.3.4 Optical properties

Understanding optical properties of a crystal leads to gain an insight into the electronic structure, band gap energy, and support the possible promising applications of the target materials, solar energy absorber for instance [350]. Therefore, we shall briefly summarize some of the optical features of molybdenum nitride in both scanned phases. Here, the predicted optical properties have been performed under the frame work of density functional theory using

the CASTEP code (Cambridge Serial Total Energy Package) [316, 351] installed in Material Studio (version 6.0) . Estimated optical properties were obtained for optimised structures based in the methodology outlined in section 4.3.4.

Through the interaction between photons and electrons, the optical properties can be illustrated with the aid of a dielectric tensor description. The dielectric function relies on the frequency as equation 4.6 states that is obtained from the momentum matrix elements between occupied and unoccupied (excited) electronic states. In regard to the real part $\varepsilon_1(\omega)$, that is associated with electronic structure, it can be utilized to illustrate the linear response of the regime to electromagnetic radiation, which relates to the interaction of photons and electrons to obtain the optical band gap. On the other hand, the imaginary component is proportional to the optical absorption spectrum of the material and is directly related to the density of state which in turn helps to explore the electronic structure of material.

The real and imaginary components of dielectric tensor are given by:

$$\varepsilon(\omega)=\varepsilon_1(\omega)+i\varepsilon_2(\omega) \quad 4.6$$

the real component of the dielectric function ε_1 is derived from the imaginary part and directly calculated by Kramers-Kroing transformation [352]. The expressions given in equations 4.7 and 4.8 below represent real and imaginary components of dielectric function. These two components are given by:

$$\varepsilon_1(\omega) = 1 + \frac{2}{\pi}\int_0^{\infty} \frac{\varepsilon_2(\omega')\omega' d\omega'}{\omega'^2-\omega^2} \quad 4.7$$

$$\varepsilon_2(\omega) = \frac{2e^2\pi}{\Omega\varepsilon_0}\sum_{k,v,c}|\Psi_k^c|\, u.r|\Psi_k^v|^2\delta(E_k^c - E_k^v - E) \quad 4.8$$

Where Ω signifies the normalization volume,Ψ_k^c and Ψ_k^v are the conduction and valence band wave functions at wave vector *k*, respectively, *u* stands for the vector defining the polarization of the incident electric field, ω characterises the light frequency and *e* is the electronic charge. Finally, loss function signifies the energy loss of fast electrons passing between bands. It can be expressed as:

$$L(\omega) = \frac{\varepsilon_2(\omega)}{\varepsilon_1^2(\omega)+\varepsilon_2^2(\omega)} \quad 4.9$$

4.4 Results and discussion

4.4.1 Structural properties

Figure 4.1 portrays optimised structures for both considered phases.

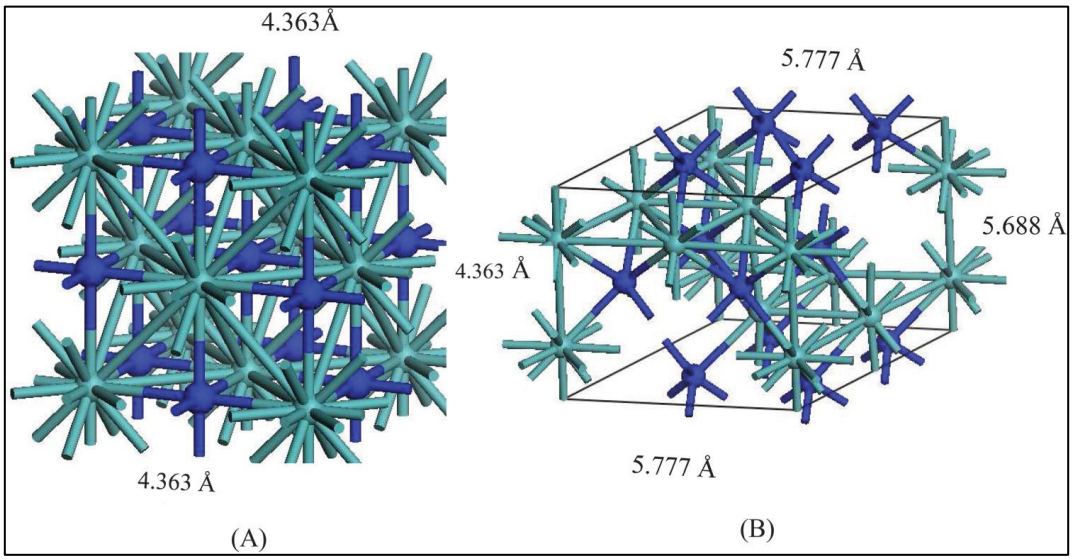

Figure 4.1: Sketched optimized unit cells (black line box): (A) c-MoN (cubic) with space group Fm3m and (B) δ_3-MoN (hexagonal) space group P63mc. Molybdenum atoms are in cyan and N atoms are in blue.

Table 4.1 lists the calculated and measured values of the lattice parameters, equilibrium molar volumes (per unit formula) and Bader charges [353]. Figure 4.2 shows energy versus volume curves for the two phases; used as input in the QHA calculations.

Table 4.1: Optimized lattice parameters a (Å), and c (Å), molar volume (per formula unit in $Å^3$), Mo–N bond distance (Å), and Bader's charges (*e*).

	c- MoN	δ_3 - MoN
Space group	Fm3m (225)	P63mc (186)
Atomic position	Mo 0 0 0 N ½ ½ ½	Mo 0 0 0 N 1/3 2/3 ¼
a (Å)	4.36,4.16[a], 4.32[b],4.32[c] 4.33[d]	5.77, 5.74[f], 5.73[h], 5.74[e]
c (Å)	-	5.68, 5.67[f], 5.66[h], 5.62[e]
Molar volume ($Å^3$/formula unit)	20.76, 20.2[i]	20.55, 20.01[g]
Mo-N bond distance(Å)	2.16	2.13
Bader charges (electron)	Mo 1.85 N -1.83	Mo 1.27 N -1.27

[a] Experiment [325]

[b] US-PP method within GGA,Ref. [354]

[c] VASP within GGA, Ref. [327]

[d] CASTEP within GGA, Ref. [344]

[f] Experiment, Ref.[74]

[h] CASTEP within GGA ,Ref.[328].

[e] Experiment ,Ref.[355].

[i] CASTEP within GGA ,Ref.[356].

[g] DFT method with GGA, Ref.[357] .

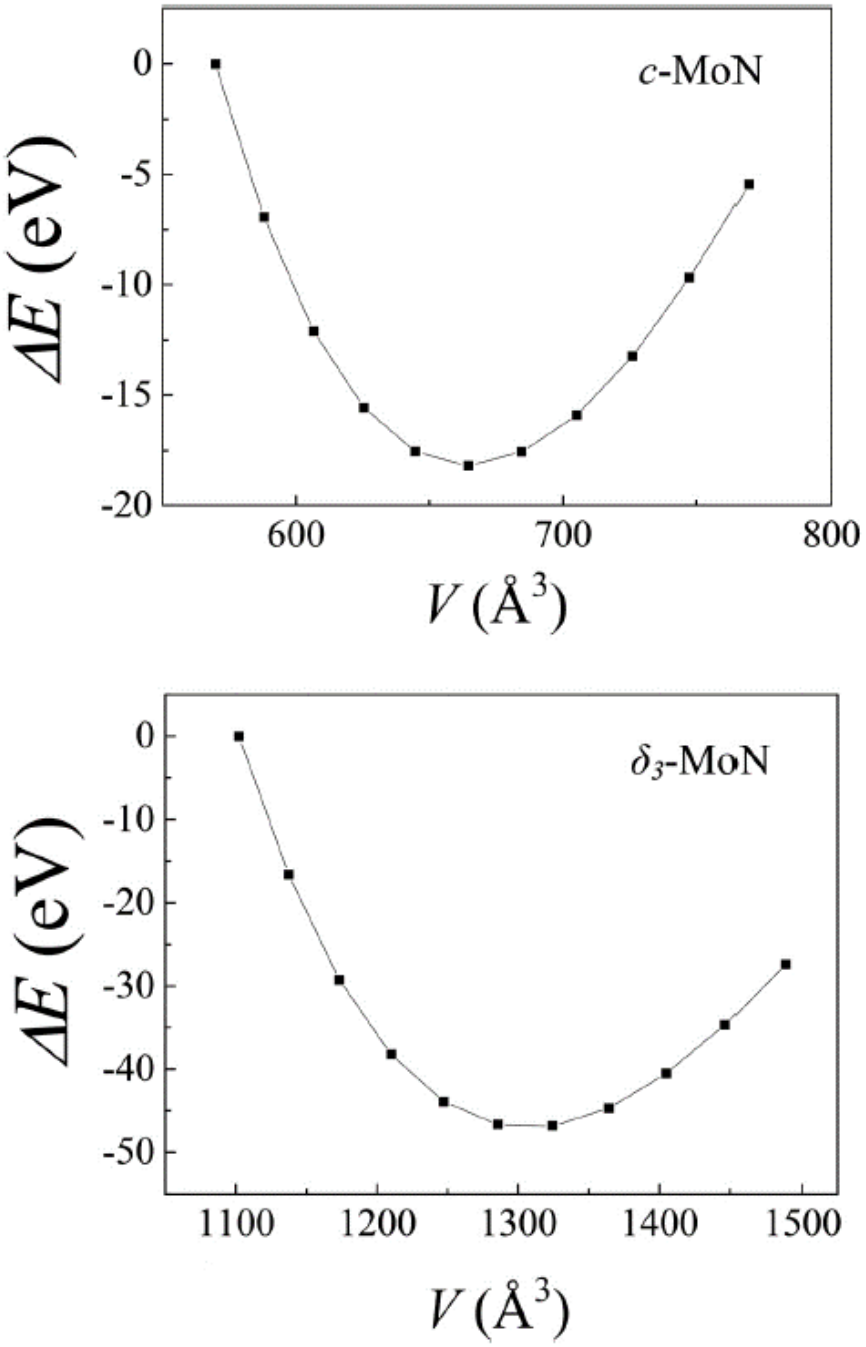

Figure 4.2: Total energy with respect to volume (the lowest energy structure) for both structures.

Our computed lattice parameters for NaCl-like structure amounts to 4.363 Å and matches very well analogous experimental measurements [325] and theoretical calculations [327, 344, 354]. The obtained lattice constants of the NiAs-MoN hexagonal phase are also in a good agreement with corresponding XRD measurements [74, 355] and previous theoretical predictions [328].

Figure 4.3 plots total and projected density of states DOSs for the two phases. The non-existence of a band gap in MoN is in accord with their well-documented behaviour as potent catalysts. As Figure 4.3 reveals, the Mo-*d* orbitals contribute significantly to DOSs values at the Fermi level resulting in high contribution to the conducting nature of MoN whereas *p* electrons do not heavily participate at the Fermi level. The valance band stretching between -17 eV to – 15 eV is mainly composed of N-*s* orbitals. Overall, our obtained DOSs curves and direct band gaps for the two phases coincide very well with other DFT accounts [316, 327, 344, 356]. Finally, calculated Bader charges indicate stronger ionic/metallic bonds of Mo and N in the MoN and δ_3-MoN, demonstrating electron transfer of 1.27 and 1.85 electron from each Mo to each N in *c*-MoN and δ_3-MoN phases, respectively, which was also discussed and outlined by others [356, 358].

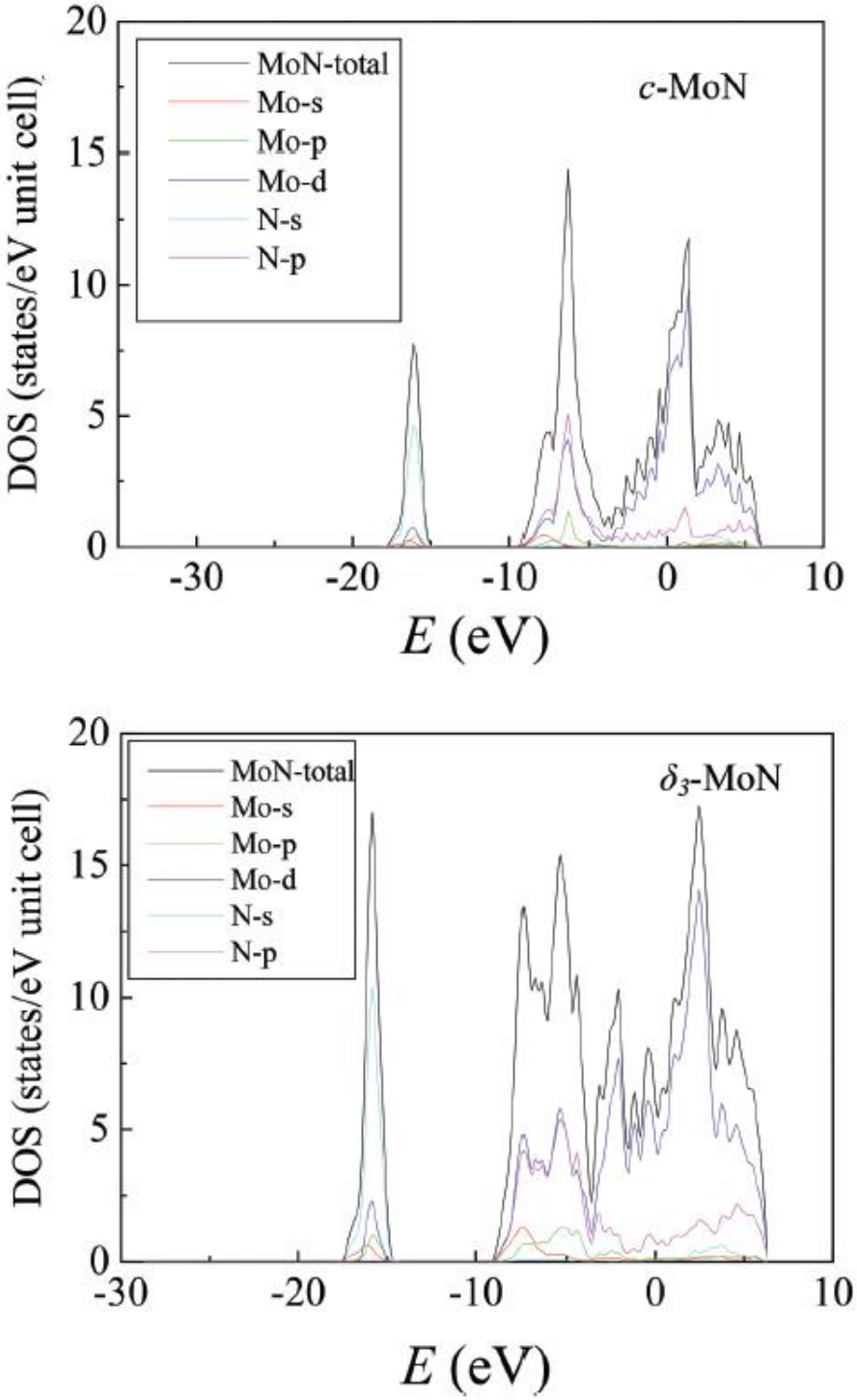

Figure 4.3: The total and partial (DOSs) for both structures.

4.4.2 Elastic stability at 0 K

In order to evaluate the ductility and brittle nature of a material, the ratio of shear to bulk modulus (*k*) should be predicted. According to Pugh [359], the ratio of shear to bulk modulus reflects the hardness of solid. It is well known that diamond is the hardest material that possess

a largest *k* of 1.2, followed by cubic-BN which considered as the second super hard material in terms of hardness having *k* value around 1.0[360]. On the other side, the trends of Poisson's ratio (*v*) towards *k* show reverse correlation. Thus, hardness tends to diminish as *v* increases. Our elastic parameters have been explored at 0 K and tabulated in Table 4.2.

It can be clearly seen that the calculated elastic stiffness coefficients do not agree with Born-Huang criteria [361] implying that MoN with the rock salt structure is mechanically unstable towards elastic deformation. These findings agree well with the other experimental and first-principles studies. For the hexagonal structure, it is noticed that it is mechanically stable due to the agreement of elastic stiffness coefficients (C_{11}, C_{12}, C_{13}, C_{33}, and C_{44}) with the Born-Huang criteria for stability fulfilling the conditions $C_{12} > 0$, $C_{33} > 0$, $C_{66} = (C_{11}-C_{12}) > 0$, $C_{44} > 0$, and $(C_{11} + C_{12})(C_{33}^2-2C_{13}^2) > 0$. The Poisson's ratio, anisotropy, and hardness are also significant to determine mechanical character of a crystal. We concluded that the hexagonal structure possesses higher resistance to plastic deformation with stiffer nature than cubic phase.

Table 4.2: Calculated independent elastic constants C_{ij} (GPa), bulk modulus B (GPa), shear modulus G (GPa), Young modulus Y (GPa), Poisson's ratio , anisotropy A, hardness H (GPa), compressibility K (1/GPa), and shear to bulk ratio (Pugh's ratio k), Vickers hardness (H_V) at zero temperature and pressure.

	c-MoN	δ_3-MoN
C_{11}	547, 551[a]	633.3, 598[a]
C_{12}	239, 225[a]	177.6, 201[a]
C_{33}	-	788.9, 807[a]
C_{44}	-57, -49[a]	227.8, 273[a]
C_{13}	-	247.4, 203[a]
B	341.8, 304[h], 351.5[b]	377.8, 345[g], 379.4[b], 380[c]
G	137, 124[d]	281.4, 216.8[e]
Y	362.4, 328[d]	676.5, 533.5[e]
v	0.32, 0.25[d]	0.219, 0.230[e]
K(1/B)	0.0029	0.0026, 0.00308[e]
k	0.4	0.74
Hv	10.5	35.6

[a] CASTEP within GGA, Ref.[356]

[b] CASTEP within GGA,Ref.[316].

[c] Experiment,Ref.[362].

[d] VASP within GGA,Ref.[327].

[e] CASTEP within GGA,Ref.[328].

[h]Experiment,Ref.[325].

[g] Experiment,Ref.[317].

4.4.3 Thermodynamic properties

The QHA approach has been deployed on the Vinet's equation of state to obtain thermo-elastic properties by computing *E*-*V* data and displacement of atoms. However, attaining convergences of predicted properties with the size of the implemented supercell is an important factor in assessing the reliability of the QHA-obtained results. Herein, thermodynamic calculations of δ_3-MoN and *c*-MoN were performed on 2×2×2 supercells of both phases.

The explored C_V, C_P and entropy *S* per formula unit of the two examined phases up to melting temperature (2030 K) and at zero pressure are presented in Figures 4.4 and 4.5, correspondingly. Results disclosed that at a studied temperature, C_V and C_P values of the NaCl structure were larger than that of their counterpart hexagonal phase as reported in Figure 4.4.

Figure 4.6 illustrates C_P of both structures as a function of temperature at selected pressures 0, 6, and 12 GPa. It is notable that when T < 1000 K, values of C_P grow strongly owing to the anharmonic approximation effects applied and any increase in the applied pressure translates into an increase in values of C_P. On the other hand, at higher temperatures the anharmonic effect is rather suppressed resulting in almost unvarying values of C_P with temperature A similar behaviour has been observed by Seddik *et al*. [363] in their investigation of the effects of external temperature and pressures on thermodynamic properties and mechanical stability of yttrium chalcogenides.

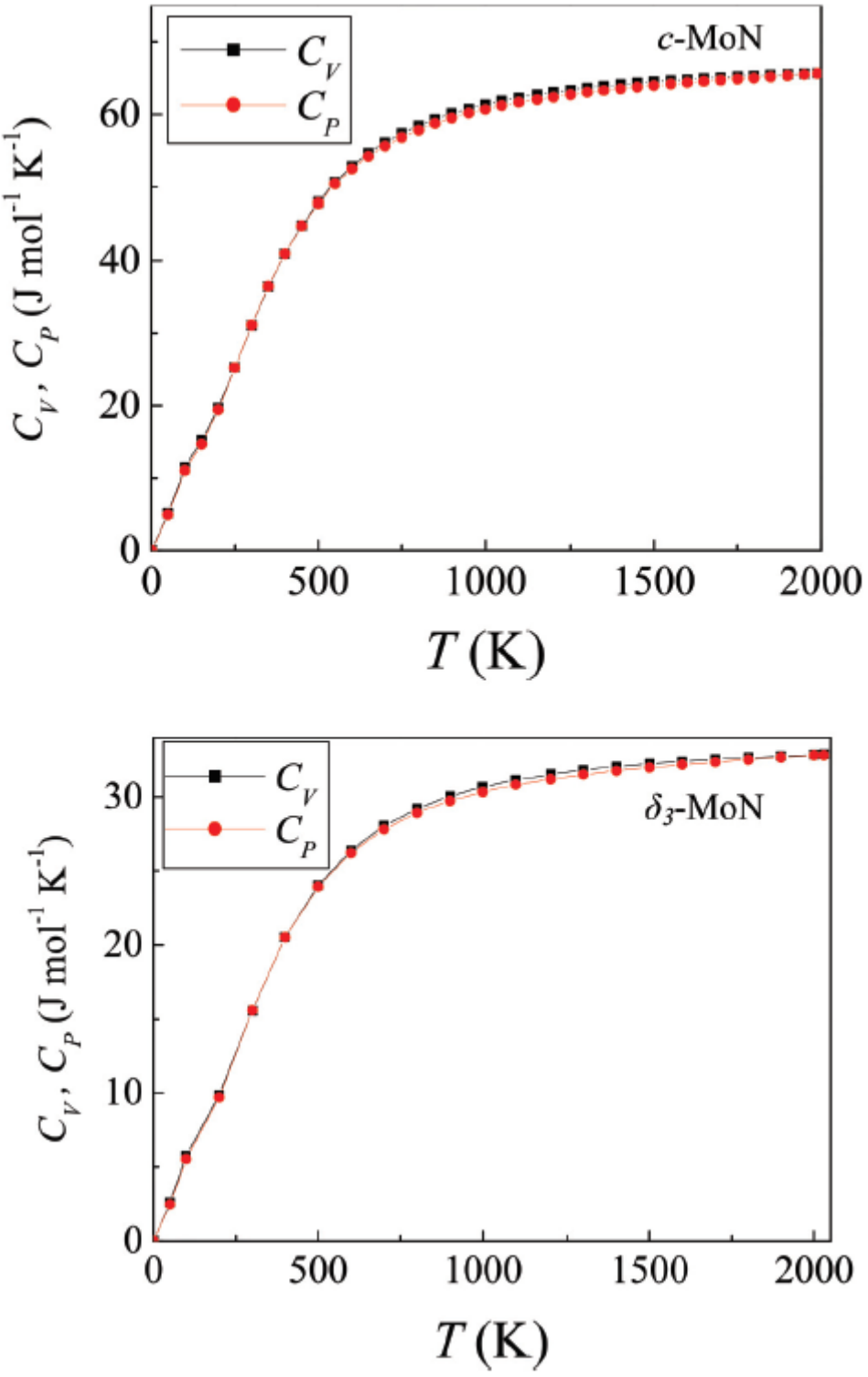

Figure 4.4: Heat capacities C_V and C_P as a function of temperature at supercell structures for both structures.

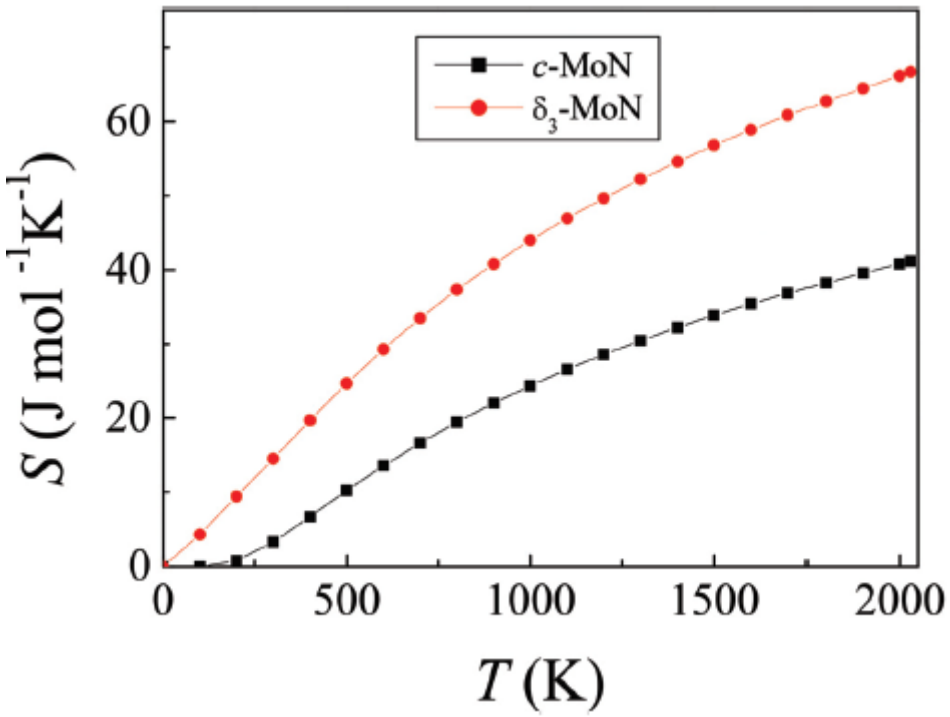

Figure 4.5: Standard entropies *S* with respect to temperature for both structures.

In reference to the primitive unit cell of NaCl-MoN (*i.e,* 8 atoms with 4 formula units), we found that values of C_P (at T = 300 K and P = 0), C_V (at T = 300 K) and S (at T = 300 K) depart by only 0.47%, 0.9%, and 1.6%, respectively in reference to values computed based on the 2×2×2 supercell (i.e., 64 atoms with 32 formula units). Matching convergence values have been obtained for the δ_3–MoN phase. This unequivocally indicates that QHA-calculated values are converged with respect to the size of the adapted supercell.

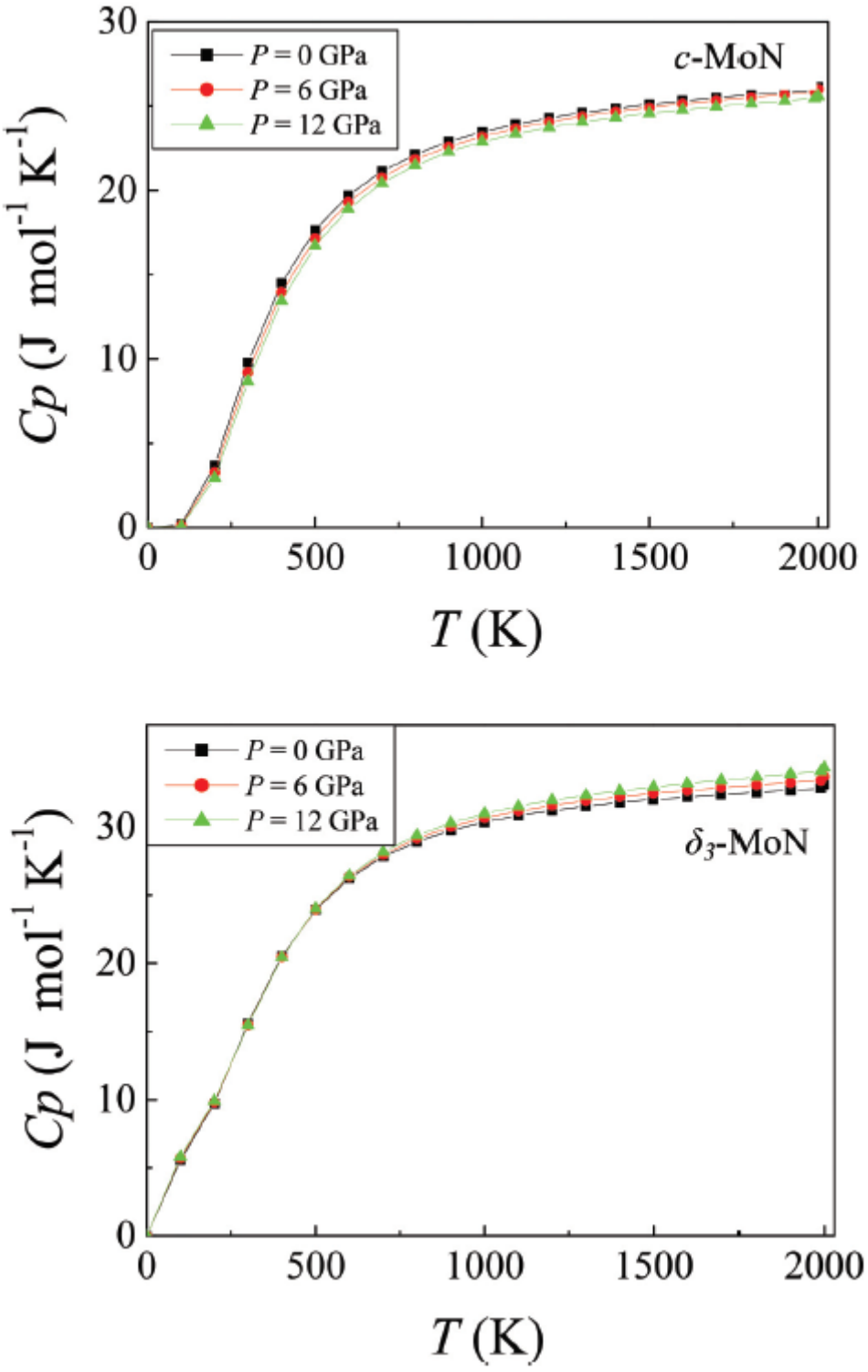

Figure 4.6**:** Specific heat capacity C_P as a function of temperature at three different pressures for both structures

Figure 4.7 plots the difference in Gibbs free energies (per unit formula) between the cubic MoN and hexagonal δ_3-MoN phases. The thermodynamic stability at all considered *T* and *P* of the

cubic phase is in accord with the consensus of experimental and theoretical findings in the literature [364].

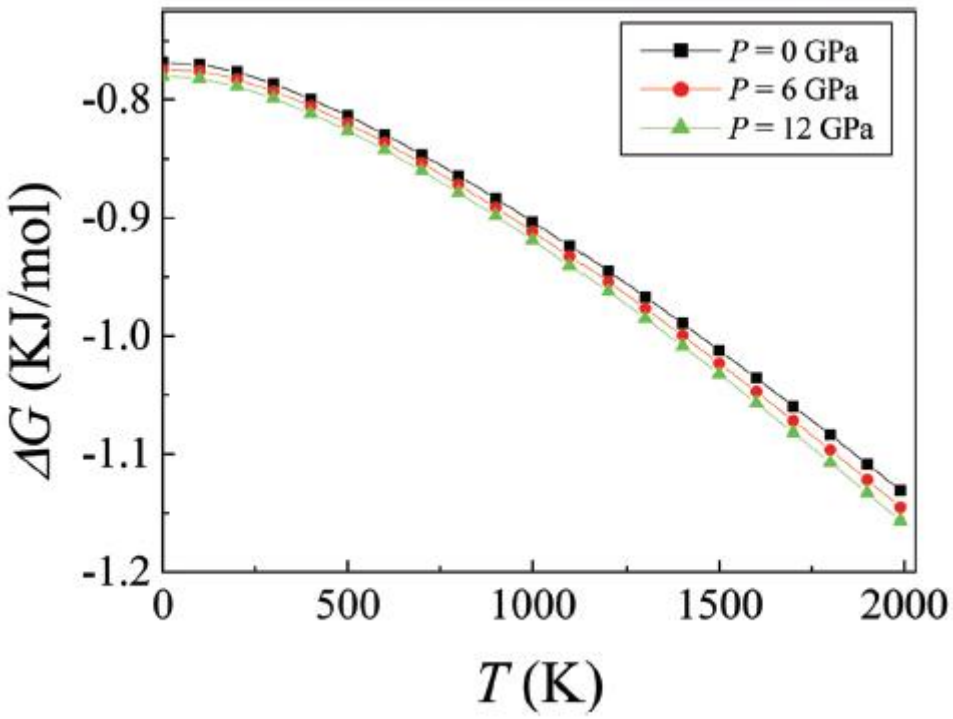

Figure 4.7: The difference in Gibbs free energy with respect to the cubic phase.

Figure 4.8 depicts values of linear thermal expansion coefficients β with varying pressure. It is evident from Figure 4.8 that the effect of QHA on β values is more significant in case of *c*-MoN where values steadily increase with temperature. Our analysis is in agreement with analogous data reported recently by Erba *et.al*. [349] in their study of α-Al_2O_3.

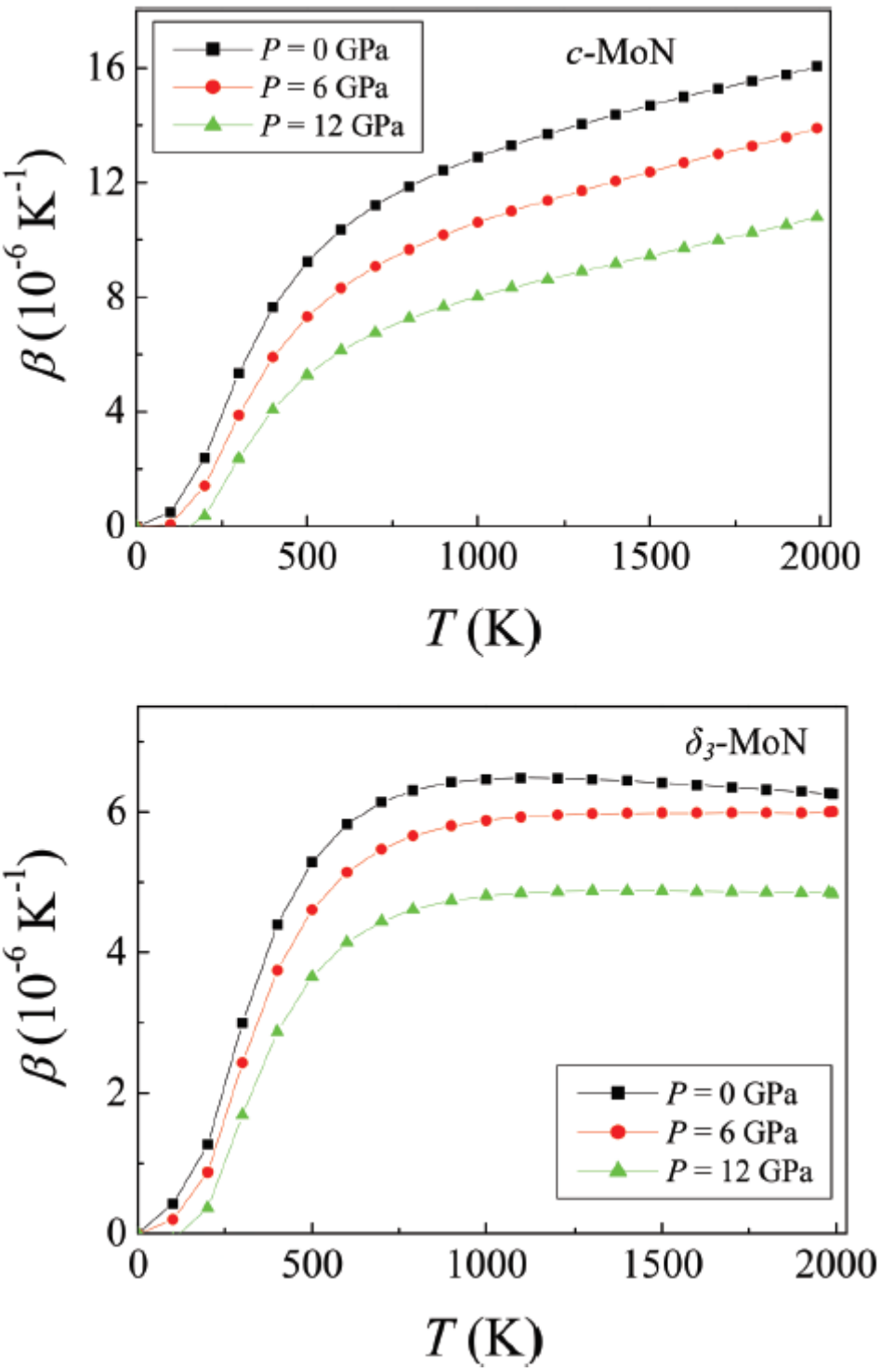

Figure 4.8: Dependence on temperature, up to 2023 K, and pressure, up to 12 GPa of the thermal expansion coefficient as computed at GGA level of approximation for 2 2 2 *c*-MoN and (1 1 1) δ_3-MoN.

Finally, Figure 4.9 shows the variation of bulk modulus (B) with T and P. As expected, the hardness of both phases decreases with temperature at a given pressure. To the best of our knowledge, no available experimental data for molybdenum nitride exists, however, the work by Liu, *et al*. [328] provided a theoretical estimation.

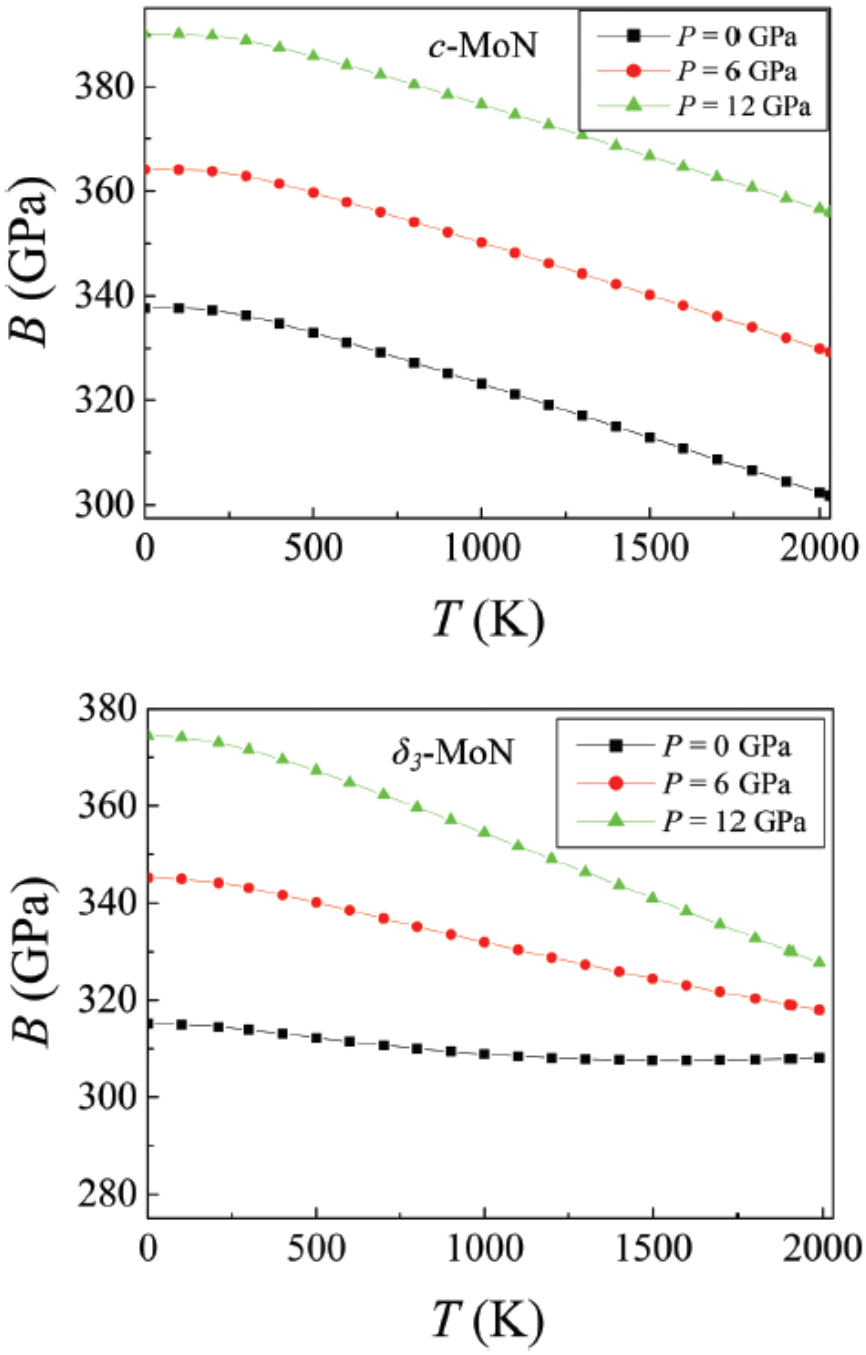

Figure 4.9: The bulk modulus versus temperature at three different pressures for both structures.

Figure 4.10 compares our calculatd C_V values with correponding Liu *et al.* [328] values. As Figure 4.10 shows, values cacluated herein significantly underestimate predictions by Liu *et al.*[328]. The absence of any experimental C_V values for the title material makes it very challenging to comment on the plausible source of significant deviation portrayed in Figure 4.10. It is worthwhile noting that Liu *et al.* [328] values were based on a deploying a Debye model while our values were obtained by utilisng the QHA approach. It is very-well documented that the Debye model provide a rather curde estimation of thermochemical functions when contrasted with the QHA estimation [365].

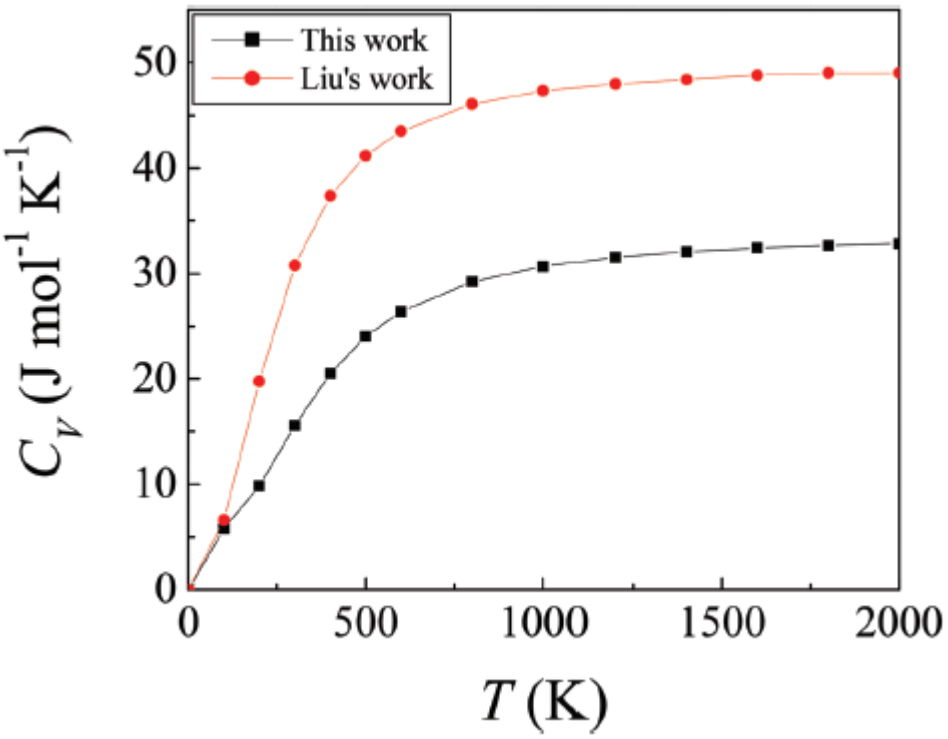

Figure 4.10: Heat capacity as a function of temperature of δ_3-MoN at P = 0 with Liu's work [328].

4.4.3. Optical properties

The predicted dielectric function includes intraband effects from free electrons (conduction electrons contribution) and interband effects (from bound-electron contribution) that represent empirical Drude term and Lorentz oscillator respectively. When calculating dielectric function, the contribution of those effects should be taking into consideration. Figure 4.11 depicts energy dependent spectrum of the real and imaginary parts of the complex dielectric function as a function of the photon energy. Main peaks of the real components extend from the top of

valence band is located at 0.3 and 0.5 eV for δ_3-MoN and *c*-MoN, respectively. This highlights matching optical spectra of both cases.

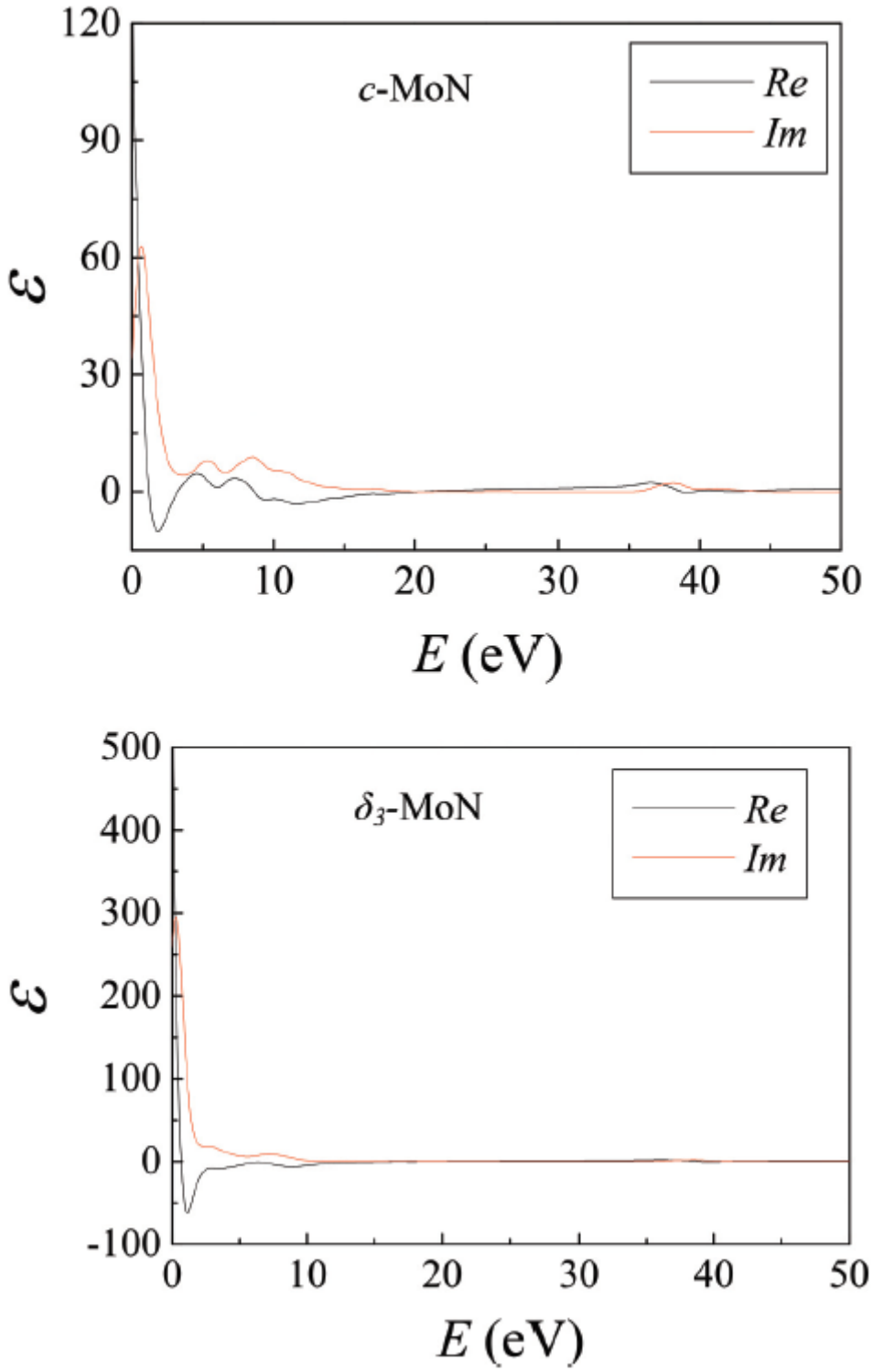

Figure 4.11: The real and imaginary parts of dielectric function for both structures.

Figure 4.12 presents absorption coefficients for both crystalline phases. Knowledge of absorption coefficients plays a vital role in providing data pertinent to the most preferable solar energy conversion efficiency and indicates how far the light with a specific energy (wavelength) can penetrate into the material before being absorbed [366]. In other words, they refer to the decrease of light intensity spreading in unit distance in medium. Owing to their metallic nature (Figure 4.3), the absorption coefficients for both phases commence at 0 eV with a maximum peak occurring at 39 eV.

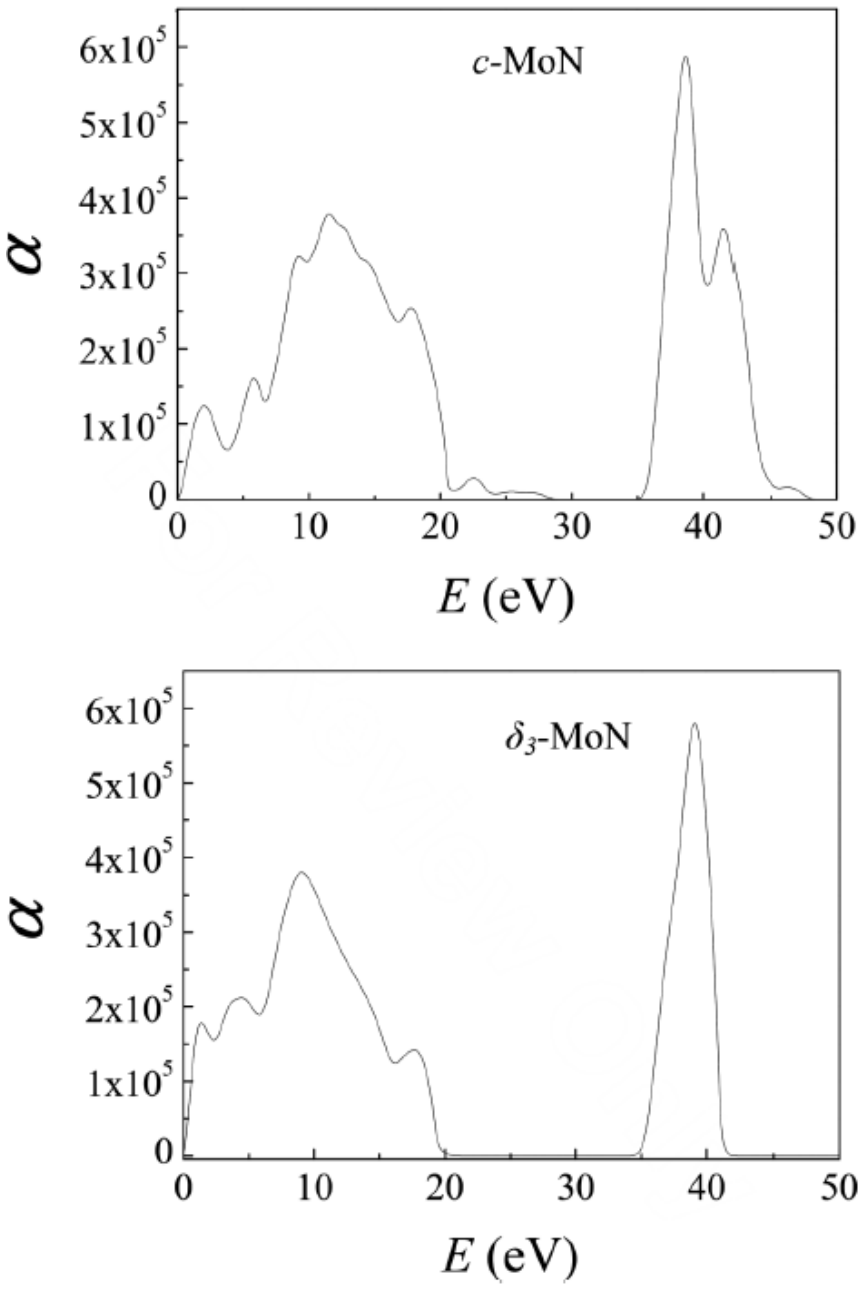

Figure 4.12: Absorption spectrum for both structures.

Figure 4.13 illustrates the reflectivity spectra as a function of photon energy. The hexagonal structure spectrum has several peaks with the highest at ~12 eV. A predominant sharp peak in the cubic structure is located at ~ 20 eV. The reflectivity is high in the visible-UV region from 250 nm up to 800 nm which corresponds to 4.96 eV -1.55 eV.

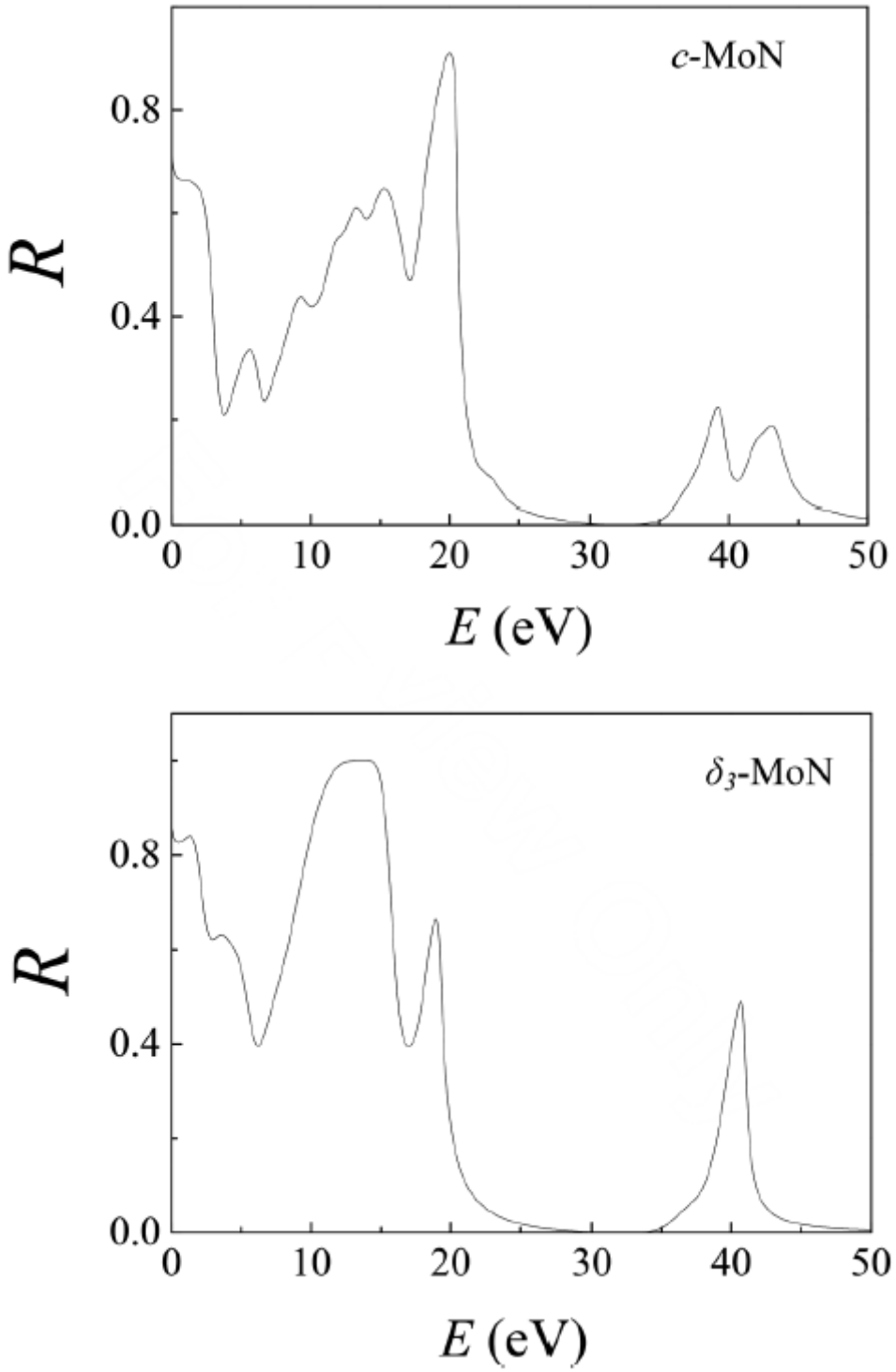

Figure 4.13: Reflective spectrum for both structures.

The reflective spectrum as a function of wave length (250-800 nm) is represented in Figure 4.14. Obviously, the figure agreed reasonably with Koutsokeras *et al.* work [367]. Most notably, both approached the same behaviour in the range 450-600 nm.

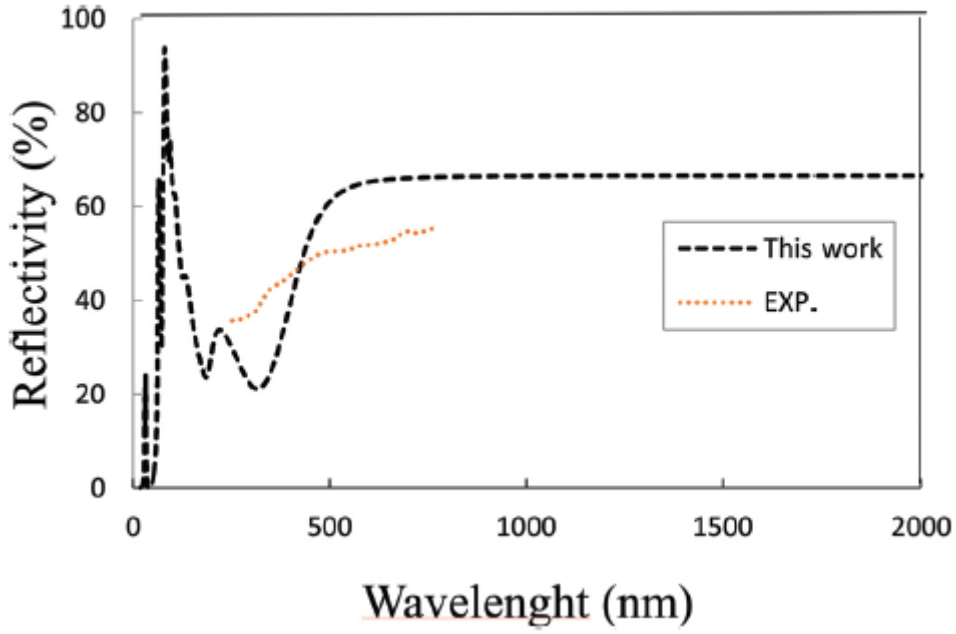

Figure 4.14: Reflectivity as a function of wavelength. The black line refers to this work while the orange one refers to experimental results [367].

Having considered dielectric constant, absorption and reflectivity, it is worth mentioning that the calculated conductivity spectrum σ starts at zero photon energy in accord with the metallic nature noted earlier. Additionally, the photon conductivity and hence electrical conductivity of a material increases as a result of absorbing photons as plotted in Figure 4.15.

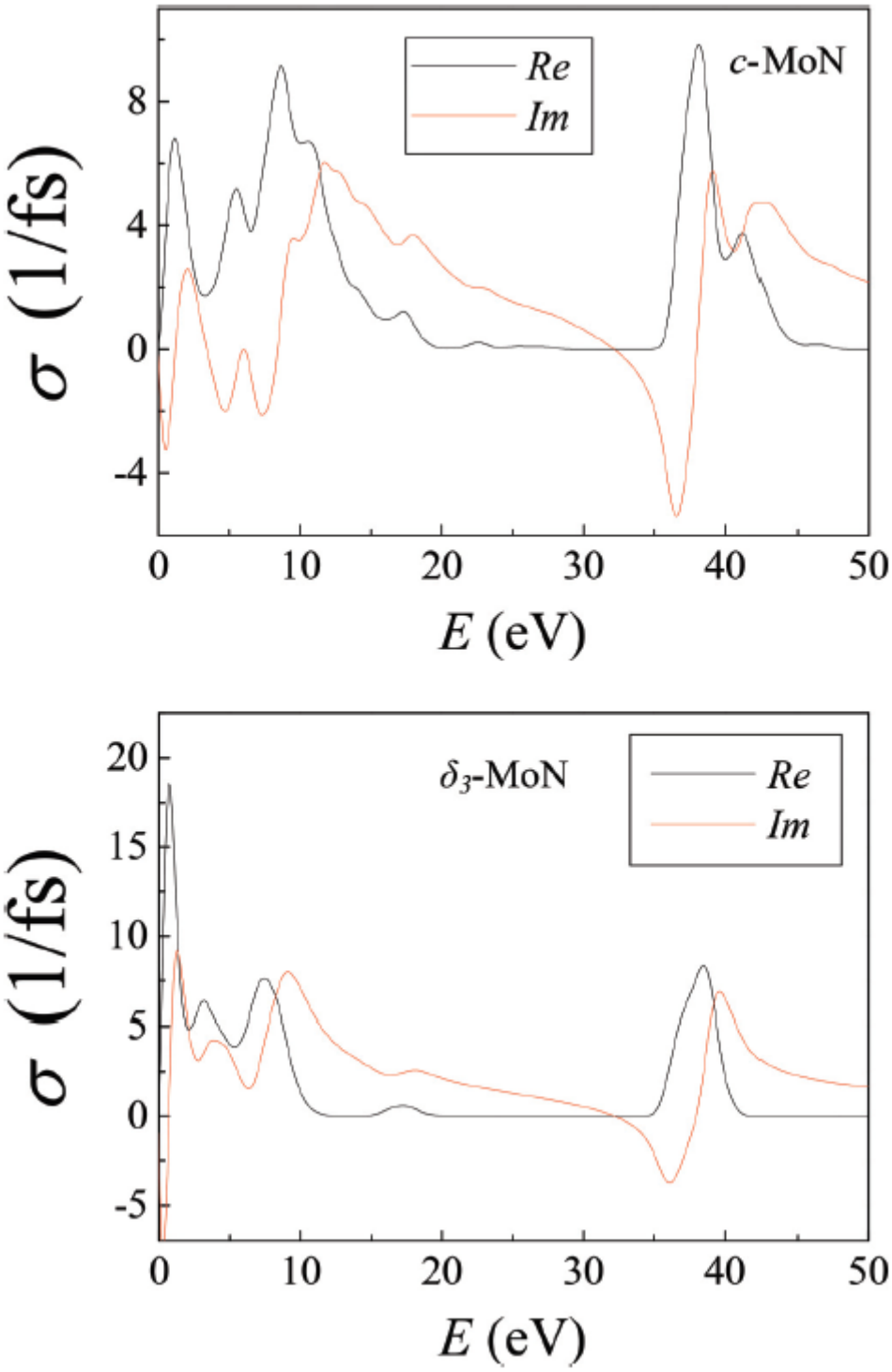

Figure 4.15: Conductivity spectrum for both structures.

Finally, refractive index *n* extinction coefficient *k*, and energy loss-functions, *L* are shown in Figures 4.16, and 4.17, respectively. From the electronic complex dielectric function, the energy loss spectrum of a fast electron traversing in the material is depicted in Figure 4.16.

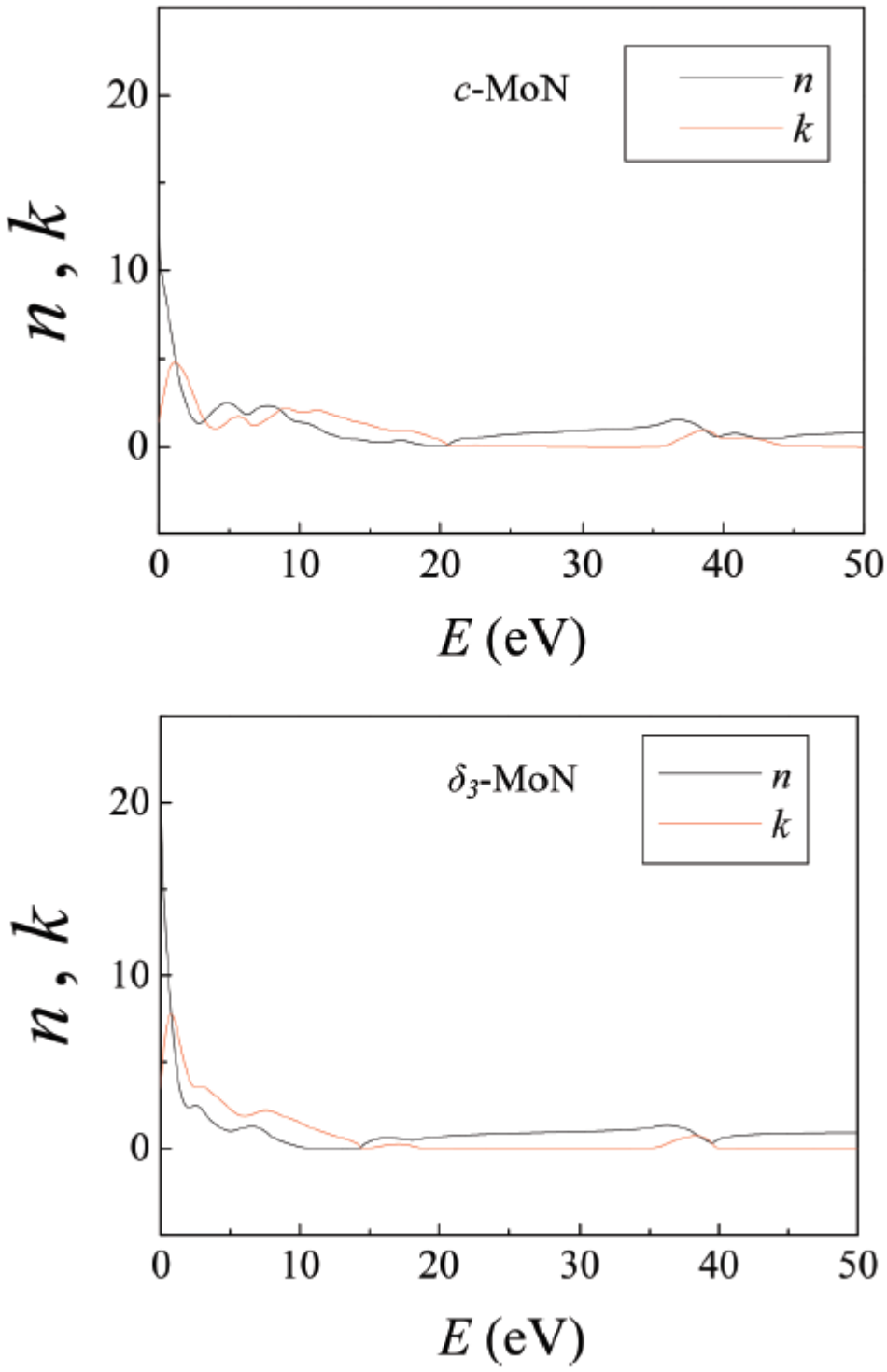

Figure 4.16: The refractive index (*n*) and the extinction coefficient (*k*) for both structures.

It can be seen that the energy loss function spectrum comprises two predominant peaks in the two phases. The main peak in the spectra refers to the Plasmon peak, indicating the energy of collective excitation of the electronic charge density in the crystal.

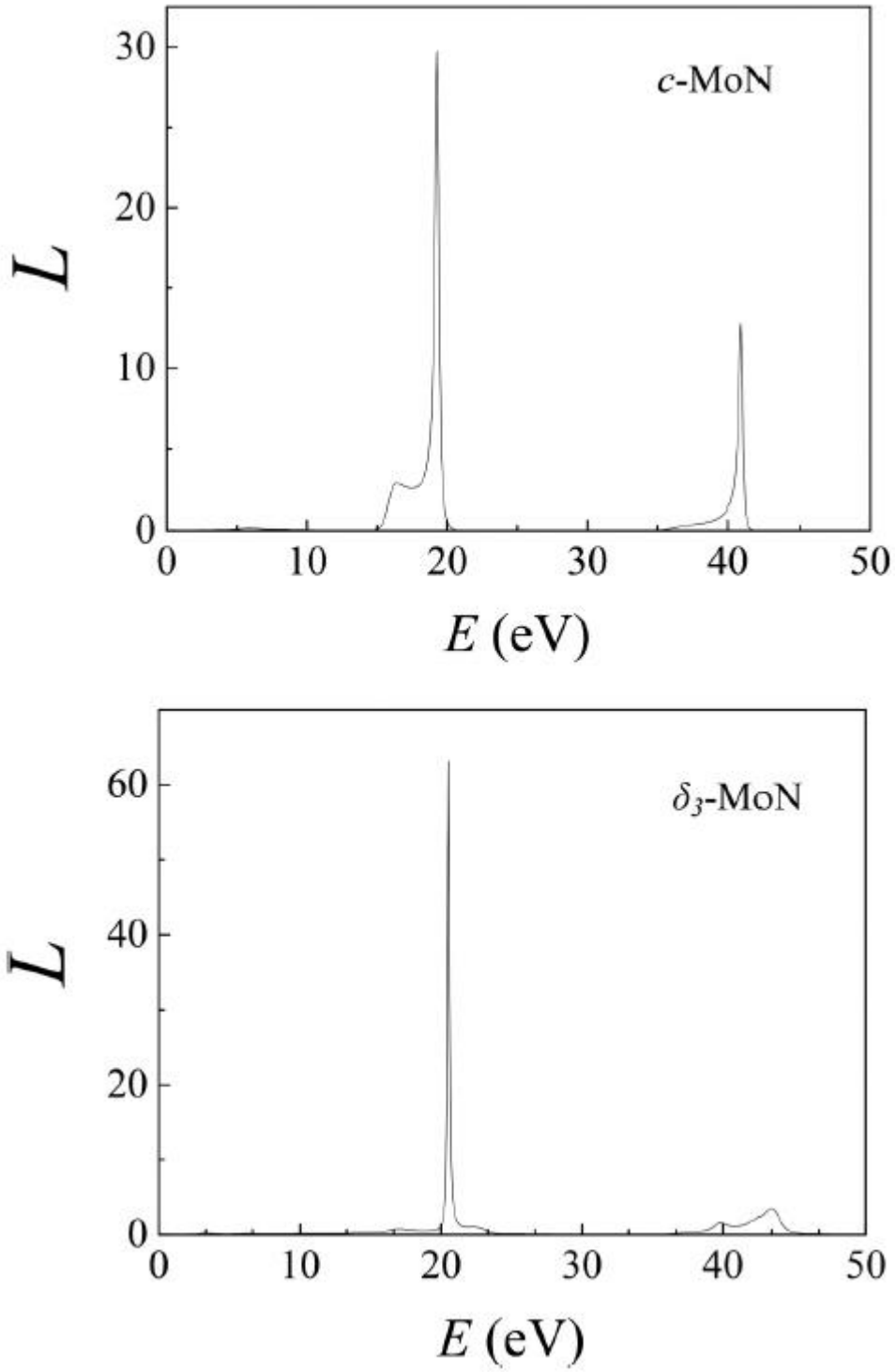

Figure 4.17: Loss function spectrum for both structures.

4.5 Conclusions

We outlined detailed analyses of the thermal, mechanical and optical properties of transition metal mononitride MoN. The ground state properties of both stoichiometric and non-stoichiometric phases demonstrate good agreement with previous experimental and theoretical accounts. The cubic *fcc* MoN structure exhibits thermodynamic stability and attain values of thermal expansion coefficients higher than the hexagonal δ_3-MoN phase. However, according to the Born-Huang criteria, the hexagonal phase is harder and mechanically stable at 0 K in contrast to the cubic phase. Predicted reflectivity in the wavelength range of 250 - 800 nm was found to be greater than 60%, indicating promising potential for the utilisation of the films as antireflection coating applications. The plotted energy dependent spectrum of the real and imaginary parts shows that the considered two phases share matching optical properties. (DOSs) curves suggest that the chemical reactivity of the MoN materials is controlled by Mo-*d* orbital. The highly cationic Mo atoms engender it as an active catalytic site for the adsorption of molecules with strong electronegative centres. Attained properties in this study should be instrumental to achieve a thorough understanding of the remarkable physical and chemical features of molybdenum nitride. In a due course, we will carry out an analogous investigation pertinent to properties of unsaturated MoN (i.e., Mo_2N). Accruing thermo-mechanical information on all possible phases of MoN/Mo_2N would enable to construct a stability phase diagram of molybdenum nitrides as a function of the nitrogen chemical potential.

Chapter 5 : Geometries, electronic properties and stability of molybdenum and tungsten nitrides low-index surfaces

Paper II

Zainab N. Jaf Mohammednoor Altarawneh, Hussein A. Miran, Zhong-Tao Jiang "*Geometries, electronic properties and stability of molybdenum and tungsten nitrides low-index surfaces*" https://doi.org/10.1088/2053-1591/aadeb6.

5.1 Abstract

Motivated by the vital role played by transition metal nitride (TMN) composites in various industrial applications, the current study reports electronic properties, thermodynamic stability phase diagram, and vacancy formation energies of the plausible surfaces of NiAs and WC-type structures of δ_3-MoN and δ-WN hexagonal phases, respectively. Low miller indices of various surface terminations of δ_3-MoN and δ-WN namely, (100), (110), (111), and (001) have been considered. Initial cleaving of δ_3-MoN bulk unit cell offers separate Mo and N terminations signified as δ_3-MoN (100): Mo, δ_3-MoN(100):N, δ_3-MoN(111):Mo, δ_3-MoN(111):Mo, and δ_3-MoN(001):Mo. However, the (110) plane reveals mix-truncated with both molybdenum and nitrogen atoms i.e. δ_3-MoN (110): MoN. Likewise, the δ-WN faces incur analogous surface terminations. Ab initio atomistic thermodynamic analyses predict that, N-terminated (111) and (100) slabs to be the most energetically favourable surface terminations amongst the explored surfaces of δ_3-MoN and δ-WN, respectively. Evidenced by plotted density of states DOSs, bulk and surfaces of δ_3-MoN and δ-WN display a metallic character. In terms of surface relaxation and reconstructions, most investigated surfaces experience mainly downward displacements of their topmost layers. Most notably, the relaxed Mo-termination in (111) and (100) surfaces of δ_3-MoN demonstrate significant reconstructions resulted in the first layer to be solely truncated with nitrogen atoms instead of molybdenum in the un-relaxed geometry. Nevertheless, no surface reconstruction has been noticed in most of considered δ-WN configurations. Calculated Bader's electronic charges reveal charge transfer from Mo/W atoms to N atoms, largely retaining the ionic bond nature in their bulk phases. Finally, vacancy formation energy (VFE) calculations showed that introducing nitrogen vacancies through the surface is an endothermic process. Furthermore, the energy required to create a vacant cite in the inner layers differ than that needed in the outer layers. Nitrogen terminated slabs for the most stable surfaces of Mo-N and W-N systems hold the highest concentrations (*i.e.*, at 300 K, MoN(100):N: +2VN and WN(100):N+2VN afford a concentration of 7.7 × 1019 cm^{-2} and 2.8×1017 cm^{-2}, respectively. Results from this study should be useful when studying the activation of doubly and triply bonded molecules such as N_2 at surface vacancies.

5.2 Introduction

Being situated between carbon and oxygen in the periodic table, nitrogen-based compounds enjoy a combination of carbide and oxide properties. Binary nitride systems, in particular molybdenum and tungsten mononitrides find significant applications as diffusion barrier layers in integrated logic circuits, scratch protection coatings in cutting machineries, and recently as heterogeneous catalysts [3, 171, 368]. The unique properties of crystalline phases of molybdenum and tungsten nitride are attributed to the incorporation of nitrogen into the lattice of metal atoms (Mo and W). This results in a profound *d*-band electronic density of states DOSs at the Fermi level (high metal →N electron transfer)[4]. This in turn leads to having elevated melting point, high hardness, good thermal stability and chemical inertness (*i.e.*, these materials are chemically inert at relatively low to medium temperatures) [3]. While profound *d*-band DOSs usually leads to high hardness, it has been shown that for rocksalt nitrides, high *d*-band DOSs leads to significant softening and even mechanical instability [164, 179, 369-372].

Inspired by the pioneering work of Levy and Boudart, who reported that transition metal nitrides exhibit high catalytic activities resembling those of platinum catalysts (Group VIII)[16], interest in studying the chemistry of Mo and W mononitrides has been emerged. Based on various preparation methods, high surface area of molybdenum/tungsten nitrides can be synthesised via temperature-programmed reaction (TPR) technique[127, 129]. This reaction involves heat treatments of molybdenum trioxide MoO_3 and WO_3 thin films in the presence of ammonia NH_3 flow. Several Mo and W-nitride phases can be fabricated depending on the reaction conditions such as the nature of the metals used (thin film or powder), the nature of the precursor[58] and temperature. For instance, non-stoichiometric cubic γ-Mo_2N belong to rocksalt-type structure with an interstices sites, these sites are partially filled with randomly distributed nitrogen atoms occupying the octahedral vacant sites of the close-packed metal lattices resulting in a face centered cubic (fcc) crystal structure [373]. This phase is well known to incur high mechanical instability due to having negative elastic stiffness coefficients C_{44} [374].

Furthermore, the fully stoichiometric metastable cubic B1-MoN phase has not yet been confirmed experimentally [375]. Hart and Klein stated that it is impossible to synthesis a stoichiometric B1-MoN structure due to elastic instability even at high pressure [376].

Conversely, Inumaru et al. [69] fabricated stoichiometric and non-stoichiometric B1-MoN films on α-Al_2O_3 (001) and MgO (001) substrates at 973 K using pulsed laser deposition techniques. While, the stoichiometric phase of MoN is hard to synthesize, non-stoichiometric phases, nearing x=1, have been synthesized in plenty. In particular, both cation and anion vacancies of molybdenum and nitrogen being present such that the net ratio between the two varying from 0.6 - 1.25 have been synthesized [84, 94, 372, 377]. Another crystalline form known as a tetragonal β-Mo_2N represents a low temperature phase with order distribution of nitrogen atoms with lattice parameters of $a = b = 4.210$ Å and doubled $c = 8.060$ Å and a space group of I 41/a md:1 [378]. Besides, the stable, hard and incompressible form of Mo nitride is suggested to be a hexagonal phase δ_3-MoN with NiAs- type structure and space group of P63/mc and a point group of 6m [379] that can be compared with diamond and *c*-BN in terms of hardness [67, 380]. For the case of Mo_2N, the phase stabilities are in the order of ε-Mo_2N (orthorhombic), β-Mo_2N (tetragonal) and γ-Mo_2N (cubic). Similarly, the most stable phase at the 1:1 composition for MoN is a monoclinic phase, although it is only 7meV/atom more stable than the NiAs phase[84, 85].

Experimentally, four different phases of the hexagonal molybdenum nitride have been synthesised by either plasma-enhanced chemical vapour deposition (PECVD) process or ammonolysis of $MoCl_5$ and MoS_2 [54]. Monochromatic synchrotron X-ray diffraction at high pressure experiment has been performed to determine the compressibility of hexagonal phase of MoN [381]. As a promising catalytically phase, hexagonal MoN has been the subjects of several studies. Xie *et al.* [106] synthesised two-dimensional atomically-thin nanosheets of bulk hexagonal MoN parallel to graphene, in which high catalytic performance in the hydrogen evolution reaction (HER) has been demonstrated. Enhanced activities of hexagonal molybdenum nitrides have been proposed towards oxygen reduction reaction (ORR) [62]. Wang *et al.* [60] reported high–pressure synthesis of hexagonal δ–MoN via an ion–exchange reaction at a pressure of 3.5 GPa. The fabricated bulk was the hardest among the known metal nitrides and reveals an exceptional hardness which was even higher than cubic γ–Mo_2N (~30 GPa versus ~23 GPa).

Another important member of the TMNs family, refractory tungsten nitride compounds have attracted considerable attention [382, 383]. Depending on the anion-to-cation ratios, WN crystallises in wide variety of phases [112, 384, 385]. DFT studies have demonstrated that WN in the NbO phase is mechanically (C_{44} = 175 GPa) and thermodynamically (H_f = −0.84 eV) more stable than other plausible WN configurations, however, it has not yet been confirmed

experimentally[384]. For this reason, we elect to study the experimentally confirmed δ-WN phase.

The majority of binary W−N system are prepared as thin films with poor crystallinity[386]. Hexagonal tungsten nitride films (δ−WN) were first synthesized by Schöenberg [387] with the P$\bar{6}$m2 structure space group No. 187, and lattice parameters of ($a = b = 2.893$ Å and $c = 2.826$ Å, $\alpha = \beta = 90°$and $\gamma = 120°$). This phase is experimentally observed at a pressure of 5 GPa. Limited number of experimental and simulation-based studies has been devoted on the hexagonal phase. Recently, crystalized δ−WN has been fabricated via solid-state ion exchange reaction under high pressure and temperature. Wang *et al.* [386] proposed synthetic procedure to prepare series of novel nitrides including, hexagonal W_2N_3, hexagonal WN and cubic W_3N_4, under moderate pressure of 5 GPa with elastic properties resembling or surpassing those of cubic-BN. Moreover, preparation, electronic, and mechanical properties of bulk δ−WN have been reported by Wang *et al.* [388]. The effectively fabricated δ−WN phase was stable up to 24.8 GPa. During the preparation process, W_2N_3 and melamine were adopted as tungsten source and nitrogen source, respectively, under high pressure and high temperature. The detected bulk modulus and Vickers hardness were 373 ± 8.3 GPa, 13.8 GPa, in that order[388]. Furthermore, tungsten nitride captured substantial interest in energy storage and conversion applications [389]. By means of the first-principle calculations, structural, elastic and thermodynamic properties of WC type structure of δ-WN were conveyed. Result showed that the δ-WN is mechanically stable [390, 391]. Another important aspect is that the effect of removing either metal or non-metal atoms on the stoichiometry of bulk/surface binary nitride systems has shown to play vital role in improving various properties. Mattsson and Mattsson [392] reported that structural relaxation can reduce the vacancy formation energy by more than 30% It is therefore important to include structural relaxation when calculating vacancy formation energies from first principles. Balasubramanian *et al.* [384] performed density functional theory calculations and compared between two stoichiometric phases of WN namely, NaCl and NbO-like structures. Their findings indicated that, the defect free rocksalt (NaCl) phase is unstable mechanically and thermodynamically. However, the WN in NbO phase having 25% of vacancies (cation and anion) showed mechanical stability. In another study conducted by Cai *et al.* [393], the influence of vacancy defects on electronic and optical properties of bulk gallium nitride (GaN) has been modelled. They concluded that introducing Ga and or N vacancies can increase the band gap by which optoelectronic performance can be controlled. Kerdsongpanya *et al.* [394] studied bulk unit cell of scandium nitride (ScN) via

DFT calculations. They suggested that Sc and N vacancies creation would induce asymmetric peaks in the density of state DOSs which in turn serve in thermoelectric purposes. Bocharov *et al.* [395] presented DFT calculations of clean and vacancy containing slabs of 2×2 and 3×3 uranium nitride (UN) supercells cleaved in along the 001 direction. They concluded that, vacancy formation energies for surface layer are smaller than those for sub-surface and central layers demonstrating a clear trend for segregation towards the surface and grain boundaries.

Density functional theory calculations and ab initio thermodynamics have mainly reported the stability of various metallic surfaces [396-399] however, neither MoN nor WN surfaces have been investigated yet excluding a work accomplished by Liu *et al.* [400] who performed first-principles calculations on Mo termination of hexagonal MoN (001) surface. Their findings revealed that this material enjoy high catalytic performance towards CO and sulfur adsorption. Due to their potential significance in material science, more knowledge on structural and surface properties is recommended. Therefore, in this chapter, we aim to shed light on (*i*) electronic and structural characters of all Mo and W nitrides plausible surface terminations, (*ii*) construct phase stability diagram via Ab initio atomistic thermodynamic approach under selected temperature and pressure, and (*iii*) to estimate the vacancy formation energies of these surfaces and their corresponding equilibrium vacancy concentrations at a temperature range of 300-1000 K.

5.3 Computational methods

5.3.1 Structural optimisation

All structural optimisation and energy calculations for the considered low-index surfaces were carried out using the VASP code [401]. Generalized gradient approximation GGA of Perdew and Wang (PW91) [282] was deployed for the determination of exchange-correlation functional. Throughout the optimisation, all layers were allowed to relax till the total energy and forces on atoms were converged to less than 10^{-6} eV and 10^{-4}eV/Å, respectively. We modelled 2 × 2 supercell symmetric slabs comprising 2-15 atomic layers. To eliminate the interactions within the periodic images of the slab, we adopted a vacuum thickness of at least 15 Å to separate each slab from its corresponding repeated images along the *z* axis. The cut-off energy used for the plane wave basis set was fixed to 500 eV with the Brillouin-zone integration carried out using Monkhorst-Pack grids sampling of 5×5×1 *k*-points. We apply

dipole slab correction to the surface to void any plausible surface deformation caused by dipole accumulation along the *z* direction.

5.3.2 Bulk calculations of δ_3-MoN and δ-WN

Bulk unit cells were optimized using an energy cut-off of 600.0 eV and a 12 × 12 × 12 Monkhorst-Pack (MP) scheme for the generation of κ-points. The calculated formation energy (E^f) is obtained according to the following formula;

$$E^f = E_{MN}^{bulk} - E_M^{bulk} - \frac{1}{2}E_{N2} \quad 5.1$$

where E_{MN}^{bulk} signifies the energies of bulk metal nitrides (δ_3-MoN and δ-WN per formula unit). E_M^{bulk} stands for the energies of bulk Mo or W per formula unit, and E_{N2} refers to the energy of a nitrogen molecule in the gas phase, respectively.

5.3.3 Ab initio atomistic thermodynamics

The state-of-art, *ab* initio atomistic thermodynamics has widely been utilised to provide insights into the thermodynamic stability of transition metal nitride surfaces in nitrogen atmosphere, literature offers comprehensive account of equations governing the *ab* initio atomistic thermodynamics approach underlying assumptions, and approximations [399]. Thus, the thermodynamic stability orderings of Mo-N and W-N facets in a nitrogen environment (one-component gas phase) described by altering the chemical potential according to the formula:

$$\gamma(T,P) = \frac{1}{2A}\left[G^{slab}(T,P,N_M,N_N) - N_M E_{MN}^{bulk} - (N_N - N_M)\mu_N(T,P)\right] \quad 5.2$$

In the above equation, $\gamma(T,P)$ refers to the surface free energy, *A* represents surface area of the slab, $G^{slab}(T,P,N_M,N_N)$ refers to the Gibbs free energy of δ_3-MoN and δ-WN slabs, N_M stands for the number of either molybdenum or tungsten atoms in the slab, and N_N denotes the number of nitrogen atoms in the slab. E_{MN}^{bulk} refers to the energy of bulk δ_3-MoN and δ-WN per formula unit and $\mu_N(T,P)$ denotes to the chemical potential of nitrogen. The chemical potential of nitrogen is calculated based on;

$$\mu_N(T,P) = \Delta\mu_N(T,P) + \frac{1}{2}E_{N2} \quad 5.3$$

The chemical potential of nitrogen $\mu_N(T,P)$ as a function of temperature and pressure can be written as [402];

$$\mu_N(T,P) = -4.86 - 0.967 \times \left(\frac{T}{1000}\right) - 0.1013 \times \left(\frac{T}{1000}\right)^2 + 0.0173 \times \left(\frac{T}{1000}\right)^3 + \frac{K_B\, T}{2} \ln(P_{N_2}) \quad 5.4$$

5.3.4 Formation of vacancies and concentrations

Herein, we perform a DFT study to address the surface properties with single and double vacancies. Positive calculated formation energies indicate that the desorption of a surface atom occurs non-spontaneously. For both studied systems, we created reduced surfaces by removing either metal (Mo/ W) or non-metal (N) from the stoichiometric slabs. The calculated vacancy formation energy E_{VFE} is defined as;

$$E_{VFE} = \frac{1}{n} \left(E_{MN-vacant} + \frac{n}{2} E_{N2} - E_{MN-perfect}\right) \quad 5.5$$

where $E_{MN-vacant}$ and $E_{MN-perfect}$ are the total energies of reduced and defect free slabs in Mo and W nitrides, respectively. *n* corresponds to the number of created vacancies. In symmetric surfaces, we deleted one and two nitrogen atoms from the top and the corresponding atoms in the bottom layer, therefore, the total number of vacancies (*n*) will be 2, 4, etc. E_{N2} signifies the ground state energy of the nitrogen molecule positioned inside a (15× 15 × 15 Å^3) box. The optimized bond length of N_2 was 1.1 Å with a total energy of -16.6 eV. After reporting vacancy formation energies, we predict the equilibrium vacancy concentration in the considered slab. A detailed derivation of the energy vacancy equation can be found elsewhere [158].

$$\Delta G_v \cong \Delta E_v X_v - T\Delta S_v(T) X_v + RT\,[X_v\, lnX_v + (1 - X_v)\ln(1 - X_v)] \quad 5.6$$

The change in entropy of molecular nitrogen was taken from [403]. The equilibrium vacancy molar fraction at temperature *T* was calculated according to;

$$X_v^e(T) = g.exp\left(\frac{-\Delta G}{RT}\right) \quad 5.7$$

Where *g* is a degeneracy factor accounting for internal degrees of freedom of the point defect.

The equilibrium vacancy concentrations were calculated using the formula;

$$C_v^e(T) = \frac{N_{Av}}{MW.S} X_v^e(T) \quad 5.8$$

in which S denotes the specific surface area per mass ($84.1 m^2/g$) [404], N_{Av} and MW refer to Avogadro's number and the molar mass of metal nitride (i.e. MoN and WN), respectively.

5.4 Results and discussion

5.4.1 Bulk δ_3-MoN and δ-WN

In our previous work, we covered in details the structural optimization of hexagonal molybdenum nitride unit cell [374]. The obtained equilibrium lattice parameters of WN were 2.87Å and 2.90Å which agreed well with the literature analogous values [405]. Our estimations of the formation energies for δ_3-MoN and δ-WN are -1.25 eV and -0.12 eV, respectively, in line with the corresponding published values [34, 385, 405, 406]. Both optimized unit cells are showing in Figure 5.1.

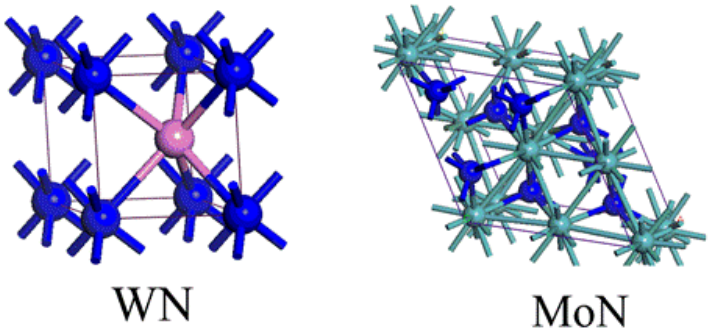

Figure 5.1: Optimized bulk unit cells of WN and MoN (pink, green, and dark blue spheres signify W, Mo, and N, in that order).

5.4.2 Geometries of δ_3-MoN and δ-WN low Miller indices

Atoms in a slab seek to stabilize themselves via relaxing to more energetically favourable positions by showing either upwards or downwards displacements [407]. To model symmetrical slabs of Mo and W nitride phases, we applied 2×2 supercell that afford four polar (non-stoichiometric) and non-polar (stoichiometric) low-index planes oriented along the (100), (111), (110) and (001) directions. Tables 5.1 and 5.2 report the relaxation of the interlayer spacing in the first three layers of MoN and WN slabs (i.e, d_{12} and d_{23}). The differences between relaxed and ideal interlayer spacing, Δd_{ij} with percentage relaxation are calculated via

$\Delta d_{ij}=(d_{ij}-d_0)\,/d_{ij}$ where d_{ij} is the interlayer spacing between two atomic layers (for instance, first and second layers in the relaxed slab) and d_0 denotes the interlayer spacing in the initial slab.

Table 5.1: First and second interlayer distances d_{ij} (Å) and analogous interlayer relaxation (as a reference to the bulk values) of the considered MoN surfaces. Positive values indicate an expansion of the distance (upward displacements) and negative values refer to a reduction occurred in the topmost layers (downward displacements).

Slab	Atomic ratio *R*	$\Delta d_{12}= d_{12}-d_0$ *(Å)*	interlayer relaxation *(%)*	$\Delta d_{23}= d_{23}- d_0$ *(Å)*	interlayer relaxation *(%)*
MoN(100)	64/80	-0.17	-27	0.68	45
MoN(100)+1V_{Mo}	64/78	-0.13	-20	0.47	37
MoN(100):N	80/64	-0.01	-2	-0.27	-50
MoN(100):N+1V_N	78/64	-0.09	-13	-0.23	-39
MoN(100):N+2V_N	76/64	-0.01	-2	-0.22	-37
MoN(100):N+1V_{N*}	78/64	-0.07	-10	-0.19	-31
MoN(110):MoN	80/80	-0.18	-15	0.04	3
MoN(110):MoN+1V_{Mo}	80/78	-0.01	-0.9	0.00	0.2
MoN(110):MoN+1V_N	78/80	0.00	0.5	0.00	0.4
MoN(110):MoN+2V_N	76/80	0.01	0.9	0.00	0.5
MoN(111):Mo	80/96	-0.29	-85	0.00	-1
MoN(111):Mo+1V_{Mo}	80/94	-0.29	-86	0.00	0.01
MoN(111):N	80/64	-0.08	-15	0.09	-16
MoN(111):N+1V_N	78/64	-0.07	-13	0.10	-19
MoN(111):N+1V_{N*}	78/64	-0.09	-16	0.07	-13
MoN(001):Mo	64/80	-0.08	-6	0.08	5
MoN(001):Mo+1V_{Mo}	64/78	-0.01	-1	0.00	0.00

Table 5.2: First and second interlayer distances dij (Å) and analogous interlayer relaxation (as a reference to the bulk values) of the considered WN surfaces. Positive values indicate an expansion of the distance (upward displacements) and negative values refer to a reduction occurred in the topmost layers (downward displacements).

Slab	Atomic ratio *R (N/M)*	Δd_{12}= d_{12}-d_0 *(Å)*	interlayer relaxation *(%)*	Δd_{23}= d_{23}- d_0 *(Å)*	interlayer relaxation *(%)*
WN(100):W	28/32	-0.19	-30	0.06	3.5
WN(100):W+1V_W	28/30	0.01	1.9	-0.08	-3.5
WN(100):W+1V_N	26/32	0.03	4.6	-0.04	-2.6
WN(100):W+1V_{W*}	28/30	0.03	4.5	-0.003	-0.2
WN(100):N	36/32	-0.44	-36	0.3	27
WN(100):N+1V_N	34/32	0.07	6	-0.14	-14
WN(100):N+1V_{N*}	34/32	0.001	0.11	-0.001	-0.16
WN(110):WN	36/36	-0.16	-13	0.05	3
WN(110):WN+1V_N	34/36	0.01	0.00	0.00	0.00
WN(111):W	36/40	-0.15	-32	-0.07	-12
WN(111):W+1V_W	36/38	0.02	4	0.00	1
WN(111):N	36/32	-0.16	-14	0.05	3
WN(111):N+1V_N	34/32	0.00	-0.59	-0.03	-2
WN(111):N+2V_N	32/32	-0.03	-3	-0.02	-1
WN(001):W	12/16	-0.04	-3	-0.01	-0.9
WN(001):W+1V_W	12/14	-0.06	-4	-0.04	-3

The surfaces are labelled according to their orientations and terminated elements. For the analysis of the optimized δ_3-MoN surfaces, we found that the ideal un-optimized molybdenum terminated surface MoN(100):Mo, comprises only Mo atoms in its outermost layers. However, the lowest energy structure undergoes surface reconstruction that resulted in downward movement by 27% via forming nitrogen dimer rows. The ideal and relaxed slabs are presented in Figure 5.2 (a) and (b), respectively. Furthermore, the interlayer spacing in the relaxed top most layer and the beneath layer amounts to d_{12}=0.17Å (in reference to bulk positions). For the MoN(100):N termination, a minor shrinkage towards the slab centre has been observed where d_{12} is only 0.01 Å as demonstrated in Figure 5.3 (a).

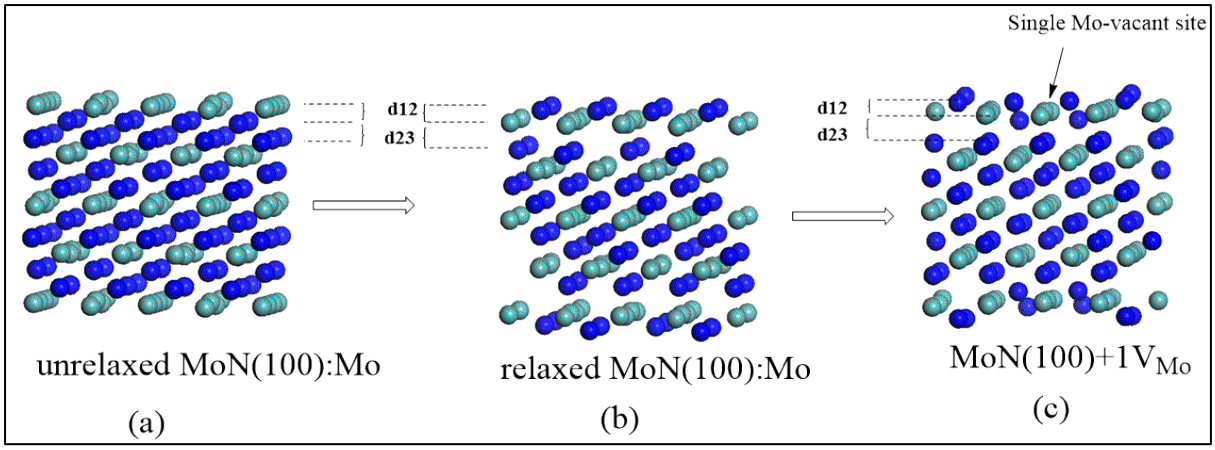

Figure 5.2: Optimised geometries of MoN slabs, showing the un-optimized MoN (100): Mo (a), optimized MoN(100):Mo (b), and (c) Mo-defect (100) surface termination. Light blue and blue spheres signify Mo and N, respectively.

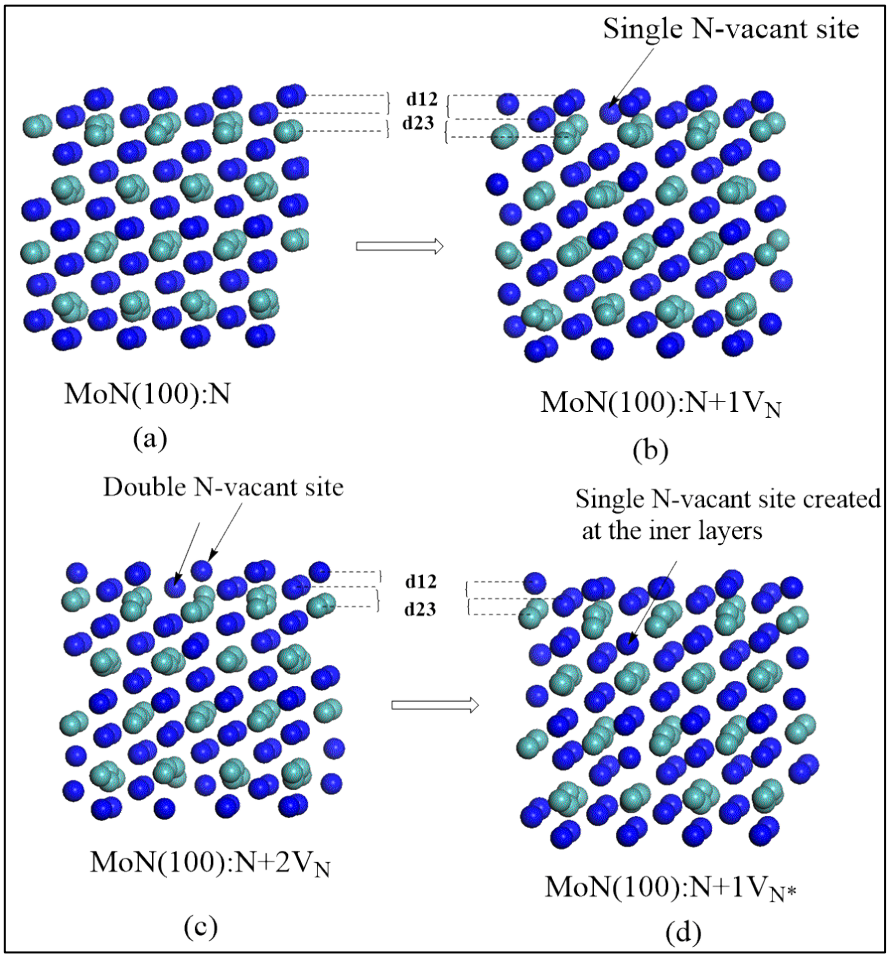

Figure 5.3: Optimised geometries of the MoN(100):N surfaces; perfect slab (a) and defected slabs (b-d). Light blue and blue spheres signify Mo and N, respectively.

Figure 5.4 (a) demonstrates cleaving bulk δ_3-MoN along the (110) direction. A stoichiometric surface that offers an equivalent number of Mo and N atoms has been optimized. A downward relaxation between the first and second layers of about 15% is observed. The relaxation between the second and third layer was only 3%. The unrelaxed polar (111) surface offers two possible terminations labelled as MoN(111):Mo and MoN(111):N.

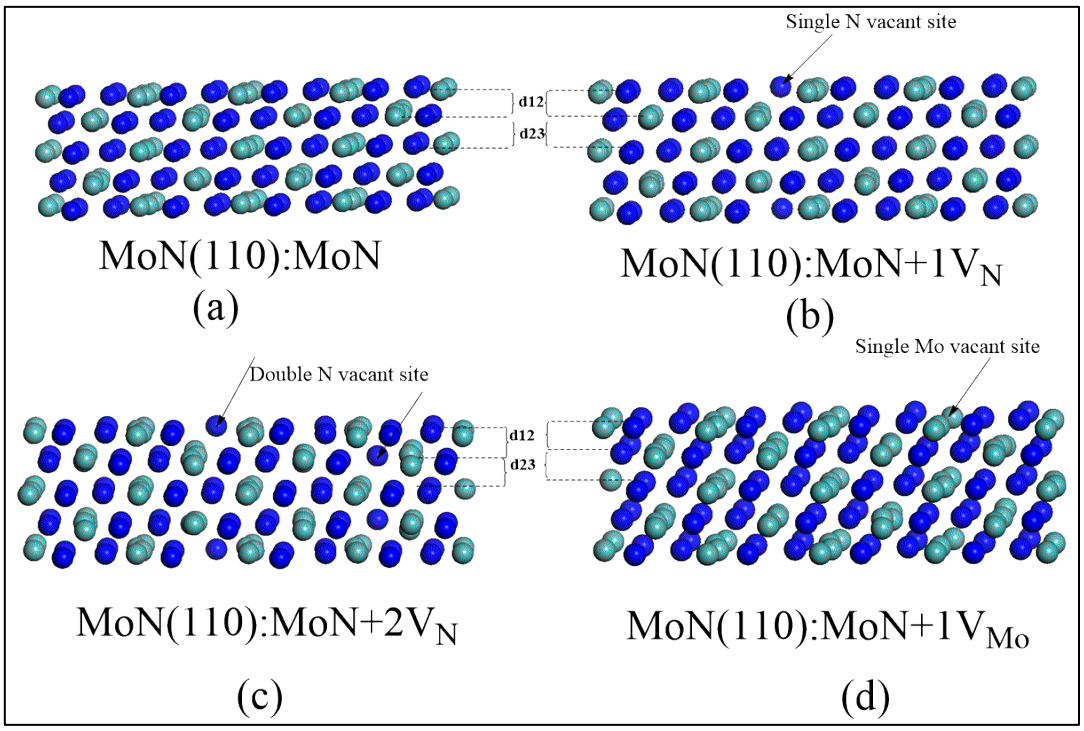

Figure 5.4: Side of views of the MoN(110):MoN optimized geometries; perfect (a) and vacant slabs (b-d). Light blue and blue spheres denote Mo and N, respectively

Optimized slab indicates that Mo truncated surface undergoes a drastic surface contraction. On the other hand, N-terminated surface exhibits a much milder contraction that allows nitrogen atoms in first top layer to shrink up to 15%. This value has been computed via the relation $\Delta d_{ij} = (d_{ij}-d_0)/d_{ij} \times 100$ %, in which d_{ij} is the interlayer spacing between first and second atomic layers and d_0 is the bulk interlayer spacing. Figure 5.5 (a-d) demonstrates side views of un-relaxed and relaxed slabs.

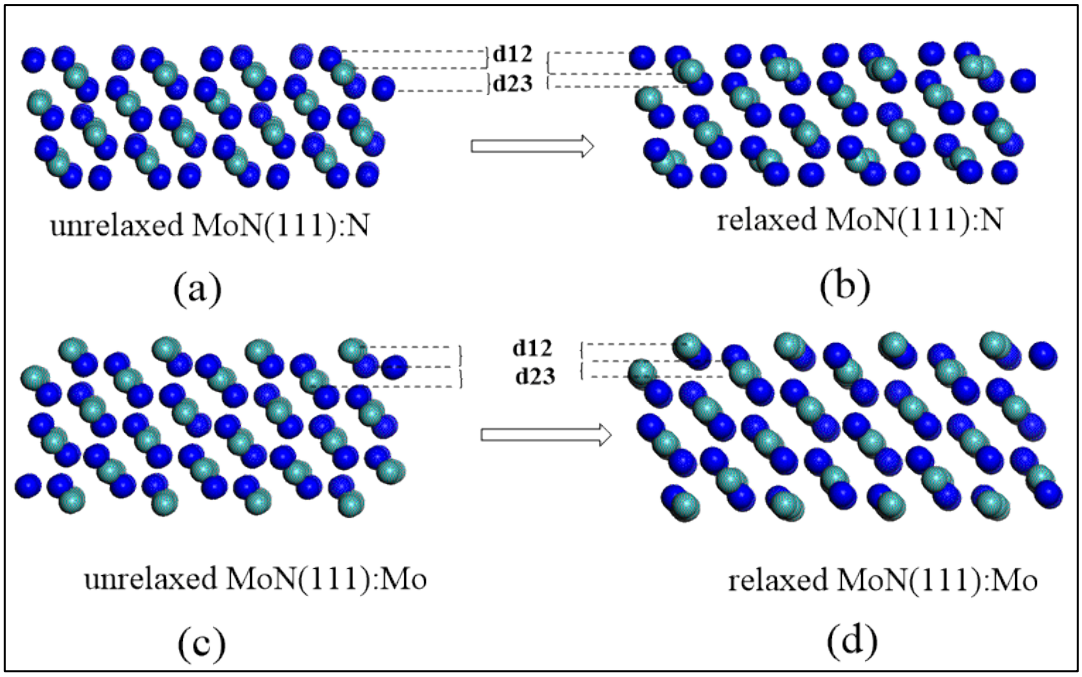

Figure 5.5: Unrelaxed and relaxed MoN (111): N and Mo terminated slabs. Light blue and blue spheres denote Mo and N, respectively.

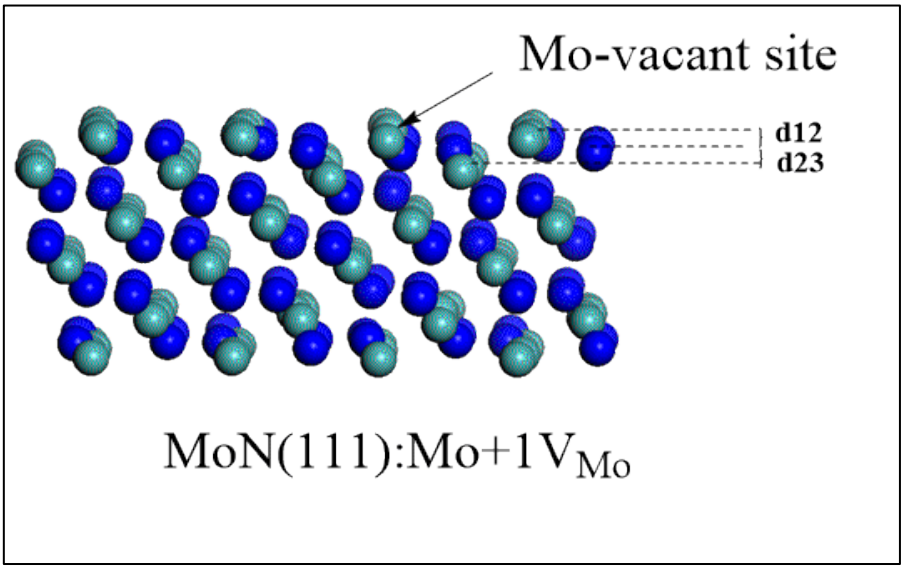

Figure 5.6: The optimized geometries of the MoN(111):Mo terminated surface containing one Mo-vacant site. Light blue and blue spheres denote Mo and N, respectively.

Finally, the (001) configuration was truncated with molybdenum atoms at the top most layer as shown in Figure 5.7(a). The MoN(001):Mo experienced a downward displacement by only d_{12} = -0.08 Å.

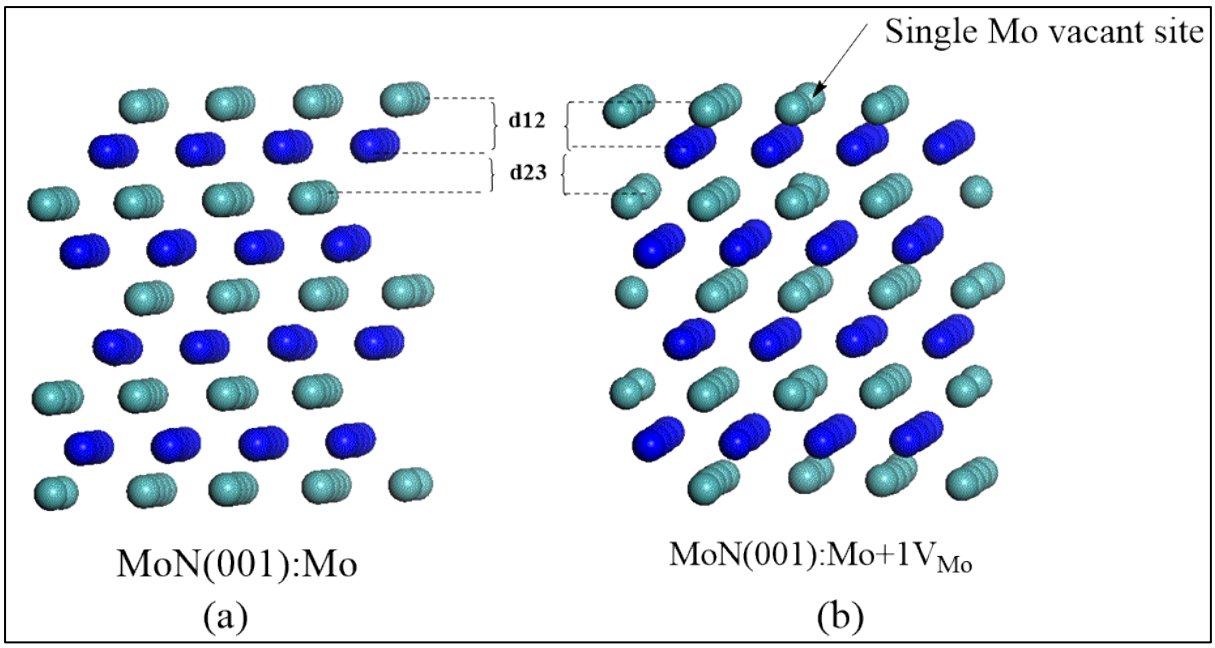

Figure 5.7: Side view of the MoN(001):Mo optimized geometry; perfect (a) and defect containing slab (b). Light blue and blue spheres denote Mo and N, respectively.

Having discussed surface terminations of hexagonal molybdenum nitride, we are now considering surface properties of hexagonal tungsten nitride (δ-WN). Herein, various atomic layers oriented along (100), (110), (111), and (001) directions have been optimized to be either N- or W-terminated planes excluding (110) plane that exhibits one stoichiometric edge denoted as WN(110):WN. The N- terminated (100) slab relaxes downward leading to shortening the W–N bond length by 36%. Similarly, the first upper layers in W-terminated (100) surface has been contracted up to 45% with no surface reconstruction noticed. Figure 5.8 (a) and (d) depict side views of tungsten nitride nitrogen and tungsten optimised geometries in (100) plane.

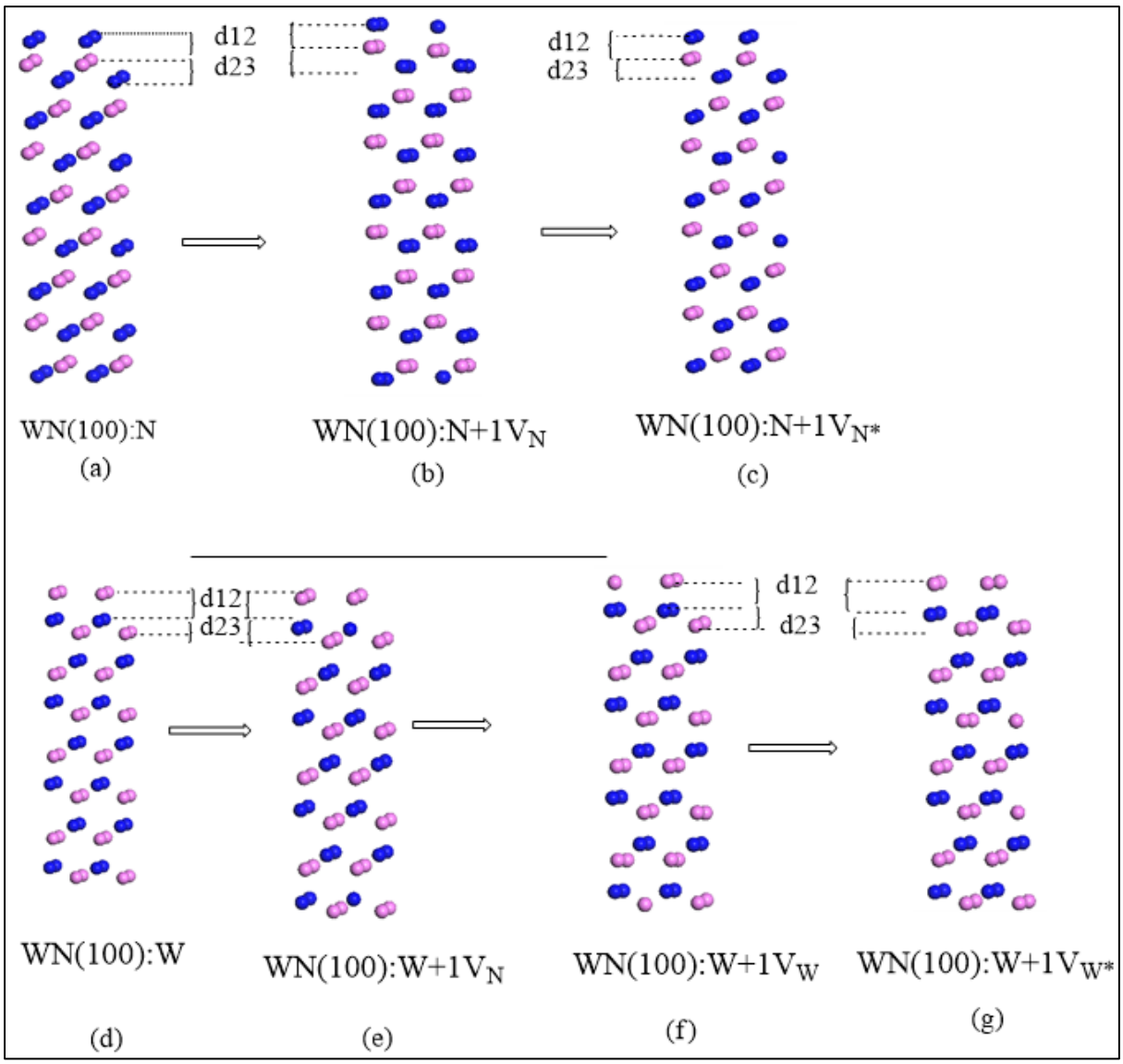

Figure 5.8: Side view of the WN (100) W and N slabs. Pink and blue spheres denote W and N atoms, respectively.

The optimized geometry of WN(110) slab demonstrates a downward displacement compared to the initial unoptimized one by 13%. Side views of WN(110) surface structure is shown in Figure 5.9 (c).

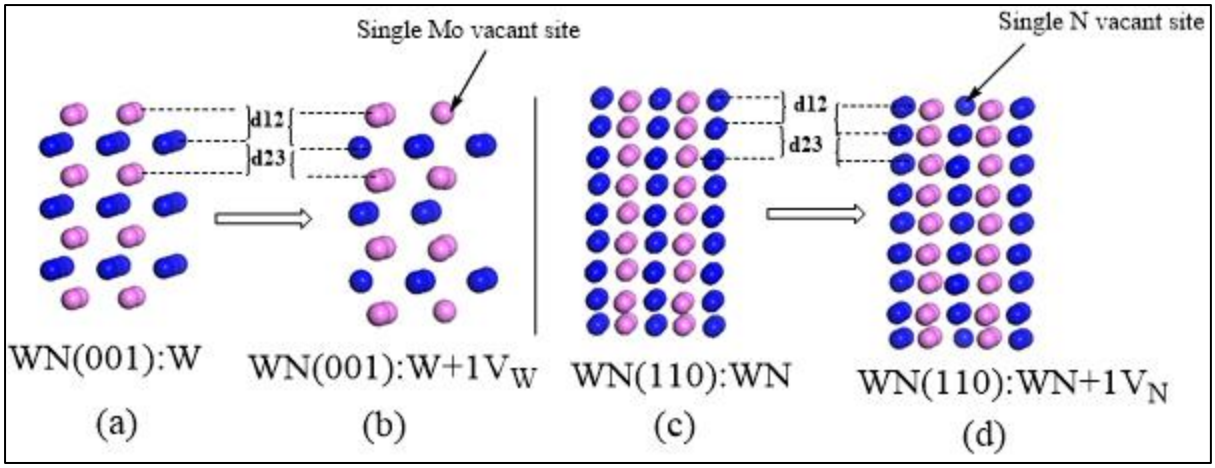

Figure 5.9: Side view of the WN (001) and WN (110) optimized slabs. Pink and blue spheres denote W and N, respectively.

For WN(111) N ended slab, inward relaxation by 14% compared to the bulk geometry is observed in Figure 5.10 (a). However, tungsten terminated slab tends to contract by 32% as a reference to the ideal geometry as depicted in Figure 5.10(d). All in all, studied molybdenum and tungsten nitride surfaces tend to mainly experience downward displacements, similarly to the observed trends in cubic boron nitride surfaces [408].

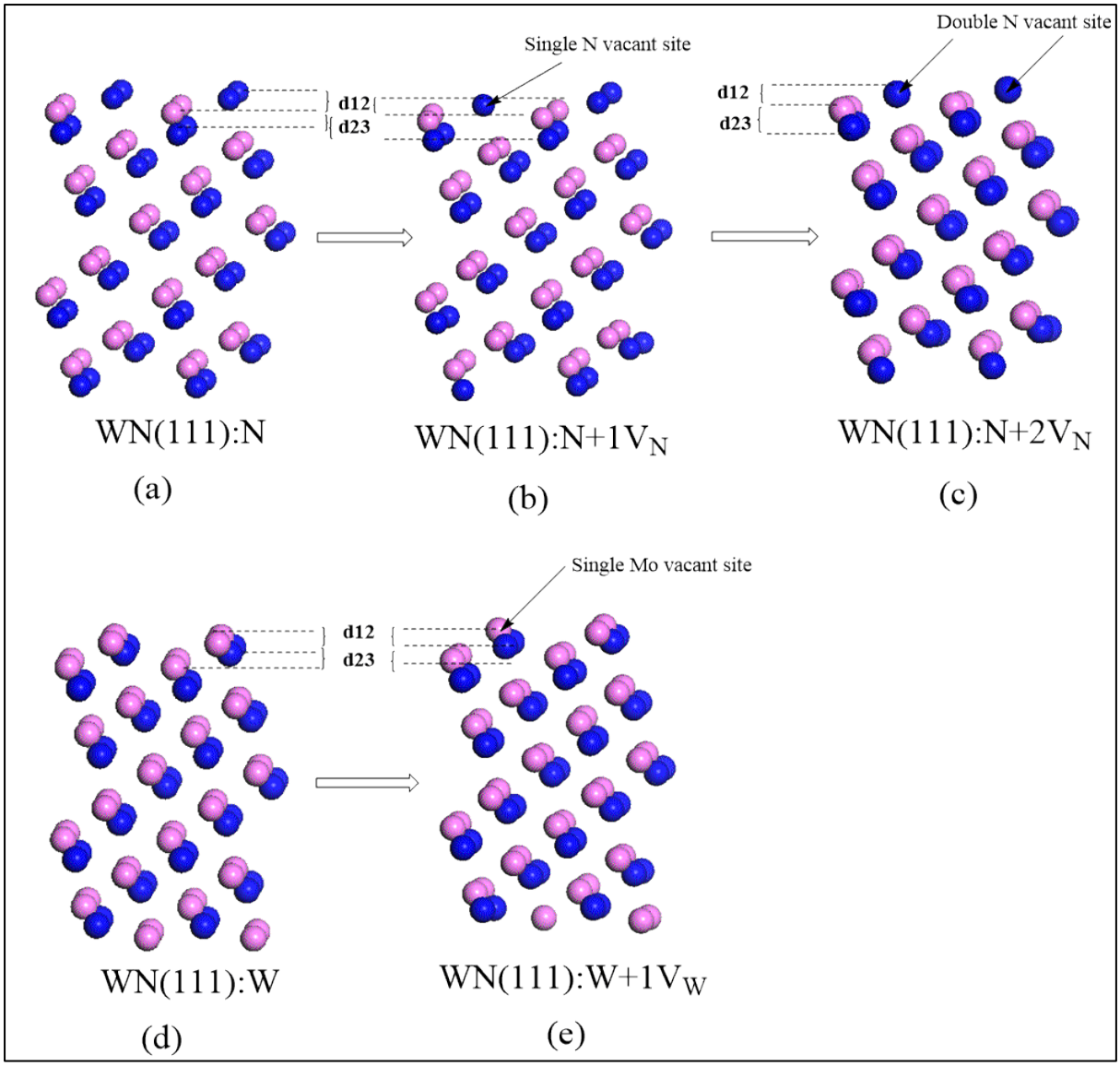

Figure 5.10: Side view of the WN (111) perfect and vacant-containing slabs. Pink and blue spheres denote W and N, respectively.

The effect of introducing an arbitrary vacant site is considered in this section. The calculated vacancy formation energies and equilibrium concentrations for the inspected surfaces are presented in Table 5.3. As we are considering symmetric slabs with top and bottom faces, removal of an atom of one side of the slab requires removal of its counterpart atom in the other side of the slab.

Thus, for the MoN(100):Mo+1V_{Mo}, we assumed a monovacancy structure when one Mo vacant site is created (*i.e.* one Mo atom is removed from the upper and corresponding bottom most layers of the slab). Upon relaxing the structure as seen in Figure 5.2 (c), the neighbouring atoms undergo significant reconstruction resulted in altering the Mo-terminated surface to be N-

terminated. This displacement is associated with downward relaxation by 20%. Calculated vacancy formation energy indicated that Mo-removal is an endothermic process by 0.55eV per Mo-vacant site.

Table 5.3: Vacancy formation energies (VFEs) and equilibrium concentrations for some selected defects-containing slabs of MoN.

Vacant slab	Total *VFE* (eV)	VFE per vacant site (eV)	Concentration $C_v^e(T)$(Cm^{-2}) at 300K
MoN(100):MoN+1V_{Mo}	1.10	0.55	-
MoN (100):N+1V_N	2.03	1.01	1.0×10^{17}
MoN(100):N: +2V_N	2.56	0.64	7.7×10^{19}
MoN(100):N+1V_{N*}	3.55	1.77	6.8×10^{13}
MoN(100):N+1V_{N**}	3.65	1.82	4.2×10^{13}
MoN(110):MoN+1V_N	3.44	1.72	2.3×10^{13}
MoN(110):MoN+2V_N	6.75	1.68	1.6×10^{14}
MoN(110):MoN+1V_{Mo}	-0.04	-0.02	-
MoN(111):N+1V_N	2.17	1.08	1.1×10^{16}
MoN(111):N+1V_{N*}	2.69	1.34	8.7×10^{14}
MoN(111):N+1V_{Mo}	-0.73	-0.36	-

(* and **) Refer to removing N atom from second and central layers, respectively.

In the case of the N vacancy in MoN(100):N+1V_N surface, the neighbouring atoms are displaced to a lesser extent when compared with the rearrangement in (100):Mo. Upon the removal of the second nitrogen atom, the resulting geometry is associated with a slight inward displacement of the outermost surface nitrogen atoms by 2% in a reference to the bulk configuration. In MoN(111):Mo+1V_{Mo} structure Figure 5.6 , the two-direction surface with two molybdenum vacancies (one at each side) experience noticeable downward relaxation at the topmost layer of about 86 % which is in line with its counterpart defect-free surface. Table 3, documents vacancy formation energies for the adopted slabs. Concerning, vacancy creation over WN surfaces, Table 5.4 shows that WN (111):N+2V_N affords the highest vacancy concentrations among the explored WN surfaces.

Table 5.4: Vacancy formation energies (VFEs) and equilibrium concentrations for some selected defects-containing slabs of WN.

Vacant slab	Total VFE (eV)	VFE per vacant site (eV)	Concentration $C_v^e(T)$(Cm^{-2}) at 300K
WN(100):N+1V_N	2.29	1.14	4.6×10^{16}
WN(100):N+2V_N	5.49	1.37	2.8×10^{17}
WN(100):N+1V_W	-2.28	-1.14	-
WN(110):WN+1V_N	3.05	1.52	1.2×10^{15}
WN(111):N+1N_V	3.38	1.69	1.8×10^{15}
WN(111):N+2V_N	7.26	1.81	2.0×10^{17}
WN(111):W+1V_W	-4.18	-2.09	-

Theoretical calculated values of Mo, W and N vacancies formation energies VFEs (eV), vacancy equilibrium concentrations $C_v^e(T)$ for the δ_3-MoN and δ-WN phases are presented in Tables 5.3 and 5.4, correspondingly. The obtained results will be valuable to understand the interaction of nitrogen with defective surfaces, in order to understand the Mars−van Krevelen mechanism [409] operating in many important catalytic reactions, most notably in ammonia formation.

Furthermore, Bader's charges were calculated using a code developed by Henkelman's group [410]. The aim is to explore the bond nature in δ_3-MoN and δ-WN composites. Tables 5.5 and 5.6 report calculated average Bader's charge of Mo, W, and N atoms in the first two topmost layers of the nominated low index surfaces. Our analysis of charge transfer suggested net charges of Mo and N atoms in bulk δ_3-MoN to be 1.44 e and −1.44 *e*, respectively. W atoms carry a net charge of 1.45 *e* and N atoms hold -1.45 *e*. This indicates a charge transfer from the metal atoms (Mo or W) to non-metal atoms (N) reflecting the bond's ionic nature [388]. Table 5.5 displays that the metal atoms in the first and second layers of the MoN and WN facets reproduce the ionic feature of their bulk. Electronegativity of N atoms in the first and second layers of studied slabs closely matches their analogous bulk with some deviation, especially in defects-containing slabs.

Table 5.5: Average bader charges in (e) for Mo, W, and N atoms, subscript numbers refers to the first and second atomic layers.

Slab	Mo_1	Mo_2	N_1	N_2
MoN(100):MoN	0.89	1.17	-1.31	-1.38
MoN(100):MoN+1V_{Mo}	0.89	1.25	-1.29	-1.37
MoN(100):N	1.68	1.46	-1.04	-1.25
MoN(100):N+1V_{N*}	1.64	1.42	-0.88	-1.25
MoN(110):MoN	1.19	1.50	-1.30	-1.36
MoN(110):MoN+1V_{Mo}	1.23	1.51	-1.41	-1.35
MoN(110):MoN+2V_N	1.15	1.46	-1.30	-1.37
MoN(110):MoN+2V_N	1.13	1.42	-1.30	-1.36
MoN(111):Mo	0.93	1.12	-1.34	-1.37
MoN(111):Mo+1V_{Mo}	0.94	1.11	-1.34	-1.37
MoN(111):N	1.16	1.39	-1.21	-1.44
MoN(111):N+1V_N	1.55	1.51	-1.13	-1.31
MoN(111):N+1V_{N*}	1.55	1.44	-1.14	-1.32
MoN(001):Mo+1V_{Mo}	0.71	1.37	-1.31	-1.42

Table 5.6: Average Bader's charges in (e) for W and N atoms, subscript numbers refers to the first and second atomic layers.

WN slabs	W_1	W_2	N_1	N_2
WN(100):W	1.06	1.44	-1.54	-1.42
WN (100):N	1.90	1.48	-1.04	-1.39
WN (100):N+1V_N	1.66	1.47	-1.00	-1.43
WN (100):N+2V_N	1.54	1.42	-1.08	-1.44
WN (100):W+1V_W	1.09	1.53	-1.40	-1.45
WN (110):WN	1.14	1.63	-1.33	-1.46
WN (001):N	1.74	1.54	-1.08	-1.42
WN (001):W	0.70	1.48	-1.43	-1.52
WN (001):W+1V_W	0.75	1.60	-1.31	-1.46
WN (111):W	0.89	1.17	-1.45	-1.40
WN (111):W+1V_W	0.95	1.27	-1.39	-1.40
WN (111):N	1.59	1.64	-1.25	-1.37
WN (111):N+1V_N	1.45	1.50	-1.37	-1.24
WN (111):N+2V_N	0.94	1.33	-1.25	-1.39

5.4.3 Stability phase diagram

Generally, the change in nitrogen chemical potential $\Delta\mu_N(T,P)$ vary between two distinct boundaries termed as nitrogen-rich conditions (zero) and nitrogen-lean limits (*i.e.* formation energy E^f). A nitrogen-lean limit describes possible value of the change in the chemical potential of nitrogen once bulk δ_3-MoN and δ-WN commence forming from the interaction of bulk molybdenum/ tungsten in a nitrogen atmosphere. On the other hand, a nitrogen-rich limit denotes the condensation of N_2 molecule. For symmetric slabs adopted in this study and according to calculated E^f values, N-lean limit of δ_3-MoN is estimated to be -1.25 eV, whilst in the case of δ-WN, it amounts to -0.12 eV. Tables 5.7 and 5.8 present surface free energy at N lean and rich limits for both considered phases.

Table 5.7: Surface free energy γ *(T, P)*, values in eV /Å^2 for all surfaces at N-lean and N-rich limits of δ_3-MoN.

Slab	N_{Rich}	N_{Lean}
MoN(100):Mo	0.208	0.130
MoN(100):Mo+1V_{Mo}	0.202	0.134
MoN(100):N	0.103	0.180
MoN(100):N+1V_N	0.110	0.178
MoN(100):N+2V_N	0.112	0.170
MoN(100):N+1N_{V*}	0.113	0.181
MoN(110):MoN	0.141	0.141
MoN(110):MoN+1V_{Mo}	0.135	0.141
MoN(110):MoN+1V_N	0.151	0.145
MoN(110):MoN+2V_N	0.156	0.145
MoN(111):MoN	0.851	0.811
MoN(111):Mo+1V_{Mo}	0.188	0.153
MoN(111):N	0.097	0.136
MoN(111):N+1V_N	0.101	0.136
MoN(111):N+1V_{N*}	0.102	0.137
MoN(001):Mo	0.246	0.159

Table 5.8: Surface free energy γ *(T, P)* values in eV /Å^2 for all surfaces at N-lean and N-rich limits of δ-WN slabs.

	N_{Rich}	N_{Lean}
WN(100):W	-3.44	-3.44
WN(100):W+1V_W	-3.22	-3.22
WN(100):N	-0.30	-0.29
WN(100):N+1V_N	-3.05	-3.05
WN(100):N+2V_N	-3.01	-3.01
WN(110):WN	-2.61	-2.61
WN(110):WN+1V_N	-2.59	-2.59
WN(111):W	-2.54	-2.54
WN(111):W+1V_W	-2.44	-2.44
WN(111):N	-2.11	-2.11
WN(111):N+1V_N	-2.08	-2.08
WN(111):N+2V_N	-2.05	-2.05
WN(001):W	-2.25	-2.25
WN(001):W+1V_W	-1.94	-1.94
WN(001):N	-3.06	-3.06
MoN(001):Mo+1V_{Mo}	0.249	0.173

Figure 5.11 plots stability phase diagram of δ_3-MoN possible surface terminations, it is obvious that in δ_3-MoN, the (111):N- truncated surface appear to be the most stable configuration competing with nitrogen vacancies containing slabs at all obtainable values of nitrogen chemical potential. There is no dependency of surface free energy on chemical potential changing for stoichiometric slabs (*i.e.*, equal numbers of atoms Mo=N as in (110) surface termination). The obtained thermodynamic stability trend suggests that the absorption of bulk Mo in a N_2 gas-phase environment only form a MoN(111):N phase. The stability of nitrogen terminated surfaces is in line with the general consensus the literature findings that surfaces terminated with electronegative atoms (such as N and Br) hold the most stable geometries [408,

411]. Based on equation 5.4 in section 5.3.3, Figure 5.11 displays the obtained stability lines relevant to practical conditions of *T-P*.

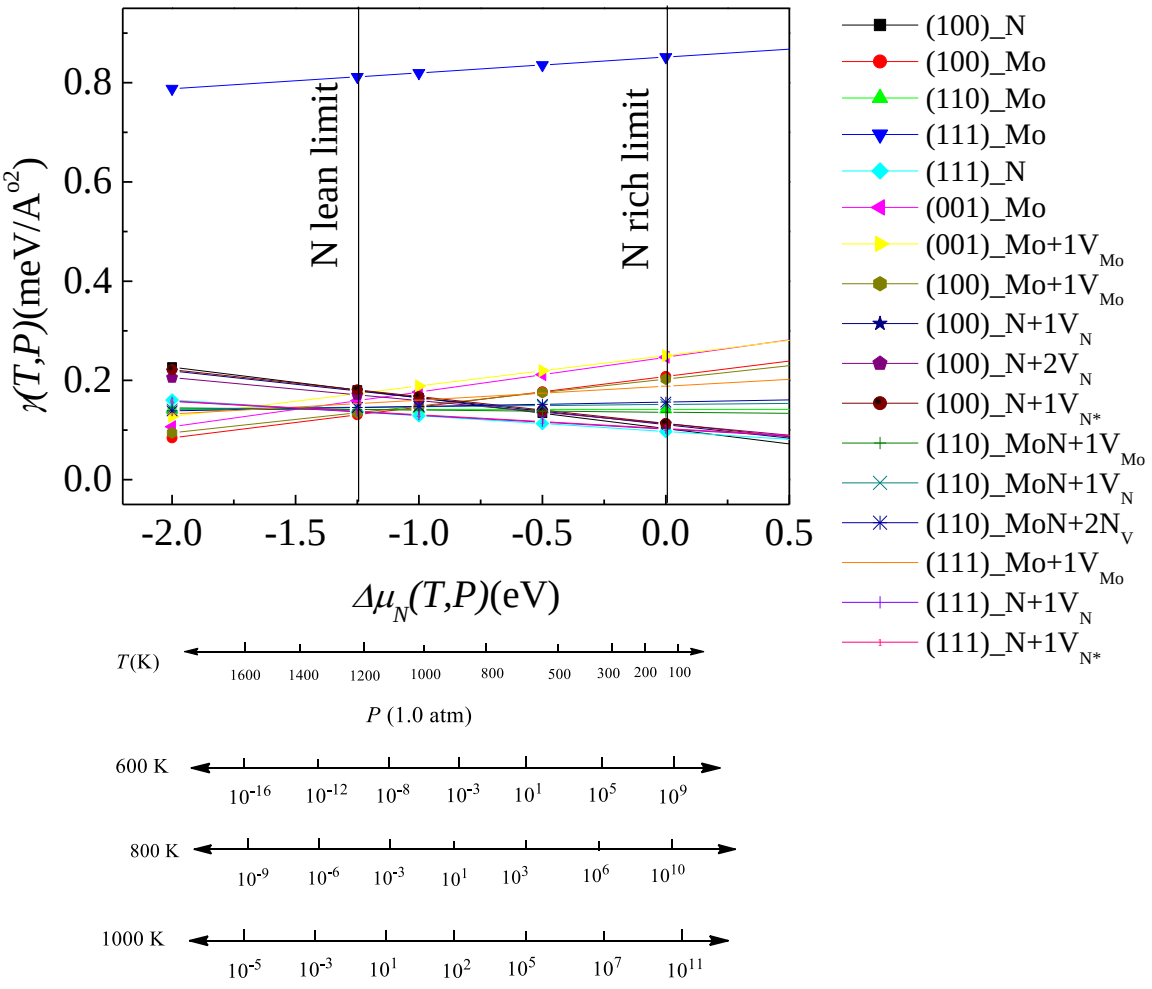

Figure 5.11: Stability phase diagram of Mo-N system represented by surface energies against the N chemical potential. The left vertical line stands for the formation energy of bulk δ_3-MoN.

To this end, several structural and electronic factors affect the thermodynamic stability ordering; such as interlayer displacements, polarity, and charge distribution. Zhu *et al.* [412] stated that surface stability is mainly governed by interplanar distance. Along the same line of enquiry, we have established that the surface terminations with a marginal inter layer relaxation assume higher thermodynamic stability in contrast with significantly relaxed terminations [411]. Nonetheless, MoN(111):Mo associates with a significant downward relaxation, MoN(111):N slab is more stable than terminations that incur lesser relaxation as reported in Table 5.1. This may be ascribed to the positive charges accumulated on molybdenum atoms.

Based on atomic ratios presented in Tables 5.1 and 5.2, the surface polarity can be excluded as the underpinning factor that determines the thermodynamic stability ordering. Overall, the stability tends can be influenced by a combination of factors as described by Rogal *et al.* [413]. Figure 5.12 depicts stability phase diagram of δ-WN possible surface terminations, it is obvious that in δ-WN phase, the (100):N- truncated surface appears to be the most energetically stable.

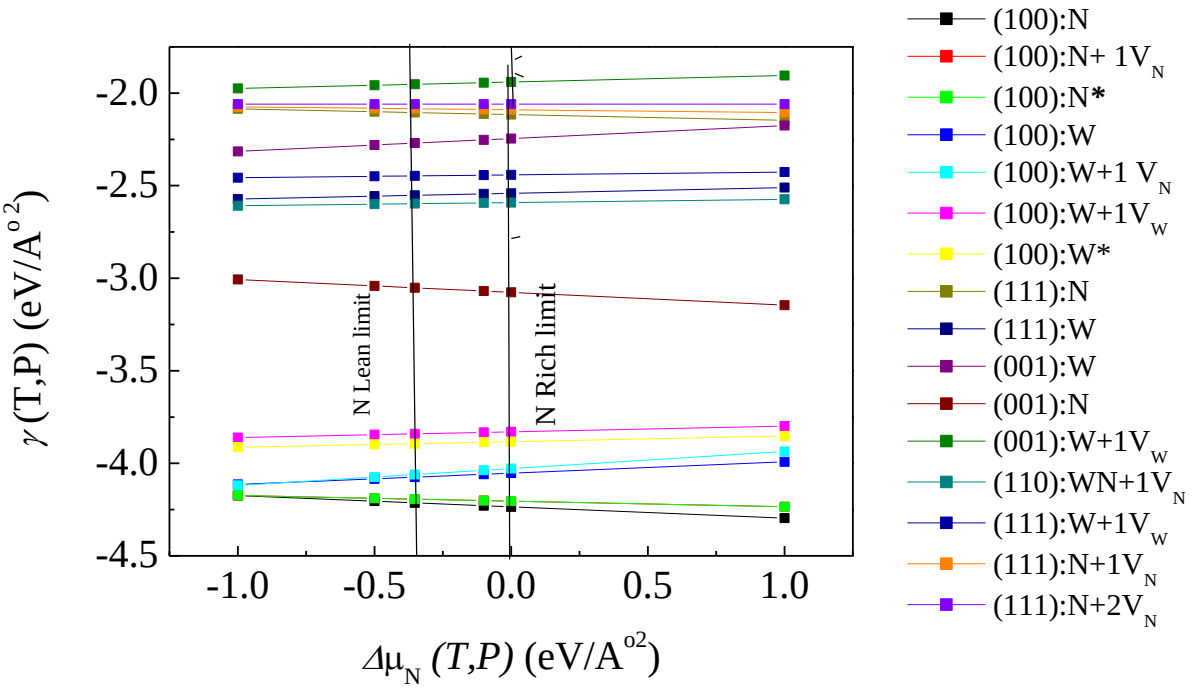

Figure 5.12: Stability phase diagram of δ-WN surfaces represented by surface energies against the N chemical potential. Nitrogen lean limit indicates the formation energy of bulk δ-WN.

We have illustrated in our recent studies that factors dictating thermodynamic stability ordering include polarity of surfaces, charge distributions, and surface relaxations[414-417]. Likewise, since δ_3-MoN and δ-WN represent 4-*d* and 5-*d* transition metal nitrides; respectively, they display different geometries space groups, charge distributions, surface relaxation, and reconstructions. These factors may have resulted in a different trend of thermodynamic stability among δ_3-MoN and δ-WN.

5.4.4 Density of state analysis

After having an insight into the geometries of perfect and defect low-index molybdenum and tungsten nitride surfaces, herein, we are looking at the electronic structure through analysing the total density of states DOSs for the most stable geometries (i.e. MoN(111):N and WN(100):N). It is well known that the presence of nitrogen atoms in the lattice of molybdenum and tungsten nitrides contribute in possessing higher *d*-band electronic density of states at the fermi level and hence relevant electronic characteristics approaching those of precious metals. In another word, the resulted metallic nature of δ_3-MoN and δ-WN systems stem from the mixture of Mo(4*d*), W(5*d*) and N(2*p*) orbitals [4]. Total and projected density of state PDOS of both bulk systems are very comparable to analogous reported values [418]. The predicted total and partial DOSs of the (111): N and (100): N surface terminations and their corresponding pure metallic are shown in Figures 5.13 and 5.14, respectively, which obviously mimicking the metallic nature of their analogues bulk unit cells. The most prominent peaks depict the hybridization of metal *d* orbitals with nitrogen *p* orbitals [112].

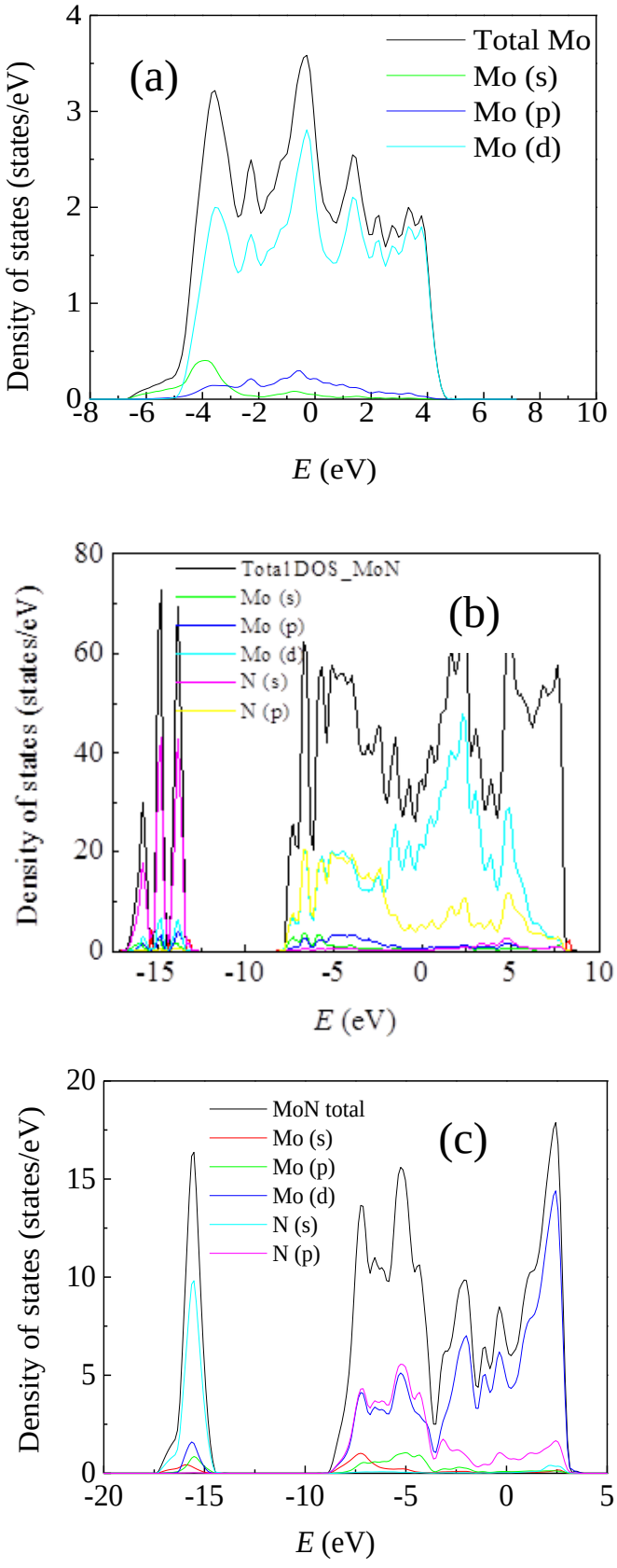

Figure 5.13: Total and partial density of states for (a) bulk Mo, (b) bulk δ_3-MoN, and (c) nitrogen terminated δ_3-MoN(111) surface.

As can be observed from Figure 5.13, the Mo-*d* orbitals strongly contribute to DOSs values at the Fermi level resulting in high contribution to the metallic nature of δ_3-MoN whereas *p* electrons do not strongly participate at the Fermi level. The valance band extending between –17 and –14 eV is mostly composed of N-*s* orbitals. In general, our obtained DOSs for the nitrogen terminated (111) plane accords very well with the DOSs of its correspondence bulk obtained in previous DFT accounts.

It is clearly seen from Figure 5.14 that the valence bands of δ-WN (100): N are comprised of three main components. The lowest states are located from -19.0 Ev to -16.0 eV and mainly contain nitrogen *2s* states. The valence bands stretched from -10 eV to -5eV eV and exhibits strong of hybridizing W*5d* and N*2s* states.

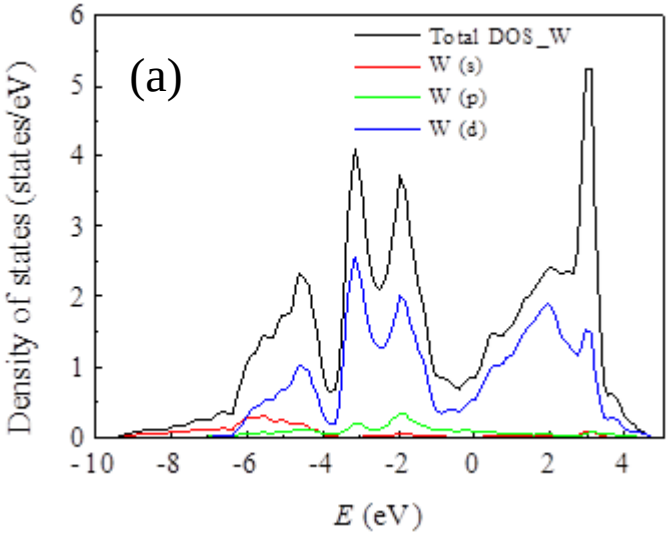

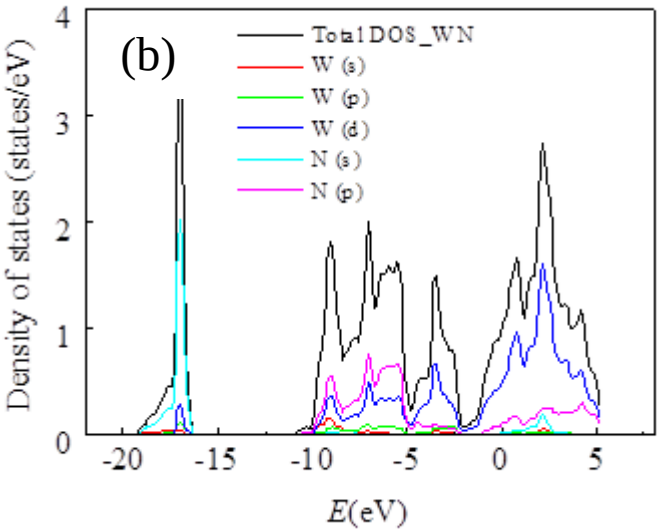

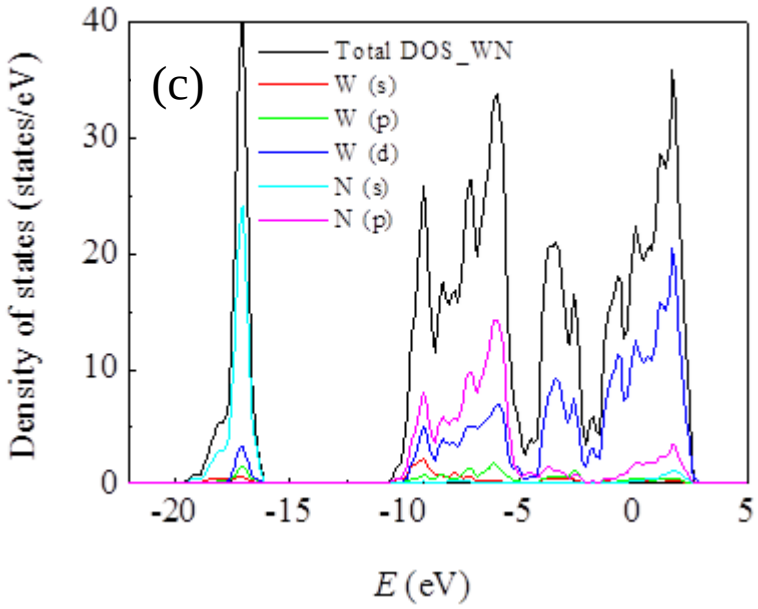

Figure 5.14: Total and partial density of states of (a) bulk W, (b) bulk δ-WN, and (c) nitrogen terminated δ-WN (100) surface.

The valence bands near the Fermi level is occupied between -5eV to 0.0 eV and is derived mainly from the to5d-states. The conduction band states located from 0 eV to 2.75eV mainly consists from the W5*d*, *p* and N2*s* states[391].

Regarding the bonding nature in δ-WN system, it can be classified as a mixture of metallic, ionic and covalent contributions. The metallic one can be ascribed to the partially filled W*5d* bands. The ionic nature of the WN bond is determined by charge transfer from W atoms to the more electronegative N atoms. Finally, the presence of a covalent bonding is indicated by hybridization of the C *2p* and W*5d* states.

Lastly, Figures 5.15 and 5.16 resemble the Nitrogen vacancy concentrations as a function of temperature for selected most stable surfaces of δ_3-MoN and δ-WN phases, respectively. These created vacancy sites in a stoichiometric geometries could serve as potential sites in the so-called Mars−van Krevelen mechanism.

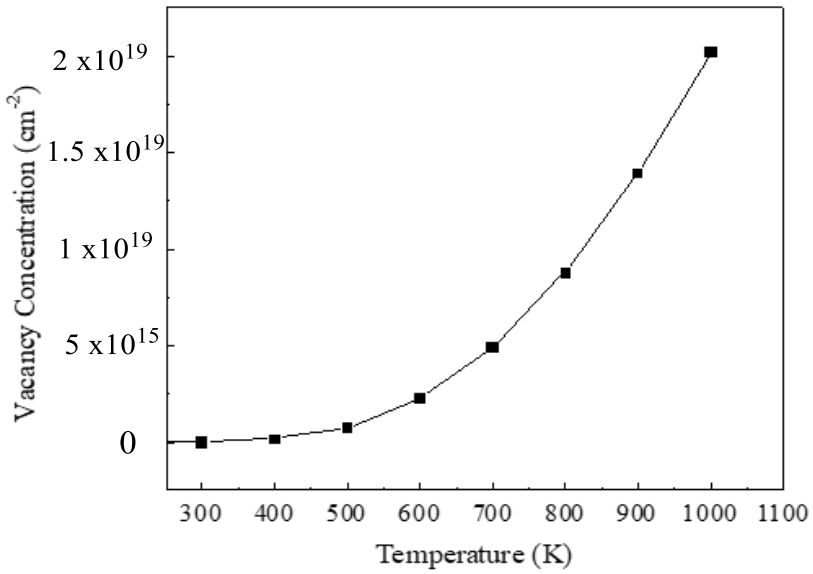

Figure 5.15: Nitrogen vacancy concentration as a function of temperature at nitrogen vacancy coverage X_v = 1/16 of MoN(111):N+1V_N surface termination.

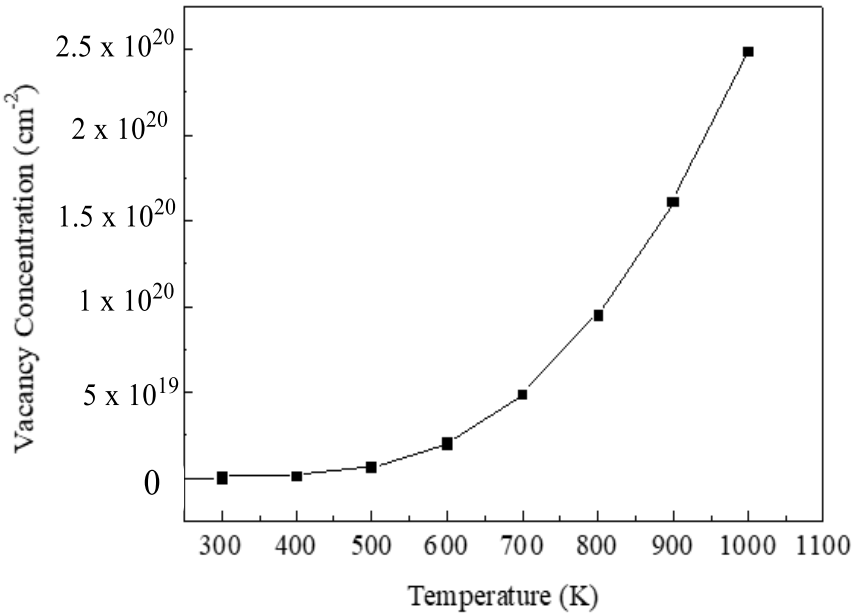

Figure 5.16: Nitrogen vacancy concentration as a function of temperature at nitrogen vacancy coverage X_v = 1/6 of WN (100):N+1V_N surface termination.

5.5 Conclusions

In this chapter, we perform spin-polarized density functional theory calculations to investigate geometries, electronic charges, phase stability diagram of δ_3-MoN and δ-WN low-index surfaces. Diverse surface terminations were inspected in terms of relaxation and reconstruction, Bader's charges, density of states, and vacancy formation energy. Phase stability diagrams indicate that nitrogen terminated (111) and (100) surface of δ_3-MoN and δ-WN, respectively are the most predicted stable surfaces.

Our findings propose that vacancy-containing slabs exhibit less charge transfer than the perfect slabs. Vacancy formation energy and concentrations were found to be the highest for nitrogen terminated surfaces. Results from this study would contribute in paving the way into more understanding of the future catalytic performance of theses phases.

Chapter 6 : Mechanisms Governing Selective Hydrogenation of Acetylene over γ-Mo_2N Surfaces

Paper III

Jaf,Z.N., Altarawneh, M., Miran, H.A., Jiang, Z-T and Dlugogorski, B.Z. (2017) ***Mechanisms governing selective hydrogenation of acetylene over γ-Mo_2N surfaces.*** Catalysis Science & Technology, 7 (4). pp. 943-960.

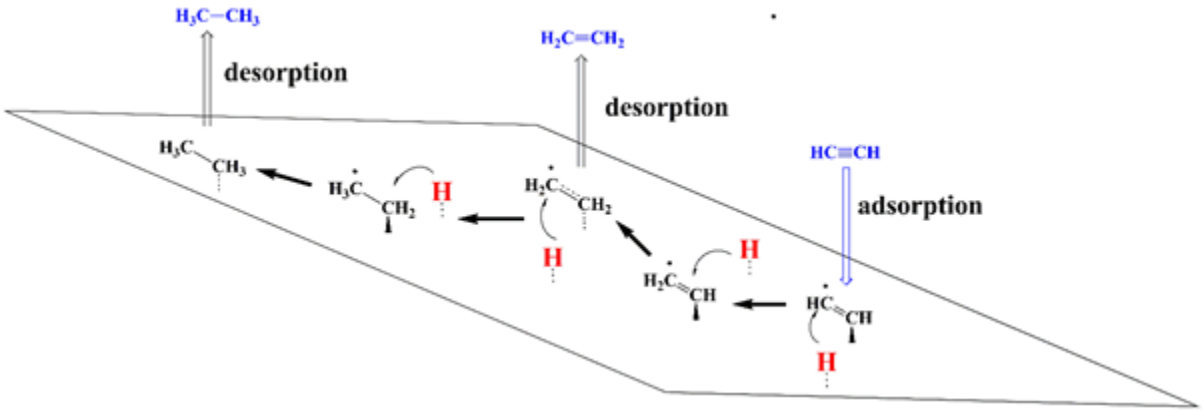

6.1 Abstract

Selective hydrogenation of ethyne in hydrocarbon feeds into ethene assumes critical importance in notable chemical applications. Stand-alone molybdenum nitride (Mo_2N) mediates surface hydrogenation of ethyene with a profound selectivity; similar to that observed over noble metals. However, the underlying mechanisms governing the H_2-C_2H_2-Mo_2N interaction leading to partial rather than complete hydrogenation remain largely unclear. We find that molecular hydrogen adapts several physisrobed states prior to its dissociative dissociation; mainly on 3-fold hollow f*cc* and 3-fold hollow *fcc* sites over the (111) and (100) terminations of Mo_2N; respectively. Our results on the interaction of hydrogen with γ-Mo_2N concur very well with analogous experimental findings pertinent to the preference for the dissociation to occur on surface nitrogen vacant sites, the mobility of surface adsorbed hydrogen atoms and the inhibition effect of pre-adsorbed oxygen on H_2 dissociation. Over the (111) surface, constructed reaction mechanism, estimated reaction rate constants, and micro-kinetics modelling provide illumination on the occurrence of the selective hydrogenation of ethyne into ethene, rather than ethane. We demonstrate that, the occurrence of selective hydrogenation rests on two aspects; distinctive energy profiles of hydrogenation steps in partial versus full hydrogenation routes, and thermodynamic selectivity entailing higher surface stability of adsorbed C_2H_2 in relative to C_2H_4. Production of ethane and oligomerisation into C_4 cuts prevail over the (100) surface. Thermo-kinetic parameters reported herein provide molecular-base understating on the unique and highly selective hydrogenation capacity of γ-Mo_2N catalysts. Such knowledge is useful to design optimum operational conditions for the catalytic operations.

6.2 Introduction

Formation of ethyne (C_2H_2 or acetylene) as a secondary by-product in olefines purification processes induces poisoning effects on deployed catalysts[419]. Likewise, while introducing carbon monoxide to the hydrocarbons feed prevents additional hydrogenation of olefins into alkanes [420] it also deactivates noble metal-based catalysts such as Pt, Pd and Ni. When using these metals as active sites on supported catalysts (i.e., alumina), alkenes can be easily hydrogenated to alkanes [421-425]. For this reason, the development of novel materials with high surface area and profound selective hydrogenation constitutes a key challenge requiring identification of active sites and molecular-level understanding of the associated reaction mechanisms. The limited availability of precious metals and their high price have hindered their widespread applications. This has paved the way for the development of alternative potent materials that mimic the catalytic behaviour of precious metals. With similar *d*-orbitals filling, transitional metal nitrides most notably molybdenum nitride (Mo_2N) display Pt-like characters [426] in many critical catalytic applications including NO_x reduction [427], hydrogenation [428], hydrodenitrogenation [429], and hydrodesulfurization [430]. Consensus of opinions in the literature evidence that, Mo_2N-facilitated hydrogenation reactions take place over nitrogen vacant sites. For instance, Perret *et al.*[431] have thoroughly compared the catalytic hydrogenation capability of β versus γ phases of Mo_2N to report higher specific hydrogenation rate on the surface of β-Mo_2N. This has been ascribed to higher Mo/N ratio (i.e., larger deficiency of surface nitrogen) for the β–phase.

Theoretical and experimental studies have illustrated structural, electronic as well as optical properties of bulk[46, 374] and surfaces[400, 432, 433] of the two phases of Mo_2N, in the pursuit to provide atomic-based insights into their remarkable properties. Mo_2N is typically synthesised via a temperature programmed reduction-nitradation process [426]. Several operational factors, including temperature, heating rate, the source of nitrogen in the gas phase composition (i.e., NH_3 versus H_2 + N_2 mixture) and the Mo-containing precursor (*i.e.*, Mo_xO_y and $MoCl_x$) influence the properties of the synthesised MoN_x phase. The nitridation process often results in wide-size distributions and irregular shapes of Mo_2N. A significant deal of recent research has focused on tailoring the morphology of Mo_2N particles into similarly shaped and sized nanostructures that could catalyse a niche category of reactions [434].

Mo_2N exhibits unique selectivity response in hydrogen mediated reactions [428]. Examples include; the preferential production of benzyl aldehyde from benzyl alcohol [434], and *p*-chloroaniline from *p*-chloronitrobenzene [431].

Along the same line of enquiry, the high selective hydrogenation capacity of Mo_2N catalysts has find direct application in producing high-purity alkene streams, to be used in synthesis of polyethylene polymers [419]. The underlying objective of selective hydrogenation of alkynes is to minimise the formation of alkanes and to produce a nearly-free alkenes stream [435]. Via careful IR measurements, Wu *et al*. [180] illustrated a highly selective hydrogenation process of 1,3-butadiene to 1-butene on γ-Mo_2N/α-Al_2O_3 catalyst. Authors attributed the highly selective nature of the γ-Mo_2N/α-Al_2O_3 catalyst to surface nitrogen atoms that weaken the interaction between the parent reactant 1,3-butadiene and the catalyst surface. Similarly, high selectivity towards conversion of ethyne to ethene of about 85% has been reported by Hao *et al*. at atmospheric pressure and reaction temperature of 232-483 K with various space velocities [177]. The selective production of ethene remains almost unchanged at around 90% after reaching a steady state. Hao *et al*.[177] explained that the occurrence of catalytic hydrogenation rests on two factors; thermodynamic selectivity entailing higher adsorption energies of alkynes in reference to alkenes, and the inaccessible re-adsorption of produced alkenes.

Hydrogenation process of alkynes commence by activation of hydrogen molecules on γ-Mo_2N surfaces. Temperature programmed desorption (TPD) study by Li *et al.* [436] has demonstrated some interesting remarks pertinent to hydrogen uptake by γ-Mo_2N surfaces. TPD results indicate that γ-Mo_2N surfaces dissociate hydrogen molecules even at room temperature; though at very low yields. This remarkable finding is on the contrary with the general consensus pointing out that dissociative adsorption of hydrogen is often regarded as the rate limiting step in catalysis hydrogenation [437]. The relatively facile conversion of C_2H_2 into C_2H_4 at a relatively low temperature of 473−523 K supports the occurrence of a low-energy hydrogen dissociation process over γ-Mo_2N-based catalysts.

While the role of γ-Mo_2N catalysts in mediating partial and full hydrogenation of alkynes is well-established, the underlying reaction mechanisms remain unclear. Furthermore, as conveyed above, it is of a fundamental interest to underpin factors contributing to the profound

selectivity toward partial rather than full hydrogenation. The unique catalytic characters of γ-Mo_2N surfaces are believed to stem from structural as well electronic aspects. On the structural side, adsorption of diatomic species such as CO [152] on γ-Mo_2N surfaces was greatly facilitated by the presence of vacant N sites. Similarly, Li *et al.* [436] postulated that adsorption of hydrogen takes place on coordinatively unsaturated molybdenum ions. A relatively narrow band gap in Mo_2N is a signature for its high catalytic activity [426].

To this end, this chapter maps out potential energy surfaces pertinent to partial and full hydrogenation of ethyne on γ-Mo_2N surfaces. Guided by experimental results for hydrogen and acetylene interactions with γ-Mo_2N and via implementing accurate density functional theory (DFT) calculations, this study has three-fold aims: to illustrate the process governing hydrogen uptake by γ-Mo_2N surface; to build reaction routes for the hydrogenation mechanisms of triple bonds (C_2H_2) to single bond (C_2H_6) through double bond (C_2H_4); and to provide robust kinetic parameters for all surveyed chemical reactions. The most intriguing question to answer here is if the selective hydrogenation of ethyne is dictated by kinetic barriers of the intrinsic hydrogen transfer reactions or simply controlled by the relative thermodynamic stability of adsorbed species. Thermo-kinetic parameters reported herein should be instrumental in the pursuit to formulate novel γ-Mo_2N-based catalytic, specifically tailored for industrial applications.

6.3 Methodology

6.3.1 Computational details

All structural optimisations and energy calculations were performed using DMol^3 package [438]. The Kohn-Sham equations were applied based on the Padrew and Wang (PAW) DFT functional along with the local density approximation (LDA) for the exchange-correlation potential [439]. The total energy converges with a tolerance of 1×10^{-6} Ha. A double numerical plus P-function (DNP) basis set (i.e. comprises one numerical function for each occupied atomic orbital) has been applied with a cut-off energy of 3.7 Å. Integration of the first-Brillioun zone was carried out at κ points samplings of $1 \times 2 \times 1$ and $2 \times 2 \times 1$ for the (111)

and (100) miller indices of γ-Mo_2N; respectively. Spin polarization was imposed in all calculations at a thermal smearing of 0.05 Ha. Optimization convergence thresholds for energy change, maximum force, and maximum displacement between the optimization cycles were set at 0.00002 Ha, 0.004 Ha/Å, and 0.005 Å, respectively. DMol^3 performs transition states calculations through the linear synchronous and quadratic synchronous transit LST/QST methods [440]. Computations of vibrational frequencies enable to derive activation enthalpies and entropies as a function temperature. Arrhenius rate parameters (*A*-factors and activation energy, E_a) were estimated by fitting reaction rate constants, $k(T)$, with the inverse of temperature ($1/T$) according to the conventional transition state theory (TST).

We calculate adsorption energies, E_{ads} (at 0 K) of γ-Mo_2N/species systems based on the energy difference between the adsorbate - surface system a non-interacting system and;

$$E_{ads} = E_{substrate\_surface} - E_{non\text{-}interacting\ \ system} \qquad 6.1$$

In the non-interacting system, the gas phase species is placed in the middle of the vacuum, separated by at least 8.00 Å from the surface.

We estimate charge transfer from the slab to the adsorbed C_2Hy species based on the Hirshfeld formalism. It is well-known that this method provide accurate electronic charge density, even when a smaller basis sets is deployed [441]. Finally, we track the change in C-C bond elongations in selected species according to the Mayer's method [442]. This in turn provides an information about bond order and charge rearrangement in the course of chemical reaction [443].

6.3.2 Mo_2N surfaces

In a recent study, we constructed a stability phase diagram for plausible terminations of γ-Mo_2N through the ab initio atomistic thermodynamics formalism [432]. A nitrogen-truncated surface along the (111) index was found to be the most stable facet at all accessible values of nitrogen chemical potential. The N/Mo ratio in this particular surface amounts to 0.57, deviating noticeably from the unsaturated γ-Mo_2N surface with N/Mo ratio at 0.50. In alike procedure to our recent investigation on NO_x reduction by γ-Mo_2N[432], we elect herein to consider the (111) and (100) terminations to simulate γ-Mo_2N. While considering the most thermodynamically stable (111) termination is intuitively appealing, our choice to study the (100) surface stems from its mixed N/Mo surface termination. We have shown throughout the discussion that, such termination induces substantial differences in adsorption energies, reaction and activation energies and reaction products in reference to the (111) surface. Furthermore, all experimental studies on H_2/C_2H_2 interaction with γ-Mo_2N were carried out in a pure argon environment (i.e., in absence of a nitrogen source) prompting us also to consider a genuinely unsaturated γ-Mo_2N surface (i.e., N/Mo ratio of 0.5) [177]. We model the two γ-Mo_2N surfaces by deploying slab models comprising four layers of 2 × 2 unit cell. Figure 6.1 portrays optimised geometry of the γ-Mo_2N (111)/(100) surfaces. In the (111) surface, five adsorption sites can be distinguished; 3-fold hollow fcc (H1), 3-fold hollow hcp (H2), on-top Mo (TMo1), on-top N (TN1) and bridge Mo-Mo (B1) sites. Similarly, the (100) surface features four distinct adsorption sites; namely on-top Mo (TMo2), on-top N (TN2), 4-fold hollow fcc (H3), and bridge Mo-Mo (B2). The 2 × 2 unit cell of (111) surface contains four H1 sites. Similarly, the 2 × 2 unit cell of the (100) surface comprise four H3 sites.

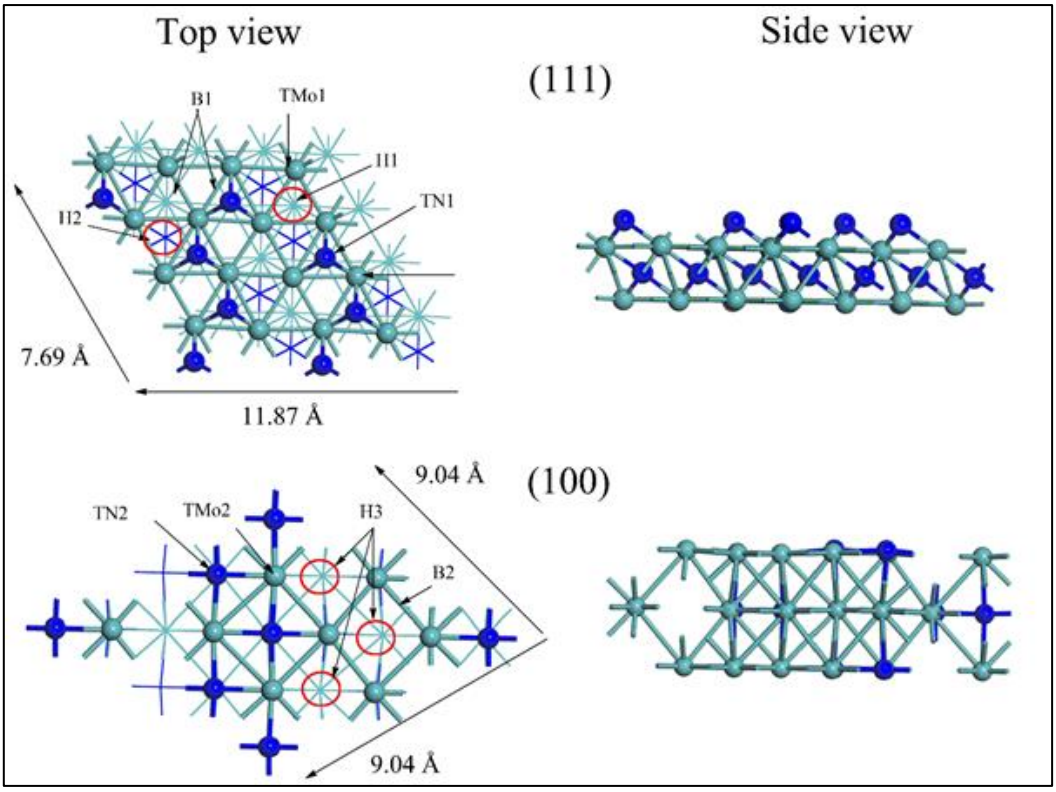

Figure 6.1**:** Optimised structures of the γ-Mo_2N(111) and γ-Mo_2N(100) surfaces with highlighted potent adsorption sites. Molybdenum atoms are in light green while nitrogen atoms are in blue.

Assuming that, these vacant nitrogen positions constitute the potent active sites, and based on the dimensions in Figure 6.1 (*i.e.*, 4 sites/9.10×10^{-19} m^2), one estimates the concentration of the active sites on Mo_2N surfaces to be 7.30×10^{-10} mol/cm^2. This value deviates by a factor of 2.27 from the experimental measurements reported by Neylon *et al.*[444] *i.e.*, 1.66×10^{-9} mol/cm^2. However, it appears that, Neylon *et al.*[444] quoted a typical value for the concentration of active sites on commonly deployed catalysts, without explicitly estimating the number of sites specifically for the case of Mo_2N. To the best of our knowledge, our calculated value of the number of active sites on Mo_2N (that amounts to 7.30×10^{-10} mol/cm^2) represents the first ever estimate.

6.4.1 Interaction of hydrogen with γ-Mo_2N surfaces

Several experimental investigations have probed the aspects dictating the adsorption of H_2 and subsequent mobility of adsorbed hydrogen atoms on the unsupported γ-Mo_2N surface. Measurements performed by NMR spectroscopy have confirmed that, hydrogen adsorbs on Mo sites associated with nitrogen defects via the homolytic dissociation pathway. The maximum uptake of hydrogen amounts to 200 μmol/g, corresponding to (at most) 10 % of the total surface area [146]. Conversely, Li *et al.*[436] and Perret *et al.*[431] proposed that, the adsorption of H_2 on γ-Mo_2N occurs via the heterolytic dissociation. At ~675 K and within a pressure range of 0.4 – 0.8 atm[436], Li *et al.*[445] measured the total hydrogen uptake to reside between 12 μmol/g and 200 μmol/g. Unfortunately, the authors did not determine the composition of the Mo_2N surface.

The H_2-TPD profiles of Zhang *et al.*[446] and Li *et al.*[436] have established the two major adsorption peaks; viz. at ~510 K and ~750 K. These two peaks represent the low and high energy adsorption sites, with the cited literature providing no identification of the exact locations of these sites. Migration of the surface hydrogen intensifies the high energy adsorption peak, following the saturation of the low energy adsorption sites. Further increase of temperature results in migration of hydrogen atoms into the low energy adsorption sites as well as the desorption of hydrogen molecules. Li *et al.*[436] attributed the high energy adsorption sites to sub-surface adsorption. Inspection of the H_2-TPD profiles in literature indicates that, the dissociative surface adsorption of hydrogen may be followed by diffusion into the sub-layer and/or bulk γ-Mo_2N phase for the intermediate to high temperature; i.e., ~700 – 750 K [445]. Very recently, Xie *et al.*[106] have demonstrated a high rate of the dissociative adsorption of hydrogen on atomically-thin molybdenum nitride Nano-sheets of γ-Mo_2N for applications related to hydrodesulfurization and CO uptake. Overall, the existing H_2-TPD results indicate that, the capacity for hydrogen adsorption on the γ-Mo_2N surface increases with the adsorption temperature. Having considered the reverse reaction as well, it would decrease the overall uptake as the temperature increases [146, 445].

6.4.1.1 Dissociative adsorption of H_2 over γ-Mo_2N surfaces

Herein, we study the various modes of interaction of H_2 with the γ-Mo_2N (111)/(100) surfaces with the aim to provide mechanistic elucidations into the H_2-TPD results demonstrated above Starting with non-dissociative molecular adsorption, molecular H_2 adapts several configurations over the two considered γ-Mo_2N surfaces signified by intermediates M1-M4 (100) and M9-M12 (111) as Figures 6.2 and 6.3 depict; respectively. Table 6.1 describes the positions of the adsorbed hydrogen molecules and atoms on the two surfaces.

Table 6.1: Description of molecular and dissociative adsorption of hydrogen at distinct sites over γ-Mo_2N(100) and γ-Mo_2N(111) surfaces. Refer to Figures 6.1-6.3. for graphical illustrations of adsorption sites.

Structure	Description
(100)	
M1	Molecular hydrogen adsorbs horizontally at a TMo2 site
M2	Molecular hydrogen adsorbs horizontally at a B2 site
M3	Molecular hydrogen adsorbs vertically at an H3 site
M4	Molecular hydrogen adsorbs horizontally at an H3 site
M5	The two hydrogen atoms are positioned at H3 sites
M6	Hydrogen atoms occupy into TN2 and H3 sites
M7	Hydrogen atoms occupy into TN2 and B2 sites
M8	The two hydrogen atoms are positioned at TN2 sites
(111)	
M9	A hydrogen molecule is adsorbed horizontally over H1 site
M10	A hydrogen molecule is adsorbed horizontally over TN1 site
M11	Molecular hydrogen adsorbs horizontally at H2 site
M12	A hydrogen molecule is adsorbed horizontally over B1 site
M13	The two hydrogen atoms are positioned at B1 sites
M14	The two hydrogen atoms are positioned at H1 sites
M15	Hydrogen atoms occupy into TN2 and H2 sites
M16	The two hydrogen atoms are positioned at TN2 sites

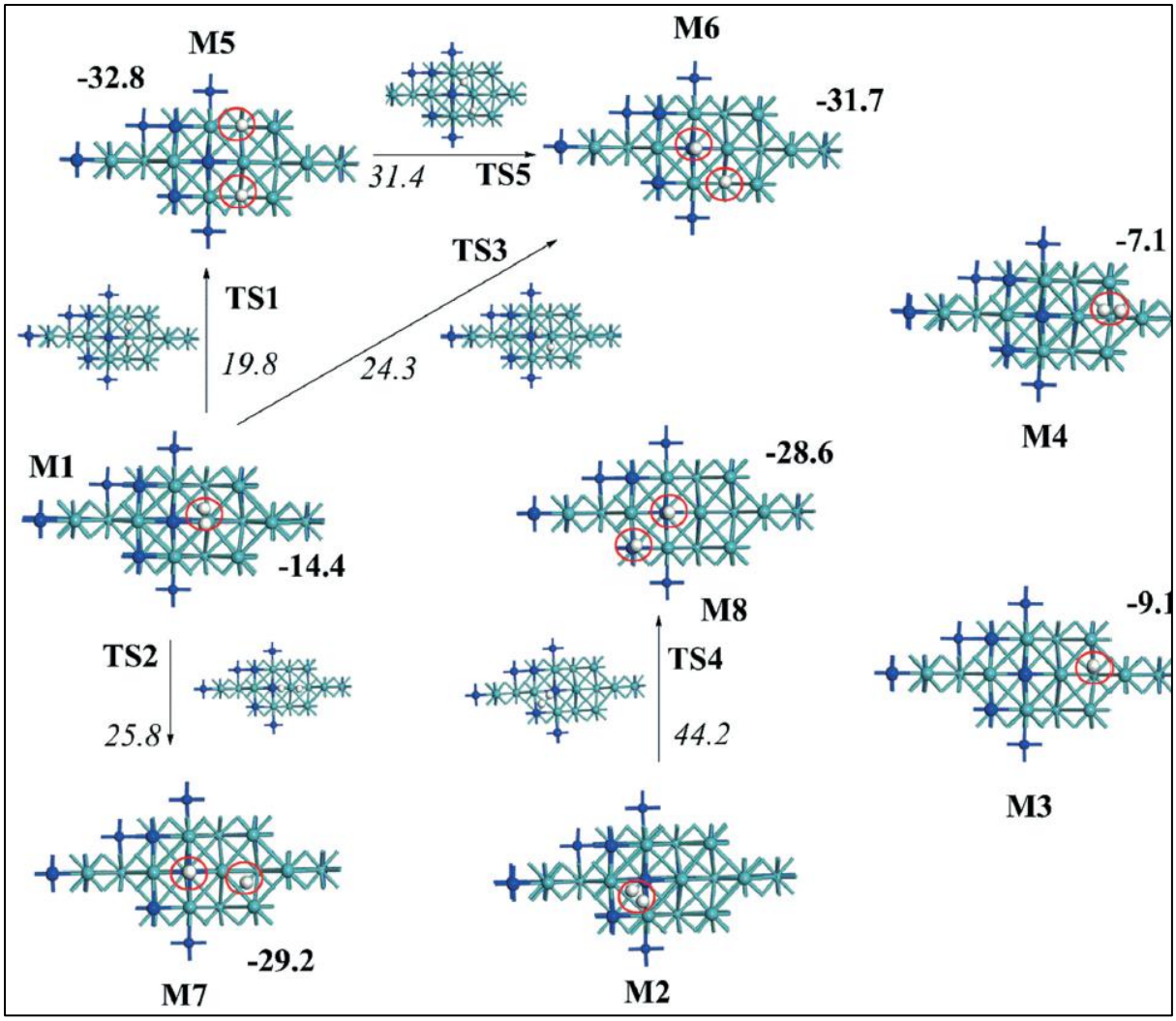

Figure 6.2**:** Reaction routes for interactions of molecular hydrogen with the γ-$Mo_2N(100)$ surface. Values in bold (reaction energies) are in reference to a non-interacting hydrogen molecule while values in italic (activation barriers) are relative to the reactant in each step. Circles denote the adsorbed hydrogen molecules/atoms (in white). All values are in kcal/mol. Refer to Table 6.1 for descriptions of adsorption sites.

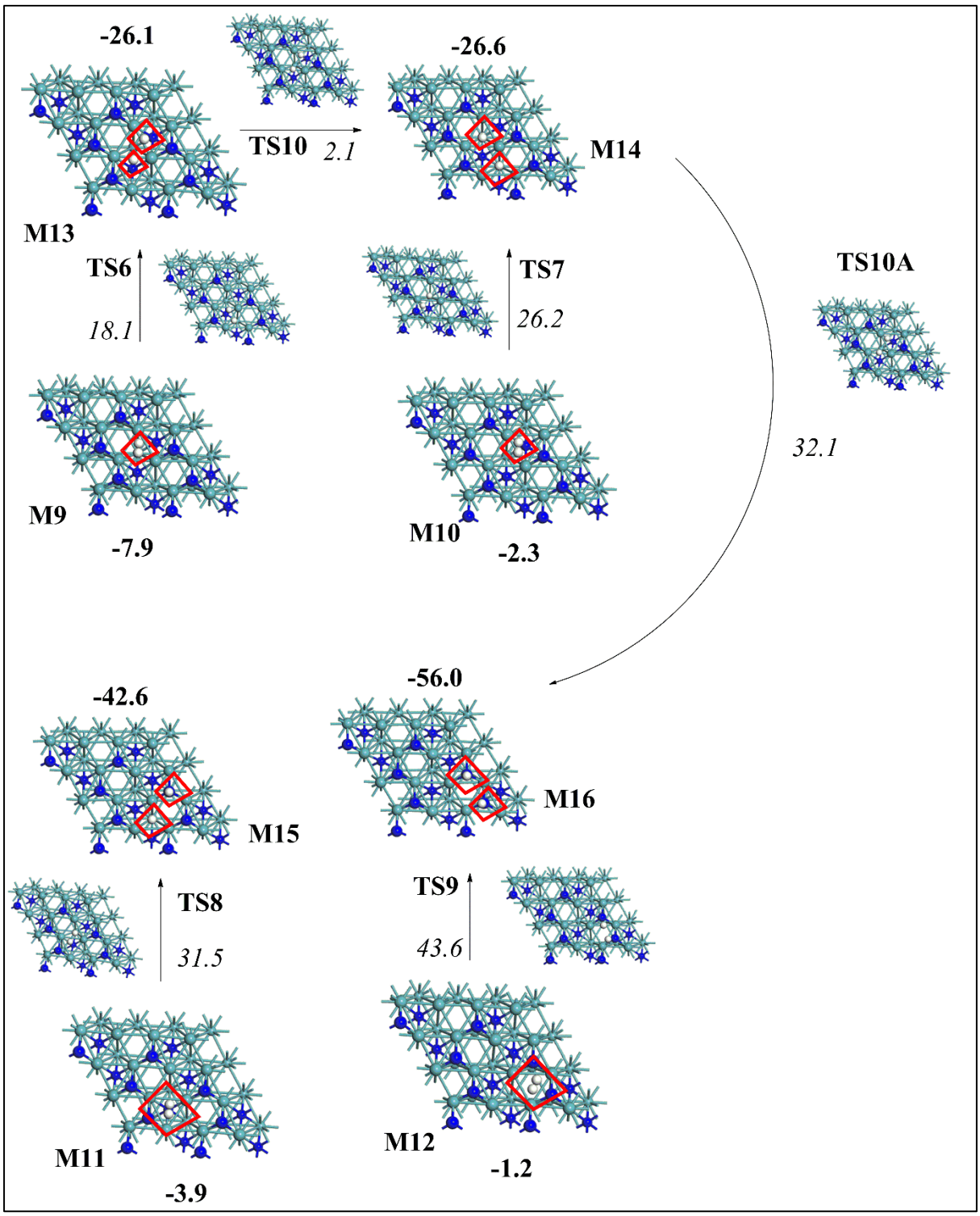

Figure 6.3: Reaction routes for interactions of molecular hydrogen with the γ-$Mo_2N(111)$ surface. Values in bold (reaction energies) are in reference to a non-interacting hydrogen molecule while values in italic (activation barriers) are relative to the reactant in each step. Circles denote the adsorbed hydrogen molecules/atoms (in white). All values are in kcal/mol. Refer to Table 6.1 for descriptions of adsorption sites.

Adsorption energies for the initial physisorbed structures on the two surfaces fall within the narrow range of - 1.2 – - 14.4 kcal/mol revealing a rather minor influence of the adsorption site on the physisorption process. In fact, the value -14.4 kcal/mol is a big energy to be assigned as a physisorption process. However, it is envisaged that H_2 goes through a chemisorption process in this adsorption energy range. Based on these figures, molecular hydrogen is weakly adsorbed on γ-Mo_2N in reference to CO (-34.3 kcal/mol) [447] and NO (-30.1 – 50.2 kcal/mol) [432] over γ-Mo_2N. The low adsorption energies for physisorbed molecular hydrogen infers that, molecular hydrogen uptake by Mo_2N is highly unlikely and that undissociated hydrogen molecules will readily desorb from the surface. In addition to sizable high reaction barrier for H_2 dissociation (to be discussed in the following paragraphs), low H_2 binding energies may have contributed to the very low H/Mo ratios measured during the irreversible uptake of hydrogen; *i.e.,* ~ 0.001 – 0.002 [448].

In studying the rupture of the H-H bond, a molecular state resembling the dissociative structure was considered as the initial reactant. Figures 6.2 and 6.3 portray schemes for the dissociation of hydrogen molecules over the (100) and (111) terminations; respectively. Starting with the (100) termination (Figure 6.2), the dissociation of the adsorbed dihydrogen molecule occurs at two H3 sites (M5); into TN2 and B2 sites (M6), TN2 and B2 sites (M7) and over two surface nitrogen atoms (M8). In reference to the initial physisorbed state, fission of the H-H bond yielding M5, M6, M7 and M8 structures entails exothermicity of 32.8 kcal/mol, 31.7 kcal/mol, 29.2 kcal/mol and 28.6 kcal/mol; respectively. The breakage of H-H bond in the gas phase requires a tremendous endothermicity of ~120 kcal/mol. Thus, while thermodynamic factors in terms of the adsorption energies reveals a spontaneous H-H cleavage process on the surface, activation of hydrogen molecules truly rests on underlying kinetic factors, embedded in activation energies. Scission of the H-H bond over the two 4-fold hollow sites B3 require the least activation barrier of 19.8 kcal/mol through the transition structure TS1. H-H bond fission into structures M6 and M7 entail very similar activation energies of 25.8 kcal/mol (TS2) and 24.3 kcal/mol (TS3); correspondingly. Attachment of H atoms on surface N atoms in structure M8 pass through sizable reaction barrier of 44.2 kcal/mol (TS4).

Interaction of H_2 with the (111) surface (Figure 6.3) exhibits similar energetic trend to that of the (100) surface (Figure 6.2). This is reflected by a sizable energy barrier for dissociation over two TN1 sites (43.6 kcal/mol) and modest energy barriers for hydrogen attachment at 3-fcc sites (26.2 kcal/mol and 31.5 kcal/mol). Hydrogen molecule rupture over two neighbouring B1 sites represents the most accessible corridor in the dissociative adsorption of H_2 over the (111) surface via an energy barrier of 18.1 kcal/mol. By contrasting the sites based on their corresponding energy barriers, sites H1 (111), B1 (111) and H3 (100) could be classified as low energy sites while the two surface nitrogen sites (TN1, TN2) characterise high energy sites. Despite of several attempts, placing hydrogen atoms at on top-Mo and H2 sites converge into other sites. The calculated dissociative adsorption energy for H_2 over γ-Mo_2N falls between -56. and -26.1 kcal/mol. At low hydrogen coverage, Guerrero-Ruiz *et al*.[448] reported an adsorption energy of -30 kcal/mol, whereas Somorjai quotes an estimate of -40 kcal/mol for polycrystalline Mo [449].

The exceedingly high barriers of TS4 and TS9 render direct attachments at two neighbouring nitrogen sites to be kinetically hindered (*i.e.* high energy sites). Practically, this means that once the γ-Mo_2N surface is fully covered by nitrogen atoms; catalytic reactivity is greatly reduced. N^{14}/N^{15} isotope analysis during the course of interaction between ^{15}NO and γ-Mo_2N indicates migration of ^{15}N into the lattice of γ-Mo_2N.[450] Nonetheless, due to the very strong bond in the N_2 molecule, it is highly unlikely that atmospheric nitrogen to de-catalyse γ-Mo_2N. All experiments on the interaction of H_2 with γ-Mo_2N were carried out in Ar environment preventing one from drawing a conclusive conclusion on the effect of atmospheric nitrogen on the uptake of hydrogen. Along the same line of enquiry, the occurrence of Mars-van Krevelen like-mechanism[451] involving γ-Mo_2N surfaces and nitrogen molecules warrants further investigation to assess the likelihood for the re-generation of γ-Mo_2N in a gaseous reservoir of a relatively weak nitrogen-bounded molecules such as N_2H_4 for instance. Such scenarios may be encountered when deploying γ-Mo_2N based catalysts to decontaminate emission from nitrogen-rich fuel; such as biomass. Table 6.2 enlists Arrhenius parameters for the dissociative desorption of hydrogen molecule along the pathways shown in Figures 6.2 and 6.3.

Table 6.2: Arrhenius coefficients of H_2 dissociative adsorption fitted in the temperature range of 300-1000 K.

Reaction	*A* (1/s)	E_a (kcal/mol)
(100)		
M1→M5	6.21×10^{12}	19.5
M1→M6	3.51×10^{12}	26.4
M1→M7	9.87×10^{11}	24.2
M2→M8	5.1×10^{12}	44.0
(111)		
M9→M13	2.10×10^{12}	17.1
M10→M14	4.21×10^{11}	27.2
M11→M15	6.10×10^{11}	32.0
M12→M16	1.10×10^{12}	42.0

Reaction rate constants in Table 6.2 confirm the dominance of the M1 → M5 (H1 site) and M9 → M13 (H3 sites) over the (111) and (100) surfaces; in that order. We find a trivial barrier of 2.1 kcal/mol (TS10) for hydrogen transfer from B1 sites into H1 sites; i.e., M13 → M14 (111). Thus, the reaction network M9 → M13 → M14 signifies a lower energy pathway for the occupation of two neighbouring H1 sites (4-fold hollow sites). Overall, the kinetic and thermodynamic preference for the dissociation of H_2 at vacant N sites supports earlier experimental interpretations by Liu *et al.* [436] and Haddix *et al.* [146] who postulated that hydrogen molecules dissociate at nitrogen deficient patches of molybdenum atoms.

Next, we assess energy requirements for two potential processes that may operate during interaction of hydrogen with the γ-Mo_2N surface; surface diffusion and dissociative adsorption over an oxygen covered γ-Mo_2N surface. We establish that hydrogen atoms preferentially

occupy N-vacant sites and their adsorption on surface N atoms is associated with a considerable energy penalty. The higher desorption temperature (~750 K) in H_2-TPD profiles by Liu *et al.*[445] and Zhang *et al.*[446] was attributed to hydrogen movement from low energy sites to high energy sites; following the saturation of the former sites. To simulate this process, we calculate energy barriers for hydrogen atom surface diffusion from H1/H3 sites (i.e., low energy sites) to TN1/TN2 (i.e. high energy sites). Calculated barriers amount to somehow sizable barriers of 32.1 kcal/mol (TS10A, Figure 6.3) and 31.4 kcal/mol (TS5, Figure 6.2). Thus, hydrogen mobility over the γ-Mo_2N surfaces is plausible at elevated temperatures and suggests that, low energy sites could serve as precursors for high energy sites. This findings concurs very well with the experimental interpretation of Li *et al.* [445] who observed by analysing H_2-TPD patterns high mobility of adsorbed hydrogen atoms from low energy sites to higher energy sites. Clearly, hydrogen subsurface diffusion is not related to the hydrogenation of alkynes; a purely surface process and thus it is not further discussed here.

Experimental studies[450] as well our recent theoretical account[432] find the NO uptake by γ-Mo_2N to result in the formation of $Mo_2N_xO_y$ configuration in which oxygen atoms occupy the vacant N sites. The interaction of γ-Mo_2N with atmospheric oxygen in practical systems may also result in the formation of a $Mo_2N_xO_y$ phase, an oxynitride. Any practical hydrogenation system requires the removal of oxygen during the start-up period and constant attention to identify and eliminate air leaks. Normally, a high-temperature flow of H_2[444] through the system or Ar ion sputtering serves to reduce or remove the surface oxygen layers formed in passivation of Mo_2N.[431] Thus, it is of interest to study the effect of oxygen presence on the dissociative adsorption of hydrogen. Figure 6.4 illustrates that, dissociation of a H_2 molecule over a $Mo_2N_xO_y$-like phase requires an energy barrier of 31.1 kcal/mol (over the (111) configuration). This barrier matches those of high energy sites (i.e., TN1 site) and indicates that, the atmospheric oxygen displays a poisoning effect on the uptake process of H_2. Thus, a highly reducing condition (i.e., very dilute concentration of oxygen) signifies an optimum operating condition for hydrogen uptake by γ-Mo_2N. Interestingly, our conclusion herein matches the experimental findings of Li *et al.*[436, 445] who observed that, hydrogen adsorption on γ-Mo_2N becomes unfeasible in the presence of the pre-adsorbed oxygen on the surface.

Experimental studies[450] as well our recent theoretical account[432] find the NO uptake by γ-Mo_2N to result in the formation of $Mo_2N_xO_y$ configuration in which oxygen atoms occupy the vacant N sites. The interaction of γ-Mo_2N with atmospheric oxygen in practical systems may also result in the formation of a $Mo_2N_xO_y$ phase, an oxynitride. Any practical hydrogenation system requires the removal of oxygen during the start-up period and constant attention to identify and eliminate air leaks. Normally, a high-temperature flow of H_2[444] through the system or Ar ion sputtering serves to reduce or remove the surface oxygen layers formed in passivation of Mo_2N.[431]. Thus, it is of interest to study the effect of oxygen presence on the dissociative adsorption of hydrogen. Figure 6.4 illustrates that, dissociation of a H_2 molecule over a $Mo_2N_xO_y$-like phase requires an energy barrier of 31.1 kcal/mol (over the (111) configuration). This barrier matches those of high energy sites (*i.e.*, TN1 site) and indicates that, the atmospheric oxygen displays a poisoning effect on the uptake process of H_2. Thus, a highly reducing condition (*i.e.*, very dilute concentration of oxygen) signifies an optimum operating condition for hydrogen uptake by γ-Mo_2N. Interestingly, our conclusion herein matches the experimental findings of Li *et al*.[436, 445] who observed that, hydrogen adsorption on γ-Mo_2N becomes unfeasible in the presence of the pre-adsorbed oxygen on the surface

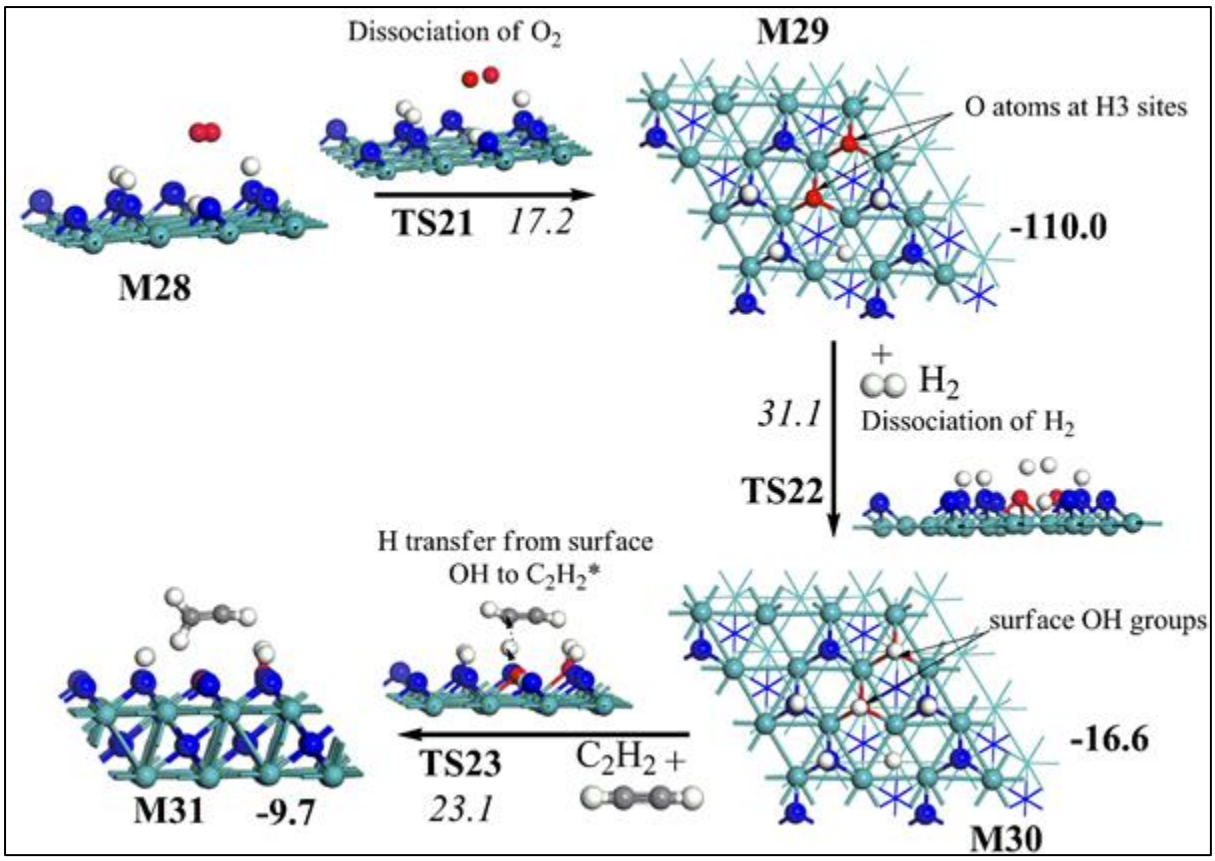

Figure 6.4: Dissociative adsorption of H_2 over a Mo_2NO_x-like phase and H transfer from an OH site to adsorbed C_2H_2 adduct over the (111) surface. Values in bold (reaction energies) and italic (activation barriers) are relative to the reactant in each step. All values are in kcal/mol. Carbon, hydrogen, and oxygen atoms are represented by grey, white and red spheres.

6.4.1.2 Kinetics of H_2 uptake

As the thermodynamic stability of the (111) facet dominates that of (100)[113], we have only considered the most kinetically preferred pathway for the dissociative addition of H_2 on the (111) surface. We calculate the rate constant for this pathway, $H_2 + \gamma\text{-}Mo_2N(111) \rightarrow$ M13 (i.e., $A_2 + 2^* \rightarrow 2A^*$, where * is an active site), based on the reaction rate expression of:[452]

$$k(T) = \frac{s}{\sigma^2}\sqrt{\frac{RT}{2\pi M}}e^{\frac{-E_a}{RT}} \qquad 6.2$$

in which σ stands for the active site density of Mo_2N[444] (1.66×10^{-9} mol/g), s denotes the sticking coefficient (assumed to be 1.0), M is the molecular mass of H_2 and E_a signifies the activation energy in reference to the gas phase hydrogen molecule (10.2 kcal/mol). The rate of hydrogen uptake is then expressed as $r(T) = k(T)C_s^{\,2}P_{H_2}$ where P_{H_2} is the partial pressure of hydrogen and C_s the surface concentration of attached H atoms (assumed to be σ/10, based on the experimental interpretation of Haddix *et al.*[146] with a corresponding surface area of 79 m^2/g). Table 6.3 lists the calculated values of $k(T)$ and $r(T)$ under selected conditions.

Table 6.3: Reaction rate constants k ($cm^5\ mol^{-2}\ s^{-1}$) for hydrogen dissociative adsorption on the γ-Mo_2N(111) surface and the corresponding rate of hydrogen uptake at 0.1 atm ($\mu mol\ g^{-1}\ s^{-1}$).

T (K)	Rate constant for surface H_2 dissociation ($cm^5/(mol^2 \cdot s)$)			Rate of hydrogen uptake (μmol/(g·s))		
	M9 → M13	M10 → M14	M11 → M15	M9 → M13	M10 → M14	M11 → M15
300	3.46×10^{9}	5.14×10^{3}	4.08×10^{2}	3.06×10^{-4}	4.54×10^{-10}	3.61×10^{-15}
350	4.21×10^{10}	4.25×10^{5}	1.81×10^{1}	3.19×10^{-3}	3.22×10^{-8}	1.37×10^{-12}
400	2.76×10^{11}	1.18×10^{7}	1.76×10^{3}	1.83×10^{-2}	7.79×10^{-7}	1.17×10^{-10}
450	1.20×10^{12}	1.57×10^{8}	6.23×10^{4}	7.09×10^{-2}	9.23×10^{-6}	3.67×10^{-9}
500	3.92×10^{12}	1.25×10^{9}	1.09×10^{6}	2.08×10^{-1}	6.63×10^{-5}	5.77×10^{-8}
550	1.04×10^{13}	6.87×10^{9}	1.13×10^{7}	5.00×10^{-1}	3.31×10^{-4}	5.47×10^{-07}
600	2.34×10^{13}	2.85×10^{10}	8.04×10^{7}	1.03	1.26×10^{-3}	3.55×10^{-6}
700	8.48×10^{13}	2.70×10^{11}	1.76×10^{9}	3.21	1.02×10^{-2}	6.65×10^{-5}
800	2.25×10^{14}	1.46×10^{12}	1.79×10^{10}	7.45	4.86×10^{-2}	5.94×10^{-4}
900	4.83×10^{14}	5.51×10^{12}	1.10×10^{11}	1.42×10^{1}	1.62×10^{-1}	3.24×10^{-3}
1000	8.96×10^{14}	1.55×10^{13}	4.71×10^{11}	2.37×10^{1}	4.23×10^{-1}	1.25×10^{-2}

Figure 6.5a contrasts our estimated rate of hydrogen uptake with experimental values while Figure 6.5b plots the total hydrogen uptake within 1 h. At 700 K and P_{H_2} of 0.6 atm, our calculated rate of hydrogen uptake exceeds that of Neylon *et al.*[444] by a factor of 5.5. We envisage that, the main source of discrepancy stems from a significant uncertainty in the degree of the hydrogen coverage of the surface. Most notably, the one-tenth coverage of the surface by hydrogen, reported by Haddix *et al.*[146], applies to 298.15 K, while Neylon *et al.*[444] measured the rate of hydrogen uptake between 670 K and 770 K. Perret *et al.*[431] determined the total hydrogen consumption as around 730.0 μmol/g. The fact that Perret *et al.*[431] reported neither the time interval nor hydrogen pressure makes it impossible to compare this value with a theoretical estimation (*i.e.*, curves of hydrogen uptake in Figure 6.5b). As pointed out by Perret *et al.*[431] the amount of consumed H_2 on the Mo_2N surfaces varies depending on the crystallographic form (β versus γ), nitride synthesis and pre-treatment conditions.

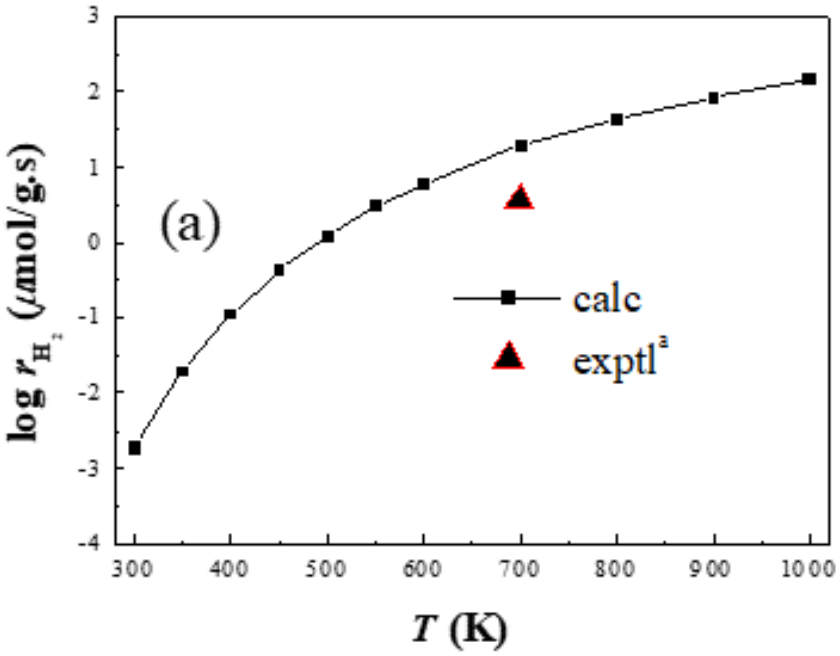

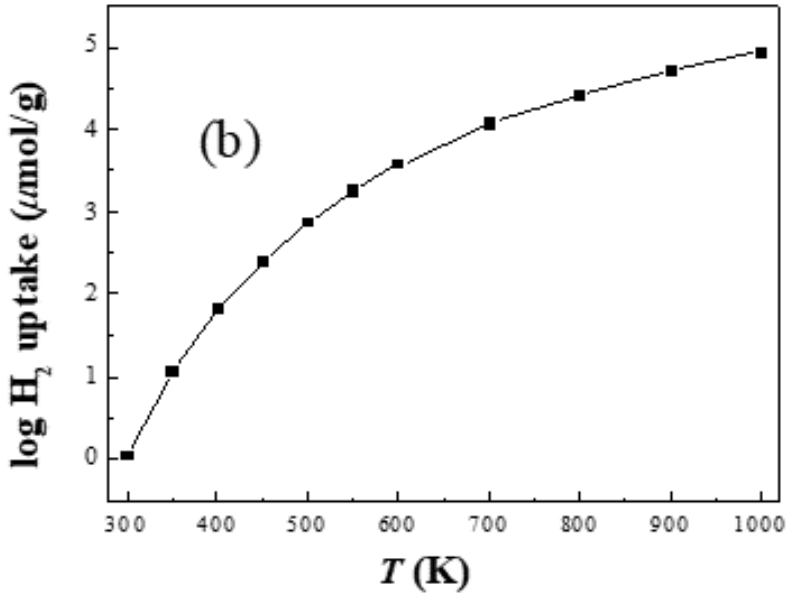

Figure 6.5: Reaction rate for hydrogen uptake by the γ-$Mo_2N(111)$ surface along the reaction H_2 + γ-$Mo_2N(111) \rightarrow$ M13 at 0.6 atm H_2 and 10 % surface coverage (a) and the total hydrogen uptake in 1 h at 0.1 atm H_2 and 10 % surface coverage. [a] ref [444].

6.4.2 Adsorbed C_2Hy species

We calculate adsorption energies for acetylene to be -87.1 kcal/mol and - 51.6 kcal/mol, respectively, over pure (111) and (100) surfaces. The adsorbed C_2H_2 moiety adopts a near-flat position over the H1 (111) and H3 (100) sites. Hao *et al*.[177] co-introduced hydrogen and acetylene into the reactor at concentrations of 1.4 % for C_2H_2) and 14.0 % for H_2. Thus, a competitive C_2H_2-versus-H_2 adsorption prevails under practical scenarios. This has prompted us to calculate the adsorption energy for ethyne over the (111) and (100) surfaces pre-covered with hydrogen. Table 6.4 gives the adsorption energies for C_2H_y moieties over vacant and hydrogen pre-occupied sites of H1 (111) and H3 (100) along with some molecular descriptors, such as C-C bond elongation in comparison to gas phase values and charge transfer from the surface to the adsorbed C_2H_y species. Positioning the C_2H_2 adduct over an H-occupied H1 site reduces the C_2H_2-γ-$Mo_2N(111)$ surface binding energy to- 6.9 kcal/mol; i.e., forming weakly bounded configuration. This indicates a hydrogen pre-covered (111) surface to be less active toward hydrogenation of ethyne molecules.

Table 6.4: Adsorption energies and molecular descriptors for adsorbed C_2H_y species.

	(111)			
	Adsorption energy (kcal/mol)		% C-C elongation in reference to gas phase (vacant H3 site)	Net charge transfer from the surface to the C_2Hy species (e), vacant H3 site
	Vacant H3 site	H pre-occupied H3 site		
C_2H_2*	- 51.6	-6.9	12.1	0.33
C_2H_3*	-82.2			
C_2H_4*	- 15.4	-2.4	1.8	0.08
C_2H_5*	-54.7			
C_2H_6*	-10.0			
(100)				
	Adsorption energy (kcal/mol)		% C-C elongation in reference to gas phase, vacant H1 site.	Net charge transfer from the surface to the C_2Hy species (*e*), vacant H1 site.
	Vacant H3 site	H pre-occupied H3 site		
C_2H_2*	-87.0	-38.2	18.4	0.46
C_2H_3*	94.5			
C_2H_4*	-48.3	-16.8	9.8	0.37
C_2H_5*	-61.8			
C_2H_6*	-3.0			

The fact that the dissociative adsorption of a hydrogen molecule requires at least - 18.1 kcal/mol of activation energy (i.e., the barrier of TS5) indicates a kinetic hindrance toward facile pre-covering of active sites by hydrogen atoms. Thus, the optimum approach necessitates the concomitant introduction of H_2 and ethyne, rather than admitting high loads of hydrogen prior to the stream of ethyne. Over the (100) surface, an ethyne molecule strongly attaches itself to a H-occupied H3 site with a binding energy of - 38.2 kcal/mol. The C_2H_4 molecule (the product of partial hydrogenation) is rather weakly attached to pre-covered active sites above the two surfaces (-2.4 kcal/mol (111) and - 16.8 kcal/mol (100)). Low binding energy for ethene over H pre-occupied active sites supports the hypothesis that, partial hydrogenation involves

subsequent blocking of active sites that prevents the re-adsorption of alkenes. Inspection of binding energies in Table 6.4 consistently indicates stronger adsorption over the (111) surface in comparison with that over the (100) surface. This is reflected by elongation of the C-C bond and increased charge transfer into the adsorbed substrates.

Ethyne pre-adsorbed on N-vacant sites blocked hydrogen adsorption in this potent location, leaving only the high-energy sites available for hydrogen, according to reactions M2 → M8 (100) and M12 → M16 (111) as shown in Figures 6.2 and 6.3, respectively.

6.4.3 Partial versus full hydrogenation of C_2H_2 over the (111) termination.

Hydrogenation of alkynes commence with the co-adsorption of the hydrocarbon adducts with hydrogen atoms on the γ-Mo_2N surface. Herein, we outline reaction profiles for partial and complete hydrogenation of ethyne over the (111) termination of γ-Mo_2N. The hydrogenation reaction mechanism is captured in Figure 6.6 and is summarised in the Langmuir−Hinshelwood reaction network:

$$C_2H_2^* + H^* \underset{R1^r}{\overset{R1^f}{\rightleftharpoons}} C_2H_3^* \qquad R1$$

$$C_2H_3^* + H^* \underset{R2^r}{\overset{R2^f}{\rightleftharpoons}} C_2H_4^* \qquad R2$$

$$C_2H_4^* + H^* \underset{R3^r}{\overset{R3^f}{\rightleftharpoons}} C_2H_5^* \qquad R3$$

$$C_2H_5^* + H^* \underset{R4^r}{\overset{R4^f}{\rightleftharpoons}} C_2H_6^* \qquad R4$$

(* denotes an adsorbed species, *f* and *r* stands for forward and reverse reaction; respectively).

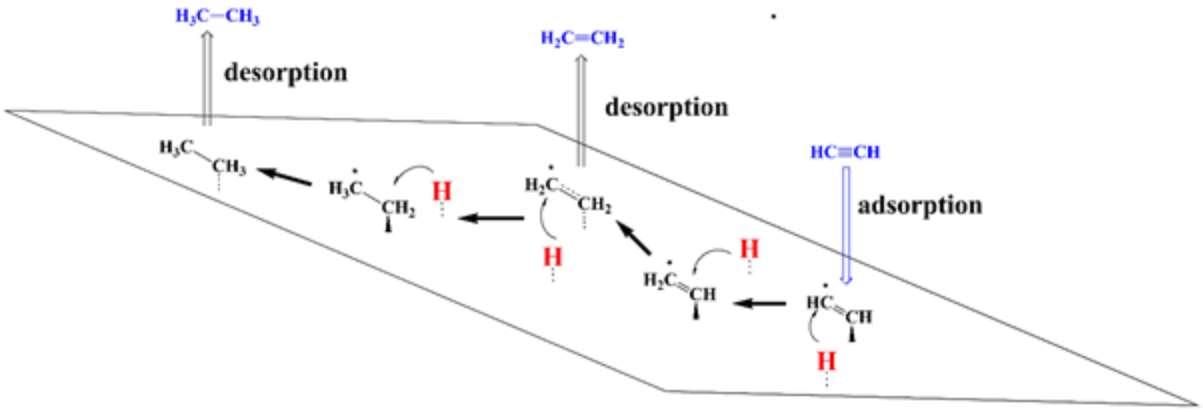

Figure 6.6: Reaction networks for partial and full hydrogenation of ethylene.

Figures 6.7 and 6.8 map out potential energy surfaces for partial and full hydrogenation of ethylene over (111) and (100) surfaces; correspondingly, with Table 6.5 and Figure 6.9 presents their Arrhenius parameters for the (111) surface.

Table 6.5: Kinetic parameters (*i.e.*, turn over frequency) of surface reactions operating in the partial and full hydrogenation over the γ-Mo_2N(111) surface, fitted in the range of 300 – 1000K.

Reaction		Reaction Scheme	A (s^{-1})	E_a (kcal/mol)
M17 $\underset{r}{\overset{f}{\rightleftharpoons}}$ M18	$R1^f$	C_2H_2*+H* → C_2H_3*	2.10×10^{12}	7.3
	$R1^r$	*C_2H_3 → C_2H_2* + H*	5.61×10^{12}	18.4
M18 $\underset{r}{\overset{f}{\rightleftharpoons}}$ M19	$R2^f$	C_2H_3*+H* → C_2H_4*	3.09×10^{12}	10.1
	$R2^r$	*C_2H_4 → C_2H_3* + H*	7.61×10^{12}	38.2
M19 $\underset{r}{\overset{f}{\rightleftharpoons}}$ M20	$R3^f$	C_2H_4*+H* → C_2H_5*	1.29×10^{12}	17.1
	$R3^r$	*C_2H_5 → C_2H_4* + H*	3.52×10^{12}	16.9
M20 $\underset{r}{\overset{f}{\rightleftharpoons}}$ M21	$R4^f$	C_2H_5*+H* → C_2H_6*	5.67×10^{12}	18.1
	$R1^r$	*C_2H_6 → C_2H_5* + H*	3.82×10^{12}	38.0

Partial hydrogenation of ethyne initiates with its near-flat adsorption on H1 site; surrounded by adsorbed H^* atoms at neighbouring H1 and N1 (on-top surface nitrogen) sites. Hydrogen transfer from the surface to the adsorbed $C_2H_2^*$ radical could occur either from H1 or N1 sites and results in the formation of an adsorbed $C_2H_3^*$ adduct (i.e., vinyl) in a well-depth of only 7.4 kcal/mol (the intermediate M18 in Figure 6.7). The transition structure TS12 characterises H^* transfer from H1 site through a modest barrier of 10.8 kcal/mol; significantly lower than the competing H^* movement from N1 site via TS11 (34.9 kcal/mol). It follows that in all subsequent hydrogenation reactions; we only consider H^* transfer from adjacent H1 sites. Mayer's C-C bond order in this vinyl adduct and all subsequently formed C_2H_y species remain around 1.0. Subsequent hydrogen transfer into adsorbed $C_2H_3^*$ adduct moiety ($R2^f$) takes place via a barrier of 8.8 kcal/mol (TS13). This reaction concludes the partial hydrogenation by producing an adsorbed ethene molecule; $C_2H_4^*$ in a well depth of 36.8 kcal/mol in reference to the entrance channel (structure M19 in Figure 6.7). Desorption of $C_2H_4^*$ from a vacant H1 site into a gas phase ethene molecule requires only 15.4 kcal/mol. This value is higher than the reverse barrier embedded in TS13 (38.2 kcal/mol). However, desorption is not a purely kinetic-driven phenomena, mass transfer factors often play a crucial roles [453]. On the other hand, full coverage of neighbouring 3-fold fcc hollow sites at excess hydrogen conditions may prevent the backward reaction of $R2^r$ (M19 → M18) by blocking the availability of preferred H intake sites.

The very distinct adsorption energies for ethyene (-51.6 kcal/mol) and ethane (-15.4 kcal/mol) is consistent with the principle of thermodynamic selectivity suggested by Bond et al.[178, 454] based on which the occurrence selective hydrogenation of ethyne into ethane was explained. However, it must also be noted that very similar adsorption energies (within 1.0 kcal/mol) for ethylene and ethene were estimated over other hydrogenation catalysts such as Pd/Al_2O_3 catalysts [420]. Herein, we argue that the occurrence of selective hydrogenation relies two on aspects; firstly, distinctive patterns of hydrogenation steps among partial and full hydrogenation, and secondly the aforementioned thermodynamic selectivity.

We analyse the full hydrogenation route over the (111) surface to elucidate rationale for the high selective nature of γ-Mo_2N towards partial hydrogenation of acetylene. Figure 6.7b shows a full hydrogenation route starting from an adsorbed $C_2H_4^*$. Pathways in Figure 6.7b follow analogous steps presented in Figure 6.7a for the partial hydrogenation. In the first step, a β-$C_2H_5^*$ intermediate is synthesised via hydrogen transfer from the H1 site to the terminal carbon atom in the adsorbed $C_2H_4^*$ adduct. This reaction is associated with a reaction barrier of 17.4

kcal/mol (TS14). It follows that the opening step in the partial hydrogenation pathway incurs higher barrier in reference to the corresponding step in the full hydrogenation (10.8 kcal/mol versus 17.4 kcal/mol). The β-$C_2H_5^*$ intermediate rests nearly at the same energy level of the starting reactant (M20 in Figure 6.7). The second hydrogenation step ($R2^f$) occurs via a matching reaction barrier of the first step; 17.1 kcal/mol and results in the formation of an adsorbed $C_2H_6^*$; the M21 structure in Figure 6.7b. The comparable energy barriers for the forward and reverse steps in the full hydrogenation and their matching reaction rate constants (Table 6.5) route indicate their highly reversible nature. This is on contrast to the largely irreversible reactions in the partial hydrogenation route (Figure 6.7a).

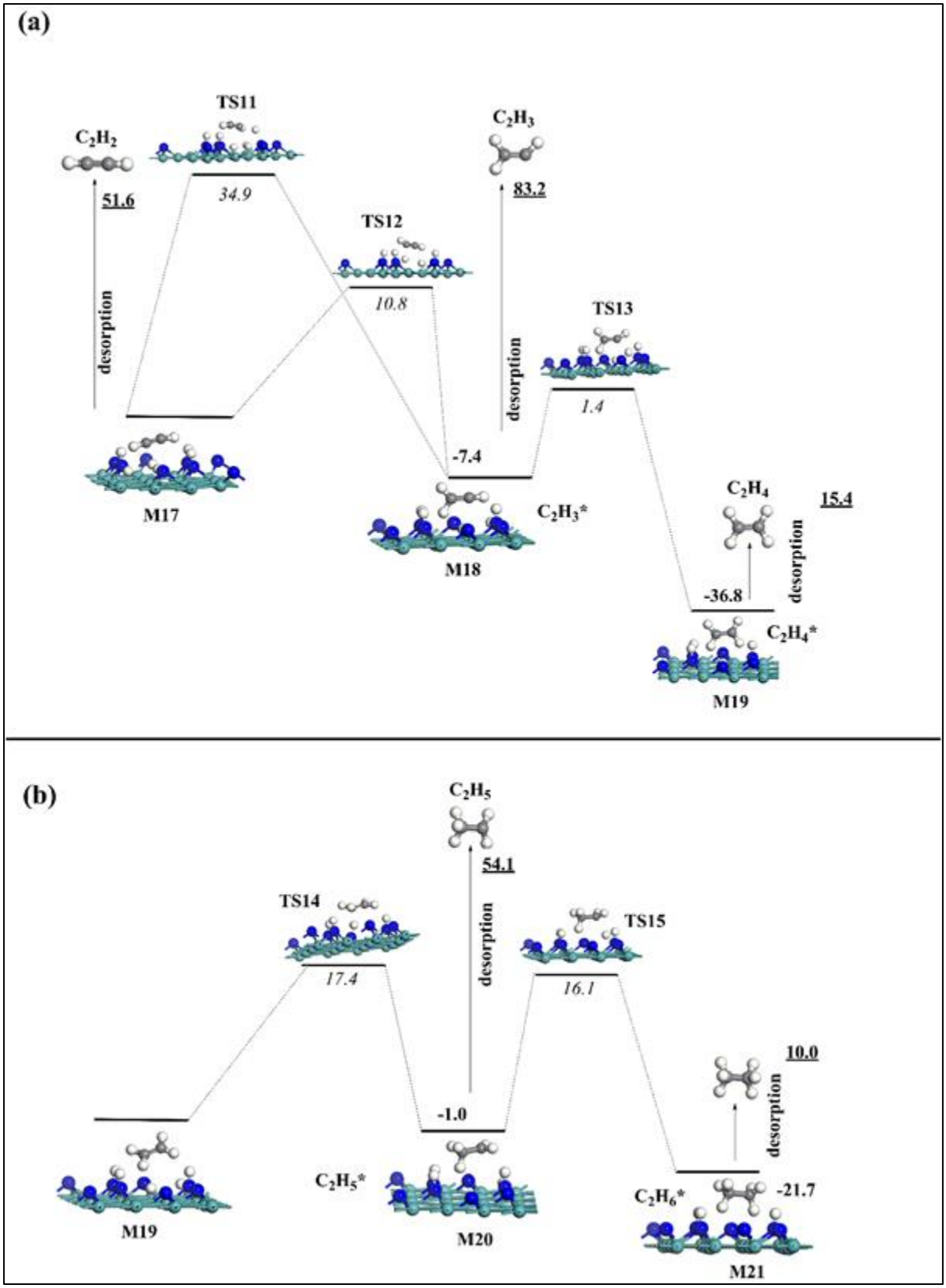

Figure 6.7: Pathways for the partial (a) and full hydrogenation (b) over the γ-Mo_2N(111) surface. All values are in kcal/mol in reference to the initial reactant. For clarity, we show only the first layer.

Elucidating reasons for the occurrence of the selective hydrogenation of ethylene requires careful inspection of the fate of adsorbed $C_2H_4^*$. With the exclusion of the reverse reaction (M19 → M18, R2^f) owing to its exceedingly high barrier (38.2 kcal/mol), two channels appear to dominate the fate of the C_2H_4*, namely desorption into the gas phase (M18 → $C_2H_{4(g)}$) and further hydrogenation into the $C_2H_5^*$ moiety (M19 → M20, R3^f). Based on reaction rate constant reported in Table 6.5 for reaction R3^f, and by utilising $\frac{k_b T}{h}$ as the *A*-factor and 15.4 kcal/mol as the energy of activation for desorption of ethane, branching ratio, i.e., $k_{R3^f} \Big/ k_{R3^f} + k_{\text{desorption}}$ for the former channel remains nearly 1.0 between 300 K – 1000 K. Thus, desorption into a gas phase ethene molecule rather than further hydrogenation marks the sole exit corridor of adsorbed $C_2H_4^*$. Clearly, desorption of $C_2H_4^*$ shuts down the full hydrogenation route and significantly contributes to the selective formation of ethene from γ-Mo_2N-mediated hydrogenation of ethylene.

We have shown that, if the first hydrogen transfer occurs from N-site, it requires significantly higher barrier than that for analogous transfer from the 4-fold hollow site (10.8 kcal/mol versus 34.9 kcal/mol). This indicates that hydrogenation capability of γ-Mo_2N, largely depends on the availability of nitrogen vacant sites. According to the low barrier of the transition state TS21 (17.2 kcal/mol), these potent sites could be readily filled out if molecular oxygen is present in the system. Figure 6.4 shows a corresponding first step hydrogenation over a hydrogenated $Mo_2N_xO_y$-like phase (the structure M29). H atom migration from H-O site requires a modest barrier of 23.1 kcal/mol (TS23). Thus, hydrogenation of ethylene is somehow feasible in an oxidative environment; however, obviously, hydrogen dissociation on the surface oxygen atoms represents a bottle-neck for such process (an energy barrier of 31.1 kcal/mol).

In a nutshell, factors contributing the selective partial hydrogenation over the (111) surface can be grouped into:

(I)- Higher Barrier for the opening hydrogenation step in full hydrogenation versus the analogous step encountered in partial hydrogenation (17.4 kcal/mol versus 10.8 kcal/mol).

(II)- Significantly higher desorption energy for $C_2H_2^*$ in comparison to $C_2H_4^*$ (over vacant H1 site). This trend is consistent with the thermodynamic selectivity assumption pioneered by Bond *et al.*[454].

(III) – The dominance of the desorption step for adsorbed $C_2H_4^*$ over further hydrogenation (i.e., R3^f).

(IV)- Competing reversibility for the β-$C_2H_5^*$; the intermediate structure in full hydrogenation in comparison to a largely irreversible analogous pathway in the case of partial hydrogenation. This can be easily observed when contrasting potential energy diagrams for partial (Figure 6.7a) and full hydrogenation (Figure 6.7b).

6.4.4 Hydrogenation mechanism over the (100) surface

Figure 6.8 depicts steps of partial and complete hydrogenation of acetylene over the (100) surface.

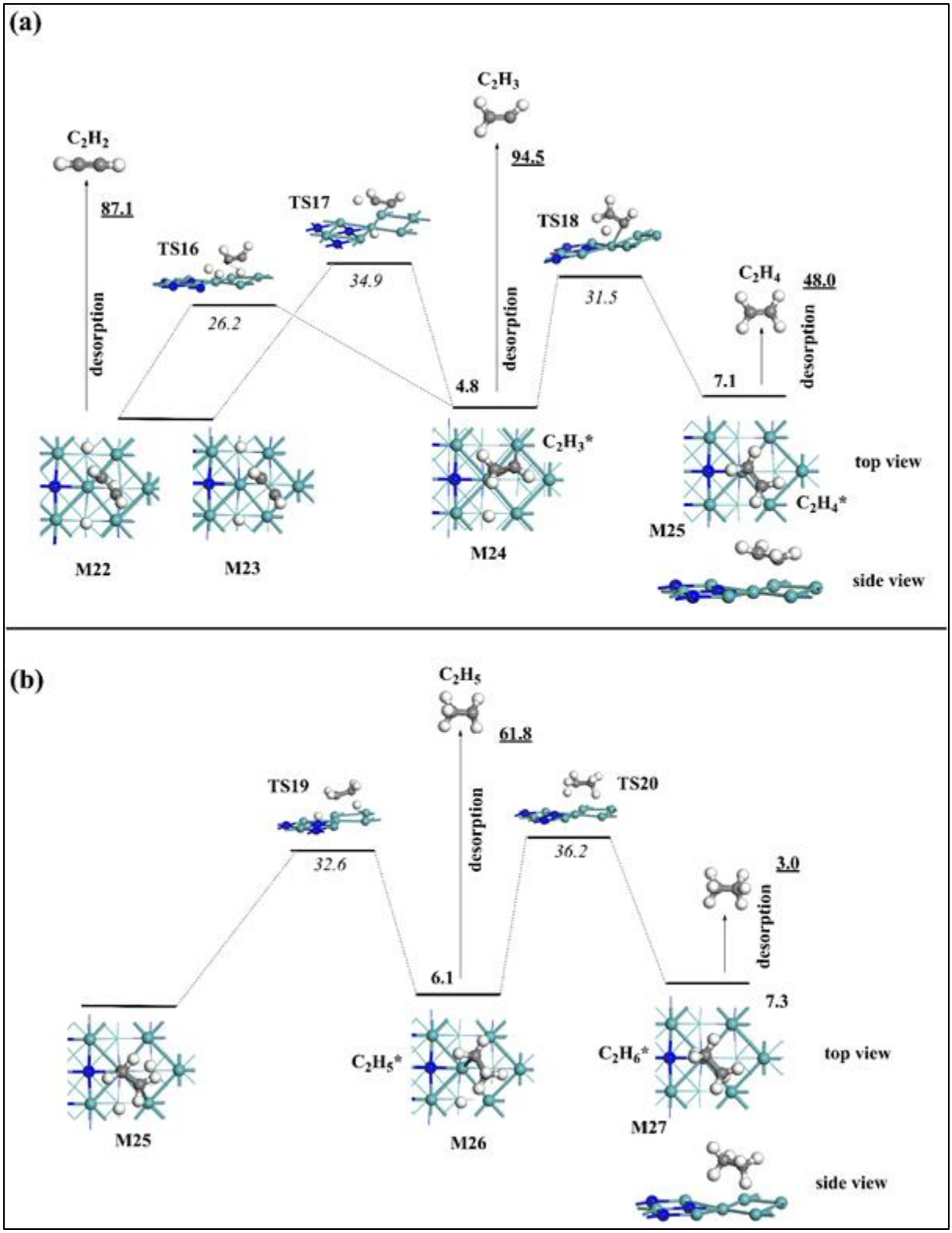

Figure 6.8: Pathways for the partial (a) and full hydrogenation (b) over the γ-Mo_2N(100) surface. All values are in kcal/mol in reference to the initial reactant. For clarity, we show only the first layer.

The hydrogenation mechanisms for the (100) and (111) surfaces share the same principal steps; albeit with distinct energy profiles reflected by the following observations:

- The (100) surface consistently feature higher energy barriers for the four hydrogenation steps in reference to the (111) surface. For example, the first hydrogenation step ($C_2H_2^*$ + H* → $C_2H_3^*$) encounters an energy barrier of 26.2 kcal/mol (TS17) if hydrogen transfer occurs from the H3 site underneath the adsorbed $C_2H_2^*$ or 34.9 kcal/mol (TS16) when the hydrogen atom moves from a neighbouring H3 site. These two values noticeably exceed that of the corresponding step operating on the (111) surface; *i.e.*, 10.8 kcal/mol.

- Barrier heights shown in Figure 6.8 (100), reveal that hydrogenation steps are reversible, in both the partial and the full hydrogenation routes. For instance, the barrier for the reaction $\mathrm{M24} \underset{r}{\overset{f}{\rightleftharpoons}} \mathrm{M25}$ in the reverse direction (24.3 kcal/mol) is slightly lower than that in the forward direction (26.7 kcal/mol). This is on the contrary to the analogous steps in the (111) surface in which energy barrier in the reverse direction overshoots the barrier height in the forward direction by 29.4 kcal/mol.

- When considering desorption of $C_2H_4^*$ from vacant H3 site, further hydrogenation into $C_2H_5^*$ is more preferred than the formation of gaseous ethene molecule (32.6 kcal/mol versus 48.0 kcal/mol).

The last two points suggest that, consecutive H^* transfer steps over (100) surface leads to full hydrogenation of ethyene into ethane. The experimental work of Hao *et al.*[177] report higher selectivity for the formation of ethane at shorter reaction time with relatively low amounts detected across the various investigated operational conditions (reaction temperatures, space velocity). The production of ethane in Hao *et al.*[177] may have proceeded via the sequential hydrogenation steps reported in Figure 6.8 upon the presence of the (100) facet. Likewise, catalysis literature have pointed out that different surface terminations often lead to variant products, and reaction rates [455]. Within the Mo_2N context, the effect of surface composition

induced by different Mo/N ratios constitutes an important contributor for a higher H_2 uptake by β-Mo_2N in reference to γ-Mo_2N.[431] The different energy profiles for the (111) and (100) substantiate that different surface termination encompasses distinct active sites toward partial versus full hydrogenation. Ethane represented the sole product from hydrogenation of ethylene on Pd/α-Al_2O_3[177] suggesting a similar nature of the active sites on Pd/α-Al_2O_3 and γ-Mo_2N(100). Higher selectivity for the production of ethene from γ-Mo_2N coincides with the dominance thermodynamic stability of the (111) surface;[432] *i.e.*, a termination that favours the partial hydrogenation route.

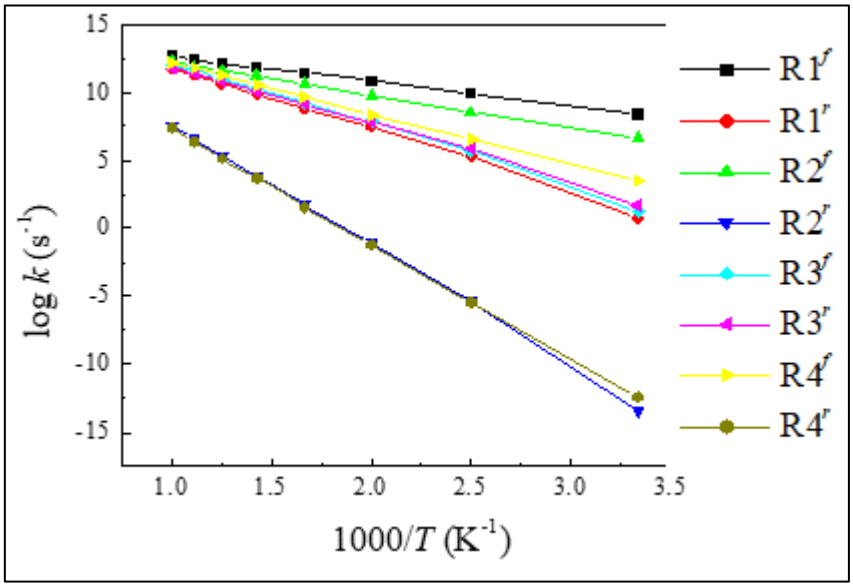

Figure 6.9: Arrhenius plots of surface reactions operating in the partial and full hydrogenation over the γ-Mo_2N(111) surface, fitted in the range of 300 – 1000 K.

6.4.5 Production of oligomers

Formation of green oil represents a chief contributor to deactivation of catalysts during hydrogenation of acetylene.[456, 457] The formed carbonaceous deposits deteriorate the catalytic activity by poisoning active sites and reducing the surface area. The unclosed carbon balance for gaseous hydrocarbons in Hao *et al.*[177] experiments suggest the formation of carbonaceous deposits on the Mo_2N surface. 1,3-butadiene (C_4H_6)[457] constitutes the most commonly discussed precursor of green oil. The high surface stability of $C_2H_3^*$ and $C_2H_2^*$

adducts (Table 6.4) assists their coupling into $C_4H_5^*$, i.e., a direct building block for C_4 oligomers:

$$C_2H_3^* + C_2H_2^* \rightarrow C_4H_5^*$$

Figure 6.10 shows that, cross-linking of two C_2 adducts on the (100) surface pass through a modest energy barrier of 15.9 kcal/mol (TS24). The corresponding process on the (111) surface proceeds without encountering an intrinsic reaction barrier. Higher stabilities of the adsorbed open-shell C_xH_y species ($C_2H_3^*$, $C_2H_5^*$) on the (100) surface in comparison to those on the (111) surface indicate increased tendency for the oligomerisation to occur on the (100) surface. Nonetheless, carrying out the catalytic reaction at higher inlet ratios of H_2/C_2H_2 will minimise the likelihood of occurrence of the bimolecular $C_2H_3^*/C_2H_2^*$ reaction.

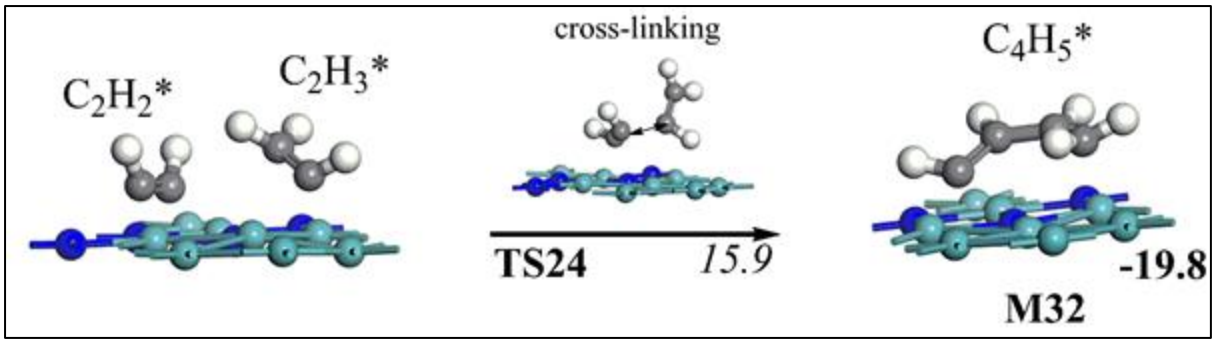

Figure 6.10: The onset of oligomerisation over the (100) surface. The value in bold signifies the reaction energy while the value in italic represents the activation barrier. All values are in kcal/mol.

6.4.6 Kinetic model

Available kinetic models on selective hydrogenation of alkynes into alkenes incorporate global one-step rather than detailed multi-steps reactions. Examples include conversion of 1-butyne over a Pd/alumina catalyst [458], selective hydrogenation of 1-hexyne mediated by Pd nanoparticles[459], and partial hydrogenation of 1-heptyne on tungsten oxide supported on alumina [460]. By utilising partial pressures for gaseous species, the concentration of active

surface sites (i.e., 1.66×10^{-9} mol/cm^2 or our own estimate at 7.31×10^{-10} mol/cm^2)[444] and surface reaction rate constants given in Tables 6.2 and 6.5, we first attempt to formulate one-step expressions for the rate of disappearance of acetylene ($-r_{C_2H_2}$) and formation of ethene ($r_{C_2H_4}$) based on the analogous aforementioned literature models. However, our unsuccessful attempts confirm that, these models were specifically fitted for the investigated catalysts and may not be generalised for the case of Mo_2N. Thus, we limit our analysis herein to provide a micro-kinetic account for our mechanistically described selective hydrogenation over the (111) plane. An approximate and representative simulation can be carried out using a simplified a plug flow reactor (PFR) model on the reaction network:

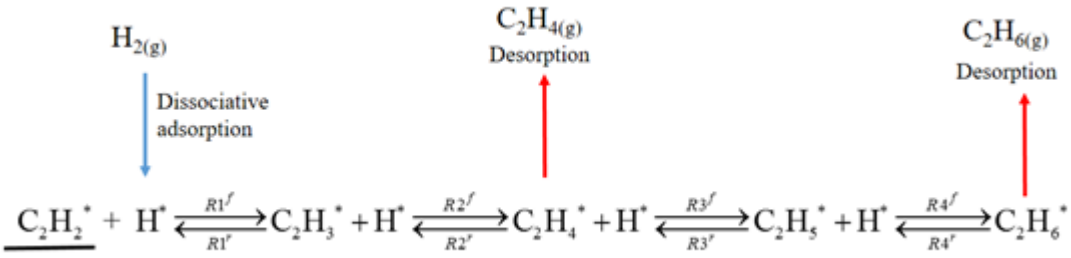

In the deployed PFR model, the governing differential equations are:

$$\frac{dF_i}{dV} = \sum_j r_i \qquad 6.3$$

in which *F*i stands for molar flow rate and $\sum_j r_i$ signifies the summation of all reactions rates that form or consume the species i, i.e., $k_j C_i C_m$. Rate constants for surface reactions (in the forward and reverse directions) are extracted from Table 6.5. Rate constants for the two adsorption steps were assumed to follow $\frac{k_b T}{h} e^{(\frac{-H_{des}}{RT})}$ where H_{des} is the desorption enthalpy for ethene/ethane. Rate constant for the dissociative adsorption for hydrogen was adapted from the reaction M9 → M13 (Table 6.2). To simulate the experimental conditions, the C_2H_2/H_2 molar flow rate ratio in the inlet stream was set to 0.1. In the simplified model, all reactants and products were treated as gas phase species. This may correspond to a full surface coverage

by the two initial reactants with a ratio of $C_2H_2^*/2H^*$ at 0.1. Figure 6.11.a compares conversion of ethylene and selectivity toward ethene with analogous experimental values between 320 – 480 K. Figure 6.11.b plots the profile of product as a function of the reactor's volume at 500 K. The simplified PFR model re-produces the experimental profiles of conversion and selectivity relatively well. The rate-determining step in the model was found to be the dissociative adsorption of hydrogen.

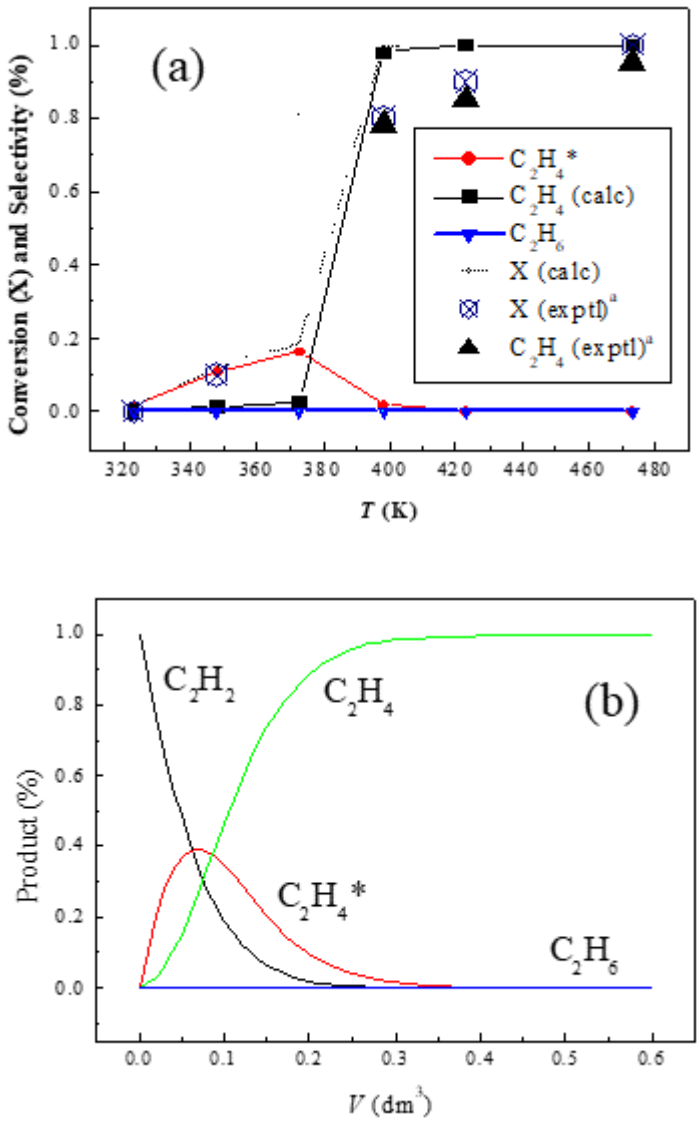

Figure 6.11: Profiles for adsorbed species as function of temperature (a) and volume of the PFR at 500 K (b). [a]Ref [177].

This is in line with an analogous finding by Maccarrone *et al.*[460] who found that, conversion of 1-heptyne into 1-heptene over WO_x/Al_2O_3 fits very well to a model in which the dissociative adsorption of hydrogen is the controlling step. Kinetic hindrance induced by the rate of the

hydrogen dissociative adsorption also agrees with the experimentally reported very low conversion of ethyne at low temperatures (i.e., below 350 K).[177]

6.5 Conclusion and future directions

In agreement with experimental observations by NMR and TPD techniques, we have illustrated that, hydrogen molecules preferentially dissociate on surface N-vacant sites on the (111) and the (100) surfaces. Surface diffusion of adsorbed hydrogen atoms from these low energy sites into other high energy sites is feasible through accessible reaction barrier at about ~ 30 kcal/mol. Pre-adsorbed oxygen atoms on vacant nitrogen sites hinder hydrogen uptake. Estimated reaction rate constants for the dissociative adsorption of hydrogen molecules enable to derive values of total hydrogen uptake as a function of the hydrogen partial pressure. Hydrogenation steps over the (100) plane require significantly higher reaction barriers when compared with the analogous steps taking place above the (111) termination. Several factors contribute to the selective hydrogenation process on the (111) surface; including higher barrier for the first hydrogenation step in partial hydrogenation in reference to opening step in the full hydrogenation corridor and lower desorption energy for the $C_2H_4^*$ intermediate when contrasted with the energy barrier for further hydrogenation. Constructed simplified PFR micro-kinetic model satisfactorily re-produces conversion of ethylene and higher selectivity toward formation of ethene. Higher surface stabilities for C_2Hy species on the (100) surface is expected to facilitate full hydrogenation and formation of oligomers.

While results from this study provide mechanistic insight into hydrogen uptake by Mo_2N and partial hydrogenation of ethyne, several intriguing aspects require further experimental confirmation, including:

The effect of the H_2/C_2H_2 ratio. We anticipate the decay of catalytic activity to be sensitive to the concentration of C_2H_2. An assessment of the extent of catalysts poisoning against relative H_2/C_2H_2 loads will serve to design optimal process conditions.

In real scenarios, the presence of trace oxygen in the reaction medium is difficult to avoid because of leaks and during start-up. Oxygen could readily occupy the potent active sites. However, our theoretical modelling suggests that, hydrogenation reactions remain feasible over the O(H) surface groups, in an analogy to the well-established role of ceria. A confirmation of this theoretical finding may involve monitoring of conversion and selectivity as function of oxygen concentration in the mixed H_2-C_2H_2 inlet stream.

The chemical change in the structure of the Mo_2N surface during the course of reaction requires further scrutiny. In this regard, surface characterisation could diagnose formation of Mo_2NH_x and $Mo_2NH_xC_y$ phases.

The literature demonstrates that, higher Mo/N ratios increase the hydrogenation capacity. Similarly, our theoretical modelling illustrates that, the occurrence of partial versus full hydrogenation depends to the type of termination, (111) versus (100) or, in other words, on the atomic composition of the surface. To the best of our knowledge, the effect of surface termination on the catalytic activity of Mo_2N has not been reported prior to the present study, requiring experimental confirmation.

Chapter 7 : Hydrodesulfurization of Thiophene over *γ*-Mo_2N catalyst

Paper IIII

Jaf,Z.N., Altarawneh, M., Miran, H.A., Jiang, Z-T and Dlugogorski, B.Z. *Hydrodesulfurization of Thiophene over γ-Mo_2N catalyst.* Molecular. Catalysis. 459. pp. 21-30. (2018)

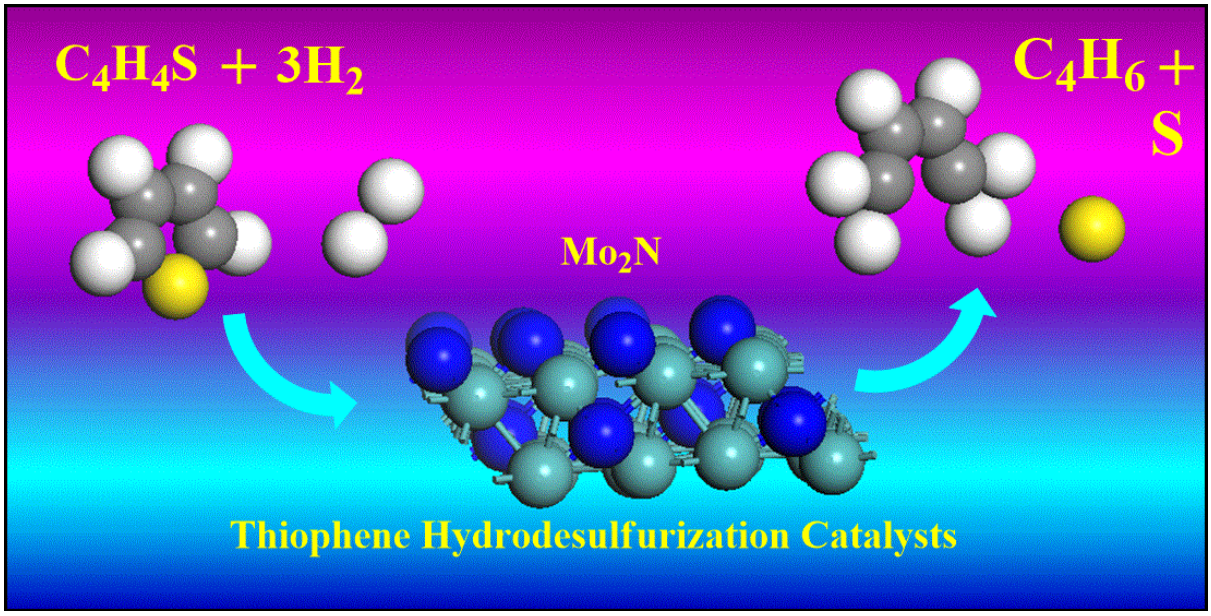

7.1 Abstract

Catalytic removal of the S-content from thiophene is a central step in efforts aiming to reduce the environmental burdens of transportation fuels. In this chapter, we investigate the hydrodesulfurization (HDS) mechanisms of thiophene (C_4H_4S) over γ-Mo_2N catalyst by means of density functional theory (DFT) calculations. The thiophene molecule preferentially adsorbs in a flat mode over 3-fold *fcc* nitrogen hollow sites. The HDS mechanism may potentially proceed either unimolecularly (direct desulfurization) or via H-assisted reactions (hydrogenation). Due to a sizable activation barrier required for the first C−S bond scission of 54.6 kcal/mol, we predict that the direct desulfurization to contribute rather very insignificantly in the HDS mechanism. Transfer of adsorbed hydrogen atoms on the γ-Mo_2N surface to the thiophene ring substantially reduces activation barrier required in the C−S bond scission to only 24.1 kcal/mol in a process that affords an adsorbed $C_4H_6^*$ species and an S atom. Further hydrogenation of the unsaturated $C_4H_6^*$ produces 2-butene. Kinetics and thermodynamics attributes dictate the occurrence of partial rather than full hydrogenation of $C_4H_6^*$. Calculated rate constants for all individual steps could be utilized to construct a robust kinetic model for the overall HDS process. Estimated conversion values of thiophene predict 50-70% consumption of thiophene at 700 K and low values of gas hourly space velocities. Reaction routes and kinetic parameters provided herein are useful to design stand-alone γ-Mo_2N-based catalysts for applications entailing partial hydrogenation and hydrodesulfurization of severely contaminated S-fuels.

7.2 Introduction

The growing demand on producing environmentally clean fuel has led to formulating strict regulations worldwide [461, 462] on oil refineries to lower the level of impurities in transportation fuels [462]. In petroleum industry, the removal of heteroatoms such as S, N, and O from organic molecules is central in the pursuit to minimise the environmental burden of the combustion of transportations fuel. Combustion of sulfur-containing complexes leads to form an oxidized species [461]. Of particular importance are sulfur and nitrogen oxides (NO_x and SO_x) that form whenever a trace load of N and S co-exists with oxygen in thermal systems. Among the various abatement technologies, catalytic-mediated destruction of heteroatomic pollutants has emerged as an effective low-temperature approach in reference to the high-temperature gas phase oxidation. For sulfur-bearing fuels, improving catalytic performance is centred toward enhancing the molecular transformation of S-species into hydrocarbons and hydrogen sulphide (H_2S).[463, 464]

HDS denotes a process that decomposes S-containing compounds into hydrocarbons and H_2S over a catalyst in H_2 atmosphere. The HDS process typically occurs within a temperature spaning from 573-773 K and operates at elevated pumping pressure of up to 130 atm [465, 466]. The conventional HDS's catalysts that effectively desulfurize aromatic molecules include CoMo and NiMo sulphides [462, 467]. Furthermore, supported and /or promoted noble metals catalysts such as Pt and Pd demonstrate high catalytic performance in the HDS process toward heterocyclic compounds [468]. Thiophene (C_4H_4S) is the simplest sulfur-containing molecules [469]. It is widely deployed as a probe model in studies that examine HDS activity of catalysts. Utilized catalysts are readily poisoned by sulfur deposition. The global reaction step for the interaction of thiophenic compounds over a catalyst surface can be expressed as;

$$C_xH_yS + nH_2 \rightarrow C_xH_y + H_2S \qquad 7.1$$

Number of reviews reported high catalytic activity of unsupported and supported Mo nitride-based catalysts, similar to or higher than those measured for sulfidic Mo catalysts. The catalytic process takes place via a series of complex reaction networks that are dictated by the so-called deep hydrodesulfurization mechanism [184, 186]. Sajkowski and Oyama [470], stated that

thiophene's hydrodesulfurization activity over unsupported molybdenum nitride (γ-Mo_2N) and alumina-supported Mo carbide catalysts under hydrotreating conditions (i.e 633K and 13.7 MPa) is about five times higher than conventional sulfided Mo/Al_2O_3 and Ni-$Mo/A1_2O_3$ catalysts. This was attributed to their metallic nature and to the incorporation of lattice nitrogen and carbon into the interstitial sites, however, XPS analysis revealed that, there is a possibility for the sulfidation of adsorption sites as probed by CO adsorption. This clearly may hinder the catalytic performance of the aforementioned catalysts in HDS applications. Aegerter *et al.* [184] tested thiophene's HDS activities of three synthetic catalysts of Mo_2C/Al_2O_3, Mo_2N/Al_2O_3 , and sulfided Mo/Al_2O_3 that having Mo loadings of about 1.5–20 wt% measured by CO's chemisorption. They found that, after 24 h and at a reaction temperature of 693 K, the proposed catalysts exhibited higher HDS activity than sulfided Mo/Al_2O_3 catalyst. The catalytic performance followed an order of sulfided Mo < γ-Mo_2N< β-Mo_2C and governed by the high density of active sites. In-situ FT-IR measurements were performed to investigate the surface chemistry of thiophene on reduced passivated and nitrided γ-Mo_2N/Al_2O_3 catalysts at temperature up to 673 K. Thiophene's probing reveals that no reaction occurs over the two catalysts even at 673 K. However, when H_2 is introduced, it becomes reactive at 573 and 373 K on reduced passivated and nitrided Mo catalysts; correspondingly. Nagai [464] evaluated the γ-Mo_2N catalysts performance under sulfidation conditions and proposed a procedure to assess the deactivation behaviour.

Wu *et al.*[471] reported that, the synthesised Mo nitride catalysts is considerably active during HDS of dibenzothiophene in the initial stage, but rapidly became deactivated because of the sulfidation effect. In HDS's catalysts, several distinct possible adsorption configurations have experimentally been observed for thiophen. Number of DFT studies have reported reaction routes of thiophene and its substituted derivatives in the course of the HDS process [472]. However, several prominent reaction steps are still not clearly understood. Literature demonstrates that pre-hydrogenation to dihydrothiophene or tetrahydrothiophene intermediates to be an important step prior to the S–C bond rupture. Experimental measurements elucidated insights into the operating reaction routes. For instance, tetrahydrothiophene was formed in appreciable quantitates at a high pressure and low temperature; whereas thermodynamic equilibrium considerations seem to act in reducing its formation at elevated temperatures [472, 473]

Recently, De Souza *et al.* [474] reported thiophene adsorption geometries, energies and reaction mechanisms over vanadium carbide VC(001) and vanadium nitride VN(001) surfaces along with the involved intermediates. They pointed out that, hydrogenation (HYD) pathway is less important than the direct desulfurization pathway (DDS) pathway over VN. Similarly, a periodic DFT study reported thiophene's dissociative uptakes over niobium nitride face centered cubic NbN(001) plane configuration. Results indicate that, the DDS route is more kinetically feasible in reference to the HYD pathway[475] . Likewise, the HDS mechanism of thiophene over γ-Mo_2N (100) surface catalyst as studied by Ren el al.[476]. They investigated the adsorption and dissociation of thiophene over the MoP(001), γ-Mo_2N(100), and Ni_2P(001) surfaces. It was established that, thiophene adsorbs dissociatively on MoP(001), while non-dissociatively over γ-Mo_2N(100) and $N_{i2}P$(001) orientations. The dissociation of the first C-S bond of adsorbed thiophene over γ-Mo_2N(100) was found to necessitate an energy barrier of 36.4 kcal/mol in an exothermic reaction of 16.8 kcal/mol.

Despite these studies, to the best of our knowledge, no effort has been dedicated to investigating the HDS mechanisms of thiophene over the thermodynamically most stable (111) termination of γ-Mo_2N. Via the implementation of the ab initio atomistic thermodynamics on all plausible terminations of γ-Mo_2N, we found the N-terminated (111) surface to incur more thermodynamic stability across all values of accessible chemical potential of nitrogen [113]. Along the same lines of enquiry, particles deployed in the HDS reactions are mostly crystallized in the (111) direction as observed in noble metals catalysts . Most of catalysis theoretical and experimental studies on γ-Mo_2N have pointed out to the predominance of the N-terminated γ-Mo_2N (111) surface [113, 477, 478]. This has motivated us to theoretically investigate the HDS's mechanism of thiophene over the γ-Mo_2N (111) plane. Herein, we report the adsorption energies and reaction rates of the involved intermediates, propose possible pathways in HDS process, and finally provide a thermodynamic and kinetic analysis to underpin dominating reaction routes.

7.3 Computational Methods

All structural optimizations and energy calculations were performed with the DMol^3 code installed in Material Studio [479]. The exchange correlation potential was represented by applying the generalized gradient approximation (GGA) with the Perdew-Burke-Ernzerhof functional (PBE)[439]. Double Numerical plus polarization function (DNP) basis set [274] (that comprises one numerical function for each occupied atomic orbital), has been applied along with the inclusion of a Grimme dispersion correction (G06) [248] (i.e., a van der Waals DFT-D functional). The unit cell of bulk γ-Mo_2N has also been optimized with considering the Grimme dispersion correction. A thermal smearing of 0.01 Ha and a real-space cutoff of 4.2 Å were considered in all computations. For numerical integration, we utilized a medium quality mesh represented by 1×3×1 *k*-point. Convergence tolerance for optimization convergence thresholds for energy change, maximum force, and maximum displacement between the optimization cycles were set at 0.00002 Ha, 0.004 Ha/Å, and 0.005 Å; respectively. In order to reduce long-range dipole interactions caused by a charge rearrangement on the surface due to thiophene adsorption, a dipole correction along the *z*-direction was deployed [480]. Transition states calculations via DMol^3 have been performed through the linear synchronous and quadratic synchronous transit LST/QST methods [440]. Merits of these two methodologies over the commonly deployed NEB method has been illustrated in our recent study [481].

The considered (2×2) supercell (11.87 Å × 9.96 Å ×18.61 Å) comprising four atomic layers together with the adsorbed chemical entity were allowed to fully relax. A vacuum region of ~18.0 Å along the z-axis averts any plausible interactions between adjacent vertical layers.

We also have tested the convergence of reaction energies with respect to the number of atomic layers. The calculated reaction energy for one reaction (the M1 → M2 step) over a six-layer slab amounts to -8.5 kcal/mol. This value differs by only 0.2 kcal/mol (~ 2.0%) from the corresponding value obtained when considering a four-layer slab". Accordingly, all computations were carried out using a four-layer slab model.

Furthermore, we have tested the effect of using various dispersion corrections functional (DFT-D methods) on the adsorption energies. Using the Ortmann, Bechstedt, and Schmidt (OBS)[250] functional, changes the adsorption energy for the molecular thiophene over a 3-*fcc* site by only 6.0%. Likewise, Moses et al [473] reported that the adsorption energies for thiophene on MoS_2 surfaces were not generally influenced by the choice of the vdW functional.

A detailed description of the surface active sites has been reported in our recent study on the selective hydrogenation of C_2H_2 over γ-Mo_2N surfaces [477].

We determine adsorption energies (at 0 K) of γ-Mo_2N/species system according to;

$$E_{ad} = E_{(surface+\ species)} - (E_{(surface)} + E_{(species)}) \qquad 7.2$$

where $E_{(surface\ +\ species)}$ refers to the energy of the surface and molecule system (physisorbed configuration), $E_{(surface)}$ is the energy of the clean surface, and $E_{(species)}$ denotes to the energy of the chemical species.

Afterwards, we perform vibrational frequencies calculations for each step in the mechanism to acquire reaction rate constants according to the classical transition state theory [482] :

$$k(T) = A \exp(-E_a/(RT)) \qquad 7.3$$

herein; $k(T)$ refers to the reaction rate constant, A represents the pre-exponential Arrhenius factor, E_a implies the activation energy in cal/mol, R stands for universal gas constant (1.987 cal K^{-1} $mole^{-1}$) and T denotes the temperature in Kelvin.

7.4 Results and Discussion

7.4.1 Thiophene Adsorption over γ-Mo_2N (111).

Figure 7.1 depicts the optimized configuration of the clean N−terminated (111) slab of γ-Mo_2N. We positioned the thiophene molecule at various orientations in order to examine potential HDS active sites.

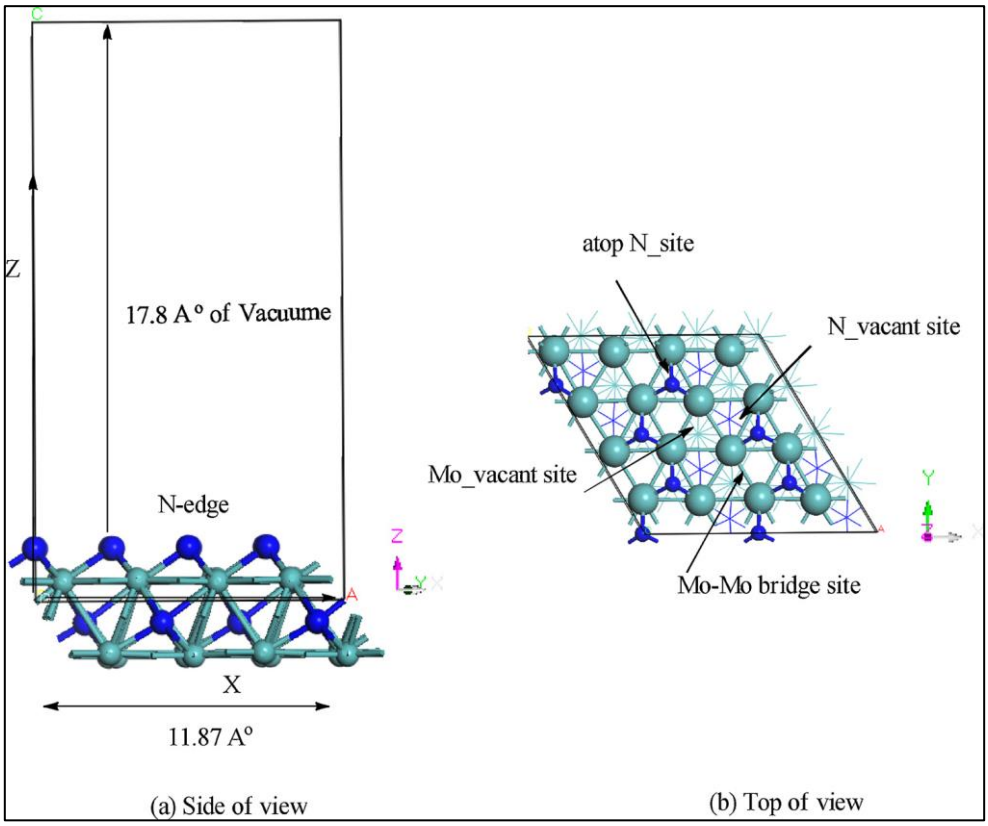

Figure 7.1: Optimized structure of γ-Mo_2N (111) slab. Grey spheres signify Mo atoms and blue spheres denote N atoms.

Figure 7.2 displays the relaxed structures of different adsorption patterns adopted by thiophene (A1−A6) while Table 7.1 enlists prominent structural parameters and adsorption energies. In the A1 configuration, the molecule ring adapts a parallel orientation above the triangle Mo vacant site (i.e. flat lying manner) and the sulfur atom is pointed to one of the molybdenum atoms at a large separation of distance of 3.065 Å.

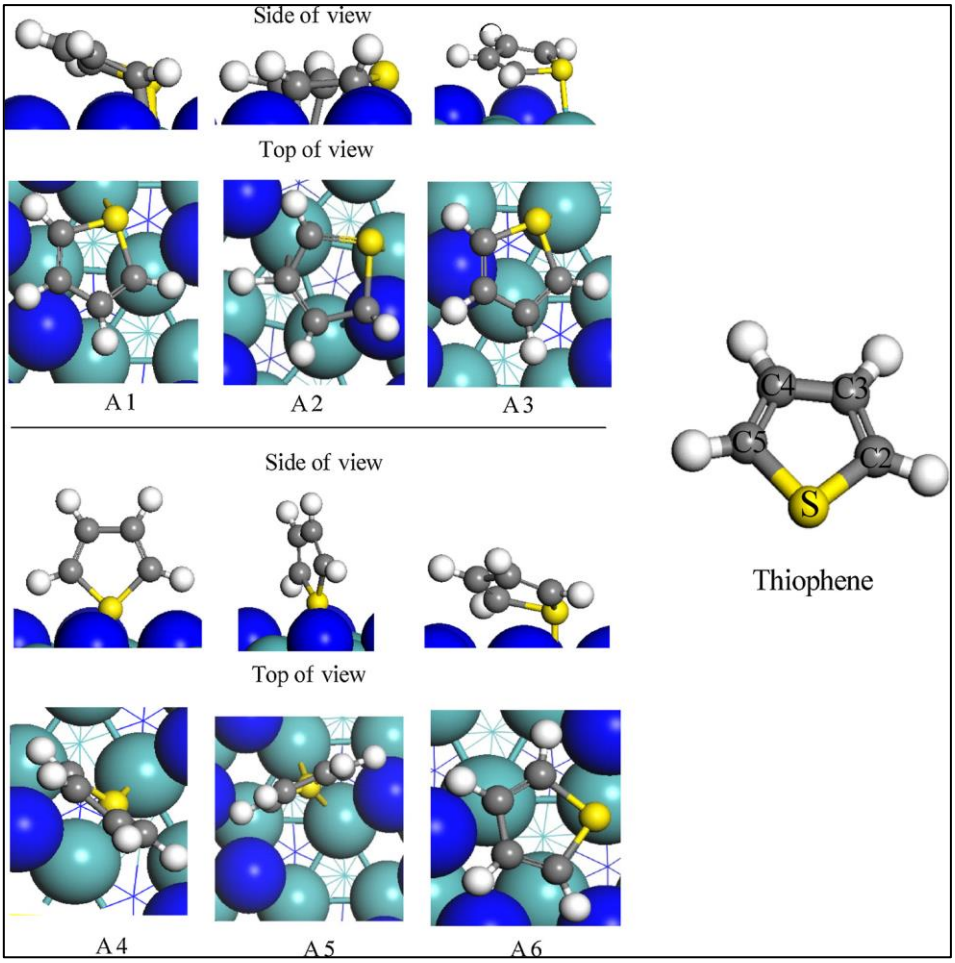

Figure 7.2: Relaxed configurations of thiophene's molecular adsorption on a γ-$Mo_2N(111)$ slab.

Table 7.1: Computed adsorption energies (E_{ads}, kcal/mol) and some structural properties of thiophene over the γ-Mo_2N(111) slab. For atomic numberings, refer to Figure 7.2.

	E_{ads}	d(C^2-C^3) (Å)	d(C^3-C^4) (Å)	d(C^4-C^5) (Å)	d(C^2-S) (Å)	d(C^5-S) (Å)	d(S-Mo) (Å)	θ(C^2-S-C^5) deg
C_4H_4S		1.390	1.411	1.390	1.760	1.760		90.18
A1-tilted	-33.8	1.388	1.413	1.375	1.784	1.735	2.635	91.61
A2-flat	-48.8	1.526	1.446	1.416	1.919	1.784	2.658	92.03
A3-tilted2	-40.0	1.388	1.422	1.371	1.761	1.741	2.694	91.30
A4-upright	-31.8	1.359	1.448	1.358	1.759	1.759	2.527	93.20
A5-upright2	-21.8	1.365	1.438	1.367	1.735	1.729	2.455	94.02
A6-tilted3	-30.3	1.366	1.432	1.367	1.749	1.759	2.577	91.45

The thiophene in the A1 structure adsorbs non-dissociatively with an adsorption energy of -33.8 kcal/mol. In the optimized configuration, the C−H bonds slightly tilt, and they experience a minimal shortening from 1.095 to 1.088 Å. The adsorption process has caused only minor shifts in the surrounding Mo−Mo, Mo−N, and N−N bond lengths from 2.973, 1.908, and 2.954 Å in the clean slab to 2.894, 1.970, and 2.976 Å in the A1 configuration, respectively. Furthermore, thiophene's intermolecular bonds display marginal stretching and/or shortening after adsorption. For instance, S−C^2, and C^3−C^4 bonds elongated after adsorption as compared to those in the gas phase from 1.760 and 1.411 Å to 1.784 and 1.423 Å in the adsorbed system, respectively. On another hand, the C^2−C^3, C^4−C^5, and S−C^5 bond lengths are slightly reduced from 1.390, 1.390, 1.760 Å in the gas phase to 1.388, 1.375, and 1.735 Å, in the adsorbed thiophene, correspondingly.

Positioning the thiophene molecule at a 3-fold *hcp* nitrogen vacant site affords the lowest energy structure (A2, -48.8 kcal/mol) in which the S atom is separated from the surface by a distance of 2.658 Å. In fact, this adsorption process does not lead to a loss of the aromaticity of thiophene, however; C^2−C^3 and C^2−S bond lengths extend to 1.919 and 1.526 Å, but without being activated. In the A3 structure, thiophene ring was positioned horizontally atop of nitrogen site at a separation of 3.109 Å, however, the structure converges into a configuration where the molecule moved toward the Mo–Mo bridge site and bonded with a surface Mo atom

at 2.694 Å. The C^3–H and C^4–H bonds tilted away and lifted from the surface; most presumably, due to the hybridization effect. Placing thiophene vertically over the 3-fold *fcc* Mo-hollow site resulted in moving the molecule toward the Mo-Mo bridge site and forming two Mo-S bonds at 2.527 and 2.504 Å. This structure (A4) resides -21.8 kcal/mol below the non-adsorbed thiophene molecule. A4 and A6 structures entail adsorption energies of -31.8 kcal/mol and -30.3 kcal/mol, correspondingly.

The calculated physisorbed energies of thiophene (extending between -21.8 – -48.8 kcal/mol) demonstrate a rather strong molecular interaction. In reference to molecule-γ-Mo_2N systems, calculated binding energies in Table 1 are in accord with analogous systems of CO (-34.3 kcal/mol) [152] and NO (-30.1 – -50.2 kcal/mol)[113]. The most stable molecular adsorption (-48.8 kcal/mol) assumes a flat orientation. Such behaviour was found to prevail in thiophene adsorption over Pt(111)[483] and MoP(001)[472] surfaces. The noticeable high adsorption energies enable the adsorbed thiophene molecule to react with surface hydrogen atoms facilitating its hydrogenation as will be illustrated in the next sections. Computational-based investigations reported that thiophene adsorbs horizontally over the γ-Mo_2N(100) plane with an estimated adsorption energy of -13.6 kcal/mol. Similarly, over the NbN(001) surface[475], molecular thiophene preferentially adapts a flat mode, with an exothermic physisorbed energy of -25.3 kcal/mol. However, over the VN(001) configuration [474], thiophene adsorbs vertically with an adsorption energy of -15.6 kcal/mol. Tominaga and Nagai [484] stated that for β-Mo_2C (001) catalysts, thiophene adsorbed vu dissociation, which in turn leads to its decomposition into sulfur, CH, and C_3H_3 species.

7.4.2 Thiophene HDS Mechanism over γ-Mo_2N(111)

In modelling the HDS mechanism, we started from a hydrogen pre-covered surface. We have shown in our recent study [477], that hydrogen molecules dissociate over the pre-covered N-terminated γ-Mo_2N (111) surface via facile activation barriers. Our detailed kinetics analysis concurs with available experimental results pertinent to the overall rate for H_2 uptake, preferred adsorption sites and the potential for the occurrence of surface H diffusion. To model the HDS reaction of thiophene, we proposed that six hydrogen atoms are randomly adsorbed on various adsorption sites (viz. *hcp*-vacant, *fcc*-vacant and atop nitrogen). This could be rationalised by the fact that H_2 dissociative adsorption typically does not constitute a rate-determining step in

catalytic hydrogenation reactions [465]. The key concept governing the HDS mechanism assumes that C−S bond scission occurs after hydrogenation of the ring. If C−S bond is cleaved first, *i.e.*, without the need of pre-hydrogenation, a direct desulfurization (DDS) route would be predominant. On the other hand, the hydrogenation (HYD) mechanism suggests that, the S−C bond rupture proceeds after several hydrogenation steps operated by adsorbed hydrogen atoms.

7.4.2.1 The direct desulfurization pathway (DDS)

As stated above, the direct desulfurization process assumes no contribution of adsorbed hydrogen atoms during S−C bonds cleavage and leads to the formation of thiolate species. From an experimental point of view, it is worth mentioning that Wu *et al.* [471] observed that, dissociation of thiophene over alumina supported γ-Mo_2N in an inert medium does not procced even at high temperatures (673 K). However, when admitting a stream of H_2, the surface of γ-Mo_2N/α-Al_2O_3 displays a profound catalytic reactivity toward thiophene's decomposition even at temperatures as low as (373 K).

Thus, it is of interest to examine the energy barriers required to split ($S–C^2$ and $S–C^5$) bonds without assistance from adsorbed hydrogen atoms. Figure 7.3 demonstrates a potential energy surface (PES) diagram for the DDS pathway. Direct fission of the $S–C^5$ bond necessitates a sizable energy barrier of 54.6 kcal/mol via the transition structure TS_a. In the intermediate structure E2, the first $S–C^5$ bond is significantly elongated from 1.745 Å to 3.31 Å, indicating a complete fission of the bond. Formation of E2 via the $S–C^5$ bond scission is endothermic by 26.1 kcal/mol. Fission of a second C^2-S bond as in the E2 configuration, leaves an adsorbed sulfur atom attached to a surface Mo atom and a $C_4H_4^*$ moiety via the transition structure TS_b. TS_b resides 50.8 kcal/mol above the E2 intermediate. The overall (DDS) process is noticeably exothermic by 21.6 kcal/mol. However, the noticeable high barriers for the first $S–C^5$ and second $S–C^2$ bond fission hinder the occurrence of the DDS process and render it as a kinetically unfavourable process. Likewise, the analogous fission of the first C-S bond over the γ-Mo_2N (100) slab requires a relatively high barrier of 36.4 kcal/mol[476]. Those high barriers of TS_a and TS_b are in accord with the experimental findings of Wu et al. [471] who found that direct decomposition of thiophene is not plausible even at relatively high

temperatures (673 K). Conversely, in the presence of H_2, the catalyst surface can partly be sulfided via thiophene's decomposition at a significantly low temperature of 373 K.

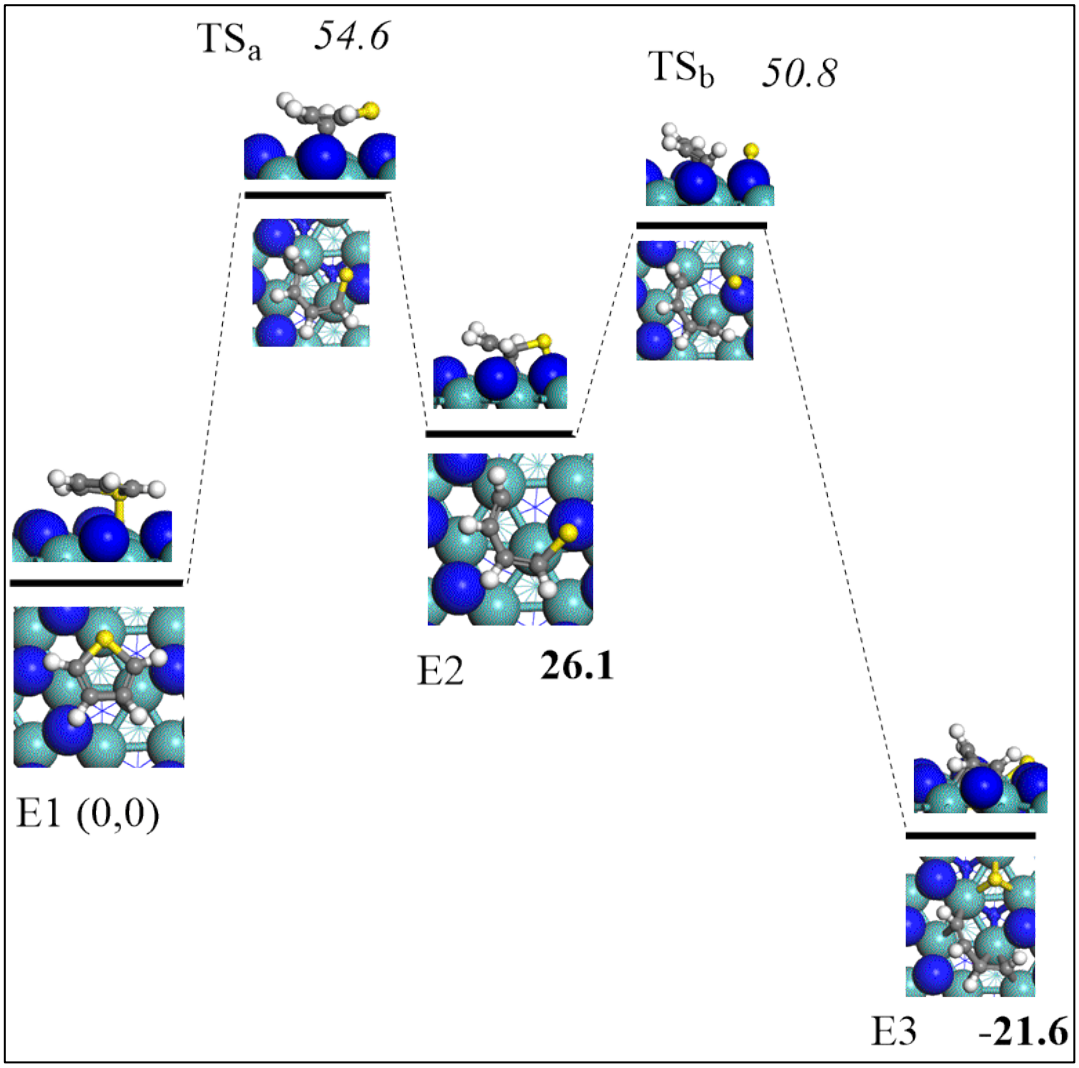

Figure 7.3: Reaction mechanism for thiophene's direct desulfurization (DDS). Values of activation barrier and reaction energy are in kcal/ mol with respect to the initial reactant (E1). Light green, blue, yellow, grey, and white stand for atoms, molybdenum, nitrogen, sulfur, carbon, and hydrogen, respectively.

7.4.2.2 The hydrogenation pathway (HYD)

Figure 7.4 depicts reaction routes for the hydrodesulfurization of thiophene over the N-terminated (111) surface. After the adsorption of thiophene, the first elementary hydrogenation step proceeds by H transfer from the surface to the C^2 atom forming a 2-hydrothiophene (M2) intermediate. The opening H-transfer reaction demands a modest energy barrier of 18.8

kcal/mol (TS1). The loss of aromaticity via this reaction is accompanied with a trivial exothermicity of only 8.3 kcal/mol. Subsequent to the first hydrogenation step, two possible reaction pathways have been proposed to generate either 2,5-dihydrothiophene (M4) or *cis*-butadienethiolate (M3) adducts. The formation of 2,5-dihydrothiophene is kinetically more plausible than *cis*-butadienethiolate.

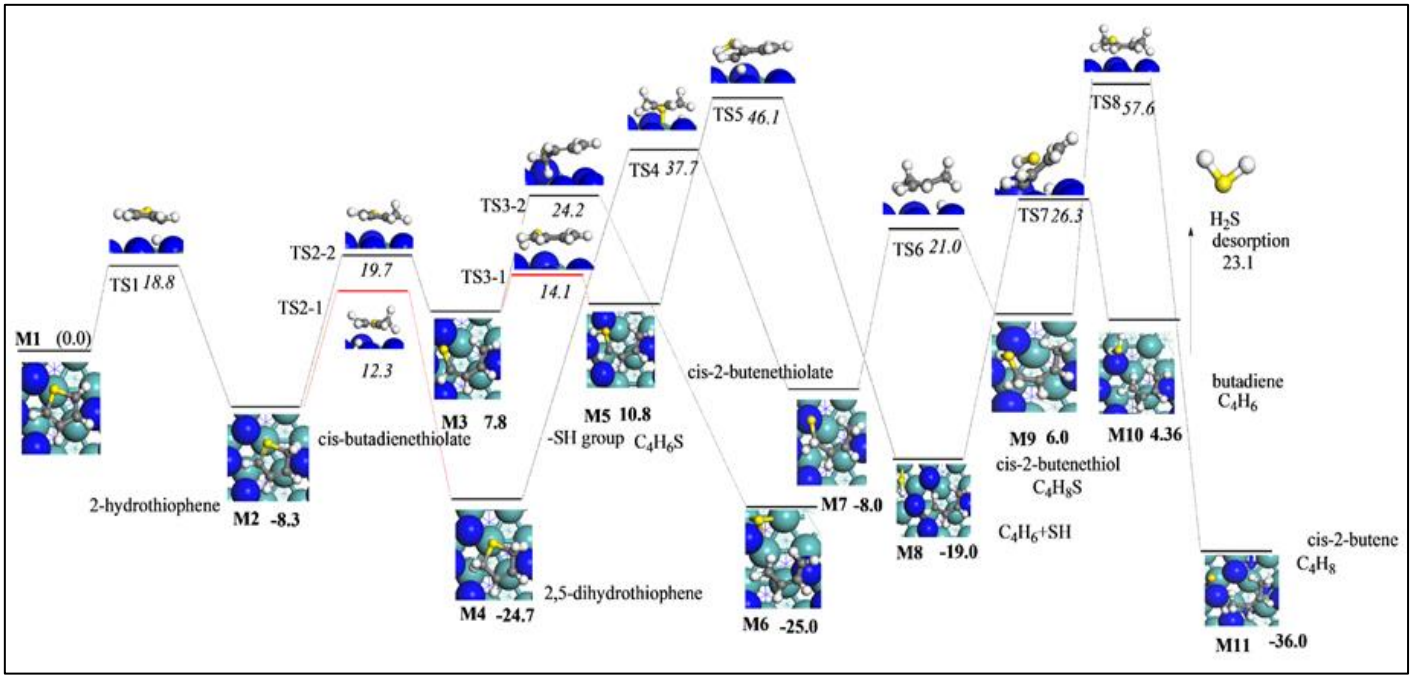

Figure 7.4: HDS's mechanism of thiophene over γ-Mo_2N slab. Values in bold (reaction energies) and italic (activation barriers) correspond to the energy of thiophene plus six atomic H adsorbed on the slab (M1). Light green, blue, yellow, gray, and white stand for atoms, molybdenum, nitrogen, sulfur, carbon, and hydrogen, respectively. All values are in kcal/mol in reference to the initial channel (M1). The adsorbed atomic H is omitted for clarity.

A DFT investigation performed by de Souza *et al.* [475] reported that *cis*-butadienethiolate synthesis has to overcome a barrier of 25 kcal/mol over NbN (001) catalyst. Our corresponding barrier for this step amounts to 12.3 kcal/mol. This finding indicates that initial steps in the catalytic hydrogenation of thiophene mediated by Mo-nitride proceeds via lower barriers when compared with niobium nitride. Further hydrogenation of 2,5-dihydrothiophene to tetrahydrothiophene has not been considered herein as the latter itself constitutes an important intermediate under low temperature and high pressure conditions [465].

The activation barrier of the subsequent hydrogen transfer to *cis*-butadienethiolate through S atom demands a trivial energy barrier of 6.3 kcal/mol through (TS3-1) forming a thiol -SH group. Formation of the M5 configuration is slightly endothermic. On the other hand, the extrusion of sulfur from *cis*-butadienethiolate proceeds via S–C bond rupture with the formation of a sulfur atom and a butadiene molecule as products (M6). This reaction takes place via an activation energy of 16.4 kcal/mol through (TS3-2). The products of these reactions reside 25.0 kcal/mol below the entrance channel. The overall barrier (24.2 kcal/mol) for the synthesis of S^{*} + $C_4H_6^{*}$ is significantly lower than in its analogous step over γ-$Mo_2N(100)$ (2.35eV ~54.1 kcal/mol) [485].

Preliminary rupture of S–C bond as a result of hydrogen transfer occurs at an energy barrier of 37.7 kcal/mol via (TS4) and generates the moiety of *cis*-2-butenethiolate (M7). To incessant the desulfurization process, another H transfer reaction is required to saturate (M5) into (M8) through (TS5) in which a modest barrier of 35.5 kcal/mol has been encountered. This reaction is exothermic by -19.01 kcal/mol and the by-products are $C_4H_6^{*}$ species and co-adsorbed HS. Another hydrogen atom transfer into the adsorbed HS group affords dihydrogen sulphide (H_2S) molecule along the reaction M8→ M10 that requires activation energy of 45.3 kcal/mol via the transition structure (TS7). The formation of butadiene (M10) and H_2S species occurs through a marginal endothermicity reaction of 4.4 kcal/mol. Desorption of H_2S* into a gas-phase species demands a desorption energy of only 23.6 kcal/mol.

In the final C−S bond scission, adsorbed *cis*-2-butene (C_4H_6*) is formed with an activation energy of 51.6 kcal/mol through the transition structure (TS8). Obviously, further hydrogenation of *cis*-2-butenethiol (M9) is predicted to be a slow process owing the sizable barrier of TS8. From a mechanistic point of view, elimination of the sulfur atom from the thiophene proceeds through two plausible intermediates namely, *cis*-butadienethiolate (M3) and *cis*-2-butenethiol (M9). The corresponding required reaction barriers are, 24.2 kcal/mol and 57.6 kcal/mol (in reference to the entrance channel), along the reactions M3→M6 and M9→M11, respectively. This indicates that, the formation of butadiene (C_4H_6) in (M6) to be a faster process than butane (C_4H_8) synthesis in (M11). In a nutshell, the PES in Figure 7.4 indicates that the HYD pathway affords adsorbed $C_4H_6^*$ and S atoms rather than $C_4H_8^*$. The high barrier of TS4 infers that further hydrogenation affording the latter is not plausible when compared with the barrier of TS3-2 that leads to the formation of the former.

The adsorbed $C_4H_6^*$ adduct constitutes a precursor for the experimentally observed products butane, butene, and 1,3-butadiene [471]. Consequently, we devote the next two sections to illustrate pathways leading to the formation of stable C_4 species commenced by hydrogenation of C_4H_6*.

7.4.2.2.1 Partial hydrogenation and the formation of cis-2-Butene

The exceptional catalytic properties of γ-Mo_2N catalysts in mediating partial rather than full hydrogenation of alkynes is comprehensively discussed in our previous work [477]. We reported that, high hydrogenation selectivity of ethyne to ethene stems from the low barrier for the first hydrogenation step in partial hydrogenation route in reference to first hydrogenation step in full hydrogenation pathway, in addition to lower desorption energy for the C_2H_4* adduct when compared with the energy barrier required for further hydrogenation.

Similarly, Wu *et al.* [180] stated that γ-Mo_2N/α-Al_2O_3 catalysts show high selectivity towards the conversion of butadiene into butene rather than butane. Figure 7.5 maps out reaction mechanism for partial hydrogenation of butadiene.

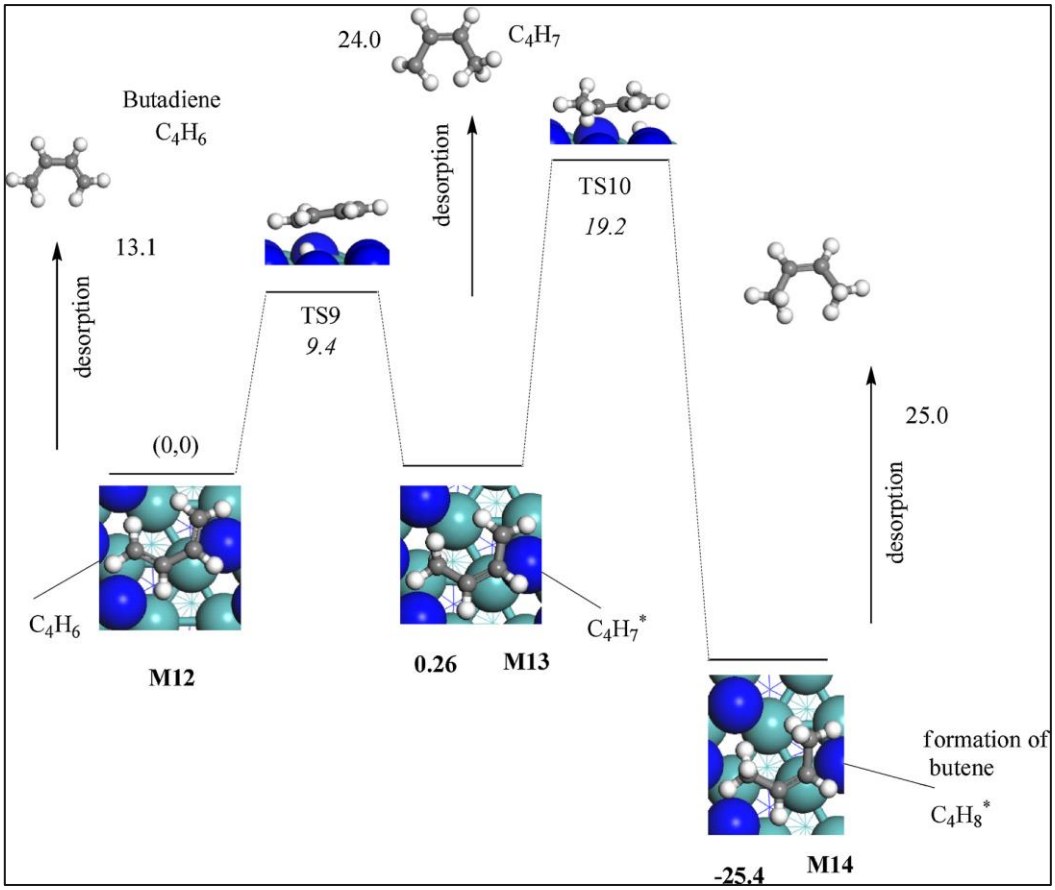

Figure 7.5: The largely irreversible pathways for the partial hydrogenation over the γ-Mo_2N(111) surface. All values are in kcal/mol in reference to the initial reactant (M12).

Hydrogenation of adsorbed C_4H_6* is carried out by consecutive transfer of atomic hydrogen placed at 3-fold *fcc* hollow sites to the carbon skeleton. In other word, a saturated alkene forms when C^2 and C^5 are fully hydrogenated. Initially, the C^5–H distance was 2.491 Å in the M12 configuration. Hydrogen transfer into the C^5 atom affords the radical C_4H_7* that is produced at the same energy level of the starting reactant. The energy barrier required for this step is only 9.4 kcal/mol. A matching low barrier of 10.8 kcal/mol was computed for the analogous reaction (C_2H_2* + H* → C_2H_3*) [477]. This may be attributed to the shared location of H atom underneath the C^5 atom in other systems (*i.e.,* 3-*fcc* fold) and the very alike electronic structure of ethylene and butadiene. Consequent hydrogen transfer to C^2 atom in the adsorbed (C_4H_7*) produces the 2-butene (C_4H_8) molecule. The calculated barrier for this step amounts to 19.2 kcal/mol at (TS10). A higher barrier for this step-in reference to the opening hydrogenation step could be attributed to the high selective nature of γ-Mo_2N catalyst toward partial hydrogenation. Formation of 2-butene is exothermic by 25.4 kcal/mol (M14). Obviously, this

excess energy stems from stabilizing the unsaturated C_4H_7* into a stable adduct. Desorption of $C_4H_8^*$ from the surface into a gas phase butene entails an energy of 24.0 kcal/mol. Thus, further hydrogenation of $C_4H_7^*$ requires less energy than its desorption (19.0 kcal/mol versus 24.0 kcal/mol).

7.4.2.2.2 Full hydrogenation and the formation of Butane

To shed more light on the high selective nature of butadiene to butene rather than butane over γ-Mo_2N surface catalyst [180, 486], we consider the full hydrogenation pathways over the (111) slab. Figure 7.6 demonstrates PES for full hydrogenation pathways.

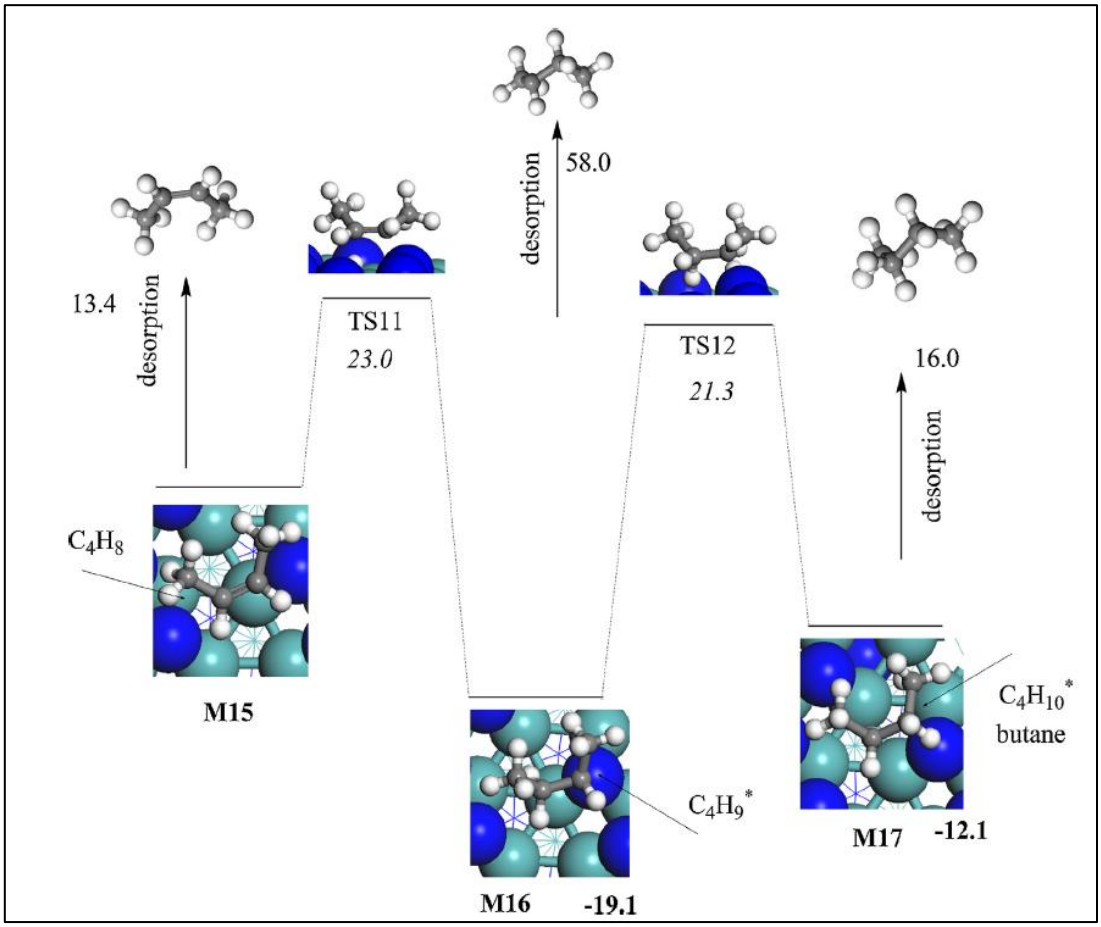

Figure 7.6: The largely reversible pathways for the full hydrogenation over the γ-Mo_2N(111) surface. All values are in kcal/mol in reference to the initial reactant (M15).

In a similar approach to the partial hydrogenation route, two H transfer reactions afford butane from the adsorbed 2-butene. The initial C^4–H distance is about 2.569 Å in (M15) and the movement of H atom from Mo vacant site toward C^4 atom produces the intermediate $C_4H_9^*$ (M16). The formation of C^4–H bond in the forward direction necessitates an energy barrier of 23.0 kcal/mol, and releases heat of 19.1 kcal/mol. Obviously, the occurrence of partial rather

than full hydrogenation is attributed to the significant difference in the energy barrier between in the opening step in both routes; *i.e.,* 9.4 kcal/mol versus 23.0 kcal/mol. This indicates that, the opening step in the partial hydrogenation pathway attains a higher barrier in reference to the corresponding step in the full hydrogenation. A similar trend was noticed during partial hydrogenation of acetylene (C_2H_2) toward ethylene (C_2H_4) instead of ethane (C_2H_6) over (111) γ-Mo_2N catalyst [477]. Reaction rate constants for the forward and reverse steps in the partial and full hydrogenation routes are documented in Table 7.2.

Table 7.2: Fitted kinetic parameters of reactions operating in the partial and full hydrogenation in the range of 300 – 1000 K.

	Reaction	A (s^{-1}.active $site^{-1}$)	E_a (kcal/mol)
M12→M13	C_4H_6*+H*→C_4H_7*	2.74×10^{17}	8.4
M13→M14	C_4H_7*+H*→C_4H_8*	2.79×10^{17}	19.8
M15→M16	C_4H_8*+H*→C_4H_9*	6.89×10^{11}	24.2
M16→M15	C_4H_9*→ C_4H_8*+H*	1.18×10^{17}	38.2
M16→M17	C_4H_9*+H*→C_4H_{10}*	2.32×10^{20}	45.2
M17→M16	C_4H_{10}*→C_4H_9*+H*	9.90×10^{13}	32.5

Finally, a butane molecule is formed upon a hydrogen transfer from the Mo-vacant site to the adsorbed $C_4H_7^*$ moiety. This process demands a modest activation barrier of 21.3 kcal/mol Further hydrogenation of $C_4H_9^*$ into butane proceeds at a very similar reaction barrier of the backward reaction into $C_4H_8^*$:

$$\text{M15} \xleftarrow{42.1\ (\text{TS11})} \text{M16} \xrightarrow{40.4\ (\text{TS12})} \text{M17}$$

The highly reversible nature that dictates the fate of the C_4H_7* moity is expected to diminish the occurrence of full hydrogenation. Overall, the occurrence of partial rather than full hydrogenation follow kinetics as well as thermodynamic rationale [487]. Based on the kinetic parameters, provided in Table 7.2, we can also shed a light into the occurrence of selective partial hydrogenation. In the partial hydrogenation route, the reaction rate constant for the first

hydrogenation step exceeds that of desorption of the C_4H_6* moity in the gas phase by six orders of magnitude at 700 K (*i.e.*, 6.5×10^{14} s^{-1} versus 8.4×10^{8} s^{-1}). On the contrary, the reaction rate constant for the desorption of the C_4H_8* moity into the gas phase largely exceeds that of the first hydrogenation reaction into C_4H_9* (*i.e.*, 8.6×10^{8} s^{-1}versus 4.4×10^{4} s^{-1} at 700 K). This indicates that the full hydrogenation pathway is blocked by the preferential desorption of C_4H_8* over hydrogenation.

7.4.3 Kinetic analysis

Table 7.3 reports predicted activation energies and pre-exponential *A* factor of HDS mechanism fitted in the temperature range of 300-1000K. Figure 7.7 portrays Arrhenius plots for the involved reactions. For instance, computed reaction rate constants (per active site) for the two S-removal reactions M3→M6 and M9→M11 500 K attain values of 3.5×10^{21} and 2.08×10^{14}, in that order.

Table 7.3: Kinetic parameters for investigated reactions fitted in the temperature range of 300-1000 K.

	Reaction	Intermediate molecules	*A*(s^{-1}or molecule.cm^{-3}.s^{-1})	E_a (kcal/mol)
M1 → M2	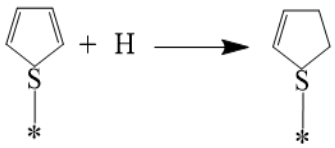	2-hydrothiophene	7.3×10^{7}	12.5
M2 → M3	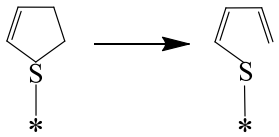	cis-butadienethiolate	3.2×10^{16}	21.8
M2 → M4	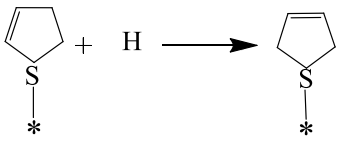	2,5-dihydrothiophene	1.9×10^{14}	14.5
M3 → M5	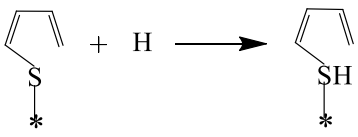	butadiene thiol	1.2×10^{14}	5.3

M3 → M6	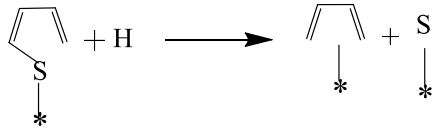	butadiene+ coadsorbed S	3.7×10^{21}	29.7
M4 → M7	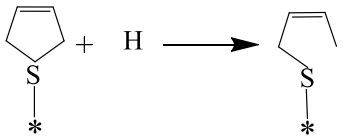	cis-2-butenethiolate	4.4×10^{14}	35.7
M5 → M8	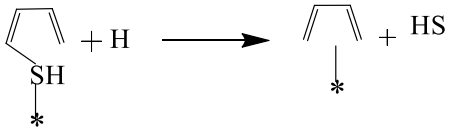	butadiene+co-adsorbed HS	1.0×10^{14}	40.2
M7→ M9	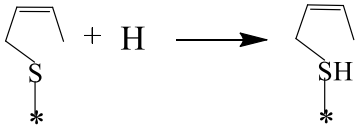	cis-2-butenethiol	4.7×10^{15}	16.2
M8 → M10	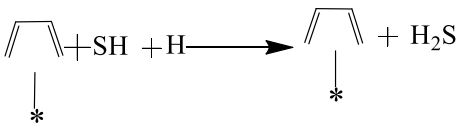	butadiene+co-adsorbed H_2S	1.1×10^{14}	30.0
M9 → M11	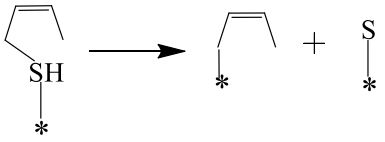	cis-2-butene + co-adsorbed S	2.2×10^{14}	52.2

Parameters in Table 7.3 could be used to construct a detailed and robust kinetic model for the decomposition of the thiophene molecule that incorporates all individual surface steps. However, we could also deduce global-like steps for the overall consumption of thiophene. The rate constant for surface catalysed reaction is expressed as [488];

$$k(T) = \frac{A}{\sigma} e^{-E_a/RT} \qquad 7.4$$

Where σ stands for the density of active sites. In our recent published study[477], we estimate σ to be 7.30×10^{-10} mol/cm^2 ; a value that reasonably match an experimental-derived value at 1.66×10^{-9} mol/cm^2. The activation energy value is taken to be the barrier of the transition state TS3-2 at 24.2 kcal/mol as it signifies the overall barrier for the most plausible pathway for removing S atom from the thiophene molecule. Likewise, a typical *A* value of 1×10^{13} s^{-1} is utilised. In the HDS experiment by Aegerter *et al.*[184] , the inlet H_2/Thiophene gas mixture

entails a ratio of 0.82/0.12. Due to the exothermic nature for the adsorption of thiophene and H_2 on the surface of γ-Mo_2N(111), it is reasonable to assume rapid conversion of gaseous H_2/thiophene partial pressures into their corresponding surface concentration. By assuming that there is no competition for adsorption sites between H_2 and thiophene, surface concentration for H atoms (C_H^*) and thiophene (C_T^*) are calculated to be 5.98×10^{-10} mol/cm^2 and 1.31×10^{-10} mol/cm^2; correspondingly. The surface rate for the disappearance of thiophene can be written as:

$$r(T) = -k(T) C_H^* C_T^* \qquad 7.5$$

Figure 7.7 plots reaction rate constants and rate of disappearance of thiophene between 400 – 1000 K. To the best of our knowledge, literature provides no analogous experimental estimates for these two quantities. As such, the calculated values in Figure 8 could serve as a benchmark for catalysts experimentalists.

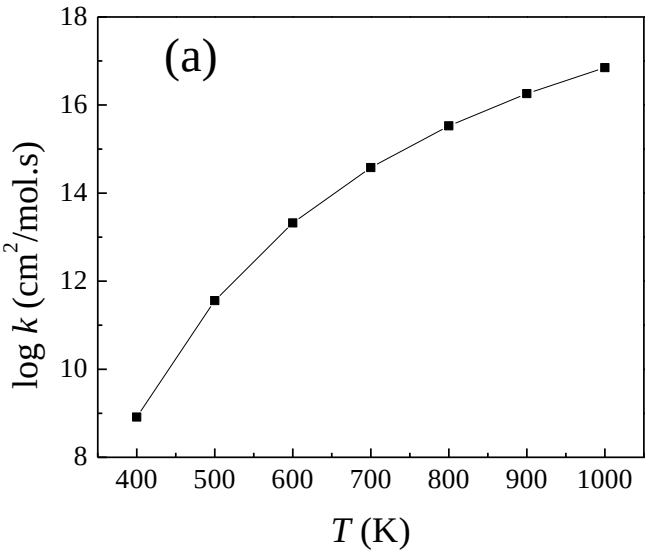

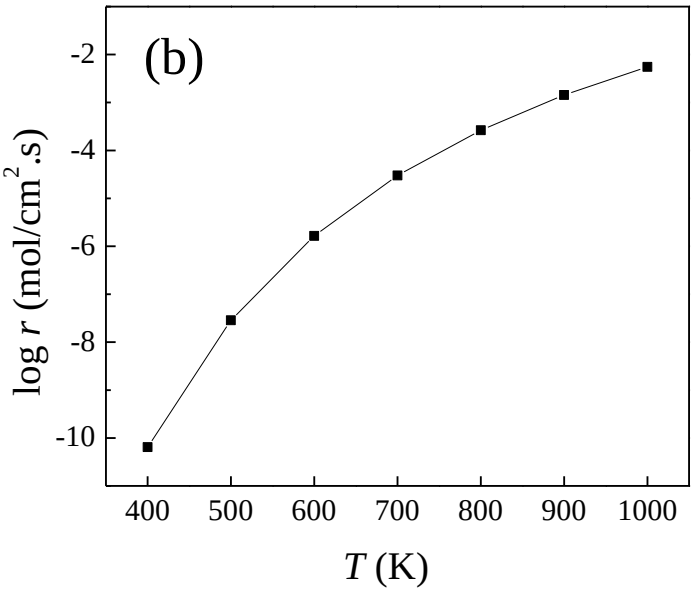

Figure 7.7**:** Reaction rate constant for the HDS of thiophene (a), and rate of the HDS process (b).

Finally, we are now in a position to deduce conversion values (*X*) for the disappearance of thiophene. By considering first-order rate law on a plug flow reactor model, *X* values can be expressed in terms of the residence time (τ), temperature and *k* values:

$$k(T) = \frac{1}{\tau}\ln[\frac{1}{1-X(T)}] \qquad 7.6$$

Arranging the equation in respect to *X* gives:

$$X(T) = 1 - \frac{1}{e^{\tau k(T)}} \qquad 7.7$$

At 700 K (the temperature at which the *X* values stabilized in the experiment[184]), the $k(T)$ value amounts to 2.78 × 10^5 s^{-1} (based on the activation barrier of the limiting reaction step at 24.2 kcal/mol; TS3-2). Accordingly, variation in τ (in s) values changes the *X* values. The only study that reports conversion values for the thiophene HDS activity was carried out by Aegerter *et al.* [184]. However, this study provided *X* values against real reaction time rather than residence time of gas hourly space velocity (GHSV, τ = 1/3600GHSV). *X* values

stabilized around 700 K at ~ 13% [184]. Table 7.4 presents *X* values at 700 K with considering GHSV values of 50 – 12,000 h^{-1}. The experimentally determined X value occurs at a GHSV of 500 h^{-1}. Calculating the GHSV requires knowing the volumetric flow rate and the reactor's volume. The flow rate in Aegerter *et al.*[184] correspondents to 8.33×10^{-6} m^3/s. Only the diameter of the reactor was given; 0.015 m. The length of the reactor was not provided in Aegerter *et al.*[184]. However, to have GHSV of 500 h^{-1}, the required reactor's length is ~ 0.3 m, which is a reasonable value. As expected, higher conversion is achieved at lower values of GHSV (*i.e.*, higher residence time).

Table 7.4: Variation of the conversion of thiophene in the HDS process with the gas hourly space velocity (GHSV) at 700 K.

GHSV (h^{-1})	*X*
50	0.79
100	0.54
300	0.23
500	0.14
1000	0.07
5000	0.02

7.5 Conclusions

This chapter reports the role of γ-Mo_2N (111) as an active catalysis in the HDS process of thiophene via spin-polarized DFT calculations. We have shown that the molecular adsorption of thiophene adapts several modes with adsorption energies in the range of -21.8 − -48.8 kcal/mol. Thiophene's HDS mainly occurs via the predominant HYD pathway affording the *cis*-butadienethiolate intermediate rather than *cis*-2-butenethiol. The most plausible initial products of the HYD process are H_2S and adsorbed $C_4H_6^*$ adducts. The latter undergoes a sequence of partial and full hydrogenation reactions leading to 2-butene and butane; respectively. We derived kinetic parameters for individual surface steps as well as global-like step for the overall HDS process. Kinetics and thermodynamics analysis indicate the preference of partial rather than full hydrogenation of $C_4H_6^*$. Calculated conversion of

thiophene indicates a 50-70% of thiophene's consumption at GHSV of 60 – 100 h^{-1}. Thermo-kinetic parameters reported herein are vital to understand the unique and highly selective nature of stand-alone γ-Mo_2N catalysts to desulfurize simple aromatic molecules as thiophene. Mechanistic routes illustrated herein could also applicable for larger S-containing molecules such as dibenzothiophene.

Chapter 8 : Catalytic Hydrogenation of *p*-chloronitrobenzene to *p*-chloroaniline Mediated by γ-Mo_2N

Paper V

Zainab N. Jaf, Mohammednoor Altarawneh, Hussein A. Miran, Almatarneh, M.H, Zhong-Tao Jiang, Bogdan. Z. Dlugogorski *"Catalytic Hydrogenation of p-chloronitrobenzene to p-chloroaniline Mediated by γ-Mo_2N". ACS Omega, 3 (10). pp. 14380-14391.*

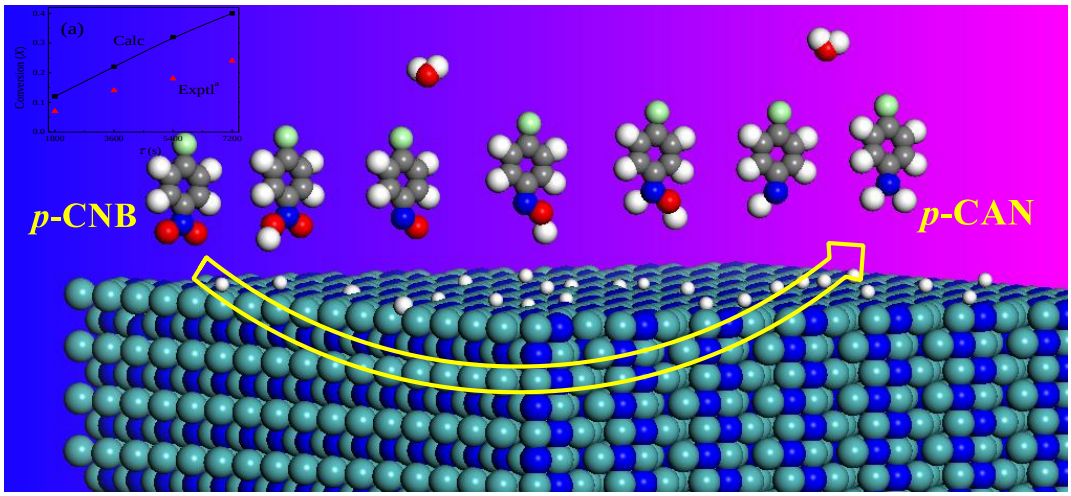

8.1 Abstract

Promoting the production of industrially important aromatic chloroamines over transition metal nitrides catalysts has emerged as a prominent theme in catalysis. This chapter provides an insight into the reduction mechanism of *p*-chloronitrobenzene (*p*-CNB) to *p*-chloroaniline (*p*-CAN) over the γ-Mo_2N (111) surface by means of density functional theory (DFT-D2) calculations. The adsorption energies of various molecularly adsorbed modes of *p*-CNB were computed. Our findings display that, *p*-CNB prefers to be adsorbed over two distinct adsorption sites namely, Mo-hollow fcc and N-hollow hcp sites with adsorption energies of -32.1 kcal/mol and -38.5 kcal/mol, respectively. We establish that, the activation of nitro group proceeds through direct pathway along with forming several reaction intermediates. Most of these intermediaries reside in a significant well-depth in reference to the entrance channel. Central to the constructed mechanism is H-transfer steps from fcc and hcp hollow sites to the NO/-NH groups through modest reaction barriers. Our computed rate constant for the conversion of *p*-CNB correlates very well with the experimental finding (0.018 versus 0.033 s^{-1} at ~ 500 K). Plotted species profiles via a simplified kinetics model confirms the experimentally reported high selectivity toward the formation of *p*-CAN at relatively low temperatures. It is hoped that thermo-kinetics parameters and mechanistic pathways provided herein to afford a molecular level understanding for γ-Mo_2N-mediated conversion of halogenated nitrobenzene's into their corresponding nitroanilines; a process that entails significant industrial applications.

8.2 Introduction

Aromatic haloamine compounds are important intermediates that are extensively deployed in the manufacturing of various prominent chemicals; most notably drugs, pesticides, and pigments [489]. The main preparation routes of these amines utilize metal–acid systems or selective hydrogenation to the analogous haloanilines (HANs) over noble metal catalysts such as platinum and palladium [490-492]. However, several parameters have hindered a mass-scale utilisation of these approaches in the production of HANs. These factors encompass high operating cost and low selectivity toward the formation of HANs. The latter is mainly attributed to hydrodehalogenation reactions that also result in the formation of aniline and nitrobenzene[195]. There are various factors that may contributed to the catalytic hydrogenation. Overall, the selectivity underpinning reaction kinetics toward the synthesis of the desired haloamine is primarily governed by the nature of catalyst that should be accurately designed in terms of metal, support and particle size), the role of stabilizers (as a promoter and an inhibitor) and reactions' condition (solvent, temperature and pressure)[489, 493, 494]. The catalytic-assisted hydrogenation reduction of aromatic molecules, in which molecular hydrogen plays a vital role as a reducing agent, has attained considerable interest. This is owing to generating less quantities of acid wastes when compared with homogenous chemical reduction reactions (i.e., the traditional Bechamp reaction) or in a metal–acid system [495], in addition of being environmentally friendly [496]. Additionally, the production of hydrogen chloride (HCl) from the hydrodechlorination reaction affects the catalytic activity of the reactor [497]. Thus, it is essential to improve heterogeneous catalysts that enforce the occurrence of selective hydrogenation of the nitro groups to the corresponding amino groups.

Recent related developments have decreased the rate of inhibiting the hydrodehalegentaion during the reduction of halonitrobenzene via using variety of metal catalysts. An activated carbon-supported Pd catalyst for instance with Pd nanoparticles size larger than 25 nm in a 500 mL reactor, was found to be highly selective towards the hydrogenation of halogenated nitrobenzenes of about 99.90% [498]. Ma et al. investigated the influence of using Ir nano-particles as a support in activated carbon catalyst (Ir/C) for the hydrogenation of halogenated nitrobenzene. They reported that high selectivity (> 99%) to *p*-chloroaniline (*p*-CAN) was accomplished with a particle size of (< 3 nm) Ir nanoparticles [499]. Furthermore, a study of gas phase hydrogenation of ortho-chloronitrobenzene (*o*-CNB) to ortho-chloroaniline (*o*-CAN) over Pd/Al_2O_3 catalyst promoted by several alkali metals was reported by Vishwanathan et al.

[500]. It was revealed that, the selectivity of the reduction of *o*-CNB depends on the polarity of N=O bond in the $–NO_2$ group.

However, the use of noble metals such as Pt and Pd is undesired due to the high cost and low catalytic stability, in which active sites could be readily blocked under high pressure of deployed hydrogen [501]. It is well established that, transition metal nitride catalysts exhibit high catalytic performance in an array of hydrogenation reactions. The partial hydrogenation of acetylene over two unsupported phases of β-Mo_2N and γ-Mo_2N has recently been investigated [179]. These synthesised catalysts were prepared by the temperature-programmed reaction of MoO_3 with $N_2 + H_2$. It was found that high selectivity (77–90%) toward ethylene formation could be attained over both β-Mo_2N and γ- Mo_2N crystallite phases. However, trivial amount of green oil formation has been detected by XPS over γ-Mo_2N in particular.

Fernando-Lizana et al [168] stated that a 100% selectivity of haloanilines was obtained during liquid phase hydrogenation of *p*-CNB, over the crystal phase Mo nitride catalysts. Furthermore, they performed a reaction over alumina supported palladium as a benchmark catalyst. Non-selective behaviour towards the production of nitrobenzene (NB) and aniline (AN) from a combined hydrodechlorination/hydrogenation effects has been detected. In another experimental work carried out under atmospheric pressure at 493 K accomplished by the same group, *p*-CAN was the only intermediate from the $–NO_2$ group's reduction via a reaction rate constant of (k = 2.0 min^{-1})[502]. From theoretical point of view, a computational study reported adsorption energies and reaction barriers for the elementary steps involved in the *p*-CNB reduction paths over two sites of Pd catalysts, namely, terrace and step[503]. Their findings suggested that, the reaction barriers of the involved reactions are about the same over Pd(111) and Pd(211) surfaces. However, to the best of our knowledge, this chapter is the first to explore the reaction pathways encountered during the *p*-CNB reduction over transition the metal nitride surface γ-Mo_2N (111) via the state-of-the-art density functional theory (DFT) calculations.

Routes for the formation of several reaction intermediates such as chloronitrosobenzene (CNSB), chlorophenylhydroxylamine (CPHA), dichloroazoxybenzene (CAOB), dichloroazobenzene (CAB), and dichlorohydrazobenzene (CHAB) have comprehensively been covered. It is known that the production of these compounds, especially chlorophenylhydroxylamine (CPHA), is critical during the hydrogenation of *p*-CNB in a batch reactor at mild conditions (i.e. low or medium temperatures) since these intermediates are

highly toxic and resist oxidative decomposition. The accumulation of these compounds on the surface of the catalyst generally hinders the formation of *p*-CAN[195]. This study has a twofold aim: (*i*) to report reaction pathways for the reduction mechanism, and (*ii*) to predict kinetic parameters for all scanned steps. Thermo-kinetic parameters reported herein should be instrumental in the pursuit to formulate novel γ-Mo_2N-based catalytic tailored for specific industrial applications pertinent to sustainable chemical treatment of halonitrobenzenes.

8.3 Computational details

All geometrical optimisations, energy and vibrations calculations were carried out by the DMol^3 code [504], using the Perdew–Burke–Ernzerhof (PBE) generalized gradient approximation (GGA) as the exchange-correlation functional [439]. Localized double-numerical basis sets along with a polarization functions (DNP)[274] afford the atomic environments. A Monkhorst–Pack κ-points mesh of (1×3×1) was used in the integration of the irreducible part of the Brillion zone. In all calculations, we set the thermal smearing at 0.01 Hartree. The convergence thresholds for energy, forces, and displacements were 2×10^{-5} Ha, 4×10^{-3} Ha/ Å, and 5×10^{-4} Å; respectively along with a global cut-off of 4.2 Å. Dispersion correction term (DFT−D2) has also been implemented [505]. The γ-Mo_2N(111) surface as reported in our previous work [506], was found to be the most energetically stable plane based on the ab initio atomistic thermodynamics approach. This plane was constructed by a periodic four-layer slab with a (2×2) supercell and a vacuum layer of 12 Å, in order to avoid interactions between periodic configurations along the *z*-direction. During the calculations, all layers and the adsorbates were allowed to relax. A test on reaction (i.e, two structures) using a global cut-off at 5.0 Å and 1×5×1 κ-points mech has changed its reaction energy only marginally by ~ 4%.

The transition states (TSs) were derived by the linear synchronous and quadratic synchronous transit LST/QST method [440]. Vibrational frequencies yield activation enthalpies and entropies as a function of selected temperatures based on the Arrhenius formula: $k(T) = A \exp(-Ea / RT)$. The two kinetic parameters (*A*-factors and activation energy, *Ea*) were estimated by fitting reaction rate constants, $k(T)$, with the inverse of temperature ($1/T$) according to the conventional transition state theory (TST) [268].

We calculated adsorption energies of γ-Mo_2N/species systems according to:

$$E_{ad} = E_{(surface + species)} - E_{(surface + fixed\ species)} \quad 8.1$$

Where $E_{surface + species}$ refers to the energy of the studied system and $E_{surface+fixed\ species}$ denotes the energy of a non-interacting system in which the chemical species is fixed in the middle of the slab separated from the surface by at least 6 Å. Finally, activation barriers represent the difference in energy between optimised transition structures and reactants in each investigated step.

8.4 Results and discussion

8.4.1 Molecular adsorption of p-chloronitrobenzene over the γ-Mo_2N (111) surface

Via probing the most energy preferable adsorption site of *p*-CNB over the *γ*-Mo_2N (111) surface, various orientations have been examined. The nature of the interaction of the *p*-CNB molecule is primarily based on the position by which the phenylene- and nitro-groups contribute in the adsorption process. Consequently, the role of the adsorption molecular orientations in a heterogeneous catalysis via the phenylene (flat) and nitro (upright) groups were often regarded to be of a prominence importance [492]. Attempts to optimize a physisrobed state along multiple rotations always converge to either a vertical or a horizontal structure. The physisorbed energies of *p*-CNB over the *γ*-Mo_2N (111) surface are listed in Table 8.1, while side and top views of all feasible geometries are shown in Figure 8.1. In the A1 configuration, the physisorption of *p*-CNB occurs when both O atoms of nitro group directly adsorb at the top of two Mo atoms via double Mo−O bonding with an average distance of 2.15 Å, yielding adsorption energy of -27.5 kcal/mol. The structure of A2 configuration depicted in Figure 8.1 infers that, when the phenylene group is flat positioned to the 3-fold fcc (i.e. molybdenum vacant site), the adsorption occurs only through a single Mo−O bond with a distance of 2.3 Å with an associated adsorption energy of -32.1 kcal/mol. When the *p*-CNB molecule is positioned horizontally and above the 3-fold hcp nitrogen vacant site, another adsorption structure can be obtained, namely, the A3 configuration.

Table 8.1: Energies and adsorption sites for the p-CNB molecule over the γ-Mo_2N(111) surface.

Adsorption configuration	Adsorption description	E_{ads} (kcal/mol)
A1	Molecular *p*-CNB adsorbs in an upright position at bridge site	-27.5
A2	Molecular *p*-CNB adsorbs in a flat posture at 3-fold fcc site (underneath Mo atom)	-32.1
A3	Molecular *p*-CNB adsorbs in a flat position at 3-fold hcp site (underneath N atom)	-22.0
A4	phenylene group *p*-CNB adsorbs in a flat position on-top of surface N atom	-28.8
A5	nitro group of *p*-CNB adsorbs vertically on 3-fold hcp site	-38.5
A6	Phenylene group of *p*-CNB adsorbs parallel on N-top site	-29.1
A7	nitro *p*-CNB adsorbs vertically on Mo-bridge site	-4.2

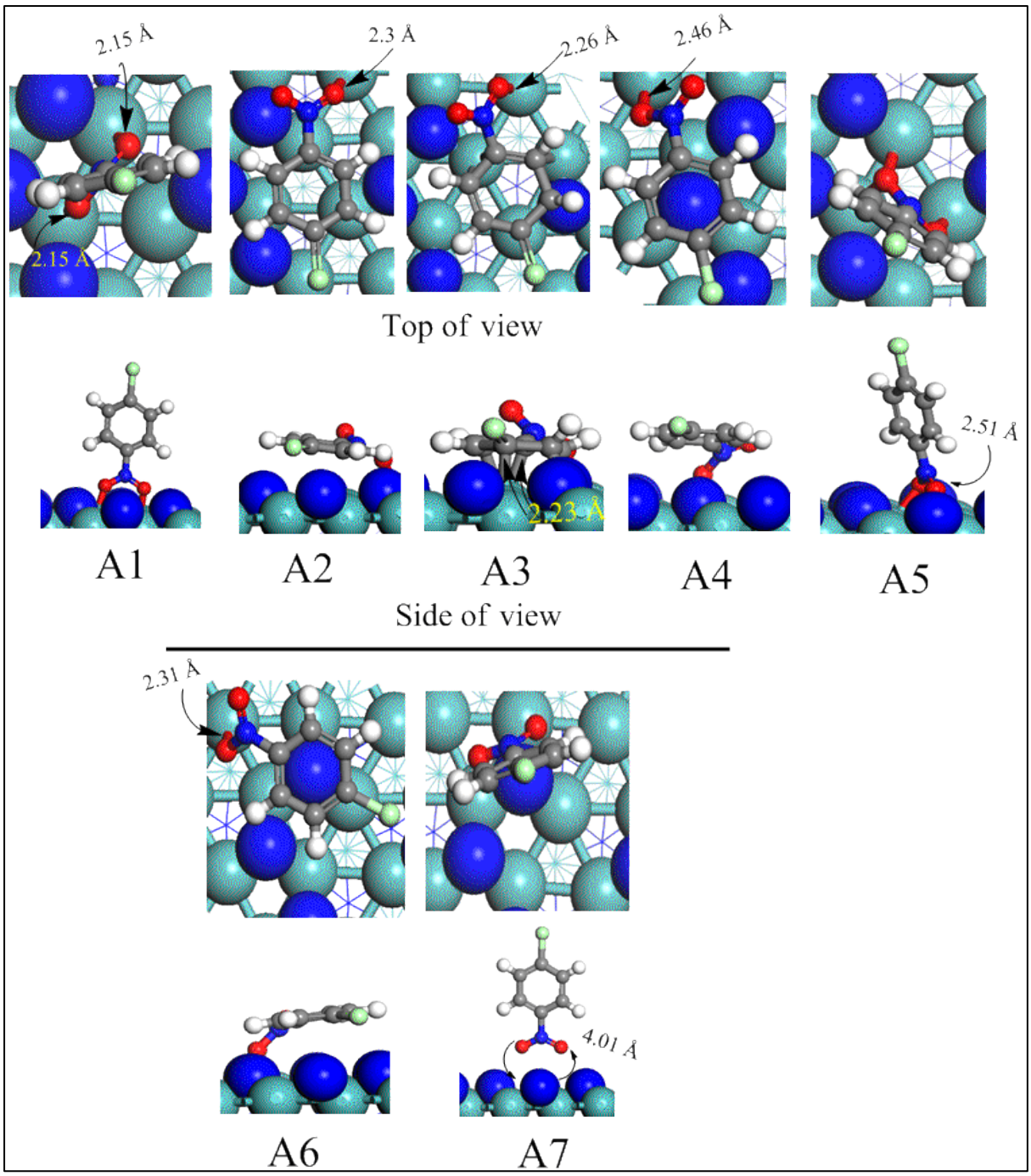

Figure 8.1: Top and side views of the optimized patterns of adsorbed para-chloronitrobenzene ($ClC_6H_4NO_2$) on the γ-Mo_2N (111) surface. Light blue: Mo, dark blue: N, red: O, grey: C, white: H, and green: Cl.

In this configuration, all of the C atoms of phenylene group are bounded to surface Mo atoms through atomic distances of ~2.26 Å with adsorption energy of -22.0 kcal/mol. A4 and A6 structures entail very similar adsorption energies of -28.8 kcal/mol and -29.1 kcal/mol, respectively, in which the *p*-CNB is placed at the top of a surface N atom. In the A5 structure, the nitro-group is linked with the surface via the two O atoms at the top of two neighbouring Mo atoms, i.e., the phenylene group is perpendicularly positioned above the γ-Mo_2N (111) plane. The formed two Mo–O bonds amount to 2.27 Å with estimated adsorption energy of -38.5 kcal/mol; indicating genuine chemical bonds. However, when the nitro group was initially situated upright at the top of a surface nitrogen atom (A7), the *p*-CNB molecule directly desorbed with a height of ~4.01 Å following full optimization. This could be attributed to the repulsion between the two negatively charged N and O entities. This phenomenon incurs the highest adsorption energy of only -4.2 kcal/mol. In a comparison with other systems, DFT calculations were utilised to estimate adsorption energies for *p*-CAN over several Pd surfaces (including steeped, flat), and clusters. Adsorption energies were found to reside in the range of -39.2 − -61.11 kcal/mol[507].

The overall aim of the hydrohalogenation process is to convert the nitro group ($-NO_2$) of *p*-CNB into an amine group ($-NH_2$) while leaving the chlorine atom at the para site of the phenyl ring. Careful inspection of the geometries in Figure 8.1 reveals that, the horizontal-like adsorbed A2 structure is a structurally suitable candidate to undergo hydrogenation of the nitro group. This adsorption mode is the most likely one to happen on the catalyst surface since it affords the lowest adsorption energy. Furthermore, the-flat-like configuration of A2 makes it more geometrically-oriented toward surface-mediated hydrogenation of its nitro group. Consequently, we elect to consider the A2 configuration as the initial structure in the hydrohalogenation mechanism of the *p*-CNB molecule.

8.4.2 Mechanisms of chloronitrobenzene hydrogenation to chloroaniline

Literature present various reaction routes for the hydrogenation of *p*-CNB molecule into *p*-CAN over a wide array of potential catalysts. Herein, guided by the experimental results [168, 508] and in view of the previously suggested analogous mechanisms [499, 503], we investigate a the reduction mechanism of *p*-CNB into *p*-CAN mediated by the γ-Mo_2N (111) surface. To avoid the formation of toxic molecules, various plausible routes inspected depending on which bond is easier to break, the C−Cl bond or N=O bond [509]. Figure 8.2 depicts proposed pathways for the surface-assisted of *p*-CNB into *p*-CAN. The direct reduction mechanism

proceeds via the formation of nitroso- and hydroxylamine-compounds (via mechanism A). However, throughout condensation–reduction, the formation of azoxybenzene and azobenzene intermediates (mechanism C) takes place. Furthermore, the formation of the undesired toxic intermediates (*i.e.*, azoxybenzene and azobenzene) must be suppressed during the hydrogenation mechanism. Further hydrogenolysis of the substituted position in parent *p*-CNB or intermediates leads to the formation of aniline (AN) and nitrobenzene (NB) [510] however, not to a large extent.

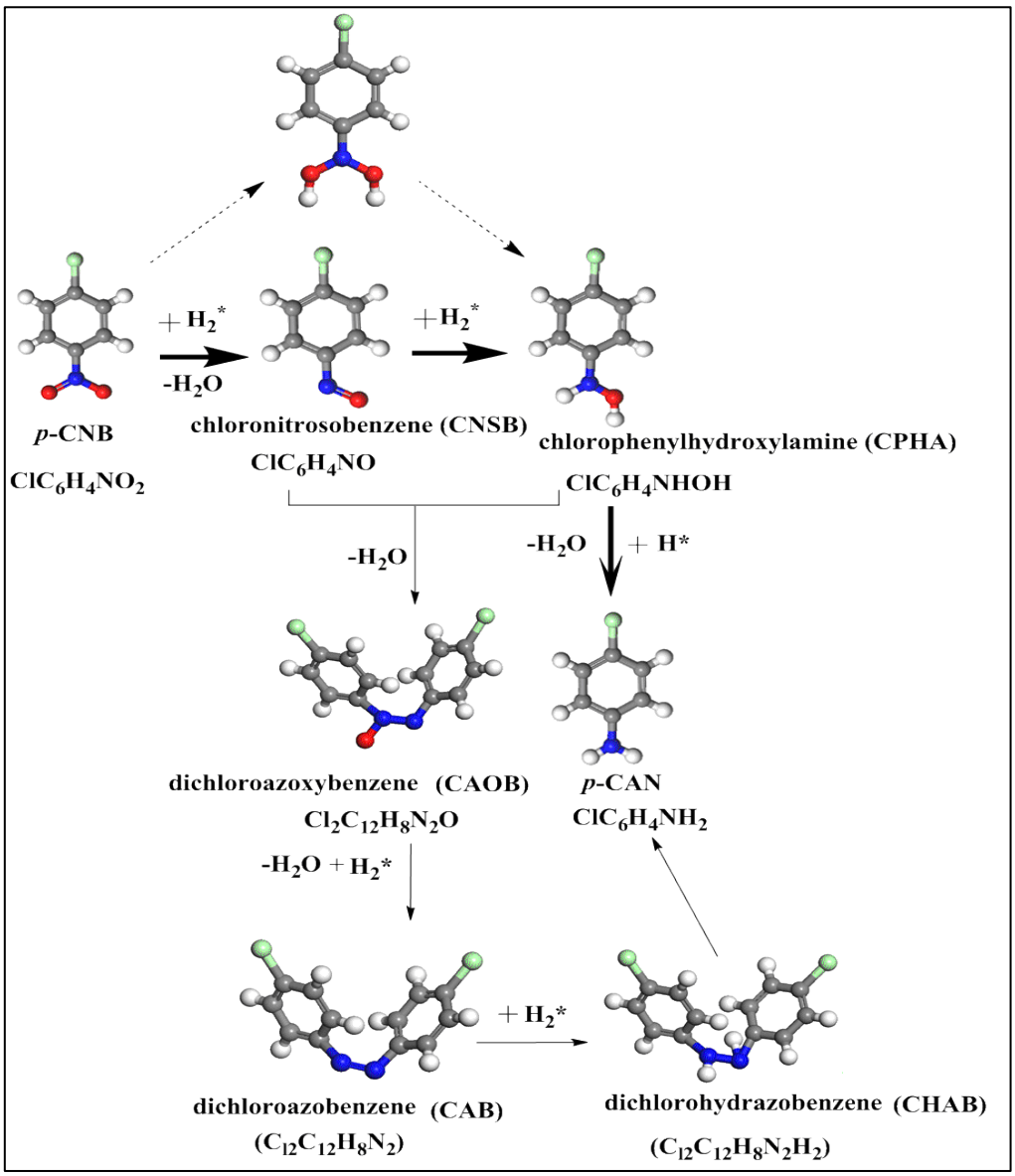

Figure 8.2: Proposed scheme for the hydrogenation of *p*-CNB to *p*-CAN. Bold arrows refer to the direct reduction (mechanism A), dashed arrows depict (mechanism B) while plain arrows represent the condensation reduction routes (mechanism C).

8.4.2.1 Direct dissociation pathways

Reduction of *p*-CNB to *p*-CAN involves subsequent fission of N−O bond by which chloronitrosobenzene (CNSB) and chlorophenylhydroxylamine (CPHA) compounds form as by-products. The corresponding structures of intermediates and transition states are depicted in Figures 8.4and 8.5; respectively. Two possible pathways feature hydrogen-induced detachment reactions, (i.e., mechanisms A and B) while a third potential mechanism involves a self-condensation route (mechanism C). Acquiring detailed potential energy surfaces for these three alternate routes determines the most kinetically preferred route for the experimentally observed products of the hydrogenation process.

8.4.2.1.1 Mechanism A

It is very experimentally challenging to determine to what extent the pre-hydrogenation of *p*-CNB contribute to the N–O bond rupture, in reference to thermal fission process (i.e., non-catalytic process). The calculated adsorption energy of the *p*-CNB molecule over pre-hydrogenated surface was -7.3 kcal/mol. This value is substantially lower than corresponding adsorption energy of the p-CNB molecule over the neat surface at -22.0 kacl/mol (for the A3 structure later). However, based on the facile process dictating the dissociative adsorption of hydrogen molecules [511], it is expected that active sites of the $Mo_2N(111)$ surface to be pre-hydrogenated at the temperature of the experiment.

This has motivated us to investigate the dissociation pathway in which the N−O bond is cleaved directly without involvement of adsorbed hydrogen atoms. Figure 8.3 displays a potential energy profile for the direct N−O bond fission. The calculated reaction energy for the reaction $ClC_6H_4NO_2^*$ (D1) → $ClC_6H_4NO^*$ + O^* is slightly exothermic by 2.8 kcal/mol, nevertheless, it associated with a sizable energy barrier of 47.7 kcal/mol via the transition state structure (TS_D). Clearly, such high barrier hinders the occurrence of the direct surface-assisted N−O bond scission at the experimental temperature of 493 K[168]. This finding correlates with the high barrier computed (37.1 kcal/mol) for the corresponding direct fission of the N−O bonds in the case of nitrobenzene ($C_6H_5NO_2$) reduction to aniline ($C_6H_5NH_2$) over Pt catalyst [512].

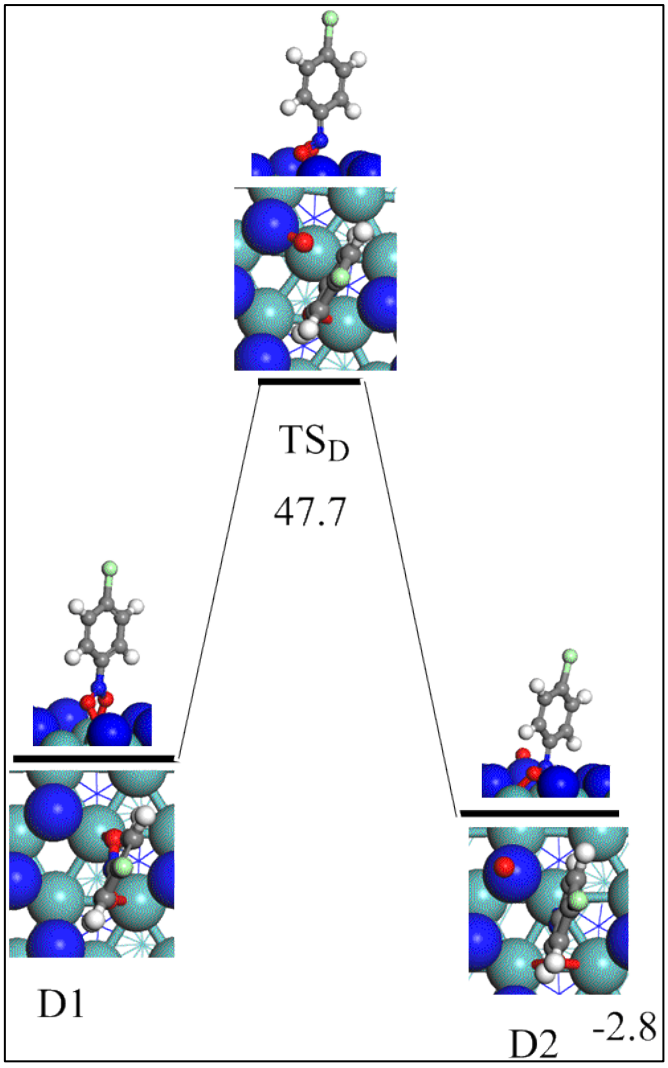

Figure 8.3: Reaction energy and activation barrier (in kcal/mol) for the direct fission of the N−O bond.

The direct dissociation pathway via hydrogen transfer from the surface proceeds by several elementary steps initiating by hydrogenating the first O atom of the nitro group (−NO_2). This process weakens the relatively strong N−O bond (70.7 kcal/mol)[6], and thus facilitates the subsequent N−O bond dissociations. Hydrogen transfer reactions from different adsorption sites i.e., top of N atom and 3-fold hcp vacant site have been investigated. We found that, hydrogen transfer from the N top-site to require a significantly higher barrier in reference to the analogues transfer from the 3-fold hcp N-hollow site, 7.5 kcal/mol versus 25.3 kcal/mol. The dependency of catalytic hydrogenation capacity of Mo_2N largely depends on the existence of nitrogen vacant sites as we demonstrated in our previous work on the selective hydrogenation of acetylene to ethene over Mo_2N surfaces.[513] Starting with the first atomic H^* transfer to the O atom in *p*−CNB via the reaction (1) $ClC_6H_4NO_2^*$ (M1) + H^* →

$ClC_6H_4NO_2H^*$, the computed reaction energy was found to be 8.1 kcal/mol above the entrance channel. The corresponding activation barrier amounts to 13.3 kcal/mol characterised by the transition structure TS1. Figure 8.4 shows structures, reaction and activation energies for all steps involved in Mechanism A, while Figure 8.5 depicts the corresponding potential energy surface in reference to the initial reactant.

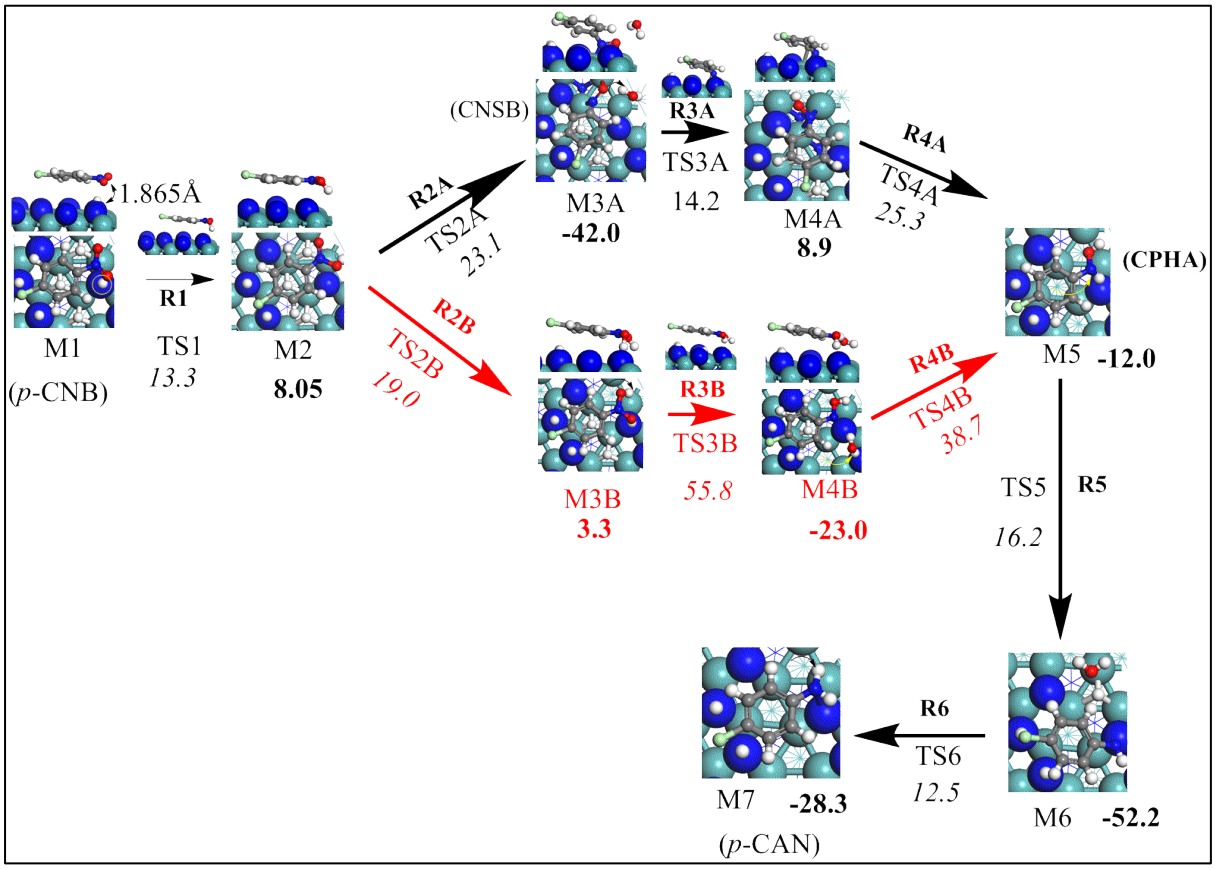

Figure 8.4: Structures of the intermediates and transition states for the steps involved in the conversion of *p*-CNB to *p*-CAN on γ-Mo_2N(111) (mechanisms A (black) and B (red) arrows). Activation barriers and reaction energies are computed in reference to the reactant in each step. All values are in kcal/mol.

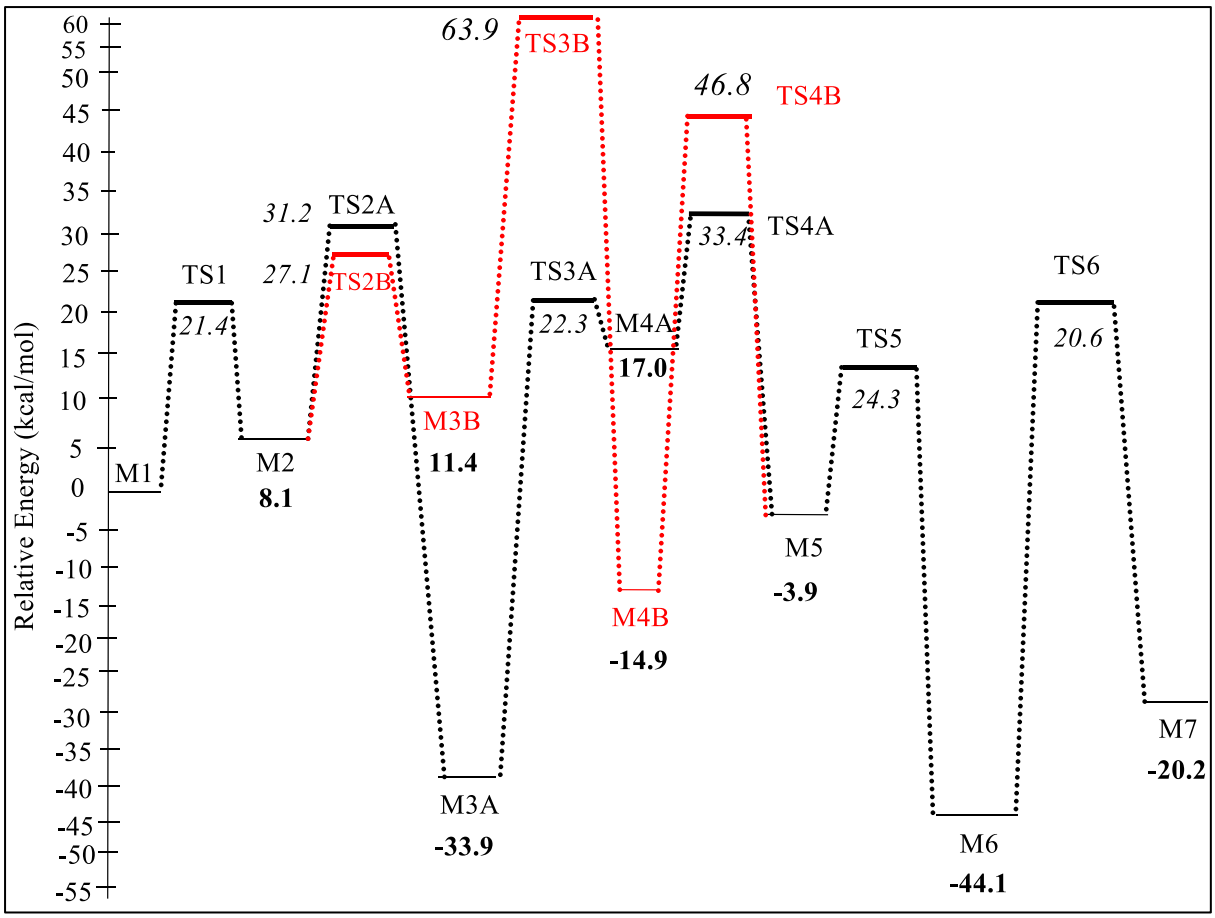

Figure 8.5: Potential energy surface for the conversion of p-CNB to p-CAN on γ-Mo_2N(111) (mechanisms A (black) and B (red) dotted lines). All energies are in reference to M1.

In order to demonstrate the catalytic capacity of the γ-Mo_2N(111), we have considered the homogenous uncatalyzed first step hydrogenation step of the NO site in the parent *p*-CBN molecule. H transfer from a hydrogen molecule to the NO site was found to incur a sizable barrier of 59.2 kcal/mol. This value significantly overshoots the analogous catalysed H transfer step at 13.3 kcal/mol.

Upon the hydrogenation of the first N-O bond into N-OH, its length stretches from 1.25Å to 1.36 Å, marking its activation. Subsequent to this step, the second reaction (2A) $ClC_6H_4NO_2H^*$ (M2) $+H^* \rightarrow ClC_6H_4NO^* + H_2O^*$ proceeds with an energy barrier of 23.1 kcal/mol (TS2A) resulted in forming adsorbed chloronitrosobenzene (CNSB) $ClC_6H_4NO^*$ as an intermediate and water molecule with an exothermic reaction energy of 42.0 kcal/mol (M3A). Desorption of H_2O^* from a surface into a gas-phase water molecule requires only 10.0 kcal/mol. While this path would expedite the deoxygenation in comparison with the direct N-O fission route (23.1

versus 47.7 kcal/mol), further hydrogenation is necessary to complete the catalytic cycle into *p*-CAN. We accordingly presumed that, after water desorption, the initial configuration of $ClC_6H_4NO^*$ and the adsorbed atomic H remain in the same initial state as in the reaction 2A. In the transition structure TS3A (reaction (3A) $ClC_6H_4NO^*$ (M3A) + $H^* \rightarrow ClC_6H_4NOH^*$), an adsorbed H^* migrates into the oxygen atom in $ClC_6H_4NO^*$ radical. This step results in the formation of the adsorbed ClC_6H_4NOH (M4A), in which the N-O bond elongates by 19% in reference to the analogous distance in M3A. This reaction is exothermic by 8.9 kcal/mol, with a modest hydrogenation barrier of 14.2 kcal/mol via TS3A. Subsequent hydrogen transfer into the adsorbed $ClC_6H_4NOH^*$ moiety via reaction (R4A), $ClC_6H_4NOH^*$(M4A) $+H^* \rightarrow$ $ClC_6H_4NHOH^*$ (M5) affords the adduct moiety of ClC_6H_4NHOH (M5). This step is exothermic by 12.0 kcal/mol and occurred via an activation barrier of 25.3 kcal/mol characterized by TS4A. In the next step (R5), a water molecule is eliminated through the movement of a surface H^* atom into the hydroxyl group of the M5 adduct. Activation barrier for this step is 16.2 kcal/mol via TS5.

Finally, an adsorbed *p*-CAN molecule is produced through the attachment of an H^* atom to the NH group in $ClC_6H_4NH^*$ (M6) as revealed in reaction (6). The reaction $ClC_6H_4NH^*$ (M6) + $H^* \rightarrow ClC_6H_4NH_2{}^*$(M7) completes the reduction mechanism of *p*-CNB into *p*-CAN. This final H* transfer is accomplished through transition state structure that signifies a reaction barrier of 12.5 kcal/mol (TS6). The adsorbed *p*-CAN in the M7 configuration resides in a well-depth of 28.3 kcal/mol in reference to M6. Consequently, it is inferred that, the hydrogenation step of chlorophenylhydroxylamine (CPHA, M5) in reaction R4A incurs the highest activation barrier and most likely to resemble the rate-limiting step. The overall reaction in mechanism A as Figure 8.5 portrays is exothermic by 116 kcal/mol.

8.4.2.1.2 Mechanism B

This mechanism differs from mechanism A with regard to the nature of reactions 2, 3, and 4. Figure 8.4 represents structure of elementary reactions in the hydrogenation of *p*-CNB (mechanism B-red arrows). Figure 8.6 portrays the corresponding potential energy surface. In reaction 2B $ClC_6H_4NO_2H^*$ (M2) + $H^* \rightarrow ClC_6H_4NO_2H_2{}^*$), the second O's atom of the nitro group is hydrogenated via another hydrogen transfer step termed as the double H-induced dissociation, in which the nitro group is doubly hydrogenated to $N(OH)_2$ group before the first N-OH bond dissociation occurs. This step requires an energy barrier of 19.0 kcal/mol (TS2B).

The reaction energy of the new synthesised intermediate $ClC_6H_4NO_2H_2^*$ (M3B) is found to be slightly endothermic by 3.3 kcal/mol. After double hydrogenation of the nitro group, hydrogen transfer from 3-fold hcp vacant site to the hydroxyl's group in M3B liberates a water molecule; in analogous reactions to those illustrated in mechanism A; i.e., via the reaction (3B) $ClC_6H_4NO_2H_2^*$ (M3B) $+H^* \rightarrow ClC_6H_4NOH^* + H_2O^*$. One of the OH group in the $ClC_6H_4NO_2H_2^*$ intermediate departs the M3B moiety simultaneously with the movement of an adsorbed H^* atom forming adsorbed ClC6H4NOH* (M4B) adduct as characterised by the transition structure TS3B via a very sizable activation barrier of 55.8 kcal/mol. This elementary step appears to be exothermic by 23.0 kcal/mol. The desorption energy of released water molecule is predicted to be 18.9 kcal/mol leaving behind an adsorbed $ClC_6H_4NOH^*$ adduct. The next step ($ClC_6H_4NOH^*$ (M4B) + $H^* \rightarrow ClC_6H_4NHOH^*$ (M5)) features a hydrogen transfer into the OH group via TS4B. Barrier for this step stands at 38.7 kcal/mol. By comparing the activation energies required for corresponding steps in both mechanisms A and B, it is obvious that the activation energy of mechanism A are generally lower than the analogous steps in mechanism B (23.1/14.2/25.3 versus 19.0/55.8/38.7 kcal/mol), nonetheless, the barrier for the opening step in mechanism B is slightly lower than that of mechanism A (i.e., 23.1 versus 19.0 kcal/mol). By reaching the M5 intermediate, the rest of the steps are the same as in mechanism A.

8.4.2.2 Aniline formation via indirect reaction pathway (i.e. condensation pathway-mechanism C)

Another expected reduction route proceeds through the formation of dichloroazoxybenzene (CAOB) as an important intermediate in the surface-assisted coupling of $ClC_6H_4NO^*$ (the structure M3A in mechanisms A). The structure of dichloroazobenzene ($Cl_2C_{12}H_8N_2^*$) (CAB) is generated by another hydrogen transfer reaction of dichloroazoxybenzene ($Cl_2C_{12}H_8N_2O^*$, (CAOB). Furthermore, dichlorohydrazobenzene ($Cl_2C_{12}H_8N_2H_2^*$) (CHAB) is the final moiety prior to the production of *p*-CAN through breaking the azo bonds. The latter term refers to the (–N=N–) bond in which two halophenylene rings are linked. Figure 8.6 displays the configurations involved in the condensation pathways that constitute unimolecular and bimolecular reactions of mechanism C. Figure 8.7 depicts potential energy surface for the condensation pathway of mechanism C. Table 8.2 lists the activation barriers and reactions energies for all the elementary steps involved in the condensation pathway.

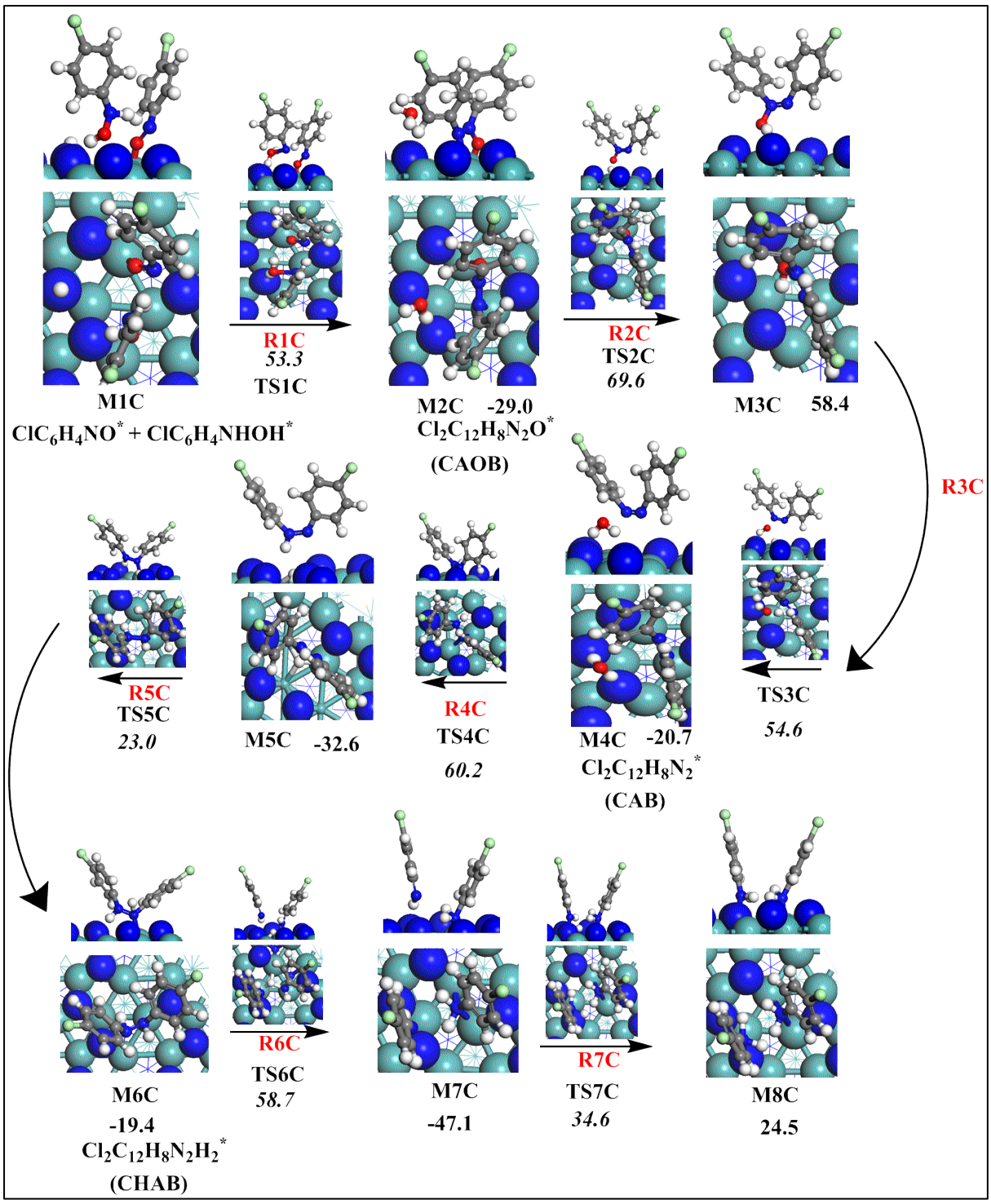

Figure 8.6: Potential energy surface for the condensation pathway (mechanisim C). Activation barriers and reaction energies are computed in reference to the reactant in each step. All values are in kcal/mol.

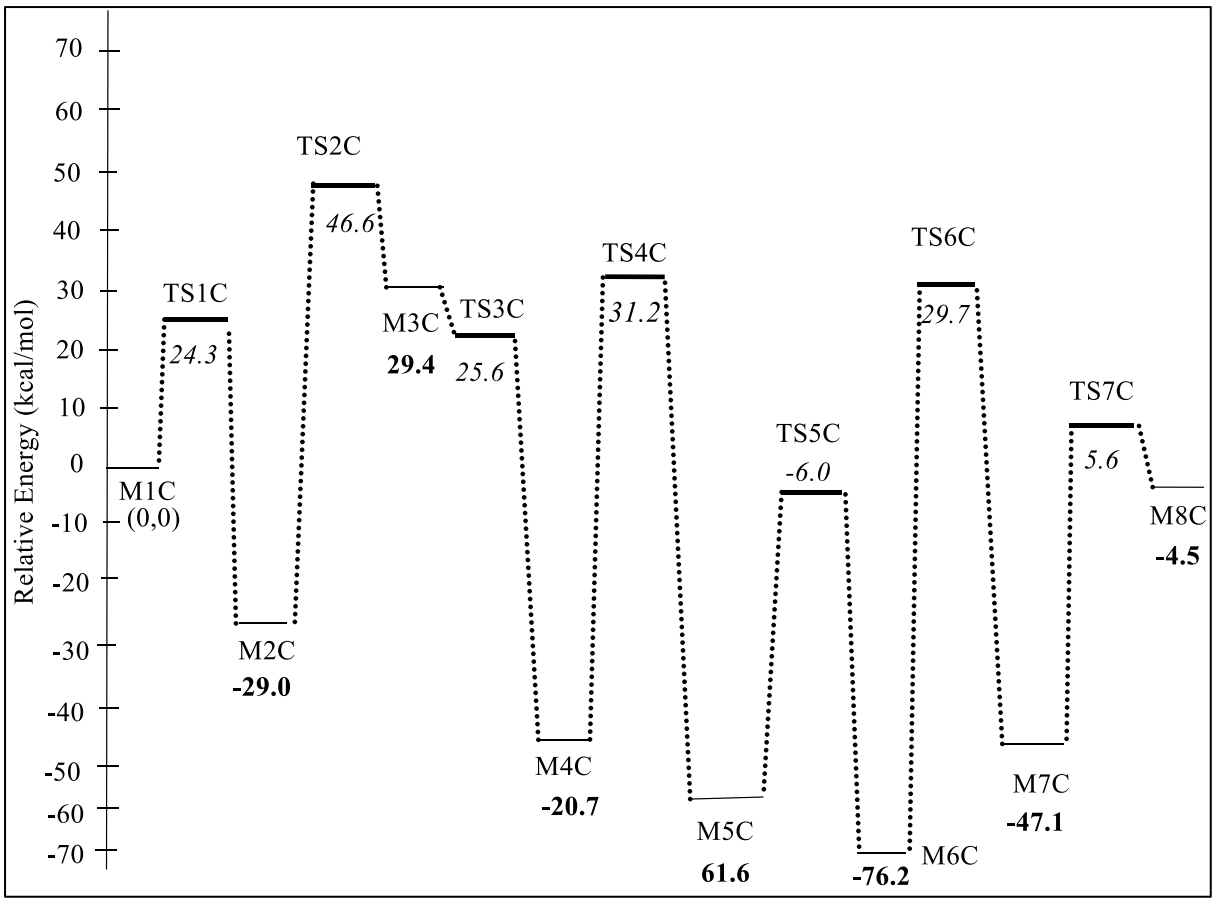

Figure 8.7: Potential energy surface for the condensation pathway (mechanism C). Values are in reference to the initial reactant M1C.

Table 8.2: Calculated activation energies (E_a) and reaction energies (ΔE) of steps involved in the condensation pathway.

Reaction	Reaction scheme	E_a(kcal/mol)	ΔE (kcal/mol)
(1C)	$ClC_6H_4NO^* + ClC_6H_4NHOH^* \rightarrow Cl_2C_{12}H_8N_2O^* + H_2O^*$ dichloroazoxybenzene (CAOB)	53.3	-29.0
(2C)	$Cl_2C_{12}H_8N_2O^* + H^* \rightarrow Cl_2C_{12}H_8N_2OH^*$	69.6	58.4
(3C)	$Cl_2C_{12}H_8N_2OH^* + H^* \rightarrow Cl_2C_{12}H_8N_2^* + H_2O^*$ dichloroazobenzene (CAB)	54.6	-20.7
(4C)	$Cl_2C_{12}H_8N_2^* + H^* \rightarrow Cl_2C_{12}H_8N_2H^*$	60.2	-32.6
(5C)	$Cl_2C_{12}H_8N_2H^* + H^* \rightarrow Cl_2C_{12}H_8N_2H_2^*$ Dichlorohydrazobenzene (CHAB)	23.0	-19.4
(6C)	$Cl_2C_{12}H_{10}N_2^* + H^* \rightarrow ClC_6H_4NH_2^* + ClC_6H_4NH^*$	58.7	-47.1
(7C)	$ClC_6H_4NH_2^* + ClC_6H_4NH^* + H^* \rightarrow 2ClC_6H_4NH_2^*$	34.6	24.5

The first four reactions are exactly the same as in mechanisms A and B. Thus, we commence tracking mechanism C by the step that leads to the generation of chlorophenylhydroxylamine (structure M2C Figure 8.6) via the presence of adjacent pre-adsorbed $ClC_6H_4NO^*$ and $ClC_6H_4NHOH^*$ adducts (M1C). The structure M2C forms via the reaction ($ClC_6H_4NO^* + ClC_6H_4NHOH^*$ (M1C) $\rightarrow$ $ClC_{12}H_8N_2O^* + H_2O^*$), in which the formation an azo bond accompanies the elimination of a water molecule. The formation of the dichloroazoxybenzene (CAOB) ($ClC_{12}H_8N_2O^*$) intermediate is exothermic by 29.0 kcal/mol. Most intermediates in the condensation pathway are linked with the surface via bonding O atoms with a Mo surface site. Desorption of H_2O into a gas-phase water molecule requires a desorption energy of 29.2 kcal/mol. While this coupling reaction is noticeably exothermic, it demands a sizable barrier of 53.3 kcal/mol (TS1C). Clearly, such high barrier presents a bottleneck for the condensation pathway and indicates that, the condensation route is highly unlikely to proceed kinetically via flat placed molecules. The barrier of TS1C is in a well accord with the analogous barrier for the corresponding step encountered in the condensation pathway over Pd3/Pt(111) surface (i.e

52.12 kcal/mol) [514]. Considering near-flat initial $ClC_6H_4NO^*$ + $ClC_6H_4NHOH^*$ structures increases the activation barrier of TS1C by~ 8.0 kcal/mol, in reference to the near-vertical structures depicted in Figure 8.7.

The reduction reaction of dichloroazoxybenzene (M2C) in the reaction (R2C) $Cl_2C_{12}H_8N_2O^*$ (M2C)+H^*→ $Cl_2C_{12}H_8N_2OH^*$ was found to be endothermic by 58.4 kcal/mol (M3C) with a very sizable activation energy 69.6 kcal/mol via (TS2C). This high barrier is attributed to energy required in breaking the surface Mo-O bond in the M2C configuration. Upon hydrogen transfer, the N–O bond is stretched by 0.10 Å in reference to the N–O bond in the M2C structure. A second third hydrogen transfer reaction generates dichloroazobenzene (CAB) (M4C) via the reaction R3C: $Cl_2C_{12}H_8N_2OH^*$ (M3C) + H^* →$Cl_2C_{12}H_8N_2{}^*$ + H_2O^*. This step proceeds via a considerable activation barrier of 54.6 kcal/mol through (TS3C) in reference to the M3C intermediate. The formed dichloroazobenzene (M4C) consequently reacts with an adsorbed H^* atom resulting in the formation of the $Cl_2C_{12}H_8N_2H^*$ intermediate (M5C) through reaction R4C. This step requires an energy barrier of 60.2 kcal/mol via transition state structure (TS4C) and releases an excess energy of about -32.6 kcal/mol. The next step in the proposed mechanism is reaction (R5C) in which dichlorohydrazobenzene moiety can be generated as a result of hydrogen transfer from 3-fold fcc vacant site. This reaction was found to be exothermic reaction by 19.4 kcal/mol (M6C) with an estimated barrier of 23.0 kcal/mol as represented in transition structure (TS5C). Fragmentation of dichlorohydrazobenzene into adsorbed *p*-CAN molecule and $ClC_6H_4NH^*$ radical proceeds by the attachment of hydrogen atom to the N atom in dichlorohydrazobenzene reaction (R6C). This reaction is highly exothermic by 47.1 kcal/mol and necessitates high activation energy of about 58.7 kcal/mol over M7C through the transition structure TS6C, correspondingly. A *p*-CAN molecule forms via attachment of a surface H^* with the NH group in the $ClC_6H_4NH^*$ moiety (M7C) along reaction R7C with an activation barrier of 34.6 kcal/mol (TS7C). All in all, the high activation barriers for the reactions could be attributed to strong N-O and N-N bonds that are broken during the course of the mechanism.

Finally, it is of interest to shed some light into the direct decomposition barriers of converting *p*-CNB to nitrobenzene (NB). We therefore investigate the dechlorination reactions of *p*-CNB into nitrobenzene ($ClC_6H_4NO_2{}^*$ → $C_6H_4NO_2{}^*$ +Cl^*) over γ-Mo_2N(111) facet. Figure 8.8 portrays optimized structures of *p*-CNB dechlorination. Our findings indicate that, direct fission the Cl-C bond is associated with a high energy barrier of 58.0 kcal/mol. This high barrier supports the experimental observation of Perret *et al.* [508] who have tested two

crystallographic phases of molybdenum nitride namely β-Mo_2N and γ-Mo_2N. They concluded that, both studied crystals promoted selective nitro-group reduction into amino-group and suppressed the dehalogenation step.

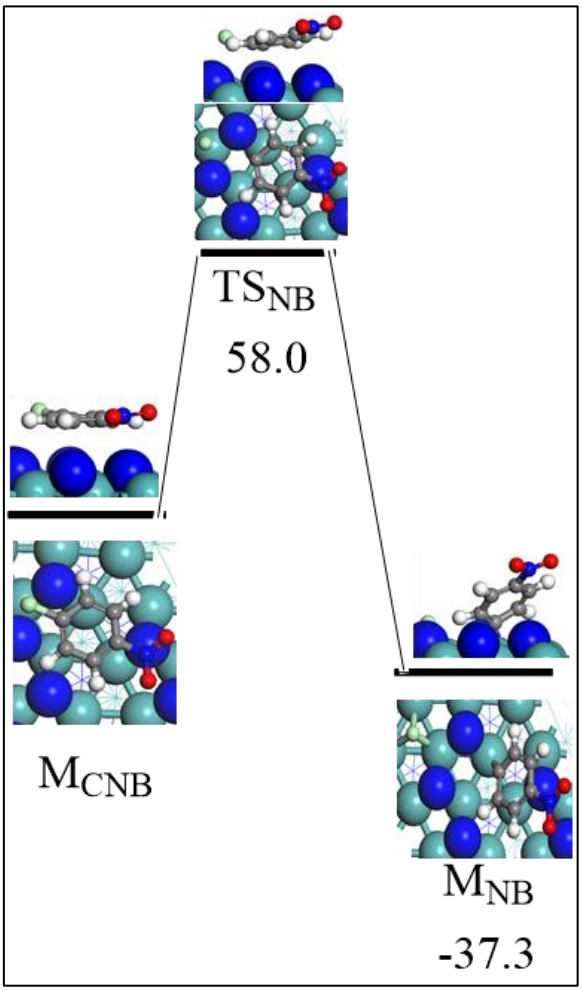

Figure 8.8: Reaction energy and activation barrier for the optimized geometries involved in in the surface mediated breakeg of the C−Cl bond in *p*-CNB. Values are in cal/mol.

8.5 Reaction rates and Kinetics

Both β and γ phases of Mo_2N display similar adsorption sites. The unit cells for both surfaces only differ in their *c*-lattice, and hence our calculated kinetics for the gamma phase should resemble experimental values for the gamma phase [67].

We predict the thermo-kinetic parameters for hydrogenation reaction of (*p*-CNB) over molybdenum nitride system. Table 8.3 reports Arrhenius parameters and activation barriers for the reactions in mechanisms A and B, while Figure 8.9 demonstrates the Arrhenius plots for

reactions in the forward directions involved in direct dissociation routs. A detailed kinetic analysis indicates that, transformation of chloronitrobenzene into chloroaniline occurs after successive addition of H to Mo−N system entities. Elimination of a water molecule occurs through its desorption after formation. Selectivity of the preferred products is essential and the kinetic parameters significantly affect the chloronitrobenzene reduction to chloroaniline over γ-Mo_2N catalysts. A useful feature of reaction rate parameters provided in Table 8.3 is to assess the relative importance of potentially competing reactions. For instance, based on reaction rate constants reported in Table 8.3, reaction R2A largely predominates the co mpeting in reaction R2B.

Table 8.3: Fitted kinetic parameters for forward and reverse surface reactions involved in the reduction mechanism of chloronitrobenzene over the γ-$Mo_2N(111)$ surface.

Reaction		Reaction Scheme	A (s^{-1})	E_a (kcal/mol)
M1→M2	$R1^f$	$ClC_6H_4NO_2^* + H^* \rightarrow ClC_6H_4NO_2H^*$	8.6×10^{12}	12.7
M2→M1	$R1^r$	$ClC_6H_4NO_2H^* \rightarrow ClC_6H_4NO_2^* + H^*$	3.3×10^{16}	3.6
M2→M3A	$R2^f$	$ClC_6H_4NO_2H^* + H^* \rightarrow ClC_6H_4NO^* + H_2O^*$	2.4×10^{15}	24.0
M3A→M2	$R2^r$	$ClC_6H_4NO^* + H_2O^* \rightarrow ClC_6H_4NO_2H^* + H^*$	1.7×10^{11}	64.7
M3A→M4A	$R3^f$	$ClC_6H_4NO^* + H^* \rightarrow ClC_6H_4NOH^*$	7.9×10^{8}	15.0
M4A→M3A	$R3^r$	$ClC_6H_4NOH^* \rightarrow ClC_6H_4NO^* + H^*$	1.0×10^{11}	22.6
M2→M3B	$R2^f$	$ClC_6H_4NO_2H^* + H^* \rightarrow ClC_6H_5NO_2H_2^*$	7.7×10^{15}	15.6
M3B→M2	$R2^r$	$ClC_6H_5NO_2H_2^* \rightarrow ClC_6H_4NO_2H^* + H^*$	8.14×10^{15}	7.6
M3B→M4B	$R3^f$	$ClC_6H_4NO_2H_2^* + H^* \rightarrow ClC_6H_4NOH^* + H_2O^*$	1.0×10^{13}	54.9
M4B→M3B	$R3^r$	$ClC_6H_4NOH^* + H_2O^* \rightarrow ClC_6H_4NO_2H_2^* + H^*$	9.9×10^{11}	71.2
M4→M5	$R4^f$	$ClC_6H_4NOH^* + H^* \rightarrow ClC_6H_4NHOH^*$	3.6×10^{12}	37.0
M5→M4	$R4^r$	$ClC_6H_4NHOH^* \rightarrow ClC_6H_4NOH^* + H^*$	3.7×10^{14}	45.0
M5→M6	$R5^f$	$ClC_6H_4NHOH^* + H^* \rightarrow ClC_6H_4NH + H_2O^*$	4.3×10^{12}	15.8
M6→M5	$R5^r$	$ClC_6H_4NH^* + H_2O^* \rightarrow ClC_6H_4NHOH^* + H^*$	1.5×10^{13}	63.5
M6→M7	$R6^f$	$ClC_6H_4NH^* + H^* \rightarrow ClC_6H_4NH_2^*$	2.8×10^{16}	19.2
M7→M6	$R6^r$	$ClC_6H_4NH_2^* \rightarrow ClC_6H_4NH^* + H^*$	1.8×10^{7}	45.6

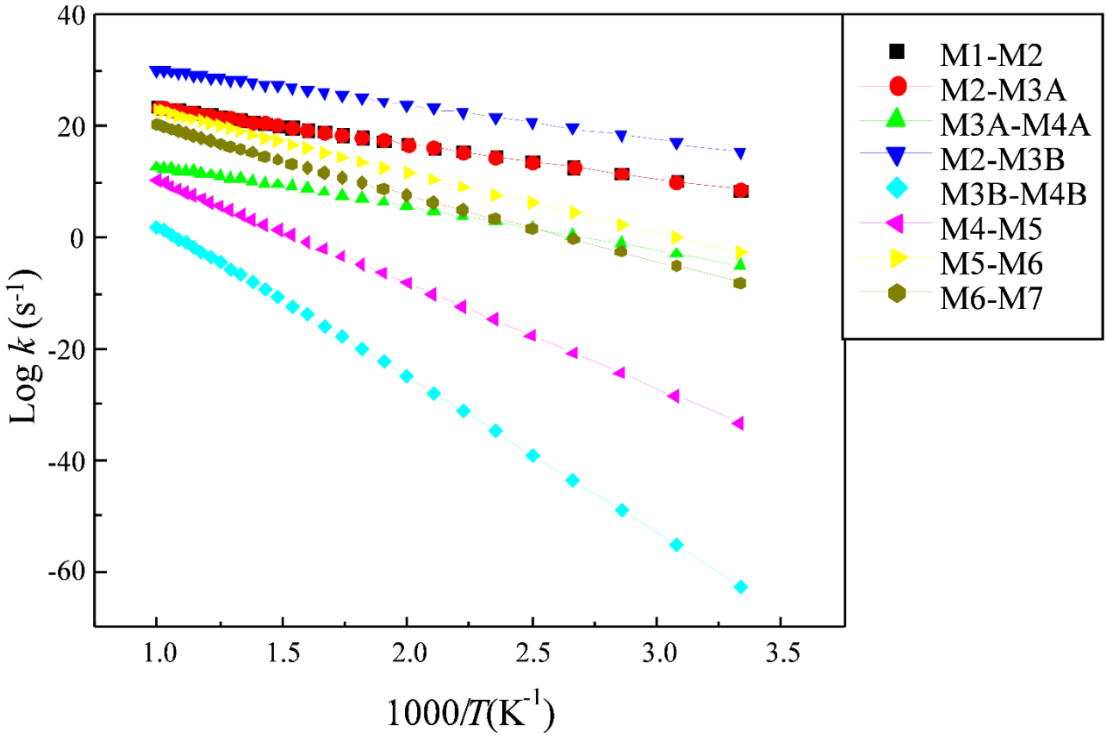

Figure 8.9: Arrhenius plots of forward hydrogenation reactions (direct dissociation routs) of *p*-CNB to *p*-CAN over the γ-Mo_2N (111) surface, fitted in the range of 300 – 1000 K.

By plotting the residence time (τ) in the plug flow reactor (PFR) against ln (1/1-*X*), where *X* is the conversion of *p*-CNB. Cárdenas-Lizana *et al.* [168] attained the overall consumption rate of *p*-CNB of~ 2.0 min^{-1} (i.e., 0.033 s^{-1}) at 493 K and τ between 1800 and 7800 s. Now, we are in a position to compare our kinetic analysis with the experimentally obtained rate constant [168]. Inspection of the potential energy surface in Figure 8.5 reveals that, the overall activation barrier for the reduction of *p*-CNB into *p*-CAN corresponds to the R2A reaction with a net activation barrier of 31.2 kcal/mol (*i.e.*, the height of TS2A in reference to M1). By considering a typical value of the *A*-factor at 1.0×10^{13} s^{-1}, we obtain an overall consumption rate for *p*-CNB at 0.018 s^{-1} (at 493 K). Clearly, our computed rate constant for the conversion of *p*-CNB correlates very well with the experimental finding of Cárdenas-Lizana *et al.*[168] (*i.e.*, 0.018 versus 0.033 s^{-1}).

Following the formation of the M3A structure, all intermediates and transition states reside below the entrance channel. Thus, formation of *p*-CAN from *p*-CNB could be modelled based on the two opening reactions R1 and R2A. Herein, we consider a simplified PFR model to compute the conversion (*X*) of *p*-CAN from *p*-CNB. Central to this simplified treatment is the

assumption that all reactions are treated as unimolecular reactions in view of the great excess of *p*-CNB in reference to inlet H_2 at the experimental conditions (i.e., 0.99 versus 0.01). The simplified PFR model utilizes the specified experimental conditions by Ca´rdenas-Lizana *et al.*[168]. These conditions comprise a reactor volume of 8.0×10^{-5} m^3 (with an internal diameter of 0.015 m) and an inlet molar flow rate of *p*-CNB at 8.0×10^{-8} mol/s. The initial concentration of *p*-CNB was fixed at 0.24 mol/m^3. The model consists of design PFR differential equations $(\frac{dF}{dV} = r)$ that relate to the change in the molar flow rate (*F*) of the three-considered species (M1, M2 and M3A) with the PFR's volume (*V*) and the rate of the reaction (*r*) along the reaction sequence:

$$\mathrm{M1} \xrightarrow{R1^f} \mathrm{M2}$$

$$\mathrm{M1} \xrightarrow{R1^f} \mathrm{M2} \underset{R2^r}{\overset{R2^f}{\rightleftharpoons}} \mathrm{M3A}$$

The reactions are considered to be elementary with respect to the concentration (*C*):

$$r_{\mathrm{M1}} = -k_1{}^f \mathrm{C}_{\mathrm{M1}} + k_1{}^r \mathrm{C}_{\mathrm{M2}}$$

$$r_{\mathrm{M2}} = k_1{}^f \mathrm{C}_{\mathrm{M1}} - k_1{}^r \mathrm{C}_{\mathrm{M2}} - k_2{}^f \mathrm{C}_{\mathrm{M2}}$$

$$r_{\mathrm{M3A}} = k_2{}^f \mathrm{C}_{\mathrm{M2}}$$

Rate constant values at 493 K for reactions R1 and R2 are taken from Table 8.2. The reverse reaction R2A was added to account for the fast reaction in the backward directions (i.e., activation energy is only 5.5 kcal/mol). Figure 8.10a contrasts our modelled *X* values with their analogous experimental values for τ between 1800 and 7800 s. The latter can be varied by adjusting the reactor's volume in reference to the volumetric flow rate. Our computed *X* values slightly overshoot corresponding experimental estimates. Nonetheless, our simplified PFR model reasonably reproduces the experimental profile pertinent to the consumption of *p*-CNB. Figures 8.10b and 8.10c portrays the computed concentrations of species and conversion/selectivity (*S*) down the length of the PFR reactor. The latter signifies the ratio for the molar flow rate of species M3A to the inlet molar flow rate of M1. It serves to provide an

estimate for the fraction of M1 that is converted into M3A. As elaborated on earlier and based on the facile nature for the all subsequent reactions (R3A-R6), we envisage that calculated S value for the intermediate M3A to largely represent the analogous value for *p*-CAN.

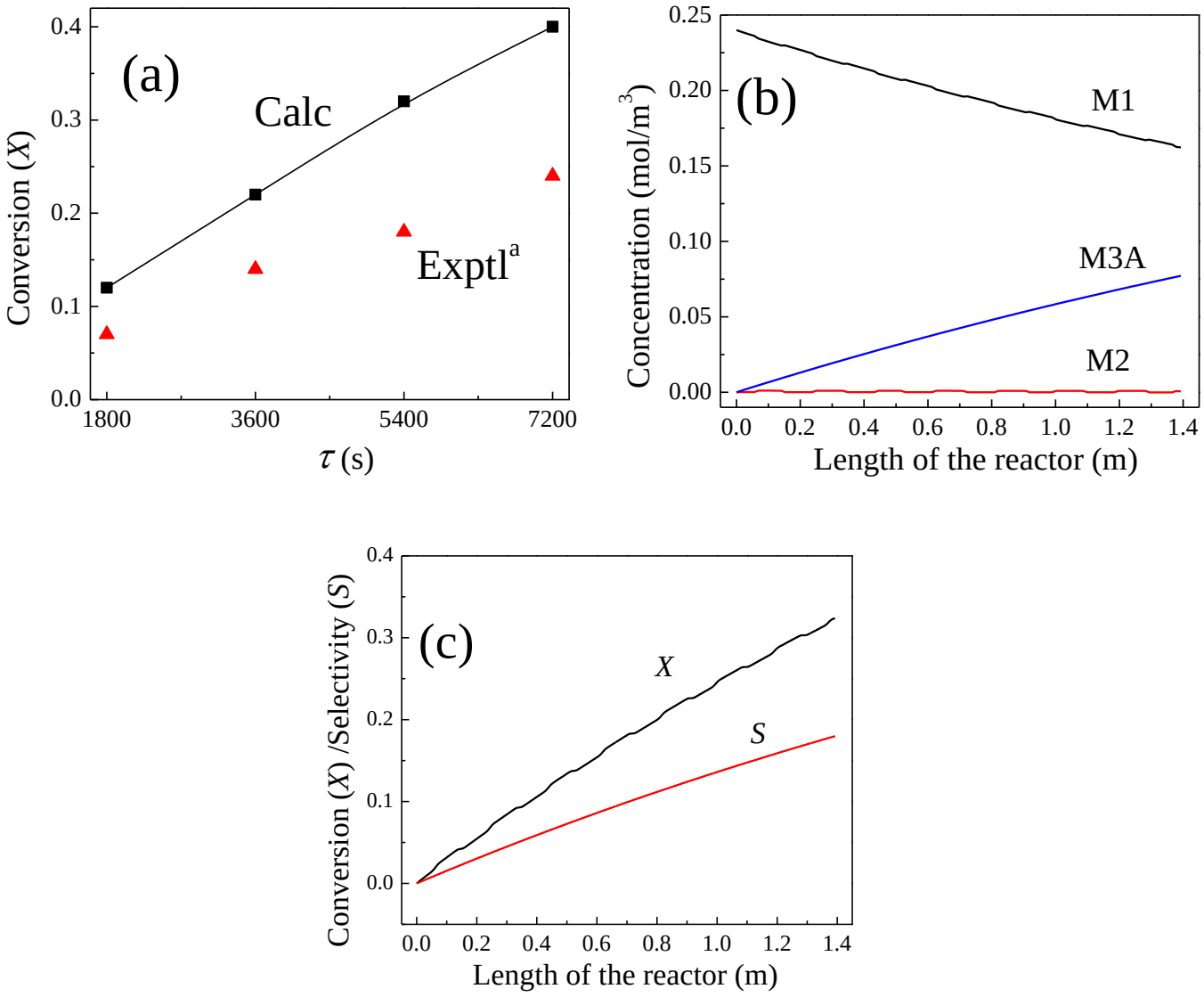

Figure 8.10: (a) Computed and experimental Conversion values. (b) Calculated concentration values for M1, M2 and M3A as a function of the reactor's length. (c) Conversion of *p*-CNB and selectivity (*S*) for the formation of M3A, [a] Ref [168].

Such deviation recorded in Figure 8.10 (c) may stem from the expected accuracy margin associated in DFT calculations. For example, binding energies by GAA-DFT is typically associated with an accuracy margin of 6 kcal/mol. Likewise, we are modelling a rather perfect

slab system while in experiments Mo2N may contain edges and terraces that normally enhance the rate of the reaction.

8.6 Conclusions

In this chapter, via density functional theory (DFT-D2) calculations, we map out mechanisms underlying the selective hydrogenation of *p*-CNB to *p*-CAN over the γ-Mo_2N (111) surface catalyst. The two most energetically favourable adsorption sites are found when the chloronitrobenzene is flat and up right positioned to the Mo-hollow fcc and N-hollow hcp of γ-Mo_2N(111) surface, respectively. We establish that, the reduction of *p*-CNB to *p*-CAN proceeds through direct and indirect (condensation) pathways, however, the direct pathway systematically requires lower activation barriers. Based on the TST theory, reaction rate constants are evaluated for the reactions involved in direct pathways (mechanisms A and B). The reduction process involves several steps of H^* transfer from the surface (mainly at fcc and hcp sites) into NO-moieties. The high barrier for direct fission of the C-Cl bond clearly hinders the formation of an aniline molecule. The hydrogenation of chloronitrosobenzene is considered to be the rate-limiting step with an energetic barrier of 55.8 kcal/mol. Desorption of water molecules entail lower desorption energies. Mechanisms and kinetic analysis (via a simplified PFR's model) presented herein illustrate pathways for the experimentally observed hydrogenation of the nitro group at relatively low temperatures. Our findings systematically provide a comprehensive understanding into the selective catalysis of such large aromatic molecule and reveal the promising role of γ-Mo_2N surface in producing commercially important organic amino-compounds.

Chapter 9 : Synthesis, Physico-chemical Properties, Combined Experimental, and Computational Studies of $Cr_xMo_{1-x}N$ Coatings

Paper VI

Zainab N. Jaf, Zhong-Tao Jiang, Mohammednoor Altarawneh, Jean-Pierre Veder, Manickam Minakshi, Hussein A. Miran, Zhi-feng Zhou, H. N. Lim, N. M. Huang, Bogdan Z. Dlugogorski *"Synthesis, Physico-chemical Properties, Combined Experimental, and Computational Studies of $Cr_xMo_{1-x}N$ Coatings"* Under Review- Thin Solid Film Journal

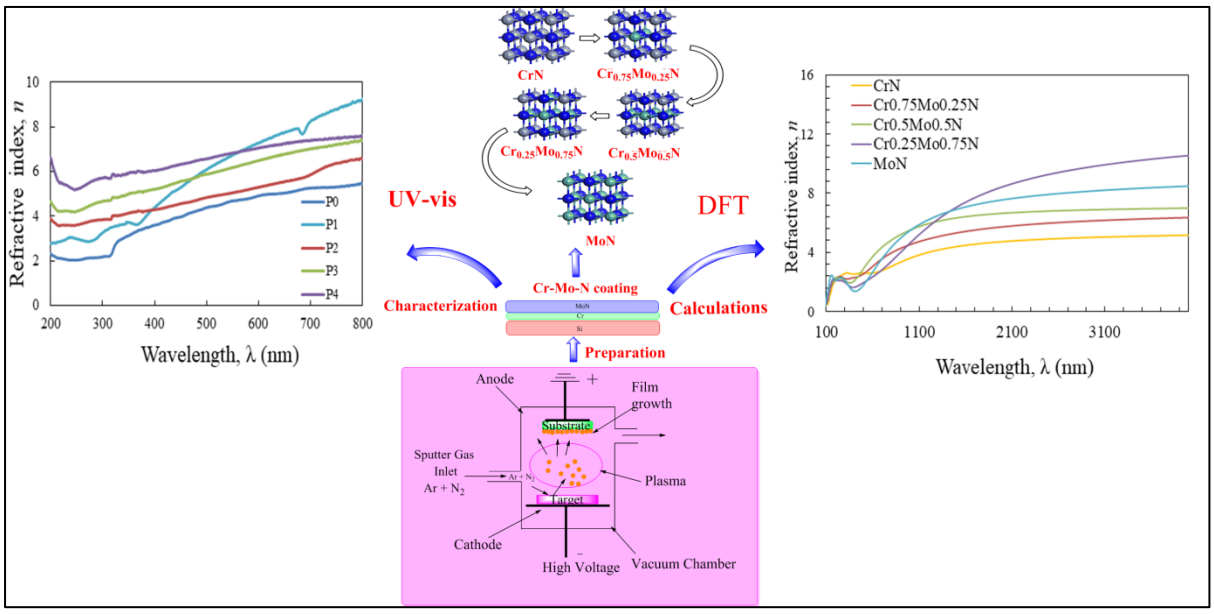

9.1Abstract

In this Chapter, Cr−Mo−N thin films with different Mo contents were synthesised *via* closed field unbalanced magnetron sputtering ion plating (CFUMSIP). The effects of Mo content on the microstructure, chemical bonding state, and optical properties of the prepared films were investigated by X-ray diffraction spectroscopy (XRD), X-ray photoelectron spectroscopy (XPS), field emission scanning electron microscopy (FESEM), and ultraviolet-visible spectrophotometry (UV-Vis). XRD results confirmed the face centered cubic (fcc) structure of pure CrN film. The incorporation of molybdenum (Mo) in the CrN matrix was approved by both XRD and XPS analyses. The CrMoN coatings demonstrate various polycrystalline phases including CrN, γ-Mo_2N, Cr with oxides layers of MoO_3, CrO_3, and Cr_2O_3. Microstructure results show that the grain size of Cr-Mo-N coatings increases with the increase of Mo content due to the formation of MoN phase, when Mo atoms interact with N atoms around the grain boundaries of CrN phase. XPS investigations confirmed the presence of Cr, Mo, N, C and O elements in the studied coatings. The optical results revealed that, the synthesised coatings exhibit low reflection magnitudes in the visible region of the solar spectrum, introducing them as good antireflection surfaces. The coatings demonstrate that, Mo-containing samples improved solar absorptance of about 76% was recorded in the wavelength range of 200 – 800 nm. However, low thermal emittance of about 20% was obtained at 2500 – 15000 nm. Furthermore, by applying density functional theory (DFT), the computational simulated geometries and the measured experimental values exhibited an absorption coefficient (α) with similar trend and to some extent, similar values within the wavelength range from 200 to 800 nm.

9.2 Introduction

Transition metal nitride composites have a wide array of outstanding properties that enable them to be applied in a variety of applications, including hard protective, and wear resistant surface layers for high temperature machinery and selective solar absorber surfaces [385, 515]. In particular, chromium nitride (CrN) ceramic based-coatings have gained considerable attention in the last decades, since they possess high hardness, low friction coefficient, enhanced wear and corrosion resistance, good thermal and chemical stability, excellent

diffusion barrier properties, superior oxidation resistance up to 700 °C, and low electrical resistivity (640 μ Ω. cm) [516-519]. Furthermore, CrN compounds have long been used as catalysts and/ or catalyst support in organic chemistry to catalyse various reactions [520, 521].

On the other hand, molybdenum nitride compounds exhibit an array of unique physical, optical, and electronic characteristics due to the extensive attention that has been paid from both fundamental and applied fields. For instance, Mo-nitrides find direct applications in field as, Cu diffusion barriers [522], corrosion protective coatings for few microns [112], and as tribological layers with low coefficients of friction [302] and catalysts [511, 513, 523]. Several fabrication methods have been deployed to synthesise CrN and MoN coatings, including magnetron sputtering-based deposition techniques fabricated coatings with high adhesion and homogeneity [133, 294, 303, 305, 384, 524].

Introducing an alloying element is an important industrial process that has widely been used as an active way to enhance microstructure, tribology, optical, oxidation behaviour and hardness of CrN. In addition, it promises the opportunity to alter the energy band gap and hence the electronic and optical properties can be enhanced. This has been observed by Hones *et al.* [525] when depositing four sets of magnetron sputtered Cr-based ternary transition metal nitride coatings $Cr_{1-x}Me_xN_y$ (Me = Mo, Ti, W and Nb) with $0 \leq x \leq 1$ over silicon, glass and high speed steel substrates. Moreover, large atomic radius elements, such as Al, Zr, W, Si, Ti and Mo have extensively been considered as dopants to develop various properties of CrN phase and form the solid solution of Cr-Me-N (where Me= Al, Zr, W, Si, Ti , Ni, and Mo) [118, 179, 307-310, 526-529]. Wo *et al*. [530] have examined the influence of Si on the microstructure and mechanical properties of CrSiN films. They stated that the integration of Si with different contents serves to improve the hardness of CrSiN coatings. It is inferred from previous literature that replacing appropriate amount of Al into the metal surface (Si) inhibits the corrosive nature of the $Mo(Si_{1-x}Al_x)_2$ nanocomposite coatings [531, 532]. Ni addition has also been found to enhance the toughness and improve damage tolerance of CrNiN thin films [533]. Notably, the oxidation resistance is increased by the introduction of Cr into Mo–N coatings prepared at different nitrogen partial pressures. This is attributed to the accumulation of molybdenum atoms in the amorphous layers which surround the columnar structured nanocrystalline (*nc*-) CrN grains. Subsequently, these amorphous layers can efficiently develop the desired coatings properties [534].

Moreover, ternary Cr–C–N and Cr–Mo–N ceramic coatings were prepared through a combination of arc ion plating (AIP) and DC magnetron sputtering techniques to compare their microstructure and mechanical properties. Results indicated that the hardness values of cation solid solution (Cr–Mo–N) and anion solid solution (Cr–C–N) coatings were 23 and 34 GPa, respectively[517]. Yuelan *et al.*[535] investigated the effect of Mo content on the structural and mechanical properties of CrMoN/MoS_2 coatings, they demonstrated that the CrMoN coating exhibited a solid and compact surface texture with large grains.

In addition to introducing alloying elements, coatings properties can be improved and tuned by varying the sputtering plasma parameters including the substrate bias voltage Vb, substrate temperature Ts, and nitrogen flow ratio $(R = N2/(N2 + Ar))$ to acquire the targeted properties of the synthesised coatings, such as grain size, preferred orientation, lattice defects, microstructure, and tribological properties *etc*. [126, 536]. Shah *et al*. [537] investigated the influence of sputtering pressure and temperature on the as-deposited magnetron sputtered CrN films. The preferred orientations, morphology, micro strain, and surface roughness of CrN films are strongly depended on deposition conditions. Furthermore, the effect of sputtering target power density influences topography and residual stress on the growth of magnetron sputtered nanocomposite $nc - TiN/a - SiNx$ films [538]. In addition to that, the influence of sputtering target power on microstructure and mechanical properties of WN and TaN coatings prepared by radio frequency (RF) reactive magnetron sputtering technique has been outlined in the literature [539].

Apart from experiment and from theoretical perspective, simulation modelling studies have been carried out to provide new insight into surface characteristics of MoN have recently been investigated via DFT approach [540]. On the other side, the effect of alloying element on elastic behaviour, hardness, and thermodynamic properties over various nitride systems such as TiN [541], $Cr_{1-x}Al_xN$ [542], and CrN [543]. Zhou *et al.* [544] investigated the structural and mechanical properties of nitrogen-deficient Cr–Mo–N and Cr–W–N systems *via* density functional theory (DFT). Results reported in [39] suggest that Cr–Mo–N and Cr–W–N solid solutions are comprising of significant amount of vacancies on the N sublattice with a chemical formula of

$Cr_{1-x}Me_xN_{1-0.5x}$ (Me = Mo and W). The determined elastic constants suggest mechanical stability along with increasing ductility with increasing Mo or W content.

To the best of our knowledge, the effect of molybdenum target power on the electronic, structural, and optical properties of Mo-doped CrN coatings has not been reported. Hence, it is of great interest to investigate the impact of depositing those coatings at various Mo target power and bring new insights on the structure, chemical bonding states, and optical properties.

9.3 Experimental and computational modelling

9.3.1 Experimental procedure

Ternary coatings of CrMoN have been synthesized by closed field unbalanced magnetron sputtering ion plating technique (termed as "CFUMSIP") (UDP650, Teer Coatings Ltd., UK). The coatings were deposited onto Si (100) wafers after being polished, ultrasonically cleaned and dried at ambient conditions. The deposition of CrMoN films was conducted in mixed N_2 and Ar atmosphere using two Cr targets and one Mo target with purity of 99.9%. The substrates were rotated at a speed of 10 rpm and the bias voltage was set to be -80 V during deposition. The flow rate of Ar (working gas for sputtering) and N_2 (reactive gas to form nitrides) were fixed at 50 and 60 sccm (Standard cubic centimeter per minute), respectively. The metallic Cr interlayer was first deposited with thickness around 0.2μm to enhance the coating adhesion with the substrate, then, a top coating of CrMoN was made with an approximate thickness of 1.4 - 1.6 μm at various Mo contents by changing the Mo target power. The coated specimens had not been exposed to any thermal treatments. Throughout this work, we identified the coatings as, P0, P1, P2, P3, and P4 corresponding to CrN (Mo- target power = 0), CrMoN (Mo target power = 281W), CrMoN (Mo target power = 620W), CrMoN (Mo target power = 1002W), and CrMoN (Mo target power = 1372W). The experimental preparation parameters employed in the current study are summarized in Table 9.1.

Table 9.1: Experimental conditions used in the sputtering deposition process of CrN and CrMoN coatings.

Sample	Targets power (V×A)	Thickness (t) µm	Power for Mo (P=VI)	OEM%
P0	308 ×4.0 Cr	1.2(CrN_X) 0.2 (Cr)	-	50
P1	281 ×1.0 Mo 312 × 4.0 Cr	1.4 ($CrMoN_x$) 0.2 (Cr)	281 W	50
P2	310 × 2.0 Mo 312 × 4.0 Cr	1.6 ($CrMoN_x$) 0.2 (Cr)	620 W	60
P3	334 × 3.0 Mo 312 × 4.0 Cr	1.5 ($CrMoN_x$) 0.2 (Cr)	1002 W	50
P4	348×4.0 Mo 308 × 4.0 Cr	1.4 ($CrMoN_x$) 0.2 (Cr)	1372 W	50

9.3.1.1 X-Ray Diffraction (XRD) measurements

A powder diffractometer D8Advance (Bruker AXS, Germany) was used to determine the crystallographic phase. The instrument was operated at voltage of 40 kV and current of 40 mA with a Cu-K_α radiation source. Reflected photon energy was detected by a LynxEye detector. The crystalline phases were identified by the Search/Match algorithm, DIFFRAC.EVA 3.2 (Bruker-AXS, Germany). The software is linked to the recent version of ICDD crystallographic database Powder Diffraction File (PDF).

9.3.1.2 XPS measurements

X-ray photoelectron spectroscopy (XPS) measurements were performed using a Kratos Axis-Ultra X-ray Photoelectron Spectrometer. These measurements were performed using an Al-K_α monochromatic X-ray source producing photon energy of 1486.6 eV operating at 150W. All samples were mounted onto a stainless-steel sample holder using double sided carbon tape, and finally positioned in the XPS analyser chamber for analysis with the vacuum pressure maintained at 3×10^{-9} Torr or above throughout the analyses.

The binding energies scale of the photoelectron lines were calibrated by the standard binding energy of *C*1*s* of C-H photoelectron line (adventitious carbon) situated at 284.8 eV. An argon gas cluster ion source operated in monoatomic mode at 5 keV was used to remove the surface of any adsorbed contaminants prior to analysis. Furthermore, in XPS composition, relative sensitivity factors supplied by the Kratos Axis Ultra manufacturer were used to determine the elemental composition rather than the use of standards. The analysis area for each measurement was set at a 700 × 300-micron slot configuration, with survey and high-resolution spectrum being measured using pass energies of 160 eV and 40 eV, respectively. CASA-XPS software was used for curve fitting and interpretation.

9.3.1.3 FESEM imaging

To determine the film thickness used to calculate optical properties, field emission scanning electron microscopy (FESEM) was performed on a commercial microscope (Zeiss Neon 40EsB and a Tescan Mira3). The CrMoN samples were prepared by mounting cross-sections in resin and polishing the mounts down to reveal the undamaged film against the substrate. The samples were then coated with approximately 3 nm Pt to make the surfaces conductive. Then, the samples were imaged using a backscattered electron detector to highlight the atomic number difference between the film and substrate. Elemental dispersive analysis (EDS) was used to verify the elemental differences. The measured thicknesses of the sputtered films by cross sectional FESEM images enlisted in Table 9.3 were taken by averaging several points on each sample.

9.3.1.4 UV-Vis measurements

Understanding the behaviour of materials that achieve the desired optical properties is known to have an extraordinary importance. Optical measurements of coatings have been the subject of intense study during the last decades and great efforts have been made to develop the mathematical formulation to describe the optical constants of various systems. The UV–Vis reflectance spectroscopy was used to examine the optical characteristics of the coatings [545]. A UV–Vis double beam spectrophotometer with 60 mm integrating sphere (Model: UV-670 UV-Vis spectrophotometer, JASCO, USA) was used to obtain UV-Vis reflectance spectra in the wavelength range from 200 to 800 nm. For a considered photon's wavelength, the UV-Vis reflectance spectroscopic data was collected to determine other important optical parameters, such as solar absorptance, band-gap, refractive index, dielectric constants, and energy loss functions.

9.3.2 Computational modelling

Ground state properties such as structural optimization and energy calculations of selected systems have been performed via density functional theory (DFT) level of calculations. Generalized-gradient approximation (GGA) [546] for the exchange-correlation energy adopted in the Cambridge Serial Total Energy Package (CASTEP) software [347, 547]. Structural optimization was performed using plane wave basis sets with a cut off energy of 370.0 eV to expand the electronic wave functions, while an energy tolerance of 2×10^{-5} eV/atom and an atomic force tolerance of 0.05 eV/Å were utilized. The integration over Brillouin Zone, a 4×4×4 *k*-points by Monkhorst grids [548] were included along with spin-polarized PAW-PBE functional [282] .

9.4 Results and Discussion

9.4.1 Structural and composition analyses

X-ray diffraction patterns of the CrMoN coatings are depicted in Figure 9.1 and all of the detected matching peaks of as-deposited CrN and CrMoN coatings are given in Table 9.2. The XRD pattern of pure CrN coating (P0) displays diffraction peaks possessing the crystallographic orientations (111), (200), (200) and (220) at the respective diffraction angles 37º, 42º, 64.2º, and 62º which corresponds to the polycrystalline structure of the face-centred cubic (fcc)-CrN phase. The (200) orientation corresponds to metallic Cr that exhibits a face-centred cubic (fcc) phase. The (220) crystal plane exhibits highest intensity. Further inspection

into the obtained patterns revealed that the addition of Mo metals to CrN stoichiometry led to an increase in the number of emerged peaks (phases) of the material while retaining the peaks that of pure CrN. Meanwhile, the extra emerged reflection peaks developed after Mo-doping are (104), (110), (112), and (222) which can be assigned to Cr_2O_3, Mo, MoO_3, and CrO_3, correspondingly. XRD results also show that significant oxidation could have occurred on the metallic CrMoN surfaces after prolonged exposure to the atmosphere, resultant peaks are probably attributed to the sample's contamination with atmospheric oxygen. Moreover, the incorporation of Mo to the coatings simulates some structural variations, specifically for higher contents (*i.e.* 16.6 and 15 at %). In other word, the intensity of the Mo_2N (200) peak increases steadily with raising Mo-target power and becomes the strongest texture intensity at a power of 1372 W. Table 9.2 documents the space group and the pdf number of the detected matching peaks. The presence of CrMoN phase is uncertain [118], due to the formation of a substitutional solid solution of (Cr, Mo) N of magnetron sputtered coatings, where larger Mo atoms replaced Cr in CrN crystal [117].

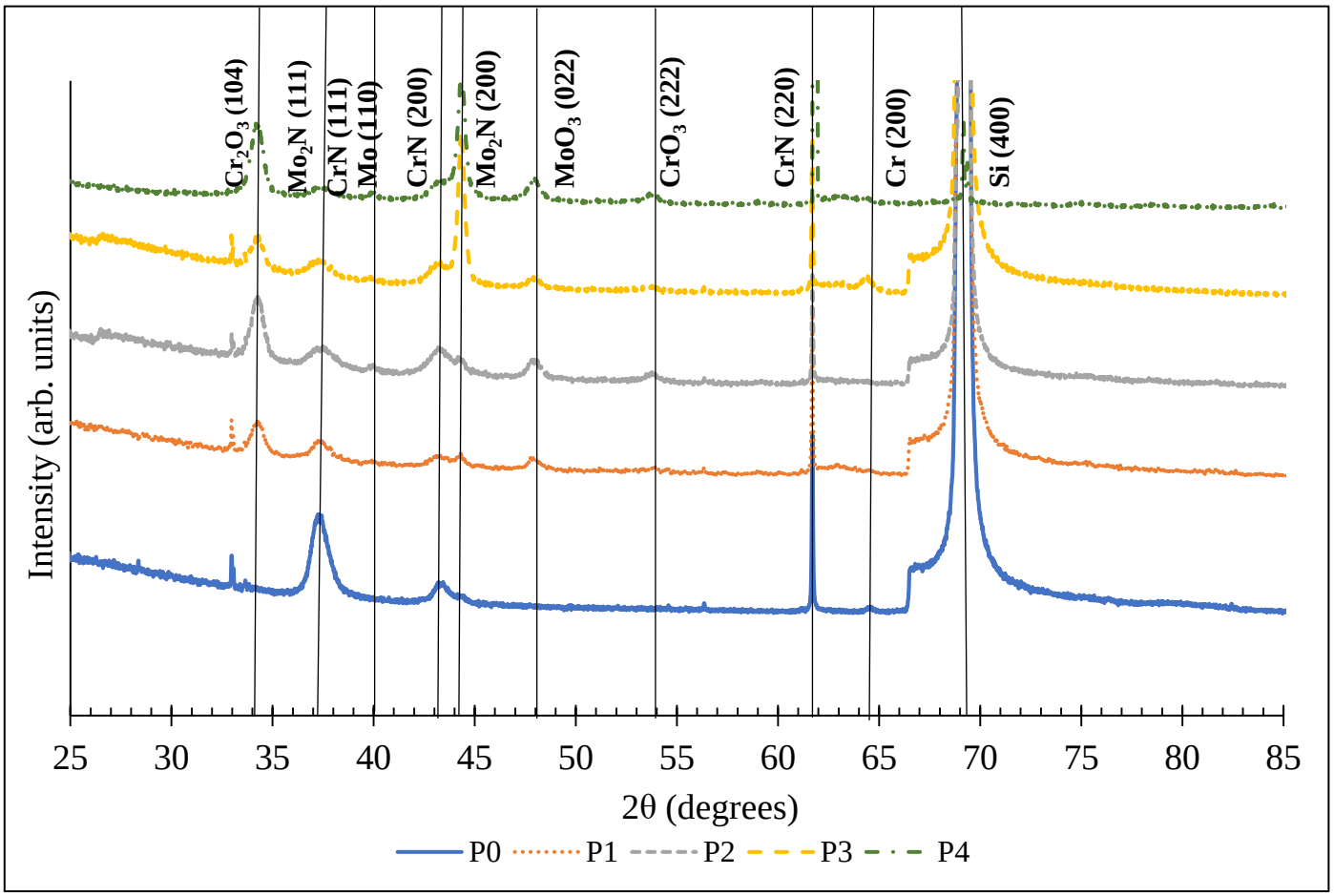

Figure 9.1: XRD patterns of Cr-Mo-N samples.

Table 9.2: XRD pattern of the detected matching peaks of as-deposited CrN and CrMoN coatings.

hkl	Space group	2θ	ICDD pdf no.
CrN(111)	Fm-3m(225)	36.3	01-080-3903
Cr_2O_3(104)	R-3c(167)	33.5	00-001-1294
CrN(200)	Fm-3m(225)	43.	01-080-3903
CrN(220)	Fm-3m(225)	61.2	01-080-3903
γ-Mo_2N(111)	Pm-3m (221)	37.3	00-025-1366
MoO_3(022)	P21/c(14)	47.0	04-007-2607
MoO_2(220)	P42/mnm(136)	53.4	04-015-7152
Cr(200)	Fm-3m(225)	64.4	00-006-0694
γ-Mo_2N(200)	Pm-3m (221)	43.4	00-025-1366
Mo(110)	Im-3m(229)	40.6	00-001-1207
Cr_2N(211)	P-31m(162)	62.4	00-035-0803
Si(311)	Fd-3m(227)	56.4	00-001-0791
Si(400)	Fd-3m(227)	69.5	00-001-0791

Based on XRD data, we estimate the average crystallite size of Debye–Scherrer relation [303] to evaluate the crystallite size of Cr-Mo-N coatings around the (220) reflection plane (since it holds the highest intensity),

$$D_g = \frac{k\,\lambda}{\beta\,\cos\theta} \qquad 9.1$$

Where D_g refers to the crystallite size, k signifies the crystallite-shape factor (k = 0.90), λ corresponds to the X-ray wavelength, β symbolizes the full width at half maximum (FWHM) of the (220) peak, and finally θ represents the diffraction angle. The calculated crystallite sizes tabulated in Table 9.3, suggests that the Mo inserted into the CrN films resulted in greater lattice parameters and grain sizes compared with pure CrN coating. This is due to the formation of MoN phases *via* Mo and N atoms interaction around the grain boundaries of CrN phase. Furthermore, it supports the idea that Mo atoms may not only substitute the Cr on their locations, but they are able to incorporate and integrate around the grain boundaries of the Cr-Mo-N matrix [535]. Figure 9.2 illustrates the compositional variations of Cr, Mo, and N concentrations of the studied films against Mo-target power.

Table 9.3: Thickness and crystallite size of the studied coatings.

sample	Sample's thickness	Crystallite size (nm)
P0	1410	135
P1	1570	220
P2	1690	270
P3	1590	270
P4	1660	270

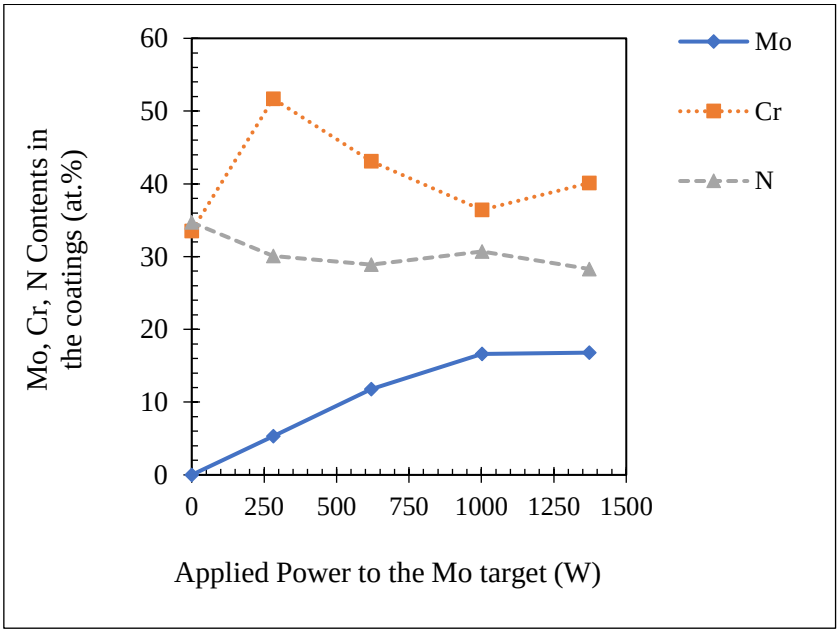

Figure 9.2: The variation of Cr, Mo, and N concentrations as a function of Mo-target power.

The surface composition and chemical bonding states of the Cr–Mo–N films were investigated *via* X-ray photoelectron spectroscopy (XPS). Due to the *p* and *d*-blocks transition metal nature of Cr and Mo, respectively, their oxy-nitrides may contain a polycrystalline phases of CrN, Cr_xO_y, Mo_xN_y, and MoO_x phases [549, 550]. While the Cr and Mo cations may occupy one of several oxidation states, each of which exhibit a different binding energy in the XPS data depending on the electron structure of the atoms involved. Consequently, XPS data for a metallic Cr and Mo surfaces are complex, comprised of overlapping spin-orbit doublets, which represent Cr [551, 552] and Mo [549, 553] phases. This makes quantitative chemical analysis of the Cr-Mo-N system difficult to perform with a high degree of certainty.

Figure 9.3 represents the XPS survey scan spectra for the studied sample systems. Survey scan analysis indicated that the films contain Cr, Mo, N, C and O atoms. The C1s peaks are attributed to surface contaminants since the samples had been exposed to the atmosphere for a period of several months. The appearance of oxygen in all Mo-alloyed films is attributed to the partial oxidation and diffusion of oxygen into the surface of the films which is consistent with the XRD findings. The presence of oxygen may also be a result of the plasma during the starting period of deposition process [554]. The main O1*s* peak from the samples has binding energy ranging from 530.32 eV – 532.06 eV. These findings are in good agreement with results expected from literature for MoO_2, MoO_3 and MoN_x phases [555-557].

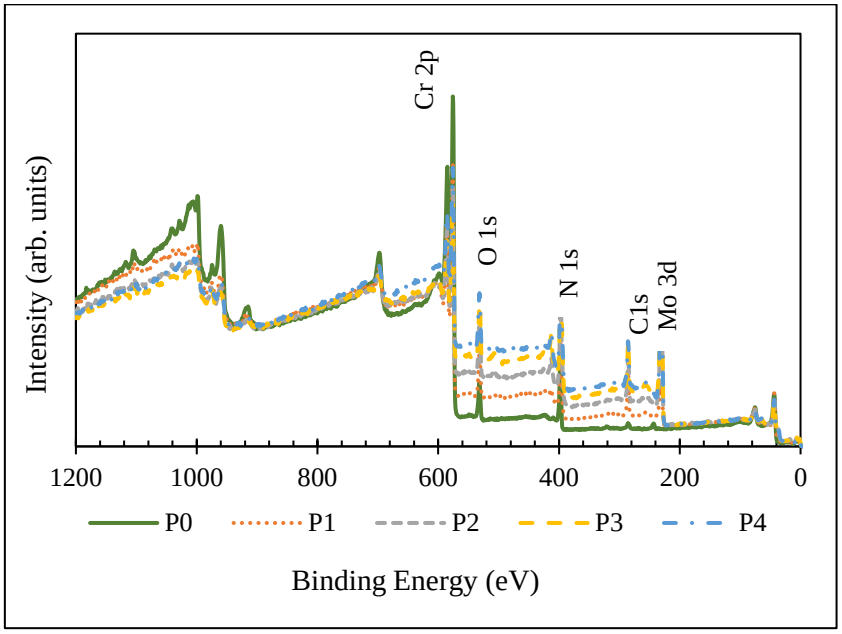

Figure 9.3: XPS survey scan spectra for the studied coatings.

Table 9.4 lists the elemental concentrations present in the studied films. Importantly, the presence of Mo 3*p* doublets in the N 1*s* region presents a challenge for elemental quantification. In order to circumvent the problem of overestimating the N 1*s* content due to the interfering contribution from Mo 3*p*, quantification was performed using the deconvoluted high resolution spectra instead of the survey spectra. Doing so enabled the Mo3*p* and N 1*s* regions to be adequately separated. From the table, it can be observed that with the rise of Mo-target power from 281 – 1372 W, the Mo contents increases from 5.3 at% to 15.0 at%, with a reduction in the Cr content from 51.7 at% to 40.1 at%. However, the nitrogen content is fluctuating from 30.1 at % to 28.3at %.

Table 9.4: Details of the elemental compositions of CrMoN coatings.

Atomic percentage of the elements (from XPS)				
Sample	Cr	Mo	O	N
P0	48.5	-	14.1	37.1
P1	51.7	5.3	12.9	30.1
P2	43.1	11.8	16.1	28.9
P3	36.4	16.6	16.2	30.7
P4	40.1	15.0	16.7	28.3

High resolution XPS measurements were carried out at the Cr2*p*, Mo3*d*, N1*s* and O1*s* core levels with the aim of characterizing the chemical bonding states. Results reported here show that significant oxidation–occurred on the coating surfaces after prolonged exposure to the atmosphere. This oxidation process was uncontrolled due to the temporal and spatial intervals between laboratories of the preparations and the characterizations.

Prior to the measurements, 5 minutes etching by Ar gas ions at 5 keV have been conducted on the films. Figures 9.4-9.8 portray the XPS core-level spectra of Cr2*p*, Mo3*d*, O1*s*, C1*s*, and N1*s*. Accordingly, each curve was deconvoluted to their components (chemical bonding states). The envelopes for the Mo3*d* and Cr2*p* doublets are clearly seen. A summary of the deconvoluted results at different Mo target power (different Mo-contents) are listed in Table 9.5. It is reported that this surface would be covered by a thin oxide layer when being in contact with the atmosphere [558]. McIntyre *et al.* [559] showed that the concentration of the oxygen anions was found to be the highest near the surface suggesting that diffusion into the materials

is the principle mechanism by which the oxidation occurs below the surface. Our XRD results confirm the diffusion of oxygen atoms into the bulk of the material *via* peaks belonging to the oxidation phases.

From the pure CrN sample (P0) as displayed in Figure 9.4, the deconvoluted chromium peak originating from Cr2$p_{3/2}$ and Cr2$p_{1/2}$ bonding states. The Cr2$p_{3/2}$ peak corresponds to two phases: Cr_7C_3, Cr (574.9 eV) and Cr_2O_3 (578.2 eV). Moreover, the Cr2$p_{1/2}$ spectrum also shows two peaks with binding energy at 584.1 eV, belongs to the Cr_7C_3, Cr states and at binding energy of 587.4 eV corresponding to Cr_2O_3. The fitted N1*s* spectra depicted in Figure 9.4 (N), display two bonding states allocated at (397.0 eV) and (397.8 eV) both corresponding both to [554]. High resolution scans of Cr-Mo-N coatings deposited at various Mo target power of (281-1372 Watt) have been considered. Previous literature reported the XPS surface elemental composition and chemical bonding states from which peaks belong to Cr–O bond were detected [560].

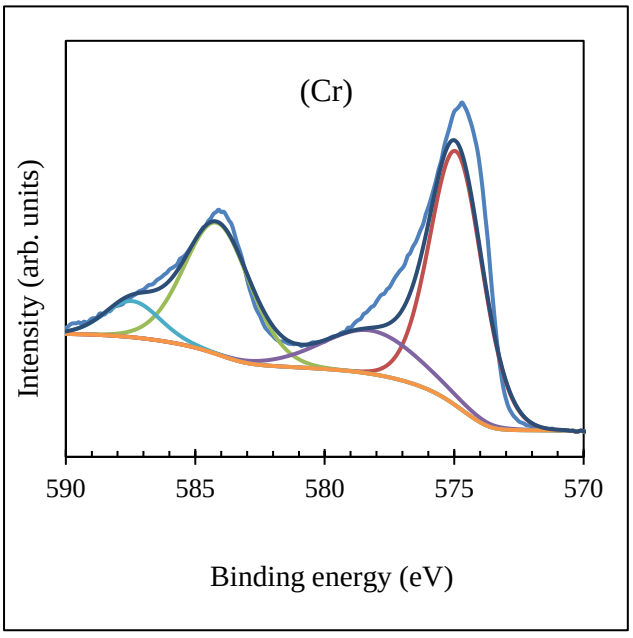

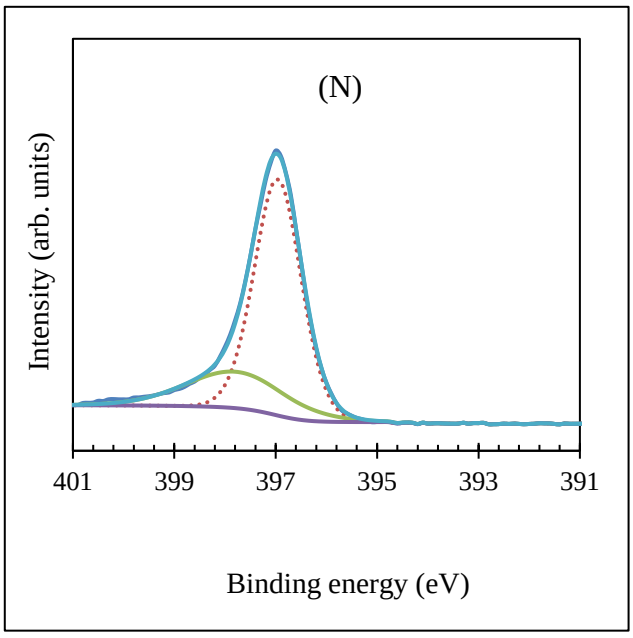

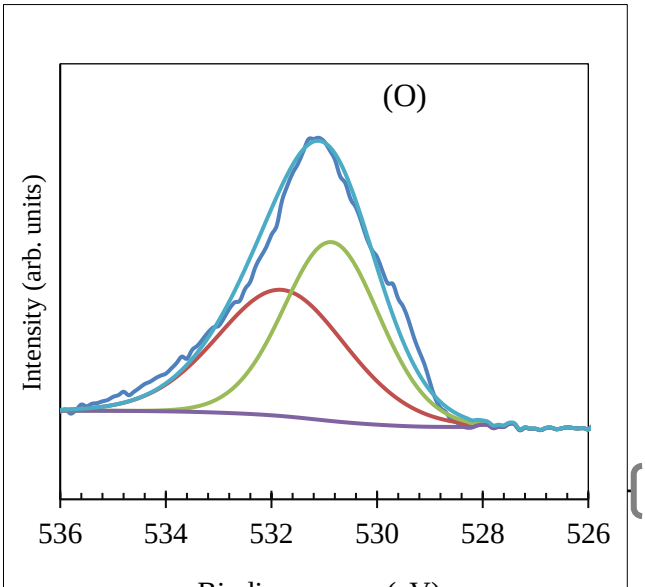

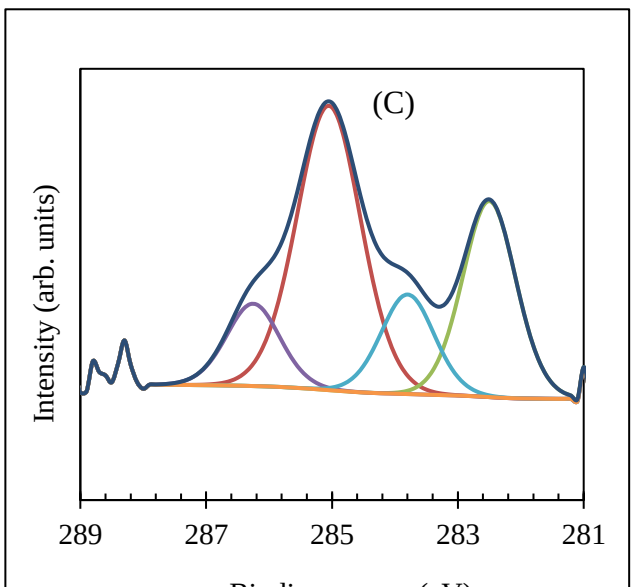

Figure 9.4: XPS core-level spectra of: Cr 2p, N 1s , C 1s, and O 1s of CrN coatings. (Sample ID; P0)

Figure 9.5 presents the XPS spectra of Cr2*p*, Mo3*d* and N1*s* of Cr-Mo-N coatings at Mo target power of 281 W. Deconvolution of Cr2*p* peak indicates that, O atoms were bonded to Cr *via* Cr_2O_3 (530.8 eV) and C to Cr through Cr_7C_3 (587.8 eV) species. The curve-fitted Mo3*d* spectra demonstrates that Mo surface atoms bind O through MoO_2 (230.2 eV) and MoO_3 (234.2 eV) and link to N *via* MoN and Mo_2N (228.9 eV). The N 1*s* spectra show bonds of N with Mo via MoN (395.1 eV) and Mo_2N (397.0 eV). Similar procedure explanation to Figure 9.6 was adapted to Figures 9.6-9.8. Table 9.5 demonstrates the XPS high resolution scan for the studied films.

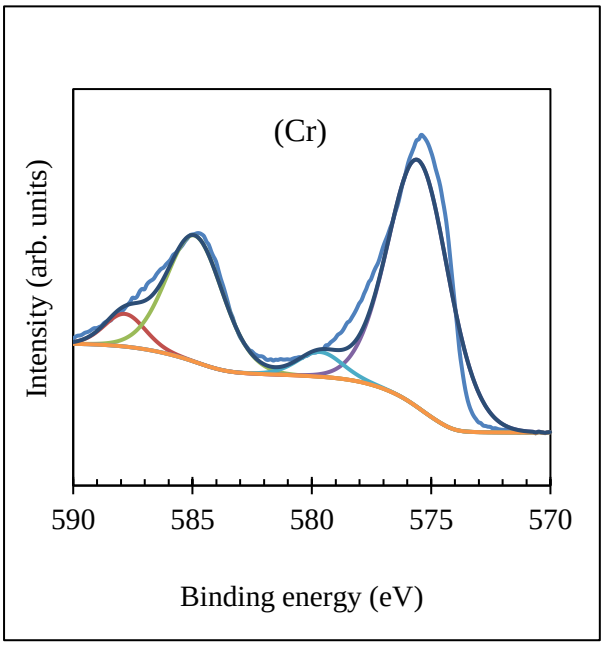

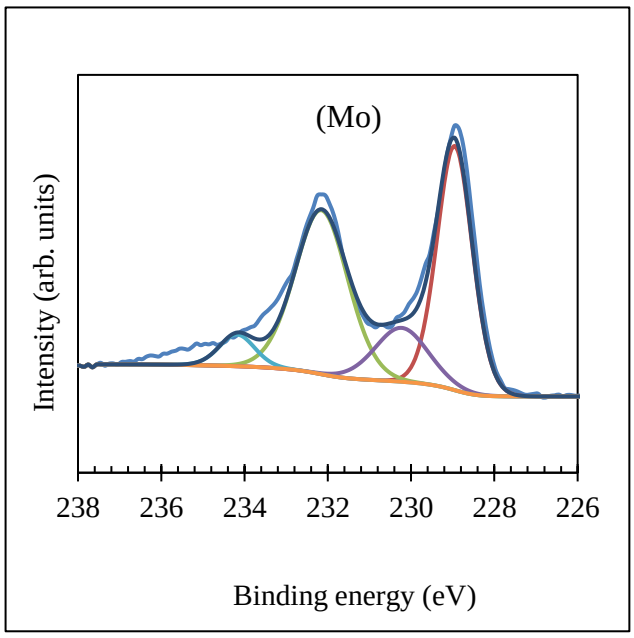

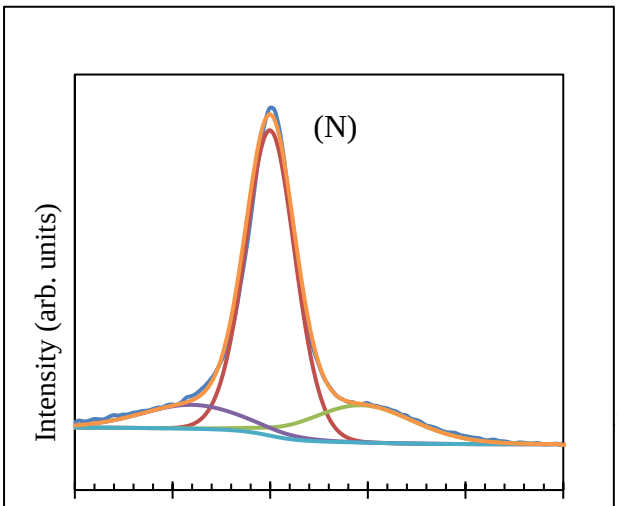

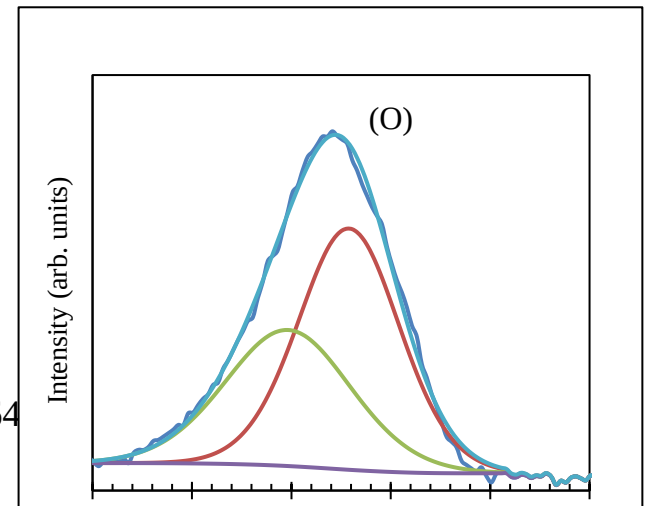

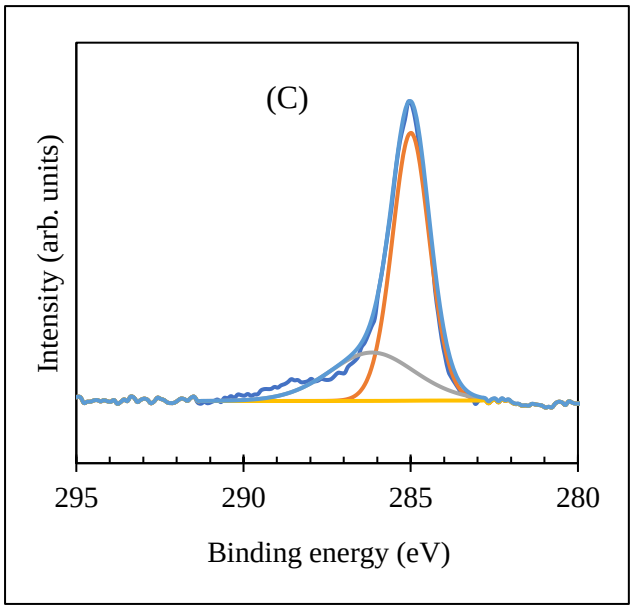

Figure 9.5:XPS core-level spectra of: Cr 2p, Mo 3d, N 1s , C 1s, and O 1s of Cr-Mo-N coatings. (Sample ID; P1).

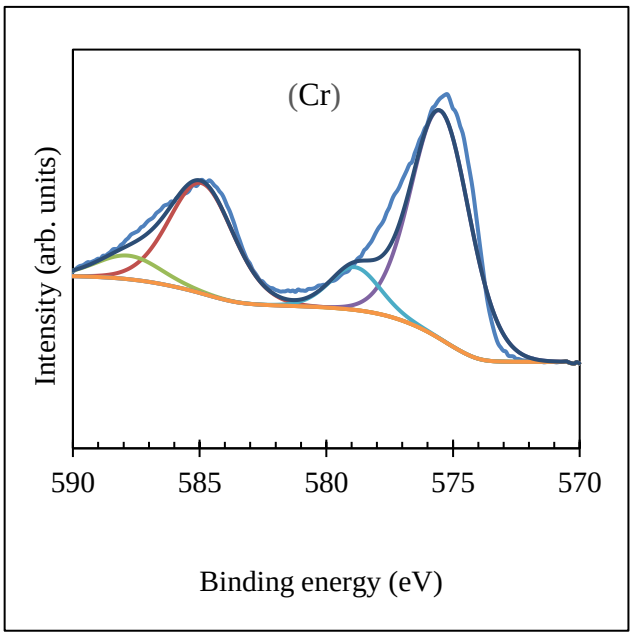

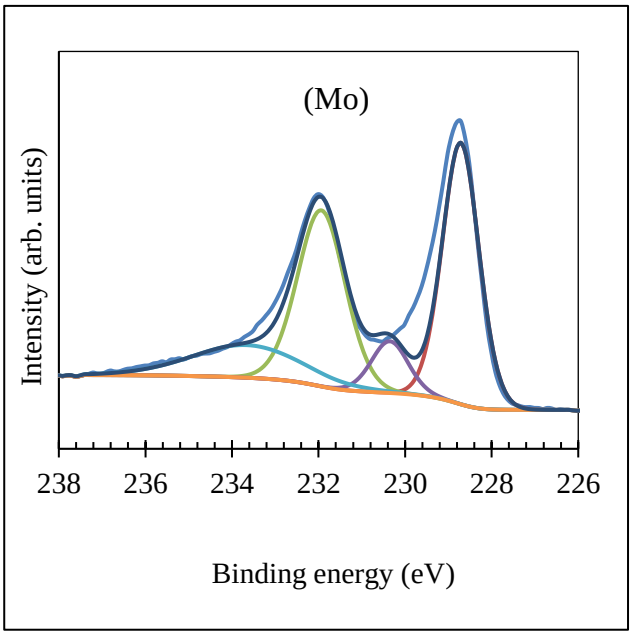

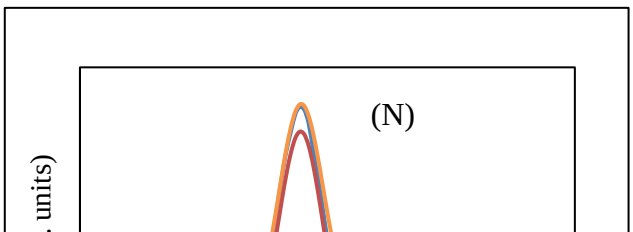

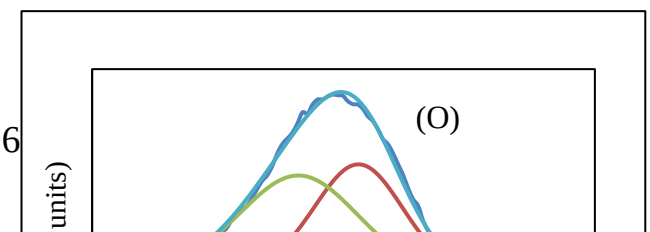

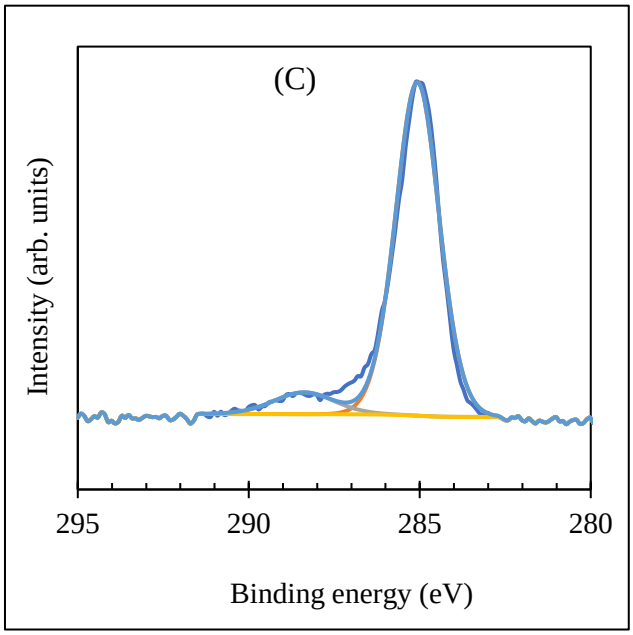

Figure 9.6: XPS core-level spectra of: Cr 2p, Mo 3d, N 1s , C 1s, and O 1s of Cr-Mo-N coatings. (Sample ID; P2).

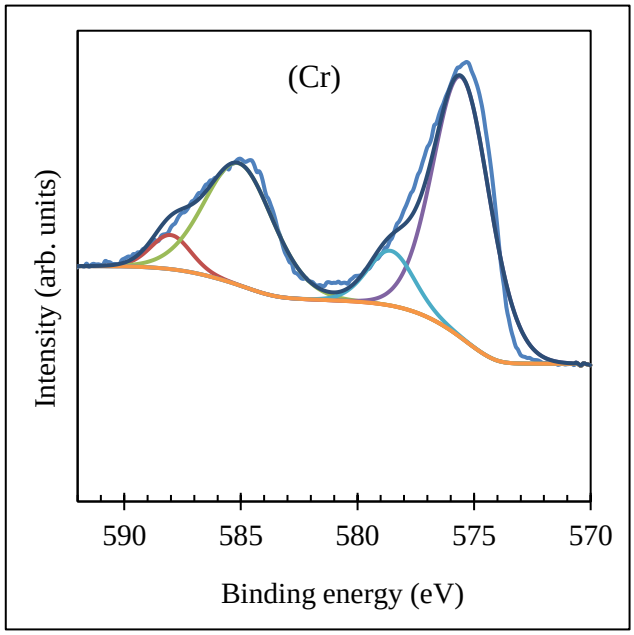
(Cr)
Intensity (arb. units)
590
585
580
575
570
Binding energy (eV)

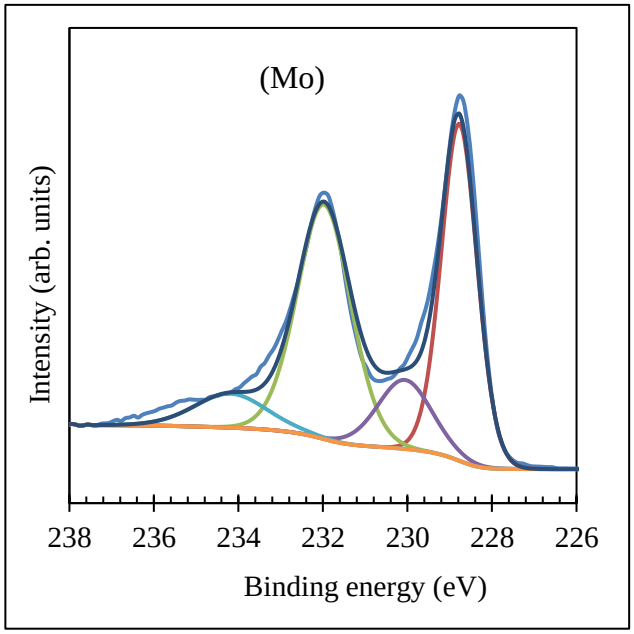
(Mo)
Intensity (arb. units)
238
236
234
232
230
228
226
Binding energy (eV)

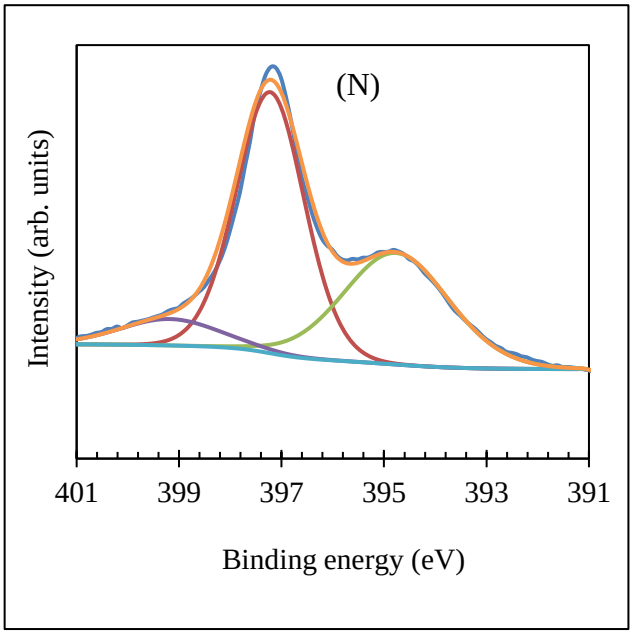
(N)
Intensity (arb. units)
401
399
397
395
393
391
Binding energy (eV)

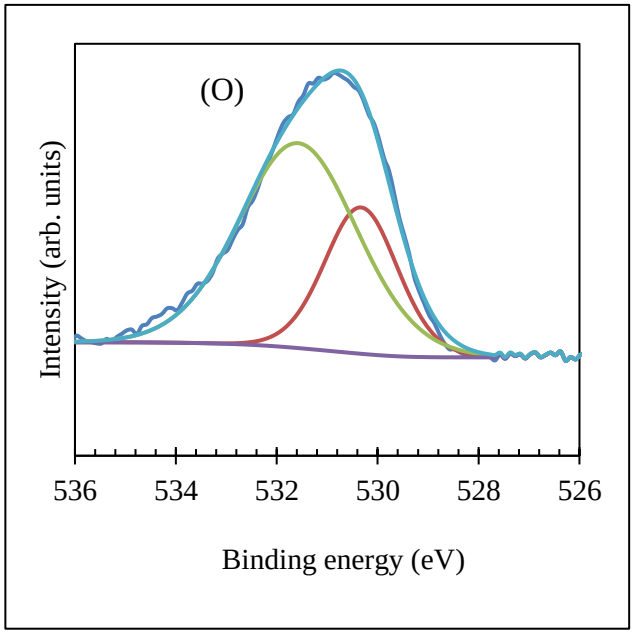
(O)
Intensity (arb. units)
536
534
532
530
528
526
Binding energy (eV)

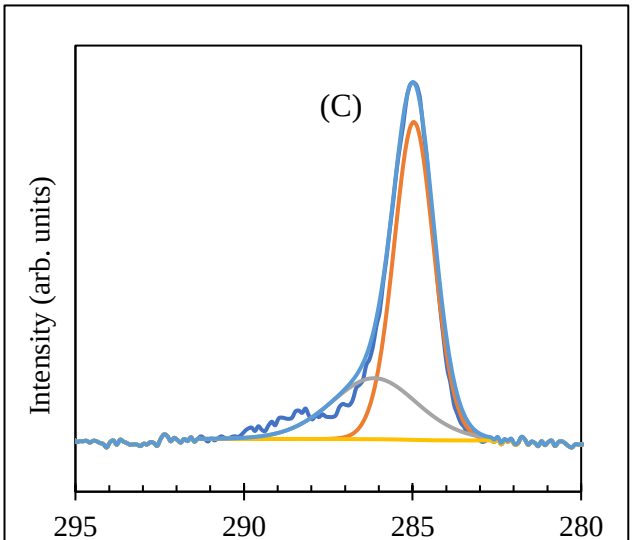
(C)
Intensity (arb. units)
295
290
285
280

Figure 9.7: XPS core-level spectra of: Cr 2p, Mo 3d, N 1s , C 1s, and O 1s of Cr-Mo-N coatings. (Sample ID; P3).

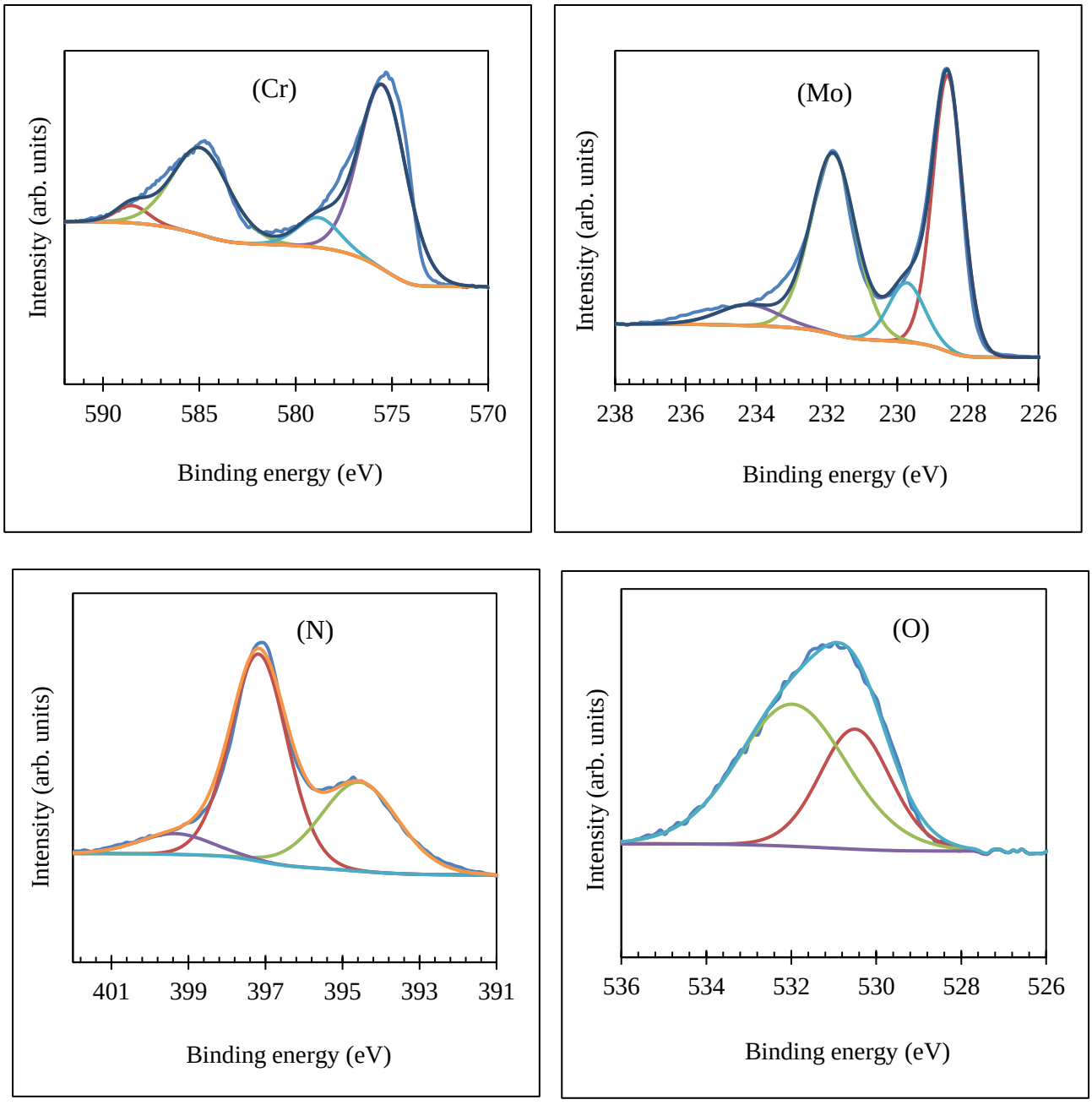

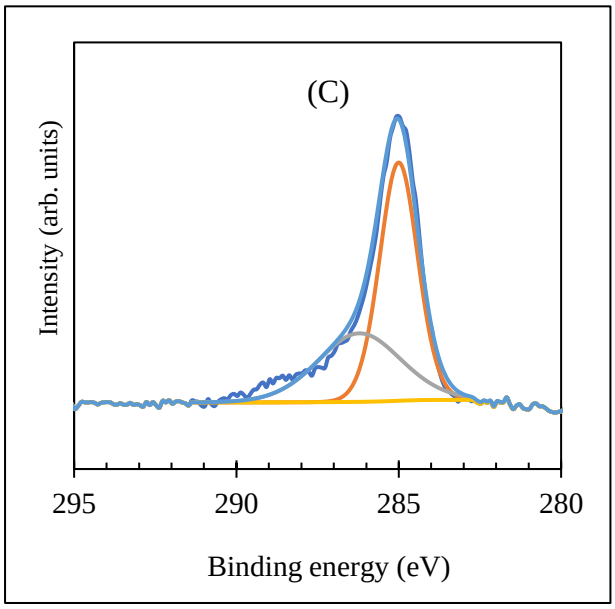

Figure 9.8: XPS core-level spectra of: Cr 2p, Mo 3d, N 1s , C 1s, and O 1s of Cr-Mo-N coatings. (Sample ID; P4).

Table 9.5: The deconvolution results of high resolution XPS spectra at O1s, N1s, Cr2p, and Mo3d photoelectron lines.

	Photoelectron line	Bonding states	Binding energy (eV)	FWHM (eV)	Percentages of the component (%)
P0	O 1s	NO	531.8	2.9	48.6
		Cr_2O_3	530.9	2.1	51.4
	N 1s	NO	397.0	1.1	75.2
		NO	397.8	2.3	24.8
	Cr 2p	Cr_7C_3, Cr	574.9	2.4	47.4
		Cr_2O_3	584.1	3.0	30.6
		Cr_7C_3, Cr	578.2	4.4	14.7
		Cr_2O_3	587.4	2.5	7.0
P1	O 1s	MoO_2, MoO_3	532.1	3.0	41.3
		Cr_2O_3	530.8	2.4	58.7
	N 1s	MoN, Mo_2N	397.0	1.2	70.7
		MoN	395.1	2.5	17.9
		MoO_3	398.6	2.5	11.4

	Mo3d	Mo_2N, MoN	228.9	1.0	40.5
		MoO_3	232.1	1.5	40.8
		MoO_2	230.2	1.5	13.4
		MoO_3	234.2	1.0	5.2
	Cr 2p	Cr_7C_3, Cr	587.8	2.0	5.4
		Cr_2O_3	584.9	2.8	29.0
		Cr_7C_3, Cr	575.5	3	61.1
		Cr_2O_3	579.6	2.2	4.5
P2	O 1s	Cr_2O_3	530.7	2.1	45.6
		MoO_2, MoO_3	531.9	2.9	54.4
	N 1s	MoN, Mo_2N	397.1	1.2	56.1
		MoN	394.9	2.9	40.3
		MoO_3	398.8	2.8	3.6
	Mo 3d	Mo_2N, MoN	228.7	1.0	40.9
		MoO_3	231.9	1.3	35.8
		MoO_2	230.3	1.0	8.1
		MoO_3	233.6	3.0	15.3
	Cr 2p	Cr_7C_3, Cr	584.9	3.9	29.4
		Cr_2O_3	587.8	3.0	6.3
		Cr_7C_3, Cr	575.5	2.7	55.5
		Cr_2O_3	578.9	2.3	8.9
P3	O 1s	Cr_2O_3	530.3	1.7	30.6
		MoO_2, MoO_3	531.6	2.7	69.4
	N 1s	MoN,Mo_2N	397.2	1.6	58.7
		MoN	394.8	2.4	38.9
		MoO_3	399.2	2.3	2.3
	Mo 3d	Mo_2N, MoN	228.8	1.0	39.2
		MoO_3	232.0	1.5	40.9
		MoO_2	230.1	1.5	12.0
		MoO_3	234.2	2.0	7.9
	Cr 2p	Cr_7C_3, Cr	588.0	2.0	5.0
		Cr_2O_3	585.1	3.5	31.1
		Cr_7C_3, Cr	575.5	2.9	54.6
		Cr_2O_3	578.6	2.3	9.3
P4	O 1s	Cr_2O_3	530.5	2.0	35.5
		MoO_2, MoO_3	532.0	3.1	64.5
	N 1s	MoN,Mo_2N	397.2	1.7	62.0
		MoN	394.5	2.3	35.9
		MoO_3	399.3	2.2	2.1
	Mo 3d	Mo_2N, MoN	228.6	1.0	41.8
		MoO_3	231.8	1.5	41.1
		MoO_3	234.2	2.0	6.3
		MoO_2	229.7	1.2	10.8
	Cr 2p	Cr_7C_3, Cr	588.5	2.0	3.7

		Cr_2O_3	584.9	3.5	32.2
		Cr_7C_3, Cr	575.5	2.9	55.9
		Cr_2O_3	578.8	2.6	8.2

Finally, the detection of Cr-O bonding suggests that an oxidation layer formed on the surface for all the samples is expected to improve the oxidation resistance of the coatings [535, 561]. Regarding surface thicknesses, Figure 9.9 depicts cross sectional FESEM images of Cr-Mo-N coatings prepared with various Mo-contents.

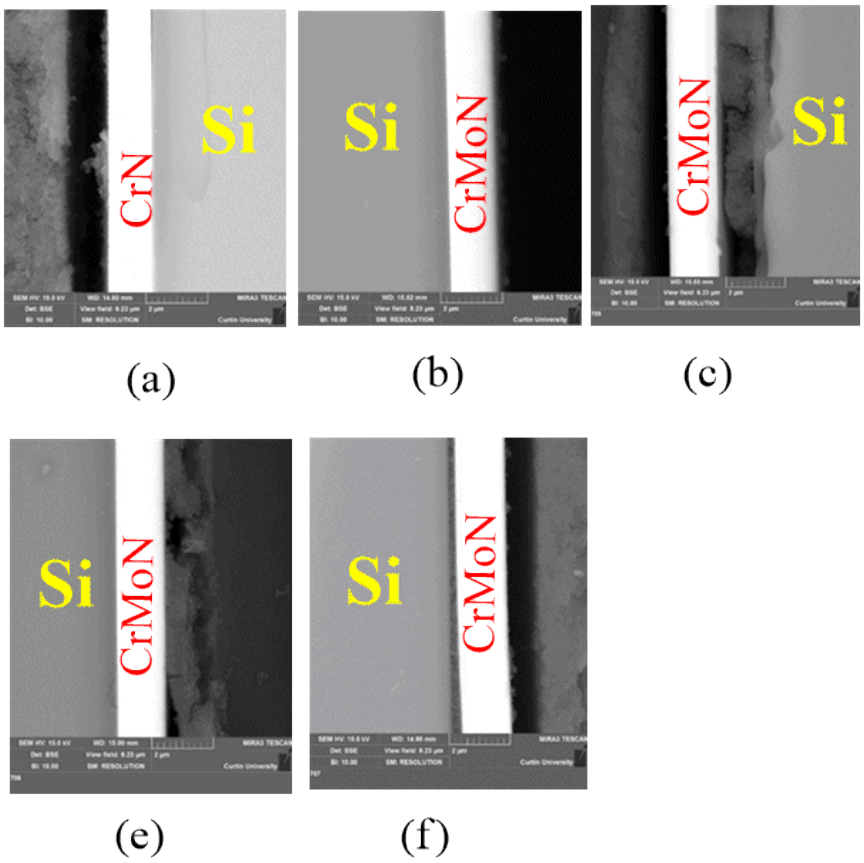

Figure 9.9: Cross sectional FESEM images of Cr-Mo-N coatings prepared with various Mo-contents.

9.4.2 Optical spectra analysis

Knowledge about electronic band structure and optical behaviour is of great interest in order to tune the desired material properties for certain applications. In this section, a series of optical constants will be discussed.

9.4.2.1. Reflectance and Urbach energy

The reflectance spectra of CrN and CrMoN coatings measured by UV-Vis in the range of 200-800 nm are shown in Figure 9.10. The target of obtaining reflectance spectra is to determine the efficiency of a substance in reflecting radiant energy. Analysis of the reflectance spectra of the coatings revealed that, all the studied films have a relatively low reflection values in the visible range of solar spectrum candidate them to be used as the pure antireflection coatings.

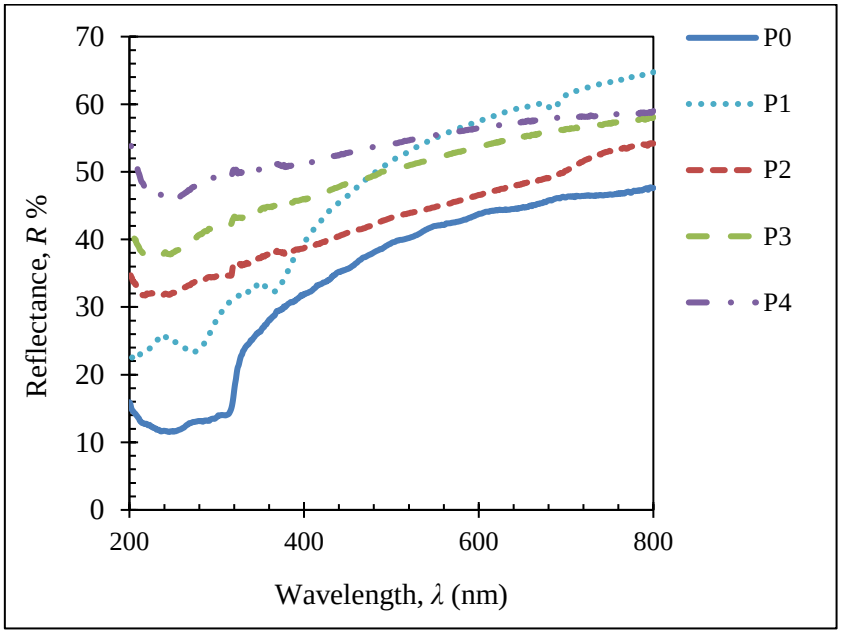

Figure 9.10: UV-Vis reflectance spectra of CrN (P0) and CrMoN (P1-P4) coatings deposited on c-silicon substrates as a function of photon wavelength.

Further, CrN film has favoured reflection characteristic over the Mo-doped CrN films. This may be due to the insertion of the metallic Mo atoms results in forming scattering centres inside the material and hence trapping the incident light [562]. Seeking to provide electronic information of the films as the optical band gap, the absorption coefficients should be obtained. The absorption coefficient (α) of the considered films was calculated according to the formula:

$$\alpha = 2.3026 \frac{A}{d} \qquad 9.2$$

Where *A* refers to the solar absorption given as percentage and *d* represents coating's thickness. Figure 9.11 depicts the variation of the optical absorption coefficient of CrN and Cr-Mo-N coatings deposited at different molybdenum target power as a function of incident photon wavelength. The variation of absorption coefficient with the photon energy helps to determine the optical band structure and the type of electron transition included in absorption process.

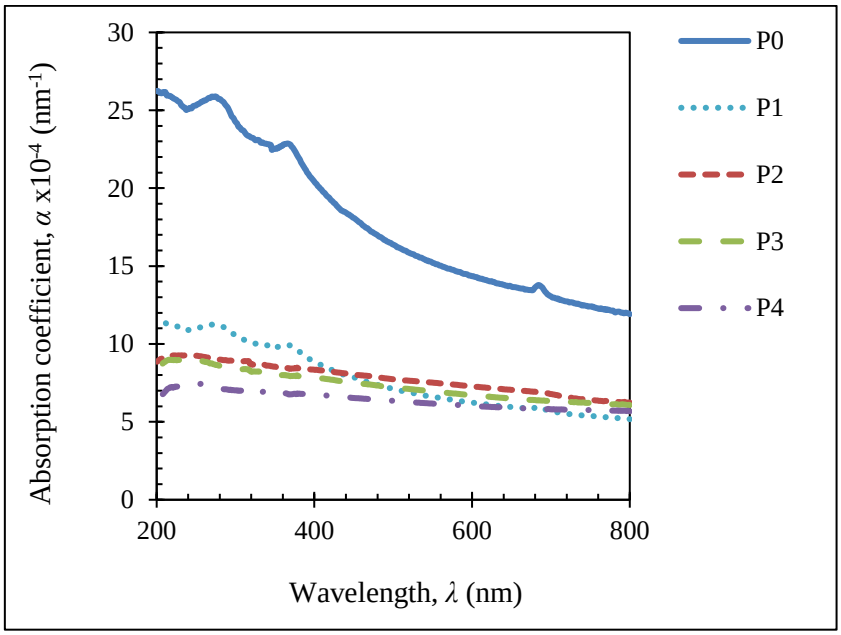

Figure 9.11: Variation of absorption coefficient with wavelength for Cr-Mo-N films deposited on c-silicon substrates.

In the case of solid materials, the incident photon absorption follows the Tauc relation [563, 564].

$$\alpha h\nu = A(h\nu - E_g)^n \qquad 9.3$$

where, α signifies the absorption coefficient, $h\nu$ stands for the photon energy, h is Planck's constant, ν represents the frequency of the incident photons, A corresponds to the probability factor of the optical transition, Eg indicates to the optical band-gap energy and n is an index depends on the type of optical transitions involved in the photon absorption process. Herein, the index n = 1/2 and 2 is for allowed direct and indirect transitions, respectively. In general, the direct band-gap can be calculated *via* plotting $h\nu$ verses $(\alpha h\nu)^2$ and extrapolating the linear part of the curve to $(\alpha h\nu)^2 = 0$ in the *X*-axis. Likewise, the indirect band-gap can be obtained by plotting $h\nu$ against $(\alpha h\nu)^{1/2}$ and inferring the linear part of the curve to $(\alpha h\nu)^{1/2} = 0$ along

the *X*-axis. Figure 9.12 portrays the plots of $(\alpha hv)^2$ versus incident photon energy (hv) of the CrN and Cr-Mo-N systems. According to the figure, the direct optical band-gap of the coatings extended from 2.85 to 3.00 eV with increasing Mo contents.

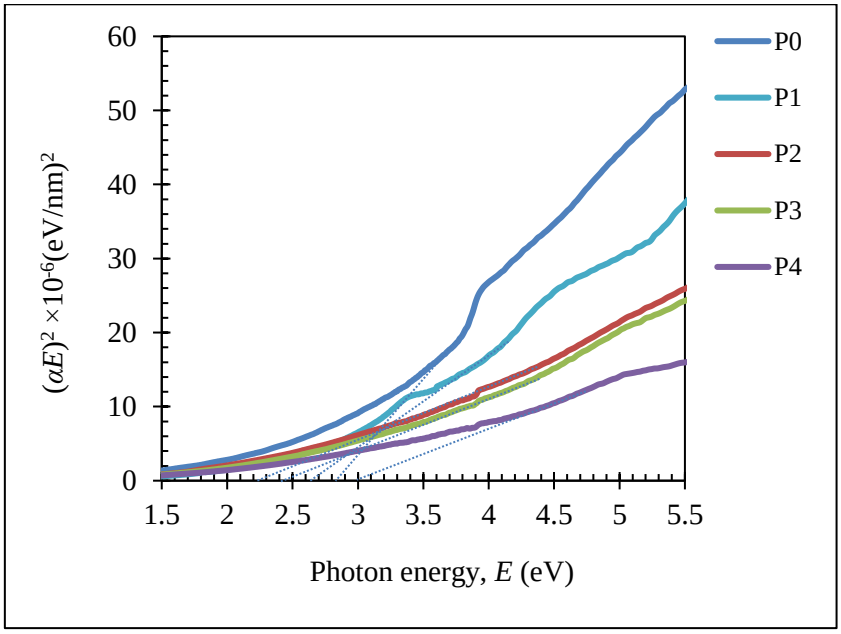

Figure 9.12: Plots of $(\alpha E)^{½}$ versus (E) of Cr-Mo-N coatings deposited on c-silicon substrates.

9.4.2.2 Determination of the dispersion constants

Knowledge about refractive index (n), and extinction coefficient (k) is of great importance to understand the optical dispersion of a crystal. In the spectral range of 200 – 800 nm, the refractive index and extinction coefficient were derived by the UV-Vis data and demonstrated in Figures 9.13 a and b. The complex refractive index is expressed as follow:

$$n^* = n + ik \qquad 9.4$$

where k denotes the imaginary part of the refractive index termed as the extinction coefficient and it is given *via* following relation:

$$k = \frac{\alpha\lambda}{4\pi} \qquad 9.5$$

The real part of the complex refractive index, n is defined by the equation below;

$$n = \left(\frac{1+R}{1-R}\right) + \sqrt{\frac{4R}{(1-R)^2} - k^2} \qquad 9.6$$

Where *R* is the reflectance data and *k* states to the extinction coefficient.

From Figure 9.13 a, it can be observed that all the spectra of refractive index for the studied films share minor differences in the considered wavelength range. Extinction spectra, as shown in Figure 9.13 b, the coatings experience relatively trivial values in the visible region. Further investigation also reveals that these films have small values of the dispersion and absorption of the solar photon energies in the visible range indicating good quality films for various optical applications.

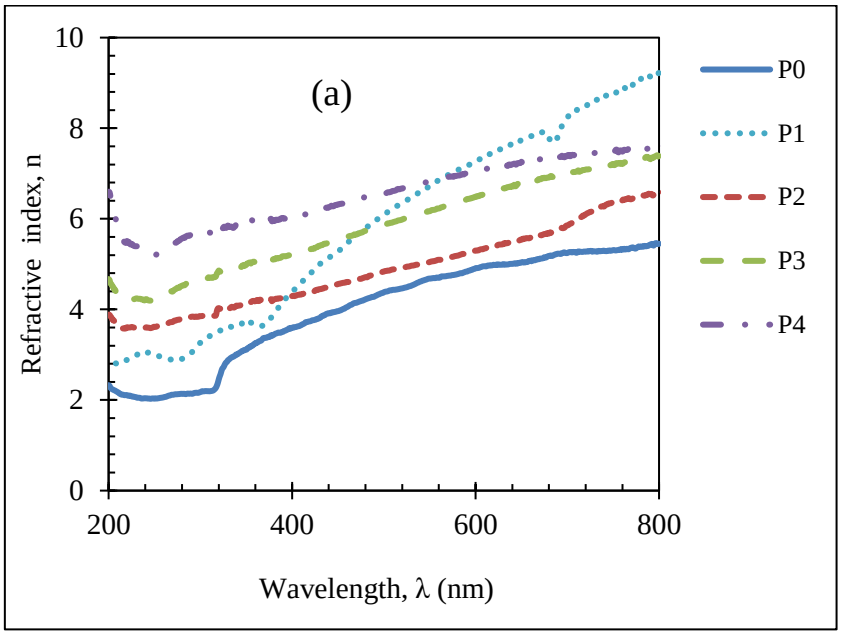

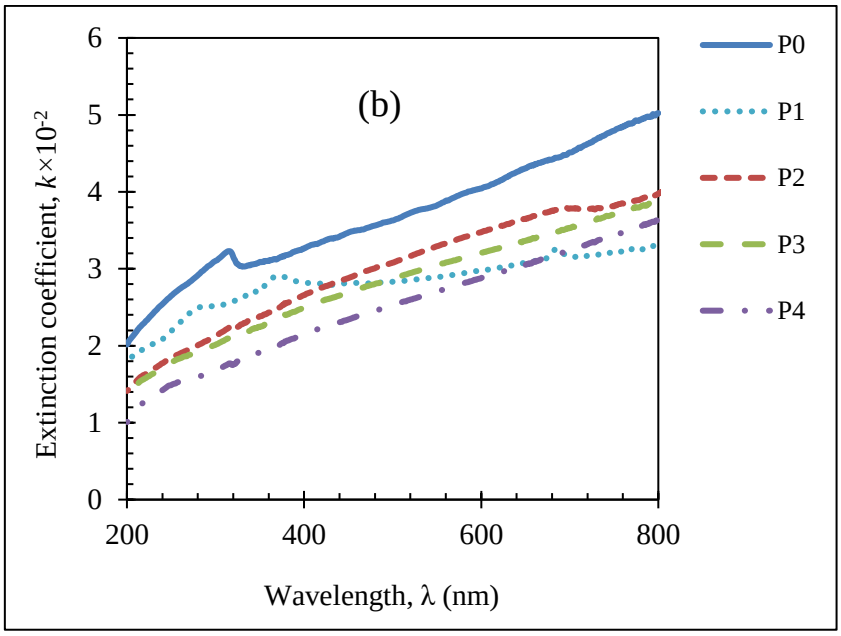

Figure 9.13: (a) Variation of refractive index; (b)Variation of extinction coefficient as a function of wavelength for Cr-Mo-N films deposited on c-silicon substrates.

9.4.2.3 Dielectric analysis

The dielectric function is based on frequency and can be obtained from the momentum matrix elements between occupied and unoccupied (excited) electronic states as shown below;

$$\varepsilon(\omega) = \varepsilon_1(\omega) + i\varepsilon_2(\omega) = (n(\omega) + ik(\omega))^2 \quad 9.7$$

Where, the real part $\varepsilon_1(\omega)$, is associated with electronic structure and illustrated the linear response of the system to electromagnetic energy. whilst, $\varepsilon_2(\omega)$ relates to the interaction of photons and electrons to obtain the optical band gap [565, 566]. The real part is described by [567],

$$\varepsilon_1 = n^2 - k^2 \quad 9.8$$

$$\varepsilon_2 = 2nk \quad 9.9$$

ε_1 (ω) resembles to the polarized material that resulted when applying an electric field, whereas ε_2 (ω) corresponds to the loss energy. From Figure 9.14a it is evidently seen that ε_1 spectra exhibit a reducing behaviour with the photon energy. Similarly, ε_2 spectra shown in Figure 9.14b demonstrates an energy dependent reducing character. However, ε_1 and ε_2 curves show small values in the visible range confirming their validity in the optical fields.

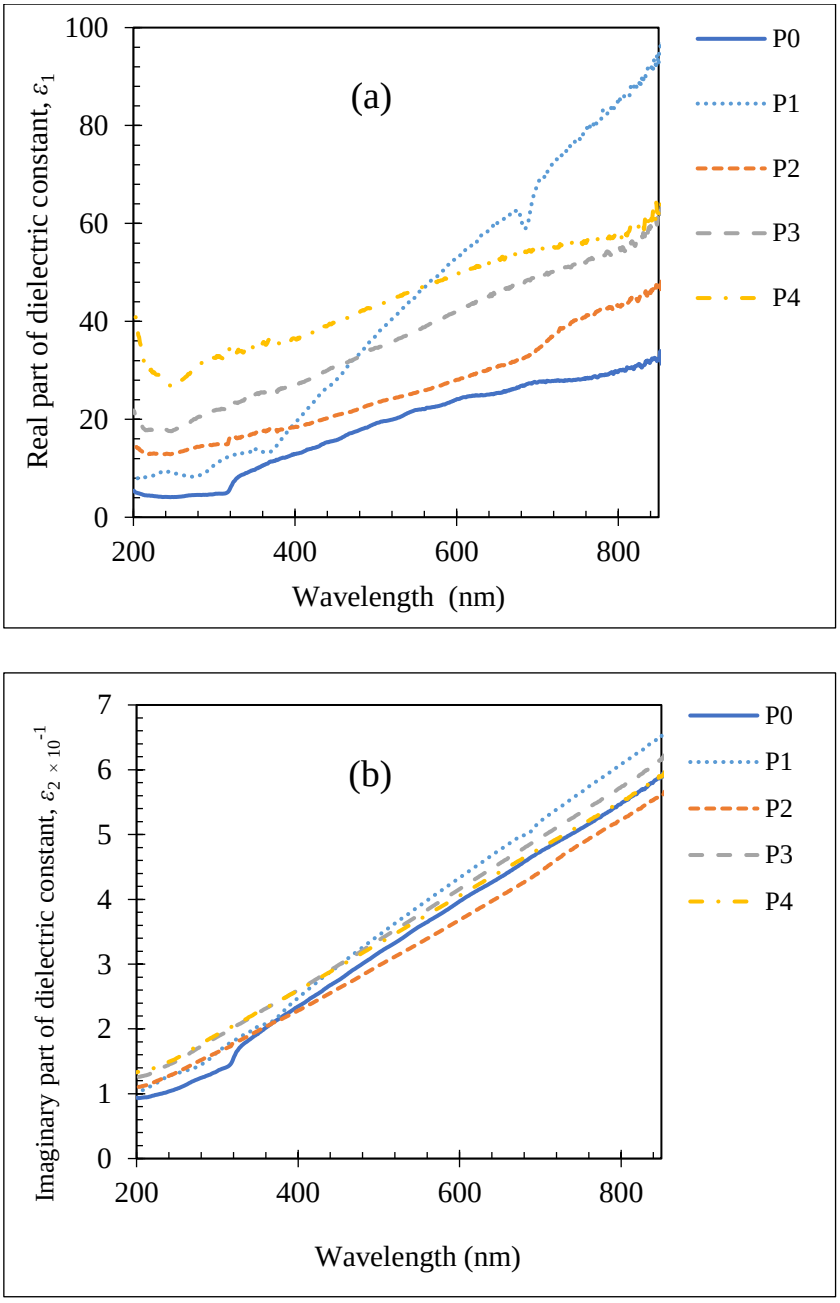

Figure 9.14: (a) Real part of dielectric constant; (b) Imaginary part of dielectric constant vs wavelength of Cr-Mo-N films deposited on c-silicon substrates.

9.4.2.4. Volume energy loss and surface energy loss functions analysis

It has been reported that the energy loss is caused by inelastic scattering process during the charge transfer and charge conduction mechanisms [568]. The energy loss is assessed by determining the loss tangent, which expressed by the following formula;

$$tan\delta = \frac{\varepsilon_2}{\varepsilon_1} \qquad 9.10$$

Figure 9.15 displays the energy dependent loss tangent of CrN and CrMoN films synthesised at different Mo content. It is clearly noticeable that doping CrN with Mo results in decreasing the amount of energy loss in the whole studied range. Our loss tangent values of the synthesised films are expected to be low due to ε_2 is far lower than that of ε_1.

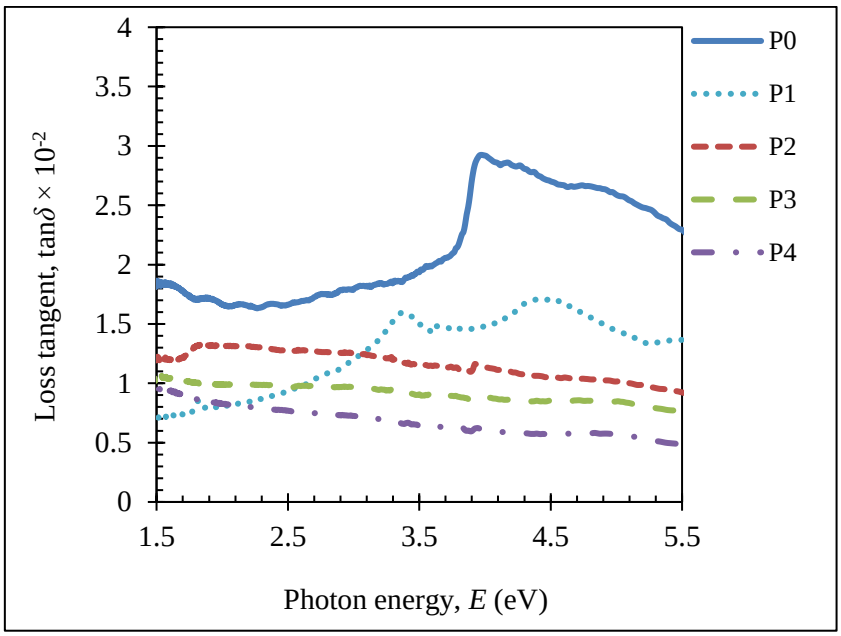

Figure 9.15: Variation of loss angle with wavelength for Cr-Mo-N coatings deposited on silicon substrates.

There are two categories of energy loss functions as volume energy loss function, V_{el} and surface energy loss function, S_{el} [569].

$$V_{el} = Im\left(-\frac{1}{\varepsilon(\omega)}\right) = \frac{\varepsilon_2}{\varepsilon_1^2 + \varepsilon_2^2} \quad 9.11$$

$$S_{el} = Im\left(-\frac{1}{\varepsilon(\omega)+1}\right) = \frac{\varepsilon_2}{(1+\varepsilon_1)^2 + \varepsilon_2^2} \quad 9.12$$

In similar situation to loss tangent, V_{el} and S_{el} are both closely related to the real and imaginary parts of dielectric function. Consequently, V_{el} and S_{el} values shown in Figure 9.16a and 9.16b are also predicted to be in their minimal values. Furthermore, adding Mo metal to the CrN material enhances the qualities of the films by reducing their energy loss for a wide range of the incident photon energies.

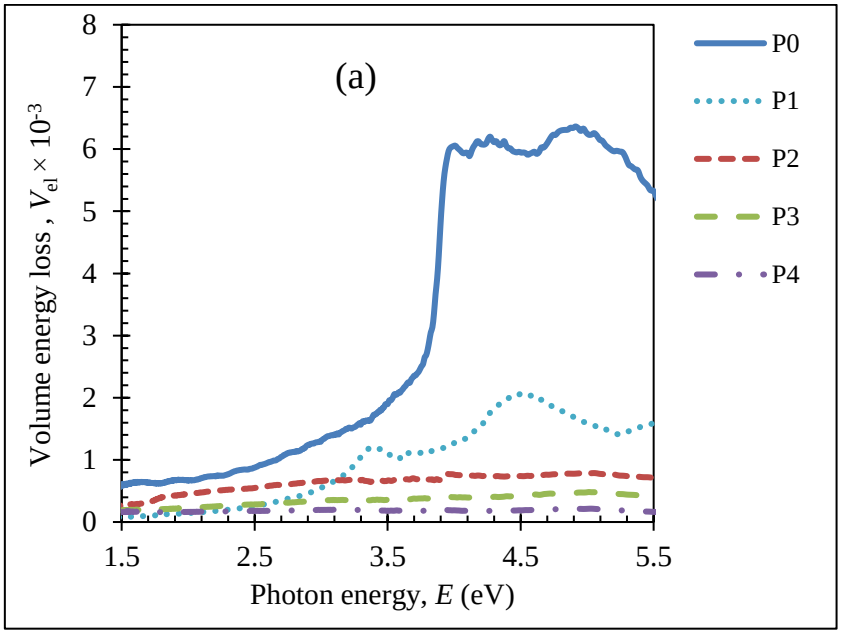

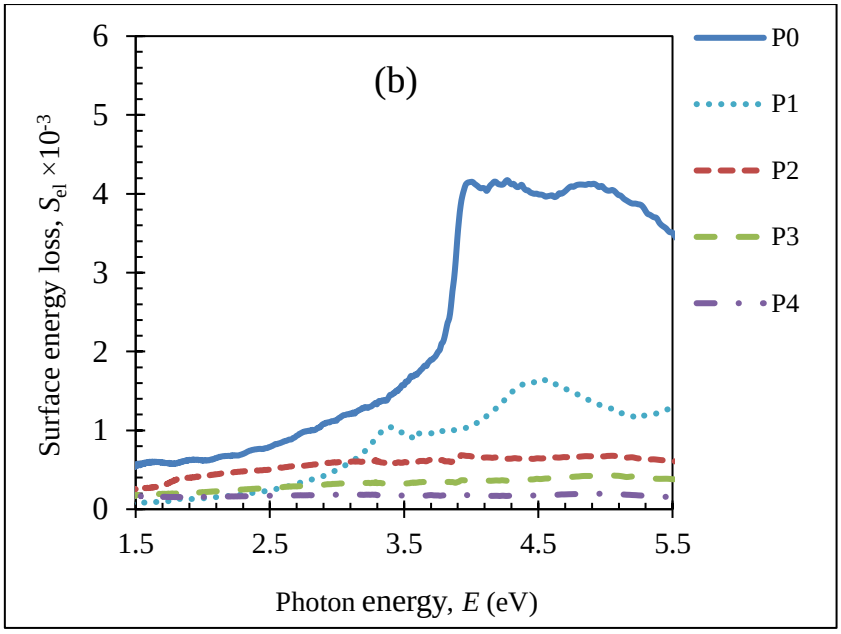

Figure 9.16: (a) Volume energy loss; (b) surface energy loss variations as a function of photon energy of Cr-Mo-N coatings deposited on c-silicon substrates.

9.4.2.5 Selective solar absorbers

Selective solar surfaces harness solar energy into heat using cermet (ceramic–metal) - based coatings. To meet the necessities of efficient spectrally selective solar absorber materials, high absorptance in the solar wavelength range and a low emittance in the infrared (IR) region are highly demanded. Extensive work has been done to optimize cermet-based solar absorbers to achieve high performance by exploring different cermet composites via different preparation methods such as electrodeposition, sputtering, pulsed laser deposition, and solution-based methods. Using FTIR spectrometer (Perkin Elmer Spectrum 100 FTIR Spectrometer, USA), the solar reflectance of the coatings has been obtained in the wavelengths of 2.5 – 15.5 mm. For a solid material, solar selective of surfaces can be estimated as a ratio between the solar absorbance A calculated from UV-Vis reflectance data and solar emittance E obtained from infrared spectra, ($S = A/E$) [570]. Using Beckmann-Duffie method, solar absorbance and solar emittance can be calculated [571]. As depicted in Table 9.6, our films record relatively good solar selectivity properties; however, the film named as P3 affords the highest solar selective value.

Table 9.6**:** thermal emittance, solar absorbance, and solar selectivity values of Cr-Mo-N synthesized with different Mo-target power.

Sample	Emittance (ε %)	Absorptance (α %)	Solar selective s
P0	38.8	67.7	1.7
P1	42.6	74.8	1.7
P2	30.0	70.2	2.3
P3	20.0	72.9	3.6
P4	27.3	75.5	2.7

9.4.3 Computational modelling

First-principle based studies are the most promising method to predict ground state properties of materials. Herein, we performed density functional theory (DFT) calculations to perform structural relaxation and energy calculation considering the *fcc*-CrN phase as predicted by XRD analysis. The optimized unit cell, shown by Figure 9.17, composed of one formula unit (*i.e.* Cr=4 atoms and N=4 atoms) exhibits NaCl type-structure with space group of Fm-3m. The estimated lattice parameters of $a=b=c$ (4.11 Å) with $\alpha=\beta=\gamma$ (90^{o}). Furthermore, the estimated lattice constants found to be 4.14 Å.

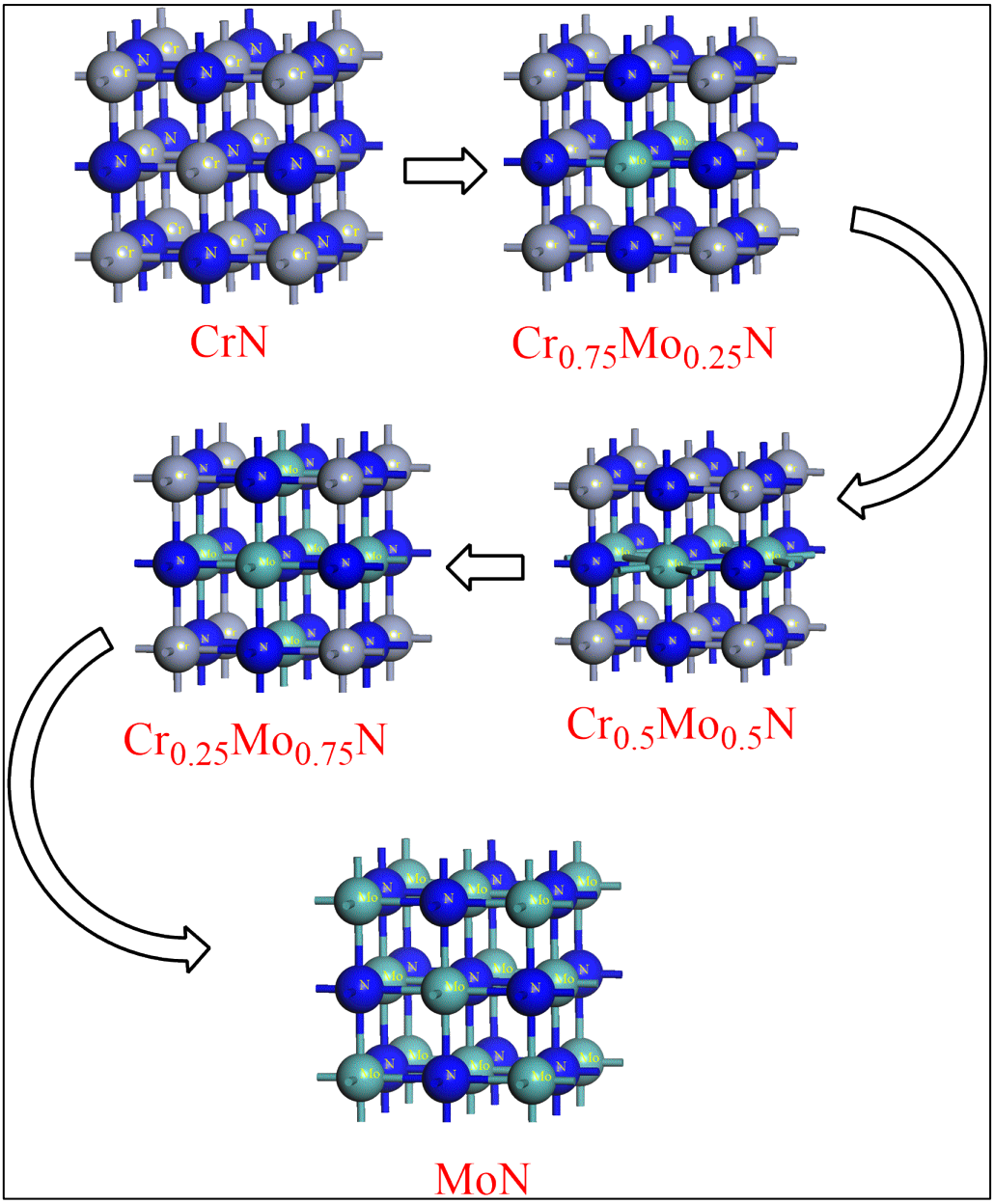

Figure 9.17: Optimized configurations of the suggested alloys. Gray, light blue, and, indigo spheres refer to chromium, molybdenum, and nitrogen atoms, respectively.

In order to check the reliability of the parameters used to theoretically calculate various optical properties, total density of states DOSs had been modelled aiming to assess and calculate the electronic structure of CrN system. Figure 9.18 depicts the electronic density of states (the incorporation of valance and conduction bands). It is apparent from calculating the total density of states at the Fermi level predicts that CrN exhibit a conducting nature and this finding was in line with what has been experimentally reported [32, 525].

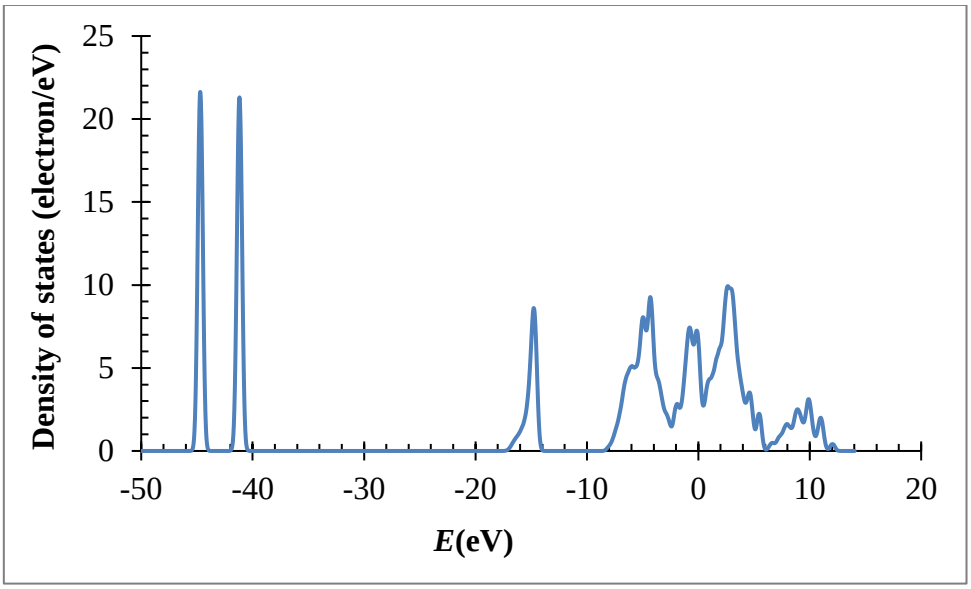

Figure 9.18: Theoretically predicted total density of states of CrN system.

Furthermore, the theoretical treatments provided the refractivity and absorption spectra as a function of wavelength of the proposed alloys as shown in Figures 9.19a – 9.19b, accordingly.

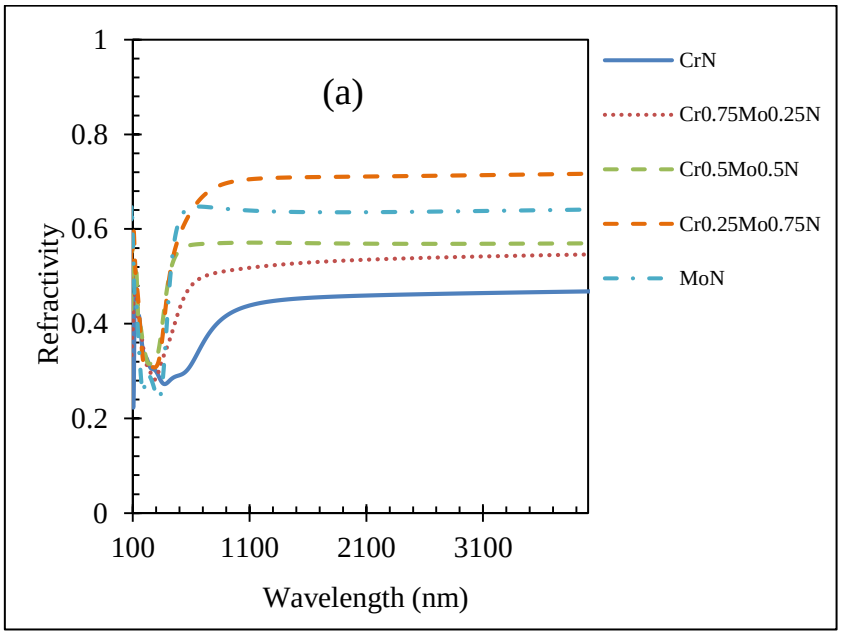

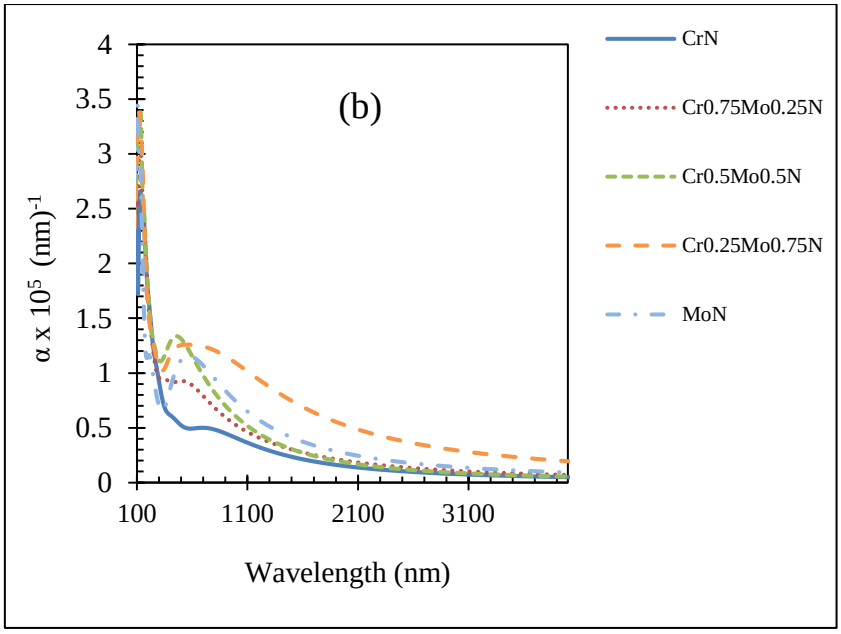

Figure 9.19: (a) Theoretical refractivity spectra; (b) Theoretical absorption spectra as a function of wavelength of the proposed alloys.

The distribution of refractance, in Figure 9.19a, indicates all thin films having transparent characteristics in the visible range, while Figure 9.19b, depicts a moderate absorption values in the same range. Refractivity spectra exhibit invariable high values in the infrared range. In contrast, absorption coefficient curves display constant small values in the same range.

The predicted refractive index (*n*) and extinction coefficient (*k*) spectra, in the wavelength range of 100 – 40000 nm, of CrN and CrMoN are shown in Figures 9.20a and 9.20b, respectively.

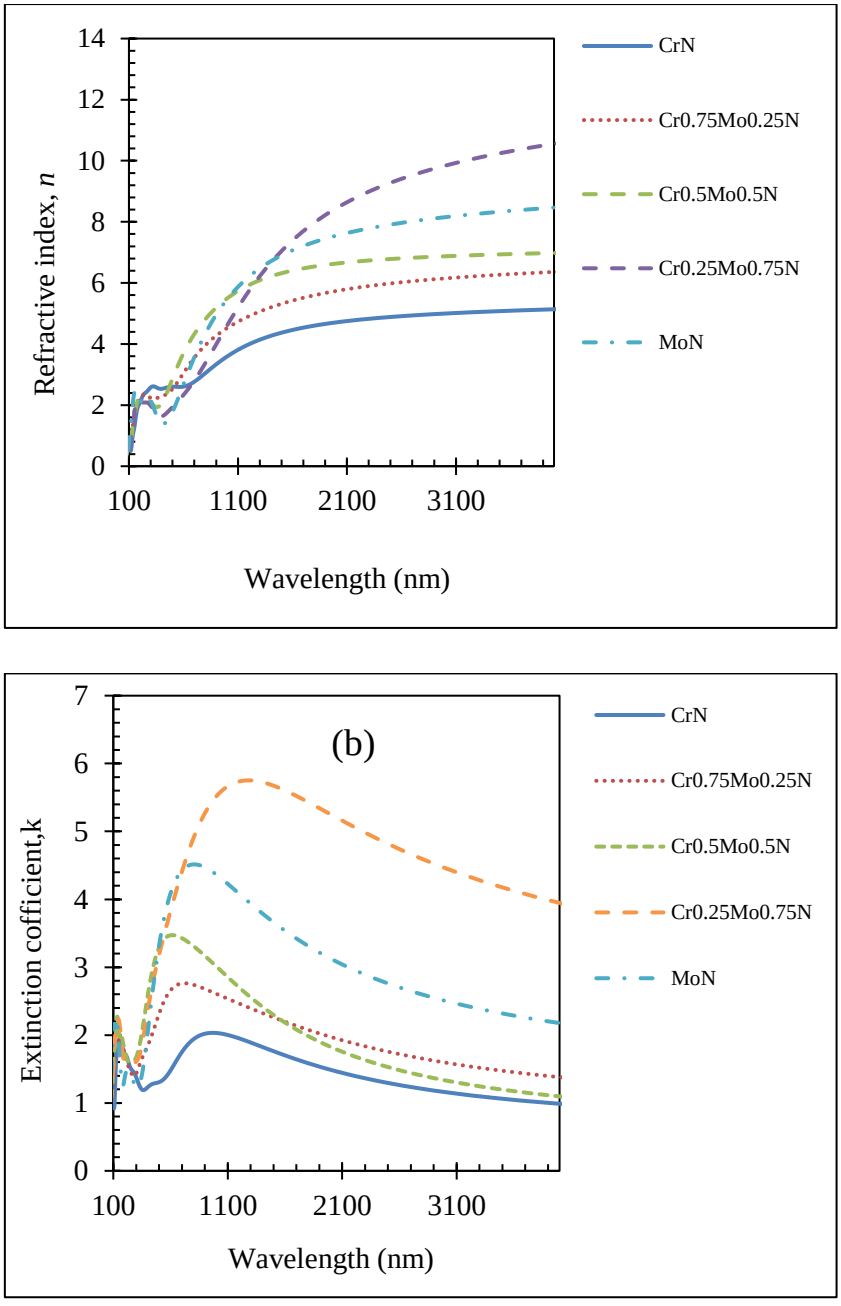

Figure 9.20: (a) Predicted variation of refractive index; (b)The calculated variation of extinction coefficient with wavelength for the proposed alloys.

Both refractive index and extinction coefficient spectra exhibit similar trend as the dielectric functions in that they both have peak values in the shorter wavelength regions. The simulated and experimental refractive index has analogous behaviours in the wavelength range from 200 to 800 nm. Finally, the calculated real and imaginary components of dielectric function are shown in Figures 9.21a and 9.21b. Theoretical predicted real and imaginary dielectric spectra

were smaller values than that from experiments in the visible range of the *E-M* spectrum suggesting a lesser loss of energies in the aforementioned region. Also, the similar dielectric behaviours of both simulated and experimental results validate our findings from this study. Real and Imaginary dielectric spectra demonstrated relatively elevated values in the Infrared range of *E-M* spectrum.

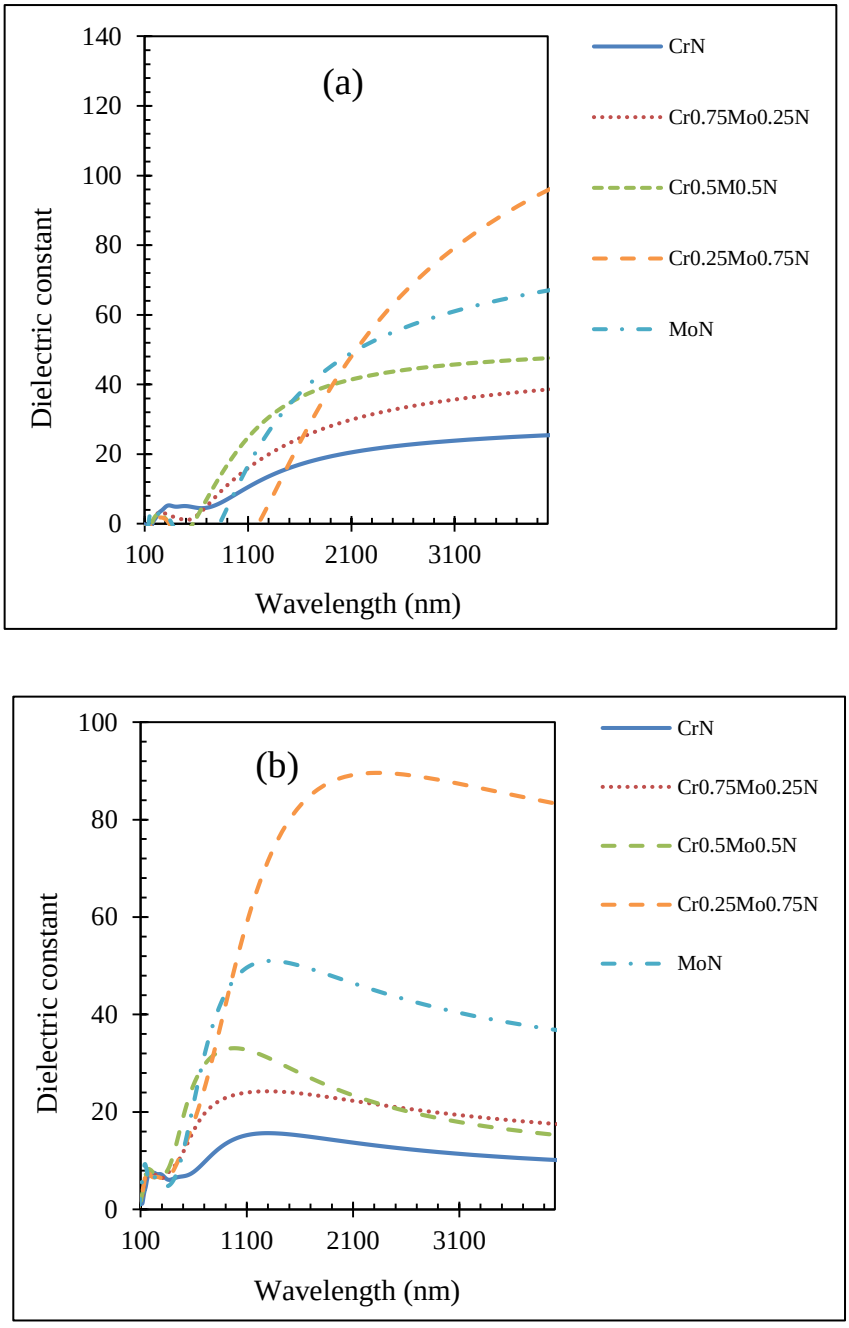

Figure 9.21: (a) The calculated real components; (b) imaginary components of dielectric function.

9.5 Conclusions

This chapter explored the physico-chemical properties of Mo-doped CrN coatings synthesized by magnetron sputtering with a mixture of $Ar+N_2$ reaction gas. All the as-deposited coatings displayed face-centered-cubic (fcc) CrN phase with multiple crystal orientations in (111), (200), and (220) directions. When the Mo-target power was augmented from 0 to 1663 W, the Mo content was found to be linearly growing in the Cr–Mo–N coating from 0 to 16.6 at. % and correlated with a corresponding reduction in Cr from 50 to 15.6 at.%. Remarkable enhancement in the solar absorptance behaviour of the coatings by the insertion of Mo interlayer was recorded to be 73% associated with 20% thermal emittance. Accordingly, Cr-Mo-N system revealed the topmost solar selectivity value of 3.7. The role of Mo addition in the CrN coating is found to be promising and has proven that CrMoN films have potential applications in solar energy industry, such as solar selective absorber surfaces.

Chapter 10 : Conclusions and Future Directions

10.1 Conclusions

This dissertation demonstrates a novel scholarly knowledge on materials modelling within the framework of DFT reporting physical and chemical properties of bulk and surfaces of γ-Mo_2N with an emphasis on catalytic-assisted reactions and optical behaviour of Cr-Mo-N coatings.

To start with, we implemented the quasi harmonic approximation approach (QHA) reporting thermo-mechanical properties for MoN phases across wide temperature range of 0-2023 K (melting point) and pressures up to 12 GPa. Calculated values were in accord with rather very limited corresponding experimental estimates. At ambient conditions, the hexagonal δ-MoN configuration affords higher mechanical stability in reference to cubic *c*-MoN. Based on predicted Bader's charges, we predicted a charge transfer from metallic to non-metallic atoms *i.e.* (Mo 1.85 *e*; N -1.83 *e* in *c*-MoN and Mo 1.27 *e* ; N -1.27 *e* in δ-MoN).

Moving towards inspecting surface characteristics of hexagonal phases of molybdenum and tungsten nitrides, we then performed periodic DFT calculations to investigate surface relaxations and construction of several low Miller indices for hexagonal phases of molybdenum and tungsten nitrides. *Ab* initio atomistic thermodynamic enabled to plot the surface free energies for atomic terminations in both materials as a function in the nitrogen chemical potential. Based on acquired thermodynamic stability trends, we predict that nitrogen terminated (111) and (100) surfaces of δ_3-MoN and δ-WN, respectively to incur higher thermodynamic stability than other plausible terminations. As we have shown in Chapter 6 of the thesis, prominent catalytic steps take place over N-vacant sites. For this reason, we computed energies required to create nitrogen vacant sites and predicted their equilibrium concentrations as a function of temperature for selected surfaces of δ_3-MoN and δ-WN. The maximum surface concentrations for N-vacant sites attain values of 7.7×10^{19} and 2.8×10^{17}, for δ_3-MoN and δ-WN, respectively.

In light of literature's experimental studies that report temperature programmed desorption (TPD), temperature programmed reaction (TPR) measurements, and catalytic tests, over surfaces of molybdenum nitrides, we constructed reactions mechanisms and developed kinetics models for surface-mediated reactions by Mo_2N.

We mapped out all steps operating in the full and partial hydrogenation of C_2H_2 over γ-Mo_2N (111) and γ-Mo_2N (111) surfaces. We computed reaction rate constants and overall uptake rate for the dissociative adsorption of hydrogen molecules; mainly over N-vacant sites. We predict that hydrogen transfer from N-vacant site to atop N site to be a feasible process owing to a relatively low surface diffusion barrier. We constructed a simplified plug flow reactor model to account for the experimentally observed profiles of products. Higher selectivity for the formation of C_2H_4 instead of C_2H_6 is mainly attributed to higher activation barrier for the opening hydrogenation step in full hydrogenation when contrasted with the analogous step encountered in the partial hydrogenation route. Overall, we illustrated the selective occurrence of partial hydrogenation based on kinetics and thermodynamics considerations. For instance, stronger binding of the adsorbed C_2H_3 adduct with the surface (in comparison to adsorbed C_2H_5) facilitates its further hydrogenation into C_2H_4, whereas the fate of adsorbed C_2H_5 is mainly dictated by its desorption into the gas phase and the backward hydrogen transfer reaction.

In the next hydrogen transfer reaction, we provide an atomic-base description of thiophene hydrodesulfurization (HDS) routes over a surface of γ-Mo_2N. Results suggested that thiophene adapts a flat molecular mode va noticeably exothermic adsorption energies. Sizable activation barrier operated in the in the C-S bond scission largely shuts down the direct desulfurization (DDS) pathway. Hydrogen transfer from N-vacant sites into a carbon atom adjacent to the S atom reduces the required activation energy to split the S-C bond in the thiophene molecules by 55.8 % in reference to the direct C-S fission route. Our calculated activation and reaction energies reveal a facile conversion of thiophene into C_4 adducts and H_2S. Developed global-like reaction model affords conversion values that are very comparable with experimental estimates.

Several experimental studies have investigated catalysis by molybdenum nitrides toward the production of the industrially important aromatic chloroamines via H-induced reaction of chloronitrobenzenes. We provide an insight into the reduction mechanisms of *p*-

chloronitrobenzene (*p*-CNB) to *p*-chloroaniline (*p*-CAN) over γ-Mo_2N (111) surface by means of DFT calculations. Transformation of the CNB molecule into CAN takes place via a series of hydrogen transfer steps. These reactions mainly comprise several hydrogen transfers reactions into the O/OH groups, N-OH bond fissions, and hydrogen transfer to unsaturated N atoms in the pre-structure of the CAN molecule. Hydrogenation of the *p*(C)Cl site was found to acquire a sizable activation barrier, and thus preventing further reduction into unsubstituted aniline. The absence of aniline from the product profiles in the catalytic experiments concurs with our kinetics analysis.

In the last part of this project, we evaluate the effect of adding various loadings of Mo into CrN coating fabricated using plasma assisted magnetron sputtering method, termed as closed field unbalanced magnetron sputtering ion plating (CFUMSIP). Structural, chemical bonding states, morphological, and optical properties of the coatings were inspected via several surface measurements techniques. XRD and XPS analyses confirm the incorporation of molybdenum (Mo) in the CrN matrix. Various polycrystalline phases including CrN, γ-Mo_2N, Cr with oxides layers of MoO_3, CrO_3, and Cr_2O_3 are present in the new fabricated coatings. The grain size of Cr-Mo-N coatings increases with the Mo content, most presumably due to the formation of MoN phase via the interaction of Mo atoms with N atoms nestled close to the grain boundaries of CrN phase. XPS investigations confirmed the presence of Cr, Mo, N, C and O elements in the studied coatings. The synthesised coatings show low reflection magnitudes in the visible region of the solar spectrum. This clearly renders the newly synthesises coatings as a promising material in for antireflection surfaces. It is found that, Mo-containing samples enhanced solar absorptance by 76% the wavelength range of 200 – 800 nm. However, the thermal emittance was reduced by 20% was between 2500 – 15000 nm.

10.2 Future Directions

Herein, we convey recommendations for potential future research;

It is insightful to construct a thermodynamic stability diagram that takes into account all plausible phases of MoN_x phases at all experimentally accessible *T-P* conditions. In this regards, the QHA approach is a robust formalism to determine values of $G(T,P)$, per bulk formula for all MoN_x phases.

Literature plots the surface free energies of Mo_2N as function of nitrogen chemical potential. Recent studies have synthesised nitrogen rich phase of MoN_2, and thus, it will be informative to explore structures, stability diagram, and to compute N-vacant equilibrium concentrations of this phase. Calculated electronic and energy values for MoN2 surfaces could shed a light on its excellent catalytic capacity toward some reactions for example oxidation of CO into CO_2.

In Chapters 6-8, we utilised global-like model to predict chemical conversion values. It would more accurate to develop step-by-step models that take into account the entire reaction networks. This could be accomplished by kinetic modelling packages such as CHEMKIN or Cosilab.

It is important to report thermo-mechanical, electronic and optical properties of other metal nitrides compounds such as, PtN_2, Zr_3N_4 Hf_3N_4, and Ta_3N_5 that are foreseen to exist from first principles point of view.

Hydrogenation mechanisms of aromatic compounds (such as benzene) into their corresponding non-aromatic compounds (for example cyclohexane) could be studied both theoretically and experimentally over Mo-N-based catalysts. Hydrogenation of benzene could serve as a source for C_2H_2 and C_2H_4 streams. Likewise, we think it is important to re-visit oxidation of CO and NOx (into CO_2 and N_2) with a focus on radical species that form as intermediates on surfaces. This could be accomplished by sophisticated DRIFT and EPR measurements.

Similarly, it is insightful to investigate another hydrotreating processes that occur during the production of fuels. Potential chemical phenomena include the HDN of other N-bearing compounds such as pyridine as well as the hydrodeoxygenation (HDO) of guaiacol and CO hydrogenation into methanol.

Annealing temperature is an important factor to probe the stability of the synthesised coatings at elevated temperature. Thus, it is important to perform an annealing test to investigate the phase stability. Mechanical test (*via* nano-indentation) is required to assure that adding molybdenum improves the hardness and bulk modulus of parent compounds. Experimentally obtained results could then be contrasted with QHA-DFT simulated results. need to be taken into account for the synthesised Cr-Mo-N coating combined with DFT calculations.

References

[1] S.T. Oyama, Introduction to the chemistry of transition metal carbides and nitrides, in: The chemistry of transition metal carbides and nitrides, Springer, 1996, pp. 1-27.

[2] H.O. Pierson, Handbook of refractory carbides and nitrides: properties, characteristics, processing and applications, William Andrew, 1996.

[3] L. Toth, Transition metal carbides and nitrides, Elsevier, 2014.

[4] J.G. Chen, Carbide and nitride overlayers on early transition metal surfaces: preparation, characterization, and reactivities, Chem. Rev., 96 (1996) 1477-1498.

[5] D.H. Gregory, Structural families in nitride chemistry, J. Chem. Soc., Dalton Trans., (1999) 259-270.

[6] Y.-R. Luo, Handbook of bond dissociation energies in organic compounds, CRC press, 2002.

[7] W. Lengauer, Nitrides: Transition Metal Solid-State Chemistry, Wiley Online Library, 2005.

[8] C. Wang, S. Akbar, W. Chen, V. Patton, Electrical properties of high-temperature oxides, borides, carbides, and nitrides, Journal of Materials Science, 30 (1995) 1627-1641.

[9] M. Wittmer, Properties and microelectronic applications of thin films of refractory metal nitrides, J. Vac. Sci. Technol. A, 3 (1985) 1797-1803.

[10] S. Vepřek, M. Haussmann, S. Reiprich, Superhard nanocrystalline W2N/amorphous Si3N4 composite materials, J. Vac. Sci. Technol. A, 14 (1996) 46-51.

[11] U. Guler, V.M. Shalaev, A. Boltasseva, Nanoparticle plasmonics: going practical with transition metal nitrides, Mater. Today, 18 (2015) 227-237.

[12] V.N. Khabashesku, J.L. Zimmerman, J.L. Margrave, Powder synthesis and characterization of amorphous carbon nitride, Chem. Mater., 12 (2000) 3264-3270.

[13] C. Mitterer, F. Holler, F. Üstel, D. Heim, Application of hard coatings in aluminium die casting—soldering, erosion and thermal fatigue behaviour, Surf. Coat. Technol., 125 (2000) 233-239.

[14] W. Lengauer, Transition metal carbides, nitrides, and carbonitrides, Handbook of ceramic hard materials, (2000) 202-252.

[15] S. Zhang, D. Sun, Y. Fu, H. Du, Recent advances of superhard nanocomposite coatings: a review, Surf. Coat. Technol., 167 (2003) 113-119.

[16] R. Levy, M. Boudart, Platinum-like behavior of tungsten carbide in surface catalysis, science, 181 (1973) 547-549.
[17] D.J. Ham, J.S. Lee, Transition metal carbides and nitrides as electrode materials for low temperature fuel cells, Energies, 2 (2009) 873-899.
[18] A.-M. Alexander, J.S. Hargreaves, Alternative catalytic materials: carbides, nitrides, phosphides and amorphous boron alloys, Chem. Soci. Rev., 39 (2010) 4388-4401.
[19] C. Giordano, M. Antonietti, Synthesis of crystalline metal nitride and metal carbide nanostructures by sol–gel chemistry, Nano Today, 6 (2011) 366-380.
[20] L.I. Johansson, Electronic and structural properties of transition-metal carbide and nitride surfaces, Surf. Sci. Rep., 21 (1995) 177-250.
[21] G. Hägg, Gesetzmässigkeiten im kristallbau bei hydriden, boriden, carbiden und nitriden der übergangselemente, Z. Phys. Chem., 12 (1931) 33-56.
[22] H.J. Goldschmid, Interstitial alloys, Springer, 2013.
[23] S.T. Oyama, Introduction to the chemistry of transition metal carbides and nitrides, in: The chemistry of transition metal carbides and nitrides, Springer, 1996.
[24] J.S. Lee, D.J. Ham, Metal nitrides, Encyclopedia of Catalysis, (2003).
[25] W.D. Sproul, Reactively sputtered nitrides and carbides of titanium, zirconium, and hafnium, J. Vac. Sci. Technol. A, 4 (1986) 2874-2878.
[26] Z. Wu, J. Meng, Ab initio study on the physical properties of CoN3 and RhN3 with skutterudite structure, Comput. Mater. Sci., 43 (2008) 495-500.
[27] Y.G. Gogotsi, R.A. Andrievski, Materials science of carbides, nitrides and borides, Springer Science & Business Media, 2012.
[28] S. Oyama, Preparation and catalytic properties of transition metal carbides and nitrides, Catal. today, 15 (1992) 179-200.
[29] L. Brewer, Bonding and structures of transition metals, Science, 161 (1968) 115-122.
[30] W. Hume-Rothery, The Engel-Brewer theories of metals and alloys, Progress in Metal Physics, 13 (1968) 229-265.
[31] N. Koutna, D. Holec, M. Friak, P.H. Mayrhofer, M. Šob, Stability and elasticity of metastable solid solutions and superlattices in the MoN–TaN system: First-principles calculations, Materials & Design, 144 (2018) 310-322.
[32] D. Papaconstantopoulos, W. Pickett, B. Klein, L. Boyer, Electronic properties of transition-metal nitrides: The group-V and group-VI nitrides VN, NbN, TaN, CrN, MoN, and WN, Phys. Rev. B, 31 (1985) 752.

[33] F. Lévy, P. Hones, P. Schmid, R. Sanjinés, M. Diserens, C. Wiemer, Electronic states and mechanical properties in transition metal nitrides, Surf. Coat. Technol., 120 (1999) 284-290.
[34] E. Zhao, J. Wang, J. Meng, Z. Wu, Structural, mechanical and electronic properties of 4d transition metal mononitrides by first-principles, Comput. Mater. Sci., 47 (2010) 1064-1071.
[35] W.M. Latimer, J.H. Hildebrand, Reference book of inorganic chemistry, The Macmillan Company; New York, 1944.
[36] M.-A. Nicolet, Diffusion barriers in thin films, Thin Solid Films, 52 (1978) 415-443.
[37] W. Schnick, Solid-State Chemistry with Nonmetal Nitrides, Angewandte Chemie International Edition, 32 (1993) 806-818.
[38] P. Hones, N. Martin, M. Regula, F. Lévy, Structural and mechanical properties of chromium nitride, molybdenum nitride, and tungsten nitride thin films, J. Phys. D Appl. Phys., 36 (2003) 1023.
[39] E. Soignard, P.F. McMillan, T.D. Chaplin, S.M. Farag, C.L. Bull, M.S. Somayazulu, K. Leinenweber, High-pressure synthesis and study of low-compressibility molybdenum nitride (MoN and MoN 1− x) phases, Phys. Rev. B, 68 (2003) 132101.
[40] D.G. Sangiovanni, L. Hultman, V. Chirita, Supertoughening in B1 transition metal nitride alloys by increased valence electron concentration, Acta Mater., 59 (2011) 2121-2134.
[41] K. Khojier, M.R.K. Mehr, H. Savaloni, Annealing temperature effect on the mechanical and tribological properties of molybdenum nitride thin films, Journal of Nanostructure in Chemistry, 3 (2013) 5.
[42] T. Suszko, W. Gulbiński, J. Jagielski, The role of surface oxidation in friction processes on molybdenum nitride thin films, Surface and Coatings Technology, 194 (2005) 319-324.
[43] J.-Y. Lee, J.-W. Park, Diffusion barrier property of molybdenum nitride films for copper metallization, Japanese journal of applied physics, 35 (1996) 4280.
[44] W. Li, X. Yan, A.G. Aberle, S. Venkataraj, Effect of deposition pressure on the properties of magnetron-sputter-deposited molybdenum back contacts for CIGS solar cells, Japanese Journal of Applied Physics, 54 (2015) 08KC14.
[45] G. Gassner, P. Mayrhofer, K. Kutschej, C. Mitterer, M. Kathrein, Magnéli phase formation of PVD Mo–N and W–N coatings, Surf. Coat. Technol., 201 (2006) 3335-3341.
[46] C.L. Bull, T. Kawashima, P.F. McMillan, D. Machon, O. Shebanova, D. Daisenberger, E. Soignard, E. Takayama-Muromachi, L.C. Chapon, Crystal structure and high-pressure properties of γ-Mo2N determined by neutron powder diffraction and X-ray diffraction, J. Solid State Chem., 179 (2006) 1762-1767.

[47] H. Ihara, Y. Kimura, K. Senzaki, H. Kezuka, M. Hirabayashi, Electronic structures of B1 MoN, fcc Mo 2 N, and hexagonal MoN, Phys. Rev. B, 31 (1985) 3177.
[48] J. Wu, C. Wu, X. Zhong, Z. Song, F. Li, Surface nitridation of transition metals by pulsed laser irradiation in gaseous nitrogen, Surf. Coat. Technol., 96 (1997) 330-336.
[49] S. Mändl, D. Manova, J. Gerlach, W. Assmann, H. Neumann, B. Rauschenbach, High temperature nitrogen plasma immersion ion implantation into molybdenum
Surf. Coat. Technol., 180 (2004) 362-366.
[50] L. Stöber, J. Konrath, S. Krivec, F. Patocka, S. Schwarz, A. Bittner, M. Schneider, U. Schmid, Impact of sputter deposition parameters on molybdenum nitride thin film properties, J. Micromech. Microeng., 25 (2015) 074001.
[51] I. Jauberteau, J.-L. Jauberteau, P. Goudeau, B. Soulestin, M. Marteau, M. Cahoreau, J. Aubreton, Investigations on a nitriding process of molybdenum thin films exposed to (Ar–N2–H2) expanding microwave plasma, Surf. Coat. Technol., 203 (2009) 1127-1132.
[52] R. Karam, R. Ward, Preparation of. beta.-molybdenum nitride, Inorg. Chem., 9 (1970) 1385-1387.
[53] J. Lowther, Lattice model for the properties of non-stoichiometric cubic and hexagonal molybdenum nitride, J. alloys Compd., 364 (2004) 13-16.
[54] A.Y. Ganin, L. Kienle, G.V. Vajenine, Synthesis and characterisation of hexagonal molybdenum nitrides, J. Solid State Chem., 179 (2006) 2339-2348.
[55] M. Kanoun, S. Goumri-Said, M. Jaouen, Structure and mechanical stability of molybdenum nitrides: A first-principles study, Phys. Rev. B, 76 (2007) 134109.
[56] E. Zhao, J. Wang, Z. Wu, Displacive phase transition, structural stability, and mechanical properties of the ultra-incompressible and hard MoN by first principles, Phys. status solidi B, 247 (2010) 1207-1213.
[57] N. Savvides, High T c superconducting B1 phase MoN films prepared by low-energy ion-assisted deposition, J. appl. Phys., 62 (1987) 600-610.
[58] R. Marchand, F. Tessier, F.J. DiSalvo, New routes to transition metal nitrides: and characterization of new phases, J. Mater. Chem., 9 (1999) 297-304.
[59] H. Jehn, P. Ettmayer, The molybdenum-nitrogen phase diagram, J. Less Common. Met., 58 (1978) 85-98.
[60] S. Wang, D. Antonio, X. Yu, J. Zhang, A.L. Cornelius, D. He, Y. Zhao, The hardest superconducting metal nitride, Sci. Rep., 5 (2015) 13733.

[61] V. Tagliazucca, K. Schlichte, F. Schüth, C. Weidenthaler, Molybdenum-based catalysts for the decomposition of ammonia: In situ X-ray diffraction studies, microstructure, and catalytic properties, J. Catal., 305 (2013) 277-289.
[62] B. Cao, J.C. Neuefeind, R.R. Adzic, P.G. Khalifah, Molybdenum nitrides as oxygen reduction reaction catalysts: structural and electrochemical studies, Inorg. Chem., 54 (2015) 2128-2136.
[63] C.L. Bull, P.F. McMillan, E. Soignard, K. Leinenweber, Determination of the crystal structure of δ-MoN by neutron diffraction, J. Solid State Chem., 177 (2004) 1488-1492.
[64] D. Papaconstantopoulos, W. Pickett, Effects of disorder on high-temperature superconductivity in cubic MoN, Physical Review B, 31 (1985) 7093.
[65] P. Ettmayer, Das System Molybdän-Stickstoff, Montash. Chem., 101 (1970) 127-140.
[66] K. Inumaru, K. Baba, S. Yamanaka, Synthesis and Characterization of Superconducting β-Mo2N crystalline phase on a Si substrate: An application of Pulsed Laser Deposition to Nitride Chemistry, Chemistry of materials, 17 (2005) 5935-5940.
[67] I. Jauberteau, A. Bessaudou, R. Mayet, J. Cornette, J.L. Jauberteau, P. Carles, T. Merle-Méjean, Molybdenum nitride films: crystal structures, synthesis, mechanical, electrical and some other properties, Coatings, 5 (2015) 656-687.
[68] K. Inumaru, K. Baba, S. Yamanaka, Preparation of superconducting molybdenum nitride MoNx (0.5⩽ x⩽ 1) films with controlled composition, Physica B Condens Matter, 383 (2006) 84-85.
[69] K. Inumaru, K. Baba, S. Yamanaka, Structural distortion and suppression of superconductivity in stoichiometric B 1− MoN epitaxial thin films, Phys. Rev. B, 73 (2006) 052504.
[70] Y. Shen, Effect of deposition conditions on mechanical stresses and microstructure of sputter-deposited molybdenum and reactively sputter-deposited molybdenum nitride films, Mat. Sci. Eng. A, 359 (2003) 158-167.
[71] T. Kawashima, E. Takayama-Muromachi, P.F. McMillan, High-pressure synthesis and crystal structure of γ-Mo2N, Physica C, 460 (2007) 651-652.
[72] K. Inumaru, K. Baba, S. Yamanaka, Preparation of superconducting molybdenum nitride MoNx (0.5⩽ x⩽ 1) films with controlled composition, Physica B: Condensed Matter, 383 (2006) 84-85.
[73] S.-Y. Lin, Y.-S. Lai, Effect of Nitrogen on the Physical Properties and Work Function of MoNx Cap Layers on HfO2 Gate Dielectrics, ECS J. Solid State Sci. Technol., 3 (2014) N161-N165.

[74] A. Bezinge, K. Yvon, J. Muller, W. Lengaeur, P. Ettmayer, High-pressure high-temperature experiments on δ-MoN, Solid state communications, 63 (1987) 141-145.
[75] X. Zhao, K.-J. Range, High pressure synthesis of molybdenum nitride MoN, J. Alloys Compd., 296 (2000) 72-74.
[76] S. Wang, H. Ge, S. Sun, J. Zhang, F. Liu, X. Wen, X. Yu, L. Wang, Y. Zhang, H. Xu, A new molybdenum nitride catalyst with rhombohedral MoS2 structure for hydrogenation applications, J. Am. Chem. Soc., 137 (2015) 4815-4822.
[77] S. Yu, B. Huang, X. Jia, Q. Zeng, A.R. Oganov, L. Zhang, G. Frapper, Exploring the Real Ground-State Structures of Molybdenum Dinitride, J. Phys. Chem. C, 120 (2016) 11060-11067.
[78] Y. Wang, Y. Ding, The hydrogen-induced structural stability and promising electronic properties of molybdenum and tungsten dinitride nanosheets: a first-principles study, J. Mater. Chem. C, 4 (2016) 7485-7493.
[79] C. Zhang, J. Liu, H. Shen, X.-Z. Li, Q. Sun, Identifying the Ground State Geometry of a MoN2 Sheet through a Global Structure Search and Its Tunable p-Electron Half-Metallicity, Chem. Mater., 29 (2017) 8588-8593.
[80] Y. Wang, Y. Ding, A first-principles study of a real energetically stable MoN 2 nanosheet and its tunable electronic structure, J. Mater. Chem. C, 6 (2018) 2245-2251.
[81] Q. Li, L. He, C. Sun, X. Zhang, Computational Study of MoN2 Monolayer as Electrochemical Catalysts for Nitrogen Reduction, J. Phys. Chem. C, 121 (2017) 27563-27568.
[82] R. Sanjinés, C. Wiemer, J. Almeida, F. Levy, Valence band photoemission study of the Ti- Mo-N system, Thin Solid Films, 290 (1996) 334-338.
[83] K. Saito, Y. Asada, Superconductivity and structural changes of nitrogen-ion implanted Mo thin films, J. Phys. F: Met. Phys., 17 (1987) 2273.
[84] F. Klimashin, N. Koutná, H. Euchner, D. Holec, P. Mayrhofer, The impact of nitrogen content and vacancies on structure and mechanical properties of Mo–N thin films, J. Appl. Phys., 120 (2016) 185301.
[85] K. Balasubramanian, L. Huang, D. Gall, Phase stability and mechanical properties of Mo1-x N x with 0≤ x≤ 1, J. Appl. Phys., 122 (2017) 195101.
[86] D.M. Hoffman, Chemical vapour deposition of nitride thin films, Polyhedron, 13 (1994) 1169-1179.
[87] S. Roberson, D. Finello, R. Davis, Phase control of MoxN films via chemical vapor deposition, Thin Solid Films, 324 (1998) 30-36.

[88] D.M. Mattox, Handbook of physical vapor deposition (PVD) processing, William Andrew, 2010.
[89] V. Anitha, S. Major, D. Chandrashekharam, M. Bhatnagar, Deposition of molybdenum nitride thin films by rf reactive magnetron sputtering, Surf. Coat. Technol., 79 (1996) 50-54.
[90] Y. Wang, R.Y. Lin, Amorphous molybdenum nitride thin films prepared by reactive sputter deposition, Mater. Sci. Eng. B, 112 (2004) 42-49.
[91] P. Hones, N. Martin, M. Regula, F. Lévy, Structural and mechanical properties of chromium nitride, molybdenum nitride, and tungsten nitride thin films, J. Phys. Appl. Phys., 36 (2003) 1023.
[92] Y. Shen, Effect of deposition conditions on mechanical stresses and microstructure of sputter-deposited molybdenum and reactively sputter-deposited molybdenum nitride films, Mater. Sci. Eng. A, 359 (2003) 158-167.
[93] D.K. Nandi, U.K. Sen, D. Choudhury, S. Mitra, S.K. Sarkar, Atomic layer deposited molybdenum nitride thin film: a promising anode material for Li ion batteries, ACS Appl. Mater. Interfaces, 6 (2014) 6606-6615.
[94] B. Ozsdolay, X. Shen, K. Balasubramanian, G. Scannell, L. Huang, M. Yamaguchi, D. Gall, Elastic constants of epitaxial cubic MoNx (001) layers, Surf. Coat. Technol., 325 (2017) 572-578.
[95] B. Bouaouina, A. Besnard, S. Abaidia, F. Haid, Residual stress, mechanical and microstructure properties of multilayer Mo2N/CrN coating produced by RF Magnetron discharge, Appl. Surf. Sci., 395 (2017) 117-121.
[96] B. Bouaouina, A. Besnard, S. Abaidia, A. Airoudj, F. Bensouici, Correlation between mechanical and microstructural properties of molybdenum nitride thin films deposited on silicon by reactive RF magnetron discharge, Surf. Coat. Technol., 333 (2018) 32-38.
[97] M. Kommer, T. Sube, A. Richter, M. Fenker, W. Schulz, B. Hader, J. Albrecht, Enhanced wear resistance of molybdenum nitride coatings deposited by high power impulse magnetron sputtering by using micropatterned surfaces, Surf. Coat. Technol., 333 (2018) 1-12.
[98] B. Wicher, R. Chodun, K. Nowakowska-Langier, S. Okrasa, M. Trzciński, K. Król, R. Minikayev, Ł. Skowroński, Ł. Kurpaska, K. Zdunek, Relation between modulation frequency of electric power oscillation during pulse magnetron sputtering deposition of MoN x thin films, Appl. Surf. Sci., (2018).
[99] G. Durai, P. Kuppusami, J. Theerthagiri, Microstructural and supercapacitive properties of reactive magnetron co-sputtered Mo3N2 electrodes: Effects of Cu doping, Mater. Lett., 220 (2018) 201-204.

[100] M. Kazmanli, M. Ürgen, A. Cakir, Effect of nitrogen pressure, bias voltage and substrate temperature on the phase structure of Mo–N coatings produced by cathodic arc PVD, Surf. Coat. Technol., 167 (2003) 77-82.
[101] L. Stöber, J. Konrath, S. Krivec, F. Patocka, S. Schwarz, A. Bittner, M. Schneider, U. Schmid, Impact of sputter deposition parameters on molybdenum nitride thin film properties, J. Micromechanics Microengineering, 25 (2015) 074001.
[102] L. Stöber, J.P. Konrath, V. Haberl, F. Patocka, M. Schneider, U. Schmid, Nitrogen incorporation in sputter deposited molybdenum nitride thin films, Journal of Vacuum Science & Technology A: Vacuum, Surfaces, and Films, 34 (2016) 021513.
[103] J.-Y. Xiang, F.-B. Wu, Gas inlet and input power modulated sputtering molybdenum nitride thin films, Surf. Coat. Technol., 332 (2017) 161-167.
[104] J. Xiang, Z. Lin, E. Renoux, F. Wu, Microstructure evolution and indentation cracking behavior of MoN multilayer films, Surf. Coat. Technol., (2018).
[105] D. Choi, P.N. Kumta, Synthesis and Characterization of Nanostructured Niobium and Molybdenum Nitrides by a Two-Step Transition Metal Halide Approach, J. Am. Ceram. Soc., 94 (2011) 2371-2378.
[106] J. Xie, S. Li, X. Zhang, J. Zhang, R. Wang, H. Zhang, B. Pan, Y. Xie, Atomically-thin molybdenum nitride nanosheets with exposed active surface sites for efficient hydrogen evolution, Chem. Sci., 5 (2014) 4615-4620.
[107] S. Joshi, Q. Wang, A. Puntambekar, V. Chakrapani, Facile Synthesis of Large Area Two-Dimensional Layers of Transition-Metal Nitride and Their Use as Insertion Electrodes, ACS Energy Letters, 2 (2017) 1257-1262.
[108] G.D. Sun, G.H. Zhang, K.C. Chou, Synthesis of molybdenum nitrides nanosheets by nitriding 2H-MoS2 with ammonia, J. Am. Ceram. Soc., 101 (2018) 2796-2808.
[109] F. Stevens, I. Carmichael, F. Callens, M. Waroquier, Density functional investigation of high-spin XY (X= Cr, Mo, W and Y= C, N, O) molecules, J. Phys. Chem. A, 110 (2006) 4846-4853.
[110] E.I. Isaev, S.I. Simak, I. Abrikosov, R. Ahuja, Y.K. Vekilov, M. Katsnelson, A. Lichtenstein, B. Johansson, Phonon related properties of transition metals, their carbides, and nitrides: A first-principles study, J. Appl. Phys., 101 (2007) 123519.
[111] D. Holec, M. Friák, J. Neugebauer, P.H. Mayrhofer, Trends in the elastic response of binary early transition metal nitrides, Phys. Rev. B, 85 (2012) 064101.

[112] Z. Liu, X. Zhou, D. Gall, S. Khare, First-principles investigation of the structural, mechanical and electronic properties of the NbO-structured 3d, 4d and 5d transition metal nitrides, Comput. Mater. Sci., 84 (2014) 365-373.
[113] M. Altarawneh, Z. Jaf, H. Oskierski, Z.-T. Jiang, J. Gore, B.Z. Dlugogorski, Conversion of NO into N2 over γ-Mo2N, J. Phys. Chem. C, 120 (2016) 22270-22280.
[114] S. Zaman, A DFT study of CO adsorption and dissociation over γ-Mo2N (111) plane, (2010).
[115] C. Subramanian, Strafford, KN, Review of multicomponent and multilayer coatings for tribological applications, Wear, 165 (1993) 85-95.
[116] B.O. Postolnyi, V. Beresnev, G. Abadias, O. Bondar, L. Rebouta, J. Araujo, A. Pogrebnjak, Multilayer design of CrN/MoN protective coatings for enhanced hardness and toughness, J. Alloys Compd, 725 (2017) 1188-1198.
[117] B. Gu, J. Tu, X. Zheng, Y. Yang, S. Peng, Comparison in mechanical and tribological properties of Cr–W–N and Cr–Mo–N multilayer films deposited by DC reactive magnetron sputtering, Surf. Coat. Technol., 202 (2008) 2189-2193.
[118] K.H. Kim, E.Y. Choi, S.G. Hong, B.G. Park, J.H. Yoon, J.H. Yong, Syntheses and mechanical properties of Cr–Mo–N coatings by a hybrid coating system, Surf. Coat. Technol., 201 (2006) 4068-4072.
[119] C. Quintela, B. Rodríguez-González, F. Rivadulla, Thermoelectric properties of heavy-element doped CrN, Appl. Phys. Lett., 104 (2014) 022103.
[120] R. Buhl, H. Pulker, E. Moll, TiN coatings on steel, Thin Solid Films, 80 (1981) 265-270.
[121] B. Navinšek, P. Panjan, I. Milošev, Industrial applications of CrN (PVD) coatings, deposited at high and low temperatures, Surf. Coat. Technol., 97 (1997) 182-191.
[122] Y. Lv, L. Ji, X. Liu, H. Li, H. Zhou, J. Chen, Influence of substrate bias voltage on structure and properties of the CrAlN films deposited by unbalanced magnetron sputtering, Appl. Surf. Sci., 258 (2012) 3864-3870.
[123] Q. Wang, F. Zhou, J. Yan, Evaluating mechanical properties and crack resistance of CrN, CrTiN, CrAlN and CrTiAlN coatings by nanoindentation and scratch tests, Surf. Coat. Technol., 285 (2016) 203-213.
[124] S. Kim, B. Kim, G. Kim, S. Lee, B. Lee, Evaluation of the high temperature characteristics of the CrZrN coatings, Surf. Coat. Technol., 202 (2008) 5521-5525.
[125] P. Hones, R. Consiglio, N. Randall, F. Leacutevy, Mechanical properties of hard chromium tungsten nitride coatings, Surf. Coat. Technol., 125 (2000) 179-184.

[126] D. Qi, H. Lei, T. Wang, Z. Pei, J. Gong, C. Sun, Mechanical, microstructural and tribological properties of reactive magnetron sputtered Cr–Mo–N films, J. Mater. Sci. Technol., 31 (2015) 55-64.
[127] L. Volpe, M. Boudart, Compounds of molybdenum and tungsten with high specific surface area: I. Nitrides, J. Solid State Chem., 59 (1985) 332-347.
[128] J.-G. Choi, R.L. Curl, L.T. Thompson, Molybdenum nitride catalysts: I. Influence of the synthesis factors on structural properties, J. Catal., 146 (1994) 218-227.
[129] J.B. Claridge, A.P. York, A.J. Brungs, M.L. Green, Study of the temperature-programmed reaction synthesis of early transition metal carbide and nitride catalyst materials from oxide precursors, Chem. Mater., 12 (2000) 132-142.
[130] C.H. Jaggers, J.N. Michaels, A.M. Stacy, Preparation of high-surface-area transition-metal nitrides: molybdenum nitrides, Mo2N and MoN, Chem. Mater., 2 (1990) 150-157.
[131] D. Mckay, Catalysis over molybdenum containing nitride materials, in, University of Glasgow, 2008.
[132] R. Marchand, X. Gouin, F. Tessier, Y. Laurent, New routes to molybdenum nitrides and oxynitrides: preparation and characterization of new phases, in: The Chemistry of Transition Metal Carbides and Nitrides, Springer, 1996, pp. 252-273.
[133] D. Mckay, J. Hargreaves, J. Rico, J. Rivera, X.-L. Sun, The influence of phase and morphology of molybdenum nitrides on ammonia synthesis activity and reduction characteristics, J. Solid State Chem., 181 (2008) 325-333.
[134] G. Haddix, D. Jones, J. Reimer, A. Bell, Characterization of NH3 adsorbed on γ-Mo2N by NMR spectroscopy, J. Catal., 112 (1988) 556-564.
[135] G. Ranhotra, G. Haddix, A. Bell, J. Reimer, Catalysis over molybdenum carbides and nitrides: I. Catalyst characterization, J. Catal., 108 (1987) 24-39.
[136] A. Roy, A. Serov, K. Artyushkova, E.L. Brosha, P. Atanassov, T.L. Ward, Facile synthesis of high surface area molybdenum nitride and carbide, J. Solid State Chem., 228 (2015) 232-238.
[137] E. Markel, J. Van Zee, Catalytic hydrodesulfurization by molybdenum nitride, J. Catal., 126 (1990) 643-657.
[138] C.W. Colling, J.-G. Choi, L.T. Thompson, Molybdenum Nitride Catalysts: II. H2Temperature Programmed Reduction and NH3Temperature Programmed Desorption, J. Catal., 160 (1996) 35-42.
[139] E. Furimsky, Metal carbides and nitrides as potential catalysts for hydroprocessing, Appl. Catal. A: Gen., 240 (2003) 1-28.

[140] R. Wise, E. Markel, Synthesis of high surface area molybdenum nitride in mixtures of nitrogen and hydrogen, J. Catal., 145 (1994) 344-355.
[141] S. Li, W.B. Kim, J.S. Lee, Effect of the reactive gas on the solid-state transformation of molybdenum trioxide to carbides and nitrides, Chem. Mater., 10 (1998) 1853-1862.
[142] A. Cairns, J. Gallagher, J. Hargreaves, D. Mckay, J. Rico, K. Wilson, The effect of low levels of dopants upon the formation and properties of beta-phase molybdenum nitride, J. Solid State Chem., 183 (2010) 613-619.
[143] A. Cairns, J. Gallagher, J. Hargreaves, D. Mckay, E. Morrison, J. Rico, K. Wilson, The influence of precursor source and thermal parameters upon the formation of beta-phase molybdenum nitride, J. Alloys Compd., 479 (2009) 851-854.
[144] H. Xu, H. Zhang, L. Fang, J. Yang, K. Wu, Y. Wang, Hierarchical molybdenum nitride nanochexes by a textured self-assembly in gas–solid phase for the enhanced application in lithium ion batteries, ACS nano, 9 (2015) 6817-6825.
[145] X.S. Li, Y.J. Zhang, Q. Xin, C.X. Ji, Y.F. Miao, L. Wang, Irreversible hydrogen uptake on Mo 2 N catalyst, React. Kinet. Catal. Lett., 57 (1996) 177-182.
[146] G. Haddix, J. Reimer, A. Bell, Characterization of H2 adsorbed on γ-Mo2N by NMR spectroscopy, J. Catal., 108 (1987) 50-54.
[147] R. Bafrali, A.T. Bell, Interactions of H2 and NH3 with Mo (100) and Mo (100)-c (2× 2) N surfaces, Surf. Sci., 278 (1992) 353-363.
[148] X.S. Li, Y.X. Chen, Y.J. Zhang, C.X. Ji, Q. Xin, Temperature-programmed desorption and adsorption of hydrogen on Mo 2 N, React. Kinet. Catal. Lett., 58 (1996) 391-396.
[149] Y. Zhang, Y. Li, C. Li, Q. Xin, Adsorption and migration of hydrogen on different surface sites of γ-Mo2N catalyst, in: Stud. Surf. Sci. Catal., Elsevier, 1997, pp. 457-464.
[150] J.-G. Choi, J.R. Brenner, C.W. Colling, B.G. Demczyk, J.L. Dunning, L.T. Thompson, Synthesis and characterization of molybdenum nitride hydrodenitrogenation catalysts, Catal. Today, 15 (1992) 201-222.
[151] S. Yang, C. Li, J. Xu, Q. Xin, Surface sites of alumina-supported molybdenum nitride characterized by FTIR, TPD-MS, and volumetric chemisorption, J. Phys. Chem. B, 102 (1998) 6986-6993.
[152] G. Frapper, M. Pelissier, J. Hafner, CO Adsorption on Molybdenum Nitride's γ-Mo2N (100) Surface: Formation of NCO Species? A Density Functional Study, J. Phys. Chem. B, 104 (2000) 11972-11976.
[153] A. Eichler, CO oxidation on transition metal surfaces: reaction rates from first principles, Surf. Sci., 498 (2002) 314-320.

[154] G. Frapper, M. Pélissier, J. Hafner, CO Adsorption on Molybdenum Nitride's γ-Mo2N (100) Surface: Formation of NCO Species? A Density Functional Study, J. Phys. Chem. B, 104 (2000) 11972-11976.
[155] M. Hillis, C. Kemball, M. Roberts, Synthesis of ammonia and related processes on reduced molybdenum dioxide, Trans. Faraday Soc., 62 (1966) 3570-3585.
[156] K.-i. Aika, A. Ozaki, Mechanism and isotope effect in ammonia synthesis over molybdenum nitride, J. Catal., 14 (1969) 311-321.
[157] S.M. Hunter, D. Mckay, R.I. Smith, J.S. Hargreaves, D.H. Gregory, Topotactic nitrogen transfer: structural transformation in cobalt molybdenum nitrides, Chem. Mater., 22 (2010) 2898-2907.
[158] C.D. Zeinalipour-Yazdi, J.S. Hargreaves, C.R.A. Catlow, Nitrogen activation in a Mars–van Krevelen mechanism for ammonia synthesis on Co3Mo3N, J. Phys. Chem. C, 119 (2015) 28368-28376.
[159] M. Neylon, S. Choi, H. Kwon, K. Curry, L. Thompson, Catalytic properties of early transition metal nitrides and carbides: n-butane hydrogenolysis, dehydrogenation and isomerization, Appl. Catal. A: Gen., 183 (1999) 253-263.
[160] W.-F. Chen, J.T. Muckerman, E. Fujita, Recent developments in transition metal carbides and nitrides as hydrogen evolution electrocatalysts, Chem. Commun., 49 (2013) 8896-8909.
[161] V.R.B. Gurram, S.S. Enumula, R.R. Chada, K.S. Koppadi, D.R. Burri, S.R.R. Kamaraju, Synthesis and Industrial Catalytic Applications of Binary and Ternary Molybdenum Nitrides: A Review, Catal. Surv. Asia, (2018) 1-15.
[162] I. Ghampson, C. Sepúlveda, R. Garcia, B. Frederick, M. Wheeler, N. Escalona, W. DeSisto, Guaiacol transformation over unsupported molybdenum-based nitride catalysts, Appl. Catal. A: Gen., 413 (2012) 78-84.
[163] R. Kojima, K.-i. Aika, Molybdenum nitride and carbide catalysts for ammonia synthesis, Appl. Catal. A: Gen, 219 (2001) 141-147.
[164] K. Balasubramanian, S.V. Khare, D. Gall, Energetics of point defects in rocksalt structure transition metal nitrides: thermodynamic reasons for deviations from stoichiometry, Acta Mater., (2018).
[165] E. Markel, J. Van Zee, Catalytic hydrodesulfurization by molybdenum nitride, Journal of Catalysis, 126 (1990) 643-657.
[166] W.F. Chen, K. Sasaki, C. Ma, A.I. Frenkel, N. Marinkovic, J.T. Muckerman, Y. Zhu, R.R. Adzic, Hydrogen-Evolution Catalysts Based on Non-Noble Metal Nickel–Molybdenum Nitride Nanosheets, Angewandte Chemie International Edition, 51 (2012) 6131-6135.

[167] D. Liu, Y. Liu, T. Zhou, C. Liu, G. Que, IN SITU FT-IR STUDY OF CO HYDROGENATION ON A MOLYBDENUM NITRIDE CATALYST, Prepr. Pap.-Am. Chem. Soc., Div. Fuel Chem, 48 (2003) 506.

[168] F. Cardenas-Lizana, S. Gomez-Quero, N. Perret, L. Kiwi-Minsker, M.A. Keane, β-Molybdenum nitride: synthesis mechanism and catalytic response in the gas phase hydrogenation of p-chloronitrobenzene, Catal. Sci. Technol., 1 (2011) 794-801.

[169] G. Dolce, P. Savage, L. Thompson, Hydrotreatment activities of supported molybdenum nitrides and carbides, Energy Fuels, 11 (1997) 668-675.

[170] M. Nagai, Transition-metal nitrides for hydrotreating catalyst—Synthesis, surface properties, and reactivities, Appl. Catal. A: Gen., 322 (2007) 178-190.

[171] J. Hargreaves, Heterogeneous catalysis with metal nitrides, Coord. Chem. Rev., 257 (2013) 2015-2031.

[172] S.T. Oyama, Crystal structure and chemical reactivity of transition metal carbides and nitrides, J. solid state chem., 96 (1992) 442-445.

[173] V. Heine, s− d Interaction in Transition Metals, Phys. Rev., 153 (1967) 673.

[174] W.-F. Chen, J.T. Muckerman, E. Fujita, Recent developments in transition metal carbides and nitrides as hydrogen evolution electrocatalysts, Chem. Comm., 49 (2013) 8896-8909.

[175] G. Haddix, J. Reimer, A. Bell, Characterization of H2 adsorbed on γ-Mo2N by NMR spectroscopy, Journal of Catalysis, 108 (1987) 50-54.

[176] E. Furimsky, Metal carbides and nitrides as potential catalysts for hydroprocessing, Appl Catal A: Gen, 240 (2003) 1-28.

[177] Z. Hao, Z. Wei, L. Wang, X. Li, C. Li, E. Min, Q. Xin, Selective hydrogenation of ethyne on γ-Mo_2N, Appl. Catal., A, 192 (2000) 81-84.

[178] G. Bond, G. Webb, P. Wells, J. Winterbottom, Patterns of behavior in catalysis by metals, J. Catal., 1 (1962) 74-84.

[179] F. Cárdenas-Lizana, D. Lamey, L. Kiwi-Minsker, M.A. Keane, Molybdenum nitrides: a study of synthesis variables and catalytic performance in acetylene hydrogenation, J. Mater. Sci., 53 (2018) 6707-6718.

[180] Z. Wu, Z. Hao, P. Ying, C. Li, Q. Xin, An IR study on selective hydrogenation of 1, 3-butadiene on transition metal nitrides: 1, 3-butadiene and 1-butene adsorption on Mo_2N/γ-Al_2O_3 catalyst, J. Phys. Chem. B, 104 (2000) 12275-12281.

[181] Z. Wu, Z. Hao, Z. Wei, C. Li, Q. Xin, Selective hydrogenation of 1, 3-butadiene on molybdenum nitride catalyst: identification of the adsorbed hydrocarbonaceous species, in: Stud. Surf. Sci. Catal., Elsevier, 2001, pp. 445-452.

[182] A. Valcárcel, A. Clotet, J.M. Ricart, F. Delbecq, P. Sautet, Selectivity control for the catalytic 1, 3-butadiene hydrogenation on Pt (111) and Pd (111) surfaces: Radical versus closed-shell intermediates, J. Phys. Chem. B, 109 (2005) 14175-14182.

[183] I. Babich, J. Moulijn, Science and technology of novel processes for deep desulfurization of oil refinery streams: a review☆, Fuel, 82 (2003) 607-631.

[184] P.A. Aegerter, W.W. Quigley, G.J. Simpson, D.D. Ziegler, J.W. Logan, K.R. McCrea, S. Glazier, M.E. Bussell, Thiophene hydrodesulfurization over alumina-supported molybdenum carbide and nitride catalysts: adsorption sites, catalytic activities, and nature of the active surface, J. Catal., 164 (1996) 109-121.

[185] M. Nagai, T. Miyao, T. Tuboi, Hydrodesulfurization of dibenzothiophene on alumina-supported molybdenum nitride, Catal. Lett., 18 (1993) 9-14.

[186] K.R. McCrea, J.W. Logan, T.L. Tarbuck, J.L. Heiser, M.E. Bussell, Thiophene hydrodesulfurization over alumina-supported molybdenum carbide and nitride catalysts: Effect of Mo loading and phase, J. Catal., 171 (1997) 255-267.

[187] U.S. Ozkan, L. Zhang, P.A. Clark, Performance and postreaction characterization of γ-Mo2N catalysts in simultaneous hydrodesulfurization and hydrodenitrogenation reactions, J. Catal., 172 (1997) 294-306.

[188] H.K. Park, J.K. Lee, J.K. Yoo, E.S. Ko, K.L. Kim, Surface properties and reactivity of supported and unsupported molybdenum nitride catalysts, Appl. Catal. A: Gen., 150 (1997) 21-35.

[189] Y. Liu, C. Liu, G. Que, Hydrodesulfurization of dibenzothiophene over cobalt− molybdenum nitride catalysts, Energy fuels, 16 (2002) 531-535.

[190] S. Ramanathan, S.T. Oyama, New catalysts for hydroprocessing: transition metal carbides and nitrides, J. Phys. Chem., 99 (1995) 16365-16372.

[191] M. Pietrowski, M. Zieliński, M. Wojciechowska, High-Selectivity Hydrogenation of Chloronitrobenzene to Chloroaniline Over Magnesium Fluoride-Supported Bimetallic Ruthenium-Copper Catalysts, Chem. Cat. Chem, 3 (2011) 835-838.

[192] F. Cárdenas-Lizana, Y. Hao, M. Crespo-Quesada, I. Yuranov, X. Wang, M.A. Keane, L. Kiwi-Minsker, Selective gas phase hydrogenation of p-chloronitrobenzene over Pd catalysts: role of the support, ACS Catal., 3 (2013) 1386-1396.

[193] H. Chen, D. He, Q. He, P. Jiang, G. Zhou, W. Fu, Selective hydrogenation of p-chloronitrobenzene over an Fe promoted Pt/AC catalyst, RSC Adv., 7 (2017) 29143-29148.

[194] L. Zhang, Z. Ni, J. Xue, H. Qian, Y. Liu, C. Jin, Selective hydrogenation of p-chloronitrobenzene on nanosized gold clusters: A theoretical study, Chem. Phys. Lett., 703 (2018) 23-28.
[195] X. Meng, H. Cheng, S.-i. Fujita, Y. Hao, Y. Shang, Y. Yu, S. Cai, F. Zhao, M. Arai, Selective hydrogenation of chloronitrobenzene to chloroaniline in supercritical carbon dioxide over Ni/TiO2: Significance of molecular interactions, J. Catal., 269 (2010) 131-139.
[196] S. Jujjuri, F. Cárdenas-Lizana, M.A. Keane, Synthesis of group VI carbides and nitrides: application in catalytic hydrodechlorination, J. Mater. Sci., 49 (2014) 5406-5417.
[197] S. Wang, H. Ge, W. Han, Y. Li, J. Zhang, X. Yu, J. Qin, Z. Quan, X. Wen, X. Li, Synthesis of Onion-Like δ-MoN Catalyst for Selective Hydrogenation, J. Phys. Chem. C, 121 (2017) 19451-19460.
[198] G. Perot, The reactions involved in hydrodenitrogenation, Catal. Today, 10 (1991) 447-472.
[199] H.F. Rase, Handbook of commercial catalysts: heterogeneous catalysts, CRC press, 2016.
[200] J.C. Schlatter, S.T. Oyama, J.E. Metcalfe III, J.M. Lambert Jr, Catalytic behavior of selected transition metal carbides, nitrides, and borides in the hydrodenitrogenation of quinoline, Ind. Eng. Chem. Res., 27 (1988) 1648-1653.
[201] K.S. Lee, H. Abe, J. Reimer, A. Bell, Hydrodenitrogenation of quinoline over high-surface-area Mo2N, J. Catal., 139 (1993) 34-40.
[202] L. Senzi, J.S. Lee, Molybdenum nitride and carbide prepared from heteropolyacid: II. Hydrodenitrogenation of indole, J. Catal., 173 (1998) 134-144.
[203] S. Li, J.S. Lee, T. Hyeon, K.S. Suslick, Catalytic hydrodenitrogenation of indole over molybdenum nitride and carbides with different structures, Appl. Catal. A: Gen., 184 (1999) 1-9.
[204] M. Nagai, Y. Goto, A. Irisawa, S. Omi, Catalytic activity and surface properties of nitrided molybdena–alumina for carbazole hydrodenitrogenation, J. Catal., 191 (2000) 128-137.
[205] M. Nagai, T. Miyao, Activity of alumina-supported molybdenum nitride for carbazole hydrodenitrogenation, Catal. Lett., 15 (1992) 105-109.
[206] X. Chen, T. Zhang, M. Zheng, Z. Wu, W. Wu, C. Li, The reaction route and active site of catalytic decomposition of hydrazine over molybdenum nitride catalyst, J. Catal., 224 (2004) 473-478.
[207] E. Furimsky, Catalytic hydrodeoxygenation, Appl. Catal. A: Gen., 199 (2000) 147-190.

[208] O. Şenol, T.-R. Viljava, A. Krause, Hydrodeoxygenation of methyl esters on sulphided NiMo/γ-Al2O3 and CoMo/γ-Al2O3 catalysts, Catal. Today, 100 (2005) 331-335.
[209] I.T. Ghampson, C. Sepúlveda, R. Garcia, L.R. Radovic, J.G. Fierro, W.J. DeSisto, N. Escalona, Hydrodeoxygenation of guaiacol over carbon-supported molybdenum nitride catalysts: Effects of nitriding methods and support properties, Appl. Catal. A: Gen., 439 (2012) 111-124.
[210] I.T. Ghampson, C. Sepúlveda, R. Garcia, J.G. Fierro, N. Escalona, W.J. DeSisto, Comparison of alumina-and SBA-15-supported molybdenum nitride catalysts for hydrodeoxygenation of guaiacol, Appl. Catal. A: Gen., 435 (2012) 51-60.
[211] C. Sepúlveda, K. Leiva, R. García, L. Radovic, I. Ghampson, W. DeSisto, J.G. Fierro, N. Escalona, Hydrodeoxygenation of 2-methoxyphenol over Mo2N catalysts supported on activated carbons, Catal. Today, 172 (2011) 232-239.
[212] N.S. Lewis, D.G. Nocera, Powering the planet: Chemical challenges in solar energy utilization, Proc. Natl. Acad. Sci. USA, 103 (2006) 15729-15735.
[213] H.B. Gray, Powering the planet with solar fuel, Nat. Chem., 1 (2009) 7.
[214] F. Mueller-Langer, E. Tzimas, M. Kaltschmitt, S. Peteves, Techno-economic assessment of hydrogen production processes for the hydrogen economy for the short and medium term, Int. J. Hydrog. Energy, 32 (2007) 3797-3810.
[215] J.R. McKone, S.C. Marinescu, B.S. Brunschwig, J.R. Winkler, H.B. Gray, Earth-abundant hydrogen evolution electrocatalysts, Chem. Sci., 5 (2014) 865-878.
[216] J.R. McKone, N.S. Lewis, H.B. Gray, Will solar-driven water-splitting devices see the light of day?, Chem. Mater., 26 (2013) 407-414.
[217] M.-S. Balogun, W. Qiu, W. Wang, P. Fang, X. Lu, Y. Tong, Recent advances in metal nitrides as high-performance electrode materials for energy storage devices, J. Mater. Chem. A, 3 (2015) 1364-1387.
[218] J. Greeley, J.K. Nørskov, L.A. Kibler, A.M. El-Aziz, D.M. Kolb, Hydrogen evolution over bimetallic systems: Understanding the trends, ChemPhysChem, 7 (2006) 1032-1035.
[219] C.-J. Yang, An impending platinum crisis and its implications for the future of the automobile, Energy Policy, 37 (2009) 1805-1808.
[220] T.F. Jaramillo, K.P. Jørgensen, J. Bonde, J.H. Nielsen, S. Horch, I. Chorkendorff, Identification of active edge sites for electrochemical H2 evolution from MoS2 nanocatalysts, Science, 317 (2007) 100-102.

[221] D.V. Esposito, S.T. Hunt, A.L. Stottlemyer, K.D. Dobson, B.E. McCandless, R.W. Birkmire, J.G. Chen, Low-Cost Hydrogen-Evolution Catalysts Based on Monolayer Platinum on Tungsten Monocarbide Substrates, Angew. Chem. Int. Ed., 49 (2010) 9859-9862.
[222] P.D. Tran, A. Le Goff, J. Heidkamp, B. Jousselme, N. Guillet, S. Palacin, H. Dau, M. Fontecave, V. Artero, Noncovalent Modification of Carbon Nanotubes with Pyrene-Functionalized Nickel Complexes: Carbon Monoxide Tolerant Catalysts for Hydrogen Evolution and Uptake, Angew. Chem., 123 (2011) 1407-1410.
[223] J.R. McKone, E.L. Warren, M.J. Bierman, S.W. Boettcher, B.S. Brunschwig, N.S. Lewis, H.B. Gray, Evaluation of Pt, Ni, and Ni–Mo electrocatalysts for hydrogen evolution on crystalline Si electrodes, Energy Environ. Sci., 4 (2011) 3573-3583.
[224] W.F. Chen, K. Sasaki, C. Ma, A.I. Frenkel, N. Marinkovic, J.T. Muckerman, Y. Zhu, R.R. Adzic, Hydrogen-Evolution Catalysts Based on Non-Noble Metal Nickel–Molybdenum Nitride Nanosheets, Angew. Chem. Int. Ed., 51 (2012) 6131-6135.
[225] W.-F. Chen, S. Iyer, S. Iyer, K. Sasaki, C.-H. Wang, Y. Zhu, J.T. Muckerman, E. Fujita, Biomass-derived electrocatalytic composites for hydrogen evolution, Energy Environ. Sci., 6 (2013) 1818-1826.
[226] W.F. Chen, J.M. Schneider, K. Sasaki, C.H. Wang, J. Schneider, S. Iyer, S. Iyer, Y. Zhu, J.T. Muckerman, E. Fujita, Tungsten carbide–nitride on graphene nanoplatelets as a durable hydrogen evolution electrocatalyst, ChemSusChem, 7 (2014) 2414-2418.
[227] B.N. Chapman, Glow discharge processes: sputtering and plasma etching, Wiley, 1980.
[228] R.A. Powell, S. Rossnagel, PVD for Microelectronics: Sputter Deposition Applied to Semiconductor Manufacturing (Thin Films), Academic Press, London, 1999.
[229] P.D. Townsend, J.C. Kelly, N.E.W. Hartley, Ion implantation, sputtering and their applications, Academic Press, 1976.
[230] J.R. Jennings, Catalytic ammonia synthesis: fundamentals and practice, Springer Science & Business Media, 2013.
[231] J.W. Erisman, M.A. Sutton, J. Galloway, Z. Klimont, W. Winiwarter, How a century of ammonia synthesis changed the world, Nat. Geosci., 1 (2008) 636.
[232] J. Hargreaves, Nitrides as ammonia synthesis catalysts and as potential nitrogen transfer reagents, Applied Petrochemical Research, 4 (2014) 3-10.
[233] A. Mittasch, W. Frankenburg, Early studies of multicomponent catalysts, in: Advances in catalysis, Elsevier, 1950, pp. 81-104.
[234] C. Liang, W. Li, Z. Wei, Q. Xin, C. Li, Catalytic decomposition of ammonia over nitrided MoNx/α-Al2O3 and NiMoNy/α-Al2O3 catalysts, Ind. Eng. Chem. Res., 39 (2000) 3694-3697.

[235] W. Zheng, T.P. Cotter, P. Kaghazchi, T. Jacob, B. Frank, K. Schlichte, W. Zhang, D.S. Su, F. Schüth, R. Schlögl, Experimental and theoretical investigation of molybdenum carbide and nitride as catalysts for ammonia decomposition, J. Am. Chem. Soc., 135 (2013) 3458-3464.
[236] S. Podila, S.F. Zaman, H. Driss, Y.A. Alhamed, A.A. Al-Zahrani, L.A. Petrov, Hydrogen production by ammonia decomposition using high surface area Mo 2 N and Co 3 Mo 3 N catalysts, Catal. Sci. Technol., 6 (2016) 1496-1506.
[237] J. Rostrupnielsen, J.B. Hansen, CO2-reforming of methane over transition metals, J. Catal., 144 (1993) 38-49.
[238] D. Pakhare, J. Spivey, A review of dry (CO 2) reforming of methane over noble metal catalysts, Chem. Soc. Rev., 43 (2014) 7813-7837.
[239] X. Fu, H. Su, W. Yin, Y. Huang, X. Gu, Bimetallic molybdenum nitride Co 3 Mo 3 N: a new promising catalyst for CO 2 reforming of methane, Catal. Sci. Technol., 7 (2017) 1671-1678.
[240] B.C. Steele, A. Heinzel, Materials for fuel-cell technologies, in: Materials For Sustainable Energy: A Collection of Peer-Reviewed Research and Review Articles from Nature Publishing Group, World Scientific, 2011, pp. 224-231.
[241] D. Xia, S. Liu, Z. Wang, G. Chen, L. Zhang, L. Zhang, S.R. Hui, J. Zhang, Methanol-tolerant MoN electrocatalyst synthesized through heat treatment of molybdenum tetraphenylporphyrin for four-electron oxygen reduction reaction, J. Power Sources, 177 (2008) 296-302.
[242] J. Qi, L. Jiang, Q. Jiang, S. Wang, G. Sun, Theoretical and experimental studies on the relationship between the structures of molybdenum nitrides and their catalytic activities toward the oxygen reduction reaction, J. Phys. Chem. C, 114 (2010) 18159-18166.
[243] E. Schrödinger, Quantisierung als eigenwertproblem, Ann. phys., 385 (1926) 437-490.
[244] I.N. Levine, D.H. Busch, H. Shull, Quantum chemistry, Prentice Hall Upper Saddle River, NJ, 2000.
[245] E.K. Gross, R.M. Dreizler, Density functional theory, Springer Science & Business Media, 2013.
[246] N. March, The Thomas-Fermi approximation in quantum mechanics, Adv. Phys., 6 (1957) 1-101.
[247] J. Pérez-Jordá, A.D. Becke, A density-functional study of van der Waals forces: rare gas diatomics, Chem. Phys. Lett., 233 (1995) 134-137.

[248] S. Grimme, Semiempirical GGA-type density functional constructed with a long-range dispersion correction, J. Comput. Chem., 27 (2006) 1787-1799.
[249] P. Jurečka, J. Černý, P. Hobza, D.R. Salahub, Density functional theory augmented with an empirical dispersion term. Interaction energies and geometries of 80 noncovalent complexes compared with ab initio quantum mechanics calculations, J. Comput. Chem., 28 (2007) 555-569.
[250] F. Ortmann, F. Bechstedt, W. Schmidt, Semiempirical van der Waals correction to the density functional description of solids and molecular structures, Phys. Rev. B, 73 (2006) 205101.
[251] A. Tkatchenko, M. Scheffler, Accurate molecular van der Waals interactions from ground-state electron density and free-atom reference data, Phys. Rev. lett., 102 (2009) 073005.
[252] R.M. Martin, Electronic structure: basic theory and practical methods, Cambridge university press, 2004.
[253] M. Popov, V. Razumovskiy, A. Reyes-Huamantinco, L. Romaner, J. Spitaler, Ab initio Calculations as a Tool for Predicting Materials Properties, BHM Berg-und Hüttenmännische Monatshefte, 159 (2014) 367-370.
[254] J.F. Nye, Physical properties of crystals, Clarendon press, 1985.
[255] G. Simmons, H. Wang, Single crystal elastic constants and calculated aggregate properties, (1971).
[256] G. Grimvall, Thermophysical properties of materials, Elsevier, 1999.
[257] G. Lu, E. Kaxiras, An overview of multiscale simulations of materials, arXiv preprint cond-mat/0401073, (2004).
[258] S. Krukowski, P. Kempisty, A.F. Jalbout, Thermodynamic and kinetic approach in density functional theory studies of microscopic structure of GaN (0001) surface in ammonia-rich conditions, The Journal of chemical physics, 129 (2008) 234705.
[259] A. Soon, L. Wong, M. Lee, M. Todorova, B. Delley, C. Stampfl, Nitrogen adsorption and thin surface nitrides on Cu (1 1 1) from first-principles, Surface Science, 601 (2007) 4775-4785.
[260] M.W. Chase Jr, NIST-JANAF thermochemical tables, J. Phys. Chem. Ref. Data, Monograph, 9 (1998).
[261] A. Togo, I. Tanaka, First principles phonon calculations in materials science, Scripta Materialia, 108 (2015) 1-5.
[262] M.T. Dove, M.T. Dove, Introduction to lattice dynamics, Cambridge university press, 1993.

[263] A.A. Maradudin, E.W. Montroll, G.H. Weiss, I. Ipatova, Theory of lattice dynamics in the harmonic approximation, Academic press New York, 1963.
[264] G.P. Srivastava, The physics of phonons, CRC press, 1990.
[265] A. Wang, S.-L. Shang, M. He, Y. Du, L. Chen, R. Zhang, D. Chen, B. Fan, F. Meng, Z.-K. Liu, Temperature-dependent elastic stiffness constants of fcc-based metal nitrides from first-principles calculations, Journal of Materials Science, 49 (2014) 424-432.
[266] D. Alfè, PHON: A program to calculate phonons using the small displacement method, Computer Physics Communications, 180 (2009) 2622-2633.
[267] H. Eyring, The activated complex in chemical reactions, The Journal of Chemical Physics, 3 (1935) 107-115.
[268] K.J. Laidler, M.C. King, Development of transition-state theory, The Journal of physical chemistry, 87 (1983) 2657-2664.
[269] T.A. Halgren, W.N. Lipscomb, The synchronous-transit method for determining reaction pathways and locating molecular transition states, Chemical Physics Letters, 49 (1977) 225-232.
[270] K.J. Laidler, The development of the Arrhenius equation, Journal of Chemical Education, 61 (1984) 494.
[271] X. Gonze, B. Amadon, P.-M. Anglade, J.-M. Beuken, F. Bottin, P. Boulanger, F. Bruneval, D. Caliste, R. Caracas, M. Côté, ABINIT: First-principles approach to material and nanosystem properties, Comput. Phys. Commun., 180 (2009) 2582-2615.
[272] P. Giannozzi, S. Baroni, N. Bonini, M. Calandra, R. Car, C. Cavazzoni, D. Ceresoli, G.L. Chiarotti, M. Cococcioni, I. Dabo, QUANTUM ESPRESSO: a modular and open-source software project for quantum simulations of materials, Journal of physics: Condensed matter, 21 (2009) 395502.
[273] G.t. Te Velde, F.M. Bickelhaupt, E.J. Baerends, C. Fonseca Guerra, S.J. van Gisbergen, J.G. Snijders, T. Ziegler, Chemistry with ADF, Journal of Computational Chemistry, 22 (2001) 931-967.
[274] B. Delley, An all-electron numerical method for solving the local density functional for polyatomic molecules, J. Chem. Phys., 92 (1990) 508-517.
[275] R. Dovesi, R. Orlando, A. Erba, C.M. Zicovich-Wilson, B. Civalleri, S. Casassa, L. Maschio, M. Ferrabone, M. De La Pierre, P. D'Arco, CRYSTAL14: A program for the ab initio investigation of crystalline solids, International Journal of Quantum Chemistry, 114 (2014) 1287-1317.

[276] M. Segall, P.J. Lindan, M.a. Probert, C. Pickard, P.J. Hasnip, S. Clark, M. Payne, First-principles simulation: ideas, illustrations and the CASTEP code, J. Phys. Condens. Matter, 14 (2002) 2717.
[277] G. Kresse, J. Furthmüller, Efficient iterative schemes for ab initio total-energy calculations using a plane-wave basis set, Physical review B, 54 (1996) 11169.
[278] B. Delley, An all-electron numerical method for solving the local density functional for polyatomic molecules, J. Chem.Phys., 92 (1990) 508-517.
[279] S.H. Vosko, L. Wilk, M. Nusair, Accurate spin-dependent electron liquid correlation energies for local spin density calculations: a critical analysis, Can. J. Phys., 58 (1980) 1200-1211.
[280] J.P. Perdew, Y. Wang, Accurate and simple analytic representation of the electron-gas correlation energy, Phys. Rev. B, 45 (1992) 13244.
[281] A.D. Becke, A multicenter numerical integration scheme for polyatomic molecules, J. Chem. Phys., 88 (1988) 2547-2553.
[282] J.P. Perdew, K. Burke, M. Ernzerhof, Generalized gradient approximation made simple, Phys. Rev. Lett., 77 (1996) 3865.
[283] B. Hammer, L.B. Hansen, J.K. Nørskov, Improved adsorption energetics within density-functional theory using revised Perdew-Burke-Ernzerhof functionals, Phys. Rev. B, 59 (1999) 7413.
[284] J.P. Perdew, A. Ruzsinszky, G.I. Csonka, O.A. Vydrov, G.E. Scuseria, L.A. Constantin, X. Zhou, K. Burke, Restoring the density-gradient expansion for exchange in solids and surfaces, Phys. Rev. Lett., 100 (2008) 136406.
[285] A.D. Boese, N.C. Handy, A new parametrization of exchange–correlation generalized gradient approximation functionals, J. Chem. Phys., 114 (2001) 5497-5503.
[286] C. Lee, W. Yang, R.G. Parr, Development of the Colle-Salvetti correlation-energy formula into a functional of the electron density, Phys. Rev. B, 37 (1988) 785.
[287] P. Stephens, F. Devlin, C. Chabalowski, M.J. Frisch, Ab initio calculation of vibrational absorption and circular dichroism spectra using density functional force fields, J. Phys. Chem., 98 (1994) 11623-11627.
[288] A.D. Becke, Density-functional thermochemistry. III. The role of exact exchange, J. Chem. Phys., 98 (1993) 5648-5652.
[289] M. Dolg, U. Wedig, H. Stoll, H. Preuss, Energy-adjusted abinitio pseudopotentials for the first row transition elements, J. Chem. Phys., 86 (1987) 866-872.

[290] A. Bergner, M. Dolg, W. Küchle, H. Stoll, H. Preuß, Ab initio energy-adjusted pseudopotentials for elements of groups 13–17, Mol. Phys., 80 (1993) 1431-1441.
[291] B. Delley, Hardness conserving semilocal pseudopotentials, Phys. Rev. B, 66 (2002) 155125.
[292] J. Hafner, Ab-initio simulations of materials using VASP: Density-functional theory and beyond, J. Comput. Chem., 29 (2008) 2044-2078.
[293] S.J. Clark, M.D. Segall, C.J. Pickard, P.J. Hasnip, M.I. Probert, K. Refson, M.C. Payne, First principles methods using CASTEP, Z. Kristallogr., 220 (2005) 567-570.
[294] A. Togo, I. Tanaka, First principles phonon calculations in materials science, Scr. Mater., 108 (2015) 1-5.
[295] J.E. Mahan, Physical vapor deposition of thin films, Physical Vapor Deposition of Thin Films, by John E. Mahan, pp. 336. ISBN 0-471-33001-9. Wiley-VCH, January 2000., (2000) 336.
[296] R. Behrisch, Sputtering by particle bombardment I. Physical sputtering of single-element solids, Vol. 47, (1981).
[297] J. Venables, G. Spiller, M. Hanbucken, Nucleation and growth of thin films, Reports on Progress in Physics, 47 (1984) 399.
[298] P. Kelly, R. Arnell, Magnetron sputtering: a review of recent developments and applications, Vacuum, 56 (2000) 159-172.
[299] B. Window, N. Savvides, Unbalanced dc magnetrons as sources of high ion fluxes, Journal of Vacuum Science & Technology A: Vacuum, Surfaces, and Films, 4 (1986) 453-456.
[300] N. Savvides, B. Window, Unbalanced magnetron ion-assisted deposition and property modification of thin films, Journal of Vacuum Science & Technology A: Vacuum, Surfaces, and Films, 4 (1986) 504-508.
[301] R.D. Arnell, P.J. Kelly, Recent advances in magnetron sputtering, Surface and Coatings Technology, 112 (1999) 170-176.
[302] B.D. Cullity, Elements of X-ray Diffraction, (1978).
[303] H.P. Klug, L.E. Alexander, X-ray diffraction procedures: for polycrystalline and amorphous materials, X-Ray Diffraction Procedures: For Polycrystalline and Amorphous Materials, 2nd Edition, by Harold P. Klug, Leroy E. Alexander, pp. 992. ISBN 0-471-49369-4. Wiley-VCH, May 1974., (1974) 992.
[304] Y. Leng, Materials characterization: introduction to microscopic and spectroscopic methods, John Wiley & Sons, 2009.
[305] B.B. He, Two-dimensional X-ray diffraction, John Wiley & Sons, 2018.

[306] R. Gazia, A. Chiodoni, E. Celasco, S. Bianco, P. Mandracci, X-Ray Analysis on Ceramic Materials Deposited by Sputtering and Reactive Sputtering for Sensing Applications, in: X-Ray Spectroscopy, InTech, 2012.
[307] L. Reimer, Scanning electron microscopy: physics of image formation and microanalysis, Springer, 2013.
[308] J.I. Goldstein, D.E. Newbury, J.R. Michael, N.W. Ritchie, J.H.J. Scott, D.C. Joy, Scanning electron microscopy and X-ray microanalysis, Springer, 2017.
[309] J.A. Duffie, W.A. Beckman, Solar engineering of thermal processes, John Wiley & Sons, 2013.
[310] A. Roos, Use of an integrating sphere in solar energy research, Solar Energy Materials and Solar Cells, 30 (1993) 77-94.
[311] T. Wang, X. Tian, Y. Yang, Y. Li, J. Wang, M. Beller, H. Jiao, Structures of Seven Molybdenum Surfaces and Their Coverage Dependent Hydrogen Adsorption, Physical Chemistry Chemical Physics, (2016).
[312] W.-F. Chen, J.T. Muckerman, E. Fujita, Recent developments in transition metal carbides and nitrides as hydrogen evolution electrocatalysts, Chemical Communications, 49 (2013) 8896-8909.
[313] I. Jauberteau, J.L. Jauberteau, S. Touimi, T. Merle-Méjean, S. Weber, A. Bessaudou, A thermochemical process using expanding plasma for nitriding thin molybdenum films at low temperature, (2012).
[314] L. Toth, Transition Metal Carbides and Nitrides (Academic, New York, 1971), and references therein, (1992) 87.
[315] S.T. Oyama, Introduction to the chemistry of transition metal carbides and nitrides, Springer, 1996.
[316] M. Segall, P.J. Lindan, M.a. Probert, C. Pickard, P. Hasnip, S. Clark, M. Payne, First-principles simulation: ideas, illustrations and the CASTEP code, Journal of Physics: Condensed Matter, 14 (2002) 2717.
[317] E. Soignard, P.F. McMillan, T.D. Chaplin, S.M. Farag, C.L. Bull, M.S. Somayazulu, K. Leinenweber, High-pressure synthesis and study of low-compressibility molybdenum nitride (MoN and MoN 1− x) phases, Physical Review B, 68 (2003) 132101.
[318] E. Jeong, J. Park, S. Choi, J. Kang, Y.C. Kang, Surface Characteristics of MoN x Thin Films Obtained by Reactive rf Magnetron Sputtering in UHV System, Bulletin of the Korean Chemical Society, 36 (2015) 2446-2450.

[319] Y. Shen, Effect of deposition conditions on mechanical stresses and microstructure of sputter-deposited molybdenum and reactively sputter-deposited molybdenum nitride films, Materials Science and Engineering: A, 359 (2003) 158-167.
[320] D. Machon, D. Daisenberger, E. Soignard, G. Shen, T. Kawashima, E. Takayama-Muromachi, P. McMillan, High pressure–high temperature studies and reactivity of γ-Mo2N and δ-MoN, physica status solidi (a), 203 (2006) 831-836.
[321] N. Gajbhiye, R. Ningthoujam, Structural, electrical and magnetic studies of nanocrystalline δ-MoN and γ-Mo2N, physica status solidi (c), 1 (2004) 3449-3454.
[322] A. Perry, A. Baouchi, J. Petersen, S. Pozder, Crystal structure of molybdenum nitride films made by reactive cathodic arc evaporation, Surface and Coatings Technology, 54 (1992) 261-265.
[323] X. Zhu, D. Yue, C. Shang, M. Fan, B. Hou, Phase composition and tribological performance of molybdenum nitride coatings synthesized by IBAD, Surface and Coatings Technology, 228 (2013) S184-S189.
[324] L. Stöber, J. Konrath, S. Krivec, F. Patocka, S. Schwarz, A. Bittner, M. Schneider, U. Schmid, Impact of sputter deposition parameters on molybdenum nitride thin film properties, Journal of Micromechanics and Microengineering, 25 (2015) 074001.
[325] C.L. Bull, T. Kawashima, P.F. McMillan, D. Machon, O. Shebanova, D. Daisenberger, E. Soignard, E. Takayama-Muromachi, L.C. Chapon, Crystal structure and high-pressure properties of γ-Mo 2 N determined by neutron powder diffraction and X-ray diffraction, Journal of Solid State Chemistry, 179 (2006) 1762-1767.
[326] J. Lowther, Lattice model for the properties of non-stoichiometric cubic and hexagonal molybdenum nitride, J. Alloys compd., 364 (2004) 13-16.
[327] R. Rajeswarapalanichamy, K. Iyakutti, Pressure induced phase transition of molybdenum nitride: A first principles study, Thin Solid Films, 525 (2012) 200-207.
[328] K. Liu, B. Dong, X. Zhou, S. Wang, Y. Zhao, J. Chang, Structural, elastic, and thermodynamic properties of hexagonal molybdenum nitrides under high pressure from first principles, J. Alloys Compd., 632 (2015) 830-836.
[329] X. Zhou, D. Gall, S.V. Khare, Mechanical properties and electronic structure of anti-ReO 3 structured cubic nitrides, M 3 N, of d block transition metals M: An ab initio study, Journal of Alloys and Compounds, 595 (2014) 80-86.
[330] Z. Liu, X. Zhou, D. Gall, S. Khare, First-principles investigation of the structural, mechanical and electronic properties of the NbO-structured 3d, 4d and 5d transition metal nitrides, Computational Materials Science, 84 (2014) 365-373.

[331] P. RICHET, F. GUYOT, G. FIQUET, P. GILLET, High-temperature thermodynamic properties of forsterite, Journal of Geophysical Research-Solid Earth and Planets, 96 (1991) 11805-11816.
[332] D.J. Adams, A.R. Oganov, Ab initio molecular dynamics study of Ca Si O 3 perovskite at P− T conditions of Earth's lower mantle, Physical Review B, 73 (2006) 184106.
[333] F. Guyot, Y. Wang, P. Gillet, Y. Ricard, Quasi-harmonic computations of thermodynamic parameters of olivines at high-pressure and high-temperature. A comparison with experiment data, Physics of the earth and planetary interiors, 98 (1996) 17-29.
[334] J.P. Perdew, K. Burke, M. Ernzerhof, Generalized gradient approximation made simple, Physical review letters, 77 (1996) 3865.
[335] P.E. Blöchl, Projector augmented-wave method, Physical Review B, 50 (1994) 17953.
[336] H.J. Monkhorst, J.D. Pack, Special points for Brillouin-zone integrations, Physical Review B, 13 (1976) 5188.
[337] J. Muscat, A. Wander, N. Harrison, On the prediction of band gaps from hybrid functional theory, Chemical Physics Letters, 342 (2001) 397-401.
[338] L. López-de-la-Torre, B. Winkler, J. Schreuer, K. Knorr, M. Avalos-Borja, Elastic properties of tantalum carbide (TaC), Solid state communications, 134 (2005) 245-250.
[339] S. Shang, Y. Wang, Z.-K. Liu, First-principles elastic constants of α-and θ-Al2O3, Applied Physics Letters, 90 (2007) 101909.
[340] I. Waller, Dynamical Theory of Crystal Lattices by M. Born and K. Huang, Acta Crystallographica, 9 (1956) 837-838.
[341] M. Levy, H. Bass, R. Stern, Handbook of Elastic Properties of Solids, Liquids, and Gases, Four-Volume Set, Academic Press, 2000.
[342] R. Hill, The elastic behaviour of a crystalline aggregate, Proceedings of the Physical Society. Section A, 65 (1952) 349.
[343] P. Steneteg, O. Hellman, O.Y. Vekilova, N. Shulumba, F. Tasnádi, I.A. Abrikosov, Temperature dependence of TiN elastic constants from ab initio molecular dynamics simulations, Physical Review B, 87 (2013) 094114.
[344] W. Chen, J. Jiang, Elastic properties and electronic structures of 4d-and 5d-transition metal mononitrides, Journal of Alloys and Compounds, 499 (2010) 243-254.
[345] Z. Liu, D. Gall, S. Khare, Electronic and bonding analysis of hardness in pyrite-type transition-metal pernitrides, Physical Review B, 90 (2014) 134102.

[346] Z. Liu, X. Zhou, S. Khare, D. Gall, Structural, mechanical and electronic properties of 3d transition metal nitrides in cubic zincblende, rocksalt and cesium chloride structures: a first-principles investigation, Journal of Physics: Condensed Matter, 26 (2013) 025404.
[347] S.J. Clark, M.D. Segall, C.J. Pickard, P.J. Hasnip, M.I. Probert, K. Refson, M.C. Payne, First principles methods using CASTEP, Zeitschrift für Kristallographie-Crystalline Materials, 220 (2005) 567-570.
[348] A. Togo, F. Oba, I. Tanaka, First-principles calculations of the ferroelastic transition between rutile-type and CaCl 2-type SiO 2 at high pressures, Physical Review B, 78 (2008) 134106.
[349] A. Erba, J. Maul, R. Demichelis, R. Dovesi, Assessing thermochemical properties of materials through ab initio quantum-mechanical methods: the case of α-Al 2 O 3, Phys. Chem. Chem. Phys., 17 (2015) 11670-11677.
[350] A. Reshak, S. Azam, Electronic Structure, Electronic Charge Density and Optical Properties Analyses of Rb2Al2B2O7 Compound: DFT Calculation, Int. J. Electrochem. Sci, 9 (2014) 975-989.
[351] M.C. Payne, M.P. Teter, D.C. Allan, T. Arias, J. Joannopoulos, Iterative minimization techniques for ab initio total-energy calculations: molecular dynamics and conjugate gradients, Reviews of Modern Physics, 64 (1992) 1045.
[352] S. Hong-Guo, Z. Zhong-Xiang, Y. Cheng-Xun, Y. Wen-Long, W. He, Structural, Electronic and Optical Properties of KTa0. 5Nb0. 5O3 Surface: A First-Principles Study, Chinese Physics Letters, 29 (2012) 017303.
[353] R. Bader, Atoms in Molecules: A Quantum Theory International Series of Monographs on Chemistry, edited by Clarendon Press, in, Oxford, 1990.
[354] E.I. Isaev, S.I. Simak, I. Abrikosov, R. Ahuja, Y.K. Vekilov, M. Katsnelson, A. Lichtenstein, B. Johansson, Phonon related properties of transition metals, their carbides, and nitrides: A first-principles study, Journal of applied physics, 101 (2007) 123519.
[355] W. Lengauer, Formation of molybdenum nitrides by ammonia nitridation of MoCl 5, Journal of crystal growth, 87 (1988) 295-298.
[356] E. Zhao, J. Wang, J. Meng, Z. Wu, Structural, mechanical and electronic properties of 4d transition metal mononitrides by first-principles, Computational Materials Science, 47 (2010) 1064-1071.
[357] E. ZHAO, J. WANG, Z. WU, Displacive phase transition, structural basic solid state physics stability, and mechanical properties of the ultra-incompressible and hard MoN by first principles, Physica status solidi. B. Basic research, 247 (2010) 1207-1213.

[358] B. Sahu, L. Kleinman, Theoretical study of structural and electronic properties of δ-MoN, Physical Review B, 70 (2004) 073103.
[359] S. Pugh, XCII. Relations between the elastic moduli and the plastic properties of polycrystalline pure metals, The London, Edinburgh, and Dublin Philosophical Magazine and Journal of Science, 45 (1954) 823-843.
[360] H. Niu, X.-Q. Chen, P. Liu, W. Xing, X. Cheng, D. Li, Y. Li, Extra-electron induced covalent strengthening and generalization of intrinsic ductile-to-brittle criterion, Scientific reports, 2 (2012).
[361] M. Born, On the stability of crystal lattices. I, in: Mathematical Proceedings of the Cambridge Philosophical Society, Cambridge Univ Press, 1940, pp. 160-172.
[362] E. Soignard, O. Shebanova, P.F. McMillan, Compressibility measurements and phonon spectra of hexagonal transition-metal nitrides at high pressure: ε− TaN, δ− MoN, and Cr 2 N, Physical Review B, 75 (2007) 014104.
[363] T. Seddik, R. Khenata, A. Bouhemadou, N. Guechi, A. Sayede, D. Varshney, Y. Al-Douri, A. Reshak, S. Bin-Omran, External temperature and pressure effects on thermodynamic properties and mechanical stability of yttrium chalcogenides YX (X= S, Se and Te), Physica B: Condensed Matter, 428 (2013) 78-88.
[364] S. Dudarev, G. Botton, S. Savrasov, C. Humphreys, A. Sutton, Electron-energy-loss spectra and the structural stability of nickel oxide: An LSDA+ U study, Physical Review B, 57 (1998) 1505.
[365] A. Otero-de-la-Roza, D. Abbasi-Pérez, V. Luaña, Gibbs2: A new version of the quasiharmonic model code. II. Models for solid-state thermodynamics, features and implementation, Computer Physics Communications, 182 (2011) 2232-2248.
[366] M. Roknuzzaman, A. Islam, Ab Initio Investigation of Nitride in Comparison with Carbide Phase of Superconducting InX (X= C, N), ISRN Condensed Matter Physics, 2013 (2013).
[367] L. Koutsokeras, G. Matenoglou, P. Patsalas, Structure, electronic properties and electron energy loss spectra of transition metal nitride films, Thin Solid Films, 528 (2013) 49-52.
[368] L. Hultman, Thermal stability of nitride thin films, Vacuum, 57 (2000) 1-30.
[369] S.-H. Jhi, S.G. Louie, M.L. Cohen, J. Ihm, Vacancy hardening and softening in transition metal carbides and nitrides, Phys. Rev. Lett., 86 (2001) 3348.
[370] G. Vilé, D. Albani, N. Almora-Barrios, N. López, J. Pérez-Ramírez, Advances in the design of nanostructured catalysts for selective hydrogenation, Chem. Cat. Chem., 8 (2016) 21-33.

[371] K. Balasubramanian, S.V. Khare, D. Gall, Valence electron concentration as an indicator for mechanical properties in rocksalt structure nitrides, carbides and carbonitrides, Acta Mater., 152 (2018) 175-185.
[372] N. Koutná, D. Holec, O. Svoboda, F.F. Klimashin, P.H. Mayrhofer, Point defects stabilise cubic Mo-N and Ta-N, J. Phys. D: Appl. Phys., 49 (2016) 375303.
[373] H. Jehn, P. Ettmayer, The molybdenum-nitrogen phase diagram, J. Less Common Met., 58 (1978) 85-98.
[374] Z.N. Jaf, Z.-T. Jiang, H.A. Miran, M. Altarawneh, Thermo-elastic and optical properties of molybdenum nitride, Can. J. Phys., 94 (2016) 902-912.
[375] D. Machon, D. Daisenberger, E. Soignard, G. Shen, T. Kawashima, E. Takayama-Muromachi, P. McMillan, High pressure–high temperature studies and reactivity of γ-Mo2N and δ-MoN, Phys. Status Solidi A, 203 (2006) 831-836.
[376] G.L. Hart, B.M. Klein, Phonon and elastic instabilities in MoC and MoN, Phys. Rev. B, 61 (2000) 3151.
[377] B. Ozsdolay, K. Balasubramanian, D. Gall, Cation and anion vacancies in cubic molybdenum nitride, J. Alloys Compd., 705 (2017) 631-637.
[378] P. Ettmayer, Das System Molybdän-Stickstoff, Monatsh. Chem., 101 (1970) 127-140.
[379] A. Bezinge, K. Yvon, J. Muller, W. Lengaeur, P. Ettmayer, High-pressure high-temperature experiments on δ-MoN, Solid State Commun., 63 (1987) 141-145.
[380] Q. Gong, Y. Wang, Q. Hu, J. Zhou, R. Feng, P.N. Duchesne, P. Zhang, F. Chen, N. Han, Y. Li, Ultrasmall and phase-pure W2C nanoparticles for efficient electrocatalytic and photoelectrochemical hydrogen evolution, Nat. Commun., 7 (2016).
[381] E. Soignard, O. Shebanova, P.F. McMillan, Compressibility measurements and phonon spectra of hexagonal transition-metal nitrides at high pressure: ε− TaN, δ− MoN, and Cr 2 N, Phys. Rev. B, 75 (2007) 014104.
[382] J.S. Becker, R.G. Gordon, Diffusion barrier properties of tungsten nitride films grown by atomic layer deposition from bis (tert-butylimido) bis (dimethylamido) tungsten and ammonia, Appl. Phys. Lett., 82 (2003) 2239-2241.
[383] M. Uekubo, T. Oku, K. Nii, M. Murakami, K. Takahiro, S. Yamaguchi, T. Nakano, T. Ohta, WNx diffusion barriers between Si and Cu, Thin Solid Films, 286 (1996) 170-175.
[384] K. Balasubramanian, S. Khare, D. Gall, Vacancy-induced mechanical stabilization of cubic tungsten nitride, Phys. Rev. B, 94 (2016) 174111.

[385] Z. Zhao, K. Bao, D. Duan, F. Tian, Y. Huang, H. Yu, Y. Liu, B. Liu, T. Cui, The low coordination number of nitrogen in hard tungsten nitrides: a first-principles study, Phys. Chem. Chem. Phys., 17 (2015) 13397-13402.
[386] S. Wang, X. Yu, Z. Lin, R. Zhang, D. He, J. Qin, J. Zhu, J. Han, L. Wang, H.-k. Mao, Synthesis, crystal structure, and elastic properties of novel tungsten nitrides, Chem. Mater., 24 (2012) 3023-3028.
[387] N. Schönberg, Contributions to the knowledge of the molybdenum-nitrogen and the tungsten-nitrogen systems, Acta Chem. Scand, 8 (1954).
[388] C. Wang, Q. Tao, S. Dong, X. Wang, P. Zhu, Synthesis and Mechanical Character of Hexagonal Phase δ− WN, Inorg. Chem., 56 (2017) 3970-3975.
[389] Y. Zhong, X. Xia, F. Shi, J. Zhan, J. Tu, H.J. Fan, Transition metal carbides and nitrides in energy storage and conversion, Adv. Sci., 3 (2016).
[390] J. Qin, X. Zhang, Y. Xue, X. Li, M. Ma, R. Liu, Structure and mechanical properties of tungsten mononitride under high pressure from first-principles calculations, Comput. Mater. Sci., 79 (2013) 456-462.
[391] J.C. Wei, H.C. Chen, W. Huang, J. Long, Theoretical investigation of the elastic, Vickers hardness and thermodynamic properties of δ-WN under pressure, Mater. Sci. Semicond. Process., 27 (2014) 883-890.
[392] T.R. Mattsson, A.E. Mattsson, Calculating the vacancy formation energy in metals: Pt, Pd, and Mo, Phys. Rev. B, 66 (2002) 214110.
[393] L. Cai, C. Feng, Effect of Vacancy Defects on the Electronic Structure and Optical Properties of GaN, J. Nanotechnol., 2017 (2017).
[394] S. Kerdsongpanya, B. Alling, P. Eklund, Effect of point defects on the electronic density of states of ScN studied by first-principles calculations and implications for thermoelectric properties, Phys. Rev. B, 86 (2012) 195140.
[395] D. Bocharov, D. Gryaznov, Y.F. Zhukovskii, E.A. Kotomin, DFT calculations of point defects on UN (001) surface, Surf. Sci., 605 (2011) 396-400.
[396] E. Heifets, S. Piskunov, E.A. Kotomin, Y.F. Zhukovskii, D.E. Ellis, Electronic structure and thermodynamic stability of double-layered Sr Ti O 3 (001) surfaces: Ab initio simulations, Phys. Rev. B, 75 (2007) 115417.
[397] P. Agoston, K. Albe, Thermodynamic stability, stoichiometry, and electronic structure of bcc-In_2O_3 surfaces, Phys.Rev. B, 84 (2011) 045311.

[398] M. Fronzi, A. Soon, B. Delley, E. Traversa, C. Stampfl, Stability and morphology of cerium oxide surfaces in an oxidizing environment: a first-principles investigation, J. Chem. Phys., 131 (2009) 104701.
[399] A. Soon, M. Todorova, B. Delley, C. Stampfl, Thermodynamic stability and structure of copper oxide surfaces: A first-principles investigation, Phys. Rev. B, 75 (2007) 125420.
[400] P. Liu, J.A. Rodriguez, Catalytic properties of molybdenum carbide, nitride and phosphide: a theoretical study, Catal. Lett., 91 (2003) 247-252.
[401] G. Kresse, J. Furthmüller, Efficient iterative schemes for ab initio total-energy calculations using a plane-wave basis set, Phys. Rev. B, 54 (1996) 11169.
[402] S. Krukowski, P. Kempisty, A.F. Jalbout, Thermodynamic and kinetic approach in density functional theory studies of microscopic structure of GaN (0001) surface in ammonia-rich conditions, J. Chem. Phys., 129 (2008) 234705.
[403] B. Younglove, J.F. Ely, Thermophysical properties of fluids. II. Methane, ethane, propane, isobutane, and normal butane, J. Phys. Chem. Ref. Data, 16 (1987) 577-798.
[404] S. Li, J.S. Lee, T. Hyeon, K.S. Suslick, Catalytic hydrodenitrogenation of indole over molybdenum nitride and carbides with different structures, Appl. Catal. A-Gen., 184 (1999) 1-9.
[405] W. Xing, X. Miao, F. Meng, R. Yu, Crystal structure of and displacive phase transition in tungsten nitride WN, J. Alloys Compd., (2017).
[406] A. Niessen, F. De Boer, The enthalpy of formation of solid borides, carbides, nitrides, silicides and phosphides of transition and noble metals, J. Less Common Met., 82 (1981) 75-80.
[407] W. Sun, G. Ceder, Efficient creation and convergence of surface slabs, Surf. Sci., 617 (2013) 53-59.
[408] E. Mohammadpour, M. Altarawneh, Z.-T. Jiang, N. Mondinos, B.Z. Dlugogorski, Electronic properties and stability phase diagrams for cubic BN surfaces, Mol. Simul., 43 (2017) 267-275.
[409] C. Doornkamp, V. Ponec, The universal character of the Mars and Van Krevelen mechanism, J. Mol. Catal. A-Chem., 162 (2000) 19-32.
[410] G. Henkelman, A. Arnaldsson, H. Jónsson, A fast and robust algorithm for Bader decomposition of charge density, Comput. Mater. Sci., 36 (2006) 354-360.
[411] M. Altarawneh, A. Marashdeh, B.Z. Dlugogorski, Structures, electronic properties and stability phase diagrams for copper (i/ii) bromide surfaces, Phys. Chem. Chem. Phys., 17 (2015) 9341-9351.

[412] J. Zhu, M. Gu, R. Pandey, Stability and electronic properties of polar and non-polar surfaces of CuI, Appl. Surf. Sci., 268 (2013) 87-91.
[413] J. Rogal, K. Reuter, M. Scheffler, Thermodynamic stability of PdO surfaces, Phys. Rev. B, 69 (2004) 075421.
[414] I.S. Altarawneh, S.E. Rawadieh, M.A. Batiha, L.A. Al-Makhadmeh, M.A. Al-Shaweesh, M.K. Altarawneh, Structures and Thermodynamic Stability of Cobalt Molybdenum Oxide (CoMoO 4-II), Surf. Sci., (2018).
[415] H. Widjaja, H.A. Miran, M. Altarawneh, I. Oluwoye, H.N. Lim, N.M. Huang, Z.-T. Jiang, B.Z. Dlugogorski, DFT+ U and ab initio atomistic thermodynamics approache for mixed transitional metallic oxides: A case study of CoCu2O3 surface terminations, Mater. Chem. Phys., 201 (2017) 241-250.
[416] M. Altarawneh, Z.-T. Jiang, B.Z. Dlugogorski, The structures and thermodynamic stability of copper (II) chloride surfaces, Phys. Chem. Chem. Phys., 16 (2014) 24209-24215.
[417] M. Altarawneh, S.A. Saraireh, Theoretical insight into chlorine adsorption on the Fe (100) surface, Phys. Chem. Chem. Phys., 16 (2014) 8575-8581.
[418] E. ZHAO, J. WANG, Z. WU, Displacive phase transition, structural basic solid state physics stability, and mechanical properties of the ultra-incompressible and hard MoN by first principles, Phys. Status Solidi B, 247 (2010) 1207-1213.
[419] H.F. Rase, Handbook of commercial catalysts: heterogeneous catalysts, CRC press, 2000.
[420] A. Bos, K. Westerterp, Mechanism and kinetics of the selective hydrogenation of ethyne and ethene, Chem Eng Proc: Process Intensification, 32 (1993) 1-7.
[421] F. Studt, F. Abild-Pedersen, T. Bligaard, R.Z. Sørensen, C.H. Christensen, J.K. Nørskov, Identification of non-precious metal alloy catalysts for selective hydrogenation of acetylene, Science, 320 (2008) 1320-1322.
[422] B. Bridier, N. López, J. Pérez-Ramírez, Molecular understanding of alkyne hydrogenation for the design of selective catalysts, Dalton Transactions, 39 (2010) 8412-8419.
[423] P.A. Sheth, M. Neurock, C.M. Smith, First-principles analysis of the effects of alloying Pd with Ag for the catalytic hydrogenation of acetylene-ethylene mixtures, J. Phys. Chem. B, 109 (2005) 12449-12466.
[424] E. Muetterties, M.-C. Tasi, S. Kelemen, Chemistry of acetylene on platinum (111) and (100) surfaces, Proc. Natl. Acad. Sci. , 78 (1981) 6571-6575.

[425] D.A. Outka, C. Friend, S. Jorgensen, R. Madix, Adsorption and hydrogenation of acetylene on copper Cu (110) and Cu (110)-O surfaces, J. Amr. Chem. Soc. , 105 (1983) 3468-3472.

[426] R.S. Ningthoujam, N.S. Gajbhiye, Synthesis, electron transport properties of transition metal nitrides and applications, Prog. Mater. Sci., 70 (2015) 50-154.

[427] C. Shi, A. Zhu, X. Yang, C. Au, On the catalytic nature of VN, Mo_2N, and W_2N nitrides for NO reduction with hydrogen, Appl. Catal., A, 276 (2004) 223-230.

[428] E. Furimsky, Metal carbides and nitrides as potential catalysts for hydroprocessing, Appl. Catal., A, 240 (2003) 1-28.

[429] H. Tominaga, M. Nagai, Reaction mechanism for hydrodenitrogenation of carbazole on molybdenum nitride based on DFT study, Appl. Catal., A, 389 (2010) 195-204.

[430] M. Nagai, Transition-metal nitrides for hydrotreating catalyst—Synthesis, surface properties, and reactivities, Appl. Catal., A, 322 (2007) 178-190.

[431] N. Perret, F. Cárdenas-Lizana, D. Lamey, V. Laporte, L. Kiwi-Minsker, M.A. Keane, Effect of Crystallographic Phase (β vs. γ) and Surface Area on Gas Phase Nitroarene Hydrogenation Over Mo_2N and Au/Mo_2N, Top Catal, 55 (2012) 955-968.

[432] M. Altarawneh, Z. Jaf, H. Oskierski, Z.-T. Jiang, J. Gore, B.Z. Dlugogorski, Conversion of NO into N_2 over γ-Mo_2N, J. Phys. Chem. C, 120 (2016) 22270–22280.

[433] I. Matanović, F.H. Garzon, N.J. Henson, Electro-reduction of nitrogen on molybdenum nitride: structure, energetics, and vibrational spectra from DFT, Phys. Chem. Chem. Phys. , 16 (2014) 3014-3026.

[434] Z. Li, C. Chen, E. Zhan, N. Ta, W. Shen, Mo_2N nanobelts for dehydrogenation of aromatic alcohols, Chem. Commun. , 51 (2014) 58-62.

[435] Y.H. Park, G.L. Price, Deuterium tracer study on the effect of carbon monoxide on the selective hydrogenation of acetylene over palladium/alumina, Ind. Eng. Chem. Res., 30 (1991) 1693-1699.

[436] X.S. Li, Y.J. Zhang, Q. Xin, C.X. Ji, Y.F. Miao, L. Wang, Irreversible hydrogen uptake on Mo_2N catalyst, Reaet.Kinet,Catal.Lett., 57 (1996) 177-182.

[437] J. Carrasco, G. Vilé, D. Fernández-Torre, R.n. Pérez, J. Pérez-Ramírez, M.V.n. Ganduglia-Pirovano, Molecular-level understanding of CeO_2 as a catalyst for partial alkyne hydrogenation, J. Phys. Chem. C, 118 (2014) 5352-5360.

[438] B. Delley, From molecules to solids with the $DMol^3$ approach, J. Chem. Phys. , 113 (2000) 7756-7764.

[439] J.P. Perdew, K. Burke, Y. Wang, Generalized gradient approximation for the exchange-correlation hole of a many-electron system, Phys. Rev. B, 54 (1996) 16533.
[440] T.A. Halgren, W.N. Lipscomb, The synchronous-transit method for determining reaction pathways and locating molecular transition states, Chem. phys. lett., 49 (1977) 225-232.
[441] F.L. Hirshfeld, Bonded-atom fragments for describing molecular charge densities, Theor. Chem. Acc., 44 (1977) 129-138.
[442] I. Mayer, Charge, bond order and valence in the ab initio SCF theory, Chem. Phys. Lett., 97 (1983) 270-274.
[443] G. Lendvay, Bond order rearrangements during chemical reactions, J. Mol Struct: THEOCHEM, 167 (1988) 331-338.
[444] M.K. Neylon, S. Choi, H. Kwon, K.E. Curry, L.T. Thompson, Catalytic properties of early transition metal nitrides and carbides: n-butane hydrogenolysis, dehydrogenation and isomerization, Appl. Catal., A, 183 (1999) 253-263.
[445] X.S. Li, Y.X. Chen, Y.J. Zhang, C.X. Ji, Q. Xin, Temperature-programmed desorption and adsorption of hydrogen on Mo_2N, Reaet.Kinet,Catal.Lett., 58 (1996) 391-396.
[446] Y. Zhang, Y. Li, C. Li, Q. Xin, Adsorption and migration of hydrogen on different surface sites of γ-Mo2N catalyst, Stud Surf Sci Catal, 112 (1997) 457-464.
[447] G. Frapper, M. Pélissier, J. Hafner, CO Adsorption on Molybdenum Nitride's γ-Mo_2N(100) Surface: Formation of NCO Species? A Density Functional Study, J. Phys. Chem. B, 104 (2000) 11972-11976.
[448] A. Guerrero-Ruiz, Q. Xin, Y.J. Zhang, A. Maroto-Valiente, I. Rodriguez-Ramos, Microcalorimetric Study of H2 Adsorption on Molybdenum Nitride Catalysts, Langmuir, 15 (1999) 4927-4929.
[449] G.A. Somorjai, Chemistry in Two Dimensional Surfaces, 1ST ed., Cornell University Press, 1981.
[450] H. He, H. Dai, K. Ngan, C. Au, Molybdenum nitride for the direct decomposition of NO, Catal. Lett. , 71 (2001) 147-153.
[451] C. Doornkamp, V. Ponec, The universal character of the Mars and Van Krevelen mechanism, J. Mol. Catal A: Chem, 162 (2000) 19-32.
[452] D.Y. Murzin, T. Salmi, Catalytic Kinetics, 2nd ed., Elsevier, London, 2016.
[453] H.S. Fogler, Elements of chemical reaction engineering, 5th ed., Pearson New York, 1999.
[454] G. Bond, P. Wells, The mechanism of the hydrogenation of unsaturated hydrocarbons on transition metal catalysts, Adv. Catal. , 15 (1965) 91-226.

[455] M. Zabilskiy, P. Djinović, E. Tchernychova, O.P. Tkachenko, L.M. Kustov, A. Pintar, Nanoshaped CuO/CeO_2 Materials: Effect of the Exposed Ceria Surfaces on Catalytic Activity in N_2O Decomposition Reaction, ACS Catal., 5 (2015) 5357-5365.
[456] A. Sárkány, A.H. Weiss, T. Szilágyi, P. Sándor, L. Guczi, Green oil poisoning of a Pd/Al_2O_3 acetylene hydrogenation catalyst, Appl. Catal., 12 (1984) 373-379.
[457] V.V. Zhivonitko, I.V. Skovpin, M. Crespo-Quesada, L. Kiwi-Minsker, I.V. Koptyug, Acetylene Oligomerization over Pd Nanoparticles with Controlled Shape: A Parahydrogen-Induced Polarization Study, J. Phys. Chem. C, 120 (2016) 4945-4953.
[458] J.A. Alves, S.P. Bressa, O.M. Martínez, G.F. Barreto, Kinetic study of the liquid-phase hydrogenation of 1-butyne over a commercial palladium/alumina catalyst, Chem Eng J, 125 (2007) 131-138.
[459] M. Crespo-Quesada, R.R. Dykeman, G. Laurenczy, P.J. Dyson, L. Kiwi-Minsker, Supported nitrogen-modified Pd nanoparticles for the selective hydrogenation of 1-hexyne, J. Catal., 279 (2011) 66-74.
[460] M. Maccarrone, G. Torres, C. Lederhos, J. Badano, C. Vera, M. Quiroga, J. Yori, Kinetic study of the partial hydrogenation of 1-heptyne on tungsten oxide supported on alumina, J. Chem. Technol. Biotechnol., 87 (2012) 1521-1528.
[461] C. Song, C. Hsu, I. Mochida, Introduction to chemistry of diesel fuels, Chemistry of diesel fuels, (2000) 1-60.
[462] H. Topsøe, B.S. Clausen, F.E. Massoth, Hydrotreating catalysis, in: Catalysis, Springer, 1996, pp. 1-269.
[463] M.L. Occelli, Hydrotreating technology for pollution control: catalysts, catalysis, and processes, CRC Press, 1996.
[464] M. Nagai, Transition-metal nitrides for hydrotreating catalyst—Synthesis, surface properties, and reactivities, Appl. Catal. A: Gen, 322 (2007) 178-190.
[465] M. Vrinat, The kinetics of the hydrodesulfurization process-a review, Appl. Catal., 6 (1983) 137-158.
[466] I. Mochida, K.-H. Choi, An overview of hydrodesulfurization and hydrodenitrogenation, J. Jpn. Pet. Inst., 47 (2004) 145-163.
[467] E. Krebs, B. Silvi, A. Daudin, P. Raybaud, A DFT study of the origin of the HDS/HydO selectivity on Co (Ni) MoS active phases, J. Catal., 260 (2008) 276-287.
[468] A. Niquille-Röthlisberger, R. Prins, Hydrodesulfurization of 4, 6-dimethyldibenzothiophene and dibenzothiophene over alumina-supported Pt, Pd, and Pt-Pd catalysts, J. catal., 242 (2006) 207-216.

[469] B. Bak, D. Christensen, L. Hansen-Nygaard, J. Rastrup-Andersen, The structure of thiophene, J. Mol. Spectrosc., 7 (1961) 58-63.
[470] D. Sajkowski, S. Oyama, Catalytic hydrotreating by molybdenum carbide and nitride: unsupported Mo2N and Mo2CAl2O3, Appl. Catal. A: Gen., 134 (1996) 339-349.
[471] Z. Wu, C. Li, Z. Wei, P. Ying, Q. Xin, FT-IR spectroscopic studies of thiophene adsorption and reactions on Mo2N/γ-Al2O3 catalysts, J. Phys. Chem. B, 106 (2002) 979-987.
[472] Y. Huang, H. Liu, X. Chen, D. Zhou, C. Wang, J. Du, T. Zhou, S. Wang, Density Functional Theory Investigation on Thiophene Hydrodesulfurization Mechanism Catalyzed by ReS2 (001) Surface, J. Phys. Chem. C, 120 (2016) 12012-12021.
[473] P.G. Moses, B. Hinnemann, H. Topsøe, J.K. Nørskov, The hydrogenation and direct desulfurization reaction pathway in thiophene hydrodesulfurization over MoS2 catalysts at realistic conditions: A density functional study, J. Catal., 248 (2007) 188-203.
[474] E.F. de Souza, T.C. Ramalho, R.B. de Alencastro, Periodic DFT Study on the Adsorption and Catalytic Desulfurization of Thiophene over VC (001) and VN (001) via Hydrogenation and Direct Pathways, J. Phys. Chem. C, 120 (2016) 4881-4894.
[475] E.F. de Souza, T.C. Ramalho, C.A. Chagas, R.B. de Alencastro, Adsorption and desulfurization reaction mechanism of thiophene and its hydrogenated derivatives over NbC (001) and NbN (001): an ab initio DFT study, Catal. Sci. Technol., 4 (2014) 2550-2563.
[476] J. Ren, C.-F. Huo, X.-D. Wen, Z. Cao, J. Wang, Y.-W. Li, H. Jiao, Thiophene adsorption and activation on MoP (001), γ-Mo2N (100), and Ni2P (001): Density functional theory studies, J. Phys. Chem. B, 110 (2006) 22563-22569.
[477] Z.N. Jaf, M. Altarawneh, H.A. Miran, Z.-T. Jiang, B.Z. Dlugogorski, Mechanisms governing selective hydrogenation of acetylene over γ-Mo 2 N surfaces, Catal. Sci. Technol., 7 (2017) 943-960.
[478] S. Zaman, DFT study of CO Adsorption and Dissociation Over γ-Mo2N (111) Plane, Bulgarian. Chem. Comm., 47 (2015) 125-132.
[479] B. Delley, From molecules to solids with the DMol 3 approach, J. Chem. Phys., 113 (2000) 7756-7764.
[480] L. Bengtsson, Dipole correction for surface supercell calculations, Phys. Rev. B, 59 (1999) 12301.
[481] H.A. Miran, M. Altarawneh, Z.-T. Jiang, H. Oskierski, M. Almatarneh, B.Z. Dlugogorski, Decomposition of selected chlorinated volatile organic compounds by ceria (CeO_2), Catal. Sci. Technol., 7 (2017) 3902-3919.

[482] K.J. Laidler, M.C. King, Development of transition-state theory, J. Phys. Chem., 87 (1983) 2657-2664.
[483] H. Zhu, W. Guo, M. Li, L. Zhao, S. Li, Y. Li, X. Lu, H. Shan, Density functional theory study of the adsorption and desulfurization of thiophene and its hydrogenated derivatives on Pt (111): implication for the mechanism of hydrodesulfurization over noble metal catalysts, ACS Catal., 1 (2011) 1498-1510.
[484] H. Tominaga, M. Nagai, Mechanism of thiophene hydrodesulfurization on clean/sulfided β-Mo2C (0 0 1) based on density functional theory—cis-and trans-2-Butene formation at the initial stage, Appl. Catal. A: Gen., 343 (2008) 95-103.
[485] K. XU, J. FENG, Q. CHU, L.-L. ZHANG, W.-Y. LI, Density Functional Theory Study of Thiophene Hydrodesulfurization on γ-Mo2N (100) Surface, Acta Phys-Chim. Sin., 30 (2014) 2063-2070.
[486] Z. Wu, C. Li, P. Ying, Z. Wei, Q. Xin, Low-temperature isomerization of 1-butene on Mo2N/γ-Al2O3 catalyst studied by in situ FT-IR spectroscopy, J. Phys. Chem. B, 105 (2001) 9183-9190.
[487] G. Bond, P. Wells, The mechanism of the hydrogenation of unsaturated hydrocarbons on transition metal catalysts, in: Adv. Catal., Elsevier, 1965, pp. 91-226.
[488] H.S. Fogler, Elements of chemical reaction engineering, Elements of chemical reaction engineering, (1999).
[489] X. Wang, M. Liang, J. Zhang, Y. Wang, Selective hydrogenation of aromatic chloronitro compounds, Current Organic Chemistry, 11 (2007) 299-314.
[490] M. Králik, Z. Vallušová, P. Major, A. Takáčová, M. Hronec, D. Gašparovičová, Hydrogenation of chloronitrobenzenes over Pd and Pt catalysts supported on cationic resins, Chemical Papers, 68 (2014) 1690-1700.
[491] V. Kratky, M. Kralik, M. Mecarova, M. Stolcova, L. Zalibera, M. Hronec, Effect of catalyst and substituents on the hydrogenation of chloronitrobenzenes, Applied Catalysis A: General, 235 (2002) 225-231.
[492] A. Mahata, R.K. Rai, I. Choudhuri, S.K. Singh, B. Pathak, Direct vs. indirect pathway for nitrobenzene reduction reaction on a Ni catalyst surface: a density functional study, Physical Chemistry Chemical Physics, 16 (2014) 26365-26374.
[493] J. Chen, N. Yao, R. Wang, J. Zhang, Hydrogenation of chloronitrobenzene to chloroaniline over Ni/TiO_2 catalysts prepared by sol–gel method, Chem. Eng. J., 148 (2009) 164-172.

[494] R.M. Machado, K.R. Heier, R.R. Broekhuis, Developments in hydrogenation technology for fine-chemical and pharmaceutical applications, CURRENT OPINION IN DRUG DISCOVERY AND DEVELOPMENT, 4 (2001) 745-755.
[495] H.U. Blaser, C. Malan, B. Pugin, F. Spindler, H. Steiner, M. Studer, Selective hydrogenation for fine chemicals: recent trends and new developments, Advanced Synthesis & Catalysis, 345 (2003) 103-151.
[496] R.A. Sheldon, I.W. Arends, U. Hanefeld, Introduction: Green chemistry and catalysis, Green Chemistry and Catalysis, (2007) 1-47.
[497] H. Chen, D. He, Q. He, P. Jiang, G. Zhou, W. Fu, Selective hydrogenation of p-chloronitrobenzene over an Fe promoted Pt/AC catalyst, RSC Advances, 7 (2017) 29143-29148.
[498] J. Lyu, J. Wang, C. Lu, L. Ma, Q. Zhang, X. He, X. Li, Size-dependent halogenated nitrobenzene hydrogenation selectivity of Pd nanoparticles, The Journal of Physical Chemistry C, 118 (2014) 2594-2601.
[499] L. Ma, J. Wang, H. Wang, Q. Zhang, C. Lu, X. He, X. Li, High halogenated nitrobenzene hydrogenation selectivity over nano Ir particles, Chin. J. Chem. Eng., 25 (2017) 306-312.
[500] V. Vishwanathan, V. Jayasri, P.M. Basha, N. Mahata, L. Sikhwivhilu, N.J. Coville, Gas phase hydrogenation of ortho-chloronitrobenzene (O-CNB) to ortho-chloroaniline (O-CAN) over unpromoted and alkali metal promoted-alumina supported palladium catalysts, Catalysis communications, 9 (2008) 453-458.
[501] F. Li, J. Liang, W. Zhu, H. Song, K. Wang, C. Li, In-Situ Liquid Hydrogenation of m-Chloronitrobenzene over Fe-Modified Pt/Carbon Nanotubes Catalysts, Catalysts, 8 (2018) 62.
[502] F. Cárdenas-Lizana, D. Lamey, S. Gómez-Quero, N. Perret, L. Kiwi-Minsker, M.A. Keane, Selective three-phase hydrogenation of aromatic nitro-compounds over β-molybdenum nitride, Catalysis today, 173 (2011) 53-61.
[503] J. Lyu, J. Wang, C. Lu, L. Ma, Q. Zhang, X. He, X. Li, Size-dependent halogenated nitrobenzene hydrogenation selectivity of Pd nanoparticles, J. Phys. Chem. C, 118 (2014) 2594-2601.
[504] B. Delley, From molecules to solids with the DMol 3 approach, J. Chem. Phys., 113 (2000) 7756-7764.
[505] S. Grimme, Semiempirical GGA-type density functional constructed with a long-range dispersion correction, Journal of computational chemistry, 27 (2006) 1787-1799.
[506] M. Altarawneh, Z. Jaf, H. Oskierski, Z.-T. Jiang, J. Gore, B.Z. Dlugogorski, Conversion of NO into N2 over γ-Mo2N, The Journal of Physical Chemistry C, (2016).

[507] X. He, J. Lyu, H. Zhou, G. Zhuang, X. Zhong, J.G. Wang, X. Li, Density functional theory study of p-chloroaniline adsorption on Pd surfaces and clusters, Int. J. Quantum Chem., 114 (2014) 895-899.
[508] N. Perret, F. Cárdenas-Lizana, D. Lamey, V. Laporte, L. Kiwi-Minsker, M.A. Keane, Effect of crystallographic phase (β vs. γ) and surface area on gas phase nitroarene hydrogenation over Mo_2N and Au/Mo_2N, Top. Catal., 55 (2012) 955-968.
[509] W. Wang, W. Xu, K.B. Thapa, X. Yang, J. Liang, L. Zhu, J. Zhu, Morpholine-Modified Pd/γ-Al_2O_3@ ASMA Pellet Catalyst with Excellent Catalytic Selectivity in the Hydrogenation of p-Chloronitrobenzene to p-Chloroaniline, Catalysts, 7 (2017) 292.
[510] F. Cárdenas-Lizana, S. Gómez-Quero, M.A. Keane, Clean production of chloroanilines by selective gas phase hydrogenation over supported Ni catalysts, Appl. Catal. A General, 334 (2008) 199-206.
[511] Z.N. Jaf, M. Altarawneh, H.A. Miran, Z.-T. Jiang, B.Z. Dlugogorski, Hydrodesulfurization of Thiophene over γ-Mo2N catalyst, Mol. Catal., 459 (2018) 21-30.
[512] T. Sheng, Y.-J. Qi, X. Lin, P. Hu, S.-G. Sun, W.-F. Lin, Insights into the mechanism of nitrobenzene reduction to aniline over Pt catalyst and the significance of the adsorption of phenyl group on kinetics, Chem. Eng. J., 293 (2016) 337-344.
[513] Z.N. Jaf, M. Altarawneh, H.A. Miran, Z.-T. Jiang, B.Z. Dlugogorski, Mechanisms governing selective hydrogenation of acetylene over γ-Mo_2N surfaces, Catal. Sci. Technol., 7 (2017) 943-960.
[514] L. Zhang, J. Jiang, W. Shi, S. Xia, Z. Ni, X. Xiao, Insights into the hydrogenation mechanism of nitrobenzene to aniline on Pd 3/Pt (111): a density functional theory study, RSC Advances, 5 (2015) 34319-34326.
[515] H. Holleck, Material selection for hard coatings, Journal of Vacuum Science & Technology A: Vacuum, Surfaces, and Films, 4 (1986) 2661-2669.
[516] W. Kalss, A. Reiter, V. Derflinger, C. Gey, J. Endrino, Modern coatings in high performance cutting applications, Int. J Refract Met H, 24 (2006) 399-404.
[517] E.Y. Choi, M.C. Kang, D.H. Kwon, D.W. Shin, K.H. Kim, Comparative studies on microstructure and mechanical properties of CrN, Cr–C–N and Cr–Mo–N coatings, J mater process tech, 187 (2007) 566-570.
[518] B. Navinšek, P. Panjan, I. Milošev, Industrial applications of CrN (PVD) coatings, deposited at high and low temperatures, Surf Coat Tech, 97 (1997) 182-191.

[519] R. Mientus, R. Grötschel, K. Ellmer, Optical and electronic properties of CrOxNy films, deposited by reactive DC magnetron sputtering in Ar/N2/O2 (N2O) atmospheres, Surf. Coat.Technol., 200 (2005) 341-345.
[520] M. Yang, R. Guarecuco, F.J. DiSalvo, Mesoporous chromium nitride as high performance catalyst support for methanol electrooxidation, Chem. Mater., 25 (2013) 1783-1787.
[521] B.M. Weckhuysen, R.A. Schoonheydt, Olefin polymerization over supported chromium oxide catalysts, Catal. today, 51 (1999) 215-221.
[522] J.-Y. Lee, J.-W. Park, Diffusion barrier property of molybdenum nitride films for copper metallization, Jpn. J. Appl. Phys., 35 (1996) 4280.
[523] Z.N. Jaf, M. Altarawneh, H.A. Miran, M.H. Almatarneh, Z.-T. Jiang, B.Z. Dlugogorski, Catalytic Hydrogenation of p-Chloronitrobenzene to p-Chloroaniline Mediated by γ-Mo2N, ACS Omega, 3 (2018) 14380-14391.
[524] A. Togo, phonopy manual, in, 2013.
[525] P. Hones, R. Sanjines, F. Levy, Sputter deposited chromium nitride based ternary compounds for hard coatings, Thin Solid Films, 332 (1998) 240-246.
[526] H.C. Barshilia, N. Selvakumar, B. Deepthi, K. Rajam, A comparative study of reactive direct current magnetron sputtered CrAlN and CrN coatings, Surf. Coat. Technol., 201 (2006) 2193-2201.
[527] P. Hones, R. Consiglio, N. Randall, F. Leacutevy, Mechanical properties of hard chromium tungsten nitride coatings, Surf. Coat. Technol., 125 (2000) 179-184.
[528] S. Zhang, L. Li, A. Kumar, Materials characterization techniques, CRC press, 2008.
[529] M.M. Rahman, A. Duan, Z.-T. Jiang, Z. Xie, A. Wu, A. Amri, B. Cowie, C.-Y. Yin, Near-edge X-ray absorption fine structure studies of Cr1− xMxN coatings, J. Alloy. Compd., 578 (2013) 362-368.
[530] P. Wo, P. Munroe, Z. Li, Z.-T. Jiang, Z. Xie, Z. Zhou, K. Li, Factors governing the mechanical behaviour of CrSiN coatings: Combined nanoindentation testing and transmission electron microscopy, Mater. Sci. Eng. A, 534 (2012) 297-308.
[531] J. Xu, D. Lai, Z. Xie, P. Munroe, Z.-T. Jiang, A critical role for Al in regulating the corrosion resistance of nanocrystalline Mo (Si 1− x Al x) 2 films, J. Mater. Chem., 22 (2012) 2596-2606.
[532] J. Xu, L. Liu, P. Munroe, Z.-H. Xie, Z.-T. Jiang, The nature and role of passive films in controlling the corrosion resistance of MoSi 2-based nanocomposite coatings, J. Mater. Chem. A, 1 (2013) 10281-10291.

[533] P.C. Wo, P.R. Munroe, Z.-T. Jiang, Z. Zhou, K.Y. Li, Z. Xie, Enhancing toughness of CrN coatings by Ni addition for safety-critical applications, Mater. Sci. Eng. A, 596 (2014) 264-274.
[534] F. Klimashin, H. Riedl, D. Primetzhofer, J. Paulitsch, P. Mayrhofer, Composition driven phase evolution and mechanical properties of Mo–Cr–N hard coatings, J. Appl. Phys., 118 (2015) 025305.
[535] D. Yuelan, Z. Ping, C. Zhihai, Y. Zhen, L. Qi, S. Wei, Effect of Mo Content on the Structural and Mechanical Properties of CrMoN/MoS2 Composite Coatings, Rare Metal Materials and Engineering, 43 (2014) 264-268.
[536] S.-K. Tien, C.-H. Lin, Y.-Z. Tsai, J.-G. Duh, Effect of nitrogen flow on the properties of quaternary CrAlSiN coatings at elevated temperatures, Surf. Coat. Technol., 202 (2007) 735-739.
[537] H. Shah, R. Jayaganthan, D. Kaur, Effect of sputtering pressure and temperature on DC magnetron sputtered CrN films, Surf. Eng., 26 (2010) 629-637.
[538] S. Zhang, D. Sun, Y. Fu, H. Du, Q. Zhang, Effect of sputtering target power density on topography and residual stress during growth of nanocomposite nc-TiN/a-SiNx thin films, Diam. Relat. Mater., 13 (2004) 1777-1784.
[539] J. Yang, B. Prakash, Z. Yuan, Y. Jiang, X. Wang, Q. Fang, Influence of sputtering target power on microstructure and mechanical properties of WN and ta-n coatings, Nanosci. Nanotech. Let., 4 (2012) 604-608.
[540] Z.N. Jaf, M. Altarawneh, H.A. Miran, Z.-T. Jiang, Geometries, electronic properties and stability of molybdenum and tungsten nitrides low-index surfaces, Mater. Res. Exp., 5 (2018) 126402.
[541] K. Chen, L. Zhao, J. Rodgers, S.T. John, Alloying effects on elastic properties of TiN-based nitrides, J. Phys D Appl. Phys., 36 (2003) 2725.
[542] L. Zhou, D. Holec, P.H. Mayrhofer, First-principles study of elastic properties of cubic Cr1− x Al x N alloys, J. Appl. Phys., 113 (2013) 043511.
[543] L. Zhou, D. Holec, P.H. Mayrhofer, Ab initio study of the alloying effect of transition metals on structure, stability and ductility of CrN, sJ. Phys. D: Appl. Phys., 46 (2013) 365301.
[544] L. Zhou, F.F. Klimashin, D. Holec, P.H. Mayrhofer, Structural and mechanical properties of nitrogen-deficient cubic Cr–Mo–N and Cr–W–N systems, Scr. Mater., 123 (2016) 34-37.
[545] R. Swanepoel, Determination of surface roughness and optical constants of inhomogeneous amorphous silicon films, J. Phys. E: Sci. Instrum., 17 (1984) 896.

[546] J.F. Nye, Physical properties of crystals: their representation by tensors and matrices, Oxford university press, 1985.
[547] M. Segall, P.J. Lindan, M.a. Probert, C. Pickard, P.J. Hasnip, S. Clark, M. Payne, First-principles simulation: ideas, illustrations and the CASTEP code, Journal of Physics: Condensed Matter, 14 (2002) 2717.
[548] H. Monkhorst, J. Pack, Special points for Brillouin-zone integrations, (2005).
[549] J. Baltrusaitis, B. Mendoza-Sanchez, V. Fernandez, R. Veenstra, N. Dukstiene, A. Roberts, N. Fairley, Generalized molybdenum oxide surface chemical state XPS determination via informed amorphous sample model, Appl. Surf. Sci., 326 (2015) 151-161.
[550] F. Esaka, K. Furuya, H. Shimada, M. Imamura, N. Matsubayashi, H. Sato, A. Nishijima, A. Kawana, H. Ichimura, T. Kikuchi, Comparison of surface oxidation of titanium nitride and chromium nitride films studied by X-ray absorption and photoelectron spectroscopy, J. Vac. Sci. Technol., 15 (1997) 2521-2528.
[551] M.C. Biesinger, B.P. Payne, A.P. Grosvenor, L.W. Lau, A.R. Gerson, R.S.C. Smart, Resolving surface chemical states in XPS analysis of first row transition metals, oxides and hydroxides: Cr, Mn, Fe, Co and Ni, Appl. Surf. Sci., 257 (2011) 2717-2730.
[552] M. Aronniemi, J. Sainio, J. Lahtinen, Chemical state quantification of iron and chromium oxides using XPS: the effect of the background subtraction method, Surf. Sci., 578 (2005) 108-123.
[553] Z.Z. Wei, P. Grange, B. Delmon, XPS and XRD studies of fresh and sulfided Mo2N, Appl. Surf. Sci., 135 (1998) 107-114.
[554] A. Lippitz, T. Hübert, XPS investigations of chromium nitride thin films, Surf. Coat. Technol., 200 (2005) 250-253.
[555] F. Jahan, B. Smith, Investigation of solar selective and microstructural properties of molybdenum black immersion coatings on cobalt substrates, J. Mater. Sci., 27 (1992) 625-636.
[556] K. Kim, W. Baitinger, J. Amy, N. Winograd, ESCA studies of metal-oxygen surfaces using argon and oxygen ion-bombardment, J. Electron Spectrosc. Relat. Phenom., 5 (1974) 351-367.
[557] T.L. Barr, C.G. Fries, F. Cariati, J.C. Bart, N. Giordano, A spectroscopic investigation of cerium molybdenum oxides, J. Chem. Soc. Dalton Trans., (1983) 1825-1829.
[558] W. Li, X. Yan, A.G. Aberle, S. Venkataraj, Effect of deposition pressure on the properties of magnetron-sputter-deposited molybdenum back contacts for CIGS solar cells, Jpn. J. Appl. Phys., 54 (2015) 08KC14.

[559] N. McIntyre, D. Johnston, L. Coatsworth, R. Davidson, J. Brown, X-ray photoelectron spectroscopic studies of thin film oxides of cobalt and molybdenum, Surf. Interface Anal., 15 (1990) 265-272.
[560] Y.L. Di, Z.H. Cai, P. Zhang, W. Shen, Research on CrN-based Ternary Films Deposited by magnetron sputtering, in: Advanced Materials Research, Trans. Tech. Publ., 2012, pp. 1650-1653.
[561] Z. Li, P. Munroe, Z.-t. Jiang, X. Zhao, J. Xu, Z.-f. Zhou, J.-q. Jiang, F. Fang, Z.-h. Xie, Designing superhard, self-toughening CrAlN coatings through grain boundary engineering, Acta Mater., 60 (2012) 5735-5744.
[562] S.K. Kumar, S. Murugesan, S. Suresh, Preparation and characterization of CuO nanostructures on copper substrate as selective solar absorbers, Mater. Chem. Phys., 143 (2014) 1209-1214.
[563] N. Mott, E. Davis, Electronic processes in non-crystalline solids, Clarendon, Oxford, 465 (1979).
[564] Z.-T. Jiang, K. Ohshimo, M. Aoyama, T. Yamaguchi, A study of Cr–Al oxides for single-layer halftone phase-shifting masks for deep-ultraviolet region photolithography, Jpn. J. Appl. Phys., 37 (1998) 4008-4013.
[565] J.H. Kang, K.J. Kim, Structural, optical, and electronic properties of cubic TiN x compounds, J. Appl. Phys., 86 (1999) 346-350.
[566] Z.N. Jaf, Z.-T. Jiang, H.A. Miran, M. Altarawneh, Thermo-elastic and optical properties of molybdenum nitride, Can J Phys, 94 (2016) 902-912.
[567] B. Barış, H.G. Özdemir, N. Tuğluoğlu, S. Karadeniz, Ö.F. Yüksel, Z. Kişnişci, Optical dispersion and dielectric properties of rubrene organic semiconductor thin film, J. Mater. Sci. Mater. Electron, 25 (2014) 3586-3593.
[568] J.F. Ziegler, The stopping and range of ions in solids, in: Ion Implantation Science and Technology (Second Edition), Elsevier, 1988, pp. 3-61.
[569] M. El-Nahass, A. Atta, H. El-Sayed, E. El-Zaidia, Structural and optical properties of thermal evaporated magnesium phthalocyanine (MgPc) thin films, Appl. Surf. Sci., 254 (2008) 2458-2465.
[570] H.A. Miran, M.M. Rahman, Z.-T. Jiang, M. Altarawneh, L.S. Chuah, H.-L. Lee, E. Mohammedpur, A. Amri, N. Mondinos, B.Z. Dlugogorski, Structural and optical characteristics of pre-and post-annealed sol-gel derived CoCu-oxide coatings, J. Alloy. Compd., 701 (2017) 222-235.

[571] W. Piskorz, F. Zasada, P. Stelmachowski, A. Kotarba, Z. Sojka, Decomposition of N2O over the surface of cobalt spinel: A DFT account of reactivity experiments, Catal. Today, 137 (2008) 418-422.